THE OPTICAL AND ELECTRICAL PROPERTIES

OF TITANIUM DIOXIDE

by

R.W.A. HILLHOUSE, BSc (Dunelm)

Thesis submitted to the University of Durham for the degree of Doctor of Philosophy

April 1981

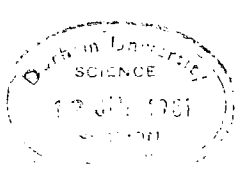

ACKNOWLEDGEMENTS

I would like to thank Professor G.G. Roberts for allowing me to use the facilities of the Applied Physics and Electronics Department and the Science Research Council for providing a C.A.S.E. award.

I am especially grateful to my supervisor, Dr. J. Woods, for his assistance and constant encouragement throughout my stay in Durham and the writing of this thesis. I also wish to extend thanks to Mr. T. Hargreaves for the polishing of the rutile crystals; to Mr. F. Spence and the staff of the workshop, and to Dr. G.J. Russell and Mr. N. Thompson for their general assistance during the course of this work. Special thanks to colleagues, friends and members of the technical staff at Durham, in particular, Dr. K. Pande, Dr. M. Petty and Dr. M. McGinnity.

I would also like to acknowledge the invaluable assistance of Dr. M. Hird and Mr. A. Riley of Tioxide International who provided expertise and assistance during the growth of the single crystal rutile. I am indebted to Dr. P. Kivits for kindly supplying a copy of his computer program for solving the TSC/TL differential equations.

Finally, my thanks to my wife, Christine, for being understanding and patient throughout the time I have been writing this thesis and for typing the manuscript.

ABSTRACT

This thesis describes the investigation of shallow and deep trap states in single crystal rutile and commercial pigments. The processes involved when rutile acts as a photocatalyst are examined and their relevance to the pigment industry is discussed.

Single crystals have been grown by the plasma flame fusion method. Oxidised (colourless) and reduced (blue) crystals were grown by altering the position of the growth pedestal relative to the plasma. Crystals doped with aluminum, niobium, manganese and iron introduced via the powder feed material were successfully grown as single crystals.

The techniques of photoconductivity, photoluminescence, photon stimulated current, thermally stimulated conductivity (TSC) and thermoluminescence (TL) have been used to probe deep and shallow levels in the single crystal rutile. The kinetic responses of PL and PC have been explained consistently in terms of a charge transfer model by considering the hole traffic through the luminescence centre as well as the electron concentration in the conduction band, and realising that the Cr^{3+} luminescence centre is only one of the many recombination centres present in these crystals.

A study of TSC and TL in the nominally 'undoped' single crystals reveals the presence of six discrete electron trapping levels. The TSC and TL curves are analysed and consistent values of the trapping parameters are obtained. Limitations of the simple insulator model and its application to single crystal rutile are discussed. Crystals from different sources all contain the same three trapping levels with ionisation energies of 0.13, 0.24 and 0.37 eV. The density of these traps increase as the crystals are chemically reduced.

An investigation of manganese, chromium, iron, cobalt and nickel

diffusion doped single crystal rutile reveals the presence of the 0.19 eV trap in chromium doped crystals and the 0.41 eV trap in nickel, chromium, iron and cobalt doped crystals.

CONTENTS

Page

Page

PREFACE

Titanium dioxide is the most stable known white compound having pigmentary qualities. It is chemically inert and resists attack by organic or inorganic acids or alkalis at ordinary or moderately raised temperatures. Titanium pigments are opaque and brilliantly white, and they find widespread industrial applications, particularly in paint, but also in plastics, paper, printing inks, floorings, manmade fibres, rubber, vitreous finishes, leather and cosmetics.

The object of the rutile research programme is to elucidate the electronic processes involved when rutile acts as an oxidising photocatalyst following the absorption of light. An understanding of this mechanism would be of major importance to the titanium pigment industry since the deleterious effects of the photocatalytic action affect the performance of a pigment, for example in reducing the durability of paint and contributing to loss of colour. It seems that in the current economic climate, industry will have to pay increasing attention to the efficient use of raw materials and conservation of resources. In the context of the pigment industry the terms conservation and durability are almost synonymous.

The present research has been undertaken with the aid of a CASE studentship in conjunction with Tioxide International Ltd., who maintain their Central Research Laboratories at Stockton-on-Tees, less than 20 miles from Durham. Tioxide pigments are made in two ways, by the familiar 'sulphate' process and by the newer 'chloride' process (Tioxide Pigments 1977). In the sulphate process ilmenite, a black mineral that looks like crushed anthracite, is transformed into one of the whitest subtances in the world. After refining, the ore is dissolved in sulphuric acid and the titanium sulphate in solution is hydrolysed by boiling to form a hydrated oxide. This is then calcined at a temperature in the vicinity of 1000 °C

and thereby converted into titanium dioxide. The waste dilute sulphuric acid and iron sulphates make the 'sulphate' process an enviromentally pollution sensitive problem.

The 'chloride' process for making titanium dioxide is very different, and its raw material is mineral rutile, which varies in colour from sandy to almost black and will not dissolve in sulphuric acid. The refined ore is made to react with chlorine to form the liquid titanium tetrachloride, and this, after having been purified by distillation, is 'burnt' in oxygen under very carefully controlled conditions to produce titanium dioxide. The chlorine formed after decomposition of the titanium tetrachloride is recycled.

The durability of a paint film will be influenced by the conditions under which a paint is applied to its substrate. Of the paint film itself, a discussion of durability may be split into two parts, the degradation of the binder and the effects of pigmentation. The photosensitised degradation of commercial polymers by titanium dioxide is believed to be related to the formation of an oxygen radical anion $O_2^{\cdot -}$ and possibly other species by electron transfer from excited state TiO_2 to molecular oxygen (Ranby and Rabek 1975, King 1968)

$$TiO_2 + O_2 \xrightarrow{\text{uv light}} TiO_2^{+} + O_2^{-}$$

The products of the reaction may then react with water to form reactive hydroxyl and perhydroxyl radicals. The hydroxyl radicals may then react with the polymer substrate and abstract a hydrogen atom and thus initiate degradation of the polymer by the well-known auto-oxidation chain mechanism for hydrocarbon polymers (Ranby and Rabek 1975, King 1968)

$$R\text{-}H + HO^{\cdot} \longrightarrow R^{\cdot} + H_2O$$

$$R^{\cdot} + O_2 \longrightarrow RO_2^{\cdot} \text{ etc}$$

The perhydroxyl radicals recombine to form hydrogen peroxide and oxygen,

$$2\ HO_2^{\circ} \longrightarrow H_2O_2 + O_2 \ .$$

The use of film forming media such as fluorinated hydrocarbons, silicone modified alkyds and polyesters, vinyl co-polymers and the better-known acrylic systems, has produced a remarkable increase in durability (Hughes 1974). Whereas a durable alkyd gloss paint film could survive for 3 to 5 years, some of the recently formulated durable paint systems are expected to yield films with a life-time of between 10 and 25 years. This improved level of performance is due primarily to successful development of the new polymers. Special surface treatment is always necessary to render pigments, either from the chloride or sulphate process, sufficiently durable for use in coating systems (Neville 1969, Tioxide 1977). Nevertheless, because of the high stability of the newer media, the weak residual photocatalytic effect of coated rutile pigments has now become a significant factor in determining durability of paint films.

The influence of titanium dioxide is both protective and destructive. The pigment protects the film in that it absorbs ultra-violet radiation to such an extent that there is little radiation left to damage the medium directly. However, the pigment is photo-active, and as a result, can initiate reactions leading to polymer breakdown. The protective aspect is demonstrated quite clearly by the difference between rutile and anatase pigments. Of the two, anatase chalks much more readily. Whilst this is partially due to the difference in photo-activity it is predominantly a result of the difference in ultra violet absorption characteristics (Hird (1976). The wavelength range, which is potentially damaging to paint films, ends at about 390-400 nm and at 375 nm the rutile absorbs more than twice as

much radiation as the anatase.

Kaempf, Papenroth and Holm (1974) have developed what they describe as a 'model conception of the micromorphological degradation processes' involved in weathering. When a titanium pigmented paint film is exposed, ultra violet degradation starts uniformly over the whole of the surface. The photo-activated process, however, occurs only where incident radiation strikes a titanium dioxide surface. Thus, this form of degradation only occurs in the immediate vicinity of the pigment particle, especially on the surface which is facing the radiation directly where the concentration of hydroxyl radicals will be highest. The medium on the other side of the particle will be effectively screened from direct attack. Also, the amount of internal scattering from other particles which could cause damage underneath the particle is low because of the high absorption of ultra violet radiation by titanium dioxide. Eventually the medium above and around the sides of the pigment particle is degraded, leaving the particle standing on a stalk or pedestal of binder.

The effect on degradation of other pigments is not well documented and in the case of inorganic pigments, the same factors as involved with titanium dioxide are likely to operate. For example, zinc oxide is known to be photo-active (Gray and Amigues 1969, Gray and Lowery 1971) and is liable to degrade the surrounding medium in the same way as titanium dioxide but to a greater extent. Also, its absorption in the ultra violet is less than half that of rutile pigments and hence the protective nature of the pigment is less. This corresponds with the well known inability of zinc oxide to impart good durability in paints. On the other hand, iron oxides are unlikely to lead to photo-degradation because of their structure. They are well known for conferring good durability. Organic pigments can be considered in the same way as the binder, absorption of ultra violet radiation can lead to degradation of the pigment, which, although not

directly leading to film destruction, may lead to fading. Organic pigment molecules are conjugated systems and any destruction of the conjugation or of the chromophoric groups will lead to fading. This theory would appear to be supported by the general observation that violet and blue organic pigments are less prone to fading than yellows and reds which tend to absorb more u v radiation.

In titanium dioxide pigments, radiation is absorbed by the pigment particle and the energy is used to form hydroxyl radicals which initiate the degradation of the binder. The reaction can be retarded if a strong electron acceptor is included in the pigment. Transition metals such as iron and chromium may be suitable for this purpose (Torlaskchi et al 1974). However, the presence of these metal ions in the pigment gives rise to discolouration which is not too desirable in a brilliant white paint film. Aluminum is not quite as efficient as these metals but, on the other hand, does not discolour the pigment and is also applied as alumina on the surface of the pigment. In practice, better results are obtained if silica molecules are bonded to those of the aluminum and this explains the common use of alumina/silica coatings on titanium pigments.

The work outlined in this thesis includes work on the growth of single crystal rutile, characterisation of these crystals and characterisation of pigment powders. Special attention has been given to the properties of transition metal doped rutile crystals and aluminum and niobium dopants which are present in some sources of rutile ores. The long term research objectives of this programme are to develop a more photostable pigment and to devise accelerated durability trials.

CHAPTER 1

PROPERTIES OF TITANIUM DIOXIDE

1.1 INTRODUCTION

Numerous studies of the titanium-oxygen diagram have been reported. The most recently reported phase diagram (Wahlbeck and Gilles 1966) is shown in figure 1.1.1.

More than 30 at % oxygen may be dissolved in octahedral interstices of titanium. Order-disorder transformations take place in the whole composition range of the Ti-O solid solutions depending on the temperature. The oxygen atoms distribute themselves on ordering in every second layer of the octaheadral interstitial planes normal to the c-axis. At a composition Ti_2O alternate planes are either empty or completely filled with interstitial oxygen, and at Ti_3O one third of the interstitial octahedral sites in the occupied planes are empty.

The higher oxides of titanium comprise TiO, Ti_2O_3, Ti_3O_5, a homologous series of oxides with the composition Ti_nO_{2n-1} and TiO_2. The structure and composition of the oxides of homologous series have in recent years received considerable attention (Anderson et al 1970). Anderson et al (1957) originally reported oxides with values of n from 4 to 10, but Bursill et al (1969) have more recently reported phases with values of n up to about 38 ($TiO_{1.974}$). Anderson and Khan (1970) found that the solid state transformations between the phases were slow, and at and below 1000°C the reactions were too sluggish to attain true equilibria.

The structure of the higher oxides of titanium may be considered to consist of TiO_6-octahedra which share corners, edges and faces in different ways, depending upon the composition of the oxide. The octahedron model for rutile is shown in figure 1.2.1. In the homologous oxides the oxygen framework of the rutile structure is essentially unchanged, and the homologous phases are determined by the arrangement of the titanium ions.

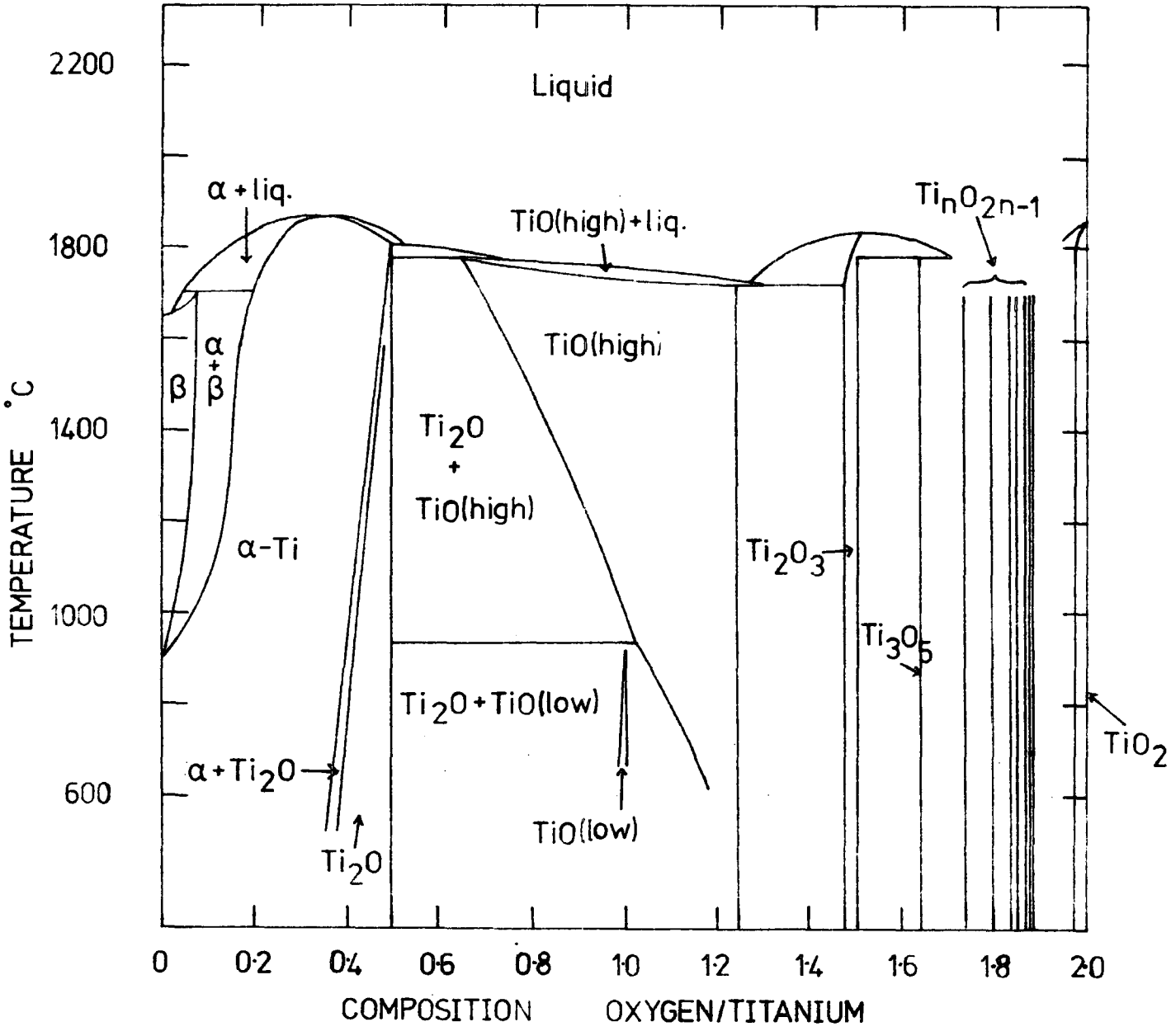

Figure 1.1.1 The titanium oxygen phase diagram. After Wahlbeck and Gilles 1966.

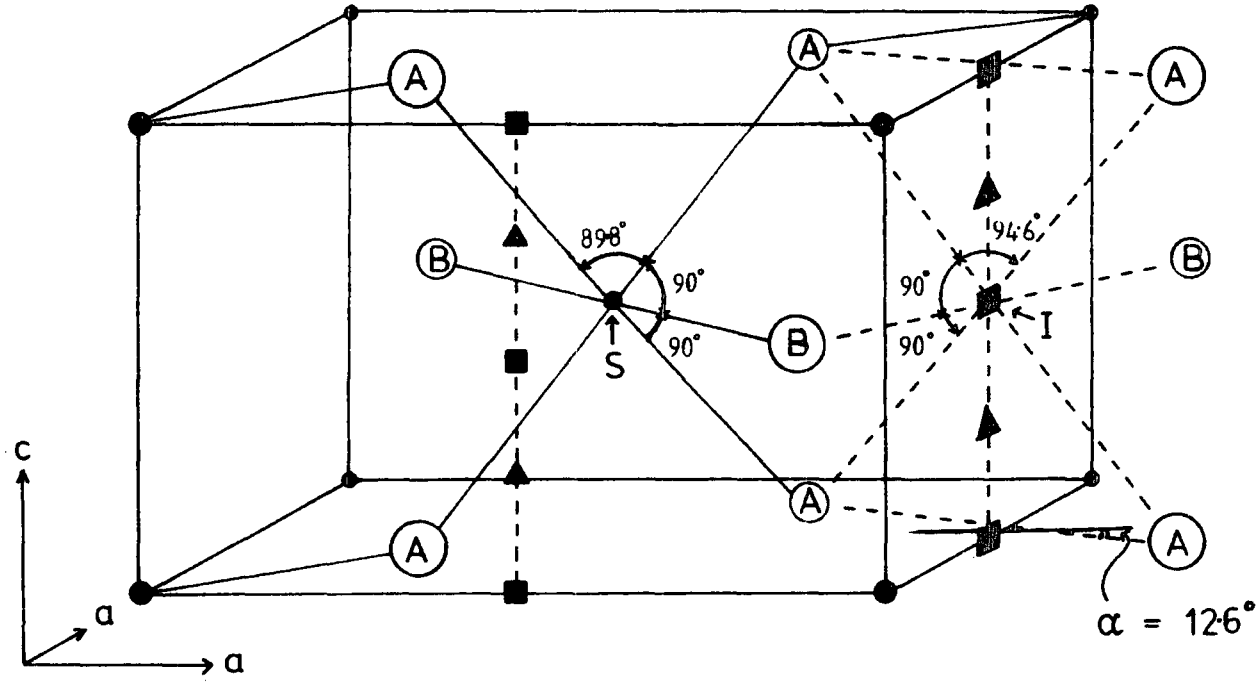

Figure 1.2.1 Crystal structure of rutile showing a unit cell and some $\frac{1}{2}0\frac{1}{2}$ (■) and $\frac{1}{2}0\frac{1}{4}$ (▲) type interstitial sites. The positions of the oxygen ions around the octahedrally coordinated substitutional ion S and around the interstitial site I are indicated

The homologous oxides may be viewed as being formed from the rutile structure by the addition of interstitial titanium ions in octahedral interstices, and the interstitial titanium ions are ordered in definite directions. In this manner the homologous series may be considered to consist of blocks or domains of the rutile structure which extend infinitely in two dimensions, but which have a finite width in the third dimension.

1.2 CRYSTAL CHEMISTRY

Titanium dioxide exists in three polymorphic forms: rutile, anatase and brookite.

The mineral rutile is one of the most important of the naturally occuring titanium ores. It is the high temperature form of titanium dioxide. Stoichiometric rutile powder is white and an important pigment for the paint, paper, plastic and textile industries. In the pure state it has a tetragonal structure similar to that of cassiterite, SnO_2.

The rutile form of TiO_2 is a tetragonal crystal belonging to the class D_{4h}^{14} (4/mmm). Usually the tetragonal axis [001] is called the c-axis. The unit-cell dimensions in the c and a directions are 2.959 Å and 4.594 Å, respectively at 250°C. Figure 1.2.1 shows the unit cell using the data of Baur (1956). The unit cell contains two nonequivalent Ti^{4+} ions; each of them surrounded by a slightly deformed oxygen octahedron. The local symmetry at a Ti^{4+} site is only orthorhombic D_{2h} (mmm), nevertheless the overall symmetry is tetragonal because the surroundings of the two nonequivalent Ti^{4+} ions differ from one another only by a rotation of 90° around the c-axis. Thus the EPR spectrum of a paramagnetic impurity substituting a Ti^{4+} ion shows a periodicity of 90° when the crystal is rotated around the c-axis.

One of the properties of the rutile lattice being responsible for the large anisotropies (for instance the diffusion of lithium (Johnson 1964)) is the existence of open channels along the c direction.

These channels may be considered as stacks of oxygen octahedra where the central Ti^{4+} ion is missing. Those central sites, indicated by ■ in figure 1.2.1, are thought to be possible locations of interstitial impurity ions. There are four sites ; $0\frac{1}{2}0$, $\frac{1}{2}00$, $0\frac{1}{2}\frac{1}{2}$ and $\frac{1}{2}0\frac{1}{2}$, which differ from one another only by rotations of $\pm\alpha_{\blacksquare}$ and $90^{\circ}\pm\alpha_{\blacksquare}$ around the c-axis, where $\alpha_{\blacksquare}=12.6$ in the undistorted lattice. Low and Offenbacher (1965) considered the space available to accommodate an ion at an interstitial site from the viewpoint of ionic radii. Following their arguments, but using the recent set of ionic radii given by Shannon and Prewitt (1969), it is concluded that ions with radii in the region 0.63-0.82 Å might prefer these interstitial sites (see table 1.2.2).

Huntington and Sullivan (1965) suggested the possibility of a second class of interstitial sites on $\frac{1}{2}\,0\,\frac{n}{4}$ type positions (indicated by ▲ in figure 1.2.1) with n odd. These sites are surrounded by four O^{2-} ions, two at a distance of 1.77 Å and two at 1.74 Å.

The mineral anatase is also of commercial importance. It is isomeric, but not isomorphous with rutile. Anatase is tetragonal with the elongated cell a = 3.785 Å and c = 9.514 Å. The unit cell contains four TiO_2 units.

The orthorhombic mineral brookite has a more complicated crystal structure. The unit cell has eight TiO_2 units and the lattice parameters are a = 9.184 Å, b = 5.477 Å and c = 5.145 Å. In all the three forms a titanium atom is octahedrally coordinated to its oxygen neighbours, but the oxygen octahedron is not regular.

1.3 DEFECT STRUCTURES IN STOICHIOMETRIC OXIDES

An exact stoichiometric composition in inorganic compounds is in principle the exception rather than the rule. Oxides in equilibrium with their surroundings are generally nonstoichiometric, except under specific conditions of temperature and partial pressure of the components.

Element	Valence state	Ionic radius (Å)
O	-2	1.36
Ti	+3	0.67
	+4	0.605
S	-2	1.74
Al	+3	0.530
Si	+4	0.400
Fe	+3	0.645
Cu	+2	0.72
Cr	+3	0.53
	+4	0.15
Ni	+2	0.68
Co	+2	0.82
Mn	+2	0.91

Table 1.2.2 Properties of some non-intentional ions which are present in single crystal rutile.

However, many inorganic compounds may be considered to be so near stoichiometry over large temperature and pressure ranges that minor deviations from stoichiometry may often be neglected in a discussion of defect concentration and defect controlled properties.

If a charged defect is formed in a stoichiometric crystal with composition MO, a complementary point defect with opposite effective charge must be formed to conserve the electrical neutrality of the crystal. Kroger and Vink (1964) list six basic types of defect structures (internal atomic disorder) which are possible in a stoichiometric compound. These are: (1) cation and anion vacancies; (2) vacancies and interstitial ions of the same component; (3) misplaced atoms; (4) vacancies and misplaced atoms for the same type of atom; (5) interstitial and misplaced atoms; (6) interstitial atoms. Types 1 and 2 which are termed Schottky and Frenkel disorder, respectively, are the only ones which as yet have been found important in oxides (see figure 1.3. 1 a and b).

1.4 DEFECT STRUCTURES IN NONSTOICHIOMETRIC OXIDES

Nonstoichiometry in oxides may consist of two main types: (1) oxygen deficiency (or excess metal) with respect to the stoichiometric composition, or (2) metal deficiency (or excess oxygen) with respect to the stoichiometric composition. Nonstoichiometry in a compound is equivalent to the presence of point defects, and the extent of nonstoichiometry is a direct measure of the net concentration of the corresponding defect or defects in a compound. While complementary point defects are formed in stoichiometric crystals, the electrical neutrality of nonstoichiometric compounds is conserved through the formation of point defects and complementary electronic defects.

Various types of defect structures may be formed depending on the type of nonstoichiometry in an oxide. The two limiting cases are the oxygen deficient oxides and the metal deficient oxides.

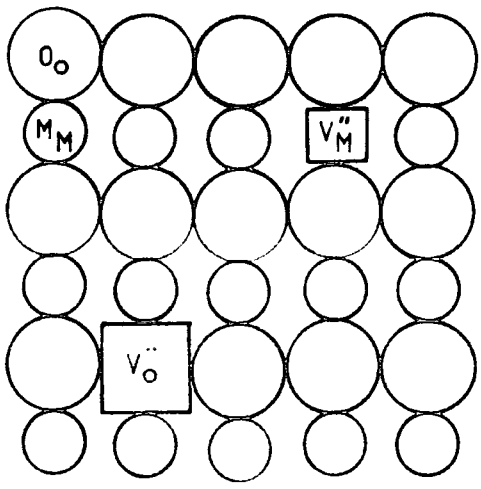

Figure 1.3.1 a

Schematic illustration of Schottky disorder with equivalent concentrations of doubly charged vacancies, V''_M and V''_O, in an oxide MO.

Figure 1.3.1 b

Schematic illustration of Frenkel disorder involving doubly charged cation vacancies and interstitial ions in an oxide MO.

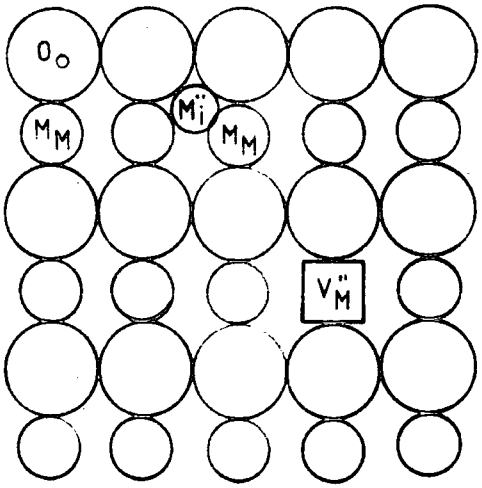

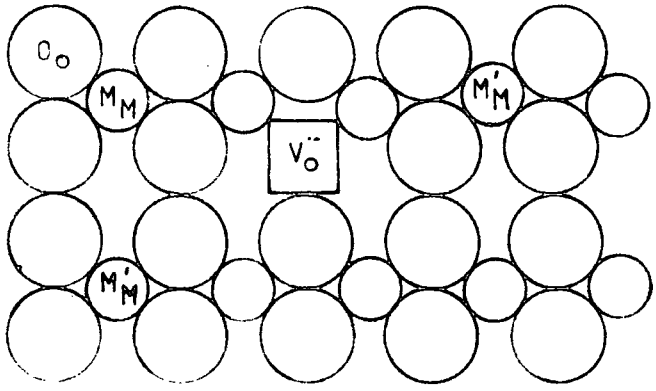

Figure 1.4.1 a

Schematic illustration of an oxygen-deficient oxide, MO_{2-x}, in which doubly charged vacancies predominate. The electrons are assumed to be localised at M-atoms on regular lattice sites.

Figure 1.4.1 b

Schematic illustration of an oxygen-deficient oxide (metal excess), $M_{1+y}O_2$, in which doubly charged interstitial cations predominate. The electrons are assumed to be localised at M_M.

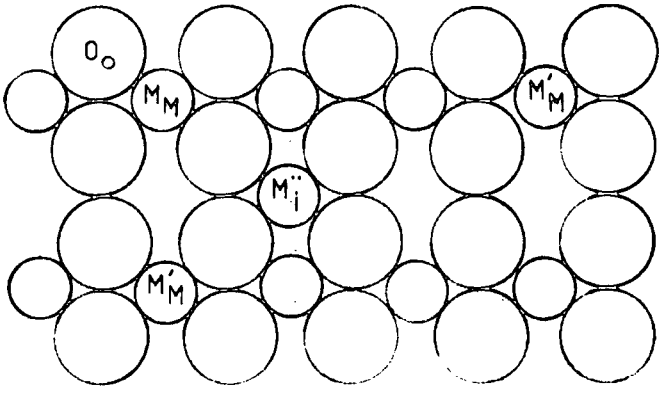

When a nonstoichiometric oxide is oxygen deficient (see figure 1.4.1 a and b), the predominating defects may be either oxygen vacancies (oxygen deficient) or interstitial metal ions (excess metal), or both types of defects. The formation of both oxygen vacancies and interstitial cations leads to the formation of complementary positive electronic defects (holes). In such oxides the electronic conductivity involves the transport of holes, and such electronic conductors are p-type. Well known examples of oxides with cation vacancy type defects are MnO, FeO, CoO, NiO and Cu_2O.

1.5 NONSTOICHIOMETRY IN RUTILE

When titanium dioxide is reduced, larger concentrations of anion vacancies and/or titanium interstitials condense into thin platelets that are removed from the structure by the formation of stacking faults, or 'shear planes'. Magneli first predicted the existence of such planes, and their existence was later confirmed by their identification in the Ti_nO_{2n-1} series. These planes, as well as the surface of the material, may act as sources or sinks of interstitial titanium. Across a Magneli shear plane, Ti:Ti pairs share common octahedral site faces and therefore represent potential electron traps. At higher temperatures, where thermal excitation empties the traps, electrostatic repulsion creates a relatively large Ti^{4+}:Ti^{4+} seperation. This is enhanced by the fact that octahedral site Ti^{4+} may act as a ferroelectric ion, becoming spontaneously displaced from the centre of symmetry of its interstice to form more stable Ti-O bonds (Goodenough 1970). The seperation is also enhanced by the formation of shear planes that allow cooperative elastic distortions across them. This elastic energy is probably the principal force stabilizing the formation of shear planes. At low temperatures, on the other hand, electron trapping permits the creation of Ti^{3+}:Ti^{3+} bonds across the shear planes.

The extent of nonstoichiometry in rutile has been extensively studied. Blumenthal and Whitmore (1963) concluded from isopiestic and emf

measurements that the homogeneity range of TiO_{2-x} at 900-1000°C extends to a value of $x \sim 0.01$. However, later studies have indicated a smaller homogeneity range. Anderson and Khan (1970) put the value of x to 0.008 at 1000°C, and at larger values of x, oxygen deficient rutile coexists with the uppermost Magneli phase. The reason for such discrepancies may be that the transitions between phases are slow and true equilibrium may be difficult to attain at and below 1000°C.

The deviation from stoichiometry as a function of temperature and partial pressure of oxygen in the homogeneity range has been studied thermogravimetrically by equilibrating in CO + CO_2 (Kofstad 1962, Forland 1964) and H_2 + H_2O + He (Moser et al 1965) mixtures. When the oxygen partial pressure dependence of x is expressed as $p^{-1/n}$, it is found when considering all the available results that n is a function of both temperature and partial pressure of oxygen (Kofstad 1967). The plots of log x against 1/T do not yield a straight line relationship. This suggests that the defect structure cannot be interpreted in terms of a simple model in which either oxygen vacancies or interstitial titanium ions predominate. Kofstad (1967) has proposed that the defect structure simultaneously comprises doubly charged oxygen vacancies and interstitial titanium ions with three and four effective charges. The proportions of these defects that exist in a rutile crystal depend on the temperature and the oxygen partial pressure.

Kofstad has proposed the following defect equilibria,

$$[V_O^{\cdot\cdot}]\, n^2 = K_{V_O^{\cdot\cdot}}\, p_{O_2}^{-\frac{1}{2}} \quad \text{(oxygen vacancy equil.)}$$

$$[Ti_i^{\cdot\cdot\cdot\cdot}]\, n^3 = K_{Ti^{\cdot\cdot\cdot\cdot}}\, p_{O_2}^{-1} \quad \text{(equil. for formation of triply charged Ti interstitials)}$$

$$[Ti_i^{\cdot\cdot\cdot}]\, n = K_a [Ti_i^{\cdot\cdot\cdot\cdot}] \quad \text{(equil. ionisation of } Ti^{\cdot\cdot\cdot} \text{)}$$

where n designates the concentration of electrons ; $K_{V_O^{\cdot\cdot}}$, $K_{Ti^{\cdot\cdot\cdot\cdot}}$, K_a are the respective equilibrium constants ; and p_{O_2} is the oxygen partial pressure. When neglecting impurities and the intrinsic electronic equilibrium, the

electroneutrality condition is given by

$$3\,[Ti_i^{\cdots}] + 4\,[Ti_i^{\cdots\cdot}] + 2\,[V_O^{\cdot\cdot}] = n$$

Expressing the point defect concentrations in numbers per mole of oxide, x becomes

$$x = \frac{2\left([Ti_i^{\cdots}] + [Ti_i^{\cdots\cdot}] + [V_O^{\cdot\cdot}]\right)}{1 + [Ti_i^{\cdots}] + [Ti_i^{\cdots\cdot}]}$$

Kofstad has fitted this model to the experimental data for the enthalpy of formation of doubly charged oxygen vacancies and triply charged titanium interstitials as 105 and 210 Kcal/mole, respectively.

The model predicts that oxygen vacancies predominate at near-atmospheric oxygen pressures, while interstitial titanium ions are dominant of the lower limit of the homogeneity range. This is illustrated in figure 1.5.1, where the calculated values of the equilibrium concentration of different defect species at 1500°C are plotted as a function of the partial pressure of oxygen. If the model is correct, it is also clear that the predominating type of defect in a particular specimen will depend on the pretreatment, e.g. state of reduction.

Barbanel et al (1969) have investigated the nature of defects in rutile by determining the change in density of crystals during their partial reduction. Figure 1.5.2 shows the results of measurements of the changes in the density of three samples (continuous curves) and the relative loss of the weight of two samples (dashed curves). Up to 500-600°C the density decreased monotonically with increasing reduction temperature (curves 1 and 3). The loss in weight increased monotonically (curves 1' and 3'). This was interpreted as an increase in the number of oxygen vacancies (donors) which were the main defects in rutile reduced in this range of temperatures. Above 600°C the reduction in the density became smaller, passed through zero at 750°C, and then the density began to increase. Assuming that the increase in the density was associated with the appearance

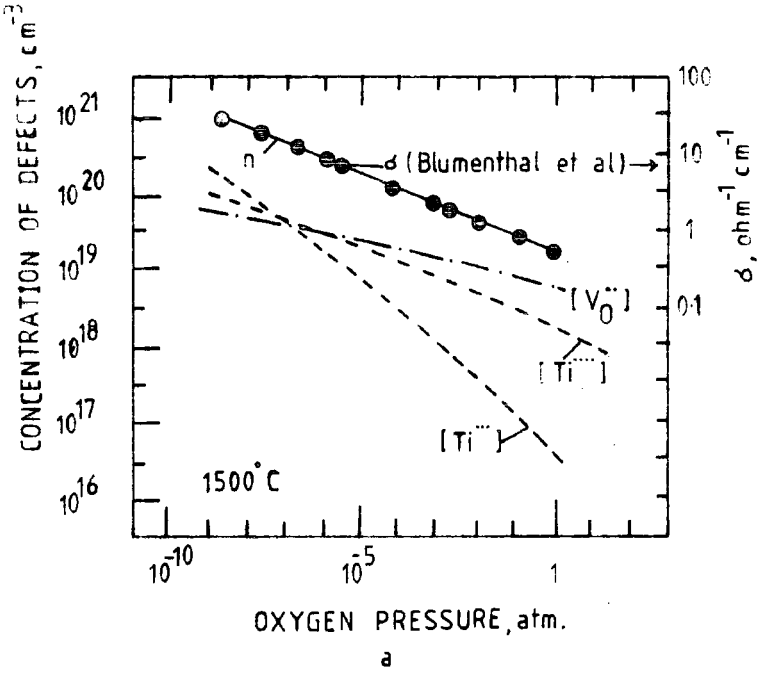

a

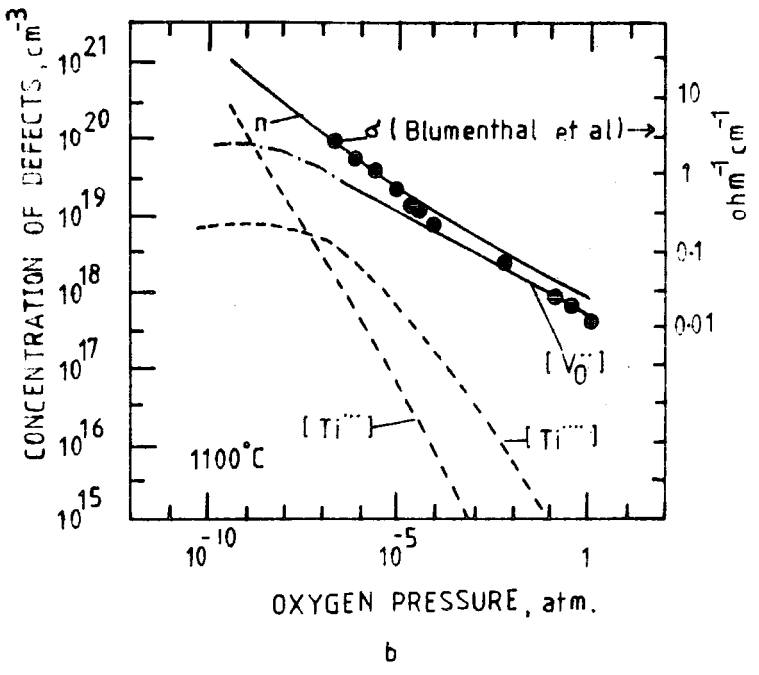

b

Figure 1.5.1 The concentrations of point defects and electrons in TiO_{2-x} as a function of the partial pressure of oxygen (After Kofstad 1972). Results of electrical conductivity after Blumenthal et al (1966) (a) 1500°C (b) 1100°C.

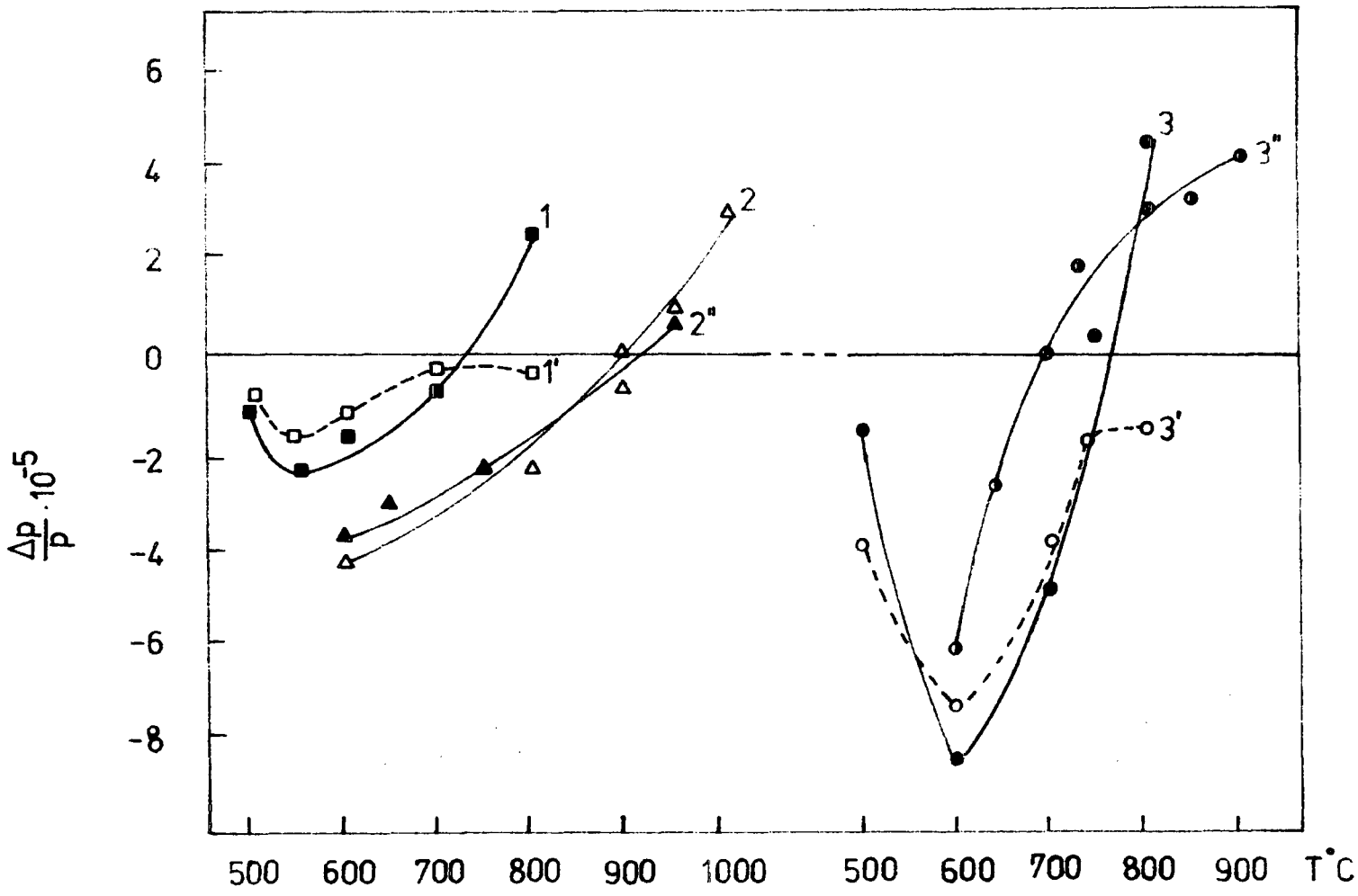

Figure 1.5.2 Dependences of the relative changes in the density (continuous curves) and weight (dashed curves) on the reduction temperature. Reduction duration (hrs) : 1, 1, 3, 3 ; (2) : 2, 2, 3, ; (0.5). Vacuum (mm Hg) 1, 1, 3, 3, 3 ($1\ 10^{-3}$) ; 2 ($1\ 10^{-4}$) ; 1 (10^{-2}).

of interstitial Ti^{3+} ions in rutile, this suggests that the interstitials began to appear at about 600°C. In the 600-800°C range both types of defect coexist.

The gradual loss of weight, due to the loss of oxygen, which occurred in spite of an increase in the reduction temperature, was explained by Barbanel et al using the following model. An important point to bear in mind when considering the motion of defects during heat treatment in vacuum, is that the rate of diffusion of defects in rutile is high as is its anisotropy (Bogomolov 1964). At T<600°C the channels in the rutile lattice are free and oxygen easily escapes along them from the interior of a sample to the surface (while oxygen vacancies move in the direction of the interior). The main defects are oxygen vacancies. At T>600°C the presence of oxygen vacancies makes the process of transfer of titanium ions from sites into interstices much easier than in stoichiometric rutile and a sample aquires two types of defect. These defects are bound to one another. Since the defects are bound, the motion of the oxygen from the interior to the surface slows down. The diffusion of Ti^{3+} ions along the channels in rutile has a higher activation energy than the diffusion of oxygen. As a result, the process of the formation of interstitial titanium ions, which takes place on an appreciable scale at temperatures T>600°C does not simply increase the number of new defects but also reduces the loss in weight by slowing down the escape of oxygen from the interior to the surface. An increase in the reduction temperature above 750°C, when only one type of defect again predominates, results in a renewed increase of the loss in weight but this is now due to the escape of oxygen from the surface of the sample. The density increases because the titanium moves from the surface into the interior.

In conclusion, Barbanel et al showed that the nature of defects produced by heat treatment in rutile in vacuum, depends on the temperature

at which the treatment is carried out. Similar conclusions were reached by Blumenthal et al (1963) from the dependence of the electrical conductivity on the oxygen pressure and temperature, as described previously.

1.6 SELF-DIFFUSION IN RUTILE

Self-diffusion of oxygen in rutile has been studied by Haul and coworkers (1960, 1962, 1965) using O^{18} tracer measurements. Figure 1.6.1 summarises their results. The self diffusion coefficient in these studies was essentially independent of the partial pressure of oxygen between 10^{-3} and 725 torr O_2, and the results suggest that oxygen vacancies are the important defects at near-atmospheric pressures. The independence of oxygen pressure indicates that the specimens were intrinsic, and Haul et al (1965) suggest that this was due to the presence of substitutionally dissolved Al-impurities. The diffusion coefficient could be written

$$D_O = 2 \times 10^{-3} \exp (-60000/RT).$$

Haul and Dumbgen (1965) further reported that oxygen diffusion proceeds more rapidiy perpendicular to the c-axis than it does parallel to it ($D_\perp/D_\parallel = 1.6$).

Venkatu and Poteat (1970) have reported self-diffusion studies of Ti^{44} in rutile in the temperature range 900-1300°C. The results shown in figure 1.6.1 can be expressed as

$$D = 6.4 \times 10^{-2} \exp (-61400/RT).$$

A comparison of the oxygen and titanium self-diffusion coefficients shows that they are both of the same order of magnitude , but that the Ti-diffusion parallel to the c-axis is faster than the O-diffusion. However, both Haul et al (1965) and Venkatu and Poteat (1970) suggest that the values represent diffusion under extrinsic conditions.

1.7 BAND STRUCTURE OF RUTILE

The early work of Cronemeyer (1952) on the electrical conductivity, optical absorption and photoconductivity of rutile shows that the forbidden

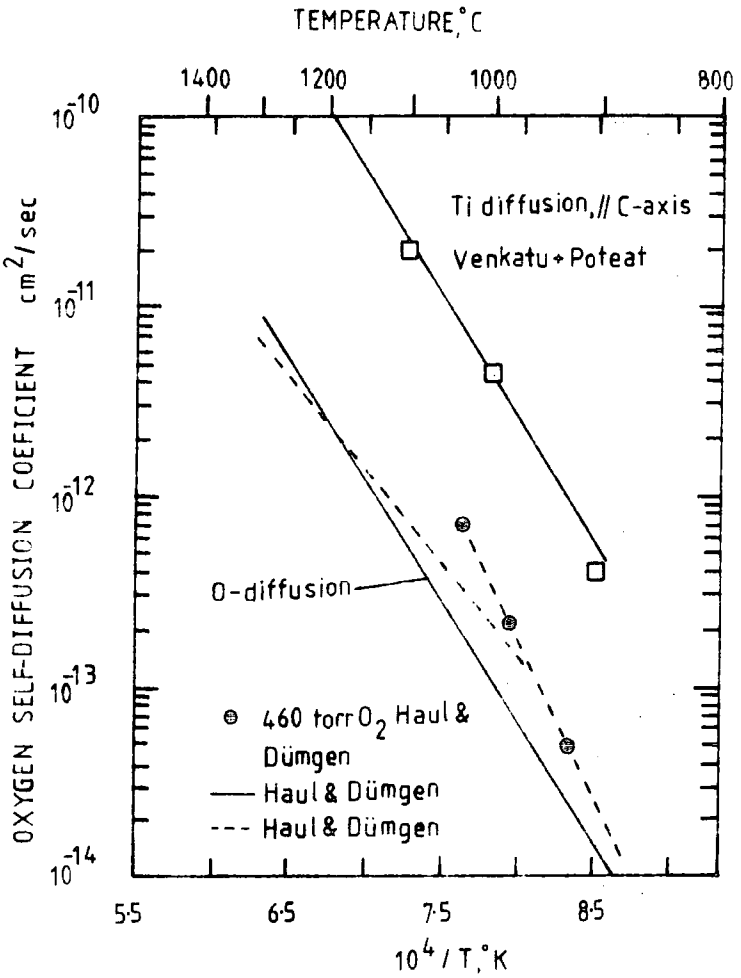

Figure 1.6.1 **Self diffusion coefficients in rutile near atmospheric pressure as a function of the reciprocal temperature. After Haul and Dumgen (1962,1965) and Venkatu and Poteat (1970).**

gap is about 3.0eV wide. Measurements of the long wavelength tail of the fundamental absorption edge with polarised radiation by Moch (1960), Soffer (1961) and Stepanor (1975) suggest that the true edge for E⊥c occurs at slightly lower energy than it does for E//c ($\sim$10 meV at room temperature and $\sim$33 meV at T=4K). The true edge difference, deduced by Arntz and Yacobi (1966) from electroabsorption spectra to be $\sim$15 meV at 77K, does not agree with the electroreflectance data of Vos (1974) who suggests a gap difference of $\sim$33 meV. Under hydrostatic pressure the absorption edge shows a blue shift as has been found by Suchan (1959).

Vos and Krusemeyer (1974, 1977) have reported optical data in the region above the energy gap from electroreflectance measurements. These low temperature electroreflectance spectra are the only optical data of rutile showing characteristic fine structure over a wide energy range.

Energy level diagrams for rutile have been proposed by Breckenridge and Hosler (1953) and Perny and Lorang (1966) who assign the onset of the absorption not to the fundamental interband absorption band edge, but to optical transitions related to excited states of lattice defects. However, most experimental data on electrical transport properties, Frederikse (1961), von Hippel (1962), Becker and Hosler (1965), Acket and Volger (1966); optical absorption, Bogomolov (1968), Pak (1975), Agekyan and Stepanov (1975); and x-ray spectroscopy, Fischer (1972), indicate that the conduction states have a predominately 3d-character and are seperated by about 3.0 eV from the oxygen 2p valence band edge. Prehaps the most convincing evidence for a band gap of 3.0 eV stems from oscillations in electroabsorption (Arntz Yacobi 1966) and electroreflectance (Vos and Krusmeyer 1974) spectra which are characteristic of band to band transitions.

An analysis of the band structure of TiO_2 has been given by Adler (1968) and a schematic diagram is shown in figure 1.7.1. These calculations were helped by the existence of a tight-binding calculation (Kahn and Leyendecker 1964) for $SrTiO_3$, which can be looked upon as a combination of SrO and TiO_2.

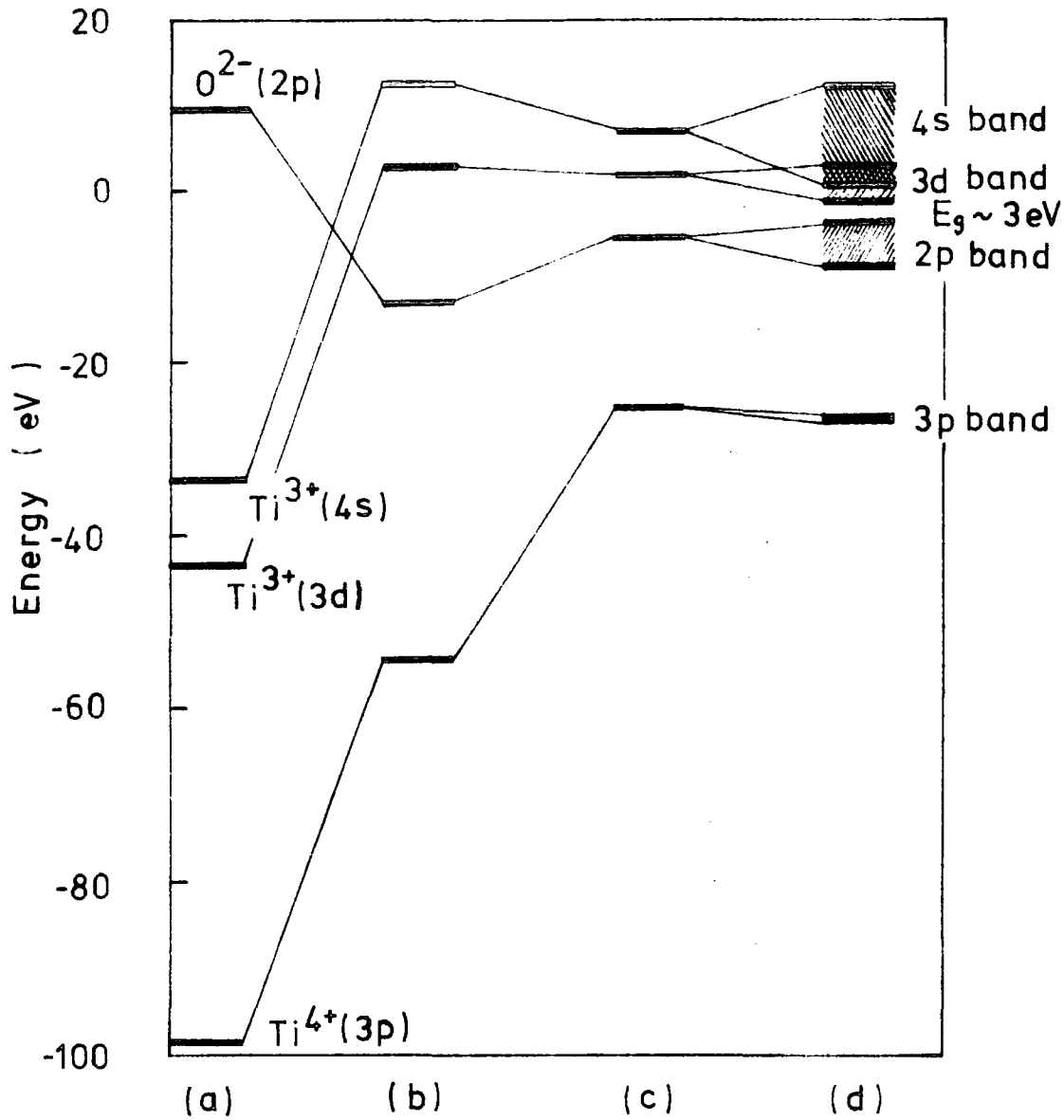

Figure 1.7.1 Sketch of the energy band structure of pure, stoichiometric TiO_2, based on a tight binding approximation; (a) free ion energies, (b) effects of Madelung potential, (c) screening and covalency effects, (d) bandwidth effects. After Adler 1970.

Adler used a screening factor of 0.5 to describe a 15% covalency in rutile. The widths of the oxygen 2p band and the titanium 3d band were taken from Kahn and Leyendecker (1964). The Ti 4s bandwidth, not evaluated by Kahn and Leyendecker was taken to be 12 eV. The result shows that TiO_2 is a semiconductor, with a 3 eV band gap seperating the filled oxygen 2p band from the empty Ti 3d band.

Recently Vos (1977) has presented a semi-quantitative picture of the band structure of rutile. He performed a linear-combination-of-orthogonalised-atomic-orbitals (LCOAO) calculation in the Slater-Koster two centre approximation (1954), using Ti-3d, O-2p and O-2s orbitals and retained only the nearest-neighbour interactions. This method has been used successfully to approximate the band structure of related compounds ($SrTiO_3$, ReO_3) computed by more elaborate methods. The energy bands of rutile TiO_2 along some high-symmetry directions in the Brillouin zone is shown in figure 1.7.2. The top of the valence band is near k = 0 with symmetry Γ_3^+ and the bottom of the conduction band is near k = ($\pi/a,\pi/a,0$) with symmetry $M_{1,2}$. The R_1^+ minimum is 0.12 eV higher in energy than the $M_{1,2}$ minimum.

1.8 CHARGE CARRIER MOBILITY IN RUTILE

The mobility of partially reduced rutile has been measured by a number of workers. Figure 1.8.1 shows the Hall mobility reported by Becker and Hosler (1962) for temperatures between 3 to 300 K. The data was interpreted as impurity level conduction at very low temperatures (T<4 K), a narrow Ti^{3+} conduction band (No. 1) at low temperatures (7-30 K) and additional contributions from another Ti^{3+} conduction band (No. 2) at intermediate temperatures (30-300 K).

Bogomolov and Zhuze (1964) measured the electrical conductivity and Hall effect in single crystal rutile at temperatures in the range 78 to 700 K. Figure 1.8.2 shows the temperature dependence of the mobility on a logarithmic

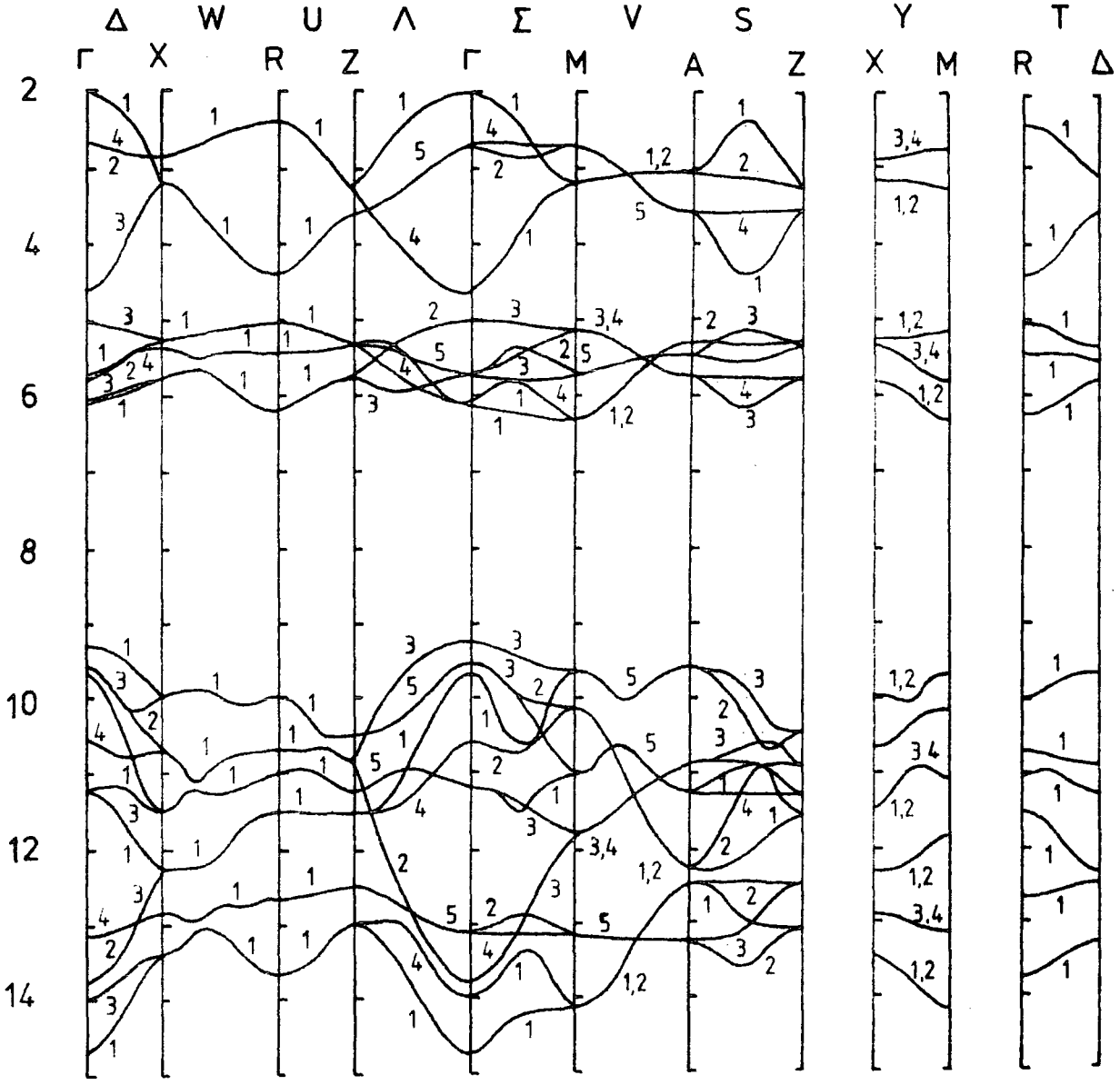

The eigenstates are labelled according to the symmetry of the corresponding eigenfunction.

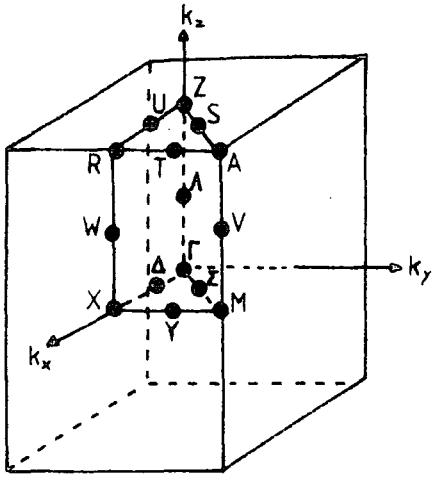

Figure 1.7.2 Energy bands of rutile TiO_2 along some high symmetry directions in the Brillouin zone. The tight binding band structure is calculated by using estimated values for the LCOAO parameters (Vos 1977).

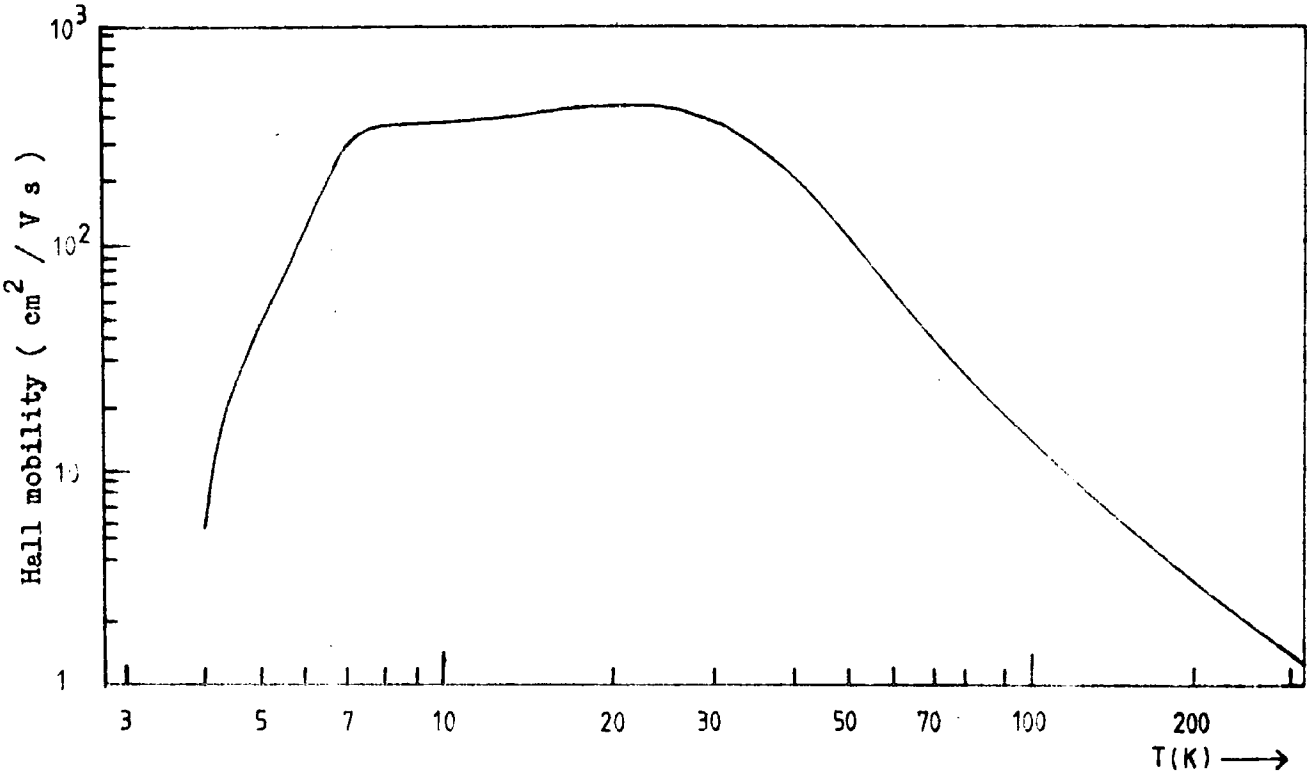

Figure 1.8.1 Hall mobility as a function of temperature, for vacuum reduced rutile (after Becker and Hosler 1963).

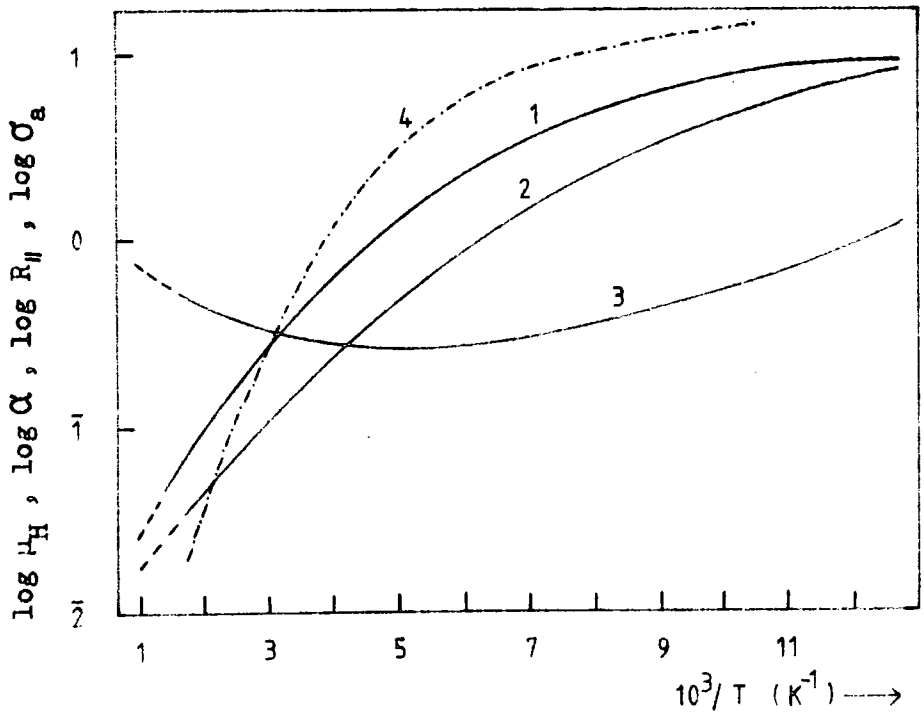

Figure 1.8.2 Temperature dependence of the Hall constant $R_{\parallel}$(1), Hall mobility $\mu_H = R_{\parallel}\sigma_a$ (2), electrical conductivity σ_a (3) and the ratio of Hall mobility to the drift mobility (4).

scale. Curve 2 which is for a bar specimen with its c-axis parallel to its length is accurately described by the T^{-n} law, where n = 2.3 for low temperatures.

Since the electron mobility is practically independent of the carrier concentration in the range 78-700 K, Bogomolov and Zhuze assumed that impurity scattering can be neglected. As for the main scattering mechanism, it must be remembered that the chemical bonding is mixed, somewhere between ionic and covalent. In this case the 'natural' scattering mechanism is determined by a combination of scattering by acoustic and optical phonons. There is no piezoelectric scattering in TiO_2, because the crystal has an inversion centre.

Bogomolov and Zhuze (1967) have interpreted their earlier work using the framework of a theory of low mobility, namely, by assuming that the electron transport is brought about by small radius polarons (Klinger 1963, 1965). This assumption leads to the conclusion that the concentration of the charge carriers cannot be calculated from the Hall constant. As can be observed in figure 1.8.2 a temperature dependence of the Hall to drift mobility ratio (μ_H/μ_D) was observed. A similar temperature dependence has been observed in silicon (Morin and Maita 1954) and interpreted to be a result of the relaxation time for intraellipsoidal and interellipsoidal scattering. However, the discrepancy between μ_H and μ_D has been shown for TiO_2 to be characteristic of small radius polarons (Bogomolov and Zhuze 1967, Austin and Mott 1969). Small polaron theory predicts a mobility which decreases with increasing temperature up to about half the Debye temperature (Θ = 670 K), but, at higher temperatures the mobility must decrease exponentially with temperature.

Yahia (1963) calculated values for the drift mobility in the range 800°C to 1000°C from conductivity and gravimetric measurements. He concluded that the electron mobility increases exponentially with temperature,

with a hopping energy of 0.6 eV, and gave μ_D (1000 K) = 10^{-5} cm^2/V s. On the other hand, Blumenthal et al (1967) have used more recent conductivity and gravimetric measurements to show that the electronic drift mobility is about 10^{-1} cm^2/V-s, and essentially independent of temperature over the range 1350 to 1500 K. Recent Hall mobility measurements on reduced rutile from 300 to 1250 K by Bransky and Tannhauser (1969), are in quite good agreement with the drift mobility value of Blumenthal et al in the overlapping temperature range (see figure 1.8.3). The facts that the measured magnitudes of the drift mobility (Blumenthal et al 1967) are essentially the same while the Hall mobility was found to decrease with increasing temperature (Bransky and Tannhauser 1969), led Bransky and Tannhauser to conclude that these results are not consistent with small polaron theory.

1.9 NATURE OF THE CHARGE CARRIERS IN RUTILE

When a free electron exists in an ionic lattice, the ions in that lattice are disturbed. Coulomb forces draw positive ions towards the electron and repel negative ions from it. The crystal is, in fact, polarised. In this way, there is a region of the solid in the vicinity of the electron in which the phonon spectrum of the lattice is noticeably perturbed. If the electron moves through the crystal, the region of polarisation moves with it, contributing an extra term to the inertia of the electron. The electron together with its polarisation field, that is, with the phonon disturbance which it creates is called a polaron. In covalent semiconductors, or in those in which the ionicity is not high, the disturbance caused by the electron as it moves in the crystal lattice is negligible, but in strongly ionic crystals like barium titanate, the effect could be strong. Indeed, if the coupling between electrons and phonons is sufficiently large, then the inertia of the polaron can become sufficiently high for the electron to become localised. The electron is trapped by the polarisation field which surrounds it. For this to

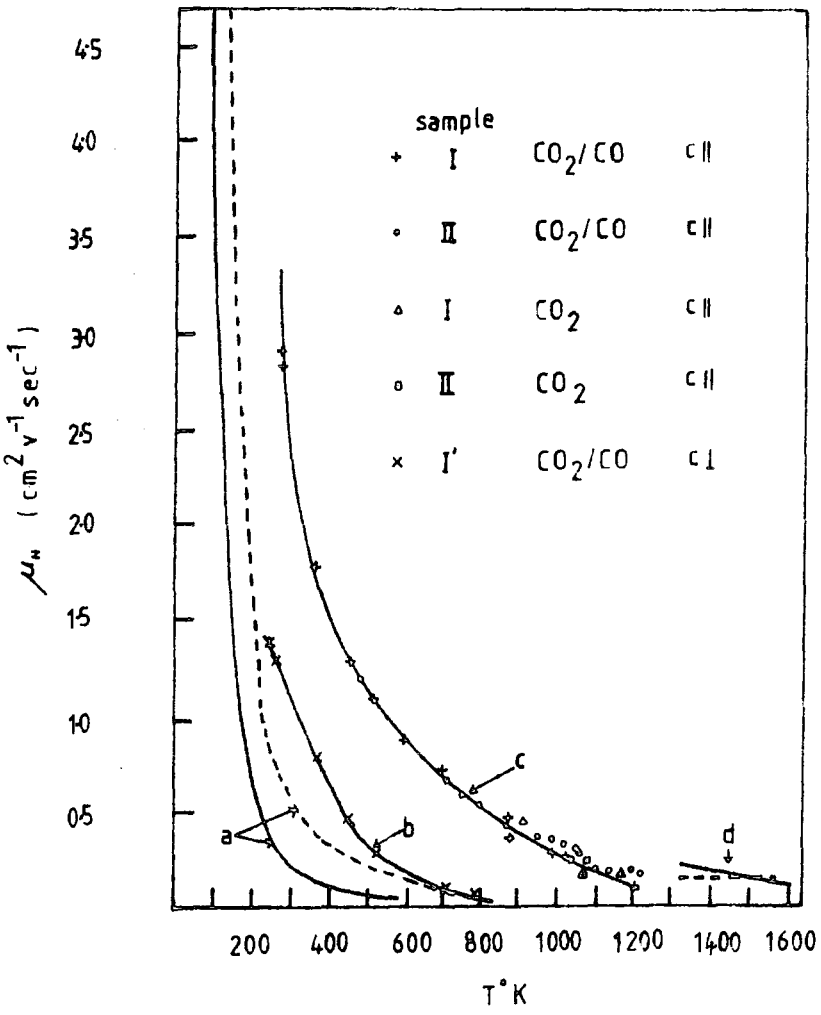

Figure 1.8.3 a Hall mobility of rutile measured by Bogomolov and Zhuze (1964) :- samples with c⊥(——), samples with c//(- - -).
b,c Hall mobility of rutile single crystal measured by Bransky and Tannhauser (1969) b c⊥ c c//.
d Drift mobility of single crystal rutile with c , calculated by Blumenthal (1967) from combined electrical conductivity and thermogravimetric measurements :- from data of Kofstad (1962) and Blumenthal (1967) (——), from data of Moser et al (1965) and Blumenthal (1967) (- - -).

happen, the spatial extent of the polaron is small (of the order of one lattice constant or less). The trapped electron can still move through the lattice if the polarisation field is temporarily broken down by thermal fluctuations. Under these conditions, however, the electron will be trapped at the next positive ion site. The motion of a small polaron in the 'hopping' mode then consists of a series of jumps from one positive ion site to the next.

Bogomolov et al (1968) in a series of electrical, optical and paramagnetic resonance experiments to 300 K, have found strong evidence for the existence of small polarons in rutile. They suggested an effective mass of 150 m_0 and a hopping energy of 0.13 eV for conduction perpindicular to the c-axis and 0.07 eV for conduction parallel to the c-axis. Analysis of the collection of experimental data on TiO_2 showed that it can all be described in terms of small polaron theory if one makes the assumption that the donors are completely ionised at T>100 K (Bogomolov and Zhuze 1967). This assumption, based on the data of Bogomolov and Zhuze, ensures automatically that the electrical conductivity above 300 K is caused by an increase in drift mobility with an activation energy E_a = 0.13 eV. Such a mobility behaviour is a feature of small polarons. The Hall constant cannot be used here to determine the current carrier concentration in the usual manner, since the drift mobility strongly differs from the Hall mobility (at about 300 K the Hall mobility in TiO_2 coincides with the drift mobility and is equal to 0.15 and 0.56 $cm^2/V\,s$ in the two directions).

A check on the assumption of complete donor ionisation and the constancy of the current carrier concentration in rutile was conducted by a method independent of the kinetic phenomena (from light absorption). This check confirmed the assumption, and consequently the polaronic nature of the conductivity (Bogomolov et al 1968).

Bogomolov, Kudinov and Mirlin (1968) have shown that the well known

absorption peak of conducting crystals (Cronemeyer 1952) is not caused by the absorption of light by defects or impurities, as is usually thought, but by the current carriers. The magnitude of the absorption at the maximum is practically independent of temperature after exhaustion of donors (above 10 to 30 K) (Becker and Hosler 1965). The resonance nature of the absorption, with a maximum near 0.8 eV, and its magnitude also agree well with the conclusions of polaron theory (Bogomolov, Kudinov and Mirlin 1968), thus providing supplementary verification that conduction in rutile is by polarons.

The frequency dependence of the absorption coefficient of rutile doped with niobium has been investigated (Kudinov et al 1968) and the temperature dependence is in agreement with small polaron theory (Kudinov et al 1968, Bogomolov and Mirlin 1968).

The observed thermoelectric power of TiO_2 is well described by the Morin formula (Morin and Maita 1954) which also argues in favour of small polarons. It should be noted that in rutile there is a weak anisotropy of the thermoelectric power (Morin and Maita 1954, Barbanel and Bogomolov 1975), which cannot be explained in the framework of the Morin formula and which obviously suggests that in the experiment there is a finite width of the polaron band. In particular in TiO_2 a situation may be realised, in which a charge carrier is localised in two directions, whereas in the third direction a motion in a narrow band occurs (Barbanel and Bogomolov 1975).

An essential argument supporting the applicability of the small polaron model to TiO_2 is given by the good agreement of the parameters obtained from the theory with results from different experimental methods. From such comparisons the following parameters result for rutile : electron-phonon coupling constant $\gamma = 4$ to 7 : activation energy $E_a \sim 0.2$ eV ; resonance integral $J \sim 0.1$ eV.

CHAPTER 2

THERMALLY STIMULATED CONDUCTIVITY AND LUMINESCENCE

2.1 INTRODUCTION

Many techniques have been used for the determination of trapping parameters of imperfections in crystals. Among these, thermally stimulated conductivity (TSC) and thermoluminescence (TL) offer the advantage of experimental simplicity and a potentially high yield of information. Essentially, the TSC technique involves the cooling of a photoconducting semi-insulator under well defined conditions to a low temperature, conveniently 77 K, where it is exposed to illumination of energy exceeding the band gap, for a period sufficient to produce saturation of photoconductivity. Traps are then occupied from which the trapped carriers cannot be freed by the available thermal energy at that temperature. When the temperature is increased, usually at a linear rate, for convenience of analysis, these trapped carriers are freed and contribute to the conductivity until they recombine with carriers of the opposite type. The conductivity measured in such a heating of the crystal, in excess of the normal dark conductivity, is called the thermally stimulated conductivity. If the recombination process is radiative then light will be emitted and this is known as thermoluminescence.

The thermal glow method was first proposed by Urbach (1930) and developed by Herman and Hofstadter (1940). Randall and Wilkins (1945) provided the first theoretical approach which was concerned with thermoluminescence in phosphors. Since 1945 numerous papers have been published on the determination of the trapping parameters from TSC and TL curves. Some methods were developed for TSC, others for TSL. In practice, however, many of the methods have been applied indiscriminately to both TSC and TL without establishing whether the procedure is valid. In several papers (Nicholas and Woods 1964, Dittfeld and Voigt 1963, Barkhalov and Lutsenko 1972, Walsh and Lightowlers 1971) results obtained using a range of these methods are

compared experimentally. It was found that different methods often do not produce the same trap depth for a given TSC or TSL peak. Some workers (Böhm and Scharmann 1971) have concluded that TSC and TSL measurements provide useful trapping parameters. Others (Kelly and Laubitz 1971) , however, state that no conclusion can be drawn from such experiments without previous knowledge about, for instance, the defect structure of the phosphor. Hagebeuk and Kivits (1976,1977) have recently reviewed TSC and TSL and attempted to evaluate the accuracy of the various methods available for different trapping and recombination kinetics.

2.2 SOLUTION OF THE THERMALLY STIMULATED LUMINESCENCE AND CONDUCTIVITY PROBLEM

The simple model commonly used (Dussel and Bube 1967, Saunders 1969, Hagebeuk and Kivits 1976) to describe the TSC and TSL phenomenon is shown in figure A. Electrons are thermally excited from trap h_1 to the conduction band (transition 1) where they contribute to the conduction. From this band they can either be retrapped (transition 2) or recombine with a hole trapped at a recombination centre (transition 3). If the recombination transition is radiative then simultaneous emission of light will occur.

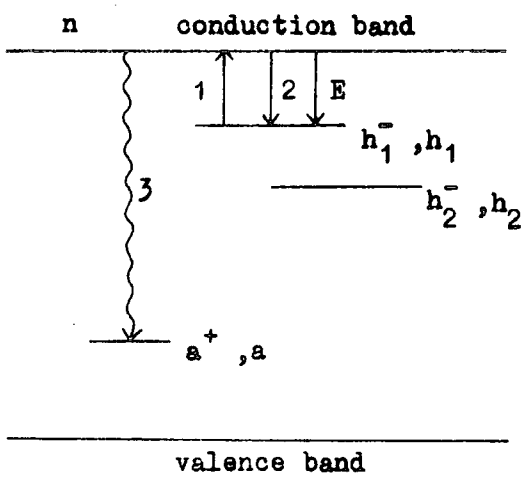

figure A

It is assumed that the occupation of deeper traps h_2 does not change during the emptying of the shallower trap. Both traps are then described as 'thermally disconnected'. In this chapter the following symbols are used ; E, trap depth (eV) ; h_1^-, h_2^- , concentration of electrons trapped at h_1 and h_2 (cm^{-3}) ; n, concentration of free electrons (cm^{-3}) ; a, concentration of recombination centres (cm^{-3}) ; a^+, concentration of holes trapped at recombination centres (cm^{-3}) ; β, trapping rate constant ($cm^3 s^{-1}$) ; α, recombination

rate constant ($cm^3 s^{-1}$) ; γ, the transition probability for electrons from trap to conduction band (s^{-1}).

Assuming full charge compensation the neutrality condition requires that

$$a^+(t) = n(t) + h_1^-(t) + h_2^-(t) \qquad (1)$$

when no free holes are present.

The differential equations for the simple model are

$$\frac{dh_1^-}{dt} = -\gamma h_1^- + \beta n (h_1 - h_1^-) \qquad (2)$$

$$\frac{dn}{dt} = -\frac{dh_1^-}{dt} - \alpha n a^+ \qquad (3)$$

$$\frac{da^+}{dt} = -\alpha n a^+ \qquad (4)$$

The initial conditions are

$h_1^-(0) = h_1$, $h_2^-(0) = h_2$, $a^+(0) = h_1 + h_2$, $n(0) = 0$. (5)

The transition probability is given by

$$\gamma = s \exp (-E/kT)$$

in which k is Boltzmann's constant and T the absolute temperature.

Kivits (1976) has shown how these equations can be solved numerically for the following range of values, assuming that these values are independent of temperature

$10^{12} < h_1 , h_2 < 10^{18}$ (cm^{-3}) , $0.1 < E < 1$ (eV) , $10^{-14} < \alpha , \beta < 10^{-8}$ ($cm^3 s^{-1}$) , $10^6 < s < 10^{12}$ (s^{-1}).

In TSC and TSL experiments the temperature is usually raised linearly, according to

$$T = T_0 + w t \qquad (6)$$

where ω is the heating rate. The TSL intensity is proportional to da^+/dT, and the conductivity is proportional to $n(T)$.

Hagebeuk and Kivits have shown that the four equations (1), (2), (3) and (4) can be reformulated by a system of two coupled equations :

$$\frac{da^{+\prime}}{dT'} = -n' a^{+\prime} \qquad (7)$$

$$\frac{1}{\alpha'}\frac{dn'}{dT'} = s' \exp(-E'/T')\,(a^{+\prime} - \xi') - n'[\,\delta' + a^{+\prime}(1-\delta') + \delta'\xi'\,] - \frac{n'}{\alpha'}(\,s' \exp(-E'/T') + \delta' n'\,) \qquad (8)$$

with the boundary conditions $a^+(1) = 1$, $n(1) = 0$, (9)

where a transformation has been made to the dimensionless quantities :

$h_1^{-\prime} = h_1^- / h_1$, $h_2^{-\prime} = h_2^- / h_2$, $n' = n/h_1$, $a^{+\prime} = a^+/h_1$,

$T' = T/T_0 = 1 + \omega t/T_0$,

$s' = sT_0/\omega$, $E' = E/kT_0$, $\alpha' = \alpha h_1 T_0/\omega$, $\delta' = \beta/\alpha$, $\xi' = h_2/h_1$.

The transformation to dimensionless form shows that two out of the seven physical quantities are non-essential. The ranges of the remaining five parameters are

$15 < E' < 150$, $10^8 < s' < 10^{16}$, $1 < \alpha' < 10^{14}$, $10^{-6} < \delta < 10^6$,

$10^{-6} < \xi < 10^6$.

Hagebeuk and Kivits have shown that the system of coupled differential equations (7) and (8) is stiff for the interesting range of the parameter α'. It cannot be solved by step wise integration procedures such as Runge-Kutta for example, unless the step, ΔT, is impossibly small ($\sim 1/\alpha$). Firstly, they solved the system using an expansion in powers of ($1/\alpha$) and found approximate analytical solutions proposed by other workers. Secondly, they solved the system by a stable numerical method which will now be described.

Equations (7) and (8) are rewritten in an approximate form for iteration :

$$a^{+\prime} = (1 + \xi') \exp\left[-\int_1^{T'} n' \, dx \right] \qquad (10)$$

$$f(n') = s' \exp(-E'/T') \, (a^{+\prime} - \xi') - n' \left[\delta' + a^{+\prime} (1 - \delta') + \delta' \xi' \right]$$

$$- \frac{1}{\alpha} \left[s' \exp(-E'/T') \, n' + \delta' n'^2 + dn'/dT' \right] . \qquad (11)$$

The iteration is started with the solution $\alpha' \to \infty$ given by

$$a_0^{+\prime}(T) = \left[1 + \int_1^{T'} s' \exp(-E'/x) \, dx \right]^{-1} \qquad (12)$$

where $a^{+\prime}(T) = a_0^{+\prime}(T) + \frac{1}{\alpha'} a_1^{+\prime}(T) + \frac{1}{\alpha'^2} a_2^{+\prime}(T) + \ldots\ldots\ldots$

This solution for $a^{+\prime}(T)$ is substituted in (11) and $n'(t)$ is solved from this equation by a Newton formula with a underrelaxation factor equal to 0.7. Then $n'(t)$ is integrated with Simpson's formula, and a new approximation for $a^{+\prime}(T)$ is obtained from (10). This process is iterated until convergence for all values of T.

The iteration procedure was obtained from P.Kivits and is shown in Appendix 2. Unfortunately, the program was written in ALGOL 66 and required some effort to convert to FORTRAN 4. The subroutine 'CURVE' in the program TSCL1 contains the modified FORTRAN 4 iteration procedure and is shown in Appendix 1. A short guide to this routine will now be given.

E, ALFA and SS are the dimensionless representations of EV, ALPHA and FREQ, respectively, where FREQ is s, ALPHA is α, EV is E, DELTA is β/α and SKSI is h_2/h_1. Lines 20 to 38 evaluate the initial value of $a_0^{+\prime}(T)$ using equation (12), A(I) = 1/(1+Q(I)). Lines 49 to 52 evaluate FIFN(T) = $-\int_1^{T'} n' \, dx$ using Simpson's rule. Line 53 determines $a^{+\prime}(T)$ using equation (10). Lines 55 and 56 evaluate R = f(n) and RR = f'(n) respectively. Line 58 is the Newton formula with an underrelaxation factor equal to 0.7. Line 60 converts the dimensionless quantity FN = n' to FNN = n. Line 61 uses equation (7) to

obtain $da^{+'}/dT = DA(T)$. Line 62 coverts the dimensionless quantity $da^{+'}/dT$ to da^{+}/dT, the TL intensity. Line 68 sets the number of iterations for the routine (ITER).

The routine was implemented on the NUMAC IBM 370 and required approximately 0.2 cpu seconds/iteration. For most values of the parameters about 10 to 20 iterations were necessary for convergence. As the algorithm is $O(\Delta T^2)$ fairly large values of ΔT can be used ($\Delta T = 1/80 \sim 1$ K). To check that the program was identical to the Hagebeuk and Kivits routine, all the curves listed in reference, Hagebeuk and Kivits 1976, were successfully reproduced. A few of these curves are shown in figures 2.2.1 to 2.2.4.

As can be seen from figure 2.2.1 the TSC and TL peak temperatures are primarily determined by the values of E' and s'. However, the peak temperatures and halfwidths are still dependent on the other parameters α', δ and ξ. From figure 2.2.2 it is seen that α' has little influence on the TSL curve, but the TSC curve depends strongly on α' if $\alpha' < 10^4$ ($\alpha' >> 10^4$ for all rutile samples examined). The shape of the TSC curve depends strongly on δ, but that of the TSL curve only if $\delta > 10^{-2}$ (see figure 2.2.3). The asymmetry of the TSC curves, which is hardly observed in experiments, is seen to disappear rapidly for small values of ξ, indicating the practical importance of assuming the presence of a second trap. The TSL curve is not significantly influenced by ξ if $\delta < 0.01$. However, it should be noted that for larger values of δ the higher temperature halfwidth slightly decreases.

2.3 SUMMARY OF APPROXIMATE METHODS

For completeness, a summary of the methods currently used to evaluate trapping parameters from TSC and TSL curves will be given. The convention used by Kivits and Hagebeuk (1977) is adopted.

(A) Methods making use of various heating rates

The following symbols are used : ω_i , the heating rate in the i th

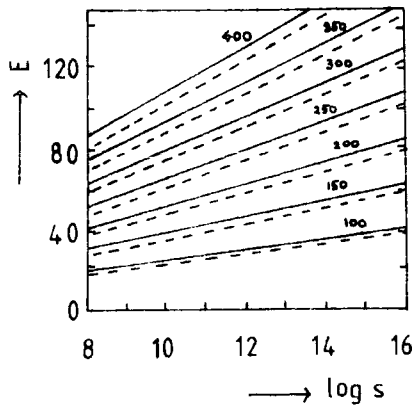

Figure 2.2.1 Lines of constant peak temperature for TSL (drawn lines) and TSC (dashed lines) for $\alpha = 10^{8}$, $\delta = 0.01$ and $\xi = 10^{-3}$.

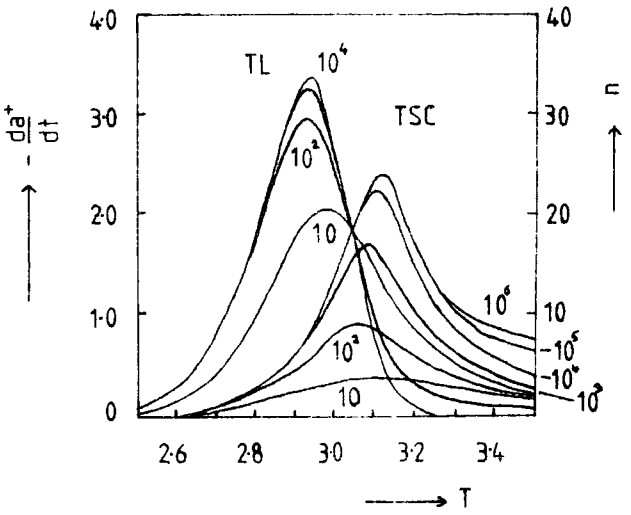

Figure 2.2.2 The influence of α on TSL and TSC curves . E = 75 , $s = 10^{12}$, $\delta = 0.01$, $\xi = 10^{-6}$.

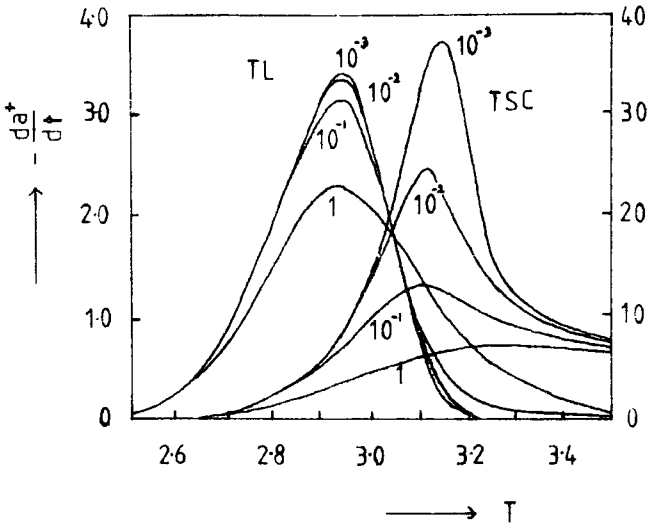

Figure 2.2.3 The influence of δ on TSL and TSC curves . E = 75 , $s = 10^{12}$, $\alpha = 10^{8}$, $\xi = 10^{-6}$.

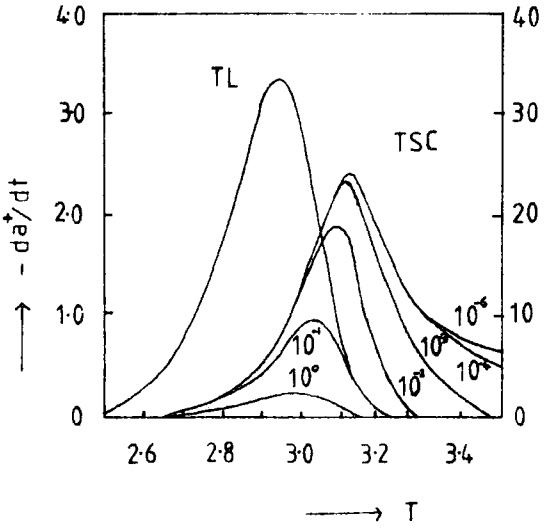

Figure 2.2.4 The influence of ξ on TSL and TSC curves . E = 75 , $s = 10^{12}$, $\alpha = 10^{8}$, $\delta = 0.01$.

Summary of the TSC/TSL curves generated by Hagebeuk and Kivits 1976.

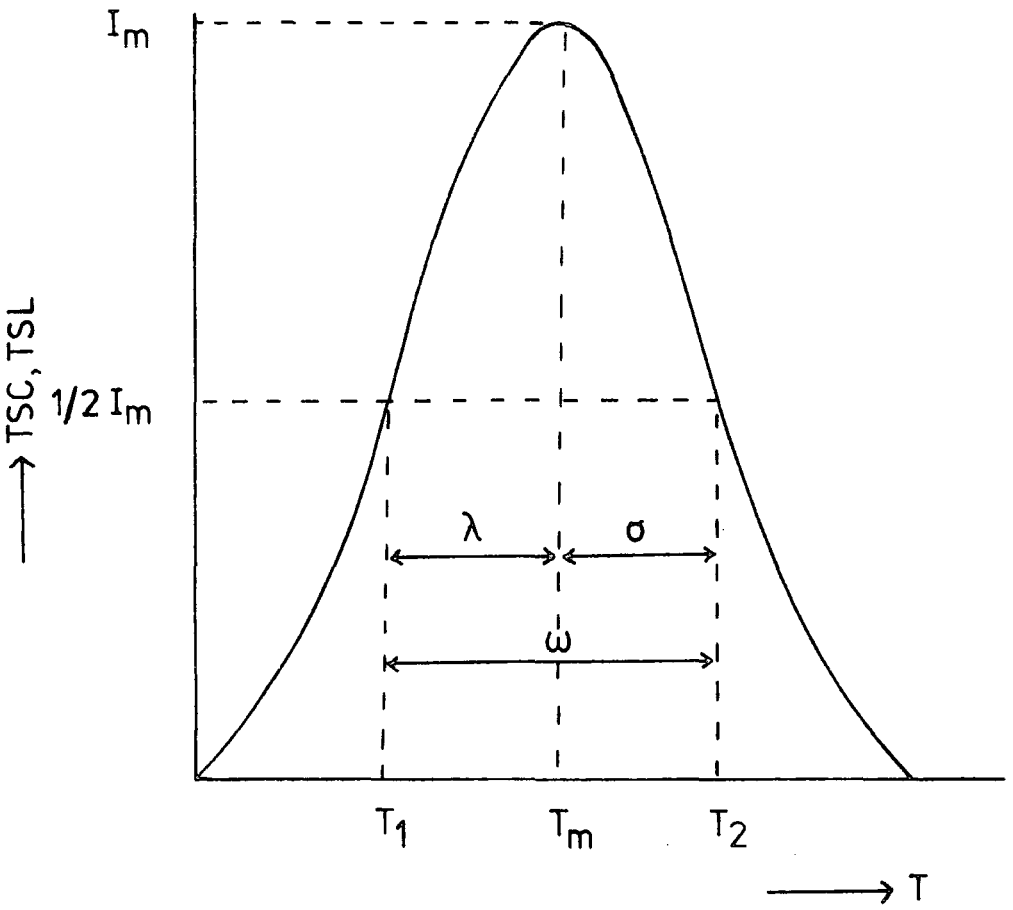

$$\omega = T_2 - T_1 \qquad \lambda = T_m - T_1 \qquad \sigma = T_2 - T_m$$

$$\mu_g = \sigma/\omega \qquad \chi = \sigma/\lambda \qquad \Delta = E/kT_m$$

Figure 2.3.1 General shape of a TSC or TSL curve with definition of some characteristic quantities .

experiment ; L_{mi} , the intensity of the TSL maximum ; n_{mi} , the maximum of the TSC curve ; T_{mi} , the temperature of the TSC or TSL maximum ; T_{1i} , the temperature at the lower side of the TSC or TSL curve where either $L = \frac{1}{2} L_{mi}$ or $n = \frac{1}{2} n_{mi}$.

(1) First class methods

Method 1 , Booth, Bohun and Parfianovitch (1954, 1954, 1954) (TSL)

$$E = k T_{m1} T_{m2} / (T_{m1} - T_{m2}) \ln (\omega_1 T_{m2}^2 / \omega_2 T_{m1}^2)$$

Method 2 , Boer, Oberlander and Voigt (1958) (TSC)

A plot of $\ln (\omega_i)$ versus $1/T_{mi}$ yields a straight line with a slope - E / k with $0.7 < \rho < 0.9$.

(2) Second class methods

Method 3 , Chen and Winer (1970) (TSL)

A plot of $\ln (L_{mi}^4 / \omega_i^2)$ versus $1/T_{mi}$ yields a straight line with a slope E / k .

(3) General class methods

Method 4 , Hoogenstraaten (1958) (TSL)

A plot of $\ln (T_{mi}^2 / \omega_i)$ versus $1/T_{mi}$ should yield a straight line with slope E / k .

Method 5 , Bube, Haering and Adams (1955, 1960)

A plot of $\ln (n_{mi})$ versus $1/T_{mi}$ yields a straight line with a slope - E / k. Haering and Adams claim that the method is valid when $E / k T_m \gg 1$.

Method 6 , Unger (1962) (TSC)

Plotting $\ln (n_{mi})$ versus $1/T_{1i}$ yields a straight line with a slope - E / k .

Method 7 , Schön (1958) (TSC)

$$E = k T_{m1} T_{m2} / (T_{m1} - T_{m2}) \ln (\omega_i T_{m2}^{7/2} T_{m1}^{3/2})$$

Method 8 , Boiko, Rashba and Trofimenko 1 (1960) (TSC)

The plot of $\ln (n_{mi} / T_{mi}^{3/2})$ versus $1/T_{mi}$ yields a straight line with a slope E / k .

Method 9 , Boiko, Rashba and Trofimenko (1960) (TSC)

The plot of $\ln (\omega_i / T_{mi}^{7/2})$ versus $1/T_{mi}$ yields a straight line of slope $- E / k$.

(B) Methods making use of geometrical approximations

See figure 2.3.1 for the definition of parameters.

(1) First class methods

Method 10 , Lushchik (1955) (TSL)

$$E = k T_m^2 / \sigma$$

Method 11 , Halperin and Braner 1 (1969) (TSL)

$$E = (1.72 k T_m^2 / \lambda) (1 - 5.16 / \Delta)$$

Method 12 , Halperin and Braner 2 (1969) (TSL)

$$E = k T_m^2 / \sigma$$

Method 13 , Chen 1 (1969) (TSL)

$$E = 2 k T_m (1.25 T_m / \omega - 1) \text{ with condition } \Delta >> 1$$

Method 14 , Chen 2 (1969) (TSL)

$$E = 2.29 k T_m^2 / \omega$$

Method 15 , Chen 3 (1969) (TSL)

$$E = (1.548 \, k \, T_m^2 / \lambda) (1 - 3.16 / \Delta)$$

Method 16 , Chen 4 (1969) (TSL)

$$E = 1.52 \, k \, T_m^2 / \lambda - 3.16 \, k \, T_m$$

Method 17 , Chen 5 (1969) (TSL)

$$E = C_6 \, k \, T_m^2 / \sigma \qquad \text{where } C_6 = 0.976 + 0.004$$

Method 18 , Chen 6a , 6b (1970,1971) (TSC)

$$E = 3 \, \sigma \, k \, T_m^2 / \omega \qquad \text{(a)}$$

$$E = 2.8 \, \sigma \, k \, T_m^2 / \omega \qquad \text{(b)}$$

(2) Second class methods

Method 19 , Halperin and Braner 3 (1969) (TSL)

$$E = (2 \, k \, T_m^2 / \lambda) (1 - 6 / \Delta)$$

Method 20 , Halperin and Braner 4 (1969) (TSL)

$$E = 2 \, k \, T_m^2 / \sigma$$

Method 21 , Halperin and Braner 5 (1969) (TSL)

$$E = (1 + \omega / \lambda) \, k \, T_m^2 / \sigma$$

Method 22 , Chen 7 (1969) (TSL)

$$E = 2 \, k \, T_m (1.77 \, T_m / \omega - 1)$$

Method 23 , Chen 8 (1969) (TSL)

$$E = 1.813 \, k \, T_m^2 / \lambda - 4 \, k \, T_m$$

Method 24 , Chen 9 (1969) (TSL)

$$E = C_7\ 2\ k\ T_m^2 / \sigma \qquad \text{where } C_7 = 0.853 + 0.0012$$

(C) Other methods

(1) First class methods

Method 25 , Randall and Wilkins (1945) (TSL)

$$E = 25\ k\ T_m$$

Method 26 , Grossweiner (1953) (TSL)

$$E = 1.51\ k\ T_m\ T_1 / \lambda$$

Method 27 , Franks and Keating (1961) (TSL)

$$1 / \Delta = (\omega / T_m) (1.2 \chi - 0.54) + 5.5\ 10^{-3} - \tfrac{1}{4} (\chi - 0.75)^2$$

with the additional conditions that $10 < \Delta < 35$ and $0.75 < \chi < 0.9$.

Method 28 , Dussel and Bube (1967) (TSC)

$$E = C_8\ k\ T_m\ T_1 / \lambda$$

$C_8 = 1.402$, 1.415 or 1.421 where $\Delta = 17$, 22 and 26 , respectively.

(2) General class methods

Method 29 , Garlick and Gibson (1948) (TSL)

In the initial rise of the curve a slope $= E / k$ is obtained when ln L is plotted versus $1/T$.

Method 30 , Sandomirskii and Zhdan (1970) (TSL)

$$E = 1.455\ k\ T_m\ T_1 / \lambda - 0.79\ k\ T_1$$

Method 31 , Voigt (1958) (TSC)

$$18\ k\ T_m \ < \ E \ < \ 25\ k\ T_m$$

Kivits and Hagebeuk (1977) have evaluated the simple insulator model for TSC and TSL analysis. After application to numerically generated TSC and TSL curves they found that of the methods considered only those of Bube, Haering and Adams, Hoogenstaaten and Unger produce reliable values of the trap depth independently of the values of the frequency factor and the retrapping ratio. An estimate of the last quantity can be made by comparing the trap depths determined with the TSL methods of Chen since these produce correct results in the cases $\delta = 0.01$ and $\delta = 1$ for TSL. They concluded that when the simple insulator model can be used, TSC and TSL measurements are a helpful tool in determining trapping parameters, in agreement with Böhm and Scharmann (1971). In chapters 7 and 8 the validity of applying the simple insulator model to single crystal rutile will be discussed.

2.4. EVALUATION OF TRAPPING PARAMETERS FROM TSL CURVES

The transition probability of thermal excitation of electrons from a trap to the conduction band, γ_h, is given by

$$\gamma_h = s_h \exp (- E / k T) .$$

The frequency factor s_h and the trapping rate constant β are related and

$$s_h = \beta N_c / g$$

where N_c is the effective density of states in the conduction band and g is the degeneracy of the trap, taken as unity here. The coefficients α and β are given by

$$\alpha = S_a v \quad \text{and} \quad \beta = S_h v$$

where v is the mean thermal velocity of free electrons (proportional to $T^{\frac{1}{2}}$) and S_a and S_h are the cross sections for the capture of electrons by recombination centres and traps, repectively. According to Lax (1959) capture

cross sections of deep centres are proportional to T^{-n} ($n \sim 2.5$ to 4). Chen and Fleming (1973) assume a range $0 < n < 4$. Following the latter authors

$$s = s_0 (T / T_0)^b \qquad -2 < b < 2$$

$$\alpha = \alpha_0 (T / T_0)^c \qquad -\tfrac{7}{2} < c < \tfrac{1}{2}$$

where α_0, s_0 and T_0 are constants. It follows that s and α vary rather slowly with temperature compared with the exponential increase of γ, when $E >> kT$. Therefore it is often assumed that s and α are independent of temperature. However, the variation of α with temperature has already been discussed in section 2.2 and an exponential dependence with reciprocal temperature of S_a and S_h has been reported by Henry and Lang (1974).

As discussed in section 2.2, the temperatures at which the TSC and TSL curves peak depend mainly on E and s. Therefore, an order of magnitude estimate of the trapping cross section, S, can be found providing that the simple insulator model applies to the system under investigation. Care must be taken in attaching undue weight to quantitative results of trap depths from TSC and TSL experiments if the model that can be applied is not known (Kelly and Laubitz 1971).

Using the numerical solution described in section 2.2 the validity of the conventional model can be tested. An estimate of ξ can be obtained from the relative areas under subsequent TSC peaks, and a knowledge of the photoconductive gain versus temperature. Difficulties can arise when the dark current prevents the detection of large quantities of deep traps.

As the model contains essentially five independent parameters E, s, α, δ and ξ, the value of the retrapping ratio can be found by curve fitting. As the shape of the TSL curve is determined by ξ and δ, providing $\alpha' > 10^4$, then the accuracy of the determination of δ depends on the value of ξ. The

difference in the temperatures at which the TSC and TSL reach their maximum values, which depends mainly on the value of ξ, can be used as a further check on the accuracy of the ξ value.

As has already been stated the trap density can be found from the complete area, ψ, under the TSC curve using

$$n_t = \psi / e V_L G$$

where V_L is the crystal volume and G is the photoconductive gain as given by :

$$G = I / e f \doteq \tau / T_r$$

I is the photocurrent excited by the absorption of f photons/second, T_r is the transit time of a free electron from cathode to anode and τ is the lifetime of a free electron. The transit time is given by

$$T_r = L / v_d = L / \mathcal{E} \mu = L^2 / V \mu$$

where v_d is the drift velocity, $\mathcal{E}$ is the electric field, μ is the mobility of free electrons and L is the spacing of the electrodes. τ can be found from the photocurrent using

$$\tau = I L^2 / \mu V e f$$

and

$$n_t = \psi L^2 / e V_L \mu \tau V . \qquad (2.4.1)$$

2.5 LIMITATIONS OF THE SIMPLE INSULATOR MODEL

Kivits (1978) has discussed extensions to the conventional simple insulator model. He showed that the values of trap depths determined after application of most of the methods described in the literature are unreliable if an extended model is used. These extensions included recombination via excited states, the presence of a trap distribution, donor-acceptor pair recombination, the presence of additional centres, temperature dependent rate parameters, thermal quenching of luminescence and scattering due to

ionised defect centres. Only Hoogenstraaten's method appeared to be rather insensitive for most of the extensions considered.

Several checks can be applied to establish whether any of these modifications to the simple model are present in a given system. For example, recombination via excited states is probable when thermoluminescence is not accompanied by simultaneous conduction. The leaking of traps via DA pair recombination can be checked by measuring the light sum in TSL experiments for various excitation levels or waiting for different lengths of time after excitation at low temperatures (Hoogenstraaten 1958).

Trap distributions can be examined using the thermal cleaning technique (Nicholas and Woods 1964). After a phosphor is excited it is alternately heated and cooled in the dark in such a way that the mean temperature increases only very slowly. When the light intensity is plotted logarithmically versus reciprocal temperature two energies may be determined from the slopes in the heating and cooling part of each cycle. The light emitted during one cycle is supposed to be only caused by recombination of electrons that were thermally excited from trapping levels between these two energies. Summing up the contributions of all cycles, the trap distribution function can be found. However, it should be mentioned that other effects can produce the same type of result, such as the presence of two thermally connected trapping levels (Samoc and Samoc 1979).

The temperature dependence of the mobility is determined by the scattering mechanism of the electrons. Often the mobility is found to be proportional to $T^{-\frac{3}{2}}$ (acoustical phonons), to T^{0} (neutral impurity centres), to $T^{\frac{3}{2}}$ (charged impurity centres) or $T^{\frac{1}{2}}$ (dipoles). In these cases the temperature dependence of the mobility will not strongly influence the shape of the TSC curve, since the number of free carriers generally changes much more rapidly with temperature. However, Kivits has pointed out that for

scattering by charged centres the mobility is also inversely proportional to the concentration of charged centres (N_i). Then after illumination at low temperatures all centres are neutralised and N_i increases when the phosphor is heated. The shape of the TSC curve is changed on the low temperature side and the methods involving the initial rise and the lower temperature side halfwidth give erroneous results. The temperature of the TSC maximum is hardly influenced and the method of Hoogenstaaten still gives a reliable value of trap depth.

Finally, it should be noted that when the mobility decreases exponentially with temperature due to polaron scattering by optical phonons (Low and Pines 1955) the TSC curve may be appreciably affected. The consequences are similar to the case of cross sections that depend exponentially on reciprocal temperature.

In conclusion, the phenomena of thermally stimulated luminescence and conductivity provide a lot of data in a series of simple experiments. However, great care must be taken in the interpretation of the data obtained. The TSC/TSL experiments should be used in conjunction with a number of different techniques in order to establish the relevant model for the system under investigation. The work described in this thesis presents photoconductivity, photoluminescence, TL and TSC experiments on a series of stoichiometric, non-stoichiometric and doped single crystal rutile in an attempt to develop a coherent model.

CHAPTER 3

CRYSTAL GROWTH

3.1 GENERAL

The growth of oxide single crystals containing transition metal ions presents a number of problems. Since the melting points of these oxides are greater than 1500°C a high temperature furnace is required, together with a crucible capable of not only withstanding the temperature but also insensitive to attack by molten oxides. Furthermore, since oxygen is a component of the system in which crystallisation is taking place, it is necessary to adjust the oxygen pressure above the melt to the correct value for equilibrium if a crystal with stoichiometric composition is to be obtained.

Almost all of the commercial growth of single crystal rutile to date has been done by the Verneuil flame fusion technique (Verneuil 1902) using an oxy-hydrogen flame. This method was invented over fifty years ago for the production of synthetic sapphire and was used extensively during the war, particularly in Germany, for the preparation of jewel bearings. Its most recent scientific application is in the preparation of artifical rubies for use in maser devices. The application of the method to the growth of single crystals of rutile has been described by Moore (1949).

The essentials of the Verneiul process are as follows. The high temperature neccessary to melt the material is obtained by means of an oxy-hydrogen burner, and the flame produced is introduced vertically into a firebrick furnace. The burner can be composed of two concentric tubes, the inner supplying oxygen and the outer hydrogen. A third outer concentric tube is often added supplying oxygen to produce a more oxidising flame whilst providing an additional means of varying the flame conditions.

The feed powder falls into a conical hopper, and then via the central tube of the burner to the flame, whence it impinges on the top of an alumina candle. The candle is connected to an automatic mechanism which rotates as the crystal is withdrawn through a muffle furnace.

The original Verneuil method described above has, however, many disadvantages. The crystal growth ambient is uncontrolled and is essentially a reducing atmosphere due to the presence of hydrogen. Difficulty arises in the precise control of the temperature and its gradient. However, the method does not require the use of a crucible to contain the growing crystal and many oxides have been successfully grown using this technique. Rutile single crystals are grown in their non-stoichiometric blue form and subsequently oxidised. Commercial crystals about 2 cm in diameter and 5 cm in length can be purchased from National Lead of America (Report NL).

The Czochralski technique of growing single crystals by pulling from the pure melt has been widely used for low-melting point materials, particularly semiconductors. This method can be used for the growth of oxides providing that a crucible material is available which is stable in the presence of both the molten material and the required atmosphere at a temperature somewhat above the melting point. Nassau and Broyer (1963) have successfully used this method to grow single crystal rutile. Pulling was performed from an iridium (m.p. 2442°C) crucible in a nitrogen atmosphere. A randomly orientated rod cut from a Verneuil-grown rutile boule was used as a seed, and a growth rate of about 2.4cm/hr was employed. The first centimetre of growth was single crystal material; after this, owing to lack of adequate temperature control, about equal length of polycrystalline material was obtained.

The rutile solidifying in the crucible was the expected blue-black colour due to chemical reduction. The pulled crystal was of the straw

colour indicative of stoichiometric rutile. However, spectrochemical analysis indicated the presence of 0.05 wt.% Ir in the crystal. No further characteristics of these crystals were reported. In addition to the Czochralski method, the heating zone method has found wide application in the growth of semiconductor crystals. This method consists in melting a narrow zone in a rotating polycrystalline rod; the zone is maintained between two solid sections of the rod by virtue of the surface tension of the liquid. The heat source is moved relative to the rod producing a single crystal from the liquid phase. The principal advantage of the method is that the liquid phase and the growing crystal do not come into contact with any foreign impurities. The material may be melted by induction heating, focused optical radiation or electron bombardment.

Holt (1965) employed the floating zone method for preparing single crystal rutile. He found that sintered rods were not suitable as an initial starting material, owing to their porosity, deformation and the contraction of the material during melting. However, good quality rods were produced by melting rutile powder in a copper container. Excess titanium was added to the starting material to produce a low resistivity rod. Such a rod could then be directly coupled to an induction coil. Holt grew his crystals in an argon atmosphere containing 0.1% oxygen. The crystals produced were non-stoichiometric and were subsequently oxidised to give a resistivity of 10^9 ohm cm.

Unlike the previous methods of crystal growth the hydrothermal technique has not been used for preparing semiconductor crystals. However, it has yielded good results in growing oxide single crystals. The hydrothermal method takes advantage of the fact that oxides, which are insoluble in only normal conditions, become soluble in water or aqueous solutions under conditions close to those of the critical point of water. The apparatus is composed of a steel autoclave, inside which a container is placed, made of a material which does not contaminate the crystal (e.g. gold or platinum).

The oxide material is then introduced into the container and the aqueous solution is added.

Inside the container a perforated diaphragm is placed, and in the upper part of the container crystal seeds are suspended. The bottom part of the system is heated to the required temperature and the upper part is cooled. The diaphragm produces two regions of aqueous solution. Owing to the relatively high temperature, the oxide in the lower part of the container is dissolved until saturation is required. Because of the temperature difference between the upper and lower parts of the container, the saturated solution passes to the upper part. Since the temperature in this part is lower, the solution becomes supersaturated, and the excess of the oxide crystallises on the seeds.

Kuznetzov (1968) has grown single crystal rutile under hydrothermal conditions. An aqueous solution of KF was used for the transcrystallisation of the rutile onto Verneuil grown seed crystals. The experiments were conducted at a solubility zone temperature of 550 °C, with an autoclave filling coefficient of 60% and ΔT = 20 - 35 °C. Under these conditions the growth rate of the {100} and {110} faces was 0.15 -0.21 mm/day and 0.26-0.31 mm / day in five day experiments. The crystals were dark blue in colour as a result of departure from stoichiometry. Introduction of oxygen (in the form of $KClO_3$, H_2O_2 up to 1%) into the autoclave did not produce a positive result.

Chandrashekhar and Title (1976) have recently described an electolytic technique for growing rutile. A mixture of TiO_2 and $Na_2Ti_3O_7$ was electrolysed in a sodium borate-sodium flouride bath (10%-NAF). A platinum disc was used as the cathode and the electrolysis was carried out at 850 °C for up to 60 hours with a current density of 25 mA/cm . Dark green crystals were produced and optical analysis showed the following impurities in ppm by weight, B:1000; Si:300; Co:100; Pb:100; Cr:30; Pt:50; Ga:50; Mg:1. These

electrolytically grown rutile crystals were generally hollow rods, a few millimetres long and about 1mm wide.

Metal oxides are hardly soluble in common solvents. They are, however, soluble in molten subtances, or in molten mixtures of appropriate substances of determined composition. Rutile is soluble in a mixture of Li_2O and MoO_3. Like the hydrothermal method the flux growth technique has been used extensively for preparing single oxide crystals. Although it requires the use of higher temperatures than the hydrothermal method these temperatures are none the less considerably lower (1825°C for rutile) than the melting points of most oxides.

Growth from the fluxed melt is performed by heating the solvent and oxide in a platinum crucible. The temperature is adjusted in such a way that the resulting solution is not saturated. By slowly cooling (1 degree/hour), the solution becomes supersaturated, and the dissolved oxide begins to crystallise. Crystal seeds are formed on the cooler parts of the crucible. The best results are obtained by introducing crystal seeds into the solution. Berkes et al (1965) have grown needlelike crystals approximately 5mm long and 0.1-0.2mm thick with the length of the sample along the c-axis. These crystals were yellowish white in colour and highly electrically insulating.

The chemical vapour deposition method may be defined as a technique to produce a solid by reacting one or more gaseous phases under controlled PVT conditions. The method, usually used in thin film epitaxial growth, has been applied to single crystals. In the most successful approach to CVD growth of large crystals a metal is reacted with chlorine gas, and the resultant chloride is passed into the oxidising astmosphere of a furnace under reduced pressure. Farrell and Linz (1975) have grown rutile crystals with this technique.

The CVD method offers several advantages. The first is that a slow

growth rate under isothermal conditions can be sustained and a consequent higher degree of crystal perfection results. The second advantage is that exact control can be maintained over the reaction rates by controlling the chlorine flow to the heated source metal.

Farrel and Linz used flame fusion crystal seeds. Crystal growth on the seed was about 15 μm/hour in a radial direction. As growth proceeded the crystal presented an obstacle to the flowing gas and turbulence occurred, consequently growth was random and polycrystalline on the seed tip. It was regular on the rest of the seed. The conditions of the successful run resulting in a large single crystal involved a duration of 96 hours at 1200 °C and 6 torr. The dimensions of the crystals were 0.5cm diameter by 3 cm in length. The crystals grew in a slightly reduced state and were later oxidised.

Although little quantitative analysis was given by Farrell and Linz they indicated that the chemical purity of these crystals was better than that of the flame fusion seed. However, the CVD method is limited by the quality of seed crystal available and the difficulty of etching the surface before crystal growth takes place. Although extremely expensive to run, a CVD growth system appears to be an interesting area of rutile single crystal growth for the future. The method could also be used for the growth of rutile thin films and heteorojunctions.

3.2 PLASMA GROWTH OF REFRACTORY OXIDES

Reed (1961) developed the induction torch and subsequently demonstrated its application to the growth of refractory crystals. By replacing the hydrogen-oxygen flame by a plasma torch as heat source, the classical Verneuil technique is modified. Three advantages of this modification are (1) higher temperatures are possible, (2) much greater control is achieved over the crystal growth enviroment and (3) hydrogen is excluded

from the growth process. Chase and van Ruyven (1969) applied the plasma growth technique to single crystal rutile. The presence of hydrogen leads to the observation of a time-dependent increase in the electrical conductivity in rutile when measurements are made with a constant voltage applied parallel to the c-axis (Van Raalte 1965). Chase and van Ruyven confirmed this conclusion and were able to demonstrate that the electrical conductivity remained constant for up to 1000 hours in crystals grown in a hydrogen-free ambient. They did not, however, report any other properties of their crystals.

The simplest induction plasma torch is obtained by producing an induced electrodeless discharge in a quartz tube. If the gas is blown through a tube, a plasma 'flame' is formed at its end, which is similar in appearance to the usual chemical flame. The power supply of such a torch is usually obtained from a tube oscillator of 5-30 kW power operating at 1-60 Mc to which the electrodeless discharge is coupled inductively. If no measures are taken to protect the quartz tube walls from the high temperatures reached in the plasma (T=9,000-10,500 K), the walls melt and the electrodeless discharge stops because of breakdown between the inductor turns. Consequently, the principal constructional element in a high frequency plasma torch is some device which provides reliable thermal insulation of the quartz tube walls. All the induction plasma torches known at the present time may be divided according to their construction into three main groups, depending on the method used to insulate thermally the quartz tube walls.

(a) Torches with forced gas cooling of the tube. The first torch of this type, working with argon mixtures, was described by Reed (1961). The same thermal insulation principle was used by Donskoi and Dresvin (1963) working with air and nitrogen.

The gas flow method of insulating the quartz tube is based on the formation of a stream of gas which, passing along the inner wall of the

tube, establishes a heat insulating zone between the quartz and the plasma. Because of its high velocity (20-30 l/min), the gas stream pushes the plasma away from the walls and establishes good conditions for the effective cooling of the tube.

In torches with gas flow insulation it is necessary to have at least three different velocities of gas flow. One stream establishes a cool zone along the inner wall of the tube; a second stream carries the powder along the centre of the plasma; while a third stream, which forms the plasma, must be supplied between the central and outer streams. The optimum relationship between the velocities of these three streams, required to provide a satisfactory supply of the powder to the seed, is not always the most convenient from the point of view of thermal insulation and reliability of the torch itself. Therefore, the selection of the optimum relationship between the velocities of these streams is a tricky problem.

(b) Torches with water cooling. Cooling water is made to flow upwards between two concentric quartz tubes, which forms a water jacket. The construction of torches of this type has been described by Reboux (1963).

Plasma torches with water cooling of the quartz tube always have an upper limit in respect of power dissipation because quartz cannot withstand thermal shock and cracks appear in it through which water seeps into the discharge zone. Therefore, it is always neccessary either to have sufficiently high velocity of the gas stream or to restrict the power consumed in torches of 20-35 mm diameter to 3.5-4 kW (in argon). Even in water cooled torches the gas stream velocities are subject to certain conditions which must be satisfied in order to provide thermal insulation.

(c) A device proposed by Dresvin, Donskoi and Patnikov (1965). This consists of a quartz tube with an internal coil comprising an assembly of water cooled copper tubes placed parallel to the inductor axis. Such a construction makes it possible to obtain an induced electrodeless discharge of several tens of kilowatts power, and to continue the discharge for an

indefinite period of time.

Dresvin claims great success for this type of plasma torch. Such a construction does not impose special conditions on the gas stream velocity. Therefore, the velocities may be selected solely on the basis of the best conditions for crystal growth. However, the replacement of a quartz tube with a copper system removes the possibility of observing the plasma and feed tubes directly. This is undersirable in the construction of a refractory growth system.

3.3 DETAILS OF THE CRYSTAL GROWTH SYSTEM EMPLOYED

3.3.1 Plasma gun and probe

The plasma gun consisted of two concentric tubes of quartz glass (see figure 3.1). The outer tube had dimensions of 43 mm I/D and 31.12 cm length. The inner tube had dimensions of 31 mm I/D and 8.89 cm length (see figure 3.2). These tubes were mounted into a brass holder using asbestos packing wool. Channels machined in the brass holder acted as gas jets and allowed gas to be admitted to the outer space between the two quartz tubes and into the inner space referred to as the plasma space. The jets were arranged in such a way that laminar flow was maintained in the central space. Any turbulence led to instability and quenching of the plasma.

The work coil was $4\frac{1}{2}$ turns of 4.8 mm copper tubing wound on a 50 mm former with 4.8 cm spacing. The coil was water cooled internally and air cooled externally. Power was supplied by an r.f. generator operating at 2.6 MHz.

The probe through which the feed material was fed consisted of two parts. The upper portion was made of brass with an outer diameter of 9.6 mm and internal diameter of 1.93 mm. The lower portion was made of copper with an outer diameter of 0.56 mm and internal diameter of 1.93 mm. The tip of the probe was water cooled.

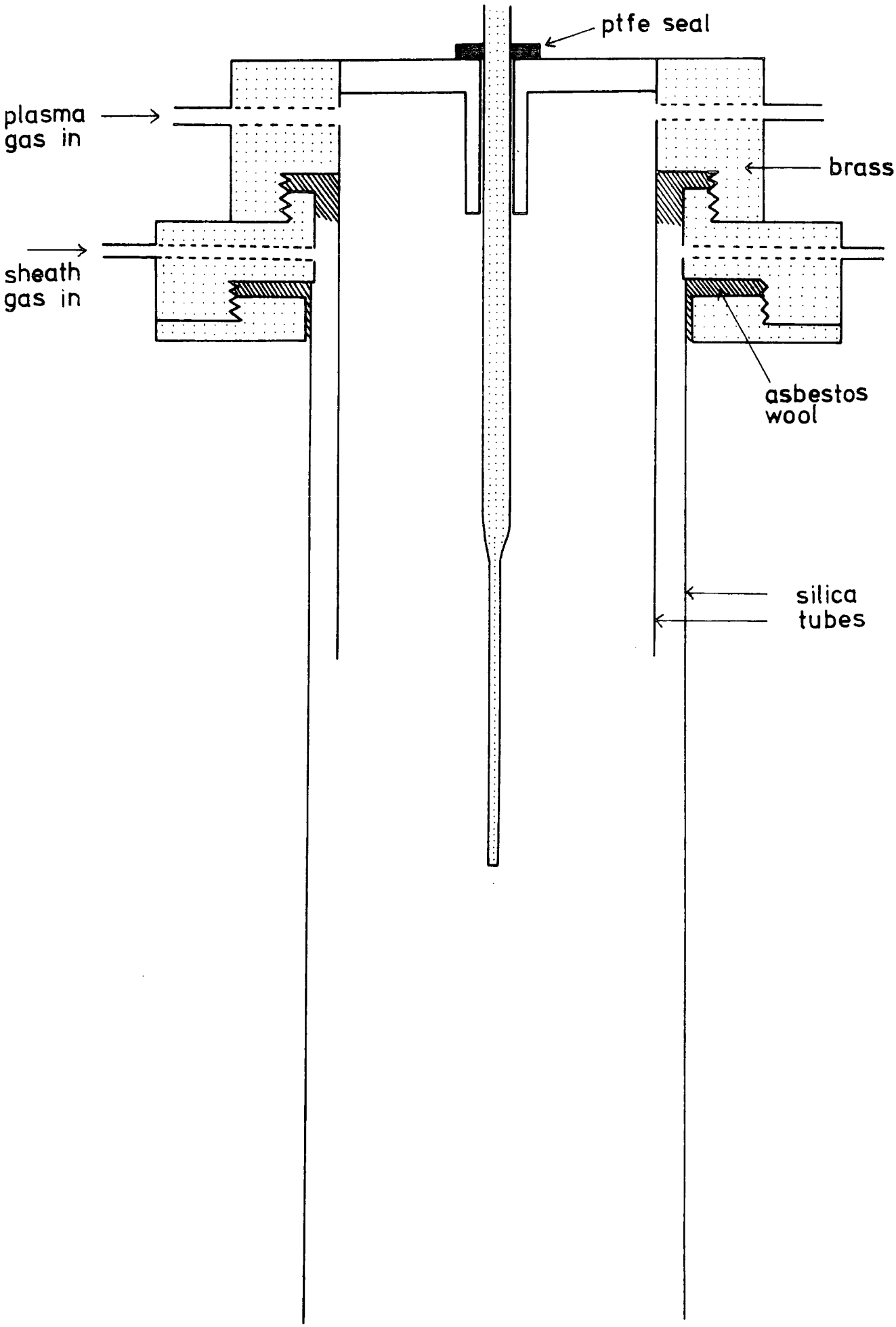

Figure 3.1 Schematic of the plasma gun

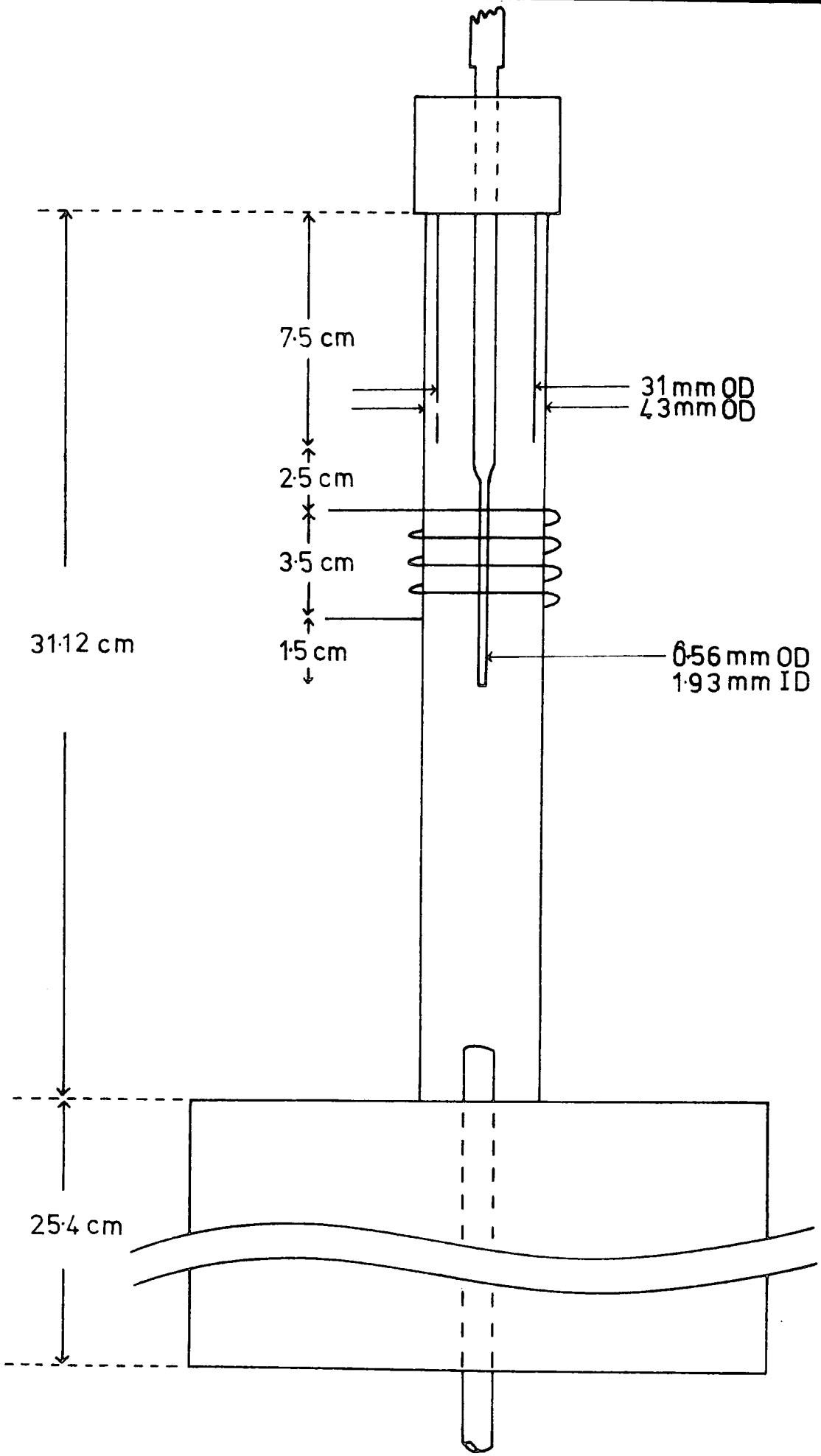

Figure 3.2 Schematic of plasma growth system

3.3.2 R.F.generator

When a large power output is required, but it is not necessary to have the highest frequency stability, an oscillator run under 'Class C' conditions is used. This is similar to the 'Class C' amplifier and gives high efficiency; it may be regarded as an amplifier with regeneration to supply the grid voltage. The mean potential is well beyond the cut-off value for the tube, and the excitation voltage must therefore have sufficient amplitude to carry the tube into the conducting region at the positive peaks.

The r.f. generator used to induce power into the plasma torch was supplied by Lepel. The unit was used with a triode anode voltage of 4.4 kV supplying 15.2 kWatts to the tank circuit. The tank capacitance was made up of two components, 1250 pf from a bank of fixed capacitors in parallel with a variable 50 pf tuning capacitor. The inductance of the tank circuit was 5μH. The r.f. power was coupled inductively to the plasma using a four and half turn copper coil.

The frequency of operation was measured at 2.58 MHz. When the plasma was ignited the frequency of operation increased to 2.61 MHz. This was caused by the reflected inductance of the plasma into the tank circuit.

3.3.3 Hopper feed

The hopper consisted of two concentric perspex tubes. The inner tube was filled with the feed material and terminated with a 200 gauge stainless steel gauze (see figure 3.3). This gauze was connected via a silver rod to a Goodman vibrator. The amplitude of the sinusoidal vibration was provided by an Advance oscillator at a frequency of 100 Hz. The millivolt output provided by the oscillator was monitored by a voltmeter.

A flow of oxygen was provided to the inner and outer perspex tubes

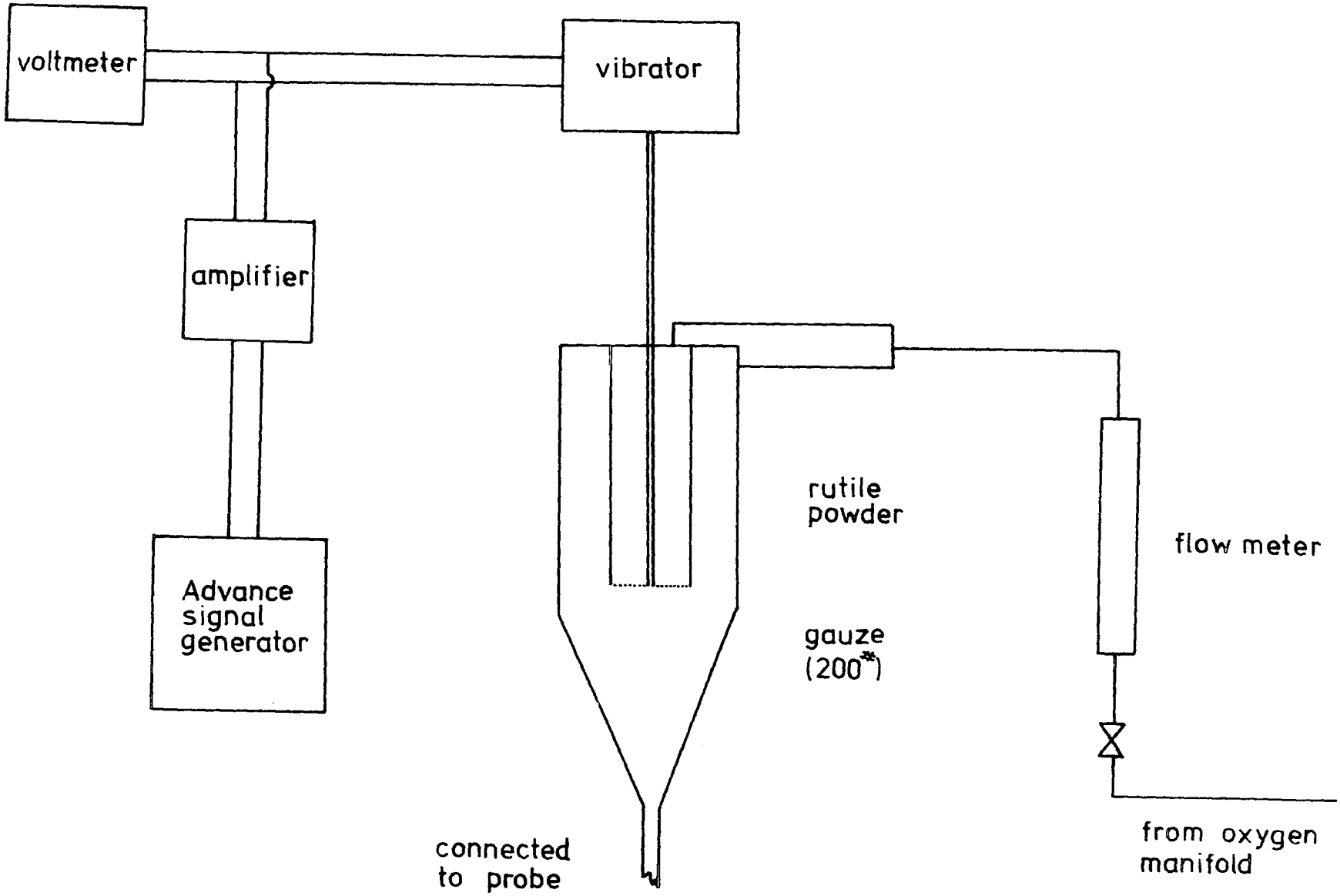

Figure 3.3 Schematic of the hopper feed system

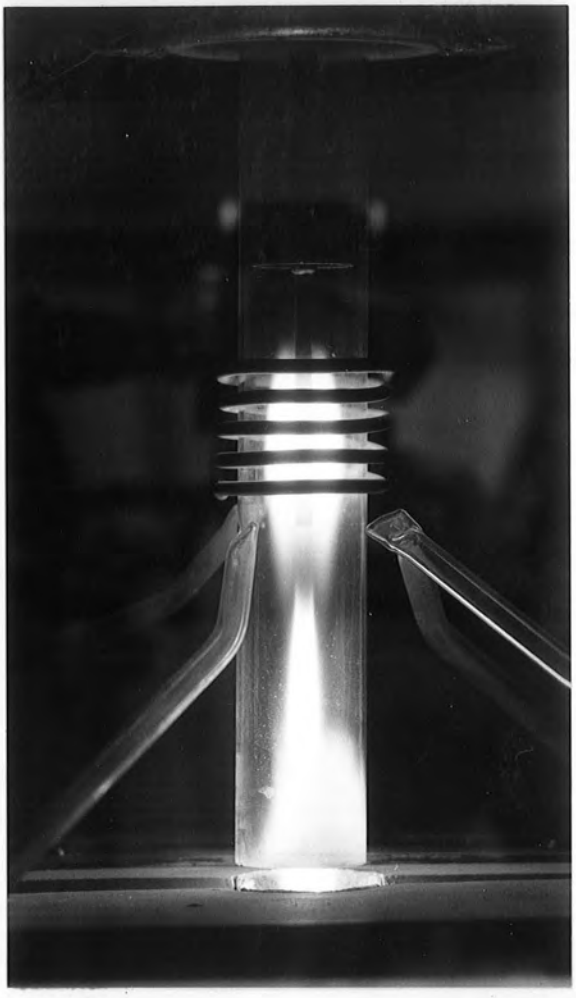

Figure 3.4

Plasma torch

Figure 3.5

Observation of rutile
crystal growth interface

to provide a constant flow of feed material to the probe. A flow of 1 litre/min was used for the growth of single crystal rutile.

The feed hopper was connected to the probe by a glass tube, drawn out to fit the hopper bottom and the top of the probe, using PVC heat shrink tubing. The feed material was provided by BTP Stockton and consisted of 'sandy' rutile powder. This powder had a particle size distribution of 40±2μ diameter. It gave an extremely uniform flow through the hopper gauze.

3.4 CRYSTAL GROWTH OF SINGLE CRYSTAL RUTILE

In order to form the plasma 8.0 kWatts was supplied to the work coil. The water cooled copper coil was externally cooled with a blast of cool air from four jets (see figure 3.4). Initially a flow of argon into the sheath space of 21 l/min was provided together with a flow of 25 l/min into the plasma space. Care was taken to eliminate the possibility of air being sucked into the system and quenching the plasma. The plasma was ignited using a Tesla coil. However, any method of reducing the ionisation potential of the argon to ignite the plasma may be used e.g. a hot wire. Immediately the plasma was formed the flow of argon into the plasma space was increased to 37 l/min, and the power was increased from 8.0 to 15.0kW. After about 5 min when the plasma had stabilised, a stream of oxygen, at a rate of 5 l/min, was admitted to the plasma space. The resultant argon-oxygen plasma was that used for the growth of the rutile crystals. Attempts to increase the oxygen content led to uncontrollable instabilities.

Since the plasma was hollow at the core, rutile powder could be introduced into it via a water cooled probe which was lowered along the axis of the plasma once stability had been achieved. The rutile powder was introduced into the feed probe from a hopper which is illustrated diagrammatically in Fig. 3.3. Chase and van Ruyven (1969) used a sub-

micron powder which tended to cake and was therefore difficult to feed at a constant rate. For our experiments a free flowing powder, described as sandy rutile, gave a uniform flow through the plasma. The rutile powder passed through the plasma at a rate which was varied between 0.05 and 0.30 g/min. The powder melted in the plasma and the liquid drops were collected on top of an alumina candle which was a rod some 60 cm long and 0.95 cm in diameter. The candle was connected to an automatic withdrawal mechanism and could be lowered at between 5 and 30 mm/hour while being rotated at 6 revolutions/min. A manual overide control was available for correcting the small changes of conditions that occurred during a growth run, which lasted between two to four hours. In practise the candle was withdrawn through a 25cm long muffle furnace which acted as an after-heater. The muffle furnace was made of magnelite bricks and was coated with alumina cement to improve its heat retention properties.

Once the feed powder was introduced into the argon-oxygen plasma, the alumina candle was positioned with its tip some 50 to 60 cm below the lowest visible portion of the plasma. With this configuration a poly-crystalline deposit was first obtained on the tip of the candle which was raised slowly until the rutile deposit melted. This position of the molten interface indicated the growth zone under the conditions of the particular run (see figure 3.5). Crystals were then grown over a period of 3 to 4 hours while the candle was lowered to maintain the growth interface at a constant depth below the bottom of the visible plasma. With the gas flow and powder feed rates described above, boules, some 1 cm in diameter and up to 6 or 8 cm in length, were grown in a reproducible manner. After a boule had been grown it was found that to avoid subsequent cracking, it was necessary to cool it slowly through the first 500°C drop in temperature. To achieve this the candle was withdrawn to the centre of the muffle; at the same time the powder feed was slowly turned off by reducing the carrier gas flow to the hopper. Next

Figure 3.6

Rutile crystal immediately after turning off plasma

Figure 3.7

Rutile crystal on the alumina candle

the flow of oxygen to the plasma space was gradually reduced to about 10 kW and then the plasma was extinguished (see figure 3.6). The streams of argon were discontinued immediately. The boule was left to cool in the muffle for 12 hrs before it was seperated from the candle (see figure 3.7). It was found by trial and error that the state of oxidation was affected by (1) the position of the feed probe in the plasma and (2) the position of the growth interface to the bottom of the visible plasma. The position of the feed probe was much the more important, and reduced crystals were obtained when the feed powder was introduced into the middle of the 30 cm long visible region of the plasma. When the powder was fed into the lower half of the plasma an oxidised crystal was produced. Generally speaking it was also desirable to maintain the growth interface some 2 to 3 cm nearer the bottom end of the visible plasma when oxidised crystals were required. To demonstrate the ease with which the state of oxidation of a boule could be changed one boule was grown with its top half produced under oxidising conditions and its bottom half under reducing conditions. The top half was colourless and transparent and was seperated from the dark-blue non-stoichiometric bottom half by a grain boundary.

Most of the boules produced were from 1.0 to 1.5 cm in diameter and from 3 to 5 cm long. With our experimental arrangement the slowest growth rate at which it was possible to produce boules with high crystallographic quality was 1.5 cm/hour. The corresponding feed rate of rutile powder was 70 mg/min, of which 50 to 60% condensed on the candle. Reduction of the feed rate below this level, in an attempt to slow the growth further, led to evaporation of the growing crystal with the consequence that a smaller and inferior quality boule was ultimately produced.

X-ray back reflection studies showed that most of the boules were mono-crystalline. They had grown with their c-axes within 5° of the axes of the approximately cylindrical boules. The X-ray investigation also showed

that the c-axis wander was negligible.

3.5 UNDOPED RUTILE CRYSTALS

The tetrachloride, $TiCl_4$, is one of the most important titanium compounds since it is the usual starting point for the preparation of most other titanium compounds. It is colourless liquid, m.p. -23°, b.p. 136°, with a pungent odour. It fumes strongly in air and is vigorously, though not violently, hydrolysed by water.

$$TiCl_4 + 2H_2O \longrightarrow TiO_2 + 4HCl$$

Naturally occurring forms of rutile are usually coloured, sometimes even black, owing to the presence of impurities such as iron. Pigment - grade material is generally made by hydrolysis of $TiOSO_4$ or vapour phase oxidation of $TiCl_4$ with oxygen.

Three batches of sandy rutile were prepared in a laboratory reactor at BTP Stockton (DN1, DN2 and DN3). The starting material was 'plant' titanium tetrachloride as used in the commercial production process. The MS7 mass spectrographic analysis of these samples is given in table 3.1. When three crystals (BS1, BS2 and BS3) were grown from this feed material and subsequently oxidised, a reddish-brown tint was noticeable. This absorption could possibly be due to the relatively high iron content of these crystals (see table 3.3).

In an attempt to obtain higher purity crystals the 'plant' titanium tetrachloride was triple distilled. The next two batches of sandy rutile, DN4 and DN5, were made from this starting material. BS10 and BS13 were two boules grown from DN4 and DN5 respectively. By examining the mass spectrometer results (table 3.2) it can be concluded that DN4 and DN5 produce a lower alumina and iron content in the rutile crystals. However, the triple distillation does not appear to have affected the two principal

	DN1	DN2	DN3	DN4	DN5
Al	<100	<100	200	<1	<1.5
Nb	<10	<10	<10	1	1
Fe	10	49	725	2	2
Ca	14	8	9	7	7
Zn	<17	<17	<17	<7	<8
Sn	<17	<17	<17	6	6
Si	600	<100	300	<47	<47
P	<100	<100	130	30	30
S	400	<100	<200	<40	<40
Zr	8	7	15	1	<1
K	12	9	38	17	16
Sb	<14	<14	<14	<1	<1
Mg				12	18
Mn				0.1	0.5
Cr				<2	0.4

All quantities in ppma .

Table 3.1 Mass spectrographic analysis of sandy rutile powders.

	Sandy rutile DN1	Single crystal BS3	Sandy rutile DN4	Single crystal BS10	Sandy rutile DN5	Single crystal BS13
Al	<100	16	<1	5	<1.5	4
Nb	<10	9	1	4	1	9
Fe	10	27	2	4	2	5
Ca	14	7	7	7	7	7
Zn	<17	<8	<7	<4	<8	<1
Sn	<17	<1	6	<1	6	<1
Si	600	47	<47	112	<47	75
P	<100	<1	30	<1	30	<1
S	400	267	<40	670	<40	200
Zr	8	1.5	1	1	<1	1
K	12	4	17	3	16	3
Sb	<14	<1	<1	<1	<1	<1
Mg		5	12	19	18	4
V		0.2	5	0.2	0.8	0.2
Mn		0.5	0.1	0.2	0.5	0.2
Cr		0.4	<2	0.4	<2	0.4

All quantities in ppma .

Table 3.2 Comparison of the mass spectrographic analysis of the sandy rutile feed material and single crystals.

CRYSTAL	BS1	BS3	BS10	BS11	BS13	BS14	BS16	BS18	BS12	BS19
DOPANT				Al		Mn	Al		Nb	Nb
Mg	7	5	19	19	4	16	8	7	26	4
Al	16	16	5	53	4	16	1060	11	11	19
Si	200	47	112	112	75	467	47	92	47	75
P	<1	<1	<1	<1	<1	<1	<1	<1	<1	<1
S	130	267	670	330	200	1300	670	250	1300	680
K	4	4	3	6	3	6	6	7	6	2
Ca	7	7	7	8	7	10	5	3	10	4
V	0.2	0.2	0.2	0.2	0.2	0.2	0.2	0.2	0.2	0.3
Cr	0.4	0.4	0.4	0.9	0.4	0.7	0.1	0.7	<4	0.2
Mn	0.5	0.5	0.2	0.5	0.2	77	0.5	0.1	0.1	0.1
Fe	18	27	4	25	5	15	3	12	12	14
Ni	<2	<2	<2	<2	<2	<2	<2	<2	<2	<1
Co	<2	<2	<2	<2	<2	<2	<2	<2	<2	<2
Cu	<1	<1	<1	<1	<1	<1	<1	<1	<1	<1
As	0.5	0.5	0.5	0.7	0.3	0.2	0.5	0.4	0.7	0.7
Sr	<1	<1			<4	0.1	0.7			0.4
Zr	1.5	1.5	1.0	1.0	1.0	3	3	1.0	3	1.5
Nb	9	9	4	6	9	9	9	6	477	140
Mo	3	3	7	13	2	2	3	3	7	2
Sn	<1	<1	<1	<1	<1	<1	<1	<1	<1	<1
Sb	<1	<1	<1	<1	<1	<1	<1	<1	<1	<1
Y			0.5	0.9					1.8	
SANDY RUTILE	DN1	DN1	DN4	DN4	DN5	DN5	DN5	DN5	DN5	DN5

All quantities in ppma.

Table 3.3 Mass spectrographic analysis of plasma grown rutile crystals.

	Crystal ppma
Al	40
Pb	15
P	207
Si	112
Mg	12
Nb	7
Ba	<1
Fe	20
V	<5
Ca	19
Zr	2
K	2
Hf	<5
Mo	<3
W	<3
Sn	3
Mn	2

Table 3.4 Mass spectrographic analysis of the National Lead crystal CA3(NL).

impurities in the crystals, that is silica and sulphur. Infact, sulphur was the only impurity to have increased substantially in concentration during growth.

3.6 DOPED RUTILE CRYSTALS

Two methods of introducing the dopant into the sandy rutile were examined i.e. via solid powders and aqueous solutions.

(a) Solid powders

The first method consisted of weighing a quantity of sandy rutile and placing it in a polythene bottle. An appropriate quantity of dopant was then added and the aggregate was then placed on rollers for 48 hours. The sandy rutile particles did not break up and retained their free flowing properties. This method worked well with dopants that were available in the form of powders with particle sizes of about 0.1μ. Aluminum powder, iron fillings and niobium oxide (Nb_2O_5) powder were introduced fairly easily using this method.

Two boules BS11 and BS16 were grown with 53 ppma and 1060 ppma aluminum impurity. Two boules BS12 and BS19 were grown with 477 ppma and 140 ppma niobium impurity. The boule BS15 was grown using iron fillings, at 100 ppma in the powder, and a single crystal was grown which appeared to have a non-uniform doping distribution. The centre of the boule was yellow, whilst the edge of the boule was dark red with an orange transition region in between. Unfortunately no mass spectrographic analysis is available for this boule.

			ppm powder calculated	ppm crystal MS7 analysis
BS11	0.0162 gms Al	100 gms TiO_2	305	53
BS16	0.1116 gms Al	289 gms TiO_2	730	1060
BS12	0.0848 gms Nb_2O_5	100 gms TiO_2	1213	477
BS19	0.0848 gms Nb_2O_5	250 gms TiO_2	485	140

(b) Aqueous solutions

Some dopants were not available in the fine powders required by the first method. Manganese dioxide was tried as the dopant but it was impossible to reduce it to a useful powder form. Hence the aqueous solution method was evaluated.

In this second method a soluble compound of the dopant was made into an aqueous solution. A known quantity of sandy rutile was then poured into the aqueous solution and then a known quantity of the solution was decanted off. The remaining slurry was placed in an oven at 120°C and the excess water was evaporated. Normally the action of water on sandy rutile is such as to break up the particles making it impossible to feed from the plasma growth hopper. However, it was found that by careful and slow mixing of the sandy rutile and the aqueous solution, this method was capable of producing good feed material.

A boule BS14 was grown using this method and an impurity content of 77 ppma Mn was obtained. Manganeous chloride ($MnCl_2 \cdot 4H_2$)) was used as the dopant.

BS14 1.220 gms of $MnCl_2 \cdot H_2O$ in 250 ml H_2O

30 ml of aqueous solution added to 100 gms TiO_2

An attempt to dope sandy rutile samples with aluminum using an aqueous solution of aluminum sulphate did not prove so successful. Samples with aluminum contents 1000 ppm and 2000 ppm were prepared, decanted and dried. However, the sandy rutile formed a hard solid mass on the dried surface with a powder underneath. This solid crust had a distinct grey colour although the sandy rutile underneath was white.

3.7 DIFFUSION DOPING OF RUTILE CRYSTALS

A limited amount of time was available for the growth of single crystal rutile and so alternative methods of doping were investigated. Metal ions

deposited onto the surface of rutile migrate into the bulk of the crystal at a rate dependent on the ion size and the temperature. Interstitial diffusion along the c-axis is strongly anisotropic, for example, lithium diffusion perpendicular to the c-axis being at least 10^8 slower than diffusion parallel to the c-axis (Kingsbury et al 1968). Diffusion of larger ions than lithium is limited almost entirely to diffusion along the c-axis channels.

A series of metals were vacuum evaporated onto a crystal face cut perpendicular to the c-axis. The crystals were then heated to 1000°C for 24 hours in a stream of oxygen. This method proved successful for nickel and chromium doping, but difficulty was found in preparing suitable evaporated films of all the metals required.

The second method of diffusion doping consisted of heating the crystal and metal together in an evacuated ampoule. The crystal and metal were placed together in a quartz ampoule, evacuated to 10^{-7} torr and heated to 500°C to drive off any residual gases. The ampoule was then sealed, placed in a furnace and heated to a predetermined temperature. Some of the vapour pressures for the metals investigated are given in table 3.7.1, the data was obtained from the Sloan technical manual and, Kaye and Laby. After a period of time at the required temperature, usually 24 hours, the sample was slowly cooled to room temperature. At this stage the crystal was black in colour and required an oxidation treatment similar to that given to non-stoichiometric as-grown crystals, whereupon the crystals attained their characteristic colours. Figure 3.7.2 shows some of the crystals doped by this method and the plasma doping method. The crystals appeared to have a uniform colour suggesting a uniform doping distribution. A complete summary and investigation of the doped rutile crystals is described in chapter 9.

	Melting point °C	Density g/cm^3	Temperature °C at vapour pressure 10^{-8}	10^{-6}	10^{-4} torr
Aluminum	660	2.70	677	821	1010
Chromium	1890	7.20	837	977	1157
Cobalt	1495	8.90	850	990	1200
Copper	1083	8.92	727	857	1017
Indium	157	7.30	487	597	742
Iron	1535	7.86	858	998	1180
Manganese	650	2.98	507	572	647
Nickel	1453	8.90	927	1072	1262
Niobium	2468	8.55	1728	1977	2287
Silver	961	10.49	847	958	1105
Titanium	1675	4.50	1067	1235	1453
Vanadium	1890	5.96	1162	1332	1547
Zinc	419	7.14	127	117	250

Table 3.7.1 Technical data of some important impurities in rutile .

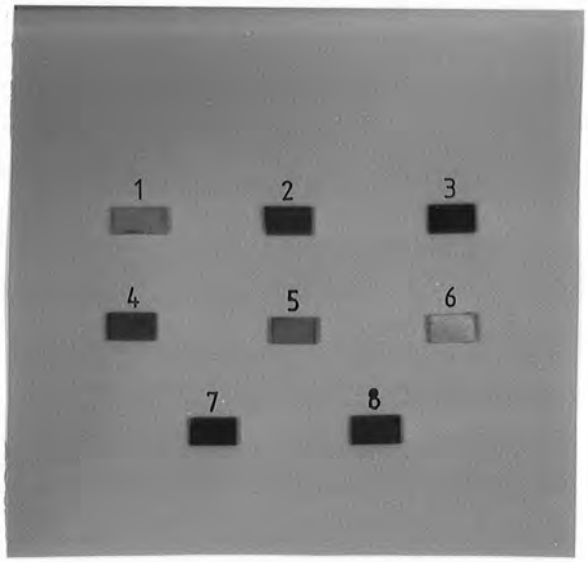

Figure 3.7.2 Photograph of the doped rutile crystals.

(1) Mn , MN(NL) ; (2) Co , CO(NL) ; (3) reduced , CA3(NL) ;

(4) Fe , FE(NL) ; (5) Ni , NI(NL) ; (6) undoped , BS18(S) ;

(7) Nb , BS12 ; (8) Mn , BS14 .

CHAPTER 4

EXPERIMENTAL TECHNIQUE

4.1 SAMPLE PREPARATION

The single crystal rutile boules were aligned using an X-ray back-reflection technique, and a diamond saw was used to cut samples with their lengths either parallel or perpendicular to the crystallographic c-axis (within $\pm 1^{\circ}$). The majority of samples were in the shape of a rectangular block, with typical dimensions of 6 x 3 x 1 mm^3.

After cutting, each sample was mechanically polished on a lapping wheel down to a diamond grit size of 1μm, and finally using 0.3μm anatase powder. The stoichiometric as-grown crystals were chemically etched in boiling concentrated H_2SO_4 for two hours in an attempt to remove surface damage. A final wash in trichloroethylene, deionised water and methanol served to remove any residual grease. Although the treatment in sulphuric acid improved the crystal surface, scratch marks could be observed on the final etched surface.

Titanium dioxide is a very stable compound resisting attack by many chemical agents. It is insoluble in water and in most hydroxide and acid solutions. It dissolves slowly in hydrofluoric acid, in hot sulphuric acid (Kwietniak and Piekarczyk 1972) and in molten potassium and sodium hydroxides (Hirthe et al 1961, Hirthe and Brittain 1962). These properties make it difficult to select a suitable etching agent. Hirthe et al (1961, 1962) used sodium and potassium hydroxides for the etchpolishing of TiO_2 surfaces. However, KOH proved to be a more active agent than NaOH and they settled on a standard etch of 8 minutes at 650°C in KOH.

Piekarczyk (1969) found that the equi-molar mixture of sodium and potassium hydroxides gave a better etch-polish than any of these hydroxides seperately, and this mixture has been used throughout the present work for

the preparation of samples from the non-stoichiometric as-grown crystals. The samples were placed in a platinum crucible containing a powdered mixture of the hydroxides. The aim of this stage was to melt the etching mixture and to remove water and carbon dioxide. When the temperature reached 700°C (dark-red glow) the crucible heater was turned off, and the sample was allowed to cool to room temperature. Pickarczyk estimated that approximately 100 μm of material was removed by this process and indeed layers 10 μm to 80 μm thick were removed from the present samples.

After cooling, the mixture of molten hydroxides, together with the crystal was dissolved in water to seperate the mixture. An etched surface had a mirror-like appearance with a white deposit which was easy to remove by boiling in hydrochloric acid for 15 minutes. After this no scratch marks could be observed in crystals with the H_2SO_4 treated crystals.

In the hydroxide etchpolishing process the crystal surface undergoes partial reduction and stoichiometric samples that were subjected to this treatment developed a blue tint. Consequently samples from stoichiometric crystals were prepared using the H_2SO_4 method. The non-stoichiometric samples were subsequently oxidised in a stream of oxygen at 1300°C for 3 days. The furnace was then cooled at about 25°C/hour using a voltage ramp in place of the thermocouple.

4.2 CONTACT FABRICATION

Vacuum deposited silver or titanium/gold have been used successfully to form excellent ohmic contacts to single crystal rutile. Durofix was used to mask that part of the surface to which no metal was to be applied. Silver or titanium/gold metal was then evaporated at a pressure of 10^{-5} torr and the Durofix removed by washing in acetone.

To enable the sample to be inserted into a cryostat, it was first mounted on a thin silica slide (20 thou thick), using an air-drying silver

paste to make contact between the evaporated metal and the contact wires. The silver paste also served to hold the sample to the silica slide. This method allowed good electrical insulation to be obtained between the sample and the metal cryostat, and also ensured mechanically strong contacts.

The silica slide was attached to the copper block of the cryostat using a thin smear of high-vacuum silicone grease which acted as an adhesive and also improved the thermal conduction between the block and sample. The temperature of the sample was measured by a copper-constantan thermocouple, the junction of which was soldered with indium to the silica slide close to the crystal. Direct contact between the thermocouple and sample was not feasible. If direct contact was made excessive electrical noise was generated which affected the measurement of small currents.

4.3 LIQUID NITROGEN CRYOSTAT

For optical and electrical measurements the crystals were mounted in the cryostat illustrated in figure 4.3.1.

The upper part of the cryostat was made of German-silver which reduced heat losses from the copper mounting block and formed a Dewar. Samples mounted on the copper cold finger could be rotated depending on the experiment. The two quartz windows were demountable and were held in position with the cryostat under vacuum by an O-ring seal. The vacuum in the cryostat was provided by a rotary pump with the option of an oil diffusion pump and liquid nitrogen trap when required.

The sample was cooled by introducing liquid into the central tube of the cryostat to which the copper block was attached. Subsequent heating of the sample was achieved by inserting a heater coil, wound inside a silica tube, into the central tube and passing a d.c. current.

The cryostat had a low thermal inertia so that heating could be

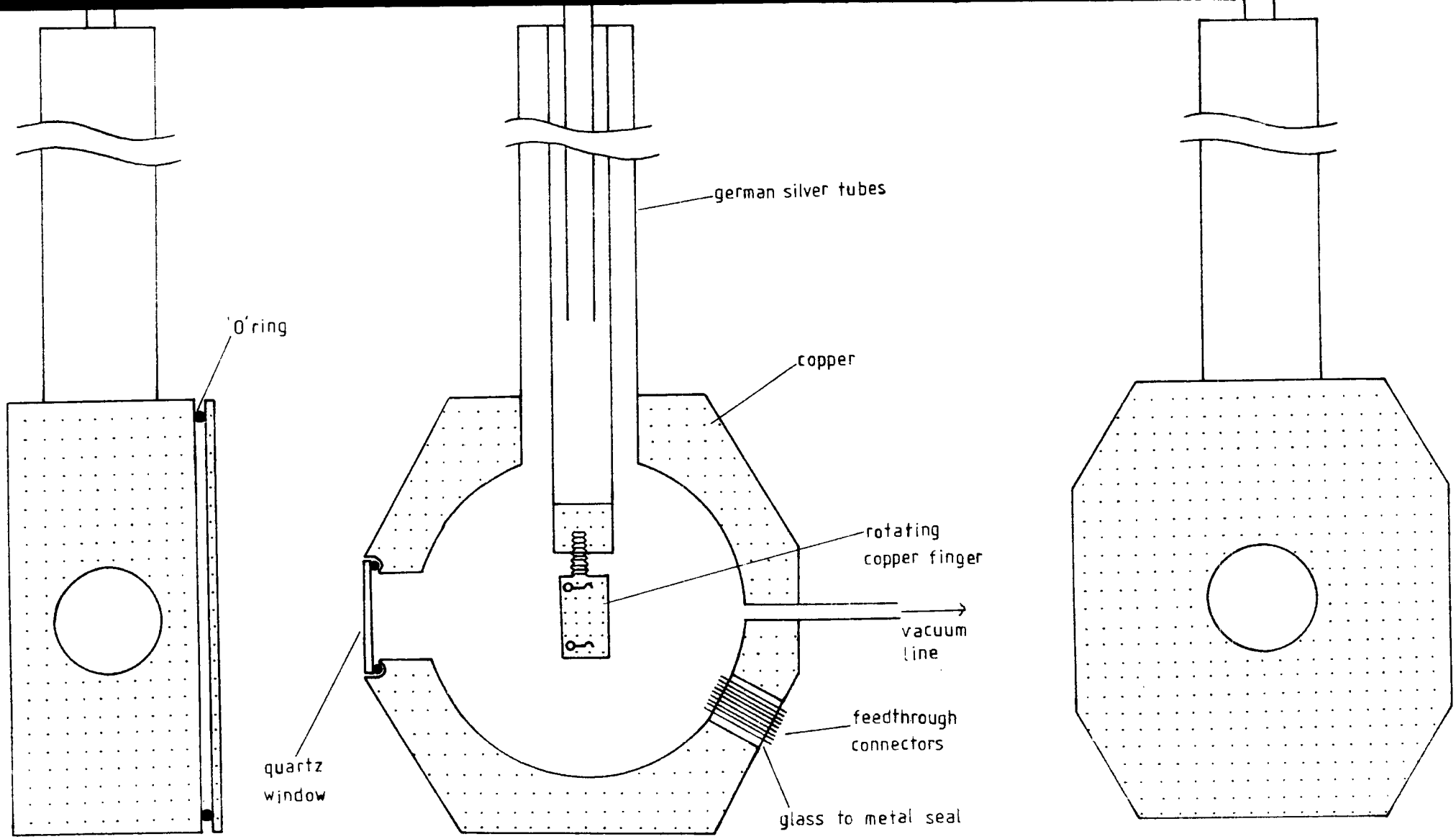

Figure 4.3.1 Liquid nitrogen cryostat.

stopped at any required temperature, or the heating rate changed quite quickly. Temperatures between 77 K and 400 K were attainable in this system, with heating rates of between 42° and 1°/ minute for heater currents of 2.7A to 0.6A. Figure 4.3.2 (a) shows the variation of the heating rate with sample temperature for various constant heater current settings. The heating rates have been calculated over ten degree increments. Figure 4.3.2 (b) shows the heating rates obtained for various heater current programs determined experimentally to obtain constant heating rate curves. The arrows indicate the temperature at which the heater current sequence, shown in the right hand column, was implemented.

The contact wires to the crystal were soldered to leads in the cryostat which were connected to BNC sockets via glass-to-metal seals. During a TSC or TL experiment a visual output was obtained by taking the output of the electrometer to a potentiometric recorder to obtain a continuous trace of current versus time. A micro-switch on the input to the recorder, when operated, produced a blip on the trace which was used to mark the temperature every five degrees.

4.4 LOW CURRENT MEASUREMENTS

The risetime of a pico-ammeter is defined as the time taken, t_r, for the output to change from 10% to 90% of its final value, in response to a step current input. Another alternative is to express the speed in terms of the time constant of an equivalent CR network. An approximate expression relating these is given by Keithley (1972)

$$t_r = \frac{0.35}{f_{3db}} = 2.2\ C\ R$$

where f_{3db} is the 3db bandwidth.

The straightforward method of measuring a current is to pass it through a sufficiently large resistor and monitor the voltage drop. This is known

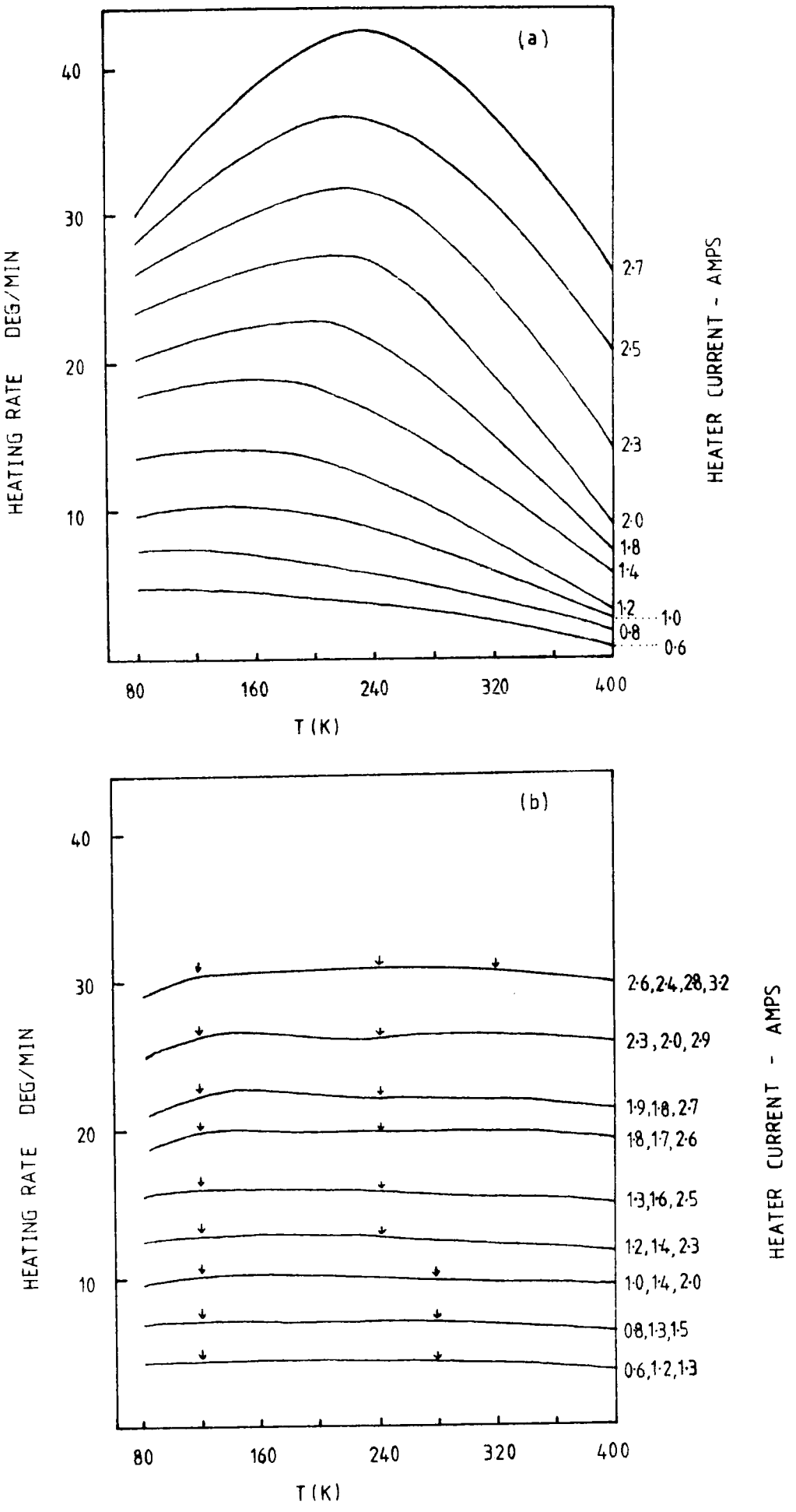

Figure 4.3.2 Heating rates obtained from the liquid nitrogen cryostat for various heating current values.

as the shunt method and requires a high input impedance voltage follower if the subsequent circuitry is not to load the resistor. The major problem concerns the capacitance present at the input, which forms a CR circuit. So for a sensitivity of IV/pA, i.e. a $10^{12}\Omega$ resistor and a stray capacitance of 10pF, the time constant would be 10 seconds. This configuration is used in the NORMAL mode on electrometers.

The alternative is to use the feedback method. This, as the name suggests, places the high value resistor in the feedback loop of a high gain amplifier. This is illustrated in figure 4.4.2 and is the configuration used in the FAST mode on electrometers.

C2 is the total effective capacitance across the input and C1 is the self capacitance of the resistor R1. The amplifier, gain K, is an electrometer, namely having very small input bias currents so as not to swamp the current being measured. The output voltage e_0, expressed as a function of time, in response to a step current of magnitude i, has been shown to be (Pragin and Nichols 1960)

$$e_0 = \frac{-\,i\,R_1}{(1 + 1/K)} \left\{ 1 - \exp \frac{-\,t}{R1\,((C2\,/\,(1 + K)) + C1)} \right\}.$$

Hence, for a sufficiently large K, the time constant is now unaffected by the input capacitance and is only dependent on the self capacitance of the resistor. Typically, this would be 1pF, giving an improvement in the time constant over the previous example from 10 s to 1 s.

The self capacitance can be mininised by the inclusion, in the feedback loop, of a compensation circuit as shown in figure 4.4.3. When this CR network has been adjusted so that

$$C_3\,R_3 = C_1\,R_1$$

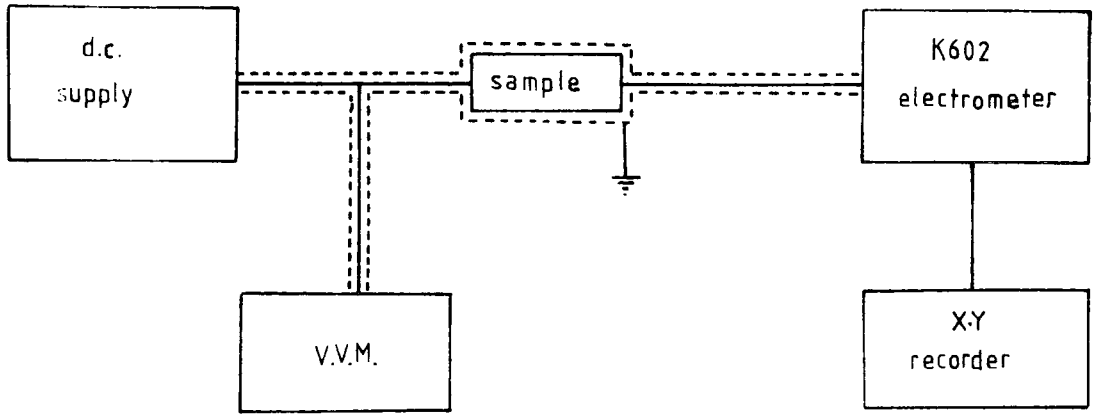

Figure 4.4.1 Electrical circuit for low current measurement.

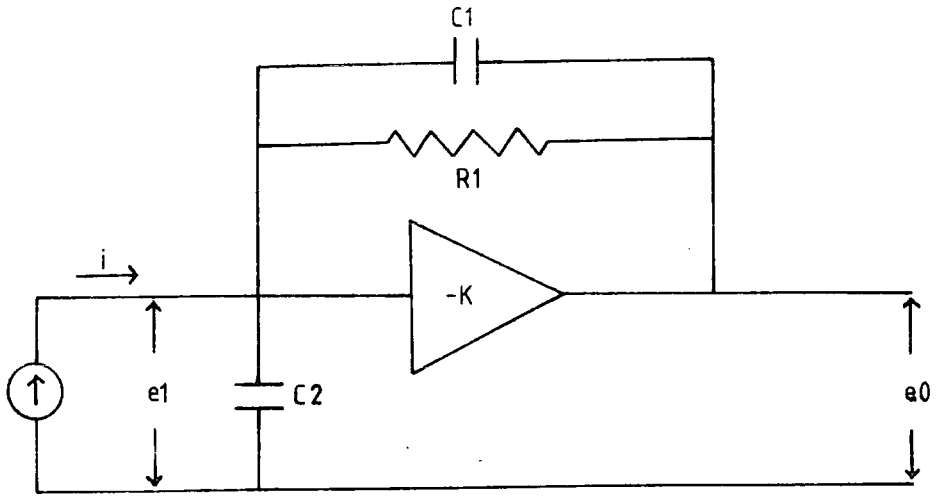

Figure 4.4.2 Circuit using feedback (Presley 1966).

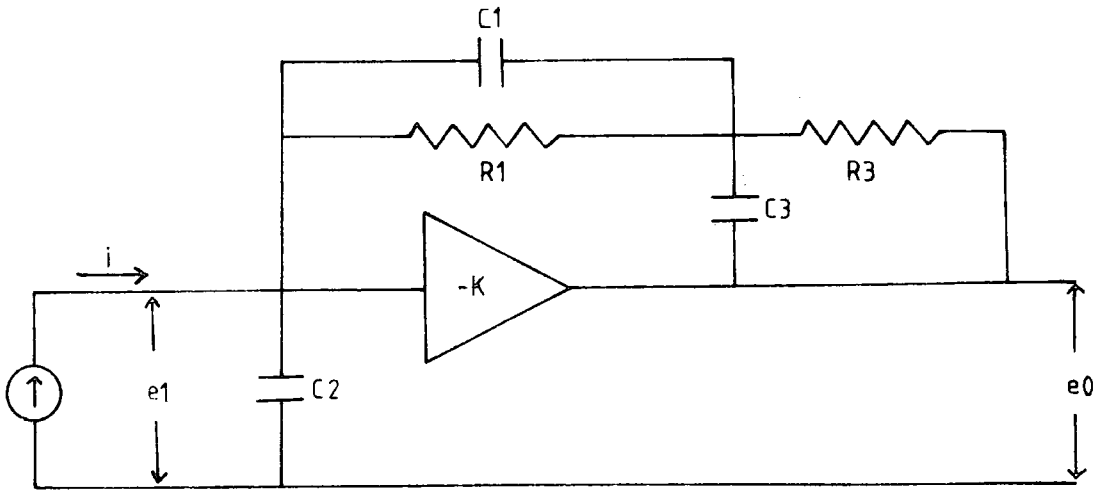

Figure 4.4.3 Circuit using compensated feedback (Presley 1966).

then the new effective time constant has been shown by Praglin and Nichols to be

$$\frac{R_1 (C_1 + C_2)}{K + 1} .$$

This implies that the response speed would now be virtually unlimited. Sadly, the above analyses assume that the self capacitance of the resistor can be lumped together as C_1, but in pratice it is distributed, thus the component acts as a delay line.

There are three major sources of noise in low current measurements:

(a) Johnson noise current in the feedback resistor

(b) Amplifier current noise

(c) Amplifier voltage noise

The RMS Johnson noise current is given by

$$i_n = \sqrt{\frac{4 k T \Delta f}{R}}$$

where Δf is the bandwidth and R is the resistance. This expression assumes that the picoammeter's bandwidth has a sharp cut off, but in practice it will have a 3dB/ octave roll off. Also resistors used never reach their theoretical noise performance, so an emprical expression often used (Weinberger 1965) is

$$i = \frac{\pi}{2} \times 2.2 \times \frac{4 k T 3.5}{R \tau_r}$$

This expression, for a 10^{12} ohm resistor and a risetime of 1 second gives a noise current of about 10^{-14} A.

The amplifier current noise depends on the particular amplifier and the overall risetime, but for modern electrometers, it would typically be 10^{-15} A, and can be ignored.

The amplifier voltage noise unlike the other sources of noise, is

unlimited by the overall bandwidth and depends on the amplifier's open loop bandwidth. This noise voltage can be expressed as an equivalent noise current, when it is referred to the input.

Cath and Peabody (1971) have shown the effect of an increase of input capacitance is an overall increase in the noise spectrum. This shows the importance of minimising this capacitance, even though it has no effect on the risetime of the amplifier in the feedback mode.

Other sources of noise include electrostatic interference and microphonic effects caused by changes in the input capacitance. The remedy is to have good shielding and to make all input connections rigid.

Figure 4.4.1 shows the experimental arrangement for the measurement of low currents. All cables were as short as possible and semi-rigid non-microphonic co-axial cable was used for all connections in an effort to minimise pick-up and noise. A system of guarded connectors was used throughout the system and care was taken to avoid earth loops. A d.c. voltage, derived from dry batteries via a series of potential dividers, was applied to the sample and was monitored using a high impedance value voltmeter. The current through the sample was measured with a Keithley electrometer model 602.

4.5 THE OPTICAL APPARATUS

The monochromator used in the PC and PL experiments was a Hilger and Watts D330/MK 11 diffraction grating device. Two gratings blazed for 0.5 μm (1200 L/mm) and 1.0 μm (600 L/mm) were available. These had dispersions of 26 and 50 Å/mm respectively. A slit width of 1 mm was used for the majority of experiments. Three scanning motors 1 RPM, 2 RPM and 5 RPM were available and were particularly useful for the PSC experiments.

Figures 4.5.1 and 4.5.2 show the throughput of the optical system which included the 500 W tungstun source, the cryostat cold finger, the

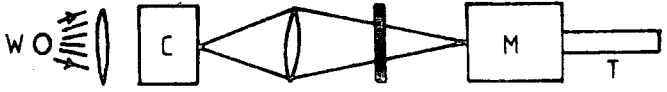

F optical filter
W 500W tungstun bulb
C cryostat
M monochromator
T thermopile

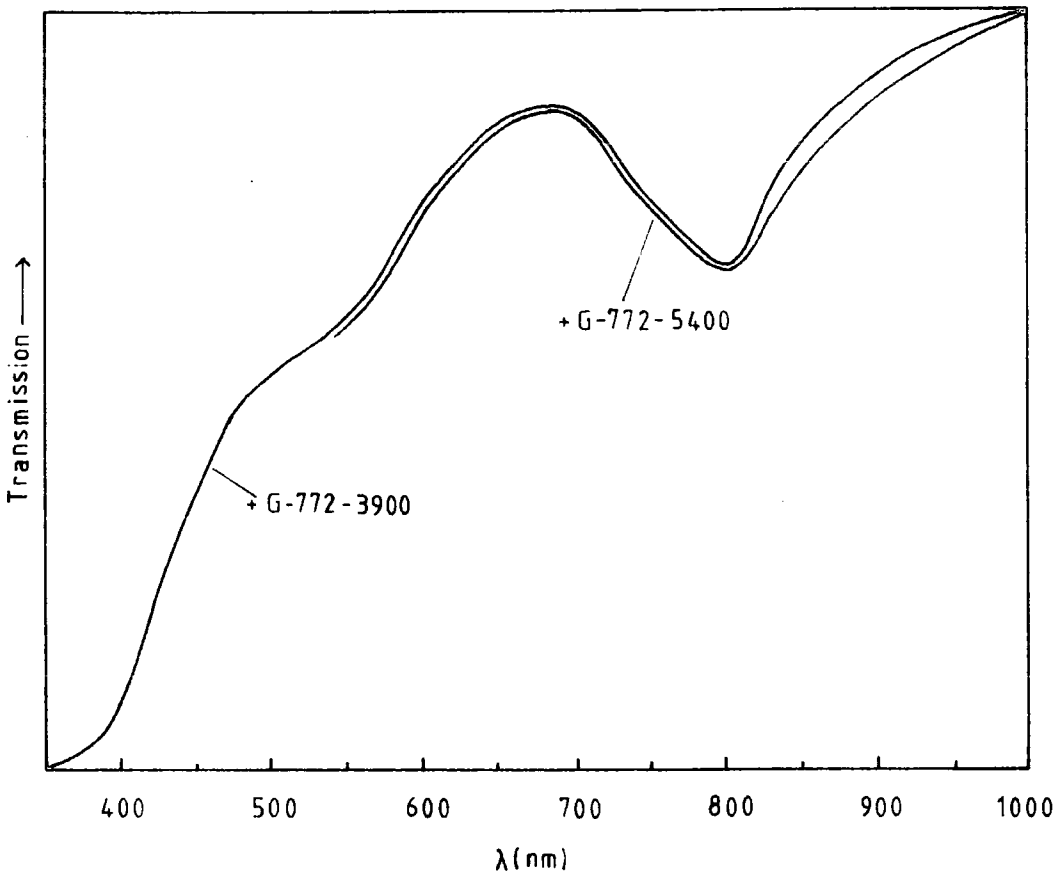

Figure 4.5.1 Throughput of the optical system using the thermopile detector, 1mm slits and the 0.5 μm grating.

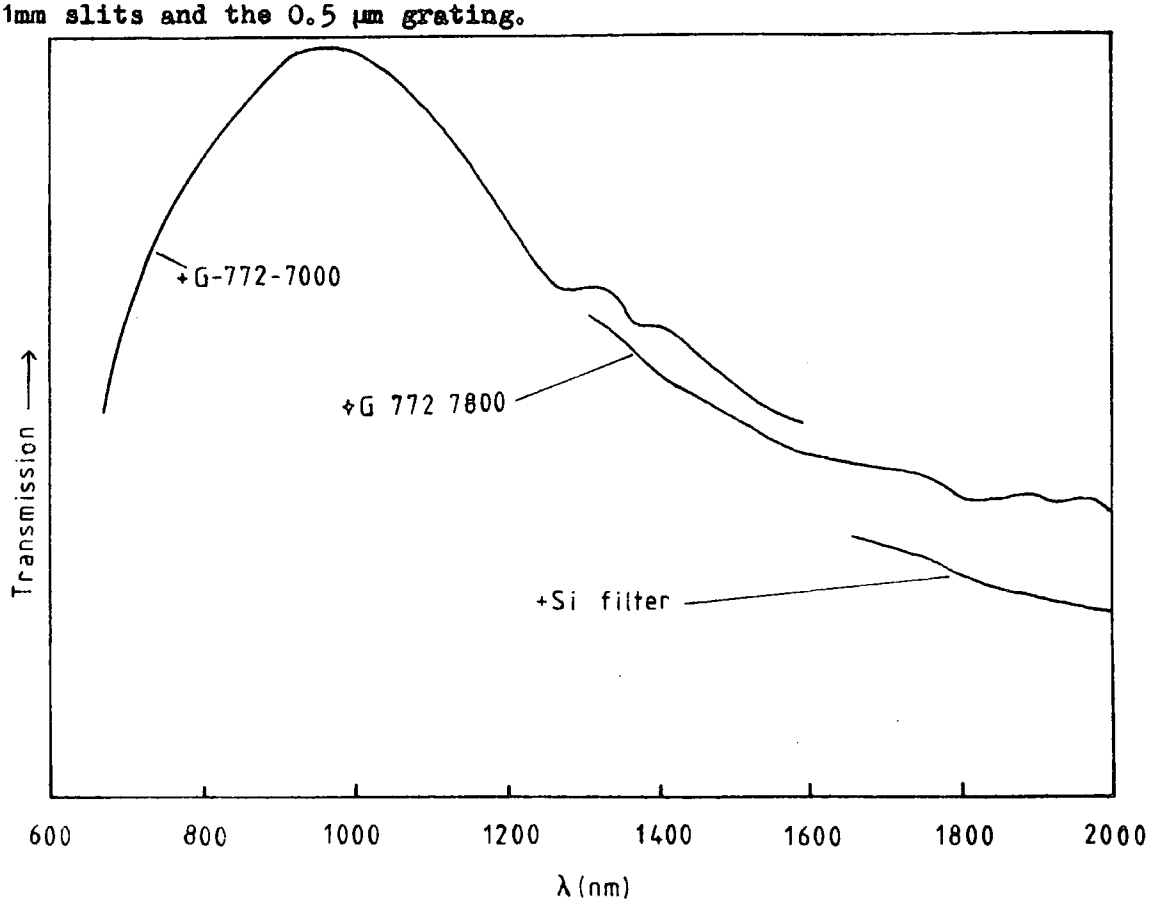

Figure 4.5.2 Throughput of the optical system for the 1 μm grating.

monochromator and lens system. A thermopile and tuned amplifier was used to detect the throughput of the system under investigation. Figures 4.5.3 and 4.5.4 show the spectral transmission of the order sorter filters used with the 1200 L/mm and 600 L/mm diffraction gratings.

An RCA deveopmental type C3 1034, 2" diameter, head-on, 11 stage Quantacon photomultiplier with a caesium doped gallium arsenide chip as the photocathode, an ultra-violet transmitting glass window, and in-line copper beryllium dynode structure, was used as the detector in the luminescence experiments. The photocathode spectral responsivity and current amplification characteristics are shown in figure 4.5.5. The only photomultiplier which extends further into the infra red employs the Cs-O-Ag S1 photocathode, has a 'peaky' spectral response, low quantum efficiency and requires a liquid nitrogen operating temperature to overcome its inherent noise properties.

4.6 PHOTOLUMINESCENCE MEASUREMENTS

The spectral transmission of the two filters G-772-4450 and G-772-7800 used in the photoluminescence experiments are shown in figure 4.5.4. A copper sulphate bath was used to eliminate infrared radiation from the output of the excitation source.

Figure 4.6.1 shows the experimental arrangement used for the observation of photoluminescence emission spectra. Excitation was provided by a 250 W compact mercury source and the photomultiplier signal was detected by monitoring the voltage across a resistor from the anode to earth. The value of this load resistor was usually 1 MΩ or 10 MΩ depending on the required signal/noise ratio required for a particular experiment. The experimental arrangement for the observation of photoluminescence excitation spectra is shown in figure 4.6.2.

Photoluminescence lifetime measurements were observed using the experimental arrangement shown in figure 4.6.3. An EG-G FX-76 xenon

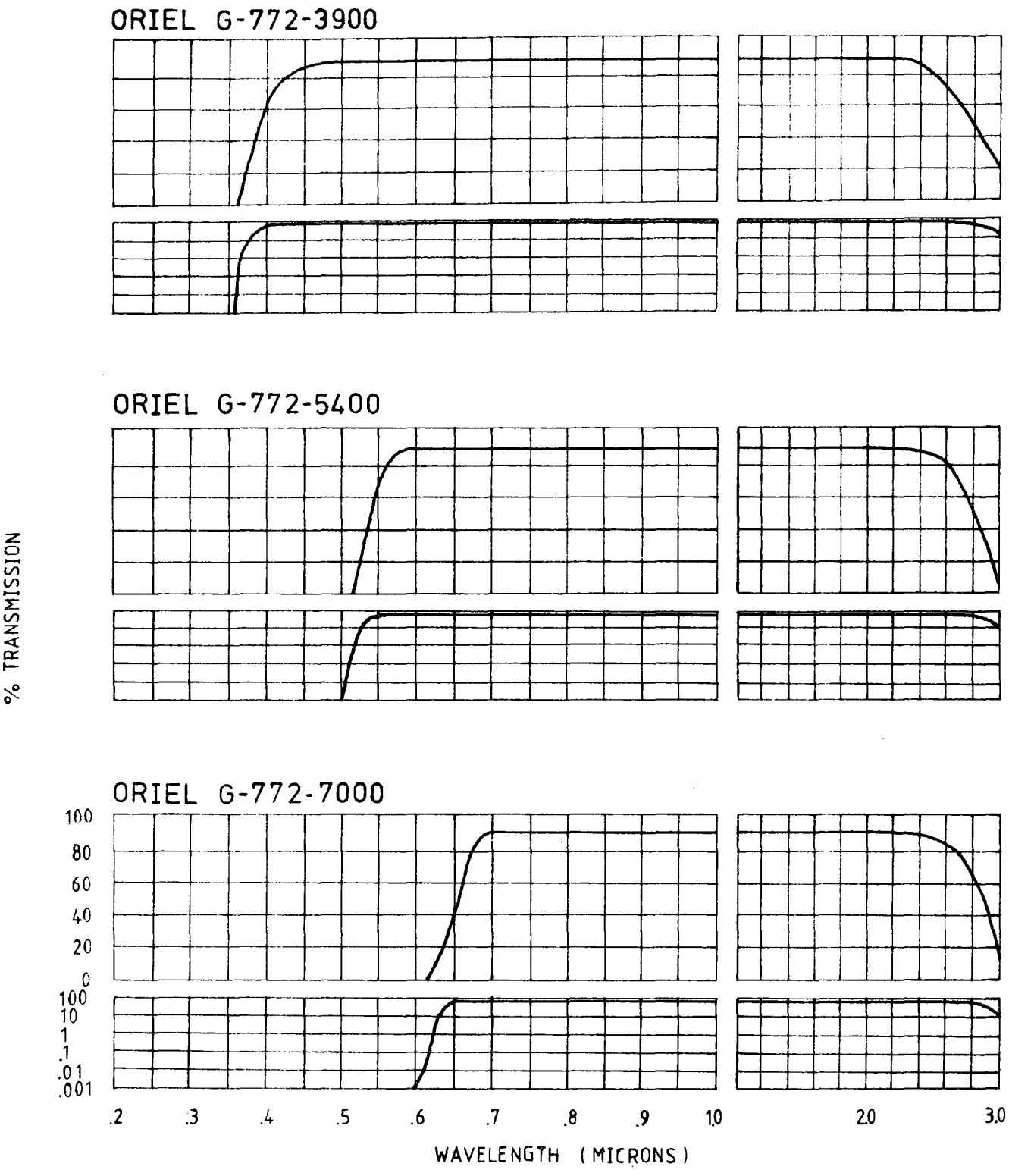

Figure 4.5.3 Spectral transmission of the order sorter filters.

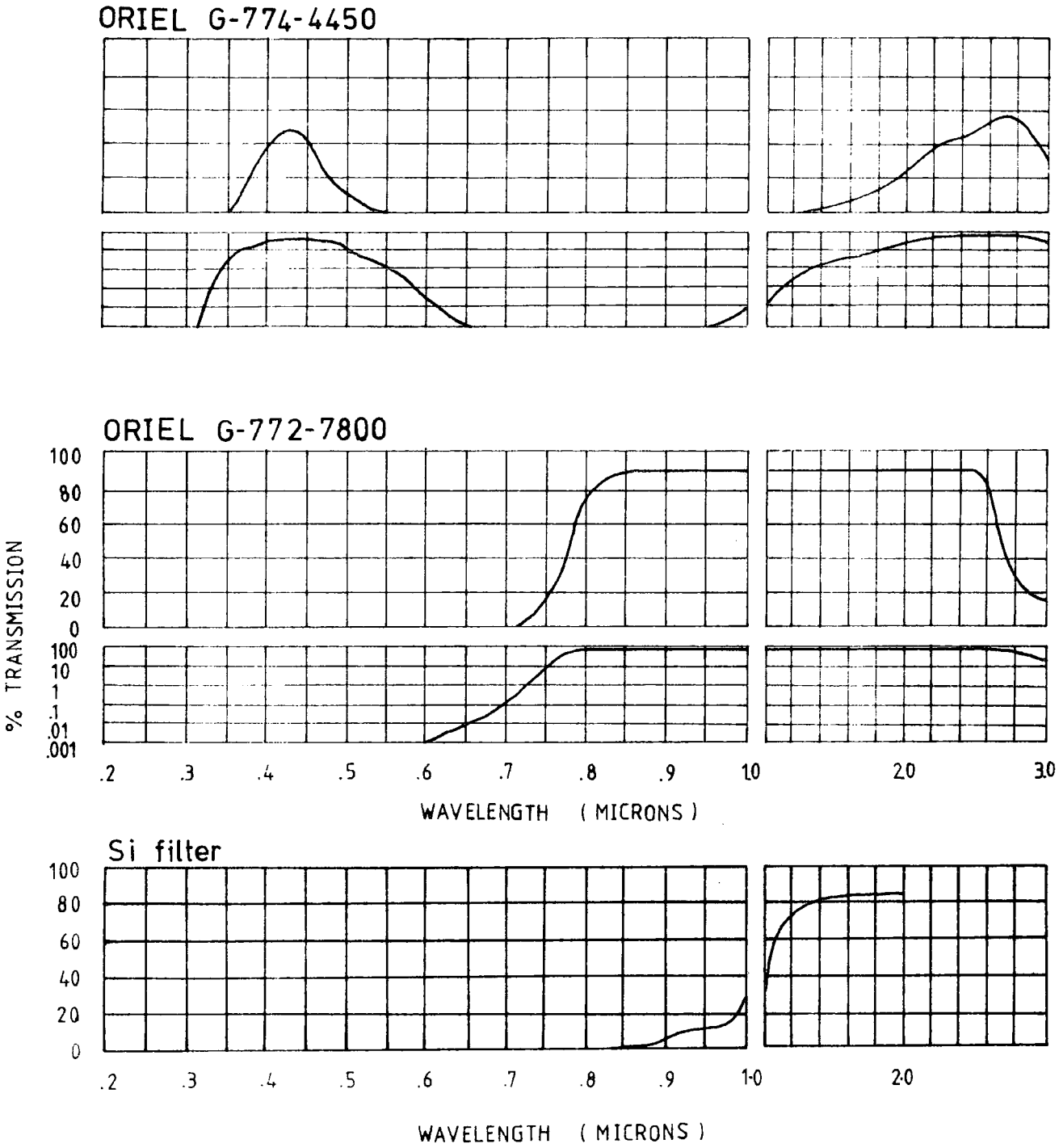

Figure 4.5.4 Spectral transmission of the order sorter filters and the uv band pass filter.

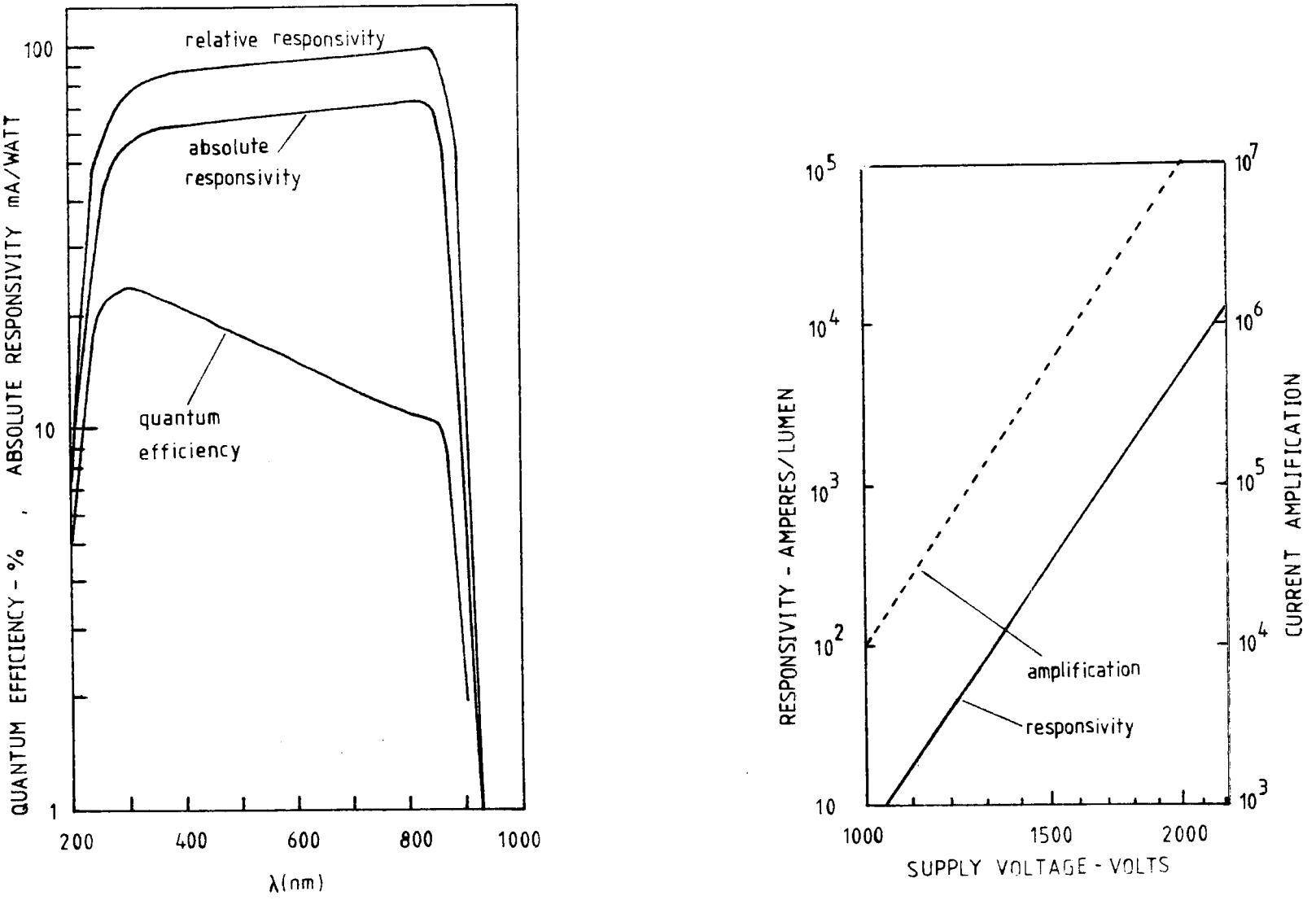

Figure 4.5.5 Photocathode spectral responsivity and current amplification characteristics for the RCA Quantacon photomultiplier type C31034.

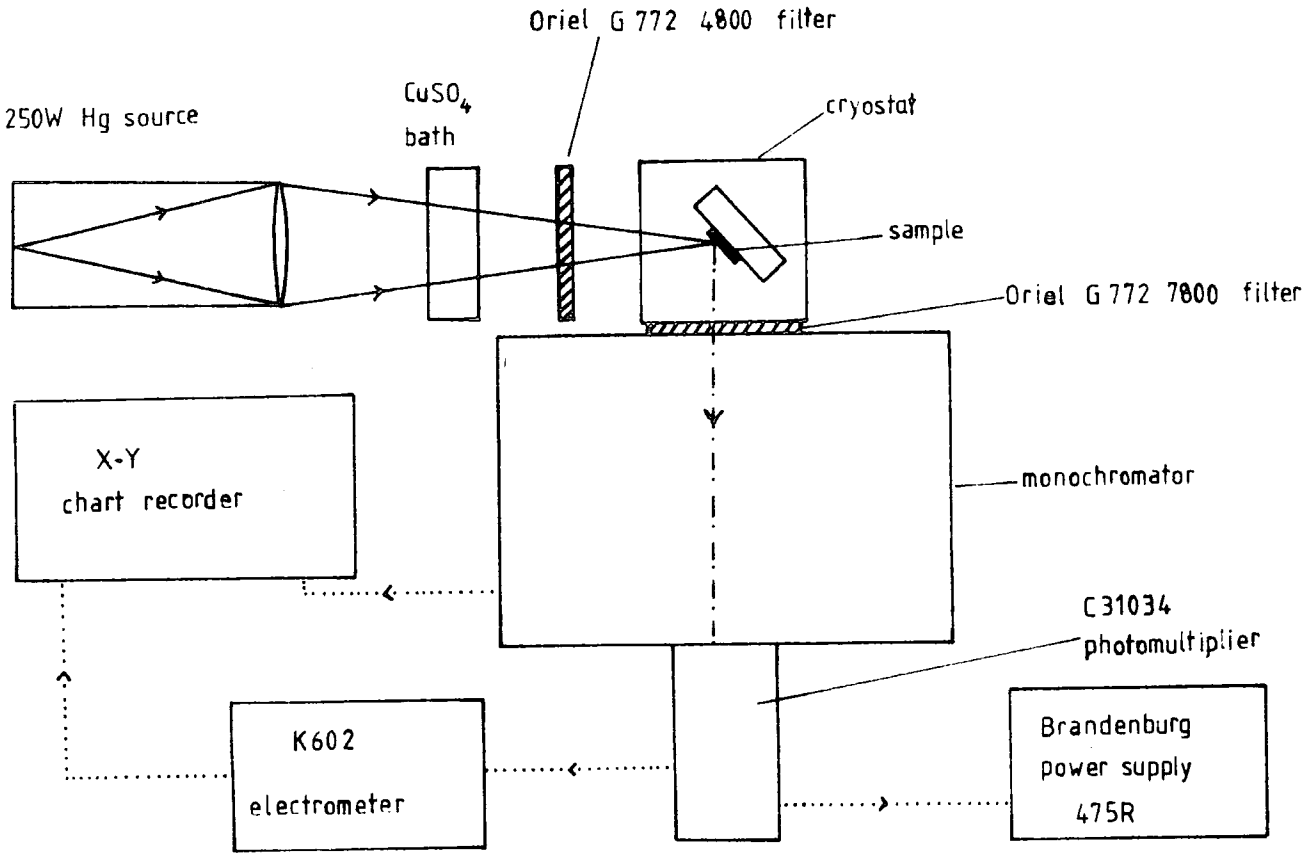

Figure 4.6.1 The experimental arrangement for observation of photoluminescence emission spectra.

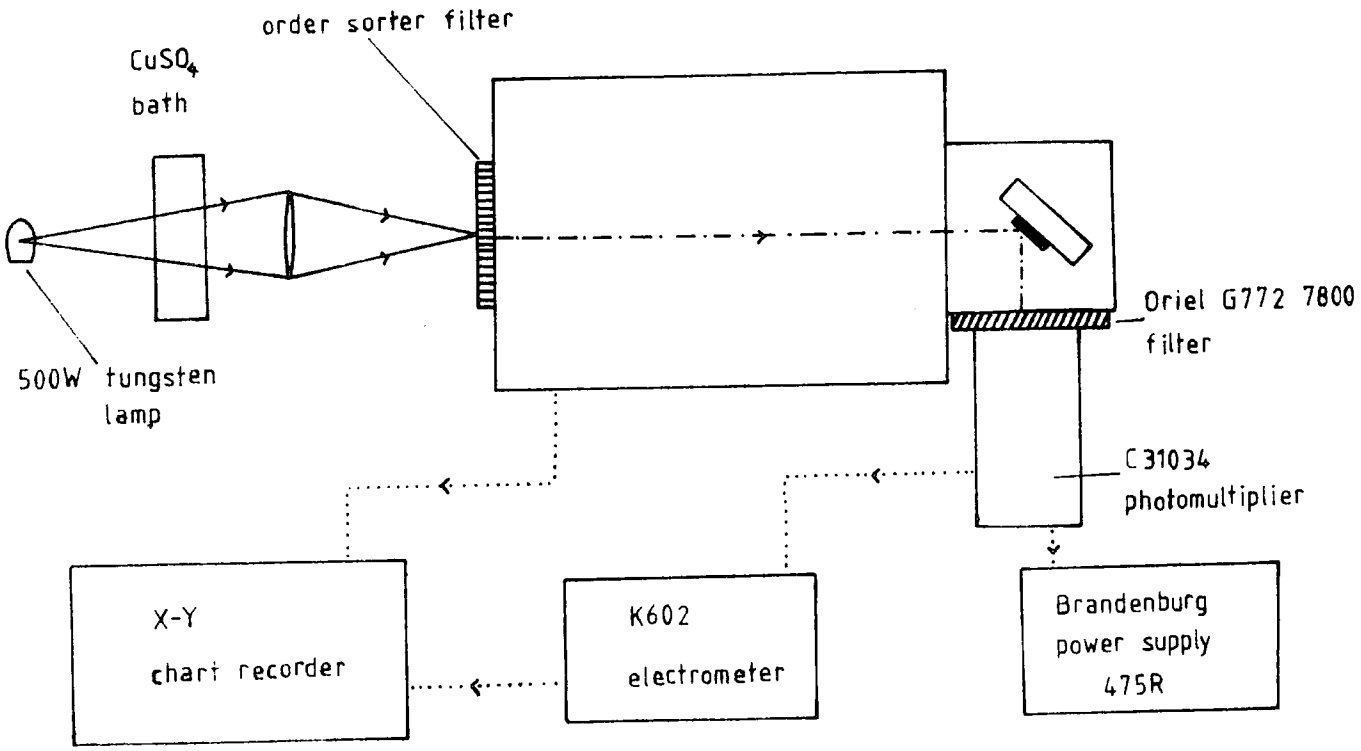

Figure 4.6.2 The experimental arrangement for observation of photoluminescence excitation spectra.

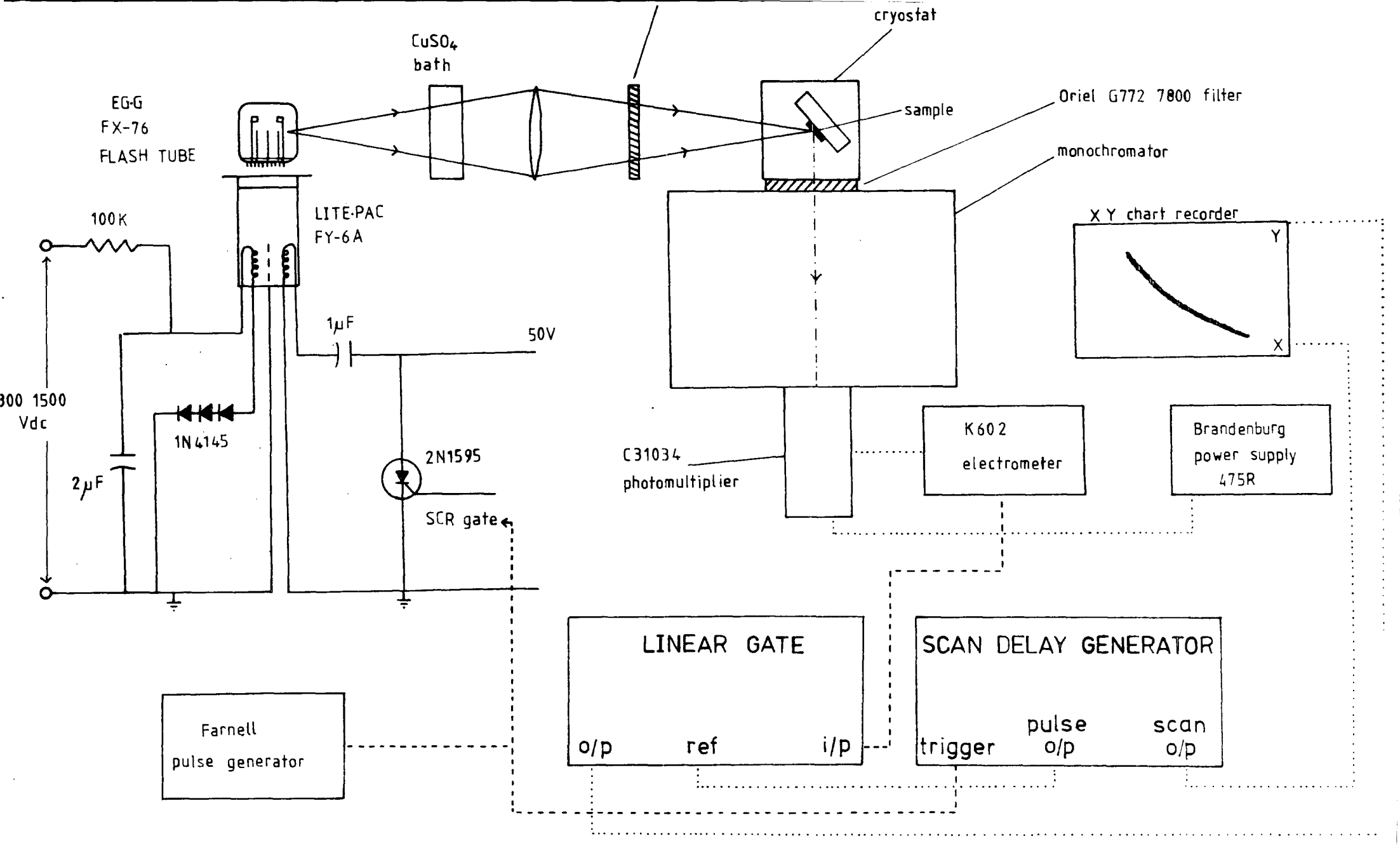

Figure 4.6.3 The experimental arrangement for the observation of photoluminescence decay times.

flash tube was pulsed at 25 pps using a square wave generator and a 2N1595 thyristor.

The same square wave signal was used as a reference for the boxcar detector to monitor the luminescence signal. The boxcar detector (Abernethy 1970) is a signal recovery instrument which is used either to retrieve the waveform of a repetitive signal from noise or to measure the amplitude of a repetitive pulse buried in noise. It has two modes of operation, 'scan' and 'single-point', the former being used in the photoluminescence lifetime experiments for waveform retrieval. Typically a 100 ns 'sampling window' and a scan speed of 100 μs in 100 seconds was used to monitor the luminescence lifetime. In practise a 2 μs delay was observed between the thyristor trigger signal and luminescence emission, and the initial delay facility on the scan delay generator was used to synchronise the signals.

CHAPTER 5

PHOTOCONDUCTIVITY

5.1 INTRODUCTION

The photoconductivity studies were made on the rutile crystals purchased from the National Lead Company, U.S.A, and those grown at BTP Stockton by the plasma fusion technique with no intentional addition of impurities. The samples were rectangular specimens with dimensions 6 x 3 x 1 mm^3 and electrical contacts were obtained by evaporating titanium on opposite ends of the crystal, so that the current flow was transverse to the direction of the incident light. The illumination was produced by using either a 450W xenon lamp or a 500W tungsten source used in combination with a Hilger and Watts grating monochromator D330 Mk11. A set of Oriel and Corning optical filters were used to eliminate order effects from the diffraction grating in the visible part of the spectrum and these were replaced by a 2 mm silicon filter in the near infra red. Neutral density filters were used to vary the light intersity. The spectral energy distribution of the source and monochromator was measured with a thermopile and the spectral response of the photoconductivity data was corrected using a simple Fortran computer program. To obtain the higher light intensities required to observe trap saturation effects the source was replaced by a 250W compact mercury lamp. The current was measured by a Keithley 602 electrometer and dc bias was applied to the sample by two 90V dry batteries connected in series with a potentiometer.

5.2 SPECTRAL RESPONSE OF INSULATING SINGLE CRYSTAL RUTILE

Photocurrents in insulating rutile single crystals were observed at liquid nitrogen temperature. A slow photocurrent rise occurs which was found to be related to electron trapping. Figure 5.1.1 shows the kinetic response curve for a plasma grown crystal (BS18) excited with 415 nm light

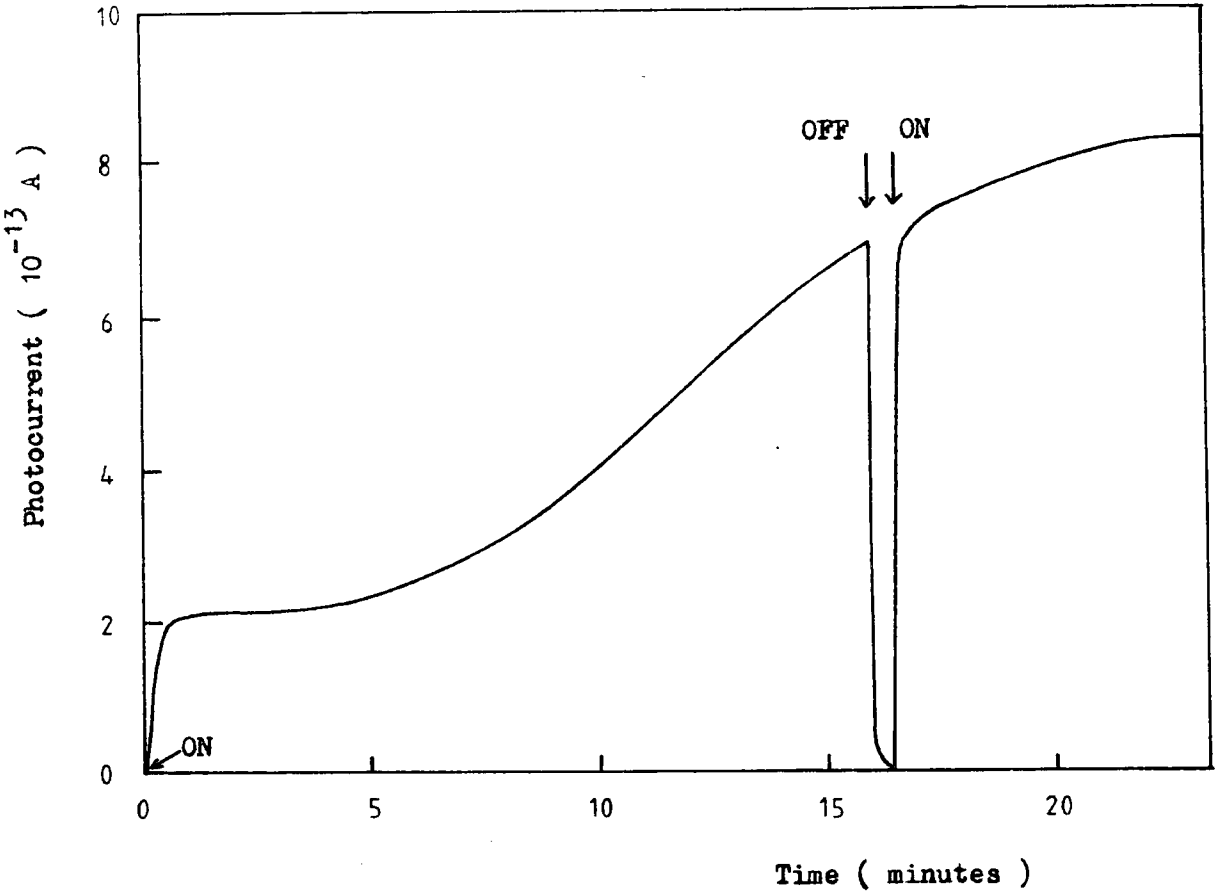

Figure 5.1.1 Slow growth of the photocurrent at 77 K for crystal BS18.

of approximate intensity 10^{12} photons/cm^2 s from a xenon lamp. The S-shaped kinetic response of the photoconductivity is usually attributed to electron trapping. During the initial part of the excitation electrons are trapped, and later when the quasi-Fermi level has been raised sufficiently, an appreciable free carrier density can be supported and the photoconductivity again increases. At higher light intensities the photocurrent increased more rapidly and saturated.

The spectral responses of the rutile single crystals were examined at 77 K after 10 minutes irradiation with a 250W mercury source to fill the shallow traps, a typical curve is shown in figure 5.2.1. Two characteristic peaks at 3.09 eV and 3.23 eV were observed in all the crystals and the low energy peak was always larger than the high energy peak even after correcting for the spectral energy distribution of the measurement system. The spectral responses were investigated under different degrees of trap population. Initially, the samples were heated to 400 K for 10 minutes and then cooled in the dark to 77 K. A voltage of 25V was applied to the samples and the photoconductivity was recorded as the monochromator was scanned from low to high energy at a speed of 50 Å/min. The samples were again heated to 400 K for 10 minutes, cooled to 77 K in the dark and illuminated with 405 nm light of approximate intensity 10^{12} photons/cm^2 s for various excitation times. Figure 5.2.3 shows a typical result of the effects of the shallow trap population on the spectral response, the corrected response is shown in figure 5.2.4. It was observed that the 3.09 eV response was sensitive to the population of the shallow traps, whereas the 3.23 eV response was not.

The spectral response of the photoconductivity at 300 K was also investigated. The samples were initally heated to 400 K and subsequently cooled to 300 K in the dark. The energy of the incident radiation was scanned at 50 Å/min from low to high energy. Curve (a) in figure 5.2.5

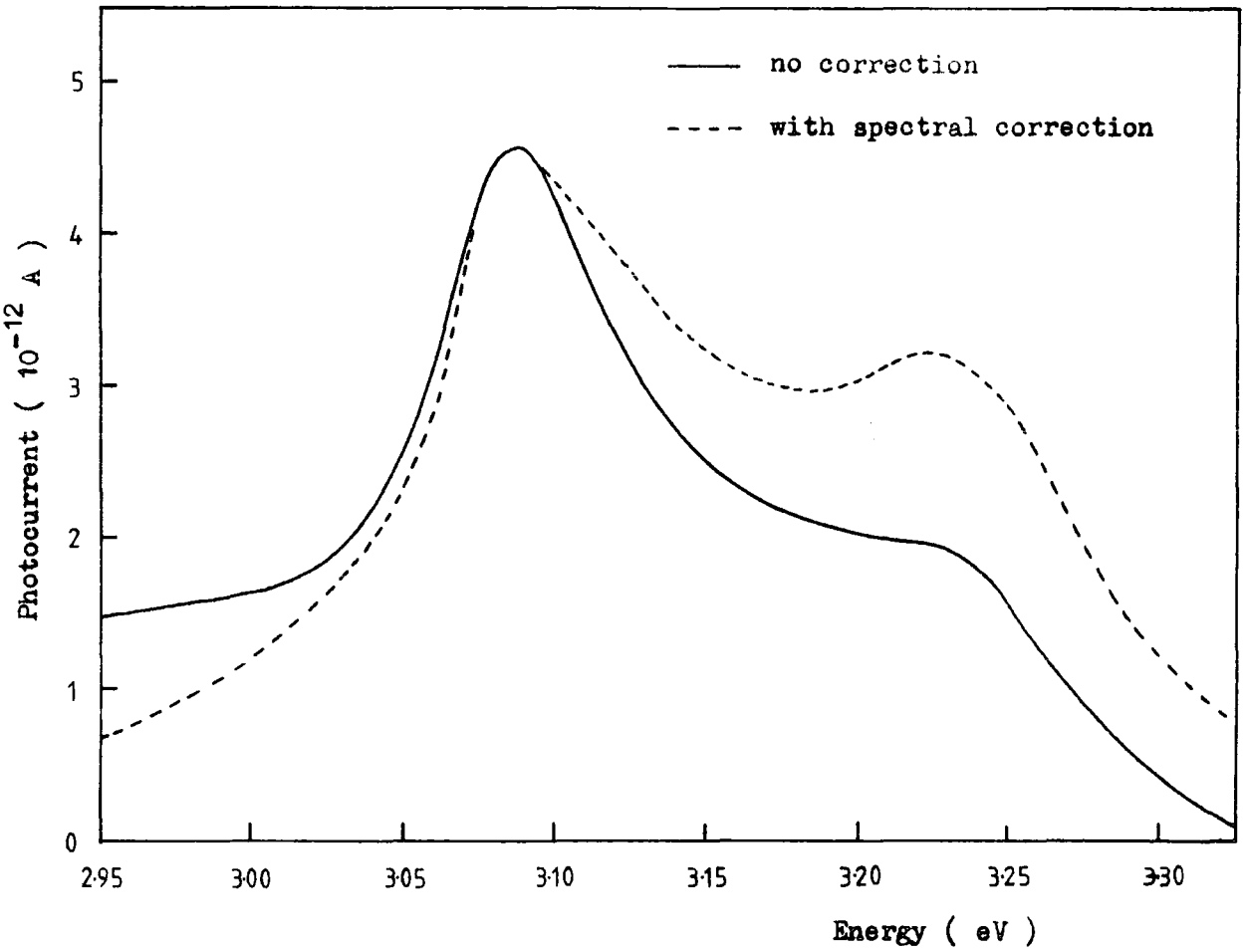

Figure 5.2.1 Spectral response of photoconductivity in crystal CA3(NL) at 77 K.

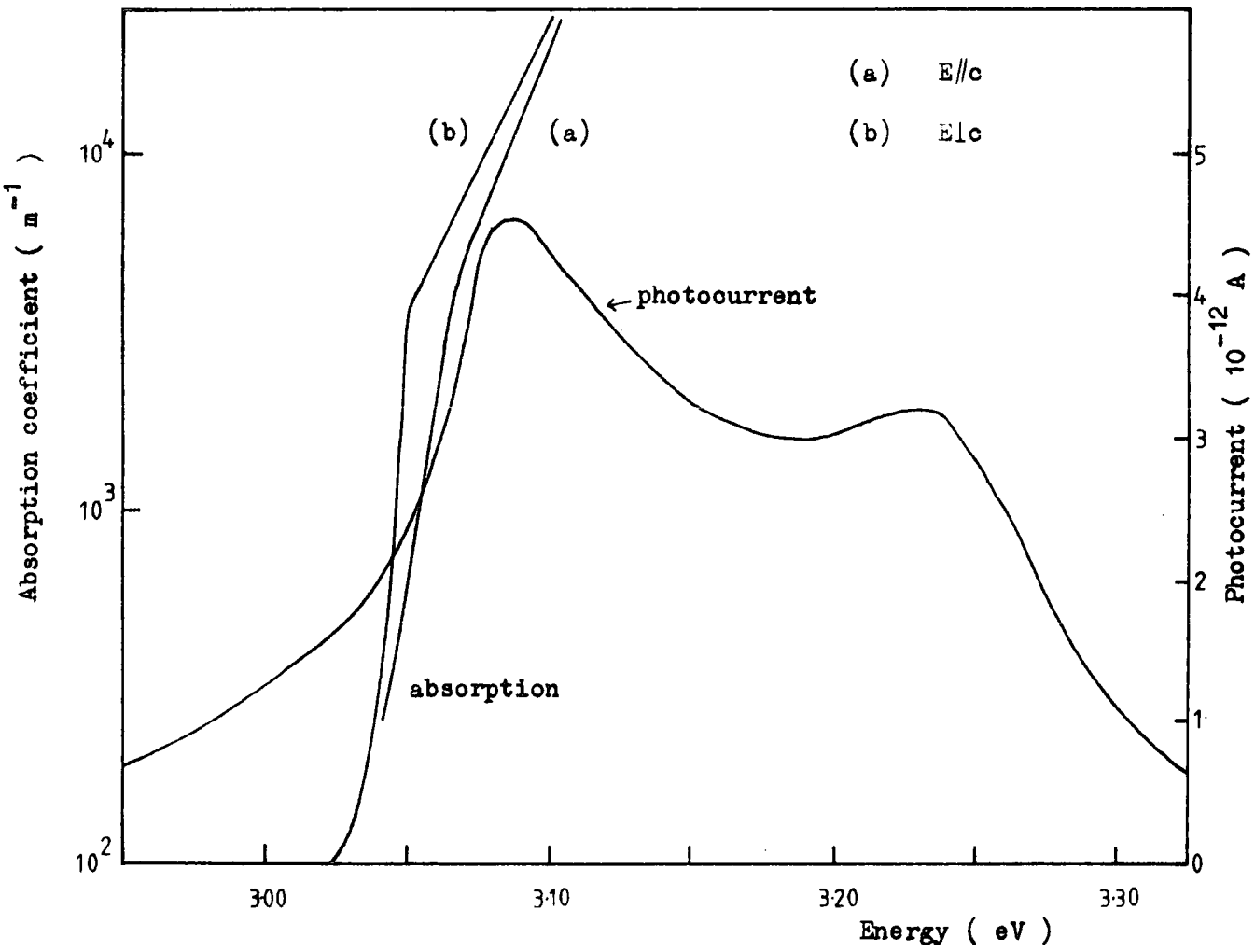

Figure 5.2.2 Comparison of the spectral response of the photoconductivity and optical absorption data at 77 K reproduced from Moch et al (1960).

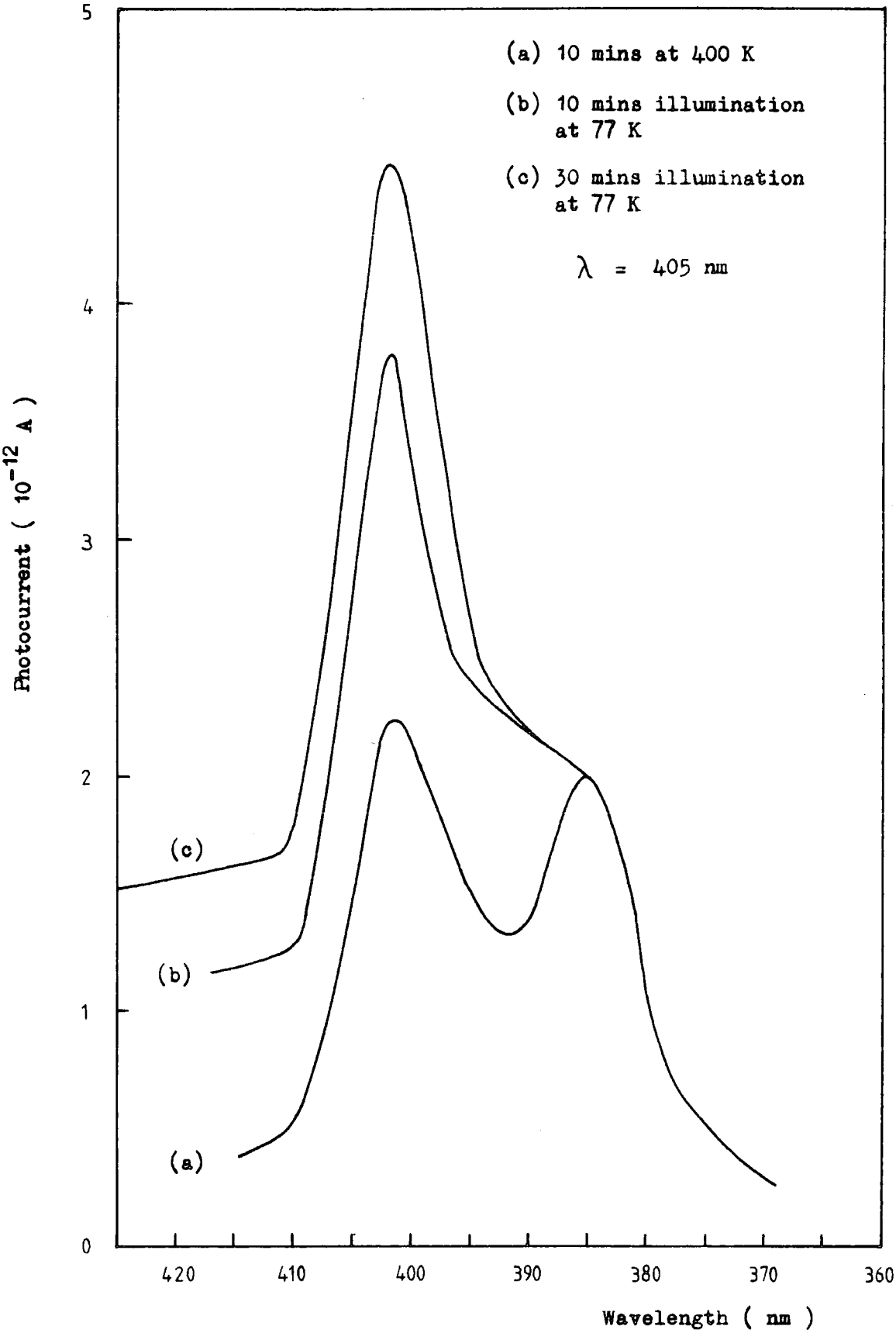

Figure 5.2.3 The spectral response of photoconductivity for crystal CA3(NL) for different shallow trap population (not corrected for the spectral response of the measurement system).

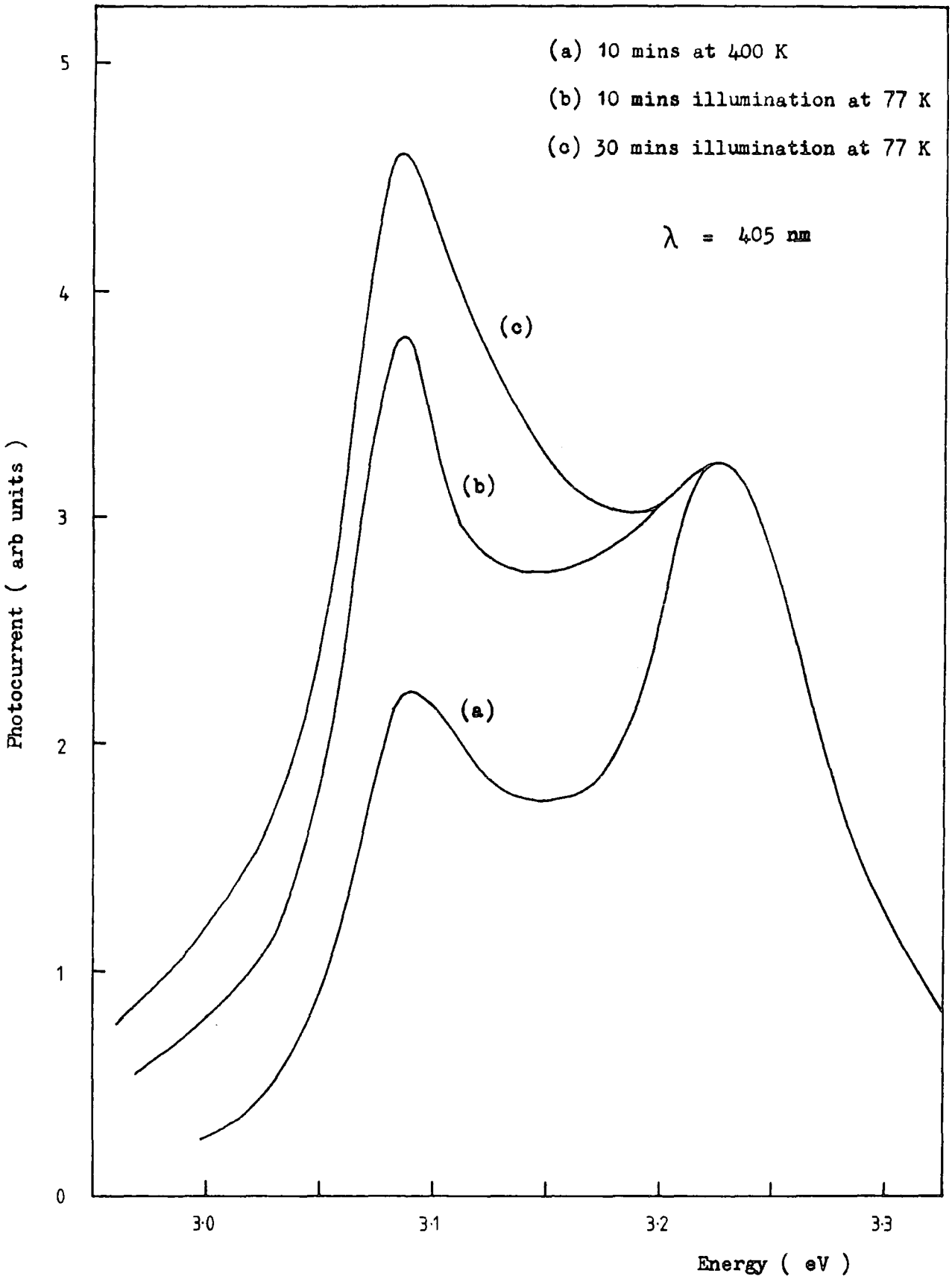

Figure 5.2.4 The spectral response of photoconductivity for crystal CA3(NL) at 77 K for different shallow trap population (includes spectral correction).

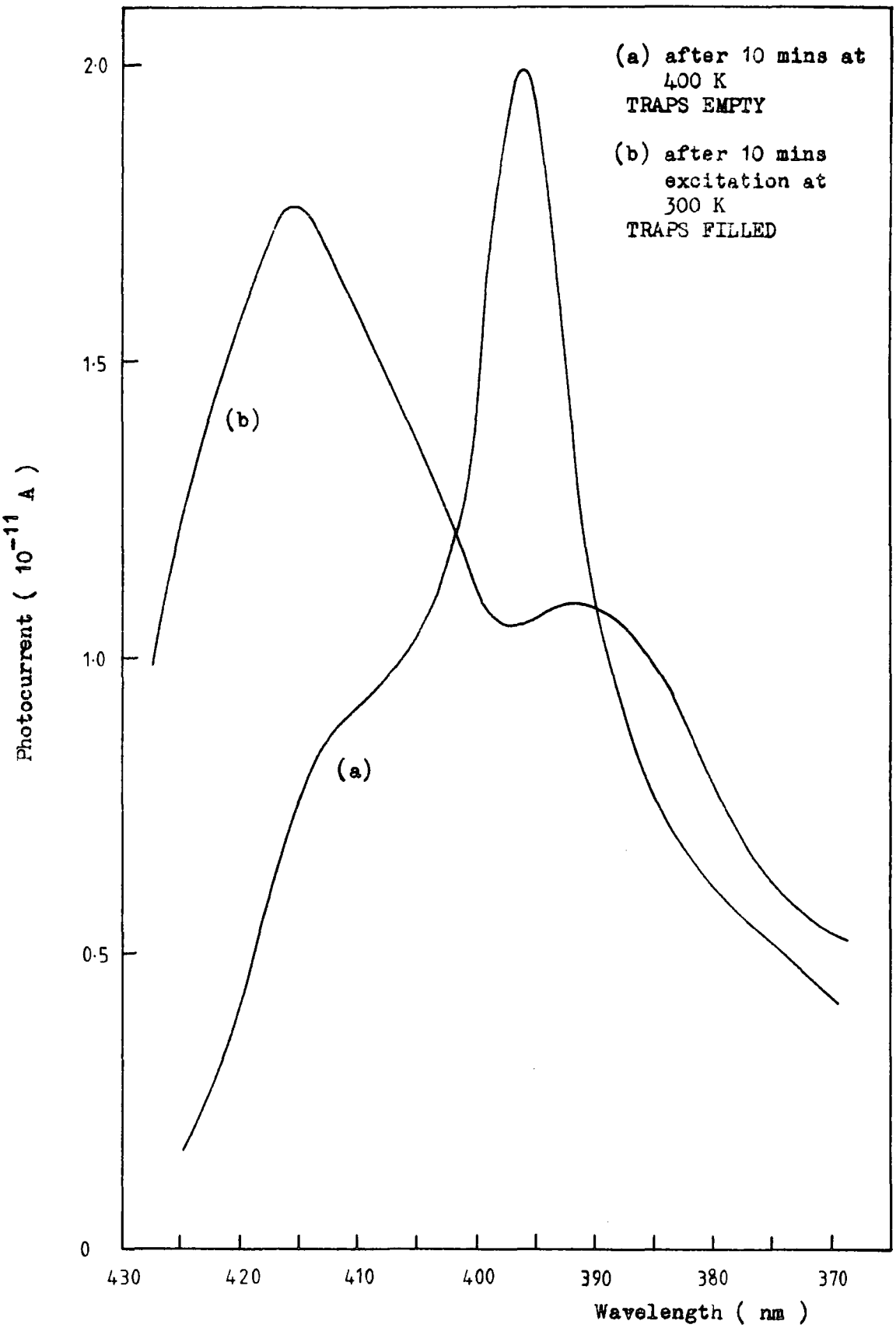

Figure 5.2.5 The spectral response of photoconductivity at 300 K for crystal CA3(NL), including spectral correction.

shows that the population of the traps was changing as the experiment progressed and this was also demonstrated by the increase of the dark current before and after the photoconductivity experiment. The experimental curve does not describe the true spectral response at 300 K and the position of the peak at 397 nm was found to be a function of the scan speed of the monochromator and the photoconductivity response time of the sample at 300 K. The experiment was repeated after 10 minutes excitation with a 250 W mercury lamp to fill the shallow traps not ionised at 300 K. The spectral response curve was obtained by allowing the current at each wavelength to stabilise before progressing to the next point. Curve (d) in figure 5.2.6 shows the corrected spectral response at 300K for the trap filled case. Because of the problems of obtaining a spectral response with varying trap population at 300 K no data on the effects of the trap population on the two characteristic peaks was observed. However, it should be noted that in the trap filled case the relative magnitude of the two photoconductivity peaks was similar at 77 K and 300 K.

The shift of the photoconductivity peaks with temperature was measured and a typical result is shown in figure 5.2.7. The temperature of the sample was allowed to stabilise at each temperature and the spectral response was obtained under steady state trap filled conditions. The results show that the temperature dependence of both the characteristic peaks was about 5.10^{-4} eV/K.

5.3 DISCUSSION OF THE SPECTRAL RESPONSE MEASUREMENTS

The early work of Cronemeyer (1952) on the electrical conductivity, optical absorption and photoconductivity of rutile shows that the forbidden gap is about 3.0 eV wide. From the dispersion of the refractive index in the visible region and a modified Sellmeier expression the major interband transitions were deduced by DeVore (1951) to occur for photon energies near w=4.3 eV. Measurements of the long wavelength tail

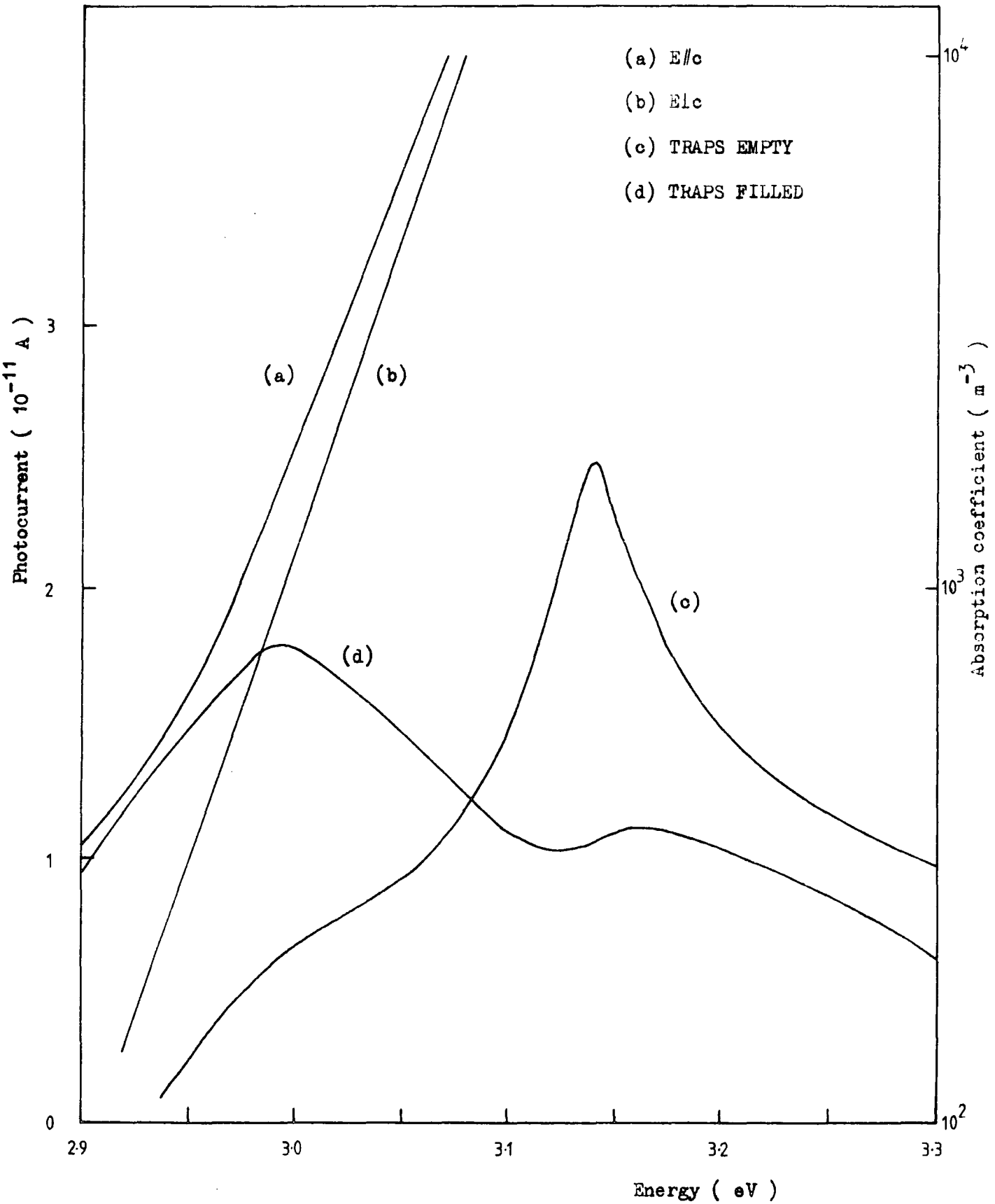

Figure 5.2.6 Comparison of the spectral response of the photoconductivity and optical absorption data at 300 K reproduced from Moch et al (1960). The photoconductivity has been corrected for the spectral response of the measurement system.

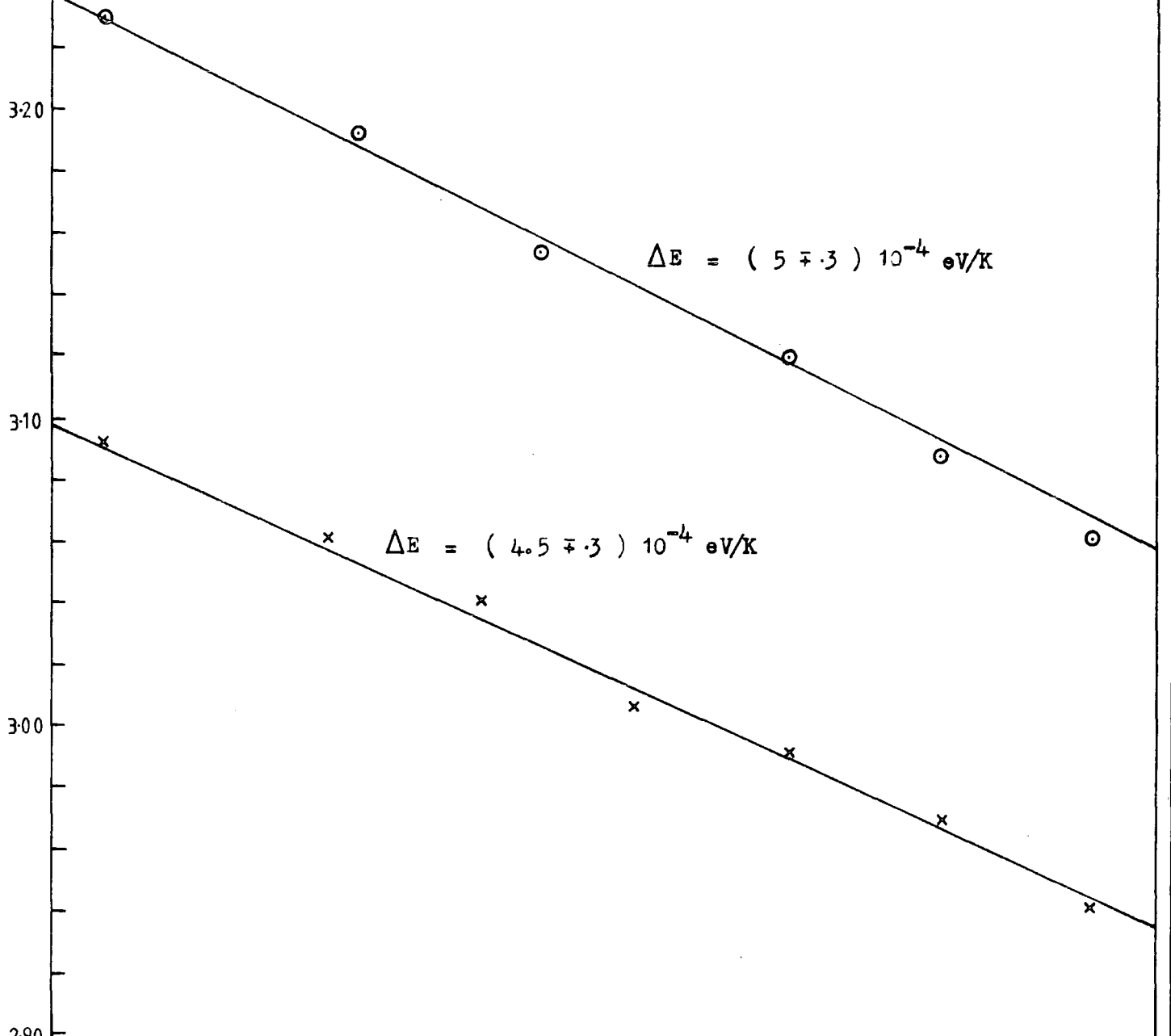

Figure 5.2.7 The temperature dependence of the two intrinsic photocond-uctivity peaks for the crystal CA3(NL).

Crystal	sample no.	R (77K)	τ sec^{-1} from Photogain
CA3(NL)	1	2.3	10^{-8}
	5	1.4	10^{-8}
	4	2.1	10^{-8}
BS1	2	2.1	10^{-8}
	3	3.4	10^{-9}
BS3	7	2.8	10^{-9}
BS10	17	1.5	10^{-8}
	18	2.7	10^{-8}
BS11	19	1.6	10^{-8}
	20	3.2	10^{-8}
BS18(S)	25	1.8	10^{-8}
BS18(NS)	26	2.4	10^{-8}

Table 5.3.1 Summary of the photoconductivity gain and the ratio of the low and high energy photoconductivity peaks after spectral correction (R) for the National Lead and plasma grown crystals .

of the fundamental absorption edge with polarised radiation by Moch (1960), Soffer (1961) and Agekyan (1975) suggests that the true edge for E⊥c occurs at a slightly lower energy than for E//c, ~ 10 meV at room temperature and ~ 33 meV at 4 K. The true edge difference, deduced from electroabsorption data, was found by Arntz and Yacobi (1966) to be ~15 meV at 77 K, but the corresponding features in the electroreflectance spectra of Vos and Krusemeyer (1974) suggest a gap difference of ~33 meV.

Energy level diagrams for rutile have been proposed by Breckenridge and Hosler (1953) and Perney and Lorang (1966) who assign the onset of the absorption not to the fundamental interband absorption edge, but to optical transitions related to excited states of lattice defects. However, most experimental data on electrical transport properties (Frederikse 1961, von Hippel 1962, Becker and Hosler 1965, Acket and Volger 1966), optical absorption (Bogomolov 1968, Pak 1975, Agekyan 1975) and x-ray spectroscopy (Fischer 1972), indicate that the conduction states have a predominantly titanium -3d character and are seperated by about 3.0 eV from the oxygen -2p valence band edge.

Vos and Krusemeyer (1977) measured the reflectance and electroreflectance spectra and Kramers-Kronig derived spectra of the dielectric constant of rutile in the 3.0-6.5 eV energy range. To interpret their data they calculated the band structure E(k) using a LCOAO calculation in the Slater-Koster two centre approximation (1954), using Ti-3d, O-2s and O-2p orbitals and retaining only nearest neighbour interactions. The electroreflectance spectra contained five major characteristics between 3.0 and 3.7 eV.

Vos and Krusemeyer proposed that the critical points in the electroreflectance which gave rise to structure at 3.030 eV with E⊥c and at 3.065 eV with E//c, are related to the $M_{1,2}$ conduction band minimum. They tentatively assigned the E⊥c structure to the indirect edge $\Gamma_3^+ \rightarrow M_{1,2}$. The transition is allowed with the participation of a M_9^+ phonon and the M_9^+ valence band as

intermediate state. The first allowed edge for E//c is $\Gamma_5^+ \rightarrow M_{1,2}$, to which they assign the 3.07 eV structure with E//c. This transition is accompanied by M_9^- phonons and the $M_{5,6}$ valence band as well as the Γ_5^- conduction band can be the intermediate state.

The electroreflectance structure at 3.12 eV was found to be described by the peak position versus $F^{2/3}$ dependence of an allowed, indirect, isotropic and non-degenerate, M_0^- edge (Cardona and Harbeke 1965). In conclusion, Vos (1977) found the structure to be well described by Franz-Keldysh oscillations belonging to the indirect edge M_0^- ($\Gamma_3^+ \rightarrow R_1^+$). The energy of the R_1^- phonon was deduced to be between 10 and 60 meV giving the energy band difference $\Gamma_3^+ \rightarrow R_1^+$ in the range 3.06 to 3.11 eV.

The structure observed by Vos (1977) in the 3.15-3.7 eV region was not well defined. This was due to several reasons, such as overlapping contributions from different critical points, either connected with other bands or due to the participation of different phonon processes. Secondly, when the excitation involves deeper valence bands or higher conduction bands, the lifetime broadening of the excited state due to interband phonon scattering may increase considerably. Two structures, observed in the E⊥c spectra, were thought to originate from an isolated critical point. The first occured at 3.17 eV and the second at 3.57 eV.

The 3.17 eV structure as well as other less well defined structures for E⊥c and E//c were thought to be due to several possible indirect and forbidden gaps in the band structure. Possible candidates for indirect transitions are the gaps $\Gamma_5^+ \rightarrow M_{1,2}$, $\Gamma_1^- \rightarrow M_{1,2}$ and $\Gamma_5^+ \rightarrow R_1^+$. All direct transitions originating from the Γ_3^+ valence band maximum are dipole forbidden for both E⊥c and E//c.

The $\Gamma_3^+ \rightarrow \Gamma_3^+$ direct gap has been proposed by Waff and Park (1970) to be about 3.75 eV wide. Vos concluded that the $\Gamma_3^+ \rightarrow \Gamma_3^+$ edge is close to 3.57 eV for E⊥c and at a slightly larger photon energy for E//c.

The spectral response data obtained from the National Lead crystal CA3(NL) , the non-stoichiometric plasma grown crystals(BS1, BS3, BS10,BS11) and the stoichiometric plasma grown crystal (BS18) is shown in table 5.3.1. All these crystals had similar photoconductivity responses in the energy range from 2.90 to 3.40 eV. The ratio of the magnitudes of the two characteristic peaks in the trap filled case, where the spectral response was least affected by the shallow trap population, was similar in all the crystals examined at 77 K. Ghosh (1969) reported that insulating rutile crystals produced a peak at 410 nm at 77 K in the trap empty case and populating of the shallow traps produced a dominant peak at 380 nm in the photoresponse. These experimental results could not be reproduced in either our NL or plasma grown crystals. The magnitude of the 3.23 eV peak was insensitive to the population of the shallow traps whilst the magnitude of the 3.09 eV peak increased as the period of excitation at 405 nm was increased.

The photoresponse at 3.09 eV is due to a combination of the $\Gamma_3^+ \rightarrow M_{1,2}$ and $\Gamma_5^+ \rightarrow M_{1,2}$ indirect transitions in the band gap of rutile. The nature of the high energy peak remains unidentified. Photoconduction can be strongly influenced by surface properties and if the surface lifetime is varying with energy relative to the bulk lifetime complex effects can result. To investigate whether such an affect was occurring a number of gases including oxygen, nitrogen, hydrogen and carbon dioxide were introduced into the sample cryostat at 77 K at a pressure of 20 torr. No affect was observed when the spectral response was remeasured. These crude experiments were not conclusive and a more extensive study of the photoresponse at ultra high vacuum would be interesting.

Examination of the band structure calculations of Vos (1977) suggests another plausible explanation of the double peak in the rutile photoresponse.

The $\Gamma_3^+ \rightarrow M_{1,2}$ indirect transition at 3.030 eV and the $\Gamma_5^+ \rightarrow M_{1,2}$ indirect transition at 3.065 eV produce the lower energy peak in the spectral response. However, examination of the rutile band structure shows another indirect gap $\Gamma_3^+ \rightarrow R_1^+$ at 3.12 eV (see figure 5.3.2). The band calculations suggest a lower effective mass and higher mobility in the R valley than in the M valley. At wavelengths shorter than the band edge the light is strongly absorbed in a surface layer which enhances recombination of holes and electrons and thus reduces photoconductivity. The possibility arises that at slightly higher energies the $\Gamma_3^+ \rightarrow R_1^+$ transition becomes possible and the increased mobility produces an increase in the photoconductivity. As the wavelength of excitation is reduced further the photoconductivity again falls with increasing absorption coefficient.

The change in the magnitude of the lower energy peak with trap filling would suggest that the shallow traps in rutile interact with the M conduction band minimum. Majerfeld and Bhattacharya (1978) have reported that for GaAs, in addition to well known capture cross section and activation energy properties of an electron trap, the conduction band minimum with which a trap level interacts is a fund mental property of the centre. These authors showed that a trap frequently occurring in GaAs emits electrons principally to the indirect L conduction band minimum rather than to the energetically lower lying direct Γ minimum. A similar result has now been established for a dominant electron trap in $Ga_{1-x}Al_xAs$, the energy level of which is rigidly coupled to the L minimum over the direct gap alloy range (Bhattacharya and Majerfeld 1978). Grushko and Gutkin (1975) found that in Fe doped InP the complementary electron and hole threshold photoionisation energies considerably exceeded the value of the fund mental energy gap and explained the results on the basis of an electron phonon interaction. Majerfeld et al (1978) have established that one trap in n-type InP is linked to the Γ minimum and two traps linked to the L minimum.

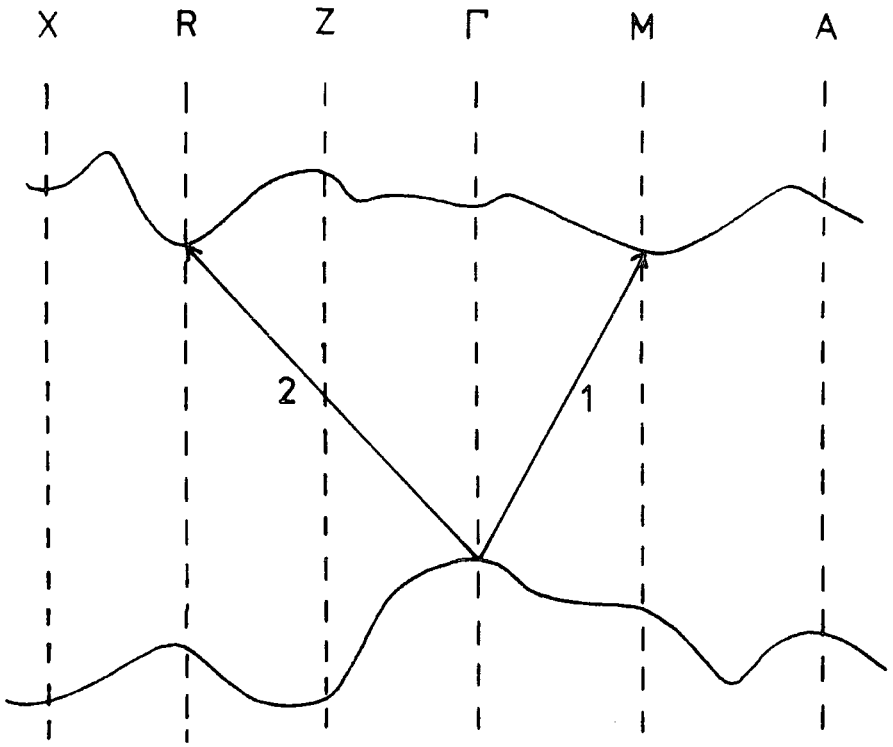

transition 1 $\begin{cases} \Gamma_3^+ \rightarrow M_{1,2} & \perp c \quad 3.030 \text{ eV} \\ \Gamma_5^+ \rightarrow M_{1,2} & \parallel c \quad 3.065 \text{ eV} \end{cases}$

transition 2 $\Gamma_3^+ \rightarrow R_1^+$ $\perp c, \parallel c$ 3.124 eV

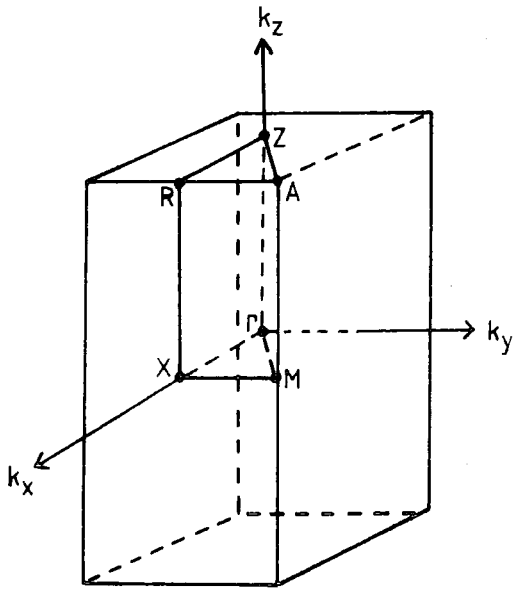

Figure 5.3.2 Schematic of rutile band structure and Brillouin zone with points of high symmetry .

5.4 ADSORPTION AND DESORPTION OF OXYGEN

The presence of surface states produces band bending near the surface. If the surface state can trap an electron, it acts as an acceptor and the bands bend upward at the surface. Conversely, if the donor-like trap can lose an electron, forming a positive charge at the surface, it will cause the bands to bend down.

If the approaching gas atom or molecule has a greater electron affinity then the work function of the semiconductor or insulator, it may capture an electron from the surface and, behaving as an acceptor, will tend to bend the bands upward. Oxygen, which is very electronegative, causes an upward bending of the bands. When oxygen is adsorbed on an n-type material, the depletion layer increases and the surface conductance decreases. On the other hand, oxygen absorbed on a p-type material causes the surface to become more negative, increasing the hole concentration at the surface, building up an accumulation layer and, therefore, increasing the surface conductance.

The adsorption process may be helped by optical stimulation, which makes more electrons available to the strongly electronegative gas, and more holes available to the donor-like species. Actually, illumination can cause either increased adsorption or the opposite effect, increased desorption (Wolkenstein and Karpenko 1962). The direction of the effect depends on the nature of the gas, the material, its doping, the bending of the bands at the surface, and such experimental conditions as temperature and pressure.

Addiss and Wakim (1969) studied the role of chemisorbed gas on the photoelectronic properties of single crystal rutile and rutile powders. At elevated temperatures exposure to oxygen produced adsorption and an increase in the resistivity. Exposure to oxygen free atmospheres, such

as helium, led to oxygen desorption and a decrease in resistivity. Oxygen adsorption was detected at 300 K and oxygen desorption was detected at temperatures greater than 80-100 °C.

Two experiments conducted by Addiss and Wakim were repeated on several plasma grown samples and results similar to theirs were obtained. Figure 5.4.1 shows the transient photocurrent response of a typical sample in one atmosphere of oxygen and in a vacuum of about 10^{-2} torr. In both cases a relatively fast initial rise was followed by a much slower rise rate which gradually decreased. However, the photocurrent saturated more rapidly in oxygen than in vacuum, resulting in a larger photocurrent in vacuum. This difference is explained on a qualitative basis by assuming that photodesorption of oxygen proceeds via the mechanism proposed by Melnick (1957); the net photocurrent is higher in vacuum because the competing oxygen adsorption process is diminished due to the much lower oxygen partial pressure. The effect of sudden exposure to oxygen on the photocurrent decay in vacuum also supported this view and exposure to one atmosphere of oxygen during the slow portion of the photocurrent decay in vacuum resulted in an increased rate of current decay (see figure 5.4.1).

The photocurrent level attained in air was increased if the air was pumped away during illumination. This effect was reversible when air was readmitted to the sample cryostat (figure 5.4.2). The difference between the photocurrents in air and vacuum is attributed to a larger photodesorption of oxygen in vacuum.

Addiss and Wakim concluded that under certain conditions, part of the photocurrent in rutile single crystals could be related to an exchange of chemisorbed gas with the ambient. However, no gas exchange effects were associated with photocurrents in ultra-high vacuum. The results of their experiments indicated that surface adsorbed gas atoms act as

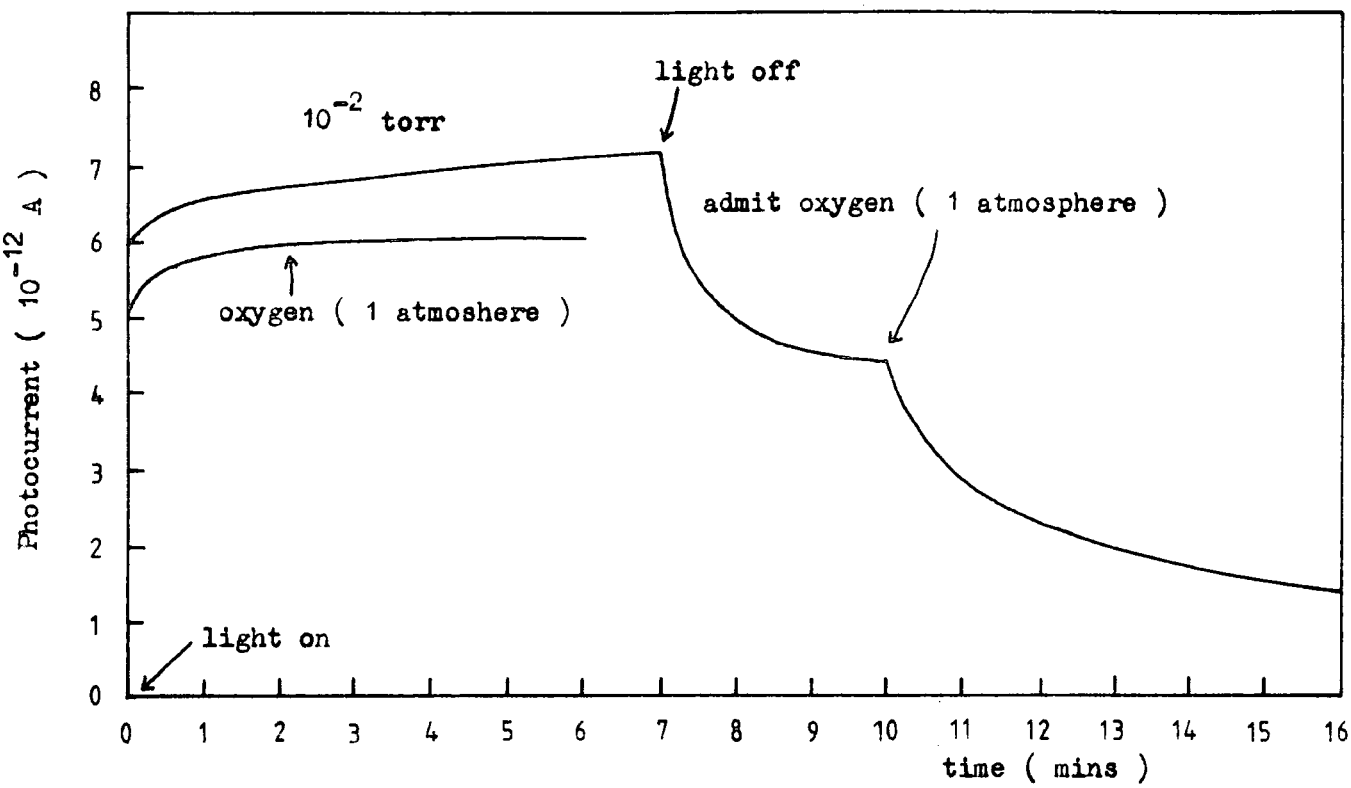

Figure 5.4.1 The photocurrent response of crystal BS18(S) in vacuum and oxygen at 300 K (λ = 400 nm).

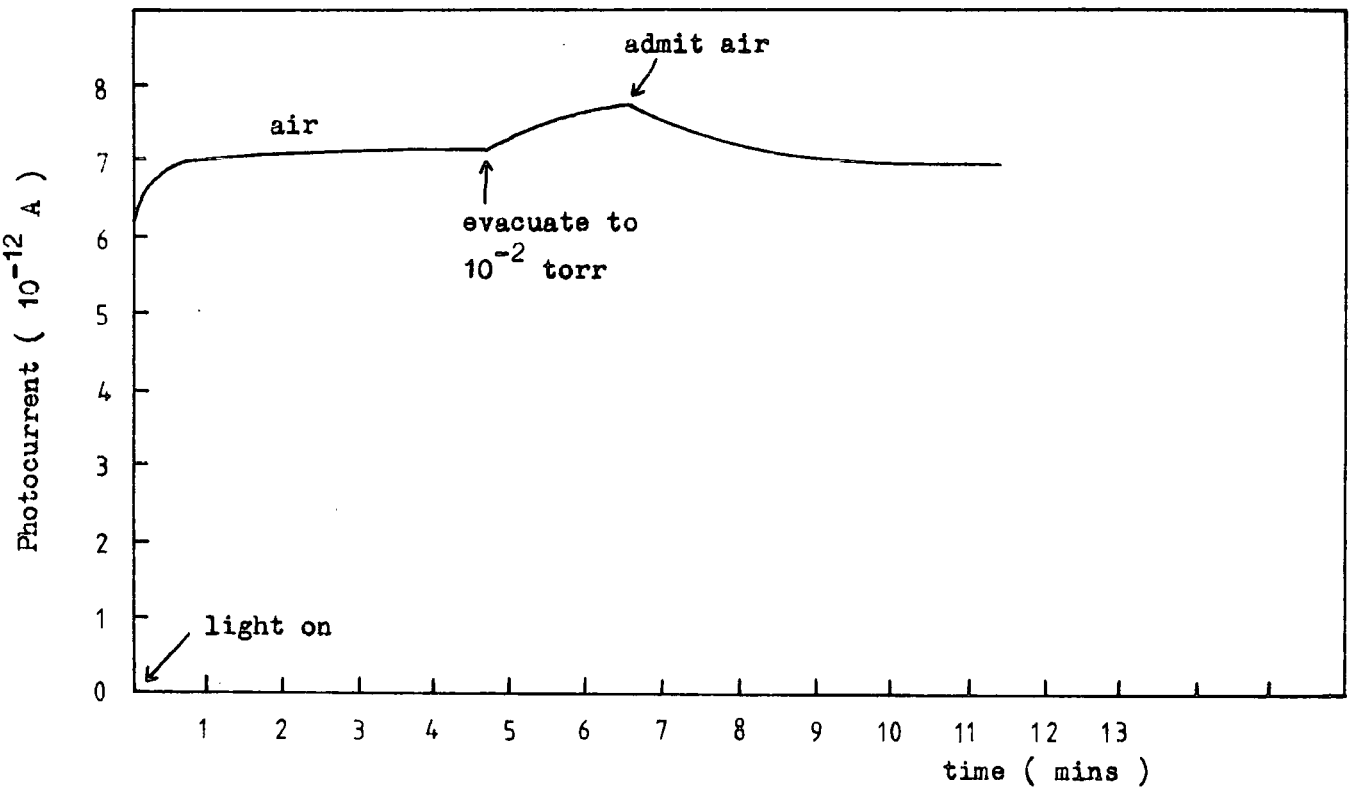

Figure 5.4.2 Photocurrent changes in crystal BS18(S) caused by changing ambient gases during excitation at 300 K (λ = 400 nm).

recombination centres, and that the long photocurrent response times are caused by shallow trap emptying rather than by chemisorption kinetics. Photocurrents in powder layers are more closely associated with the gas exchange process which affects the conduction across Schottky surface barriers between particles.

5.5 THE EFFECT OF INFRA RED EXCITATION AND LIGHT INTENSITY ON PHOTOCONDUCTIVITY

Insulators have a more or less continuous distribution of defect states throughout the forbidden zone. The density of certain levels may appear dominant against this quasi-continuum of states. Those near the bottom of the conduction band are most likely to trap electrons. Those near the top of the valence band are most likely to trap holes. Somewhere in between, probabilities of capture are comparable and recombination is most likely. Such defects are called recombination centres.

The classification must not be taken too rigidly, as recombination can also occur at any of the traps. However, the probability of recombination is much lower than the probability of trapping in the centres classified as trapping centres. A suitable demarcation level may be defined as that at which an electron has equal chances of free hole capture or thermal excitation to the conduction band. Centres closer to the ~~valence~~ conduction band are electron traps. Centres closer to the valence band are electron recombination centres. A similar criterion may be taken for hole traps near the valence band.

Traps in regions A and C of figure 5.5.1 are in thermal contact with the appropriate transport band and their occupancy is determined by a Boltzmann factor. Since the capture cross section S will vary with the type of centre, each centre has its own demarcation level. A particular

type of centre will have a demarcation level at an energy E, below the conduction band given by

$$p \; v \; S_p \;\; = \;\; S_n \; v \; N_c \;\; \exp(\; -E_1/kT \;)$$

where S_n is the free electron capture cross section for a hole occupied centre and S_p is the free hole capture cross section for a centre already occupied by an electron. The centres will act as recombination centres when

$$p \; S_p \;\; >> \;\; S_n \; N_c \;\; \exp(\; -E_1/kT \;)$$

that is, for energies well above

$$E_1 \;\; = \;\; k \; T \;\; \ln(\; pS_p/nS_n \;).$$

Similar expressions apply for hole demarcation levels. The electron demarcation level is displaced from the electron Fermi level by an energy (Rose 1963)

$$k \; T \;\; \ln(\; nS_n/pS_p \;).$$

Illumination of the insulator with light of band gap energy produces electron hole pairs and the electron and hole demarcation levels move towards the respective bands as the intensity increases.

Since the steady state Fermi levels E_{fp} and E_{fn} are defined by the relations

$$| \; E_{fp} \; , \; E_v \; | \;\; = \;\; -k \; T \;\; \ln(\; p/N_v \;)$$

and

$$| \; E_{fn} \; , \; E_c \; | \;\; = \;\; -k \; T \;\; \ln(\; n/N_c \;)$$

then at a fixed light intensity they will recede from the band edge at a rate proportional to the absolute temperature.

5.6 INFRA RED QUENCHING AND THE EFFECT OF LIGHT INTENSITY ON THE TEMPERATURE DEPENDENCE OF PHOTOCONDUCTIVITY IN SINGLE CRYSTAL RUTILE

The infra red quenching experiments were performed under dynamic conditions. The crystal was first excited by 405 nm light at 77 K. After the photoconductivity had reached steady state values the crystal was irradiated simultaneously with IR light from a 500 W tungstun source passed through a 2 mm silicon filter. The results obtained from an oxidised NL crystal CA3 (NL) are shown in figure 5.6.1. After steady state values

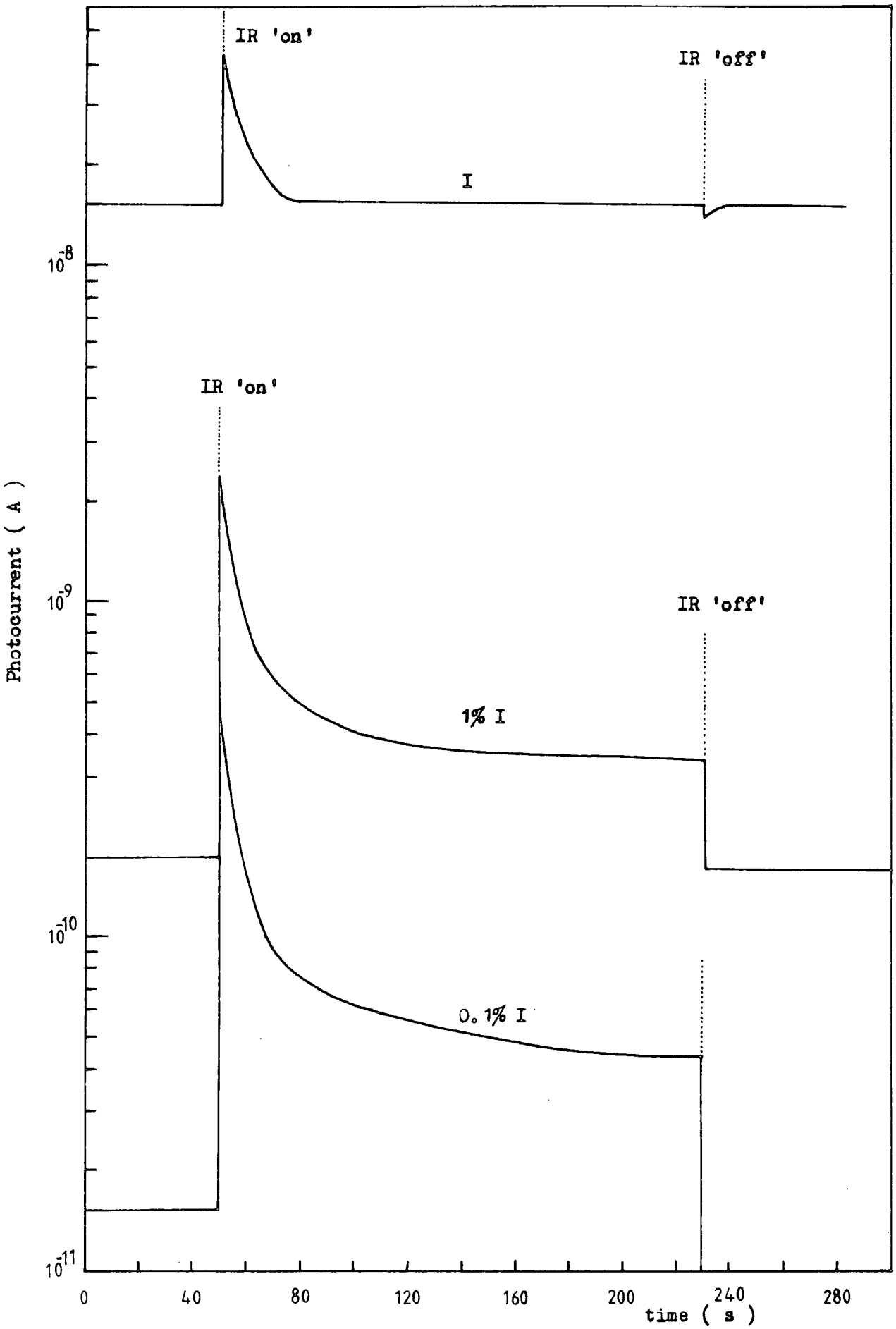

Figure 5.6.1 Photoconductivity stimulation due to infra red light as a function of 400 nm light intensity at 77 K for the unquenched CA3(NL) crystal.

were reached, photoconductivity stimulation was observed in these crystals, the degree of IR stimulation increased as the IR light intensity was reduced. Similar results were obtained from all the plasma grown and NL flame fusion crystals that were either grown as stoichiometric crystals or subsequently oxidised by heating at 1300°C in a stream of oxygen for 5 days and slowly cooling to room temperature at 1°/minute.

The temperature dependence of the photoconductivity was investigated as a function of the excitation intensity. Figure 5.6.2 shows the results obtained for the NL crystal CA3 (NL). The photocurrent decreased as the temperature was increased from 77 K to 170 K and then steadily increased as the temperature was further increased to 400 K. As the intensity of the incident light was reduced the photocurrent minimum was gradually shifted to lower temperatures.

Ghosh, Lauer and Addiss (1973) have previously reported infra red quenching of photoconductivity in NL single crystal rutile. As no IR quenching was observed in the oxidised crystals described above an attempt was made to see if a suitable treatment would lead to the appearance of the phenomenon. The oxidised crystals were heated for 4 hours at 1000°C and then quenched by withdrawing the crystals from the furnace under forced air cooling. The subsequent response to infra red radiation was investigated as shown in figure 5.6.3. It can be seen that IR quenching was induced into the NL(CA3) crystal at high excitation intensities. As the excitation intensity was reduced IR stimulation was observed.

The temperature dependence of the photoconductivity changed after treatment quenching of the NL(CA3) crystal from 1000°C. At high light intensities the minimum photoconductivity was observed at 190 K and a larger reduction in photoconductivity was observed from 77 K to 190 K than in the unquenched crystal. As the light intensity was reduced the

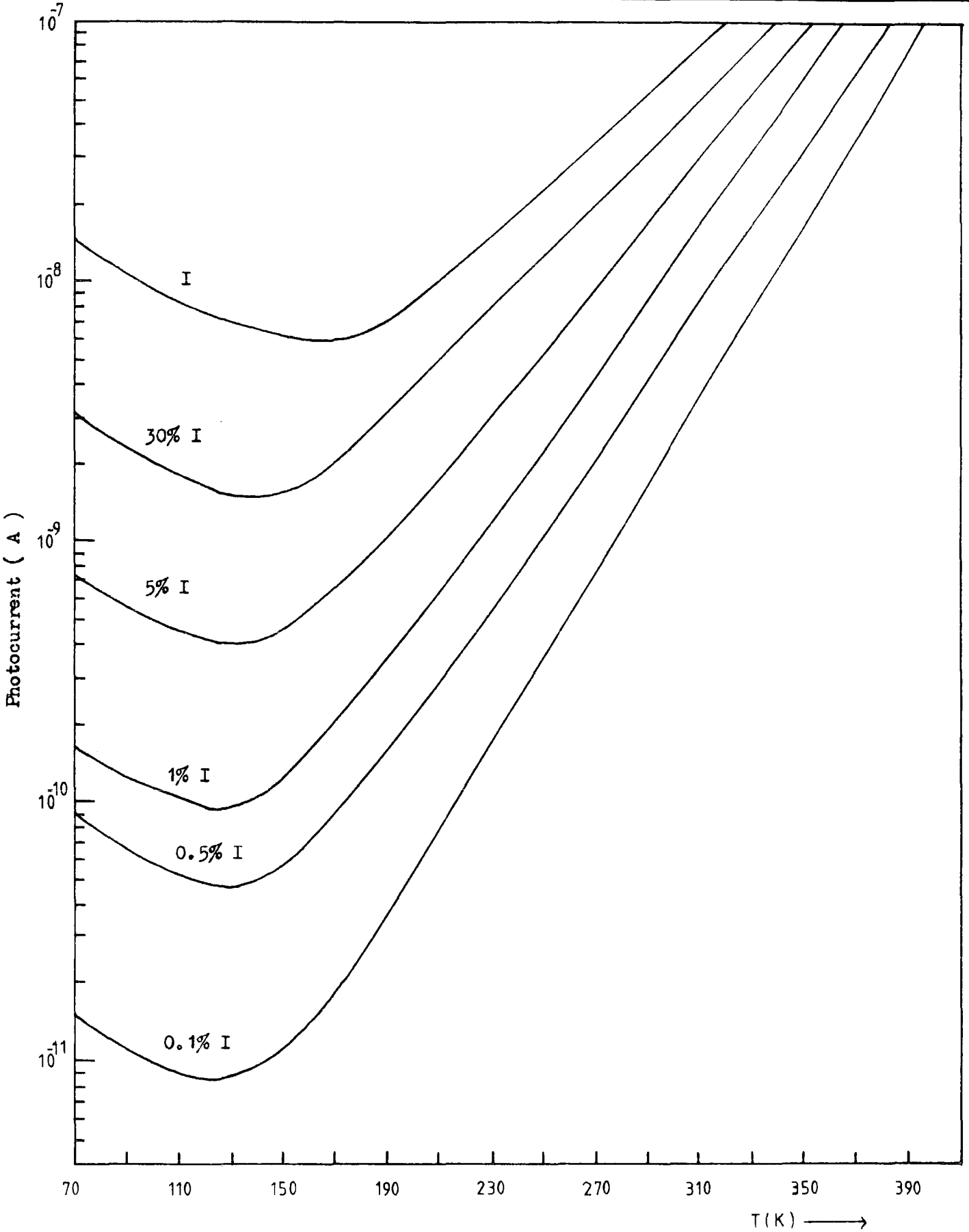

Figure 5.6.2 Temperature dependence of photoconductivity at various excitation intensities for the unquenched CA3(NL) crystal.

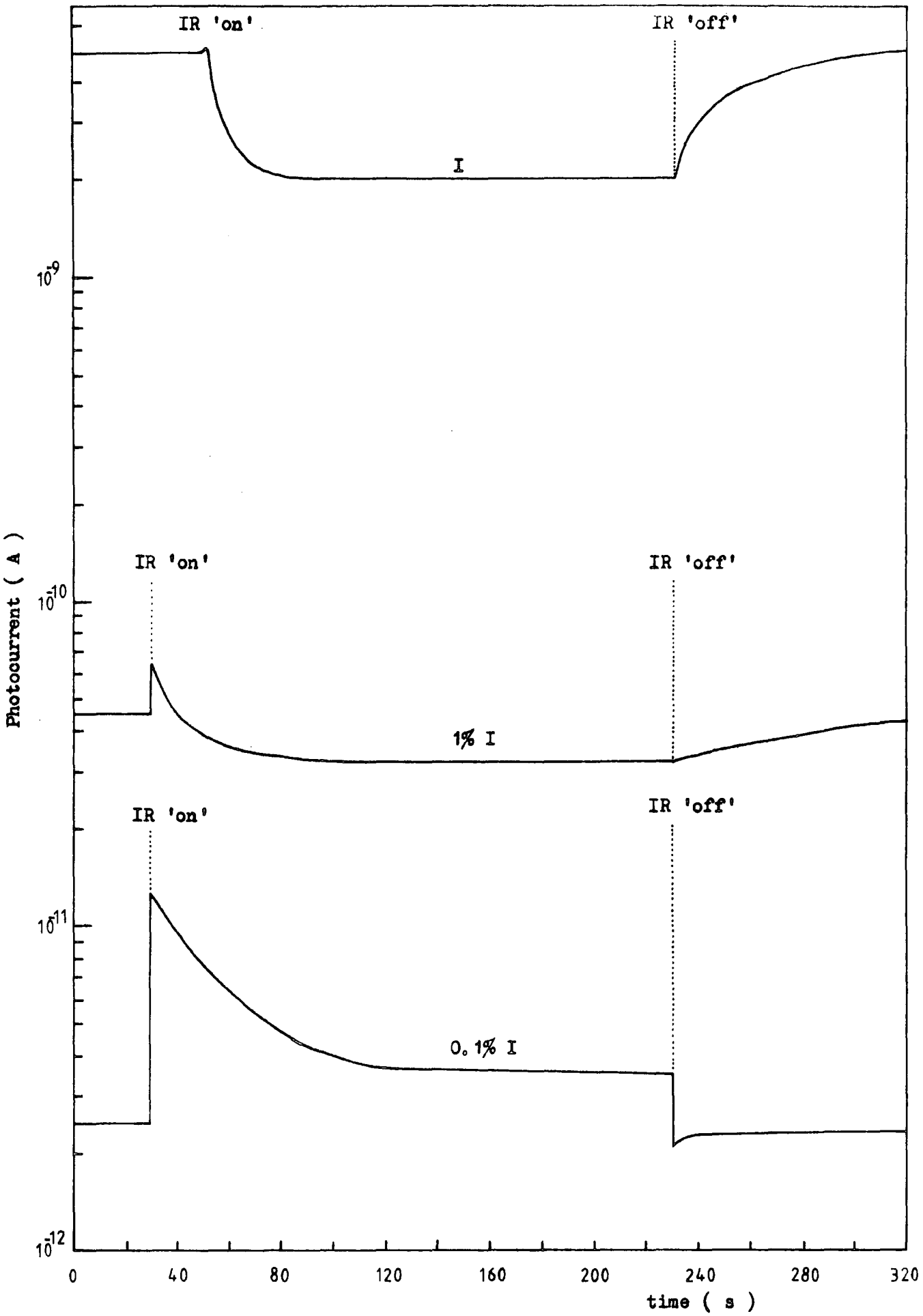

Figure 5.6.3 Photoconductivity quenching and stimulation due to infra red light as a function of 400 nm light intensity at 77 K for a quenched CA3(NL) crystal .

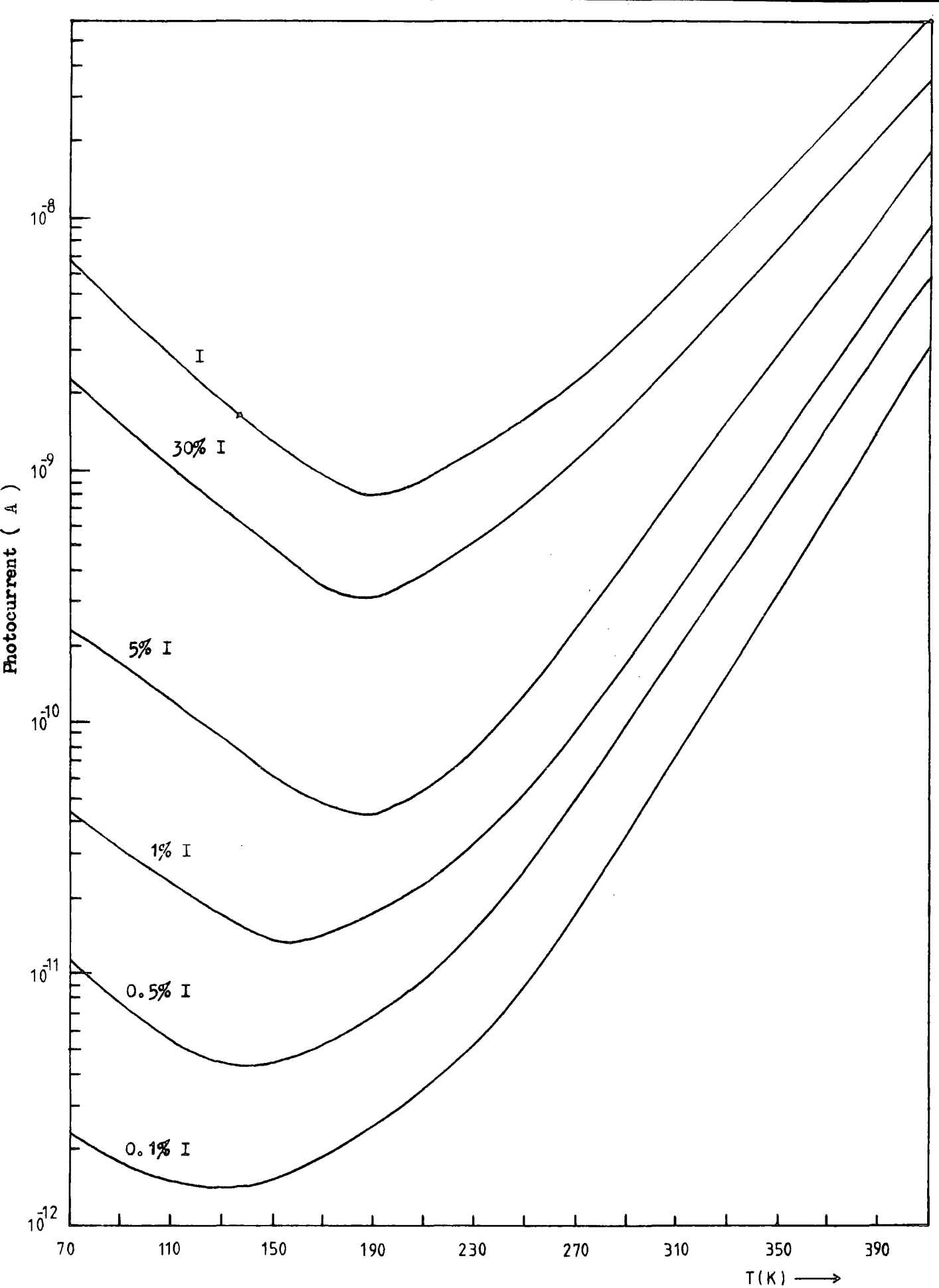

Figure 5.6.4 Temperature dependence of the photoconductivity at various excitation intensities for the quenched CA3(NL) crystal.

minimum moved to 125 K at 0.1% I.

5.7 DISCUSSION OF THE QUENCHING AND THE TEMPERATURE DEPENDENCE OF THE PHOTOCONDUCTIVITY

Figure 5.7.1 shows the variation of the photocurrent with light intensity at 77 K, 230 K, 350 K and 400 K for the quenched CA3(NL) crystal. The photocurrent was initially proportional to the light intensity at 77 K but became increasingly sublinear until it was proportional to the square root of the intensity at 400 K. Similar results were obtained on all the NL and plasma crystals both after annealing and after quenching.

Rose (1963) suggests several models relating particular trap distributions to the variation of the photocurrent with light intensity. In general, $I_p \propto I^n$, where I_p is the photocurrent, I is the light intensity and n varies between 0.5 and 1.0, depending on the mechanism of photo-conduction. The observation of a photocurrent proportional to the light intensity suggests the presence of traps which have a continuous distribution in the forbidden gap in the neighbourhood of the Fermi level or are concentrated below the Fermi level. For a trap free photoconductor, the photocurrent should be proportional to the square root of the light intensity. The latter result is also true when the number of traps is small compared to the number of free electrons.

The IR quenching experiments can be interpreted using the models shown in figures 5.7.2 and 5.7.3. In the annealed oxidised crystals at high light intensities the electron fermi level was raised above a large concentration of electron traps. The application of IR light emptied approximately equal numbers of holes and electrons, and little change was observed on the photocurrent. However when the intensity of the excitation light was reduced the electron fermi level was moved through the electron recombination centres converting them to electron traps. Now when IR light was applied to the crystal an increase in the photocurrent

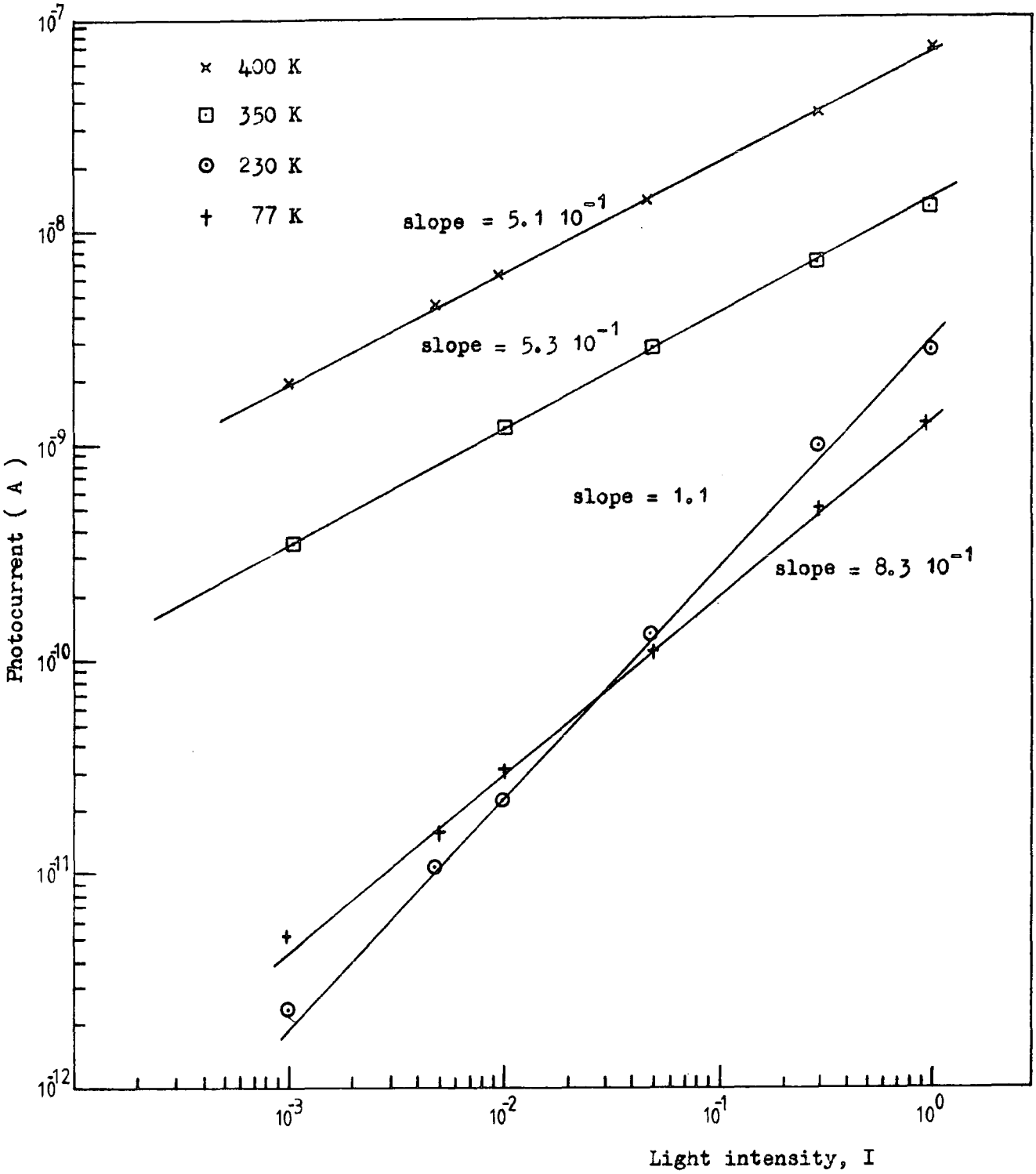

Figure 5.7.1 Photoconductivity versus light intensity at different temperatures for crystal CA3(NL).

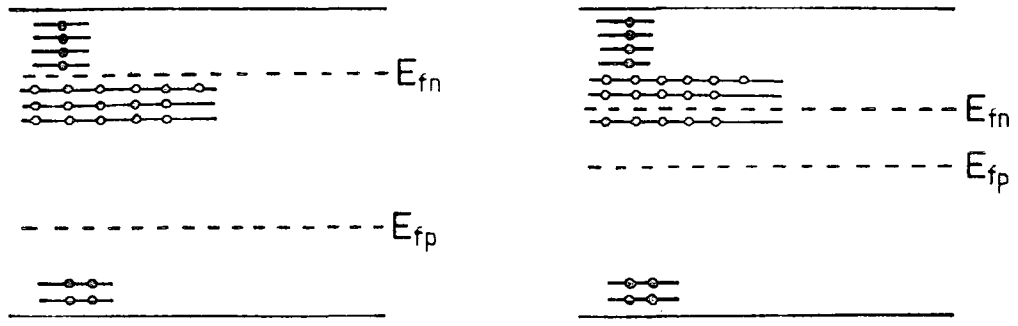

high light intensity

low light intensity

Figure 5.7.2 Model for IR quenching in annealed oxidised crystals.

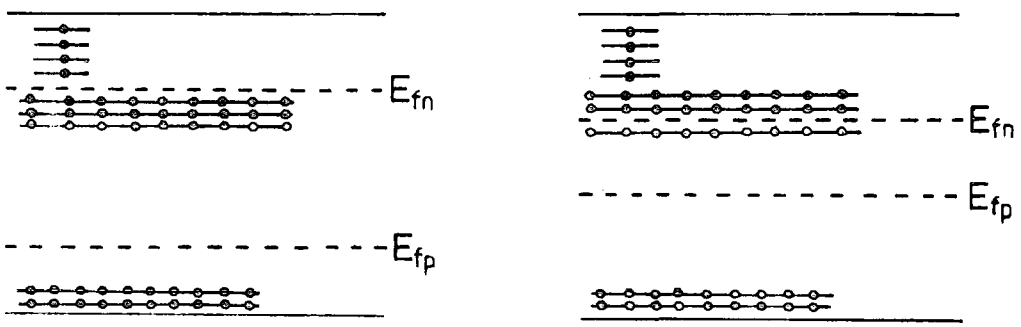

high light intensity

low light intensity

Figure 5.7.3 Model for IR quenching in quenched oxidised crystals.

stimulation was observed because more electron traps were being ionised than hole traps. The lower the intensity of the uv excitation the more electron recombination centres were converted to electron traps and the larger the photocurrent stimulation.

The IR quenching of the photocurrent in the quenched oxidised crystals can be explained if quenching the crystals from 1000°C increases both the density of the shallow hole traps and the electron traps as shown in figure 5.7.3. Evidence to support this model will be provided from TSC measurements in chapter 5. At high light intensities the number of hole traps exceeded the number of electron traps, and the application of IR light produced more ionised holes than electrons so that photocurrent quenching was observed. As the light intensity was reduced so more electron recombination centres were converted to electron traps and eventually more electrons were excited by the IR light than holes and photocurrent stimulation was observed.

The temperature dependence of the photocurrent was affected by the thermal ionisation of the traps and the position of the electron and hole fermi levels, which were controlled by the combination of light intensity and temperature. With the annealed crystals the photoconductivity decreased as the temperature was increased from 77 K due to the thermal ionisation of the shallow hole traps. At higher temperatures many of the deeper electron traps became ionised and the free electron lifetime increased producing an increase in the photocurrent. As the intensity of the light increased so more electron traps became available for thermal ionisation and the temperature of the photocurrent minimum moved to slightly lower temperatures. With the quenched oxidised crystals the initial decrease in photoconductivity was larger due to the increase in the population of the hole traps. The movement of the photocurrent minimum to lower temperatures as the light intensity was reduced was

larger due to the changing dominance of the electron and hole traps.

5.8 PHOTON STIMULATED CURRENTS

It was found that after preliminary illumination in the fundamental band region, an induced impurity photoconductivity could be observed in the rutile single crystals. This photosensitivity due to an nonequilibrium population of the impurity centres remained for several hours at liquid nitrogen temperatures.

The PSC experiments were performed by initially cooling a sample to 77 K and then illuminating it with band gap light for 10 minutes. The excitation light was removed and a bias voltage was applied to the charged sample. The conduction current was monitored as the sample was illuminated with light of progressively increasing photon energy which was always less than the band gap. The light was scanned low to high photon energy at 62nm/min in the 0.33μm to 1μm range and 125 nm/min in the 0.67μm to 2μm range. A 500 W tungstun lamp and a Hilger Watts D330 monochromator were used to provide the light source. The optical region from 1.0μm was scanned using a 1200 L/mm grating blazed at 0.5μm with a reciprocal dispersion of 26Å/mm. A 600 L/mm diffraction grating blazed at 1.0μm and a reciprocal dispersion of 50Å/mm was used to scan from 2μm to 0.67μm. The slit width at the input and output was 3mm and high order diffraction effects were reduced by using a series of Oriel filters in the visible region, a Dow Corning C57-56 and a silicon filter were used in the near infra red.

The PSC spectra for the CA3(NL) crystal are shown in figure 5.8.1. Curve a was obtained after filling the shallow traps during a 10 minute illumination with band gap light from a 250W mercury lamp passed through an OX1 glass filter and a 10% solution of copper sulphate. After heating the sample to 205 K and subsequently cooling to 77 K curve b was obtained.

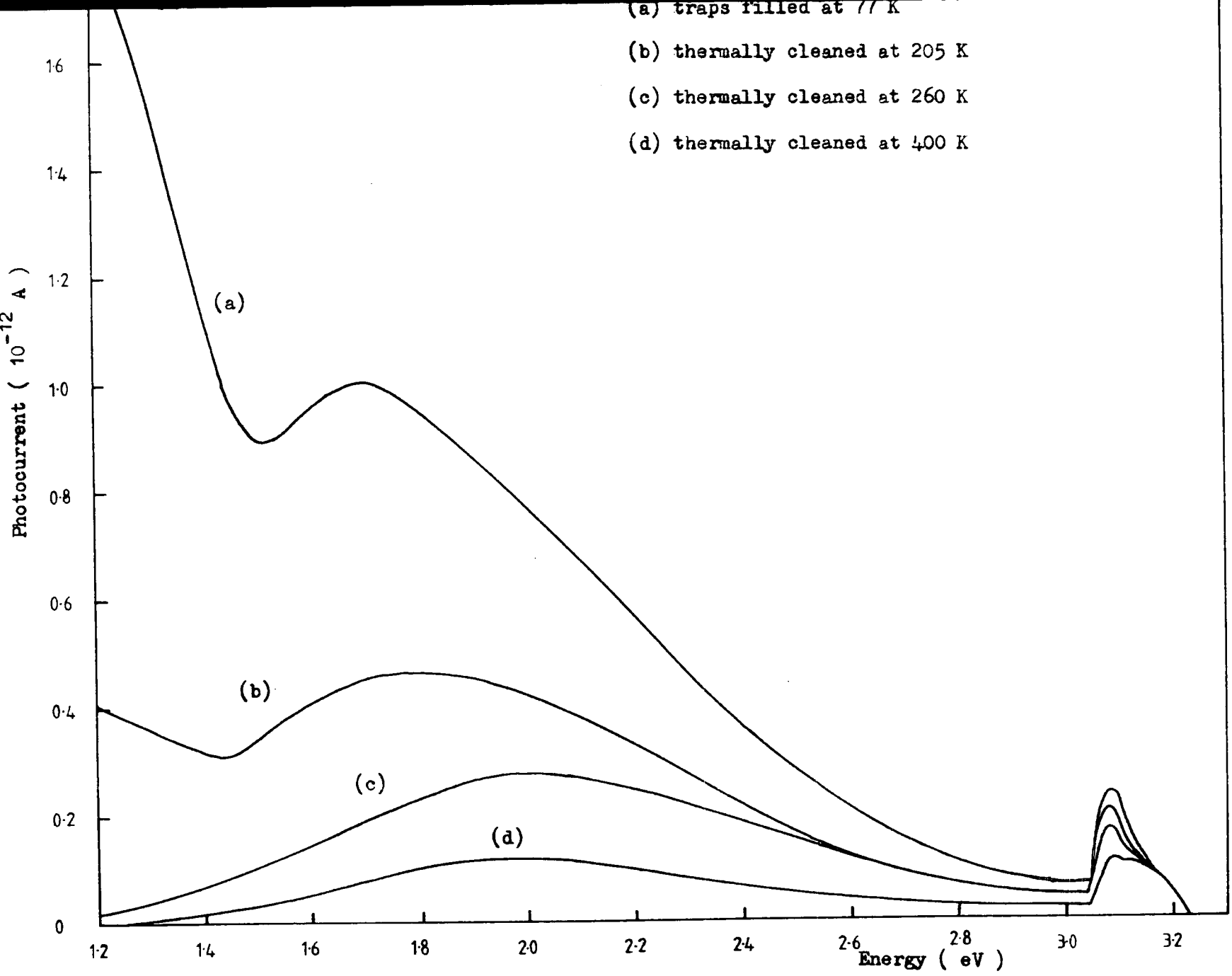

Figure 5.8.1 Induced photoconductivity in crystal CA3(NL) at 77 K after thermal cleaning at 205 K, 260 K and 400 K.

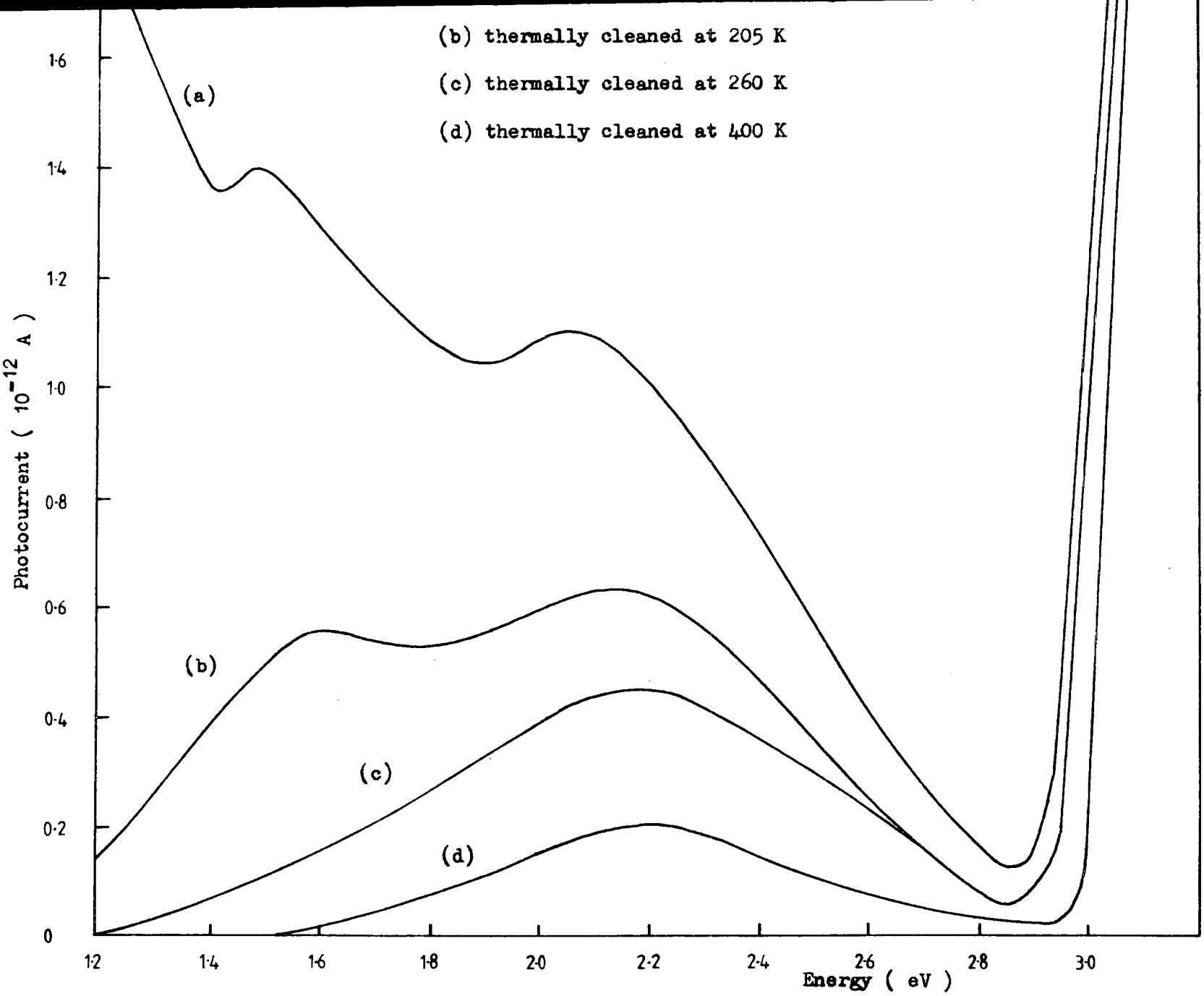

Figure 5.8.2 Induced photoconductivity in crystal CA3(NL) after spectral correction.

It can be observed that a large response at low energies, less than 1.2eV, was thermally cleaned by heating the crystal to 205 K. A smaller response at a peak energy of 1.6eV was thermally cleaned by heating to 260 K. The remaining photocurrent peak at 2.2eV was not removed by heating to 400 K and was probably due to an absorption centre in rutile which was not a trapping centre. The change in the magnitude of the 2.2eV peak after various stages of thermal cleaning was produced by the decrease in the free carrier lifetime as more trapping centres became thermally ionised after thermal cleaning.

The corrected PSC spectra for crystal CA3(NL) in the 2μm to 0.67μm range is shown in figure 5.8.3. A response which peaked at 0.8eV was thermally cleaned by heating to 140K. The large photocurrent peak at 1.2eV was thermally cleaned by heating to 205 K. Curves c and d are the PSC spectra after thermally cleaning the crystal at 205 K and 400 K respectively.

5.9 DETERMINATION OF THE TRAP DEPTH FROM PSC SPECTRA

As the energy of the light irradiating the sample approaches the trap energy E_t, some of the trapped carriers (electrons, say) are excited into the conduction band and a current is measured. Ideally, the current should not increase above the background level for energies $hc/\lambda < E_t$ and consequently the long wavelength cut-off of the photocurrent E_λ should be identical to the trap energy. However there may be a considerable long tail in the photocurrent due to the 'tailing-off' of the density of states distribution (N_c), from the conduction band (or valence band, in the case of holes) into the forbidden band. This 'tailing' is the result of lattice imperfections which are inevitably present in a real crystal. Thus the observed long wavelength cut-off point may in practice occur at energies which are less than the difference in energy between the trap energy and the 'true' conduction band edge (the mobility shoulder).

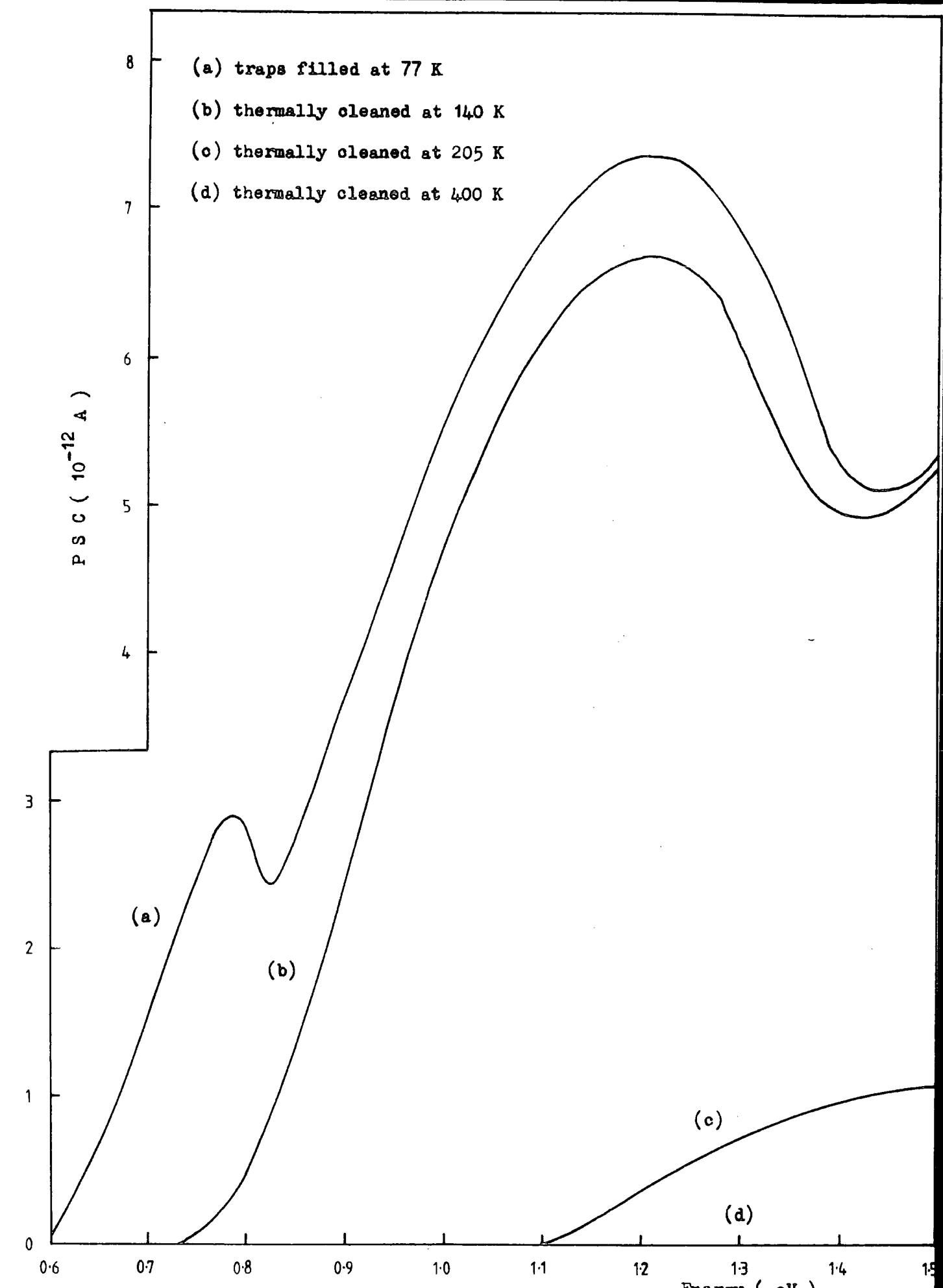

Figure 5.8.3 PSC spectra for the 0.63 eV and 0.86 eV traps in crystal CA3(NL) after thermal cleaning at 140 K, 205 K and 400 K.

Arkad'eva et al (1962) have evaluated trap energies in CdS, CdSe and CdTe, by taking $E_\lambda = E_t$ as the point at which the photocurrent is about 1% of its peak value. Nakayama (1970) discarded the initial part of the tail in the photocurrent and obtained the trap energy from the extrapolation of a graph of I^2 versus E onto the energy axis. The assumption implicit in this procedure is that the spectral photocurrent response follows approximately the density of states distribution ($N_c \propto E^{\frac{1}{2}}$) in the conduction band.

The problem of obtaining the trap energy from the PSC spectrum is similar to the problems of evaluating the band-gap energy (E_g) from an absorption spectrum. In the latter case, E_g is often taken as the energy at which the absorption coefficient changes most rapidly as a function of energy, but such a criterion can presumably be used in the present experiments only in the case of a discrete trap level.

Nakayama (1970) obtained a PSC response over a bandwidth of light energies 0.6 eV wide and considered the carriers to be excited from a discrete trap level into a broad continuum. That the trapping level involved is discrete was shown by carrying out a wavelength scan after first partially discharging the sample using light of a fixed energy; it was observed that the PSC response was smaller over the whole spectral range compared with the result obtained immediately after charging the sample. On the other hand, Thomas et al (1968) have considered a distribution of trap energies in SiO_2; when a PSC scan was carried out after discharging at a fixed energy; E', the spectral response was diminished only in the region of $hc/\lambda = E'$.

The spectral response of the photocurrent may in practice be distorted by the fact that the experimental conditions change during the course of a PSC scan, since the reservoir of trapped charge decreases

continually during the scan. It follows that the peak in the current-wavelength spectrum tends to shift to longer wavelengths compared with the result which would be obtained if the experimental conditions were constant during the experiment. However, if the scan is sufficiently slow that the total number of carriers released is small compared with the trapped charge density, the shift in the peak will be negligible.

The PSC spectra for all the rutile single crystals were found to decrease over the whole wavelength range after partially discharging the samples using light of fixed energy. This indicated the presence of three discrete traps in the crystal. Figures 5.9.1 and 5.9.2 show the I^2 versus E plots for the three traps and the extrapolation of the linear portion of the graph onto the energy axis. It can be observed that there was some uncertainty in the actual value of trap depth obtained. A comparison between the trap depth obtained from the I^2 versus E extrapolation and 1% of the energy peak is given in table 5.9.1. The 0.86eV and 1.18eV traps were observed in all the rutile crystals examined, the 0.68eV trap was only observed in the NL crystal and the plasma grown crystals BS1 and BS3.

5.10 THE KINETICS OF PSC

When a charged sample is illuminated with light of energy $h\nu = E_t$, a transient current response is measured as the released carriers move through the sample. The basic equations governing the rates of change of the free and trapped charge densities are

$$\frac{dn}{dt} = \alpha h_1^- I + \gamma h_1^- - \beta n (h_1 - h_1^-) - \alpha n a^+ \qquad (1)$$

$$\frac{dh_1}{dt}^{-1} = \beta n (h_1 - h_1^-) - \alpha h_1^- I - \gamma h_1^- \qquad (2)$$

I is the photon density illuminating the sample ($m^{-2}s^{-1}$), α is the capture cross section of the trapped carrier for a photon, the rest of the notation is the same used in chapter 2 and is represented diagrammatically in

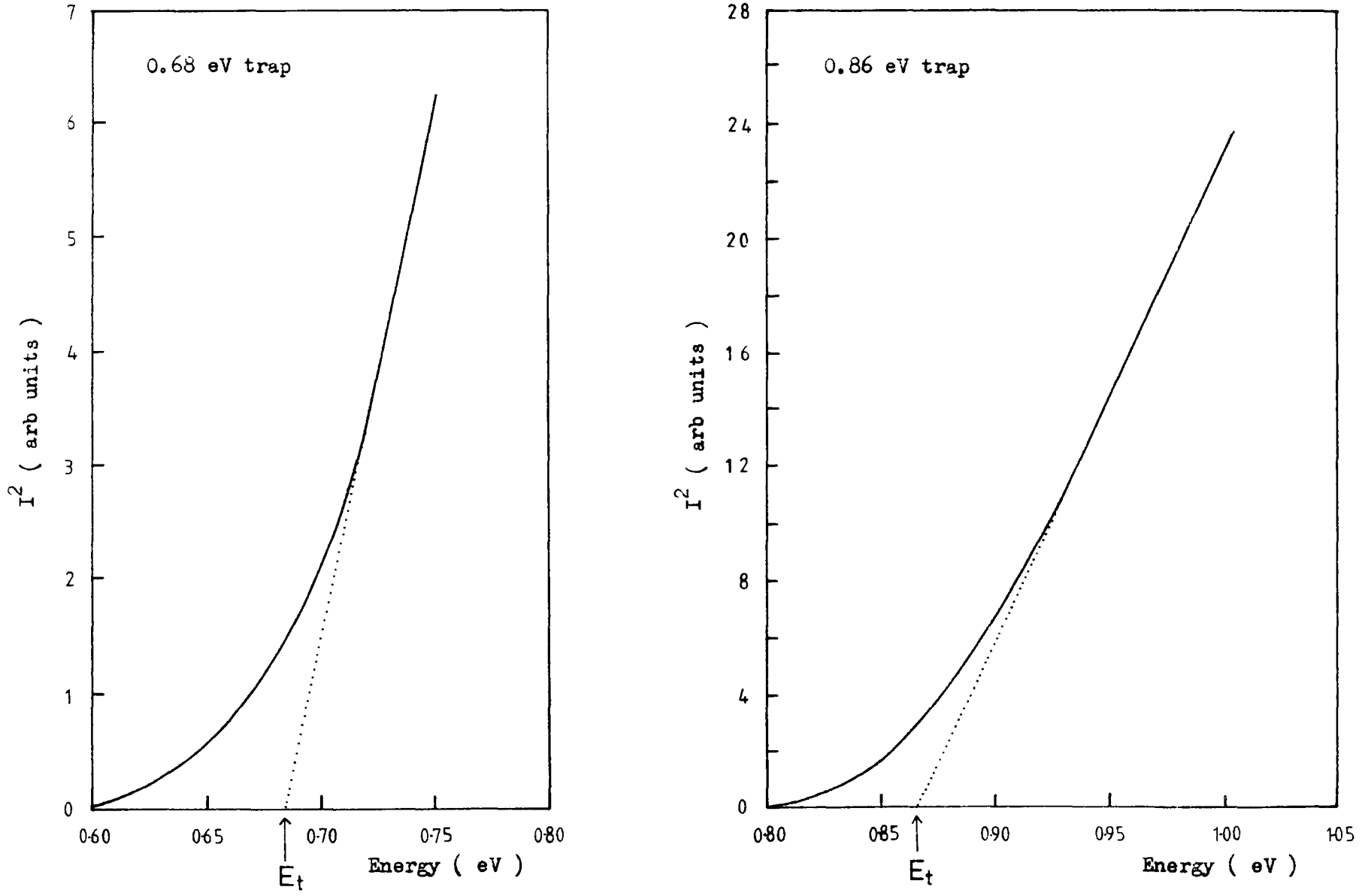

Figure 5.9.1 I^2 **versus E plots for the o.68 eV and the 0.86 eV trap in crystal CA3(NL).**

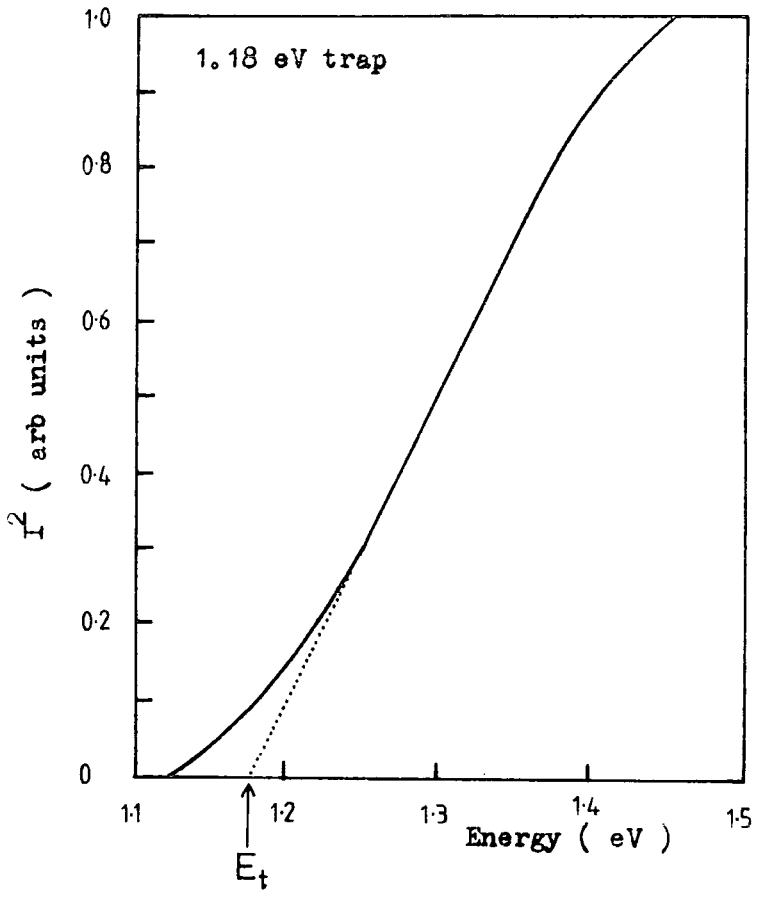

Figure 5.9.2 I^2 versus E plot for the 1.18 eV trap in crystal CA3(NL).

Method	Trap depth		Energy of PSC peaks after thermal cleaning at temperature T K				
	I^2 versus E eV	1% E_{max} eV					
Crystal			77K	140K	205K	260K	400K
CA3(NL)	0.68	0.60	0.79	-	-	-	-
	0.86	0.74	1.23	1.23	-	-	-
	1.18	1.10	1.60	1.60	1.60	-	-
			2.20	2.20	2.20	2.20	2.20
BS3	0.66	0.60	0.75	-	-	-	-
	0.85	0.73	1.31	1.31	-	-	-
	1.15	1.13	1.65	1.65	1.65	-	-
			2.25	2.25	2.25	2.25	2.25
BS10	0.84	0.73	1.29	1.29	-	-	-
	1.21	1.18	1.67	1.67	1.67	-	-
			2.15	2.15	2.15	2.15	2.15
BS13	0.85	0.73	1.29	1.29	-	-	-
	1.19	1.11	1.63	1.63	1.63	-	-
			2.16	2.16	2.16	2.16	2.16
BS18(S)	0.83	0.74	1.28	1.28	-	-	-
	1.17	1.14	1.65	1.65	1.65	-	-
			2.20	2.20	2.20	2.20	2.20
BS18(NS)	0.86	0.74	1.30	1.30	-	-	-
	1.19	1.14	1.65	1.65	1.65	-	-
			2.17	2.17	2.17	2.17	2.17
BS1	0.64	0.60	0.78	-	-	-	-
	0.84	0.74	1.26	1.26	-	-	-
	1.16	1.13	1.63	1.63	1.63	-	-
			2.01	2.01	2.01	2.01	2.01

Table 5.9.1 Summary of the trap depths obtained from the PSC experiments.

figure 5.10.1.

A factor g may be written such that

$$g = I \alpha k$$

where k is an arbitary term representing the efficiency of the process whereby a trapped charge can accept energy from a photon of energy $h\nu = E_t$. However, since energy is absorbed from the detrapping light in exciting carriers from the traps into the conduction band g will be a decreasing function of distance from the illuminated side of the crystal and we should write

$$g(x,t) = I(x,t) \alpha k$$

where x is the distance into the sample from the illuminated side of the crystal and t is the time after the illumination starts. In order to consider whether the variation of g with x is sufficiently large to warrant its inclusion in the equations it is necessary to know the order of magnitude of g. Brodribb et al (1972) have obtained values of g in the range 10^{-1} to 10^{-2} s^{-1} in anthracene and in this case, the total number of photons absorbed during an experiment is at most

$$I = h_1 V$$

where V is the volume of the sample. In the results quoted by Brodribb $h_1 \sim 10^{16}$ m^{-3} and $V \sim 10^{-7}$ m^3 from which $I = 10^9$ photons, which is negligible compared with the incident flux on the area of the sample of approximately 10^{14} s^{-1}. Consequently, in these circumstances it can be assumed that g is independent of x.

If the sample is at low temperature, thermal ionisation of carriers can be ignored and, (1) and (2) can be rewritten as

$$\frac{dn}{dt} = \alpha h_1^- I - \alpha n a^+ \qquad (3)$$

$$\frac{dh_1^-}{dt} = -\alpha h_1^- I \qquad (4)$$

for no retrapping.

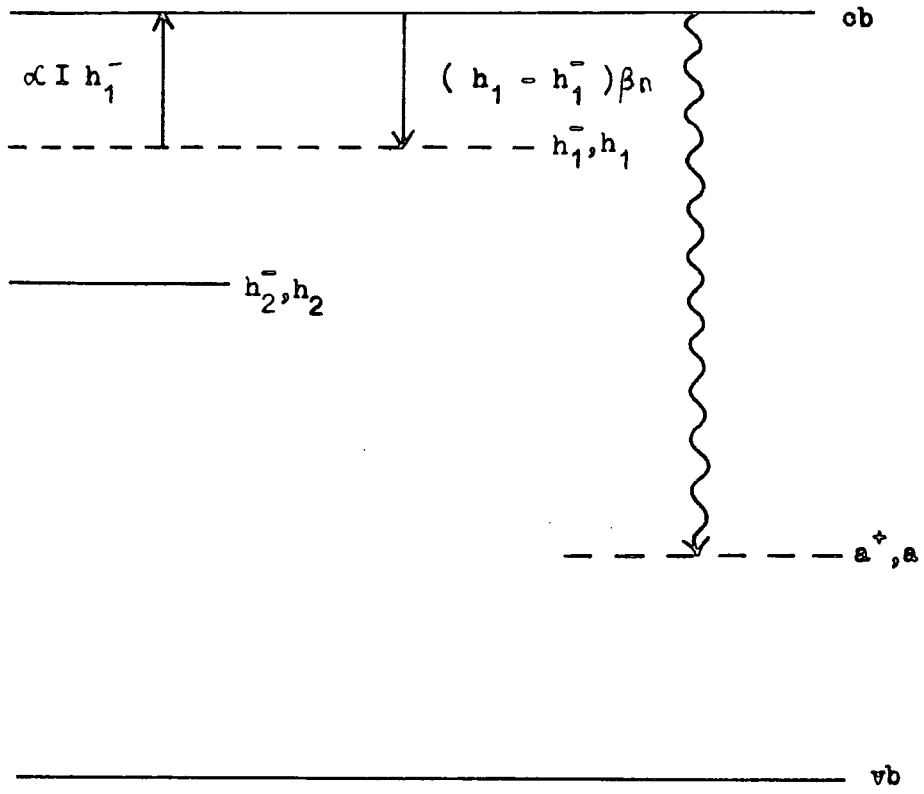

Figure 5.10.1 Simple insulator model used to describe the PSC spectra .

If $(h_1^- + n) \sim a^+$ and we ignore thermally disconnected deep charge in the sample then we can assume $1/\alpha a^+ = \tau$ and the equation (3) can be written as

$$\frac{dn}{dt} = \alpha h_1^- I - n/\tau .$$

Integration of the system for the case of illumination i.e., when the initial conditions are $n = 0$, and $h_1 = h_1^-$ when $t = 0$, gives the following expression for the electron density in the conduction band (Ryvkin 1964).

$$n = \frac{\alpha I h_1^-}{1/\tau - \alpha I} \quad (\exp(-\alpha I t) - \exp(-t/\tau)) \quad (5)$$

If in addition $\alpha I \tau << 1$ as indicated by the fast rise of the photocurrent to its peak value then for $t >> \tau$ equation (5) reduces to

$$n = \alpha I h_1^- \tau \exp(-\alpha I t) . \qquad (6)$$

Hence the current measured in the external circuit is

$$I_n = n \mu e E A$$
$$= \alpha I h_1^- \tau A E e \mu \exp(- \alpha I t) .$$

If $\ln(I_n)$ is plotted against t for the decaying portion of the curve, a straight line is obtained provided that τ is a constant, the slope of which gives $g = \alpha I$ and the intercept on the I_n axis yields $\mu \alpha I \tau h_1^- E A e$. By dividing the intercept on the I_n axis by the slope we may obtain the initial concentration of trapped charge if the product $(\mu \tau)$ is known.

The above method of determining h_1^- is essentially equivalent to obtaining the area under the I_n-t curve as follows. We may write approximately that

$$n = -\tau \frac{dh_1^-}{dt} .$$

Hence

$$| I_n | = \left| \frac{dh_1^-}{dt} \tau \mu e E A \right|$$

from which the total charge released is

$$Q = \int_0^t I_n \, dt = \tau \mu e E A g h_1^-$$

which is identical to the expression obtained by dividing the intercept of the ln(I_n) versus t curve by its slope. Thus by integrating the charge released, h_1^- may be obtained if the product ($\mu\tau$) is known. This is the procedure used by Thomas et al (1968) to estimate the trap density in SiO_2.

As with TSC this method of evaluating h_1^- is valid only if the applied voltage is sufficiently large that the electric field in the sample is unipolar.

5.11 DETERMINATION OF THE TRAP DENSITIES AND PHOTON CAPTURE CROSS SECTIONS FROM PSC DECAY CURVES

The PSC spectra were investigated further by initially cooling the crystal to 77 K and filling the shallow traps by illuminating with band gap light from a 250W mercury source. A voltage was applied to the sample which was irradiated with light of a fixed energy. The optically stimulated current was monitored as a function of time. A typical result is shown in figure 5.11.1. The sample was irradiated with light of wavelength 1.2μm and approximate intensity 10^{14} photons/s. Figure 5.11.2 shows the ln (n) versus t plots for the excitation wavelengths 1.2 μm, 1.0 μm and 0.9 μm. The difference in initial PSC was due to the variation in optical energy output of the measurement system. The 2 μm to 0.67 μm diffraction grating was blazed at 1.0 μm and had a maximum output at this wavelength. Table 5.11.8 shows the g factors obtained from the slopes of the ln (n) - t curves. The photon capture cross sections were evaluated by measuring the number of photons irradiating the sample using a calibrated thermopile. Values of trap density (h_1) were obtained from the intercept of the ln (n) axis at t=0. Similar results are shown for all the three traps seen in crystal CA3(NL).

In practice it was found that the ln (n) - t plots were not straight lines. This indicated that the free carrier lifetime was not constant with time or that some retrapping of carriers was occurring, or a combination of both effects were present. In the case of retrapping a

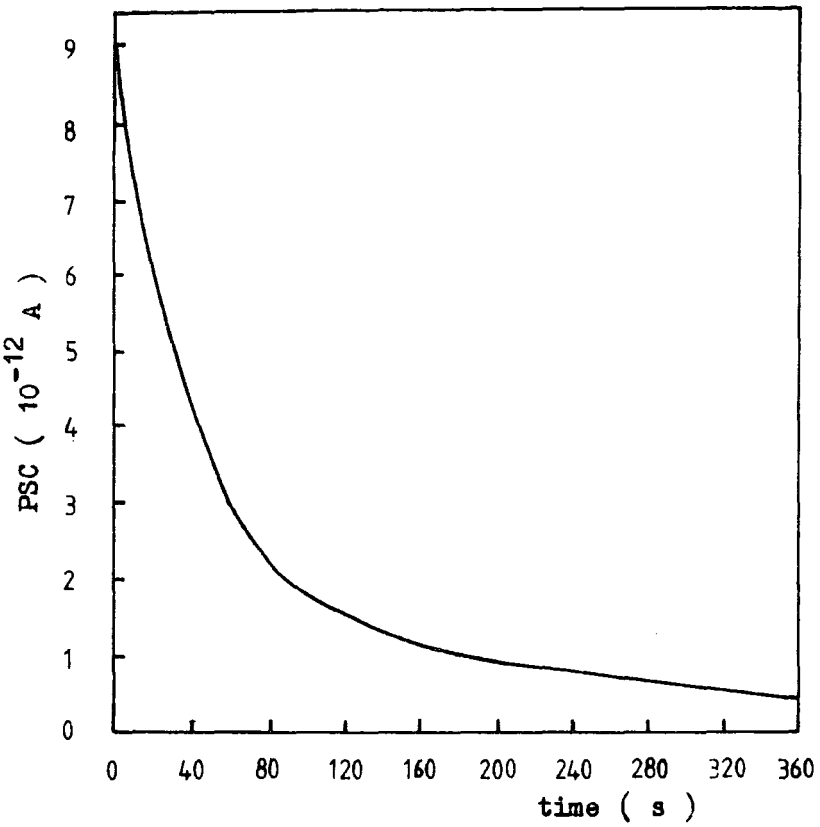

Figure 5.11.1 The emptying of the 0.86 eV trap in crystal CA3(NL) after excitation with light of wavelength 1.2 μm .

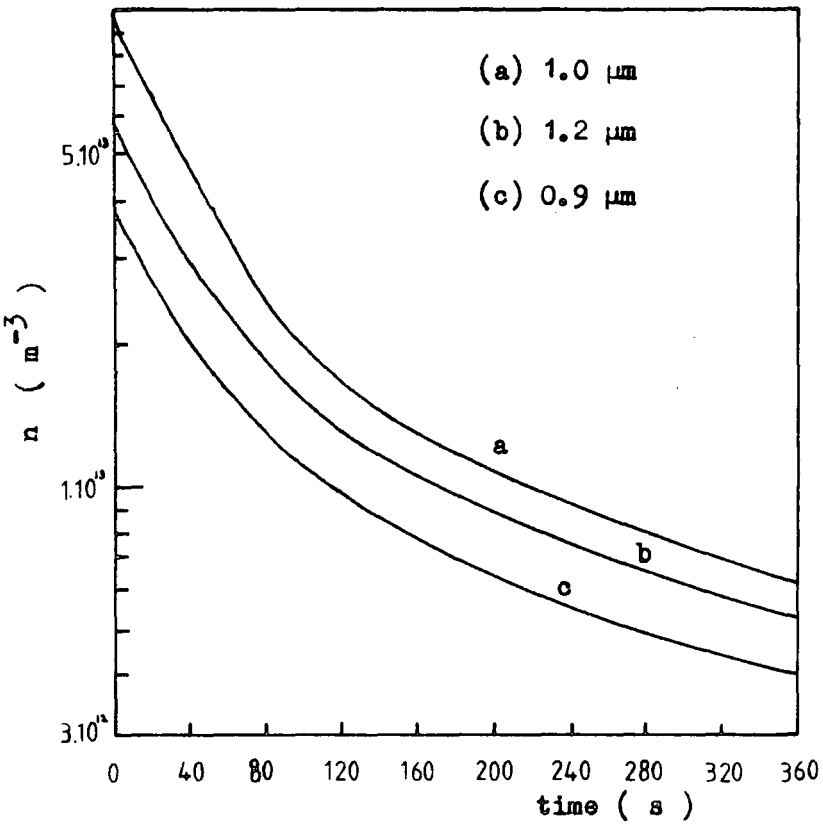

Figure 5.11.2 The emptying of the 0.86 eV trap in crystal CA3(NL) after excitation with light of wavelength 1.2 μm, 1.0 μm and 0.9 μm .

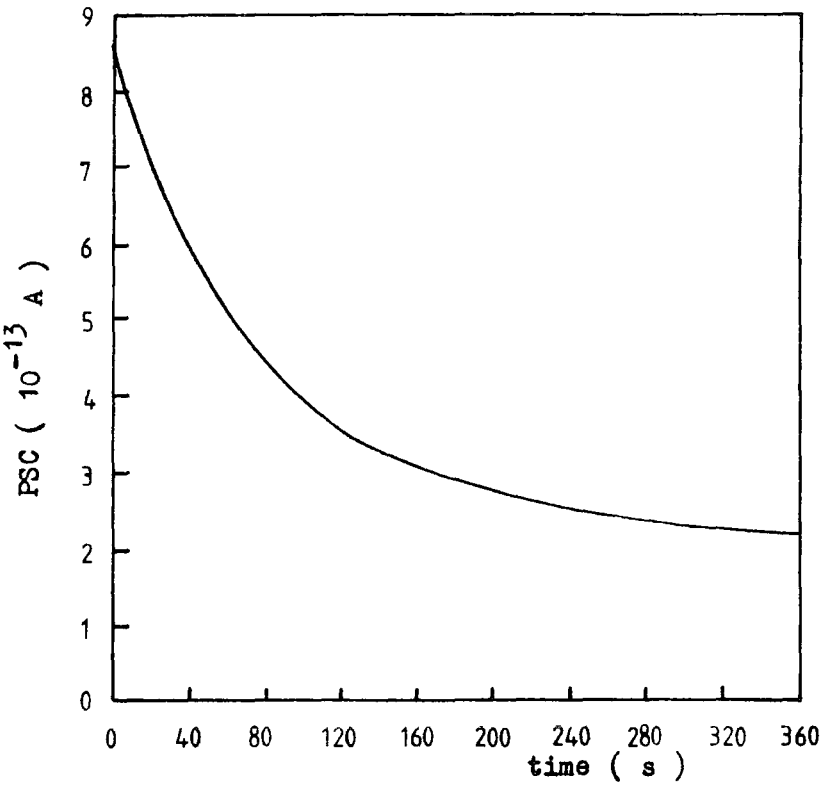

Figure 5.11.3 The emptying of the 0.68 eV trap in crystal CA3(NL) after excitation with light of wavelength 1.5 μm .

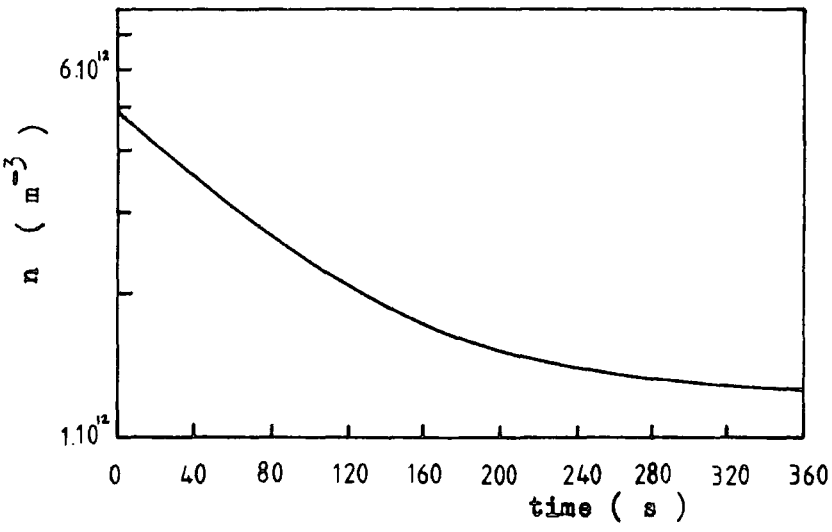

Figure 5.11.4 The emptying of the 0.68 eV trap in crystal CA3(NL) after excitation with light of wavelength 1.5 μm .

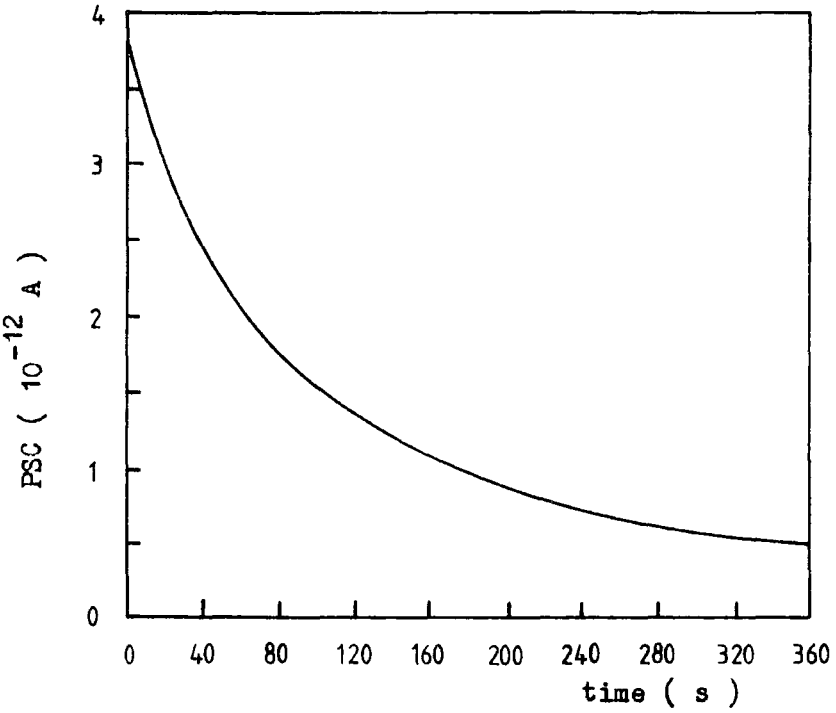

Figure 5.11.5 The emptying of the 1.18 eV trap in crystal CA3(NL) after excitation with light of wavelength 0.75 μm .

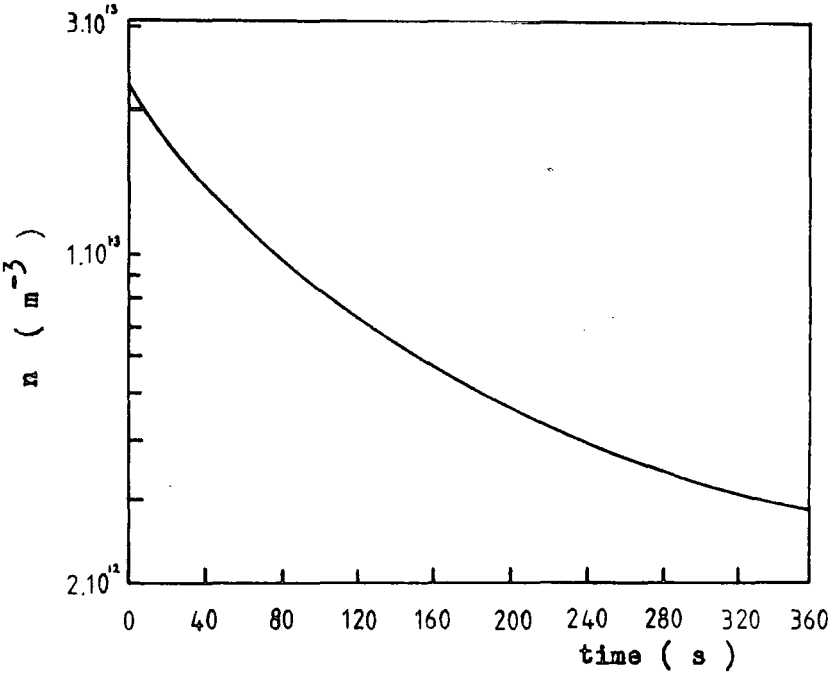

Figure 5.11.6 The emptying of the 1.18 eV trap in crystal CA3(NL) after excitation with light of wavelength 0.75 μm .

Excitation μ	E eV	ε cm^2/s	α cm^2	h_1 cm^{-3}
1.2	1.04	$2.26\ 10^{-2}$	$2.8\ 10^{-16}$	$2.5\ 10^{17}$
1.0	1.24	$1.66\ 10^{-2}$	$1.6\ 10^{-16}$	$2.6\ 10^{17}$
0.9	1.38	$1.53\ 10^{-2}$	$2.1\ 10^{-16}$	$2.4\ 10^{17}$
1.5	0.83	$1.02\ 10^{-2}$	$1.9\ 10^{-16}$	$5.0\ 10^{16}$
0.75	1.66	$1.11\ 10^{-2}$	$2.8\ 10^{-16}$	$1.9\ 10^{17}$

Table 5.11.8 Summary of the optical trapping parameters determined by PSC for crystal CA3(NL) .

Crystal	E eV	α cm^2	h_1 cm^{-3}
CA3(NL)	0.68	10^{-16}	$5\ 10^{16}$
	0.86	10^{-16}	$2\ 10^{17}$
	1.18	10^{-16}	$2\ 10^{17}$
BS1	0.64	10^{-16}	$3\ 10^{16}$
	0.84	10^{-16}	$4\ 10^{17}$
	1.16	10^{-16}	$1\ 10^{17}$
BS3	0.66	10^{-16}	$1\ 10^{16}$
	0.85	10^{-16}	$3\ 10^{17}$
	1.15	10^{-16}	$2\ 10^{17}$
BS10	0.84	10^{-16}	$9\ 10^{16}$
	1.21	10^{-16}	$4\ 10^{16}$
BS13	0.85	10^{-16}	$2\ 10^{17}$
	1.19	10^{-16}	$6\ 10^{16}$
BS19(S)	0.83	10^{-16}	$4\ 10^{16}$
	1.17	10^{-16}	$4\ 10^{16}$
BS18(NS)	0.86	10^{-16}	$1\ 10^{17}$
	1.19	10^{-16}	$8\ 10^{16}$

Table 5.11.9 Summary of the optical trapping parameters obtained from PSC for National Lead and plasma grown crystals .

gradual transition from the case of 'no retrapping' to the case where retrapping is present may occur during the course of a PSC transient. Arkad'eva et al (1962) have observed such a transition as indicated by the current response shown in figure 5.11.7. In the region 'a' the 'no retrapping' condition is considered to hold and the current decays relatively quickly. Recombination is considered to occur within the sample rather than at the electrodes and the density of recombination centres $a \sim h_1$. Hence as the traps discharge the trapping lifetime τ_t becomes larger and the recombination lifetime τ_R smaller which results in fast retrapping at long times (i.e. region 'b' in figure 5.11.7).

For the case of 'no retrapping' Arkad'eva derived an expression which is identical to equation 5, assuming τ to be constant. In the case of fast retrapping it was assumed that the total number of carriers in the sample ($N = n + h_1^-$) remains constant for times of the order of minutes and the following expressions were obtained for the variation of the current with time when the light illuminating the sample was switched off and on as shown in figure 5.11.7. For the rising portion of the current transient

$$n = \frac{g N}{h_1 v S + g} \left\{ 1 - \exp - (h_1 v S + g) t \right\}$$

$$\text{i.e.} \qquad \tau_{rise} = \frac{1}{h_1 v S + g}$$

and for the current decay

$$n = \frac{gN}{h_1 v S} \exp - (h_1 v S) t$$

$$\text{i.e.} \qquad \tau_{decay} = \frac{1}{h_1 v S} .$$

Since the values of τ_{rise} and τ_{decay} predicted by these expressions were too small to be measured for the small current levels encountered in the present

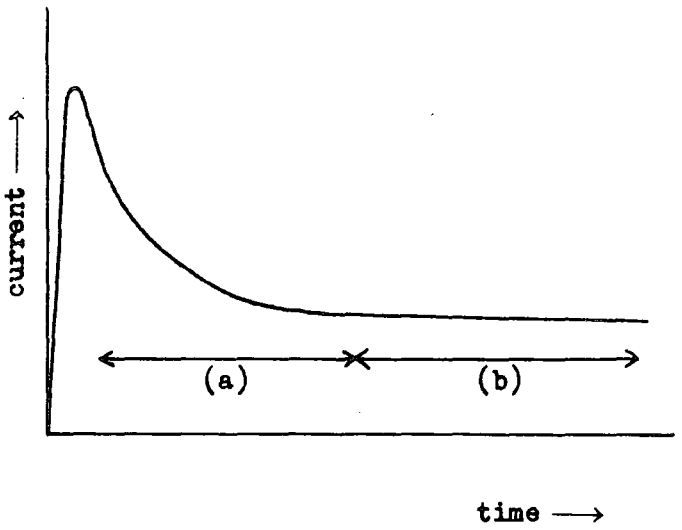

Figure 5.11.7a Optical detrapping current transient after Arkad'eva et al (1960).

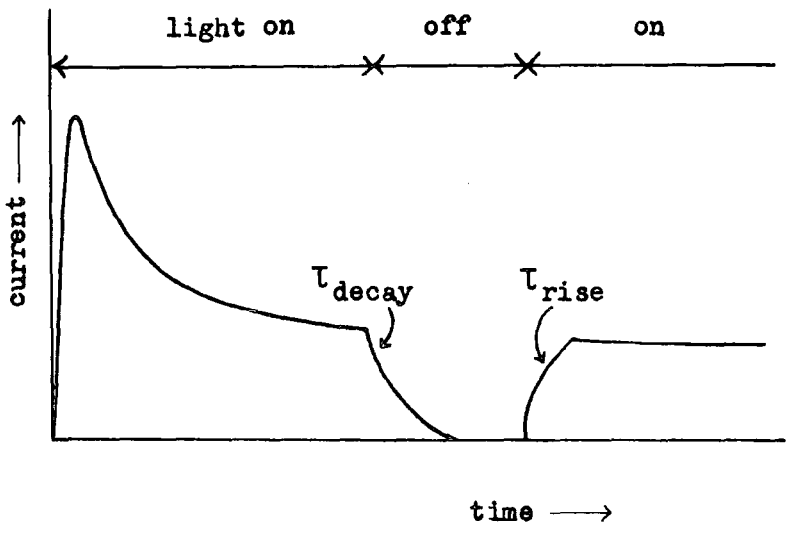

Figure 5.11.7b Response of the discharge current as the detrapping light is switched on and off.

work on rutile, it was not possible to apply this technique to find values of trapping cross section.

All the NL and plasma grown crystals were examined using the PSC technique. A summary of the results obtained is given in table 5.11.9. Two traps at 0.85 eV and 1.18 eV were present in various densities in all the crystals examined. A trap at 0.65 eV was observed in the NL crystals and the plasma crystals grown using 'impure' sandy rutile. Photon capture cross sections were estimated at 10^{-16} cm^2 for all the traps and probably reflected the insensitive nature of the analysis. Electron and hole capture cross sections were not evaluated due to the difficulties in interpreting the complex nature of the PSC decay curves. Some attempt was made to use analysis presented by Brodribb et al (1975) for PSC under retrapping conditions, but with little success. It was found impossible to seperate the contributions of retrapping and the variation of the free carrier lifetime on the non-linearity of the PSC decay curves.

CHAPTER 6

PHOTOLUMINESCENCE

6.1. INTRODUCTION

Photoluminescence measurements were made on all the undoped plasma grown and NL flame fusion crystals. The excitation radiation was supplied by either a 500W tungstun source or a 250W compact mercury source in series with a chance OX1 glass filter and a 10% solution of copper sulphate. The luminescence was monitored with a RCA Quantacon photomultiplier type C31034 in combination with a Hilger Watts grating monochromator D330 MK11. Two Oriel filters G-774-4450 and G-772-7800 were used to observe luminescence emission and excitation spectra in the single crystal rutile. An Egginc-Salem pulsed xenon flashtube, type FX-76, was used as the source for the luminescence lifetime measurements. A Brookdeal scan delay generator, type 425A, and a Brookdeal linear gate, type 415, were used to form a boxcar detector. The external voltage from a pulse generator was used to trigger the xenon flashtube with a thyristor and provide a reference signal for the boxcar.

6.2 EMISSION AND EXCITATION SPECTRA IN UNDOPED SINGLE CRYSTAL RUTILE

The photoluminescence emission spectrum was observed using the system described previously in section 4.6. The emission was observed with a RCA C31034 photomultiplier and an Oriel G-772-7800 filter in series with a monochromator. The two filters were ideally matched and no phase-sensitive detection was necessary to observe the emission spectrum. A typical result is shown in figure 6.2.1 which includes an emission spectrum corrected for the spectral response of the measurement system. A thermopile was used to calibrate the photomultiplier against the combined energy output of the source, filter and monochromator. In order to establish the spectral response of the filter and monochromator combination it was necessary to know the energy output spectrum of the tungstun source used to calibrate

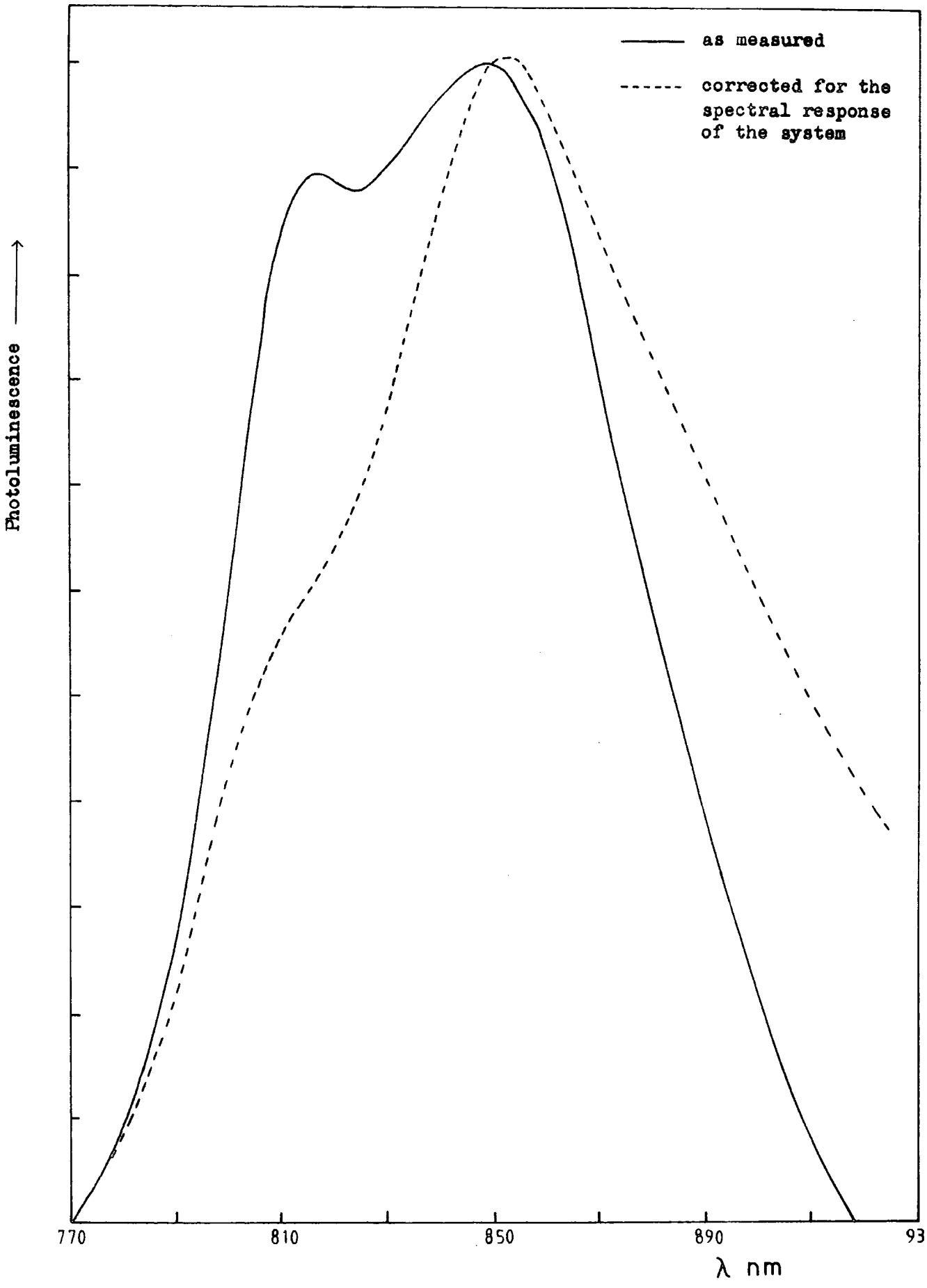

Figure 6.2.1 Photoluminescence emission spectrum at 77K for the crystal CA3(NL).

the system. No standard light source was available and so the manufacturer's typical response curve was used. As the correction was only over a small wavelength range from 770 nm to 930 nm errors were considered minimal.

Photoluminescence emission was examined from all the crystals grown by the plasma induction torch. As shown in figure 6.2.2 the photoluminescence intensity from the National Lead crystal CA3(NL) was an order of magnitude larger than any of the plasma grown crystals. All the crystals were the same size and illuminated with the same excitation intensity.

The temperature dependence of the emission spectrum is shown in figure 6.2.3 for crystal CA3(NL). Variation of the photoluminescence intensity with temperature differed from samples cut from different boules and these effects will be discussed later in the chapter. As the temperature increased the halfwidth of the emission broadened and the experimental results for CA3(NL) are shown in figure 6.2.3.

Photoluminescence excitation spectra were observed using the experimental system described in section 4.6. A 500W tungstun lamp and an Oriel G-774-4450 filter was used in series with the D330 monochromator as the excitation source. The total emission luminescence was observed with the C31034 photomultiplier and an Oriel G-772-7800 filter. A typical excitation spectrum is shown in figure 6.2.4, the as measured spectrum was corrected for the combined energy output of the measurement system. In all the crystals examined the sharp response at 395 nm was always present and the peak at 450 nm was only seen in NL flame fusion crystals.

6.3 DEEP LEVELS IN TiO_2

Before discussing the photoluminescence experiments, it will be useful to consider some of the theoretical problems posed by deep levels in titanium dioxide. A useful introduction to metal substitutes in

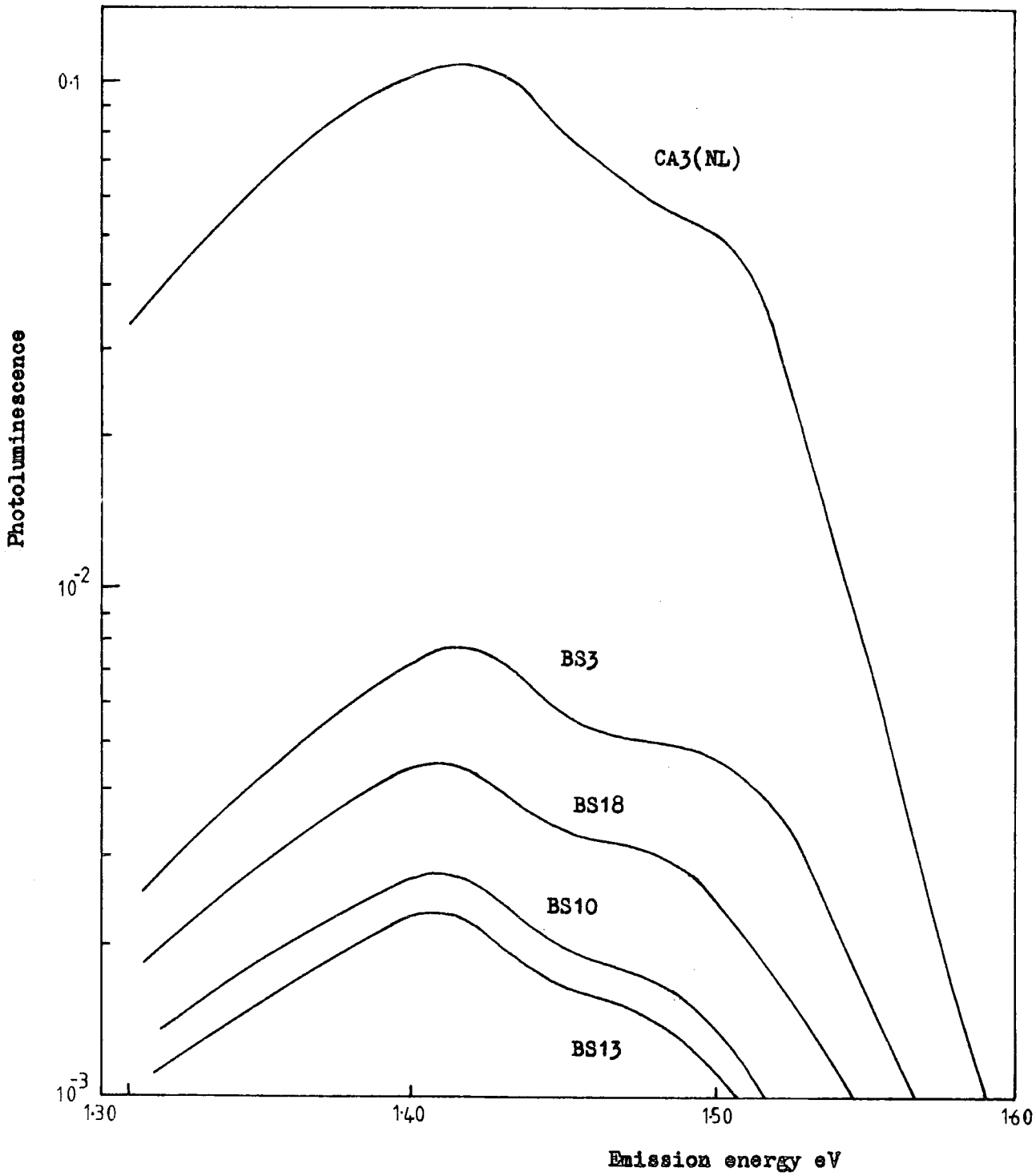

Figure 6.2.2 Comparison of the photoluminescence emission spectra for the flame fusion and plasma grown crystals.

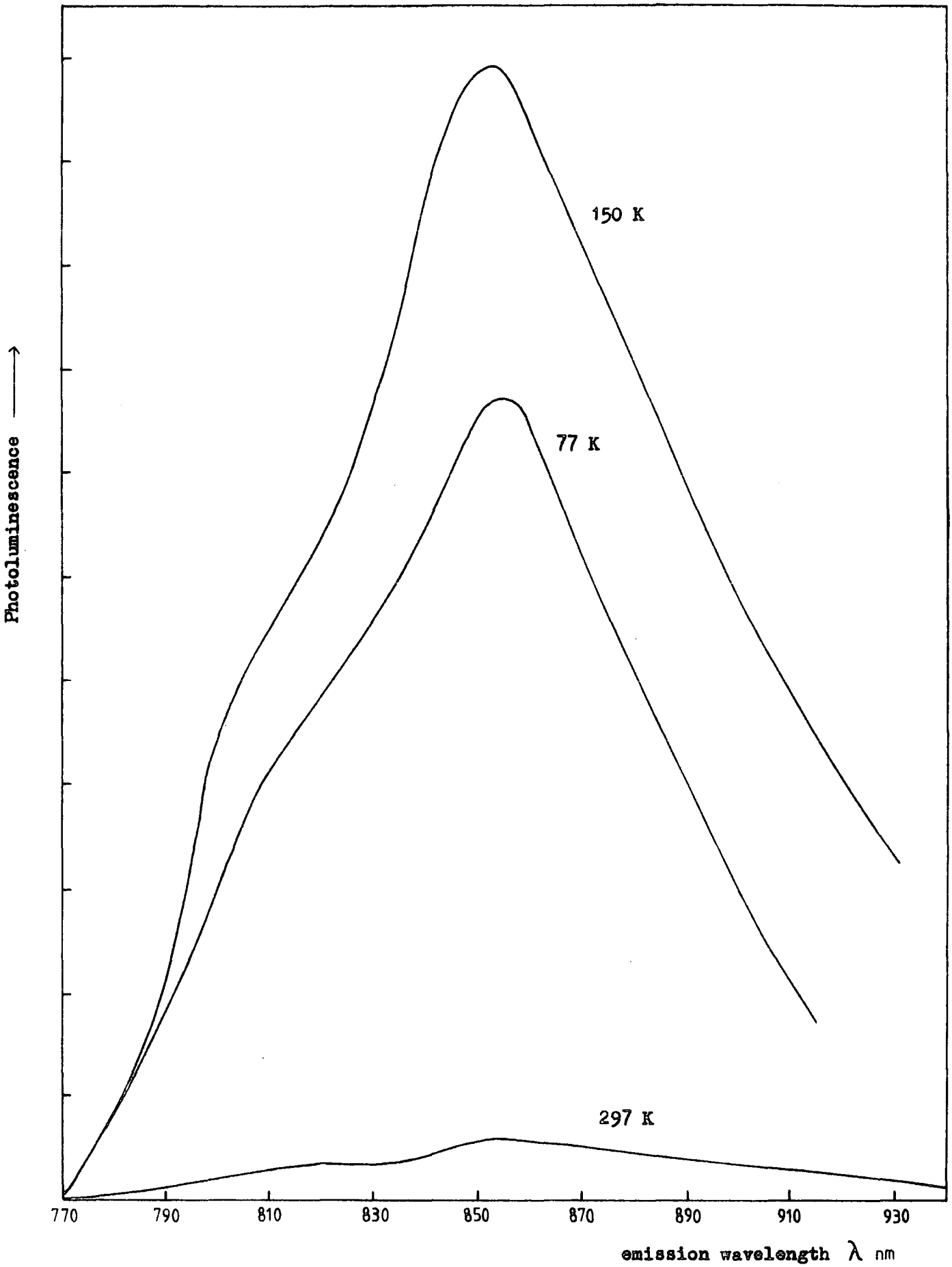

Figure 6.2.3 The temperature dependence of the photoluminescence emission spectrum for the crystal CA3(NL).

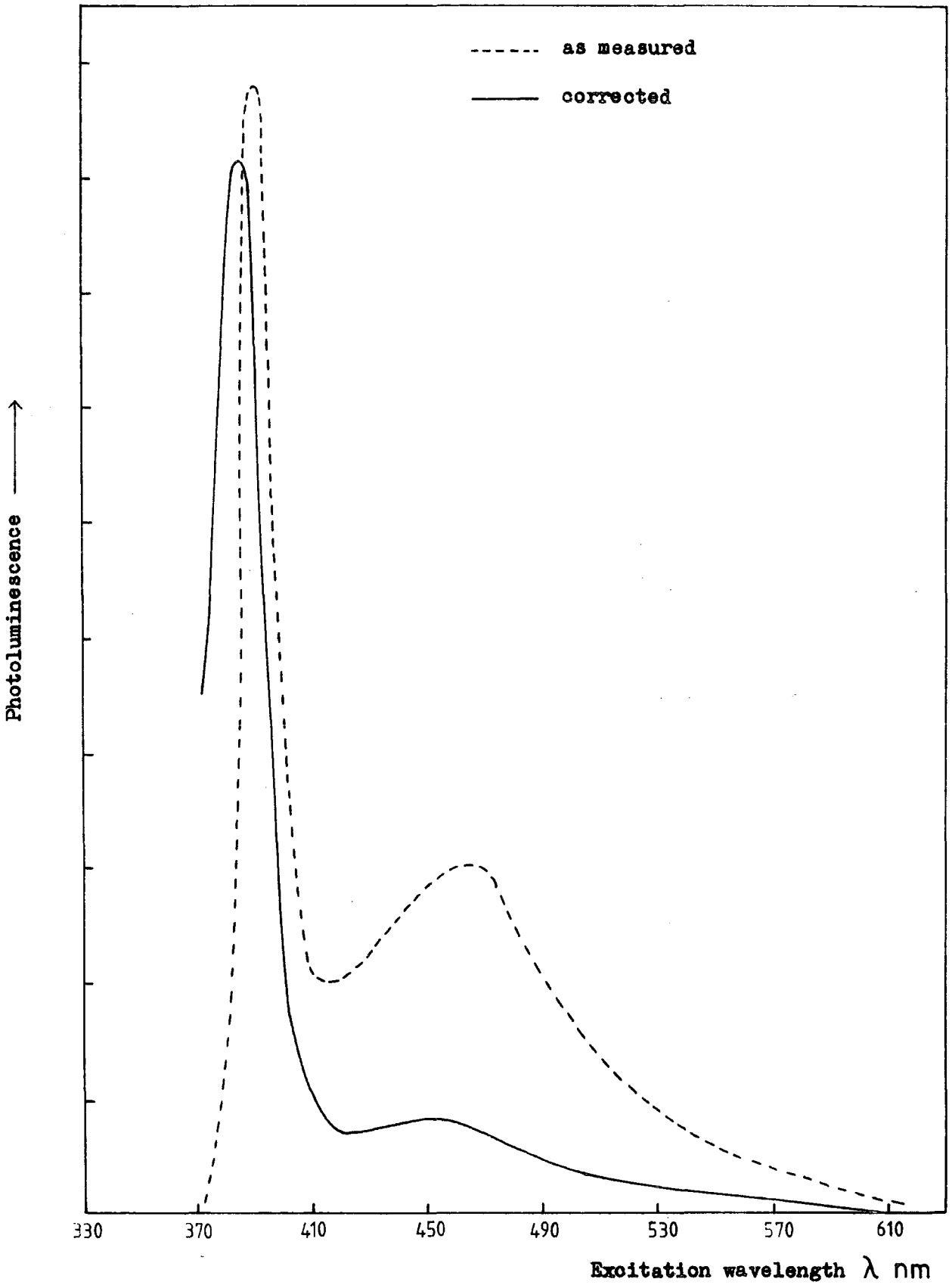

Figure 6.2.4 Photoluminescence excitation spectrum at 77 K for crystal CA3(NL).

semiconductors and phosphors is given by Robbins and Dean (1978); their notation will be used here.

Transition metal ions, such as chromium, often show variable valency in their chemical behaviour, the most stable oxidation state being determined by the environment of the ion. When a transition element is present as a substitutional impurity in a semiconductor or insulator, the energy differences between the oxidation states will be reduced with respect to the free ion values because of the high relative permittivity. So, more than one oxidation state can be important in determining the electrical properties of transition elemenments in semiconductors. An example of such variable valence is found in the compound magnetite Fe_3O_4, which contains both ferric (Fe^{III}) and ferrous (Fe^{II}) ions at different lattice sites in the same compound.

When an impurity has the same oxidation state as the lattice ion for which it substitutes, e.g. Cr^{IV}_{Ti} (the superscript denotes the oxidation state, which is squal to the charge on the nucleus minus the number of core electrons, while the subscript is the atom for which the impurity substitutes), the impurity is said to be 'iso-electronic' and will be denoted by (A). Any particle within the parenthesis can be considered as within the impurity core, where the periodic potential of the lattice will have little influence on its behaviour. A particle outside the impurity core can be thought of as effective-mass like as a first approximation. Any excitation of the form (A^*) within the core can be thought of as an excitation of essentially atomic-like electrons.

When the impurity has an oxidation state one unit lower than that of the atom for which it substitutes, e.g. Cr^{III}_{Ti}, an acceptor like state (A^-) will occur. The negative sign indicates that the impurity core is charged with respect to the lattice. An intermediate charge transfer state (CTS) may exist where a hole in the valence band is in an effective-mass-

like band due to the coulomb potential of the charged impurity core.

In the first approximation, the electronic levels of the impurity core can be treated using point-ion crystal field theory. Here one assumes that the host lattice is static and that its effect on the substituent ion can be simulated by an effective crystalline electrostatic potential (Hutchins 1963). For an impurity on a titanium site in TiO_2, the crystal field will have octahedral symmetry. The splittings of the free ion terms in an octahedral crystal field are shown for two oxidation states of chromium in figure 6.3.1.

If a crystalline defect has orbital degeneracy in the ground state, then the system is unstable with respect to at least one asymmetric displacement of the neighbouring atoms (the Jahn-Teller theorem). This will lead to a further splitting of the energy levels. For a review of this effect see Sturge (1967).

In the simple crystal-field treatment, the wave functions are taken to be those of the free ion. This approximation is often made in the EPR literature and is found to give good results. However in a more general treatment (Ligand field theory), the wave functions of the electrons of neighbouring atoms are admixed with the wave functions for the central, impurity ion. This takes into account the partially covalent nature of the bonding. Also spin-orbit and spin-spin splitting of the energy levels must be taken into account.

In most of the experimental work which follows, the explanations are couched in terms of single-ion crystal field theory. It is this notation which is used by most researchers in the field, even though it can only provide a poor approximation to the actual systems.

6.4 DISCUSSION OF THE PHOTOLUMINESCENCE MEASUREMENTS

Ghosh et al (1969) were first to observe a broad unsymmetrical emission band at 850 nm in undoped TiO_2 at 77 K. This emission was

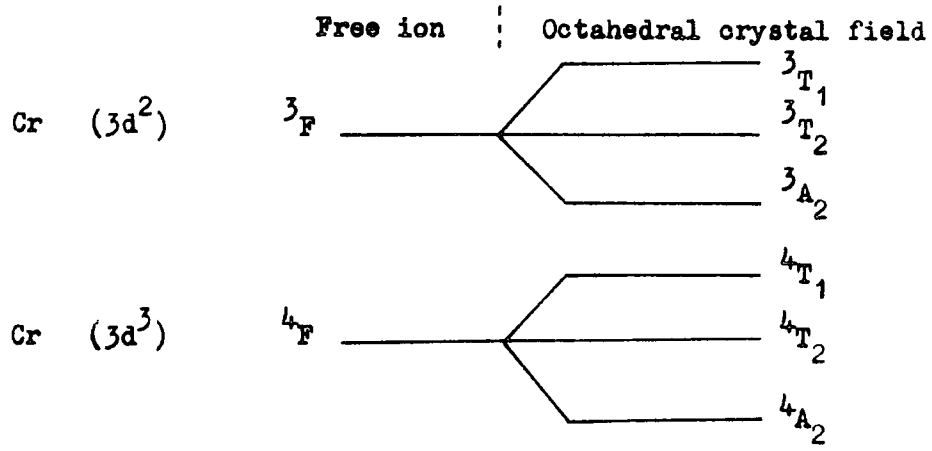

Figure 6.3.1 The energy levels for the lowest energy terms of chromium in an octahedral crystal field. Two charge states are shown .

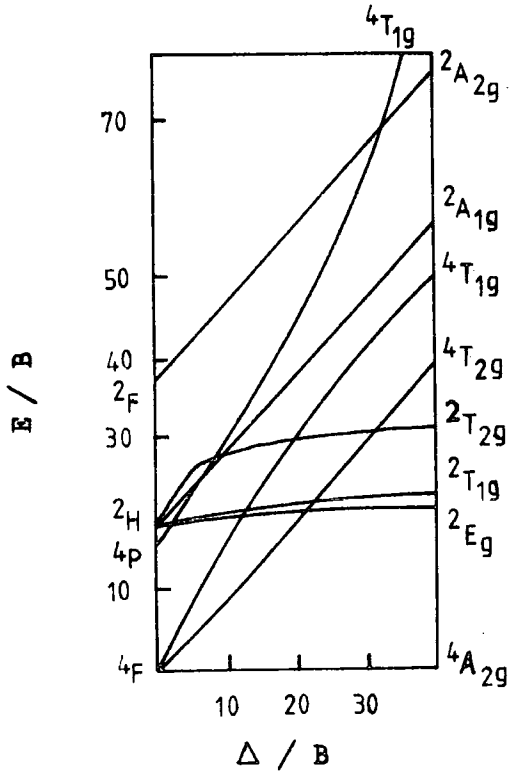

Figure 6.3.2 Tanabe-Sugano diagram for d^3 in an octahedral field .

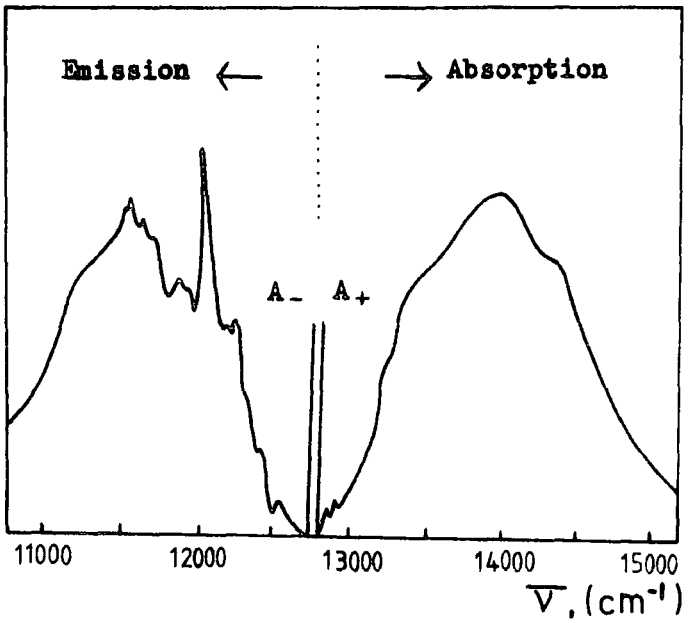

Figure 6.4.1 Comparison of absorption and emission of the Cr^{3+} ion in TiO_2 at 4 K. A_- and A_+ are no-phonon lines (after Grabner et al 1970).

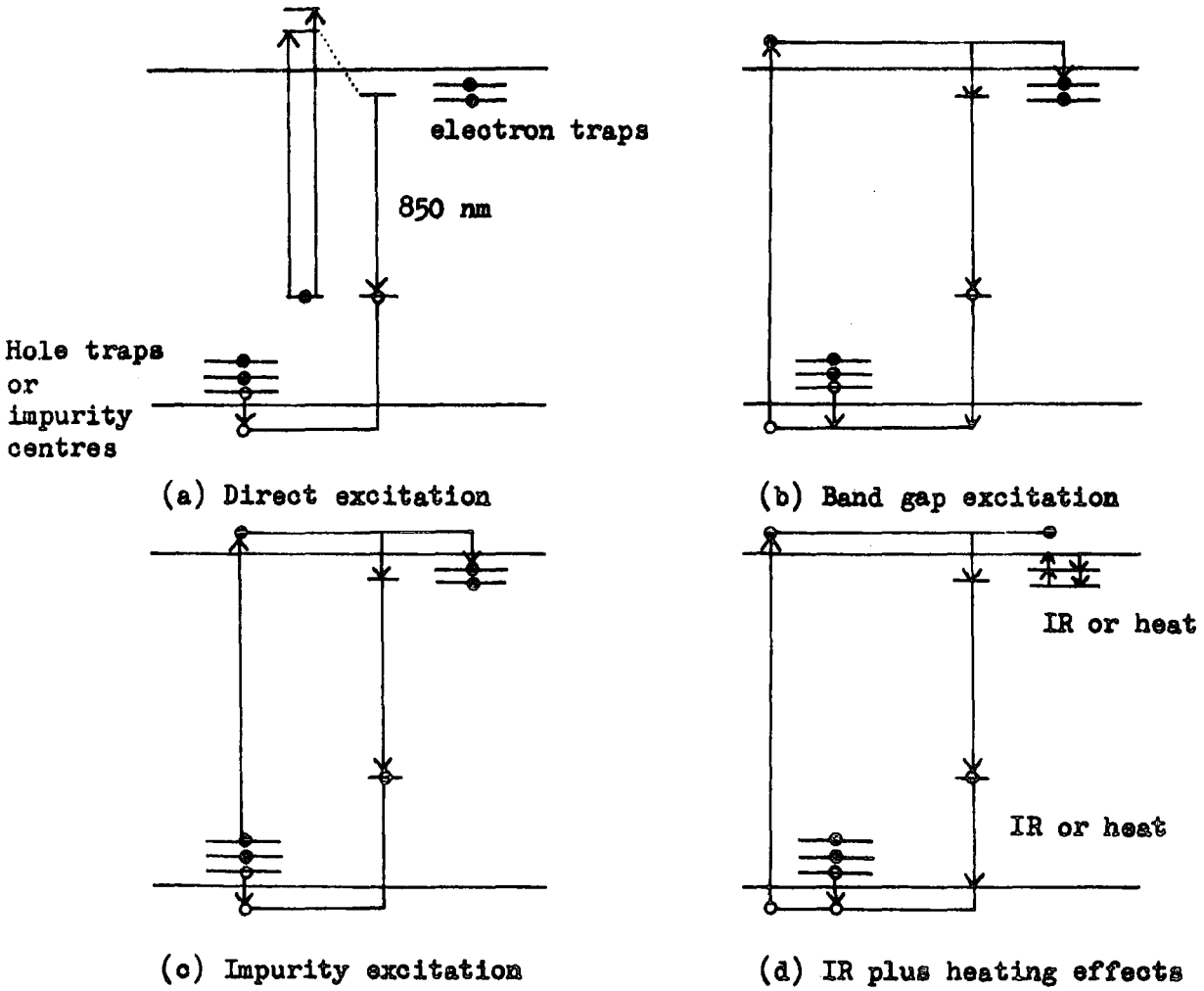

Figure 6.4.2 Phenomenological energy-level diagram of the luminescence centre and traps in rutile showing the different excitation processes.

tentatively attributed to an interstitial Ti^{3+} ion. In undoped rutile and under similar low spectral resolution, the same emission has been observed in both undoped NL and plasma grown crystals. Under high resolution at 4.2K (see figure 6.4.1) Grabner, Stokowski and Brower (1970) found that this emission band breaks up into a spectrum of considerable structure, and attributed the emission to substitutional Cr^{3+} ions present as unintentional impurities in the rutile lattice. They attributed the 850 nm photoluminescence to a $^4A_{2g} \rightarrow {}^4T_{2g}$ transition with the corresponding absorption occurring at 725 nm. This difference results in a Stokes shift of 125 nm. In addition to the broadband emission, two sharp zero-phonon lines associated with the same transition were observed. The energy difference between the two zero-phonon lines is of the same magnitude as the splitting of the $^4A_{2g}$ ground state as reported from EPR measurements (Gerritsen et al 1960). The lifetime and the excitation spectra for both the zero-phonon lines and the 850 nm band were found to be the same.

In spite of the impressive evidence relating to the ground state splitting of the $^4A_{2g}$ level, Ghosh et al (1973) retained some reservations concerning this identification. They were not able to observe an increase in the intensity of photoluminescence emission with chromium concentration. The energetic location of the $^4T_{2g}$ state with respect to the usually energetically lower-lying ^2E_g state and the implied small value of the crystal field parameter was considered troublesome. Finally, the phonon structure of the absorption and emission bands is asymmetrical about the zero-phonon line.

Grabner et al (1970) considered the possibility that the zero-phonon lines originated from the $^2E_g \rightarrow {}^4A_{2g}$ transition of Cr^{3+}, commonly known as the R lines. They found that the lifetime of the Cr^{3+} fluorescence in TiO_2 is 45 μsec compared to the R-line lifetime of 4.3 msec in Al_2O_3, 11.6 msec in MgO and 18.4 msec in $SrTiO_3$. In fact, a lifetime of the order

of milliseconds is characteristic of the $^2E_g \rightarrow {}^4A_{2g}$ transition of Cr^{3+} in any host lattice. In support of their suggestion that the $^4T_{2g}$ is the lowest lying excited state in TiO_2 they quote values of lifetime for $LiNbO_3$ (10 μsec), $LiTaO_3$ (11 μsec) and $ZnWO_4$ (10 μsec) which are similar to the 45 μsec for Cr^{3+} in TiO_2. Although a zero-phonon line has not been observed in these other oxides,a broad,almost structureless band has been observed in emission and absorption similar to the observations of Cr^{3+} in TiO_2. They also point out that the small value of the crystal field parameter Dq = 1380 cm^{-1} in TiO_2 would favour the $^4T_2$ as the lowest excited state.

Grabner et al also examined in detail the vibronic spectra of the luminescence centre. Inspection of the phonon structure showed that none of the phonons in absorption matched any of the phonons in emission. They concluded that the vibronic side bands are principally composed of defect modes and that participation by lattice phonons occurs only in combination with defect modes.

The Cr^{3+} level can be considered as a filled (or ionised) acceptor level in the dark (or ground state). The absorption due to the $^4A_{2g} \rightarrow {}^4T_{2g}$ transition is approximately 725 nm (1.7 eV). However,no absorption was found in the excitation spectra at 1.7 eV. Ghosh (1973) suggests that this lack of a peak is due to overlapping impurity absorptions and to the small oscillator strength of the $^4A_{2g} \rightarrow {}^4T_{2g}$ transition. In addition to the $^4A_{2g} \rightarrow {}^4T_{2g}$ there are other absorption bands which should occur at higher energies e.g. $^4A_{2g} \rightarrow {}^4T_{1g}$ and $^4A_{2g} \rightarrow {}^2T_{2g}$. Ghosh observed a similar excitation response to that observed in the present work with an increase in the excitation at photon energies of about 3 eV. He concluded that the luminescence was produced from the direct excitation of the Cr^{3+} ion as in the case of Cr^{3+} in Al_2O_3 and MgO. However, it seems likely that the excitation of the Cr^{3+} ion is produced by the creation of free charge carriers in the TiO_2 lattice at 3 eV rather than the direct excitation of the Cr^{3+} centre. Stokowski and Schawlow (1968) have observed similar 'background' impurity

absorption in the case of Cr^{3+} in $SrTiO_3$.

The direct excitation of the luminescence centre is represented as follows:

$$Cr^{3+} + h\nu \longrightarrow (Cr^{3+})^{*}$$

$$(Cr^{3+})^{*} \longrightarrow Cr^{3+} + 850 \text{ nm.}$$

The 850 nm emission can also be excited by band gap light. Electron-hole pairs recombine at the luminescence centre giving rise to the observed luminescence (see figure 6.4.2).

$$h\nu \longrightarrow e + p$$

$$Cr^{3+} + p \longrightarrow Cr^{4+}$$

$$Cr^{4+} + e \longrightarrow (Cr^{3+})^{*}$$

$$(Cr^{3+})^{*} \longrightarrow Cr^{3+} + 850 \text{ nm.}$$

The luminescence centre can be excited indirectly by excitation of an impurity centre. The initial excitation of impurity centre (X) results in ionisation of the centre

$$X + h\nu \longrightarrow X^{+} + e .$$

The ionised centre is equivalent to a trapped hole and a free electron.

$$X^{+} \longrightarrow X + p$$

The trapped hole can be thermally ionised and can recombine with a free electron at the luminescence centre

$$Cr^{3+} + p \longrightarrow Cr^{4+}$$

$$Cr^{4+} + e \longrightarrow (Cr^{3+})^{*}.$$

6.5 LUMINESCENCE LIFETIME MEASUREMENTS IN UNDOPED SINGLE CRYSTAL RUTILE

The photoluminescence lifetime measurements were observed using the experimental set up described in section 4.6. A FX-76 xenon lamp was pulsed using a square wave generator and a thyristor at 25 pps. The same square wave signal was used as a reference for the boxcar detector used to monitor the luminescence signal. A typical result is shown in figure 6.5.1 using a 100 ns sampling 'window' and a scan speed of 100μs in 100

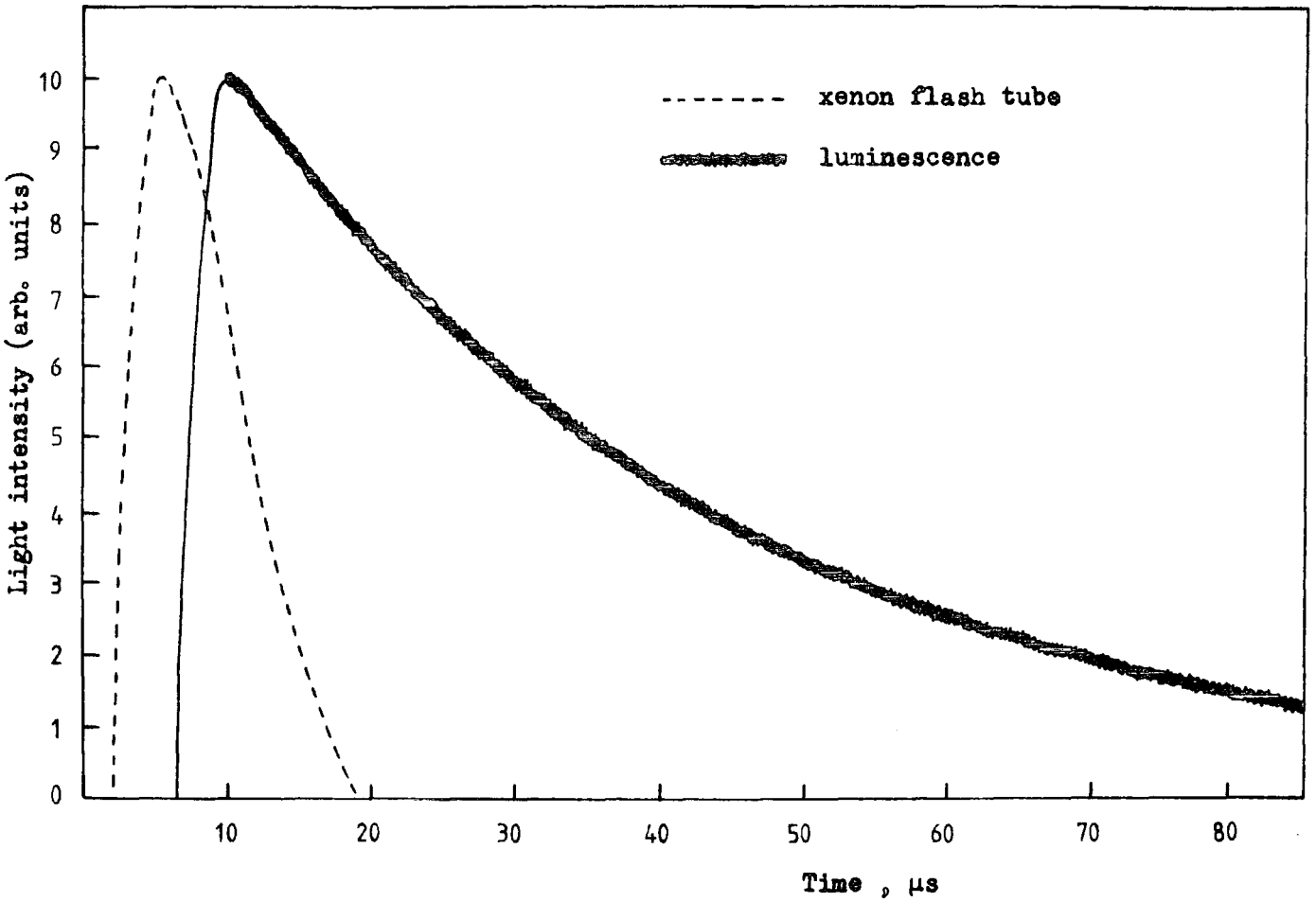

Figure 6.5.1 Luminescence decay curve at 77 K for crystal CA3(NL) .

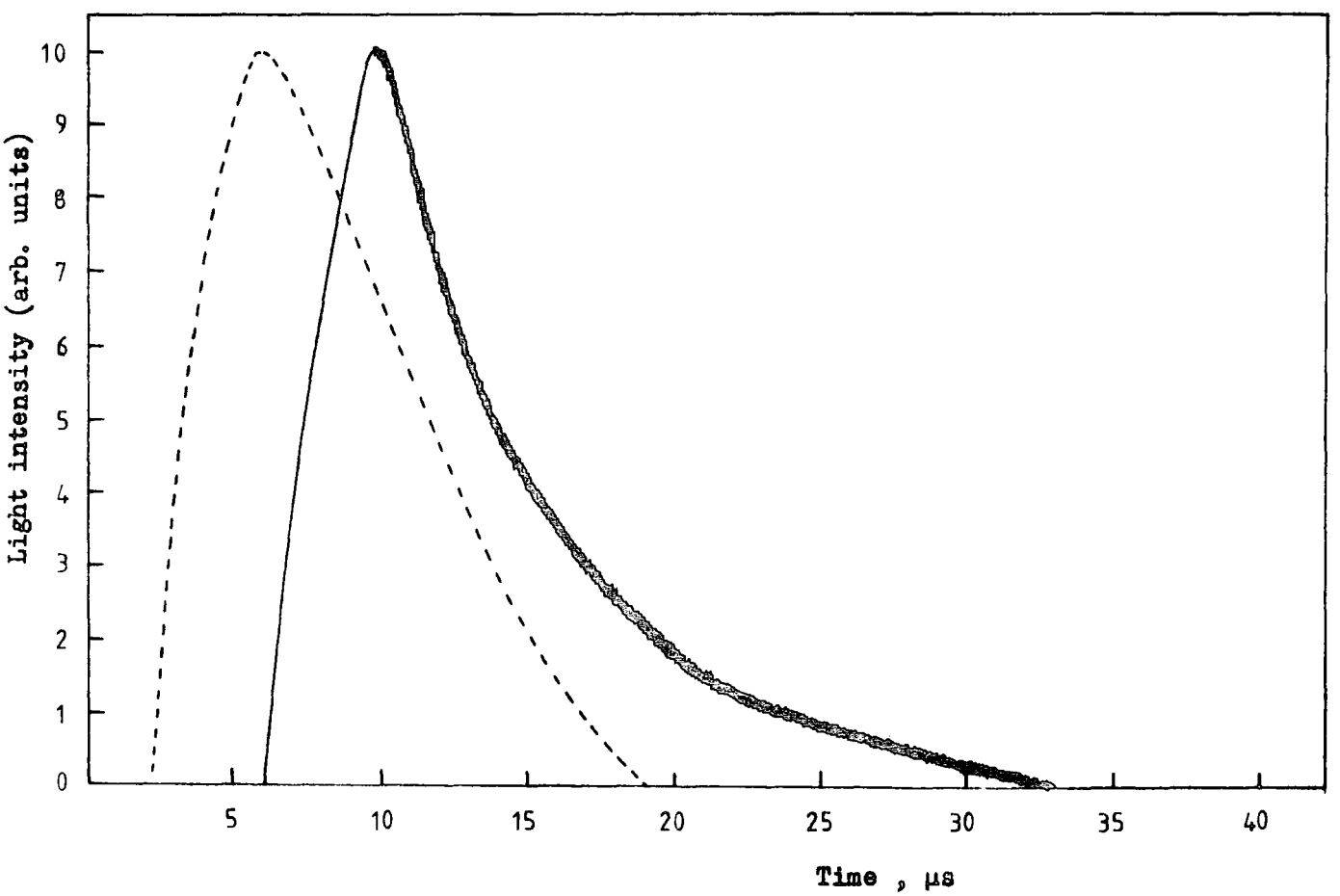

Figure 6.5.2 Luminescence decay curve at 300 K for crystal CA3(NL) .

seconds. The xenon flash tube output was observed using no filter on the emission output. To observe the luminescence decay curve an Oriel G-772-7800 filter was inserted between the crystal and photomultiplier to cut out the more intense uv excitation radiation. All time was measured from the time the square wave voltage was applied to the gate of the thyristor. It can be observed that there was about 2μs delay before light was emitted from the pulsed xenon source. At 77K the luminescence decay curve was longer than the decay curve of the xenon source. However, as can be seen in figure 6.5.2 at 300K the excitation and emission decay curves were similar. As the temperature was increased beyond 300K it became difficult to produce any meaningful results using the FX-76 flash tube.

It is generally accepted that the decay processes in luminescence in solids is governed by either monomolecular or bimolecular kinetics (Curie 1963). The luminescence intensity, I, is given by the following equation if monomolecular kinetics is the case:

$$I = n_0 \alpha \exp(-\alpha t) = I_0 \exp(-\alpha t)$$

where n_0 is the number of excited electrons at $t = 0$ and α is the probability with which excited electrons disappear. On the other hand, if the bimolecular kinetics is responsible, the equation

$$I = \frac{R n_0^2}{(1 + n_0 R t)^2} = \frac{I_0}{(1 + n_0 R t)^2}$$

holds, where R is the rate of recombination of excited electrons or holes with ionised centres. The decay rate in the bimolecular case becomes more rapid as the excitation intensity is increased, whereas the rate in the monomolecular case is independent of the excitation intensity.

The decay rate for a number of undoped crystals was examined for two orders of magnitude change in the excitation intensity. No difference was found and monomolecular kinetics were implied. The decay curves were examined

as a function of temperature and a typical set of results is shown in figure 6.5.3. It was found that the decay curves can be exactly expressed by single exponential functions. The more complicated decay curves observed at 300K and above were due to the emission of luminescence from the long tail of the excitation pulse rather than bimolecular kinetics.

The temperature dependence of the luminescence decay time (τ) for crystal CA3(NL) is shown in figure 6.5.4. The fact that the decay constants at room temperature are nearly ten times faster than those at liquid nitrogen temperatures could be associated with the existence of competitive non-radiative recombination centres. Another possibility presented by Ghosh al (1973) is that an electron in the excited state of the luminescence centre can undergo a transition to the ground state which results in luminescence emission, or it can be thermally excited into the conduction band. At sufficiently low temperatures the luminescence efficiency (η) is unity and all excited state electrons undergo luminescent transitions. The luminescence decay time (τ) at low temperatures corresponds to the intrinsic lifetime of the excited state (τ_L) and the reciprocal of this lifetime gives the probability per unit time of the luminescence transition (P_L).

At elevated temperatures the luminescence efficiency (η) is reduced as electrons are thermally excited into the conduction band. If E is the seperation of the excited state from the conduction band, the probability per unit time of thermal ionisation (P_T) is given by $P_T = \nu \exp(-E/kT)$, where ν is the attempt to escape frequency of the electron in the excited state. The fraction of excited state electrons which undergo the luminescence transition to the ground state is given by the probability of the luminescence transition to the sum of the probabilities of both transitions, $\eta = P_L/(P_L+P_T)$. Substituting for P_L and P_T gives

$$\frac{1 - \eta}{\eta \tau_L} = \nu \exp(-E/kT) \qquad (6.4.1)$$

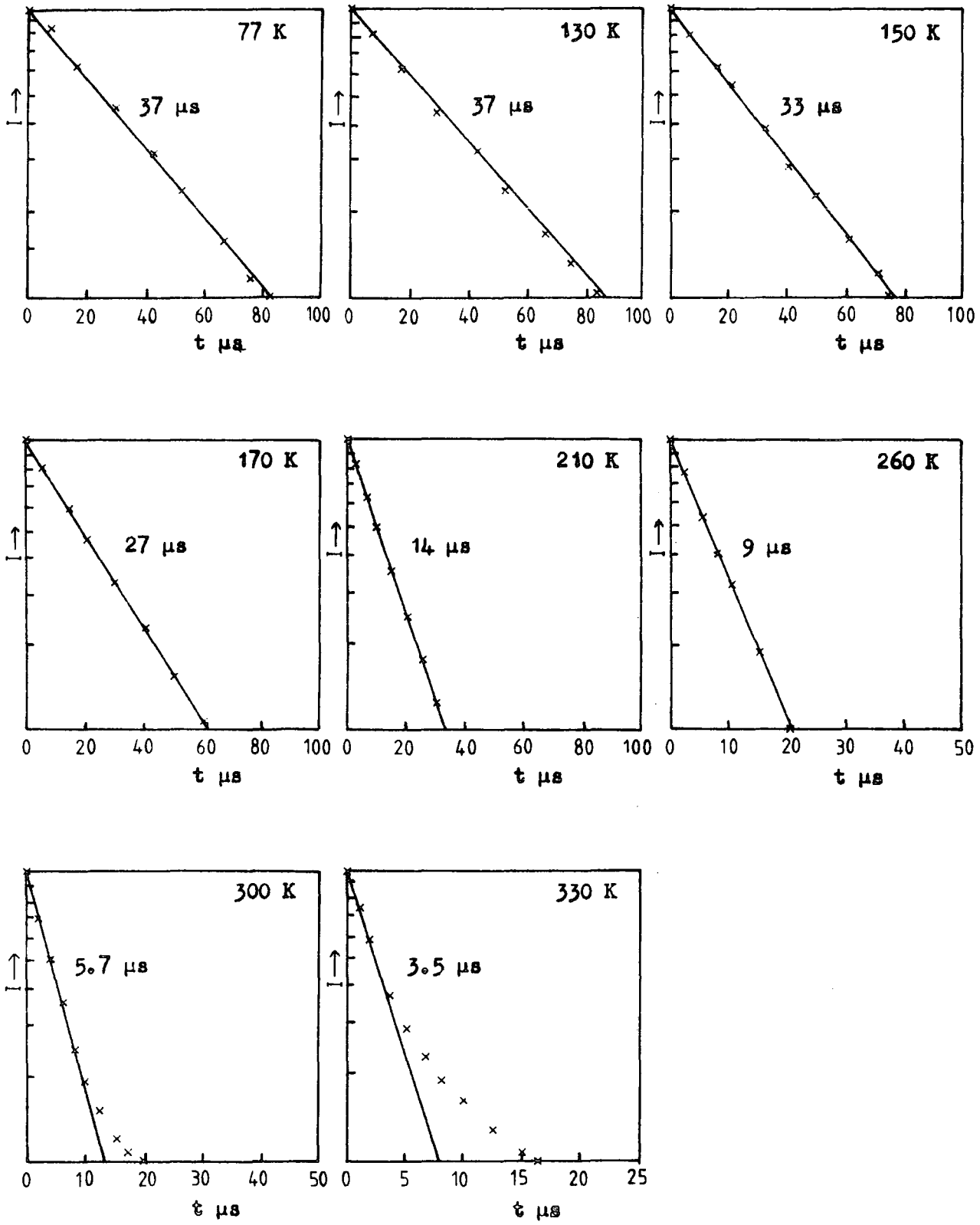

Figure 6.5.3 Luminescence decay curves for the crystal CA3(NL) at different temperatures.

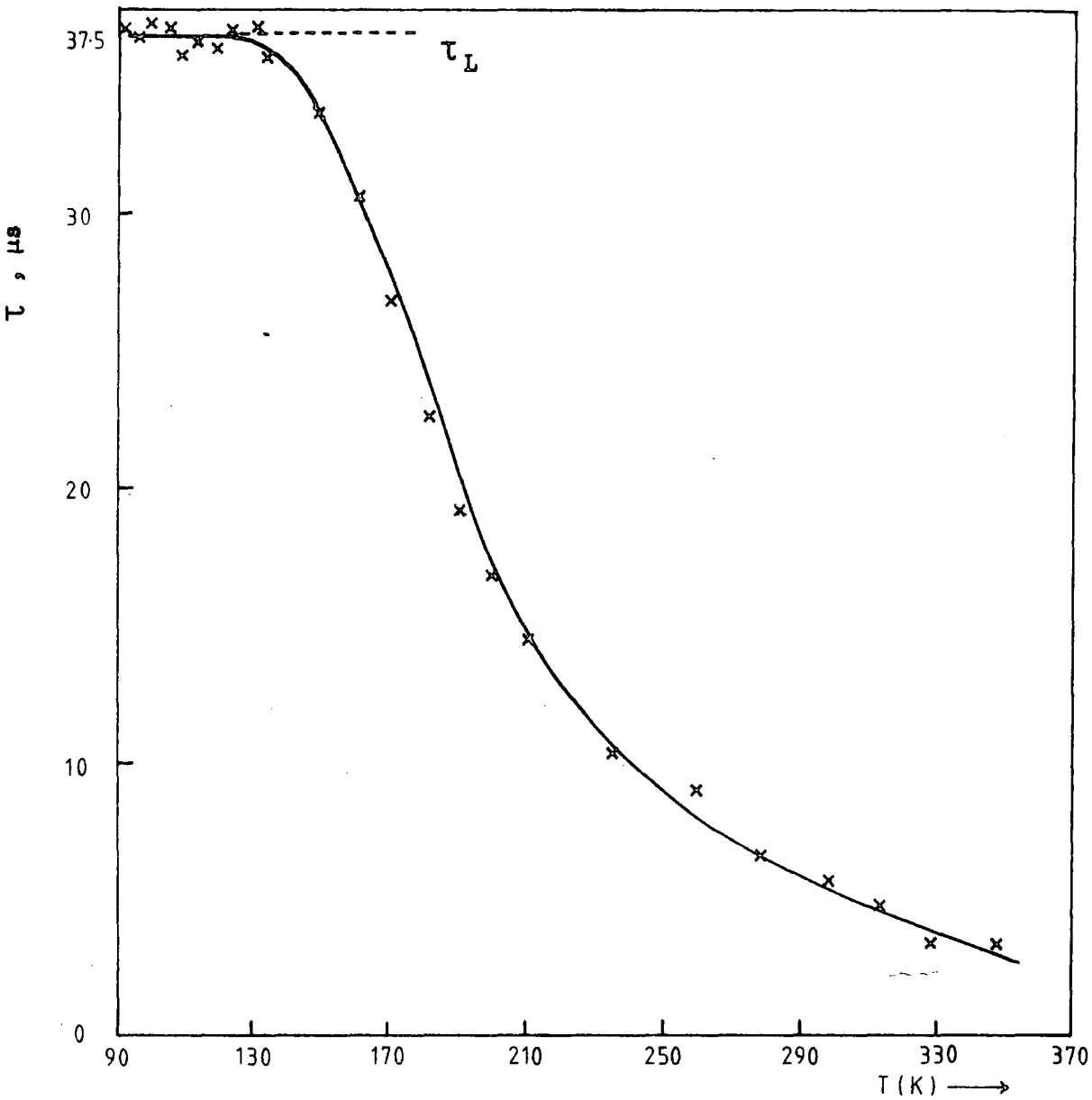

Figure 6.5.4 Temperature dependence of the luminescence decay time in the crystal CA3(NL).

Also the reciprocal of the luminescence decay time is the total probability per unit time of a transition from the excited state either to the ground state or to the conduction band, $P_L + P_T = 1/\tau$

$$\frac{1}{\tau} - \frac{1}{\tau_L} = \nu \exp(-E/kT) \qquad (6.4.2)$$

At low temperatures the decay time represents the intrinsic lifetime of the excited state of the luminescence centre. As the temperature is raised thermal ionisation of the excited state becomes a competing process and the measured decay time represents an effective lifetime of the excited state. Although in this model the thermal excitation gives rise to a conduction band electron completely free from the luminescence centre, the resulting descriptions of the thermal quenching of the luminescence emission and the decay time are identical to those obtained from the classical configuration co-ordinate model of an isolated centre (Klick and Schulman 1957).

The activation energy plot of $\ln (1/\tau - 1/\tau_L)$ is shown in figure 6.5.5 for crystal CA3(NL). The value of the intrinsic lifetime of the luminescence centre, $\tau_L = 3.6\ 10^{-5}$ s, was obtained from the low temperature limit of figure 6.4.4. There were two portions of the activation energy plot, one with an attempt to escape frequency $\nu = 5 \mp 1\ 10^{8}\ s^{-1}$ and an energy level of 0.16 ∓ 0.01 eV, and another with $\nu = 5 \mp 3\ 10^{6}\ s^{-1}$ and an energy level of 0.09 ∓ 0.02 eV. Similar results were obtained from the plasma grown crystals and a summary is shown in table 6.5.6.

6.6 THE TEMPERATURE DEPENDENCE OF THE LUMINESCENCE INTENSITY

The total integrated photolumnescence emission intensity was observed by exciting the crystal with a 250W mercury source via an Oriel G-774-4450 filter, and the emission was monitored with a C31034 photomultiplier and an Oriel G-772-7800 filter. Figure 6.6.1 shows the temperature dependence of the photoluminescence emission and the thermally stimulated

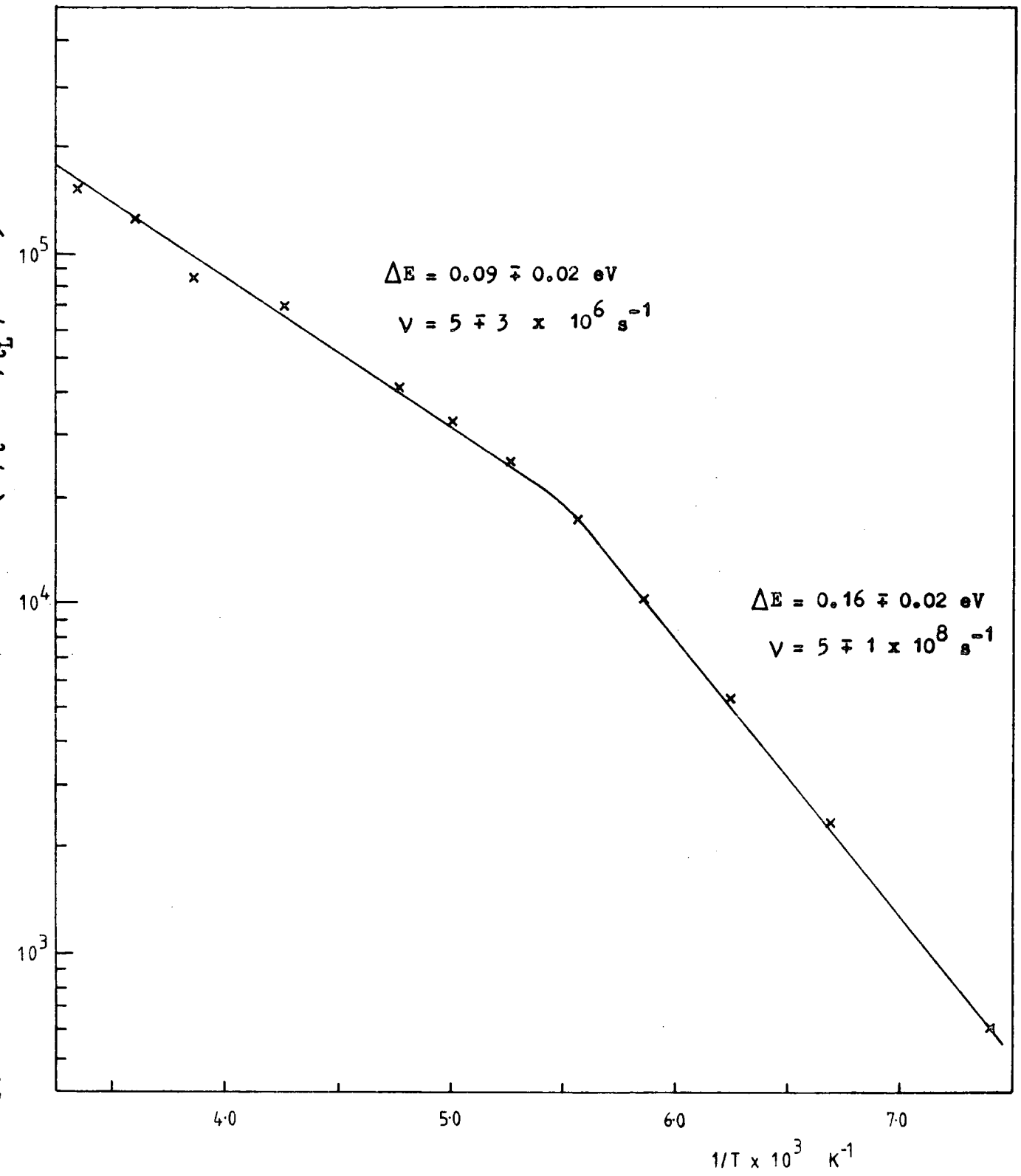

Figure 6.5.5 Activation energy plot of ln ($1/\tau - 1/\tau_L$) versus 1/T for crystal CA3(NL).

Crystal	Attempt to escape frequency ν_1 s^{-1}	Energy E eV	Attempt to escape frequency ν_2 s^{-1}	Energy E eV	Luminescence lifetime at 77K τ_L s
CA3(NL)	$5 \mp 3 . 10^8$	0.16∓0.01	$5 \mp 3 . 10^6$	0.09∓0.02	$3.6 . 10^{-5}$
BS1	$7 \mp 3 . 10^8$	0.16∓0.01	$6 \mp 3 . 10^6$	0.07∓0.02	$3.5 . 10^{-5}$
BS3	$6 \mp 2 . 10^8$	0.17∓0.01	$4 \mp 3 . 10^6$	0.07∓0.03	$3.6 . 10^{-5}$
BS10	$8 \mp 2 . 10^8$	0.18∓0.01	$3 \mp 2 . 10^6$	0.11∓0.02	$3.7 . 10^{-5}$
BS13	$9 \mp 3 . 10^8$	0.17∓0.01	$9 \mp 3 . 10^6$	0.06∓0.03	$3.5 . 10^{-5}$
BS18(S)	$7 \mp 2 . 10^8$	0.18∓0.01	$7 \mp 3 . 10^6$	0.08∓0.02	$3.5 . 10^{-5}$
BS18(NS)	$5 \mp 3 . 10^8$	0.18∓0.01	$6 \mp 3 . 10^6$	0.09∓0.03	$3.6 . 10^{-5}$

Table 6.5.6 Summary of data obtained from activation energy plots of $\ln (1/\tau - 1/\tau_L)$ versus $1/T$.

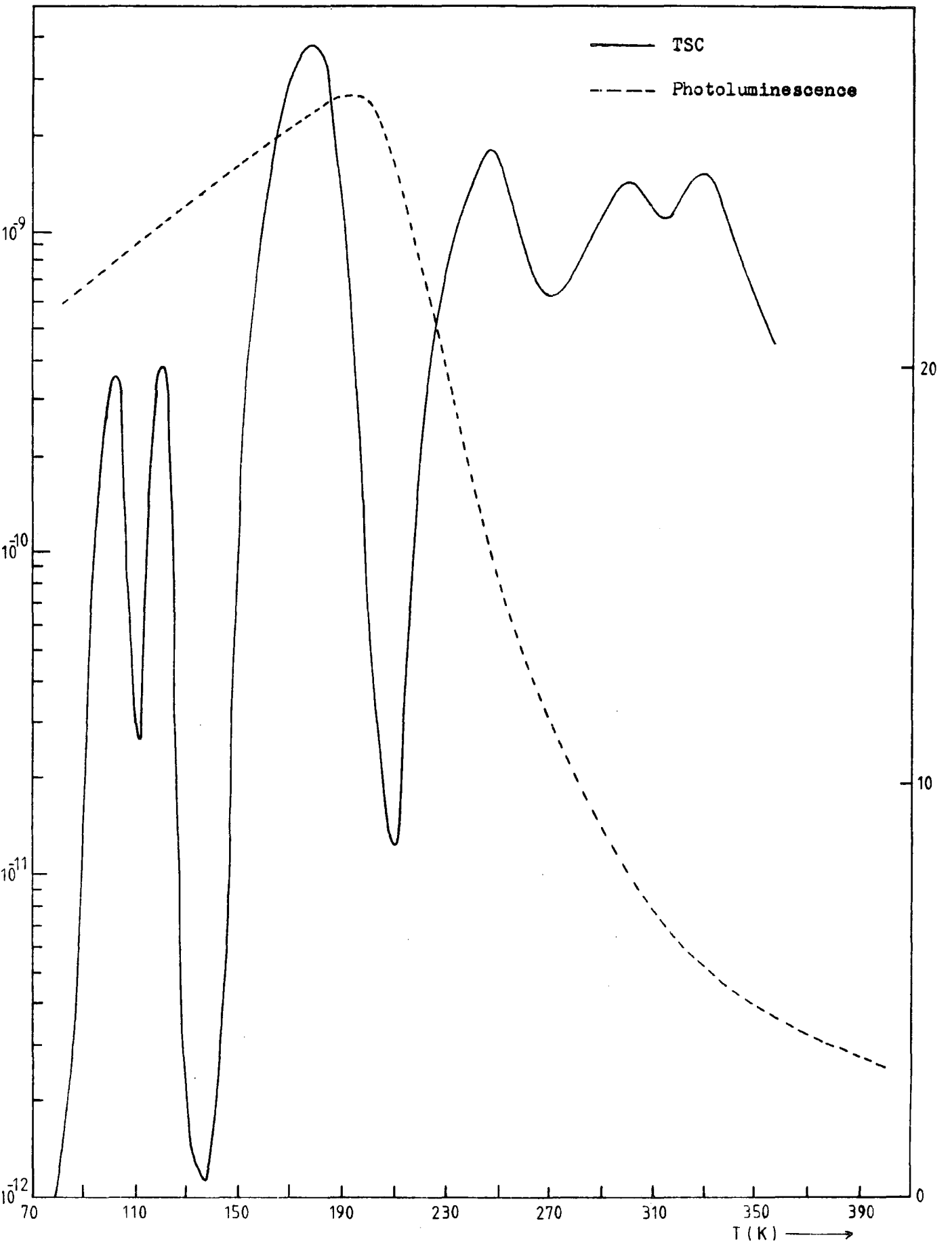

Figure 6.6.1 The thermal quenching of the photoluminescence in crystal CA3(NL).

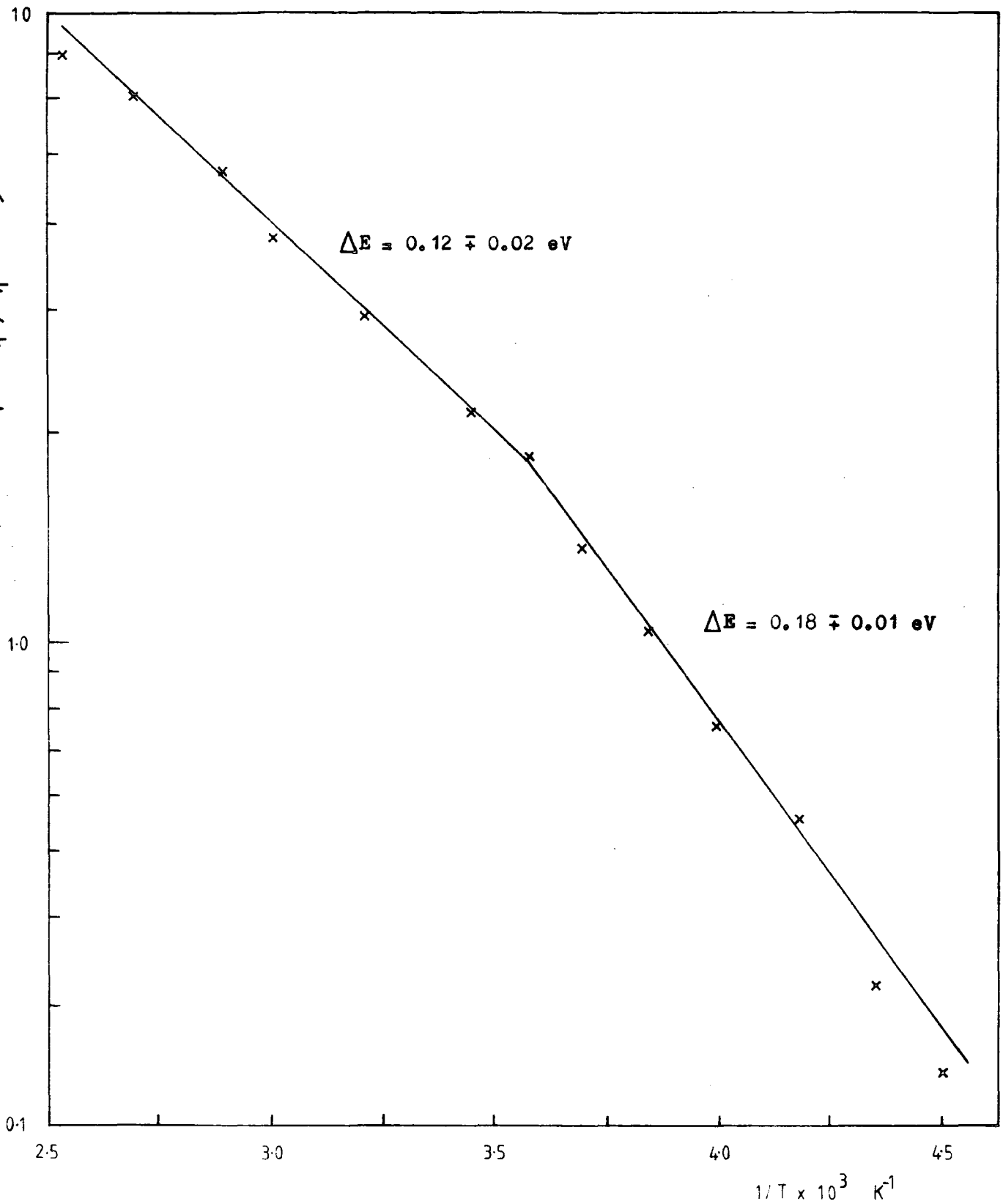

Figure 6.6.2 Activation energy plot for the thermal quenching of photo-luminescence in the crystal CA3(NL).

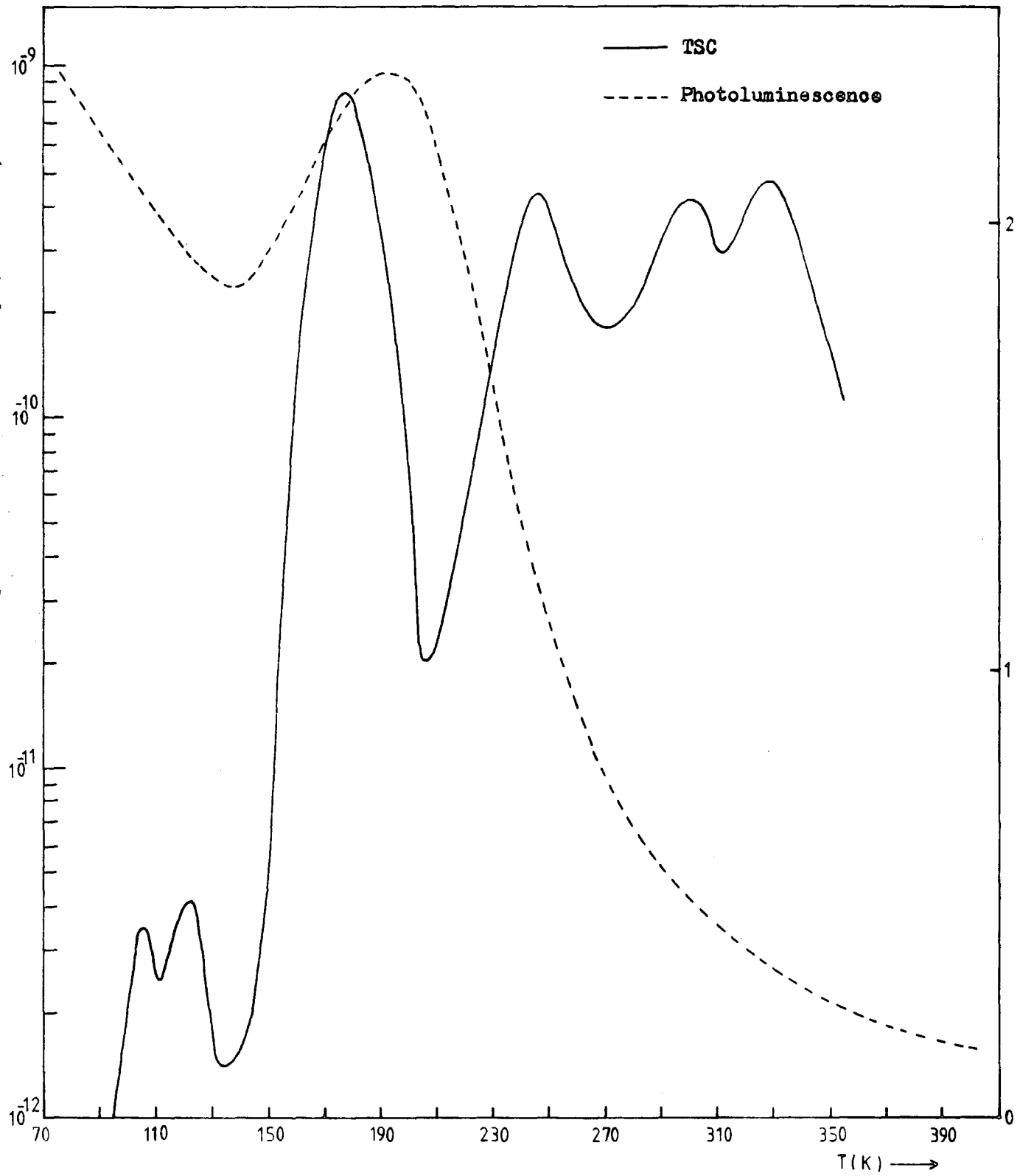

Figure 6.6.3 Thermal quenching of the photoluminescence in the crystal BS18(S).

current spectra for crystal CA3(NL). If the maximum luminescence emission is assumed to be $\eta = 1$ then a plot of $\ln (1 - \eta)/\eta$ against $1/T$ will yield a straight line with slope E/k. Figure 6.6.2 shows the result for crystal CA3 (NL) and two portions of the graph are observed, one with an energy $E = 0.12 \pm 0.02$eV and the other with $E = 0.18 \pm 0.02$ eV. These activation energies compare well with the ones obtained from the lifetime measurements although the transition temperature from one activation energy to the other is significantly different.

All the National Lead rutile samples examined showed a photoluminescence temperature dependence similar to one shown in figure 6.6.1 for crystal CA3 (NL). The photoluminescence intensity gradually increased as the temperature was increased to about 190 K and then the intensity began to decrease with increasing temperature. The plasma grown crystals produced in the non-stoichiometric form and subsequently oxidised in oxygen at 1300 °C showed the same type of behaviour. However, the stoichiometric as-grown crystals had a different photoluminescence temperature dependence as shown in figure 6.6.3 for crystal BS13(S). After quenching these type of crystals from 600 °C to room temperature in a stream of oxygen it was possible to produce a photoluminescence temperature behaviour similar to the non-stoichiometric as-grown crystals (see figure 6.6.5).

It has already been established that the lifetime of the radiative transition in rutile, probably due to the Cr^{3+} centre, is constant with temperature until 190 K and then it decreases as the temperature is raised. It might be expected that the luminescence intensity would also be a constant value from 77 K to 190 K. However, it was found that the photoluminescence intensity varies with temperature and depends on the concentration of the shallow traps. The more shallow traps present in the rutile crystal the larger the reduction in photoluminescence.

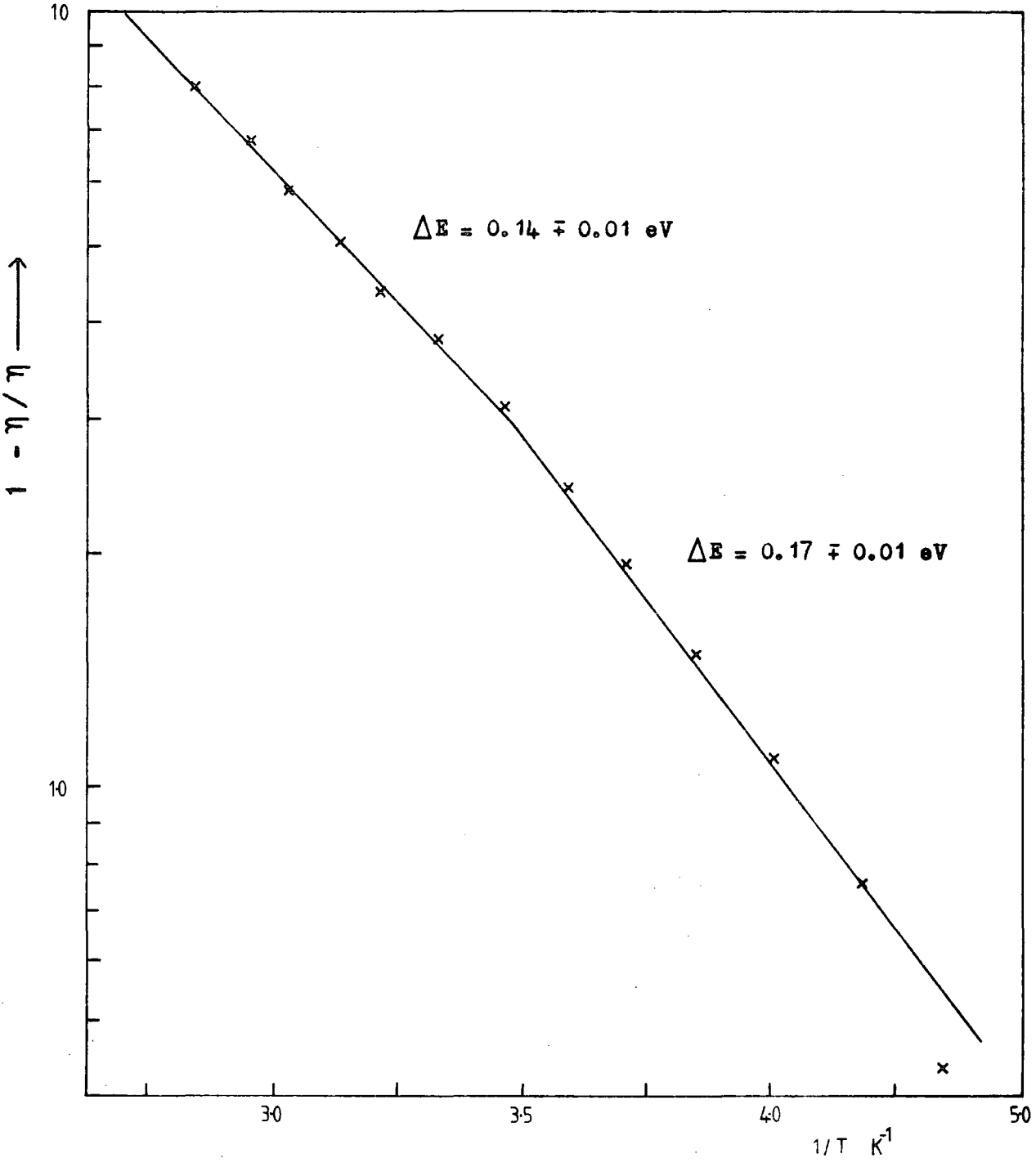

Figure 6.6.4 Activation energy plot for the thermal quenching of photo-luminescence in the crystal BS18(S).

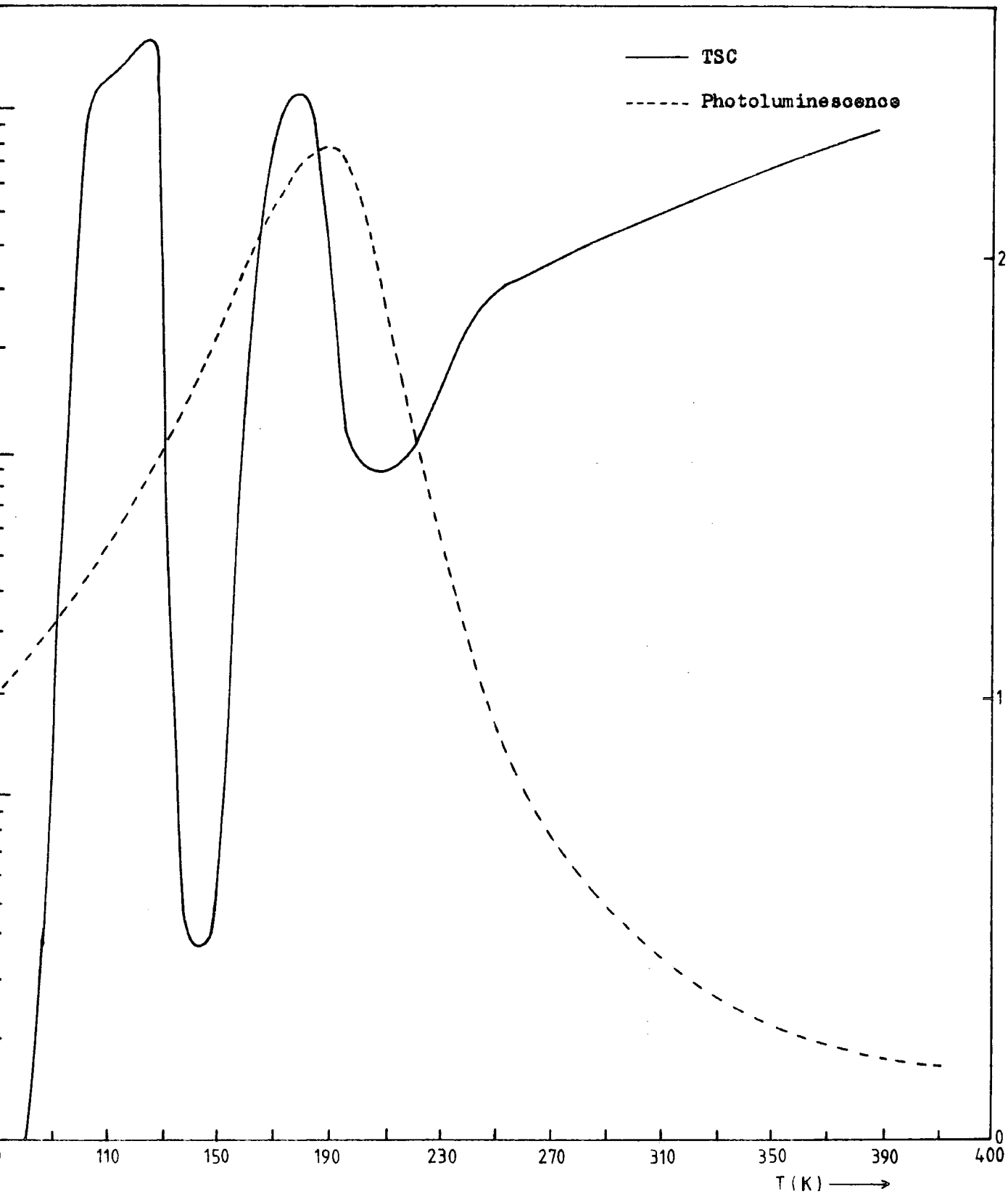

Figure 6.6.5 Thermal quenching of the photoluminescence in the crystal BS18(S) after quenching from 600°C.

It would appear that the introduction of shallow traps into the rutile lattice affects the luminescence efficiency of the Cr^{3+} centre. Radiative recombination results in photon emission, whereas non-radiative recombination is indefinite, vaguely indicating any process that does not emit a photon and leaving to one's ingenuity and imagination the construction of plausible models. One of the main competitors of a radiative transition is recombination via the Auger effect in which a second electron absorbs the energy given up by the first electron and then dissipates this energy by emitting phonons. Corresponding to each type of single electron transition there are equivalent Auger mechanisms as shown in figure 6.6.6. In the rutile case, an electron dropping into a recombination centre from the conduction band may lose its energy by exciting a trapped electron to the conduction band via an Auger-type interaction. Since the luminescence emission band overlaps with the absorption band of some of the traps, as determined by photon stimulated current experiments described earlier, energy transfer between these two centres is possible when the traps are populated. As the temperature is raised whilst measuring the photoluminescence intensity, the shallow trap population gradually decreases and the photoluminescence increases due to less competition from Auger non-radiative recombination. An Auger process very similar to this type has been observed in GaP by Tsang et al (1968). An alternative mechanism involves a more conventional Auger recombination process, followed by impact ionisation of the shallow traps, which accomplishes the same result as the previously described process. It is worth noting that either of these Auger processes, if they occur, would contribute to the observed increase in free-carrier lifetime when the shallow traps become populated.

6.7 THE EFFECT OF CHEMICAL REDUCTION AND THERMAL QUENCHING ON LUMINESCENCE EFFICIENCY

The effect of quenching in crystal defects on the luminescence efficiency was investigated. A number of crystals were heated to a

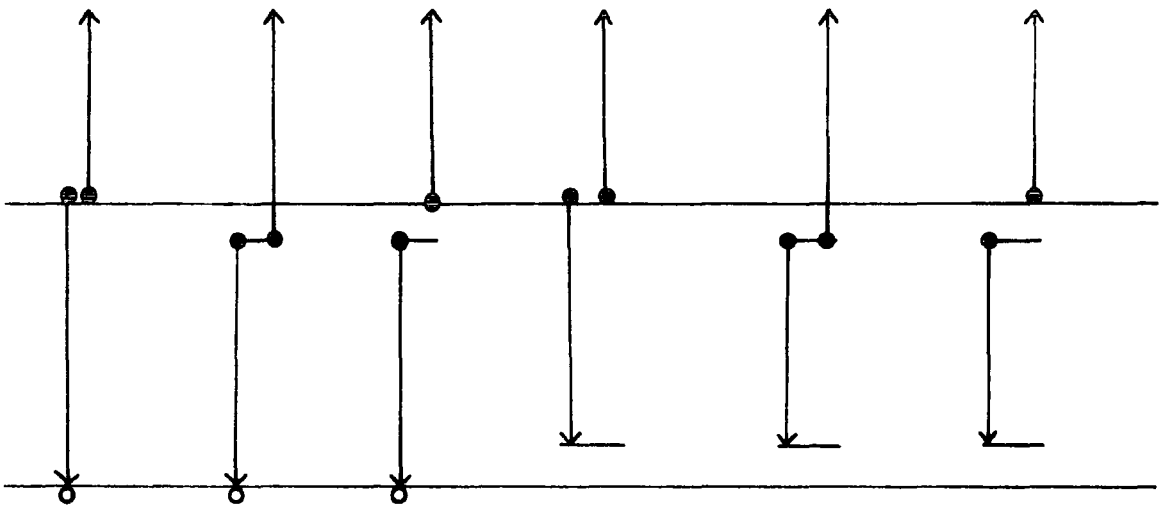

Figure 6.6.6 Diagram of some Auger processes in a n-type semiconductor.

temperature T°C for 24 hours in a stream of oxygen and then they were quenched to room temperature under forced air cooling. The results shown in figure 6.7.1 are typical of all the crystals investigated and a gradual reduction of the luminescence efficiency was observed as the temperature of quenching was increased above 600°C.

A similar investigation of the variation of luminescence with chemical reduction showed a more dramatic decrease in the luminescence efficiency. The crystals were reduced by heating in a vacuum of 10^{-5} torr at temperatures between 600°C and 700°C. The reduction was accompanied by an increased blue colouration and decreasing resistivity. Figure 6.7.2 shows the results obtained for crystal BS18 (NS) and BS18 (S) after various stages of reduction. No photoluminscence was detected at crystal resistivities below 10^{8} Ωcm due to the limit in sensitivity of the detection system.

The decrease in luminescence efficiency with increasing quenching temperature is similar to the effect described in the last section. However, when the temperature of quenching is increased from 600°C to 1000°C the luminescence efficiency falls by an order of magnitude. The Auger processes described in section 6.6 can explain these results, and an increase in the shallow trap population produces less radiative recombination.

The reduction of rutile produces donor levels, Becker and Hosler (1965) have suggested that these donors are Ti^{3+} ions at interstitial positions whilst Hasiguti et al (1961) have concluded that a model of oxygen vacancies is more likely. The low temperature photoluminescence efficiency of semiconductors generally decreases rapidly when the concentration of neutral donors or acceptors is increased above some threshold concentration. In GaP the threshold concentration is about 10^{18} cm^{-3}. At low concentrations and up to 10^{18} cm^{-3} the efficiency is constant, but at 10^{19} cm^{-3} the

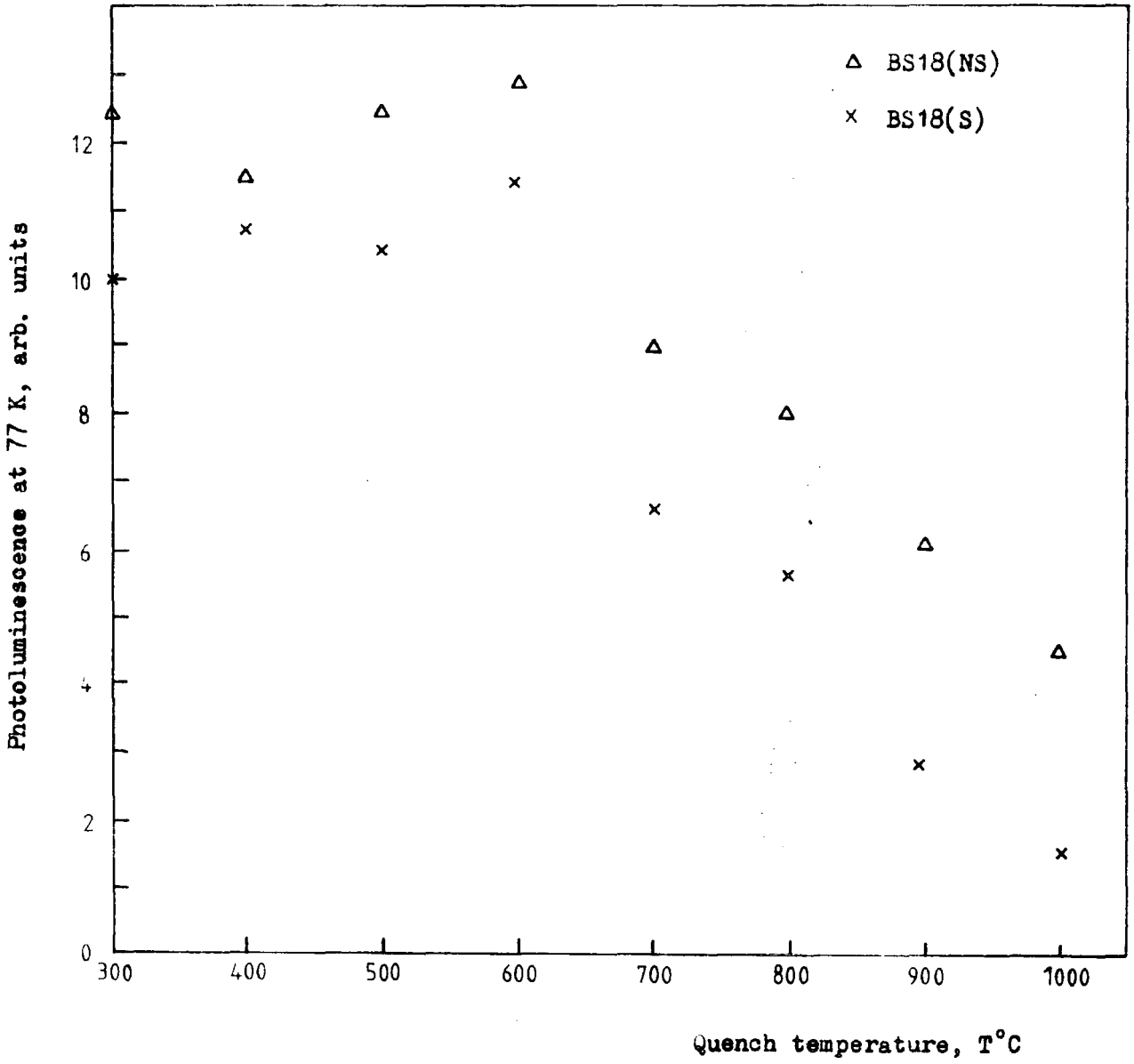

Figure 6.7.1 The photoluminescence intensity in the non-stoichiometric as grown crystal BS18(NS) and the stoichiometric as grown crystal BS18(S) after quenching from a temperature T°C.

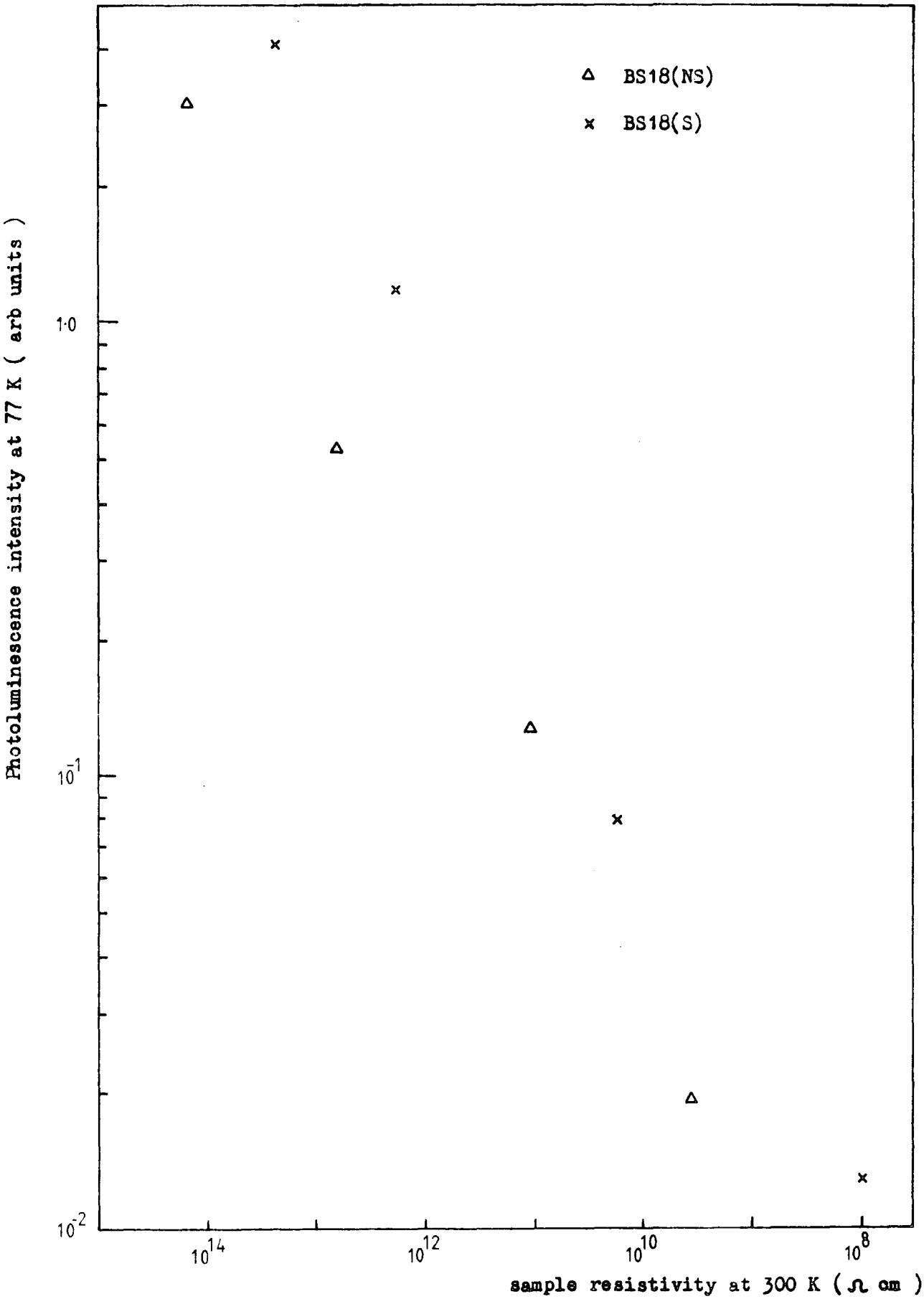

Figure 6.7.2 The photoluminescence intensity in the non-stoichiometric as grown crystal BS18(NS) and the stoichiometric as grown crystal BS18(S) after chemical reduction.

efficiency drops by a factor of 10^4 from its value at low concentrations (Tsang 1968).

At concentrations beyond 10^{18} cm $^{-3}$ the electron wavefunctions of adjacent impurities overlap, thus delocalising the electrons (or holes) and increasing the chances for an Auger excitation of the delocalised carrier. The energy of the excited carrier would then be dissipated in a cascade emission of optical phonons to conserve energy and momentum. Although a critical concentration of about 10^{18} cm $^{-3}$ may be predicted on theoretical grounds for the onset of Auger recombination, other mechanisms set in at these concentrations such as the formation of precipitates (Kressel et al 1968).

6.8 PHOTOLUMINESCENCE AND CHROMIUM DOPING

The diffusion of chromium into the rutile crystals along 'c-axis channels' has been described in chaper 3. Five crystals cut from the boules BS13,BS10,BS18,BS3 and CA3(NL) were placed in an ampoule at 10^{-5} torr with some chromium metal and heated for four hours at 1050 °C. At this stage the crystals appeared blue/black in colour which resulted mainly from absorption in the near infra red by small radius polarons (Bogomolov and Mirlin 1968). After heating for 36 hours in a stream of oxygen the crystals became light yellow in colour and were semi-transparent. Five different crystals were cut from the same five boules and they were subjected to a diffusion time of 24 hours at 1150 °C. These crystals appeared opaque and yellow after subsequent oxidation.

The intensity of the photoluminescence was measured at 77 K for all the crystals before doping and after doping with chromium. An increase in the photoluminescence was observed in all the crystals after chromium doping (see figure 6.8.1). These results would support Grabner et al (1970) in their conclusion that Cr^{3+} is the radiative centre in rutile at 850 nm. It would be interesting to repeat the experiment and measure the number of

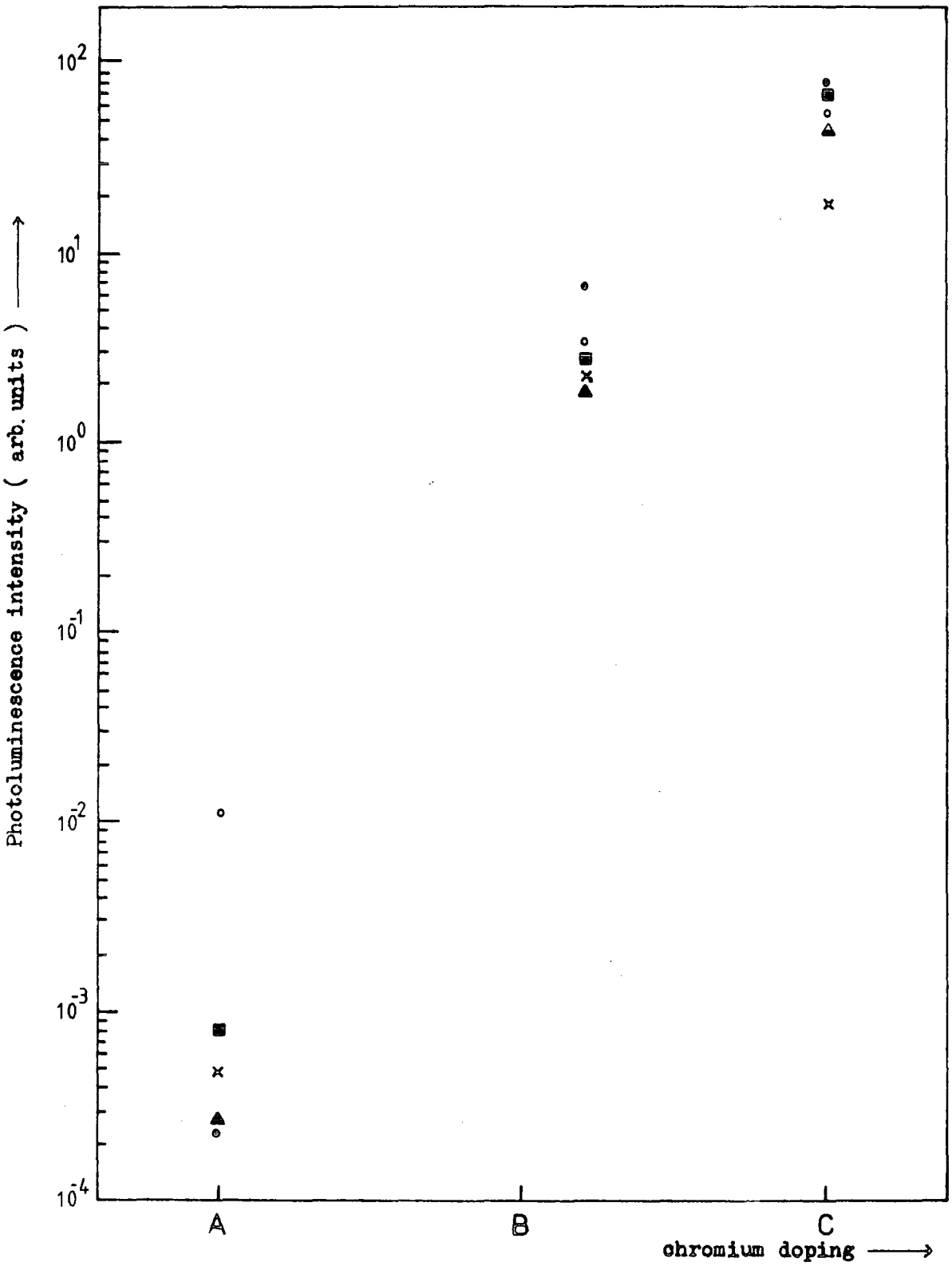

Figure 6.8.1 The affects of chromium doping on the photoluminescence at 77 K.

° BS13, ▲ BS10, × BS18, ■ BS3, ◦ CA3(NL)

A - undoped

B - chromium doped, 4 hrs at 1050°C + 36 hrs at 1000°C in O_2

C - chromium doped, 24 hrs at 1150°C + 36 hrs at 1000°C in O_2

Cr^{3+} ions present in each crystal from ESR and compare with the total amount of Cr from mass spectrographic analysis.

6.9 KINETIC RESPONSE OF PHOTOLUMINESCENCE AND PHOTOCONDUCTIVITY

Upon irradiation of a rutile crystal with uv light at 77K, it was found that the photoluminescence emission saturates much earlier than the photoconductivity. The kinetic response curves for crystal CA3 (NL) are shown in figure 6.9.1. At higher intensities than shown in figure 6.9.1, where the PC grows much faster, the PL still saturates much earlier. This effect was observed in all the crystals investigated.

The differences between the PL and PC growth curves can be explained consistently in terms of a charge transfer model by considering the hole traffic through the luminescence centre as well as the electron concentration in the conduction band, and realising that the luminescence centre is only one of the many recombination centres present. Under these conditions only a small fraction of the total recombination traffic takes place through the luminescence centre, and the electron concentration in the conduction band is determined primarily by these recombination centres rather then by the luminescence process.

6.10 TEMPERATURE QUENCHING AND INFRA RED QUENCHING OF LUMINESCENCE

The temperature dependence of the photoluminescence at various excitation intensities was investigated using a 250W mercury lamp as the excitation source. Figure 6.10.1 shows the results obtained for the stoichiometric crystal BS18(S),A, and the quenched NL crystal CA3(NL), B. At low excitation intensities the release of trapped charge from shallow trapping states produced more luminescence than direct band gap excitation of the Cr^{3+} centre. The thermoluminescence behaviour of the rutile crystals will be discussed in the next chapter and it is sufficient to note that the luminescence centre is coupled to other processes within the crystal.

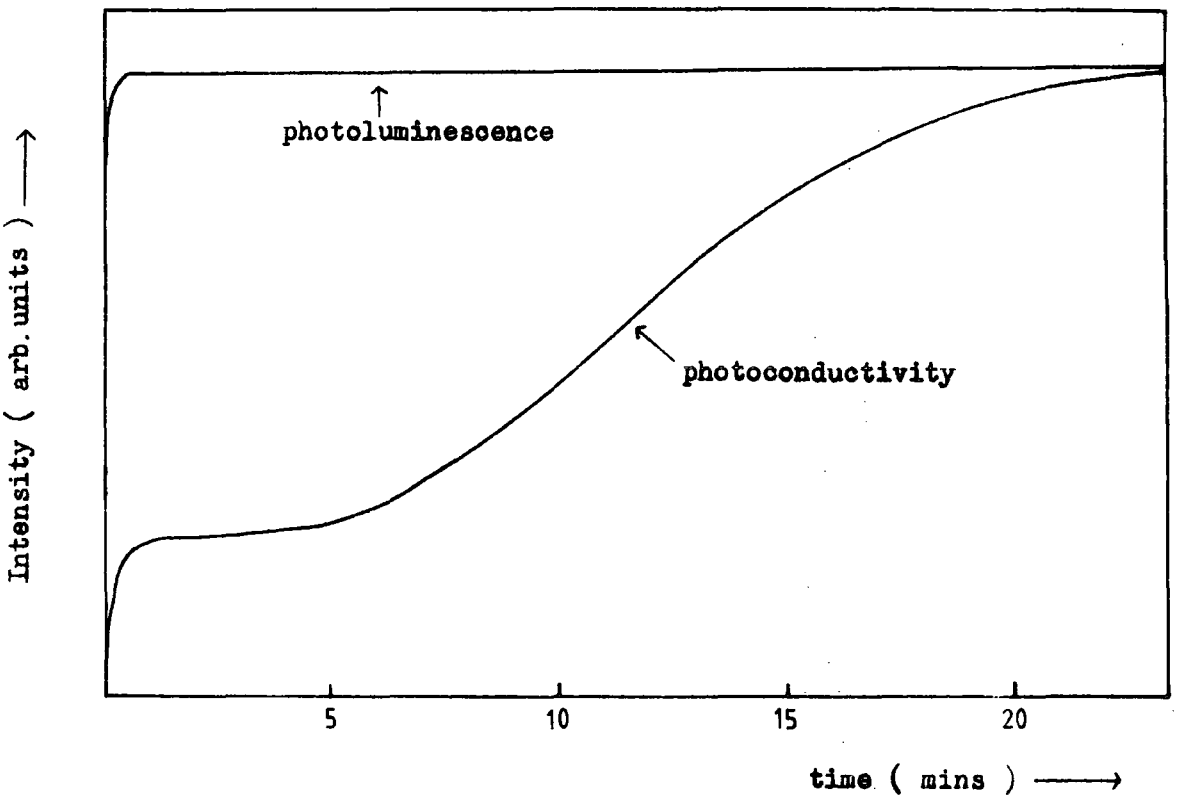

Figure 6.9.1 Kinetic response of PL and PC due to excitation with 410 nm light at 77 K.

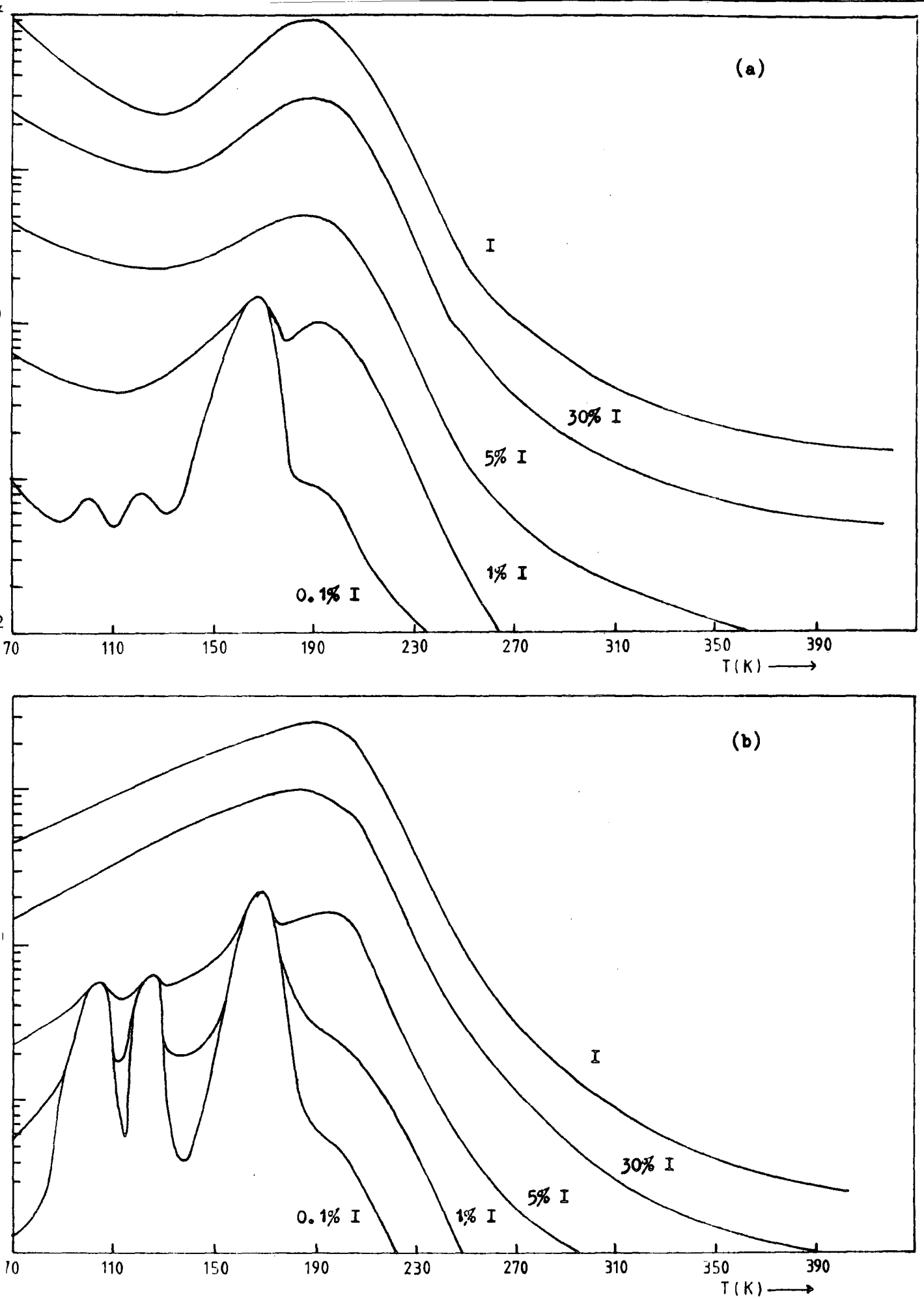

Figure 6.10.1 Temperature dependence of the photoluminescence at various excitation intensities for (a) the stoichiometric as grown crystal BS18(S) and (b) the quenched crystal CA3(NL).

The temperature dependence of the PC spectra of the crystals BS18(S) and CA3(NL) has been discussed in section 5.7. It is interesting to observe that the temperature at which the luminescence begins to fall, at 190K, does not change with excitation intensity and is similar in both crystals. This is not surprising as thermal ionisation of the Cr^{3+} excited state into the conduction band is responsible for the observed decrease in luminescence efficiency with increasing temperature.

Figure 6.10.2 shows the PC and PL response under dynamic conditions after the crystal was first excited by band gap light at 77K. After the PC reached steady state values, the crystal was irradiated simultaneously with infra red light. In both PC and PL, transients were observed when the IR light was turned on and off. The IR stimulation and quenching of PC at low and high excitation intensities has already been discussed in section 5.7. In both cases photoluminescence stimulation was observed. These results can be understood in terms of the charge transfer model as follows. The 410 nm light can excite the luminescence centre by direct excitation or indirectly by impurity excitation (see figure 6.4.2). This excitation process also gives rise to trapped holes and electrons which can be excited subsequently by IR light. It is the excitation of trapped holes and electrons by IR light which gives rise to the observed stimulation and quenching effects. Release of trapped holes always results in stimulation of the PL, because the steady-state PL depends only on the hole traffic through the luminescence centre independent of the electron concentration in the conduction band. Quenching of the PL centre would only be possible if the hole in the ground state of the excited luminescence centre could be ionised to the valence band. Since photoluminescence quenching was not observed under any circumstances, it is concluded that the IR light has insufficient energy (<1.1 eV) to photoionise the Cr^{3+} centre directly.

Finally, it should be noted that the lifetime of the Cr^{3+} excited

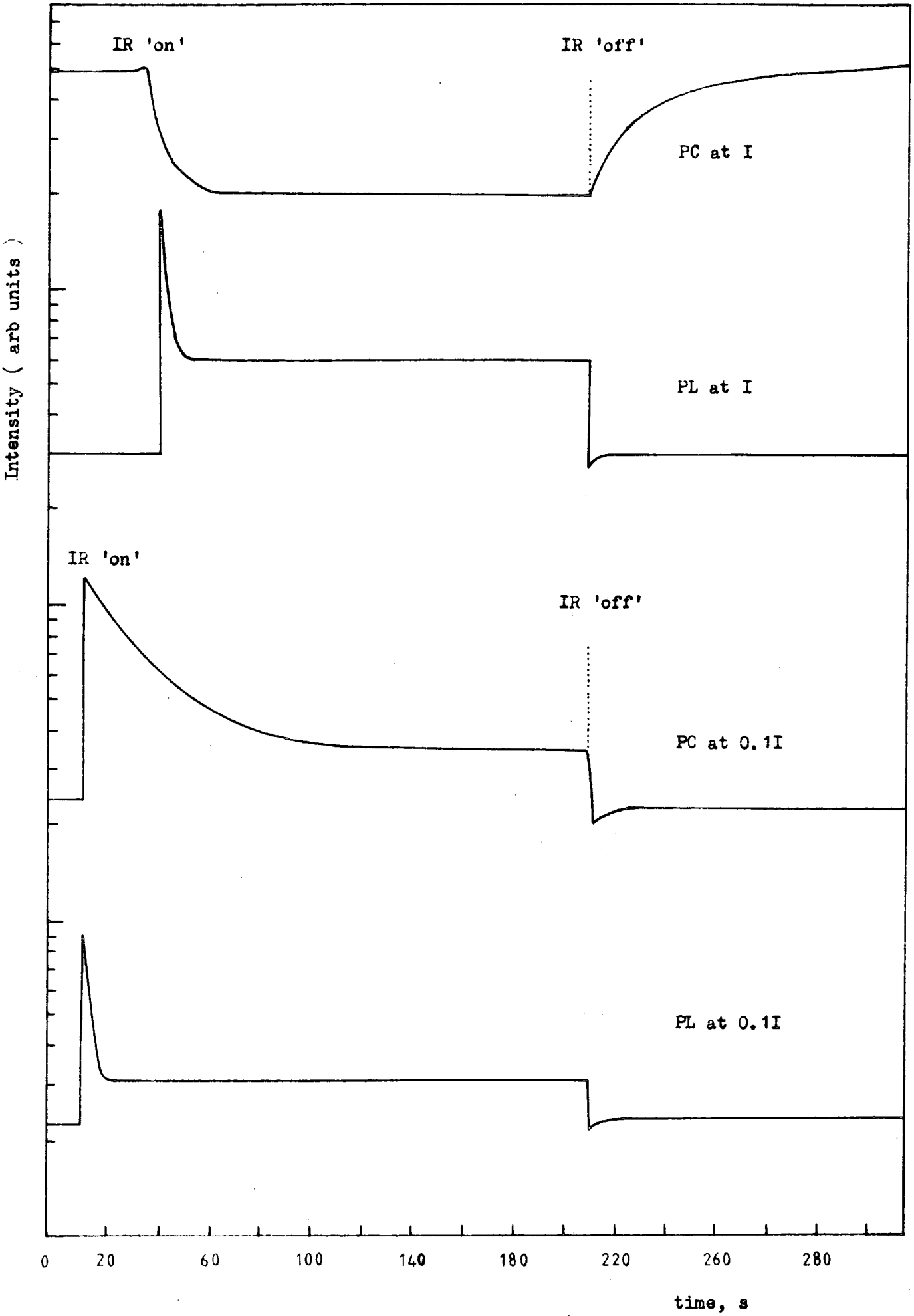

Figure 6.10.2 PC and PL response due to IR light under dynamic conditions at 77 K for crystal CA3(NL) after quenching.

state of 36 μs determined previously is large compared to the lifetime estimated from photoconductive gain measurements, 10^{-8} s. The results presented in this chapter can only be understood if there are faster recombination centres in the rutile crystals compared to the Cr^{3+} luminescence centre.

CHAPTER 7

THERMALLY STIMULATED CURRENT MEASUREMENTS

7.1 INTRODUCTION

Samples with dimensions of 6 x 3 x 1 mm^3 were cut from slices which had previously been cut perpendicularly to the c-axes of the boules. This was done using a diamond saw and the resultant bars were then polished mechanically down to a diamond grit size of 1μm, and chemically polished in boiling concentrated sulphuric acid for two hours. Vacuum deposited silver or titanium electrodes formed ohmic contacts, to which thin copper wires were attached with silver paste. The samples were then mounted on to thin silica slides, 0.17 mm thick, which in turn were mounted on to the copper block of an all metal vacuum cryostat. Prior to measuring the TSC the sample was heated to 400 K in the dark and then cooled to 77 K. The sample was then illuminated with light with wavelength 365 nm filtered from a 250 W compact source mercury lamp using OX1 chance glass and a 10% solution of copper sulphate. After 10 minutes the illumination was extinguished and the TSC was measured by applying 25 V dc and raising the temperature at a uniform rate. Currents down to 10^{-14} A could be measured using a Keighley electrometer model 602.

7.2 THERMALLY STIMULATED CURRENTS

The TSC investigations were carried out on three different types of single crystal rutile. One boule had been obtained commercially from the National Lead Company, U.S.A. and had been grown by a flame fusion technique and almost certainly contained hydrogen as an impurity. TSC measurements were made on the as-grown stoichiometric and non-stoichiometric crystals grown at Stockton by the plasma fusion technique. A typical TSC curve for a NL crystal is shown in figure 7.2.1. Six clearly resolved peaks were quite apparent, of which that with its maximum at 176 K was much the largest

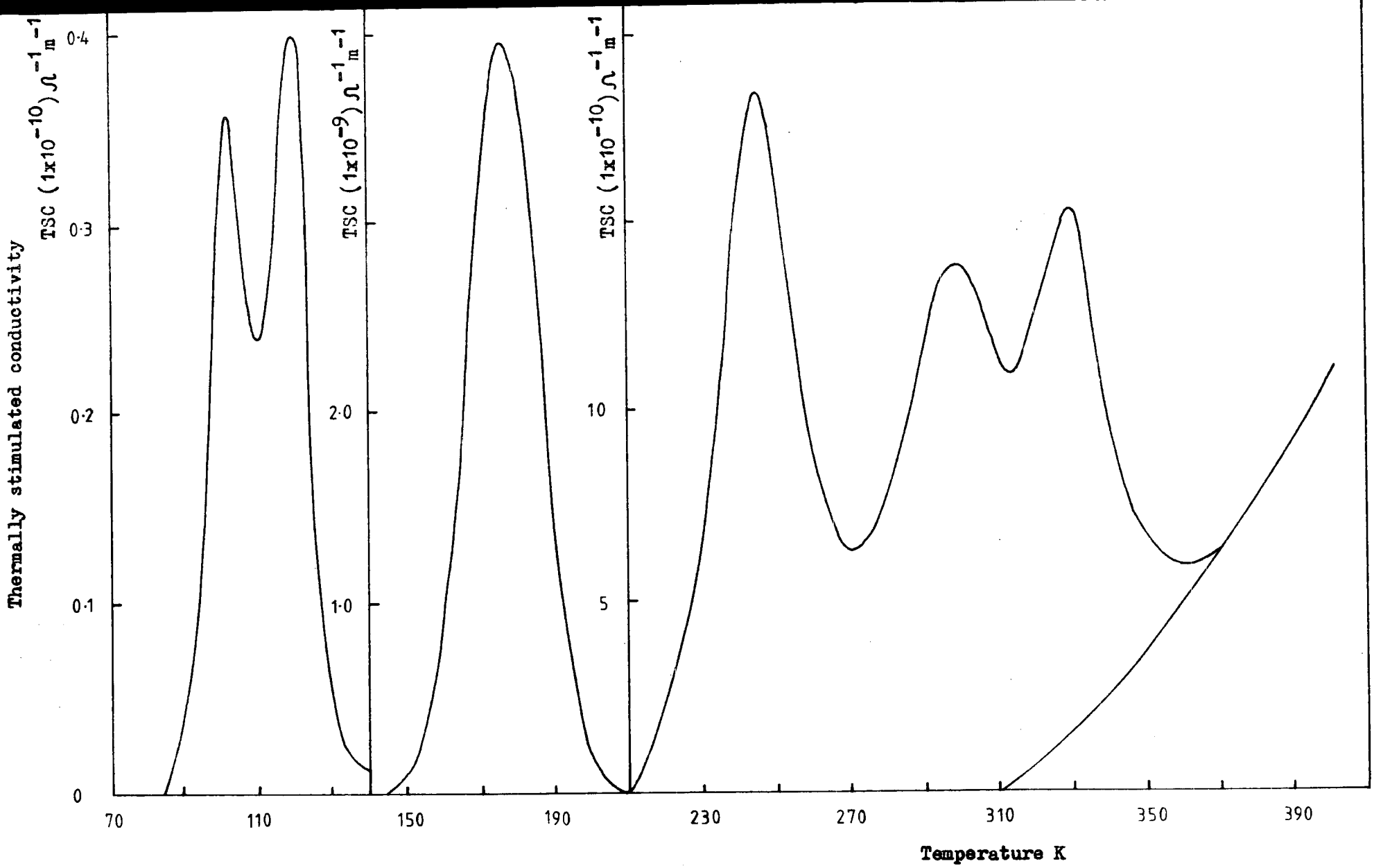

Figure 7.2.1 TSC spectra of the NL crystal CA3(NL).

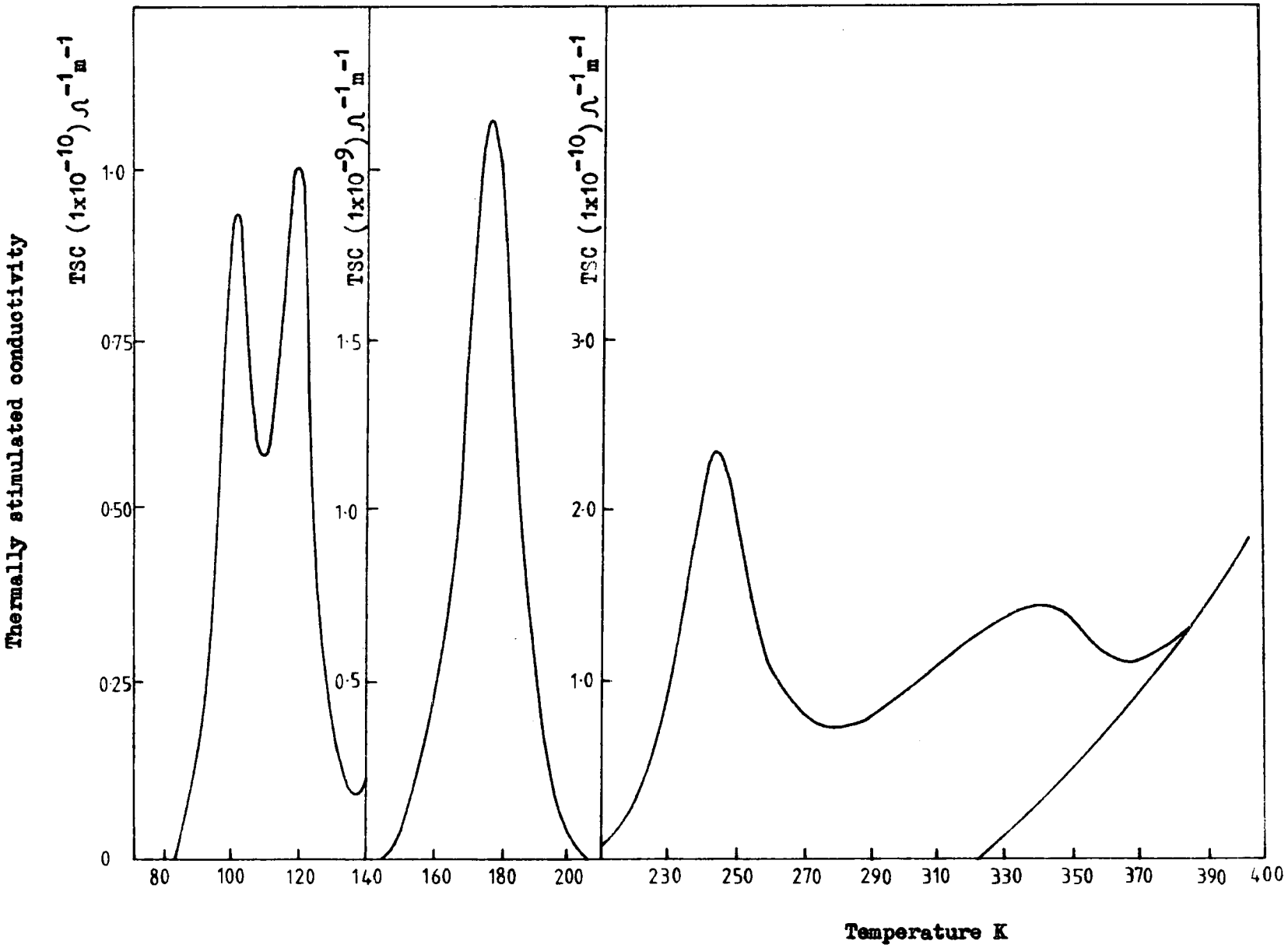

Figure 7.2.2 Thermally stimulated conductivity of an oxidised crystal which was grown in a reduced condition , BS18(NS) .

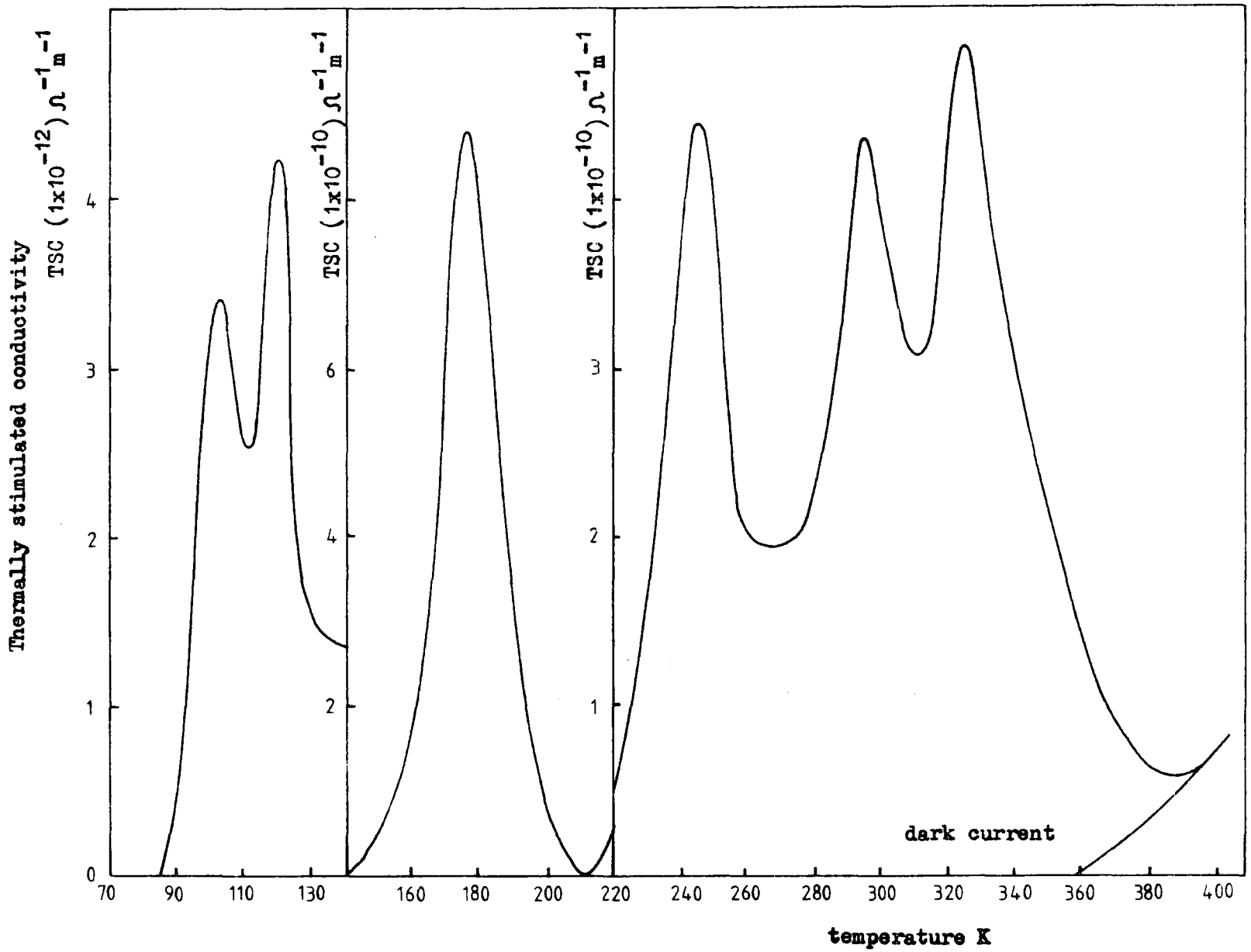

Figure 7.2.3 TSC spectra of an as-grown stoichiometric crystal BS18(S) .

(note the change of scale of the ordinate in the diagram). To help compare our results with those of Ghosh et al (1969) a measurement of TSC was made at the heating rate of $0.5K^{-1}s^{-1}$ which they had employed. The TSC spectra of the as-grown stoichiometric crystals (a typical curve is shown in figure 7.2.3), contain the same six peaks observed in the NL crystal. However, the magnitudes of these are not as large as the corresponding ones in the NL crystals.

The as-grown non-stoichiometric (reduced) crystals grown by the plasma fusion technique were subsequently oxidised by being heated in a stream of oxygen at 1300 °C. In these samples only five TSC peaks could be detected (see figure 7.2.2). All five had previously been observed in the stoichiometric samples, but there was no sign of the high temperature peak at 294 K.

7.3 THERMALLY STIMULATED CURRENTS AFTER ILLUMINATION WITH MONOCHROMATIC LIGHT

TSC spectra were measured following illumination with monochromatic light obtained from a monochromator with 450 W Xenon lamp source as described in section 3. The bandwidth (80 Å) was the same for each wavelength and the energy flux ($0.015\mu W/mm^2$) was adjusted prior to each illumination. Because of the low intensity of excitation the crystal was illuminated for 20 minutes after cooling to complete the trap filling.

Figure 7.3.1 shows the variation of the peak height of the 176 K peak after excitation at different wavelenghts. The maximum response occurs at the band edge (410 nm at 77 K) and decreases rapidly as the wavelength of excitation is decreased due to the increase of the absorption coefficient when most of the incident light is absorbed in a thin surface layer. The generation of TSC spectra at energies less than the band gap shows that the shallow traps can be filled by optically exciting electrons to the conduction band from deep levels as well as from the valence band. Figure

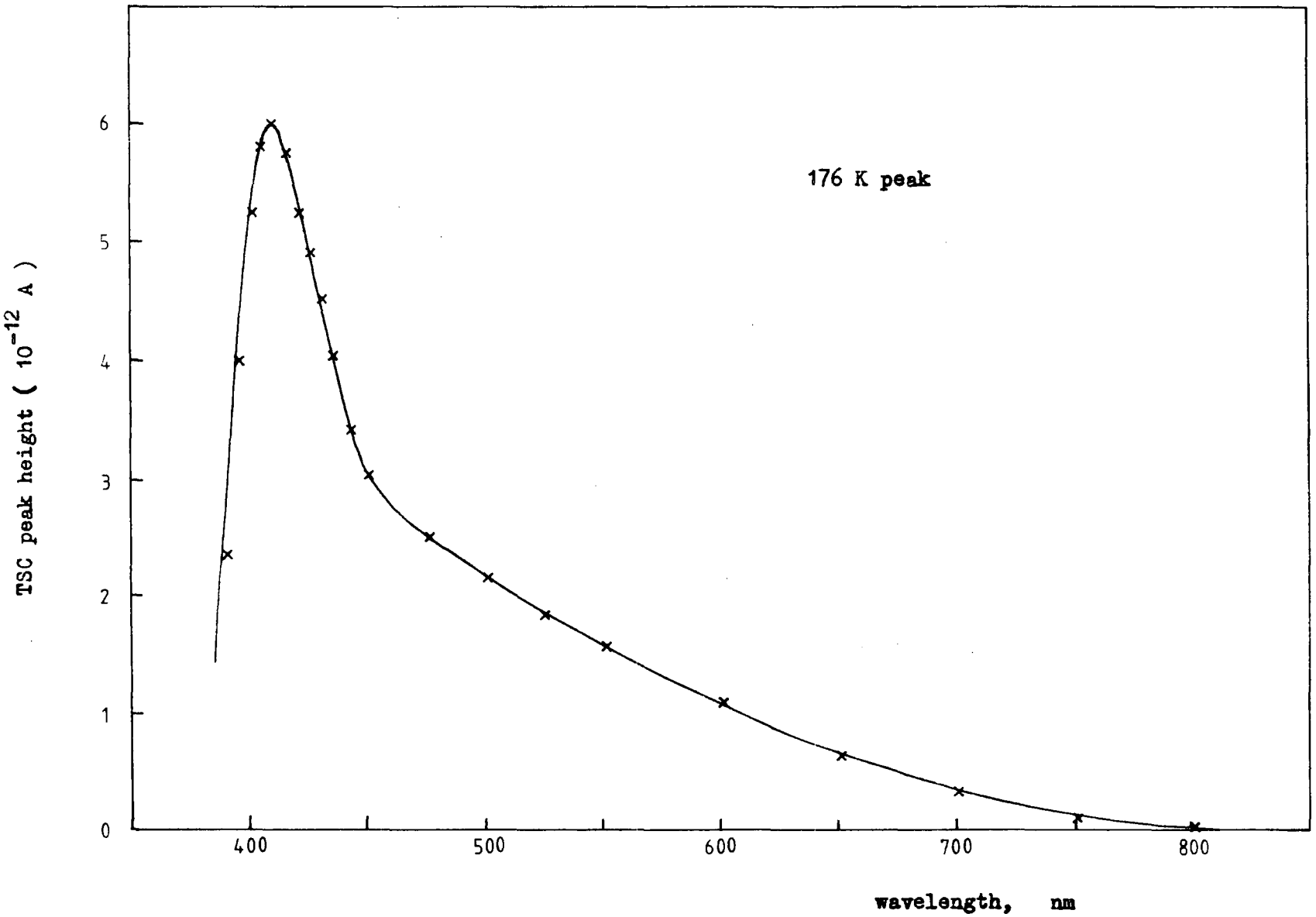

Figure 7.3.1 TSC peak height for 20 minutes excitation (0.015 $\mu W/mm^2$) at different wavelengths .

7.3.2. shows the increase of the heights of these TSC peaks with increasing duration of the excitation. The sample was heated at 400 K for 30 minutes and cooled in the dark to 77 K before each subsequent illumination. It is interesting to observe the different rates at which the various traps fill. A qualitative comparison is made later between the shapes of these curves and the computed capture cross-sections.

7.4 THE EFFECT OF EXCITATION INTENSITY AND SAMPLE THICKNESS ON TSC MEASUREMENTS

The experiments with monochromatic excitation radiation demonstrated that the traps were filling slowly with an excitation intensity of $0.015\mu W/mm^2$. The 250 W compact mercury source using an OX1 chance glass filter and a 10% copper sulphate filter allowed a maximum excitation intensity of about $10\mu W/mm^2$. It was found that the traps within a 1mm sample became saturated after 5 minutes excitation with the mercury source. An excitation time of 10 minutes was adopted for experimental purposes.

Figure 7.4.1 shows the variation of the heights of the 176 K TSC peak with the intensity of illumination for a 1 mm thick sample at a constant excitation time of 10 minutes. The saturated response with excitations between 5.10^{-2} I and I suggests that the traps have been filled throughout the 1mm thickness of sample. The decrease of the TSC peak height with excitation intensities below 10^{-2} I suggests that not all the crystal was being irradiated by light of high enough intensity to saturate the traps. This region of the curve is primarily dependent on the absorption coefficient and reflectivity of the sample. In conclusion it appears that the experimental system using the 250 W mercury source saturated the traps in a 1 mm thick rutile single crystal.

A vacuum cryostat was used in the TSC experiments as described in chapter 4. The sample was mounted onto a copper block and as a result

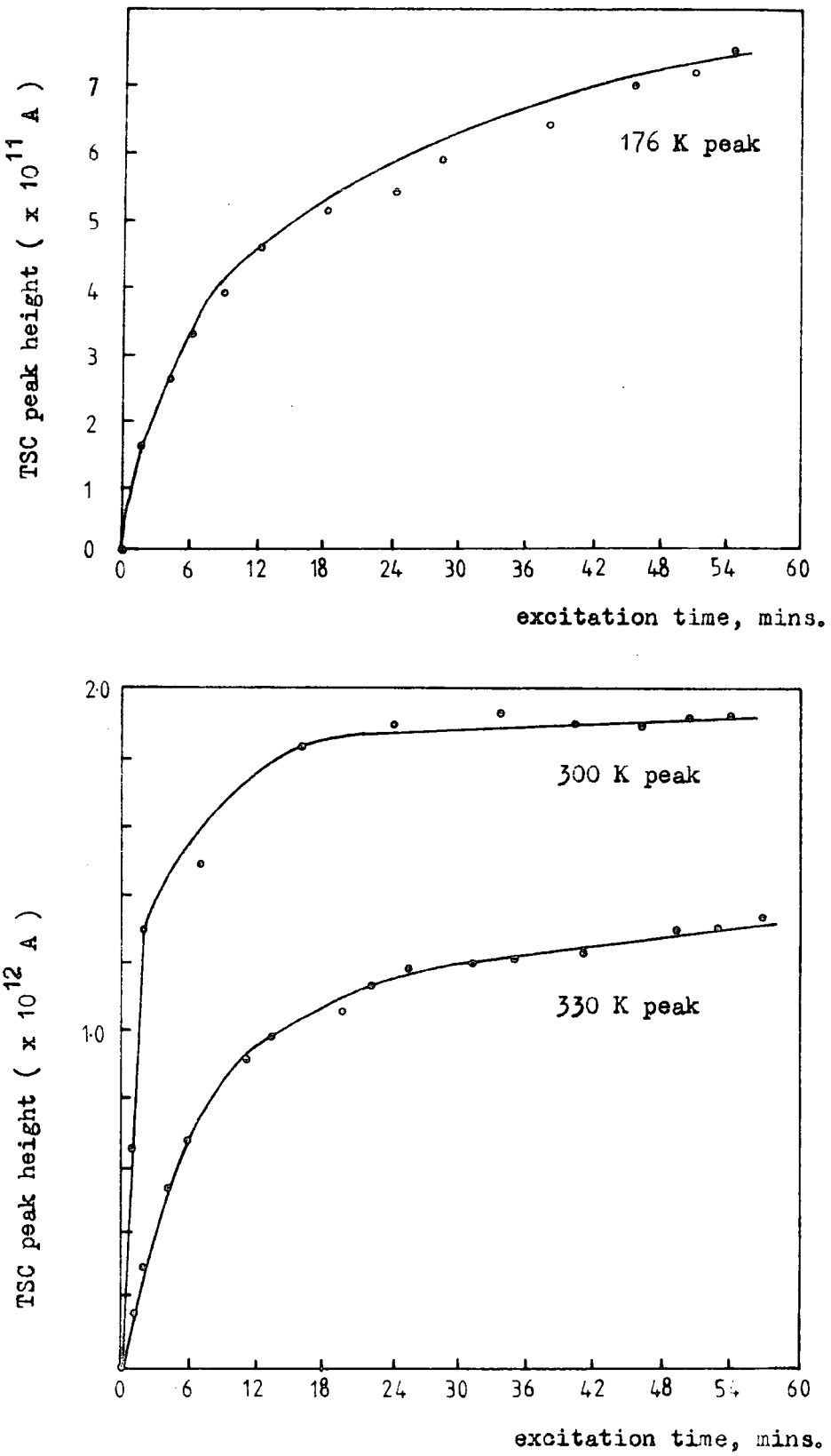

Figure 7.3.2 TSC peak height for different excitation times with an illumination intensity of 0.015 $\mu A/mm^2$.

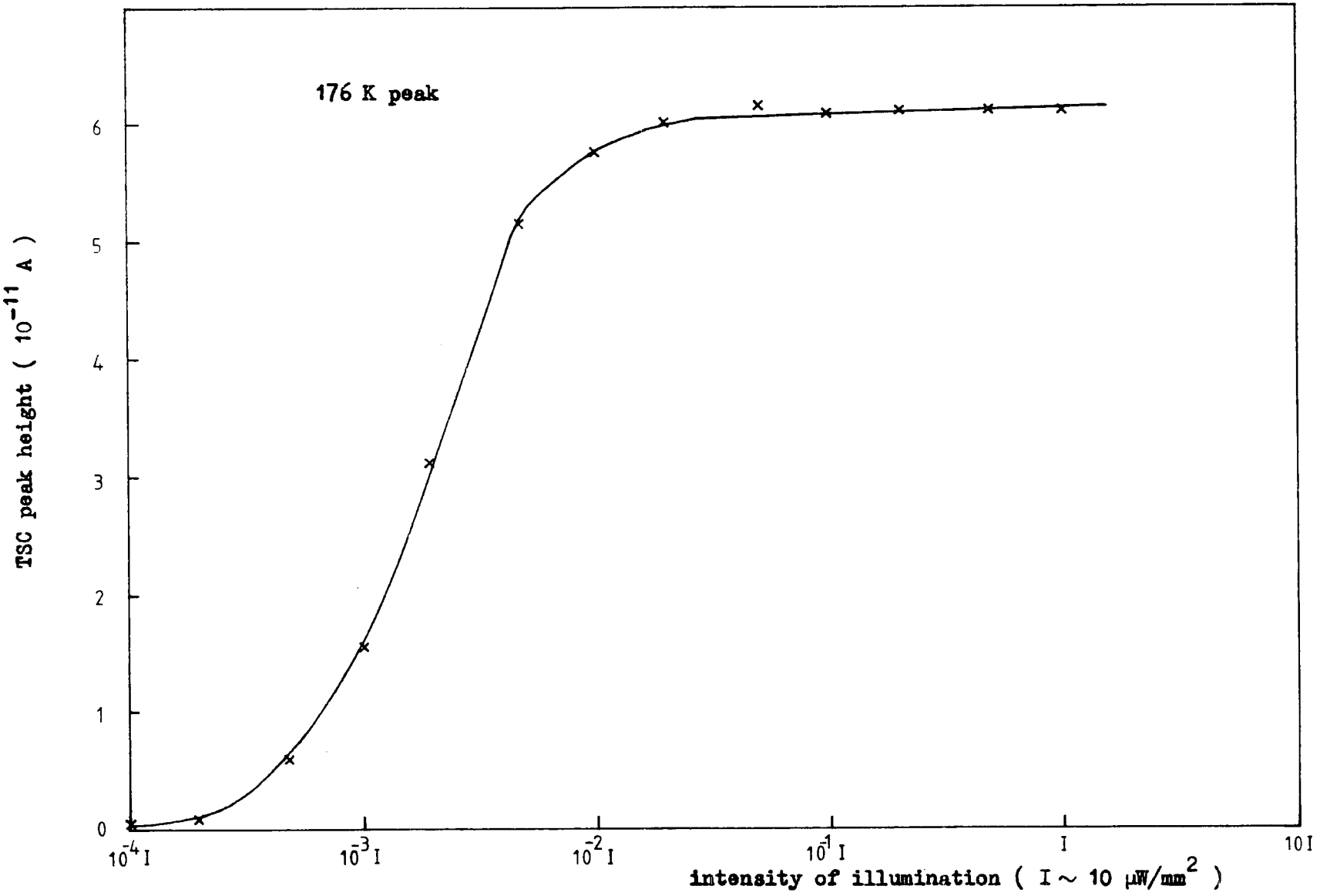

Figure 7.4.1 The variation of the TSC peak height with the intensity of illumination for a 1 mm thick sample .

a temperature gradient existed between the front and back faces of the sample as the copper was heated. A series of experiments were performed to investigate the effect of sample thickness on the TSC characteristics. Figure 7.4.2 shows the variation of the temperature of the 176 K TSC peak as the sample thickness was increased. At a thickness of about 1.5 mm there appears to be a small decrease in the temperature of the TSC maximum. However, the experiment does not appear conclusive mainly because of the problem of obtaining good thermal contact between the rutile, glass slide and copper block each time the sample was mounted. Also, the position of the thermocouple could add an error of about 1 degree each time the sample was mounted. However, the temperature of the TSC half-width is a relative temperature measurement and it showed a gradual increase as the sample thickness increased. These experiments indicated a desirable sample thickness of less than 1.2 mm for the TSC measurements.

7.5 ANALYSIS OF THE T.S.C. CURVES

The evaluation of the trapping parameters, i.e. the ionisation energy of the trap, its capture cross section and concentration, from the experimental TSC curve, is a matter of considerable complexity (Nicholas and Woods 1965, Kivits and Hagebeuk 1977). In chapter 2 a great variety of methods for the calculation of trap depths has been described. All these methods were derived assuming a simple model with one trapping level and one recombination level. Kivits and Hagebeuk applied these methods to TSC and TSL curves that were generated numerically for a more realistic model. Since in these investigations the correct trap depth was known it was possible to establish the reliability of different methods. Kivits and Hagebeuk found that the methods of Haering and Adams, Hoogenstraaten and Unger produce reliable values for the trap depth independent of the values of the frequency factor and the retrapping ratio. In any case the deviations of all methods with respect to the correct trap depth can be calculated.

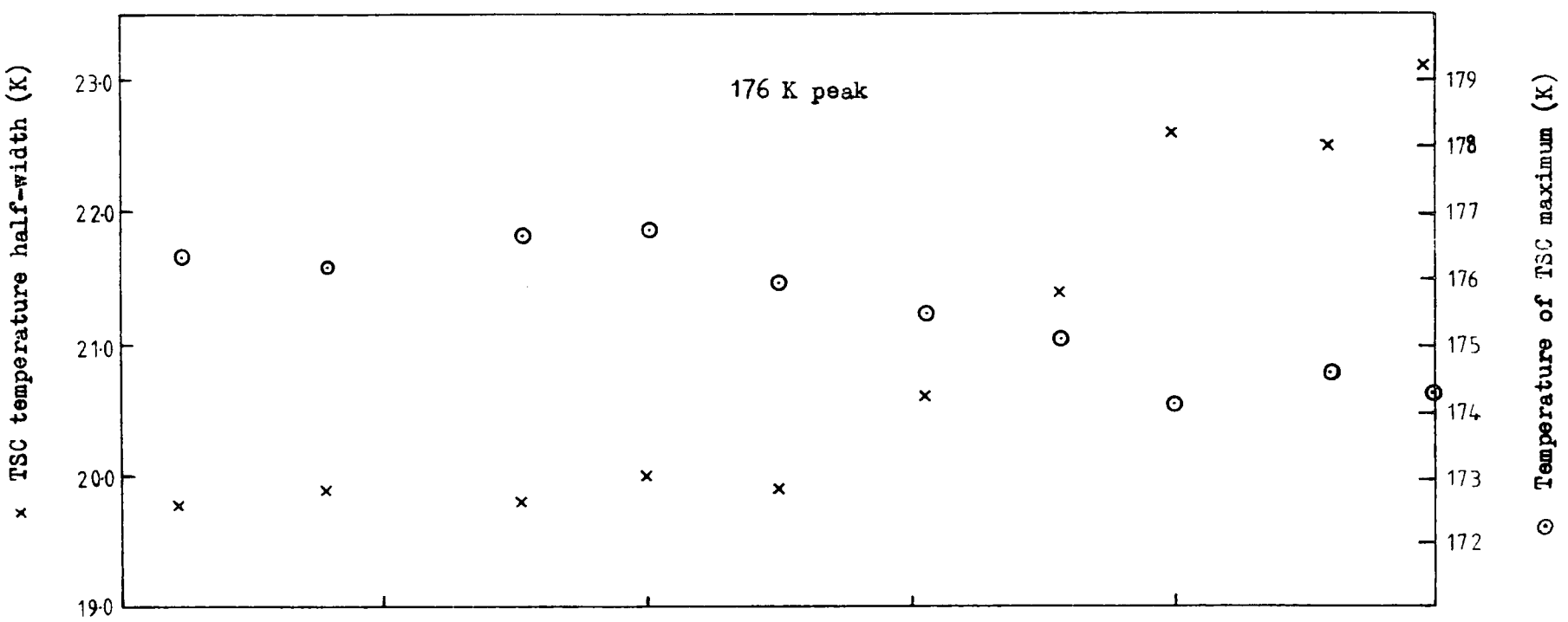

Figure 7.4.2 The variation of the TSC temperature half-width and TSC temperature maximum with sample thickness .

This can be used in testing the simple model against experimental results.

Initially, the results obtained for the dominant TSC peak at 176 K will be discussed. This peak was well isolated from the other TSC maxima and did not require any thermal cleaning. Table 7.5.1 shows the results obtained on the three rutile crystals BS18(NS), BS18(S) and CA3(NL). The methods of Hoogenstraaten, Haering and Adams, Chen and Winer, and Garlick and Gibson gave self consistent values for the trap depth. The other methods gave a range of trap depth energies.

The amount of charge released during a TSC experiment can be calculated from the area under the TSC curve. To obtain a value of the trap concentration it was necessary to know the electron mobility and the free carrier lifetime. Mobilities were not measured and values reported by Breckenridge and Hosler (1965) and Bogomolov and Zhuze (1964) for reduced rutile have therefore been used. Estimates of the free electron lifetimes have been determined experimentally, however, by measuring the photoconductive gain factor under conditions of steady-state illumination when the photocurrent was comparable in magnitude to the TSC peak under investigation. It has been assumed that the lifetime measured in this way, which was of the order of 10^{-8} second, is identical with the mean time an electron remains free following detrapping in the TSC experiment. This assumption is more likely to be correct at the lower end of the temperature range where the occupancy of the recombination centres with holes was more probably identical in the two different experiments.

In order to attempt a better appreciation of the experimental trap depths listed in Table 7.5.1, a series of theoretical TSC curves were generated using the Kivits theory. The computer program is listed in appendix 1. The ratio of thermally connected trap density to thermally disconnected trap density (ξ) was known, and it was assumed that the trap depth was 0.37 eV as indicated by the agreement of the five methods mentioned

	BS18 non-stoichiometric crystal + oxidation	BS18 stoichiometric as-grown crystal	CA3(NL) National Lead crystal
Hoogenstaaten	0.37 ∓ 0.02	0.36 ∓ 0.01	0.36 ∓ 0.01
Haering,Adams	0.37 ∓ 0.02	0.37 ∓ 0.01	0.37 ∓ 0.02
Chen,Winer	0.38 ∓ 0.02	0.37 ∓ 0.02	0.37 ∓ 0.02
Unger	0.37 ∓ 0.02	0.37 ∓ 0.02	0.37 ∓ 0.01
Garlick,Gibson 10%	0.39 ∓ 0.02	0.38 ∓ 0.03	0.38 ∓ 0.02
Garlick,Gibson 20%	0.38 ∓ 0.02	0.38 ∓ 0.03	0.38 ∓ 0.02
Boiko,Rashba,Trof.A	0.32 ∓ 0.02	0.33 ∓ 0.02	0.33 ∓ 0.02
Boiko,Rashba,Trof.B	0.31 ∓ 0.02	0.32 ∓ 0.02	0.32 ∓ 0.02
Chen 1	0.32	0.30	0.28
Chen 2	0.32	0.30	0.29
Chen 4	0.40	0.46	0.40
Chen 5	0.25	0.21	0.21
Chen 6a	0.47	0.60	0.51
Chen 6b	0.44	0.56	0.47
Luschik	0.26	0.22	0.22
Grossweiner	0.42	0.48	0.42
λ	9.0	8.0	9.1
σ	10.1	12.2	12.3
ω	19.1	20.2	21.4

Table 7.5.1 Experimental TSC analysis for the 176 K peak .

previously. Initially, a value of retrapping ratio (δ) of 1.0, suggesting an equal probability of retrapping or recombination, was fed into the computer program. These curves were normalised so that their shapes could be compared with the experimental TSC curve. A value of the trapping frequency (FREQ) was found which gave a theoretical temperature maximum indentical to the experimental value. The curve fitting was completed by varying the retrapping ratio until a good fit was obtained.

The temperature of a TSC curve maximum is primarily dependent on the value of the trap depth energy and the trapping frequency. A series of combinations of these two can be found to give a fit to almost any TSC peak. The values of ξ and δ are of secondary importance in the determination of the temperature of the TSC maximum. As an order of magnitude estimate of the trapping frequency is being sought, the effects of variation in ξ and δ can be ignored. The value of the recombination rate constant, α, only influences the TSC temperature position when α is small (Kivits, Hagebeuk 1977). In the rutile crystals this would correspond to free carrier lifetimes larger than 1 millisecond. In fact the measured lifetimes of the order of 10^{-8} second gave values of α of the order of 10^{10} cm^3/sec. Therefore the effects of variation in α on the position and shape of the TSC curves can also effectively be ignored in our calculations for the rutile crystals. The curves in figure 7.5.1. demonstrate the effect of varying the retrapping ratio, δ, for the 176 K peak. The area under the TSC curve remains constant indicating than an equal amount of charge is released in each case considered. As δ is increased we can observe a large effect on the high temperature side of the TSC curve. In figure 7.5.2 a comparison of the geometrical shapes of the experimental and theoretical curves for different retrapping ratio, indicates a value of $\delta = 0.5$ as best fit for the 176 K peak. This suggests that the recombination kinetics are intermediate between monomolecular ($\delta = 10^{-2}$) and bimolecular ($\delta = 1.0$), so that the assumption of fast retrapping made by Ghosh et al (1969) is almost certainly incorrect. In Bube's

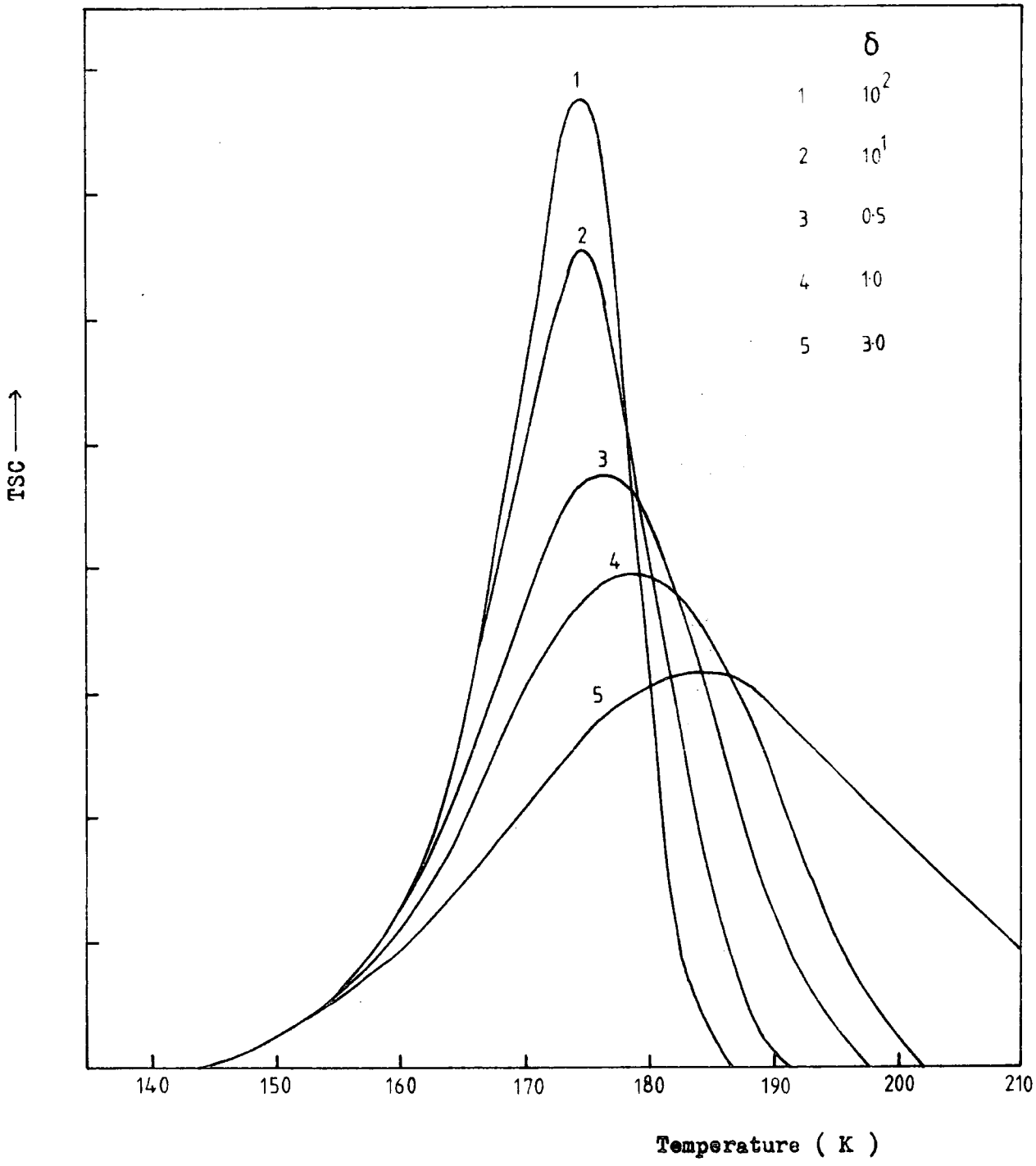

Figure 7.5.1 Variation of TSC curves with retrapping ratio δ .

E = 0.37 eV ; hs = 2.0 10^{17} cm^{-3} ; hd = 1.7 10^{16} cm^{-3} ; τ = 10^{-8} s ;

FREQ = 7.39 10^{9} s^{-1} ; β = 0.5 s^{-1} .

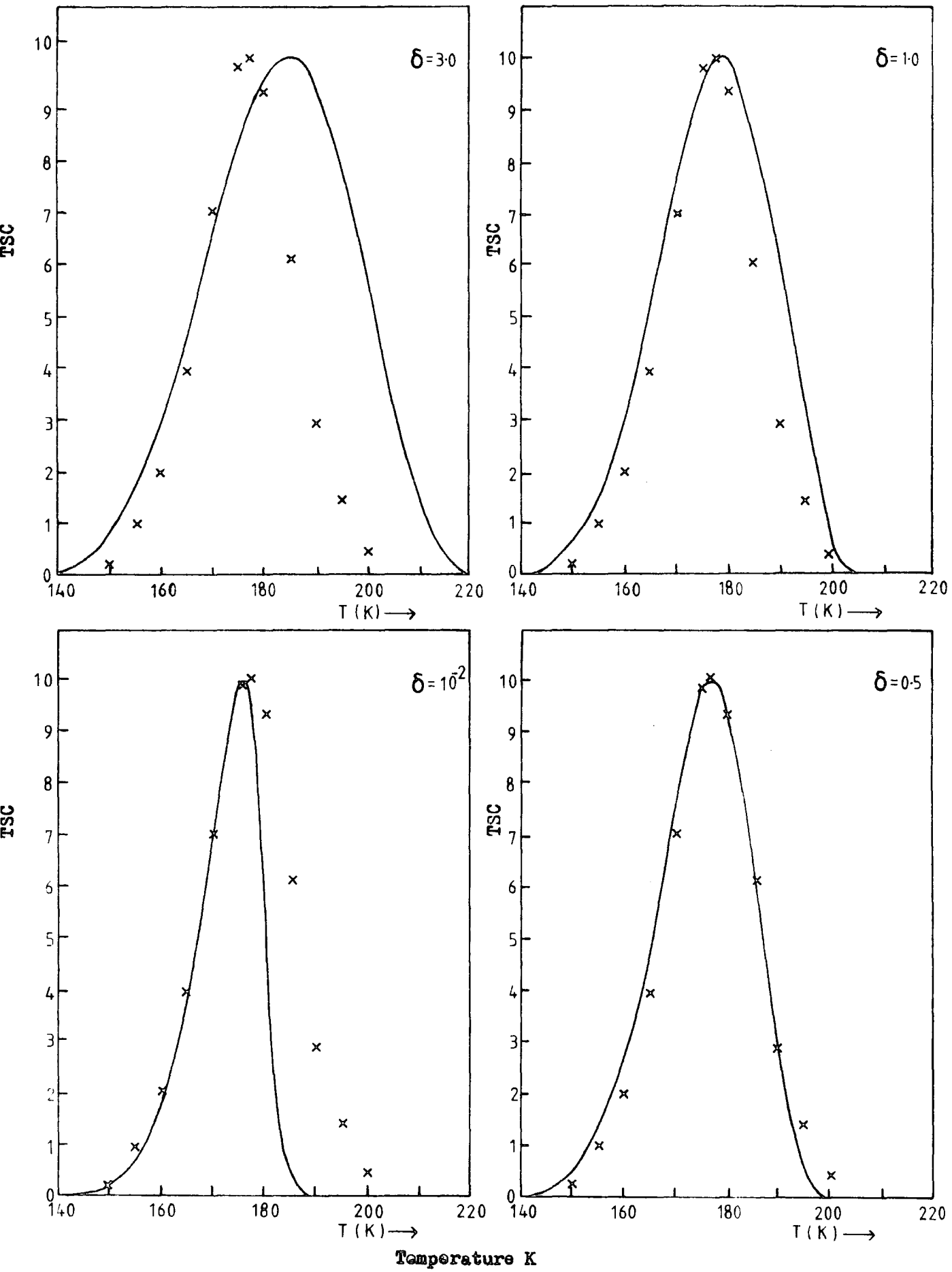

Figure 7.5.2 Comparison of the geometrical shapes of TSC curves for different retrapping ratios . E = 0.37 eV ; hs = 2.0 10^{17} cm^{-3} ; hd = 1.7 10^{16} cm^{-3} ; τ = 10^{-8} s ; FREQ = 7.39 10^{9} s^{-1} ; β = 0.5 $^{\circ}s^{-1}$.

quasi-fermi level analysis (Bube 1964), the ionisation energy is computed from the value of the sample conductivity at the peak of the TSC curve. It is assumed that the quasi-fermi level coincides with the level of the trap associated with the peak when $T=T_m$. For this analysis to be valid, retrapping must dominate over competing recombination processes i.e. $\delta=3.0$. A value of trap depth of 0.43 eV was obtained for the NL (CA3) crystal when applied to the 176 K peak. In order to obtain a good fit to the theoretical curve for 0.43 eV, a trapping frequency of 10^{13}/s had to be used in the computer program.

The theoretical data presented in table 7.5.2. include the results obtained using values of $\xi=0.85$ and $\xi=0.085$. The value 0.85 was derived experimentally by measuring the photoconductive gain at 77 K and calculating the area under the TSC curve. The value 0.085 was indicated by some thermoluminescence experiments to be presented in chaper 8. It is interesting to compare the trap depths calculated by Chen, Grossweiner and Luschik to the experimental values obtained from crystal CA3. The correlation was marginally better on the data given for $\xi=0.085$ although it was difficult to attach any significance to this observation. The errors quoted in the table are the standard deviations calculated from a 'least squares' straight line fit. In all cases, eight values of heating rate between 0.6 /s and 0.05 /s were used.

The theoretical data in table 7.5.3 shows how various methods gave spurious results depending on the value of δ and ξ taken with the constant values of E=0.37 eV and FREQ = $7.39.10^9$. Again it is clearly demonstrated, as already stated by Kivits and Hagebeuk (1977), that the methods of Hoogenstraaten, Haering and Adams, Chen and Winer, Unger and Garlick and Gibson give reliable results independent of values of δ and ξ. However, the method of Garlick and Gibson was not an easy method to apply. The experimental and theoretical data became non-linear at 18.9% of the

	Experimental crystal CA3(NL)	Theoretical HS = 2.00E+17 HD = 1.70E+17 ξ = 0.85	Theoretical HS = 2.00E+17 HD = 1.70E+16 ξ = 0.085
Hoogenstraaten	0.36 ∓ 0.01	0.3704 ∓ 0.0001	0.3707 ∓ 0.0001
Haering,Adams	0.37 ∓ 0.02	0.3713 ∓ 0.0001	0.3714 ∓ 0.0001
Chen,Winer	0.37 ∓ 0.02	0.3695 ∓ 0.0001	0.3700 ∓ 0.0001
Unger	0.37 ∓ 0.01	0.3704 ∓ 0.0001	0.3690 ∓ 0.0001
Garlick,Gibson 10%	0.38 ∓ 0.02	0.3681 ∓ 0.0001	0.3593 ∓ 0.0001
Garlick,Gibson 20%	0.38 ∓ 0.02	0.3652 ∓ 0.0001	0.3683 ∓ 0.0001
Boiko,Rashba,Trof.A	0.33 ∓ 0.02	0.3497 ∓ 0.0001	0.3520 ∓ 0.0001
Boiko,Rashba,Trof.B	0.32 ∓ 0.02	0.3488 ∓ 0.0001	0.3513 ∓ 0.0001
Chen 1	0.28	0.336	0.277
Chen 2	0.29	0.341	0.282
Chen 4	0.40	0.382	0.331
Chen 5	0.21	0.324	0.234
Chen 6a	0.51	0.824	0.379
hen 6b	0.47	0.757	0.354
uschik	0.22	0.382	0.234
rossweiner	0.42	0.383	0.354

Table 7.5.2 Comparison of trap depths obtained from theoretical and experimental data for the 176 K peak .

Theoretical input data : E, 0.37 eV ; DELTA, 0.5 ; FREQ, 7.39E+09 .

TSC	HS = 2.0E+17 HD = 2.0E+14 ξ = 1.0E-3				HS = 1.7E+17 HD = 2.0E+17 ξ = 0.85				HS = 1.7E+18 HD = 2.0E+17 ξ = 8.5			
Retrapping ratio, δ	10^{-2}	0.1	1.0	3.0	10^{-2}	0.1	1.0	3.0	10^{-2}	0.1	1.0	3.0
Hoogenstraaten	.371	.371	.367	.366	.371	.371	.371	.371	.370	.368	.370	.371
Haering,Adams	.372	.371	.372	.325	.371	.372	.372	.372	.371	.369	.371	.372
Chen,Winer	.370	.370	.404	.410	.371	.372	.372	.372	.369	.367	.369	.370
Boiko,Rashba,Trof.A	.350	.350	.350	.354	.350	.351	.350	.350	.350	.348	.349	.350
Boiko,Rashba,Trof.B	.349	.348	.352	.358	.349	.350	.350	.349	.349	.348	.349	.350
Unger	.370	.369	.379	.378	.373	.373	.371	.372	.368	.372	.371	.371
Garlick,Gibson 10%	.368	.369	.368	.369	.367	.368	.368	.368	.367	.367	.367	.367
Garlick,Gibson 20%	.370	.368	.359	.357	.367	.365	.361	.359	.365	.365	.365	.364
Chen 1	.835	.579	.481	.320	.413	.359	.342	.339	.377	.367	.362	.340
Chen 2	.793	.559	.469	.310	.405	.355	.343	.338	.372	.363	.358	.339
Chen 3	.545	.428	.301	.239	.439	.399	.364	.304	.407	.404	.399	.379
Chen 4	.520	.398	.265	.119	.411	.369	.320	.270	.379	.374	.370	.349
Chen 5	.451	.340	.272	.123	.419	.350	.429	.494	.379	.362	.357	.334
Chen 6a	1.12	.881	.619	.538	.904	.821	.687	.626	.838	.829	.821	.781
Chen 6b	1.05	.822	.587	.502	.843	.766	.643	.584	.783	.649	.643	.612
Luschik	.462	1.44	2.79	3.18	.429	.359	.438	.506	.389	.371	.366	.342
Halperin,Braner 1	.582	.456	.321	.242	.468	.426	.419	.325	.435	.425	.419	.405
Halperin,Braner 2	.665	.522	.367	.283	.535	.486	.417	.371	.497	.491	.486	.462
Grossweiner	.542	.420	.288	.119	.433	.391	.341	.292	.400	.395	.391	.371

Table 7.5.3 Values of trap depth calculated from theoretical curves for different δ and ξ.

Theoretical input data : E, 0.37 eV ; FREQ, 7.39E09 .

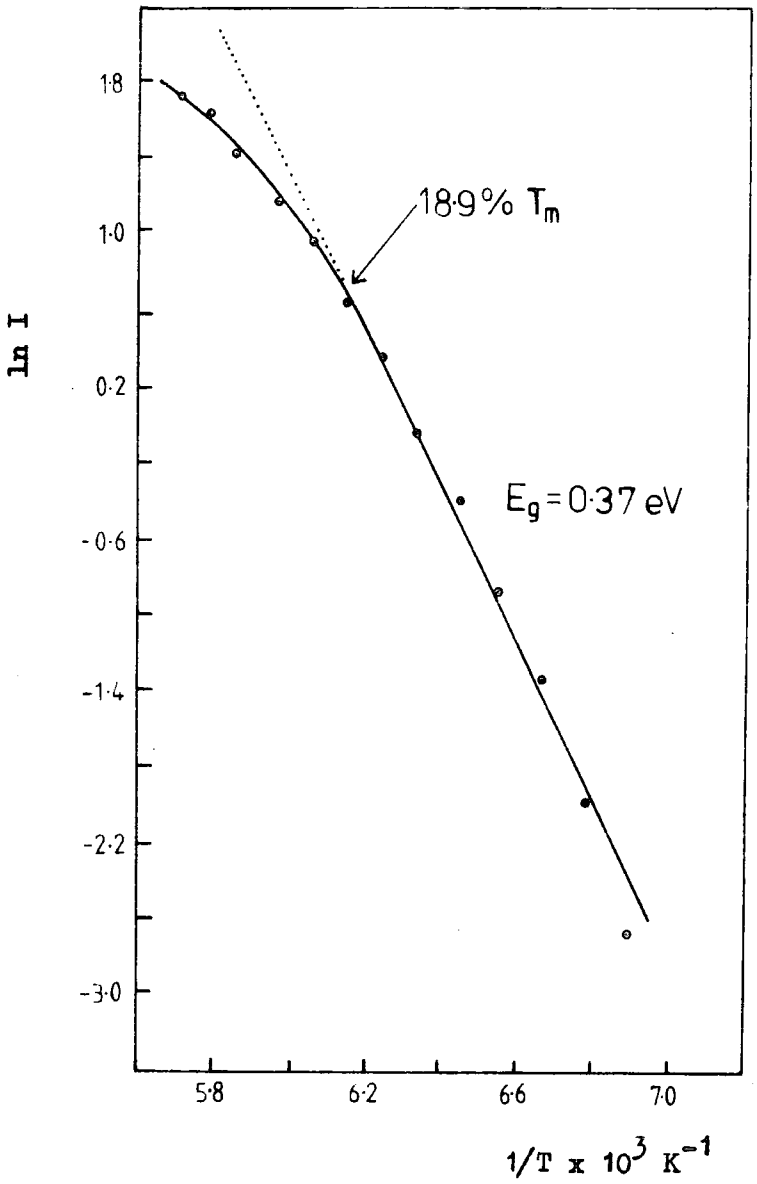

Figure 7.5.3 Garlick and Gibson plot for the NL crystal CA3(NL) .

temperature maximum when ln (I) was plotted against $1/T_m$ (see figure 7.5.3). This did not produce a problem with the theoretical data but with experimental data it limited the accuracy of the trap depth determination. The experimental lower temperature portion of the curve was non-linear because of inaccuracies in the measurement of low currents and the high temperature portion became non-linear as a consequence of the theoretical limitations of the method.

7.6 EXPERIMENTAL TSC RESULTS

A complete TSC analysis as described for the 176 K peak in the preceding section was performed on each computer TSC curve. The thermal ionisation energies of the six traps in the National Lead crystal CA3(NL) calculated by fifteen different methods are listed in Table 7.6.1. Again it can be seen that the first five methods gave extremely self consistent results. The other methods gave various answers, although extremely consistent results from all the methods were obtained for the 103 K peak. The erroneous results obtained using Bube's quasi-fermi level analysis are not surprising. The analysis assumes fast retrapping which conflicts with the conclusion from the rest of the TSC analysis. It does assume that the values of carrier mobility and effective mass taken from published work on reduced rutile can be used for insulating samples.

The concentrations of the various traps were calculated on the assumption that all the traps were completely filled by the initial radiation. The values obtained are listed in table 7.6.2 which provides a summary of the ionisation energies of the various traps and their concentrations for the three types of crystal examined. Trap depths reported by Ghosh et al are included for comparison purposes. Finally in evaluating trapping parameters the curve fitting method of Cowell and Woods (1967) has been used to obtain values of the capture cross sections. A comparison between the values obtained from the Kivits method and the Cowell and Woods method is listed

TSC PEAK	103 K	120 K	176 K	245 K	300 K	330 K
Hoogenstraaten	0.14 ∓ 0.01	0.23 ∓ 0.01	0.36 ∓ 0.01	0.51 ∓ 0.01	0.61 ∓ 0.01	0.69 ∓ 0.01
Chen,Winer	0.13 ∓ 0.01	0.24 ∓ 0.01	0.37 ∓ 0.01	0.52 ∓ 0.01	0.60 ∓ 0.02	0.69 ∓ 0.02
Haering,Adams	0.14 ∓ 0.01	0.24 ∓ 0.01	0.37 ∓ 0.01	0.51 ∓ 0.01	0.61 ∓ 0.01	0.68 ∓ 0.01
Unger	0.13 ∓ 0.01	0.24 ∓ 0.01	0.37 ∓ 0.01	0.51 ∓ 0.02	0.61 ∓ 0.02	0.69 ∓ 0.02
Garlick,Gibson 10%	0.18 ∓ 0.03	0.25 ∓ 0.03	0.38 ∓ 0.02	0.51 ∓ 0.01	0.60 ∓ 0.02	-
Boiko,Rashba,Trof.A	0.12 ∓ 0.02	0.23 ∓ 0.02	0.35 ∓ 0.02	0.47 ∓ 0.03	0.55 ∓ 0.03	0.61 ∓ 0.03
Chen 1	0.15 ∓ 0.01	0.20 ∓ 0.01	0.28 ∓ 0.02	0.48 ∓ 0.03	0.47 ∓ 0.03	0.61 ∓ 0.03
Chen 2	0.15 ∓ 0.01	0.20 ∓ 0.02	0.29 ∓ 0.02	0.48 ∓ 0.03	0.48 ∓ 0.04	0.61 ∓ 0.03
Chen 4	0.15 ∓ 0.01	0.18 ∓ 0.02	0.40 ∓ 0.02	0.59 ∓ 0.03	0.73 ∓ 0.03	1.06 ∓ 0.03
Chen 5	0.15 ∓ 0.01	0.24 ∓ 0.02	0.21 ∓ 0.02	0.40 ∓ 0.03	0.33 ∓ 0.02	0.40 ∓ 0.03
Chen 6a	0.15 ∓ 0.01	0.15 ∓ 0.02	0.60 ∓ 0.03	0.66 ∓ 0.03	0.98 ∓ 0.04	1.47 ∓ 0.04
Chen 6b	0.14 ∓ 0.01	0.14 ∓ 0.01	0.56 ∓ 0.03	0.62 ∓ 0.03	0.92 ∓ 0.04	1.37 ∓ 0.04
Luschik	0.15 ∓ 0.01	0.25 ∓ 0.02	0.22 ∓ 0.02	0.41 ∓ 0.03	0.34 ∓ 0.02	0.41 ∓ 0.03
Grossweiner	0.16 ∓ 0.01	0.25 ∓ 0.02	0.22 ∓ 0.01	0.41 ∓ 0.02	0.62 ∓ 0.03	0.99 ∓ 0.03
Bube quasi-Fermi level analysis	0.28	0.32	0.43	0.66	0.83	0.93

Table 7.6.1 Thermal ionisation energies of six traps in the National Lead crystal CA3(NL) calculated by fifteen different methods from TSC data .

Crystal BS18(S)				Crystal BS18(NS)				National Lead crystal CA3(NL)				Ghosh et al	
T_m K	E_t eV	S cm^2	n_t cm^{-3}	T_m K	E_t eV	S cm^2	n_t cm^{-3}	T_m K	E_t eV	S cm^2	n_t cm^{-3}	T_m K	E_t eV
												91	0.27
103	0.13	10^{-21}	2×10^{13}	103	0.13	10^{-21}	6×10^{14}	104	0.13	10^{-21}	3×10^{14}	106	0.28
120	0.24	10^{-19}	4×10^{13}	120	0.24	10^{-18}	1×10^{15}	121	0.24	10^{-18}	4×10^{14}	121	0.32
176	0.37	10^{-19}	1×10^{16}	176	0.37	10^{-18}	9×10^{16}	176	0.37	10^{-18}	2×10^{17}	169	0.48
												200	0.56
245	0.51	10^{-19}	2×10^{16}	245	0.51	10^{-19}	6×10^{15}	245	0.51	10^{-19}	9×10^{16}	241	0.62
294	0.61	10^{-19}	2×10^{16}					300	0.61	10^{-19}	6×10^{16}	296	0.76
326	0.69	10^{-19}	3×10^{16}	340	0.81	10^{-19}	1×10^{16}	330	0.69	10^{-19}	8×10^{16}	336	0.87

Table 7.6.2 TSC data for the as-grown stoichiometric crystal BS18(S) ; the non-stoichiometric crystal BS18(NS) after oxidation ; and the National Lead crystal CA3(NL) . The results of Ghosh et al (1969) are shown for comparison.

E_t = trap depth, S = capture cross-section and n_t = density of traps .

in table 7.6.3. The Cowell and Woods method is only correct for the special case of monomolecular kinetics and depends on a fit to the low temperature side of the TSC peak. However, the recombination kinetics in the rutile crystals was such that $1.10^{-2} < \delta < 1.0$ so that good aggreement was obtained between the two methods.

7.7 T.S.C. ANALYSIS OF REDUCED CRYSTALS

An inspection of the concentrations of traps listed in table 7.6.2 will show that the National Lead crystal contained a much larger trap density than the plasma grown crystals. The trap, with an ionisation energy of 0.37 eV, was the dominant low temperature trap in all of the samples. The stoichiometric as-grown crystal had the lowest concentration of these traps. Heating such samples at 1300°C in a stream of oxygen had no effect on the concentration. In contrast the progressive chemical reduction of a stoichiometric, as-grown crystal led to a steady increase in the densities of the three shallowest traps. The crystal was reduced by being heating in a sealed quartz tube in a vacuum of 10^{-5} torr at 600°C. The reduction was accompanied by an increased blue colouration and a decreasing resistivity. Curve a in figure 7.7.1 shows the TSC spectrum of a crystal which had been reduced by being heated at 600°C for 2 hours. Curve b shows the large dark current and demonstrates that all evidence of the high temperature trap is swamped. At each stage of reduction the photoconductive gain was measured so that the trap concentrations could be calculated. The results which are recorded in table 7.7.1 show that the densities of all three shallow traps increased with increasing chemical reduction.

A series of experiments was performed to determine whether the trap concentration was effected by heat treatment only. For this a crystal was cleaned and placed in a quartz boat under a continuous stream of oxygen. The temperature of the furnace surrounding the sample was taken to a temperature T°C and left for 24 hours, whereupon, the sample was withdrawn

	Cowell and Woods curve fitting	Kivits theory curve fitting	
	S cm^2	S cm^2	δ
103	10^{-21}	10^{-21}	10^{-2}
120	10^{-18}	10^{-18}	0.3
176	10^{-18}	10^{-18}	0.5
245	10^{-19}	10^{-18}	0.3
300	-	10^{-19}	0.5
330	-	10^{-19}	0.5

Table 7.6.3 Summary of the retrapping ratio (δ) and the capture cross section calculated for the six traps in the NL crystal CA3(NL).

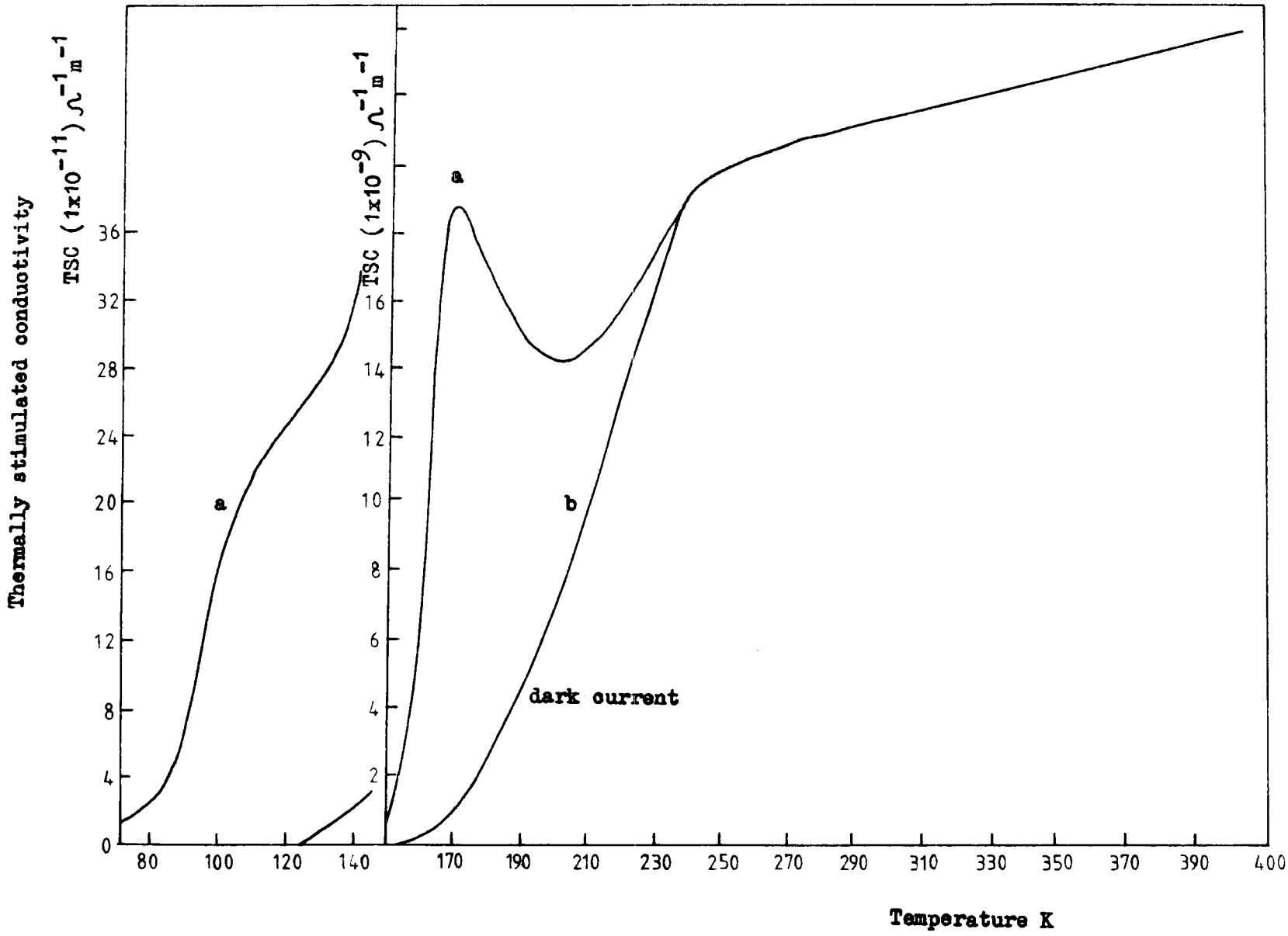

Figure 7.7.1 Thermally stimulated conductivity of a crystal reduced by heating in a vacuum at 600°C for 2 hrs .

STAGE	Resistivity ohm cm at 300K	T_m K	n_t cm^{-3}
1	$2\ 10^{14}$	103	$2\ 10^{13}$
		120	$4\ 10^{13}$
		176	$1\ 10^{16}$
2	$8\ 10^{12}$	103	$3\ 10^{14}$
		120	$4\ 10^{14}$
		176	$9\ 10^{16}$
3	$5\ 10^{9}$	110	$2\ 10^{15}$
		176	$2\ 10^{17}$
4	$5\ 10^{5}$	110	$7\ 10^{17}$
		175	$3\ 10^{18}$

Table 7.7.1 Densities of the shallow traps in the as-grown stoichiometric crystals at various stages of chemical reduction.

rapidly and quenched under forced air cooling. The TSC spectrum was measured and the experiment was repeated for several different quenching temperatures. The results obtained for a sample of the as-grown stoichiometric crystal BS18 is shown in figure 7.7.2. There was a rapid increase in the 103 K and 120 K TSC peaks at a quenching temperature of about 500 °C, the total trap densities increased from $8.10^{13}/cm^3$ to about $10^{16}/cm^3$. The concentration of these two traps continued to increase at a decreasing rate as the quenching temperature was raised from 500 °C to 1000 °C. In contrast the magnitude of the 176 K peak showed a gradual increase over the temperature range from 600 °C to 1000 °C.

7.8 DISCUSSION

The TSC spectra of the oxidised NL crystal, the oxidised as-grown non-stoichiometric plasma crystal and the as-grown stoichiometric plasma crystal were very similar in the temperature range up to 220 K. Thus all three types of crystal contained the same three shallow traps with ionisation energies of 0.13, 0.24, and 0.37 eV. The concentrations of these shallow traps were least in the as-grown stoichiometric samples.

Although there were similarities in the shapes of the TSC curves from a large number of different crystals in the temperature range up to 220 K, there were substantial differences in the range from 220 to 400 K. The as-grown stoichiometric crystals had very low dark currents and exhibited well defined TSC peaks at the higher temperatures. As such a crystal was progressively reduced, the densities of the low temperature traps increased. The dark current also increased and the deeper traps became populated with electrons as the thermal equilibrium Fermi-level moved closer to the conduction band. Thus as the dark current rose the high temperature peaks in the TSC curves began progressively to disappear. However, when the crystal was reoxidised at 1300 °C in a stream of oxygen, the original TSC curve reappeared, i.e. the reduction could be reversed by oxidation. Surprisingly when crystals were grown under reducing conditions

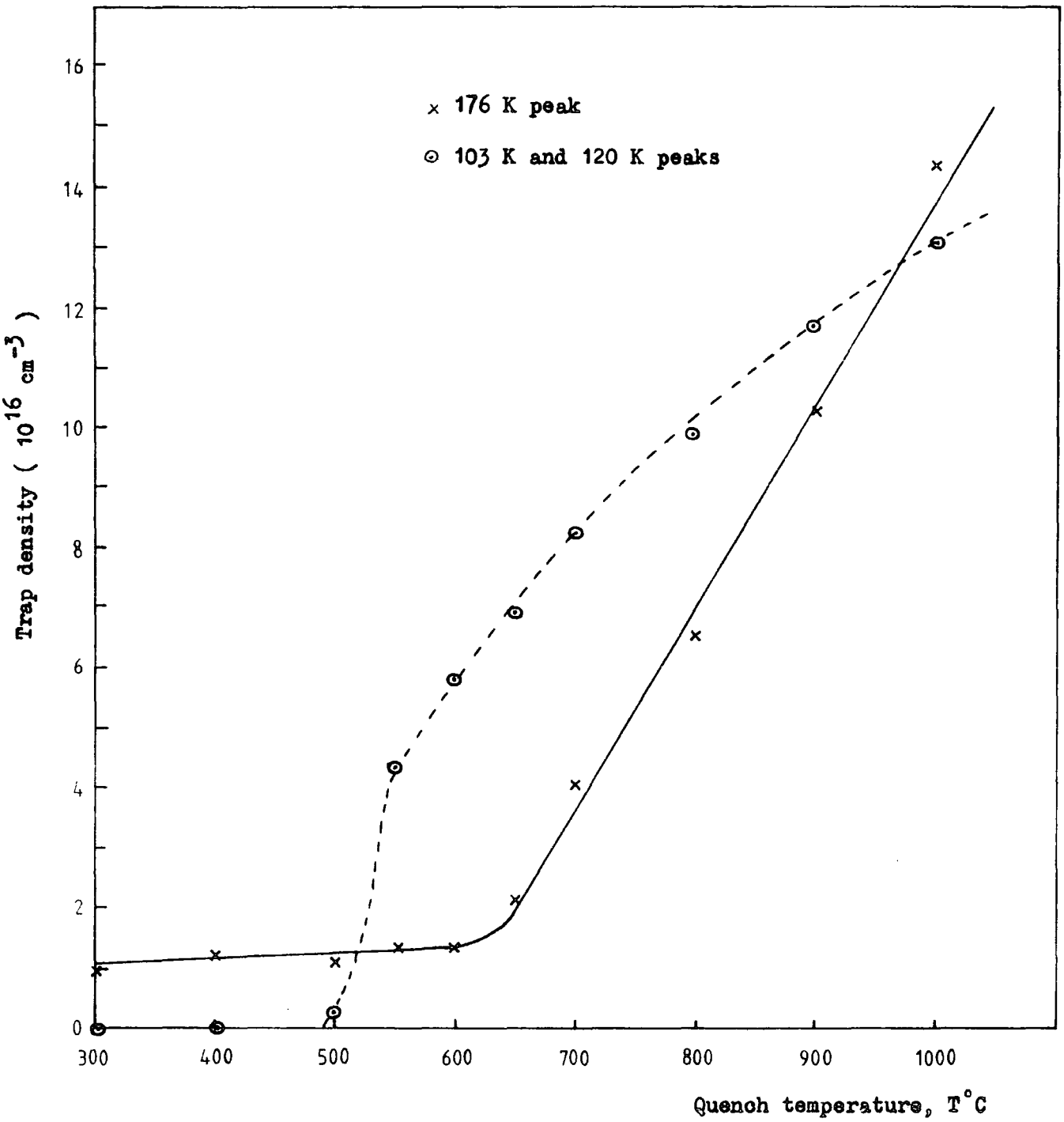

Figure 7.7.2 Densities of the shallow traps in the as-grown stoichiometric crystals after quenching from T°C .

and then oxidised at 1300 °C in oxygen, the TSC curves obtained were different in the high temperature region, from those of as-grown stoichiometric crystals. Neither was it possible to obtain TSC curves like that in figure 7.2.3 from a crystal which had been grown under reducing conditions no matter how many times it was oxidised, reduced and reoxidised. In other words the effects of post-growth reduction can be reversed by oxidation, but as-grown, reduced crystals are different from reduced, as-grown crystals. This could occur, for example, if post-growth treatment merely affected the concentration of oxygen vacancies, while growth under reducing conditions led to a high concentration of Ti^{3+} interstitials in addition to oxygen vacancies.

The conditions necessary for the formation and the nature of defects, which appear in rutile crystals during their partial chemical reduction, are still controversial. It seems reasonable that deviation from stoichiometry due to a reduction of rutile can lead to the formation of oxygen vacancies or the displacement of Ti^{3+} ions to interstitial positions, or some combination of these two processes.

In chapter 1 a summary of earlier studies has been given. Barbanel and Bogomolov (1969) attempted to establish the nature of defects in rutile by investigating the change in the density of crystals during partial reduction. They argued that the two main types of defect (vacancies and interstitial atoms) should produce opposite changes in the density of the crystals. At temperatures less than 600 °C the channels in the rutile lattice are free and oxygen escapes easily along them from the interior of a sample to the surface. They suggested that the main defects in this region are oxygen vacancies. At temperatures greater than 600 °C the presence of oxygen vacancies would make the process of transfer of titanium ions from sites into interstices much easier than in stoichiometric rutile, a sample would aquire two types of defect, and these defects would be bound to one another. Since the defects would be bound, the motion of the oxygen from the interior to the surface would slow down. The diffusion of Ti^{3+} ions along the channels in rutile has a higher activation energy than the diffusion of oxygen (Bogomolov 1964).

Therefore, the process of the formation of interstitial titanium ions, which takes place on an appreciable scale only at temperatures T > 600 °C does not simply increase the number of new defects but also reduces the loss in weight by slowing down the escape of oxygen from the interior to the surface.

The results obtained from the measurement of TSC curves from quenched crystals , see figure 7.7.2, could be explained by the model suggested by Barbanel and Bogomolov. The concentration of traps associated with the 103 K and 120 K TSC peaks show a large increase in the range 500-600 °C, whilst the trap concentration associated with the 176 K peak remains constant. This might occur if the 103 K and 120 K TSC peaks were associated with the formation of oxygen vacancies. Above 600 °C the rate of formation of these defects begins to diminish. In contrast the 176 K peak begins to increase steadily and could be associated with the formation of interstitial titanium ions.

THERMOLUMINESCENCE

8.1 INTRODUCTION

Simultaneous measurements of thermally stimulated conductivity and thermoluminescence can determine whether a transport of charged carriers takes place during thermal stimulation or whether the carriers remain localised in a luminescence centre. The experimental procedure for the TSC investigations has been described in the previous chapter and a description of the cryostat is given in chapter 4. A RCA Quantacon photomultiplier type C31034 in combination with an Oriel G-772-7800 filter was used to monitor the thermoluminescence signal.

8.2 THERMOLUMINESCENCE RESULTS

The thermoluminescence spectrum for the National Lead crystal CA3 (NL) after post growth oxidation is shown in figure 8.2.1. Investigation of the thermoluminescence signal with and without the Oriel G-772-7800 filter demonstrated that all the observed thermoluminescence originated via the 850 nm centre which is as described in chapter 6 and attributed to substitutional Cr^{3+} ions present as unintentional impurities in the rutile lattice. Any other TL emission at wavelengths longer than 1 μm was beyond the sensitivity of the detection system. The new generation of Quantacon photomultipliers using ternary semiconductor targets may prove useful in the investigation of photoluminescence and TL in rutile.

A comparison of the TL and TSC spectra for crystals BS18(NS), CA3(NL) and BS18(S) is given in figures 8.2.3, 8.2.2 and 8.2.4 respectively. Several differences can be observed between the TSC and TL spectra. Initial inspection shows a one to one correspondence between TSC and TL peaks with the TL maximum always appearing at a lower temperature than the TSC maximum. If the recombination lifetime is a rapidly increasing function of

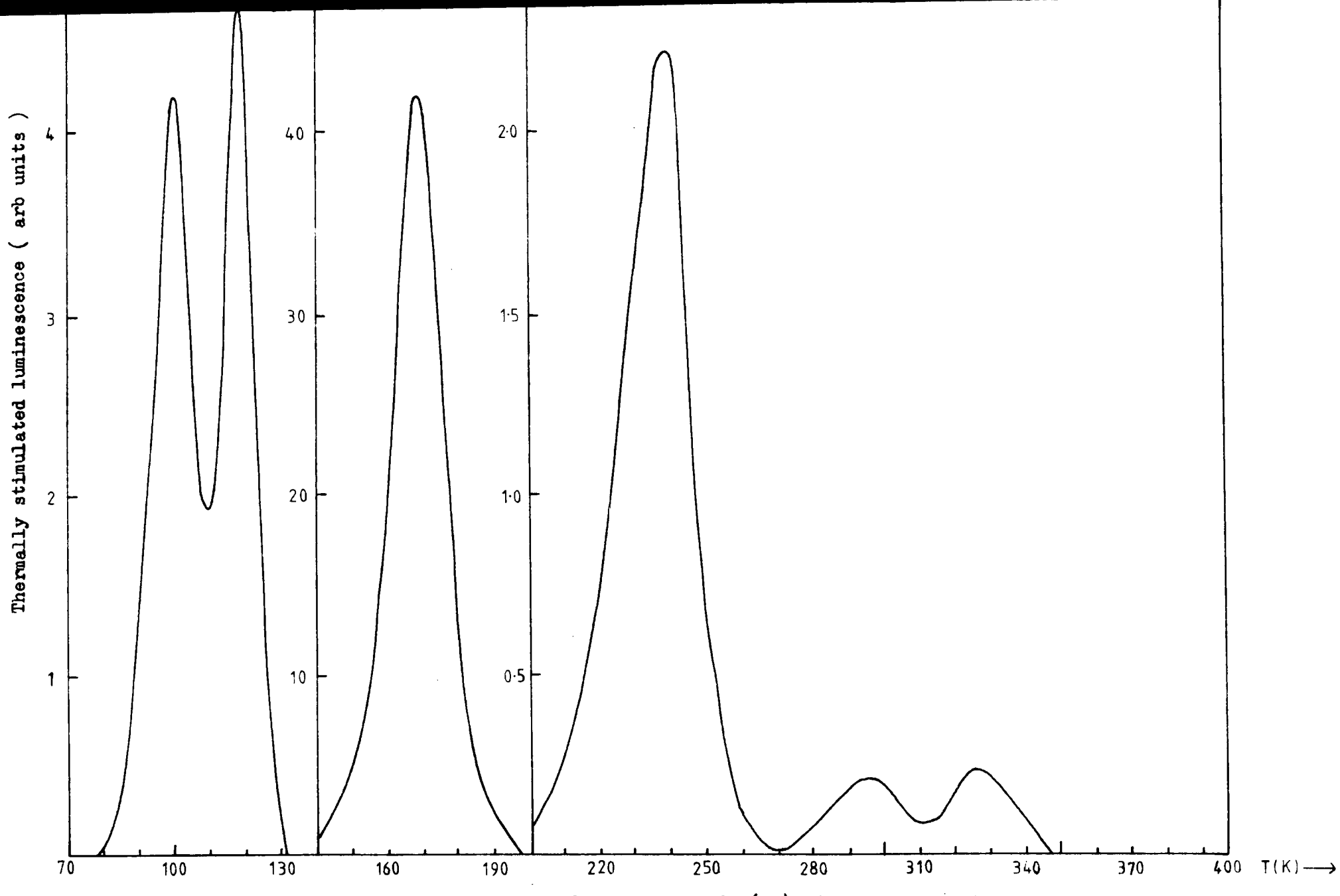

Figure 8.2.1 Thermoluminescence spectrum of the crystal CA3(NL) after post growth oxidation.

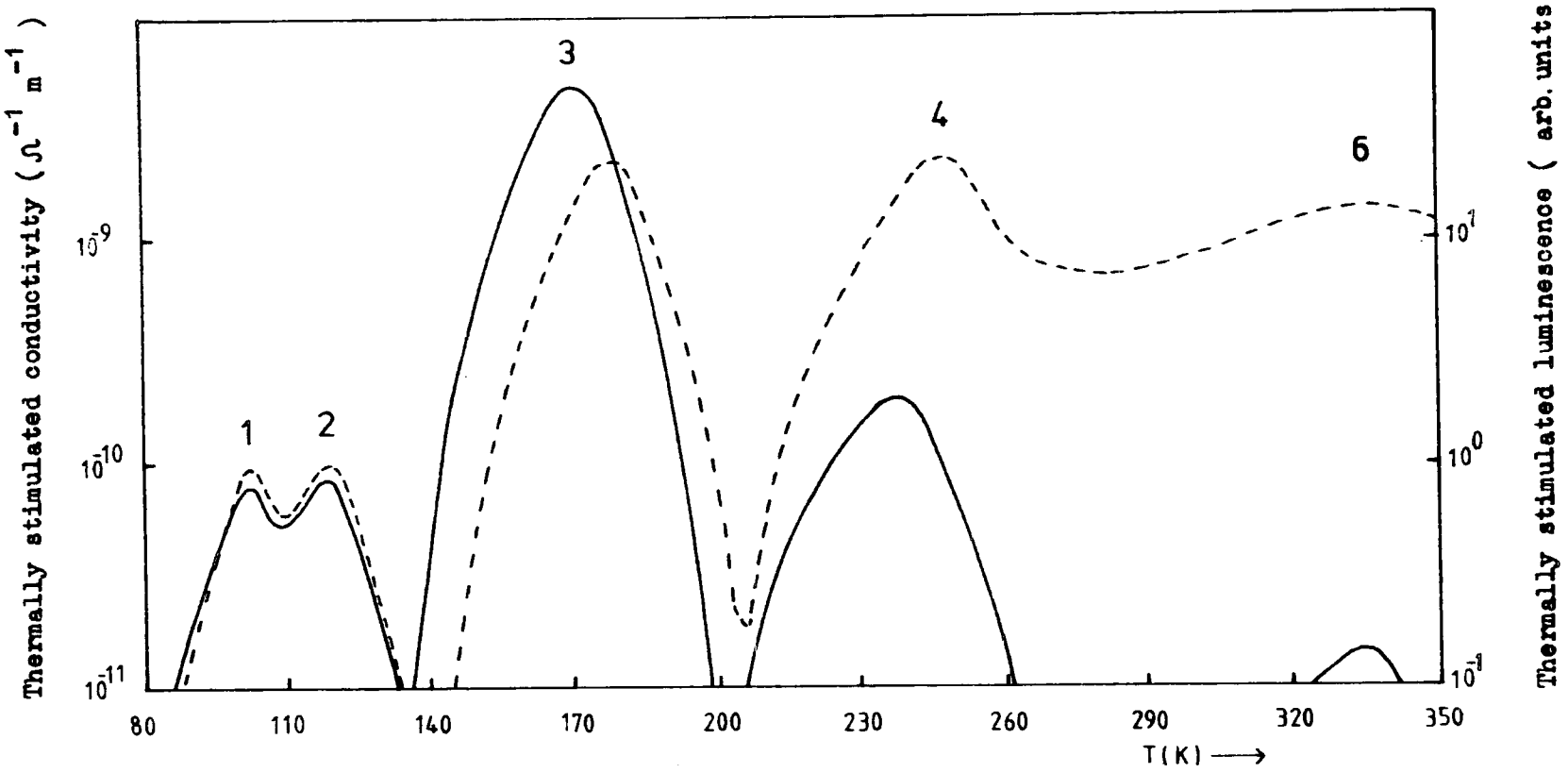

Figure 8.2.2 Comparison of the TSC and TL spectra for the non-stoichiometric as-grown crystal BS18(NS) .

TL ——— TSC - - - - -

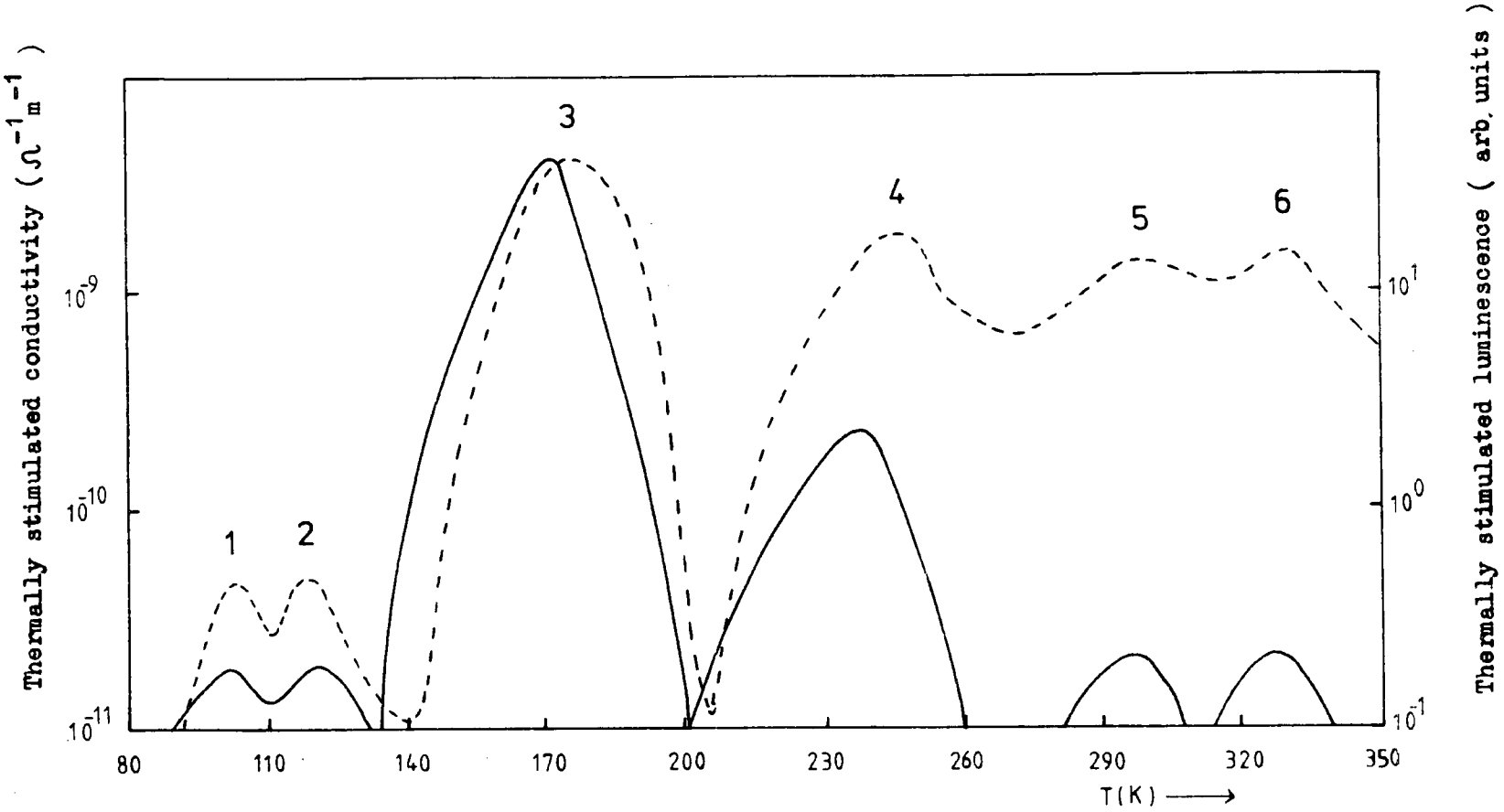

Figure 8.2.3 Comparison of the TSC and TL spectra for the NL crystal CA3(NL) .

TL ——— TSC - - - -

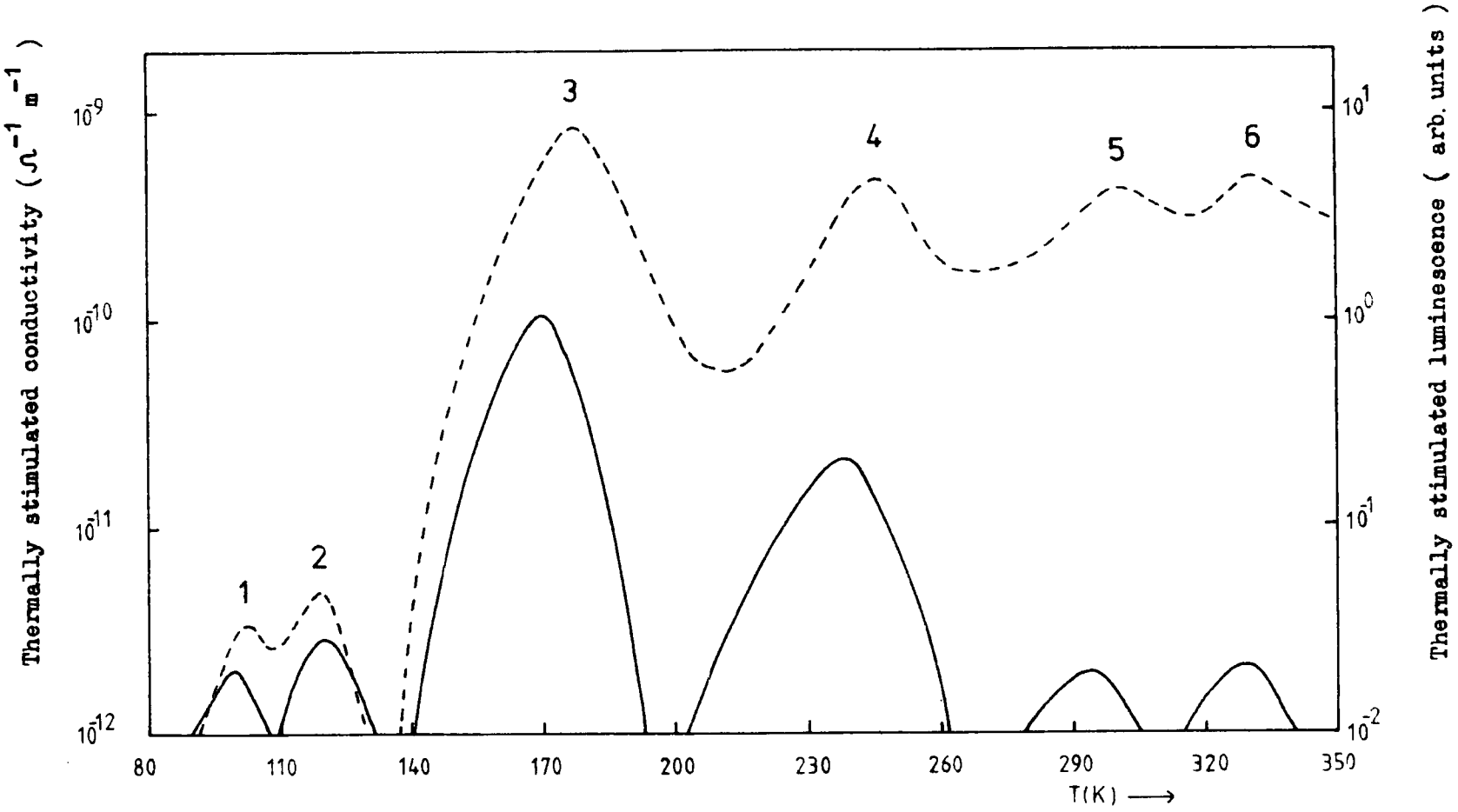

Figure 8.2.4 Comparison of the TSC and TL spectra for the stoichiometric as-grown crystal BS18(S) .

TL ——— TSC - - - -

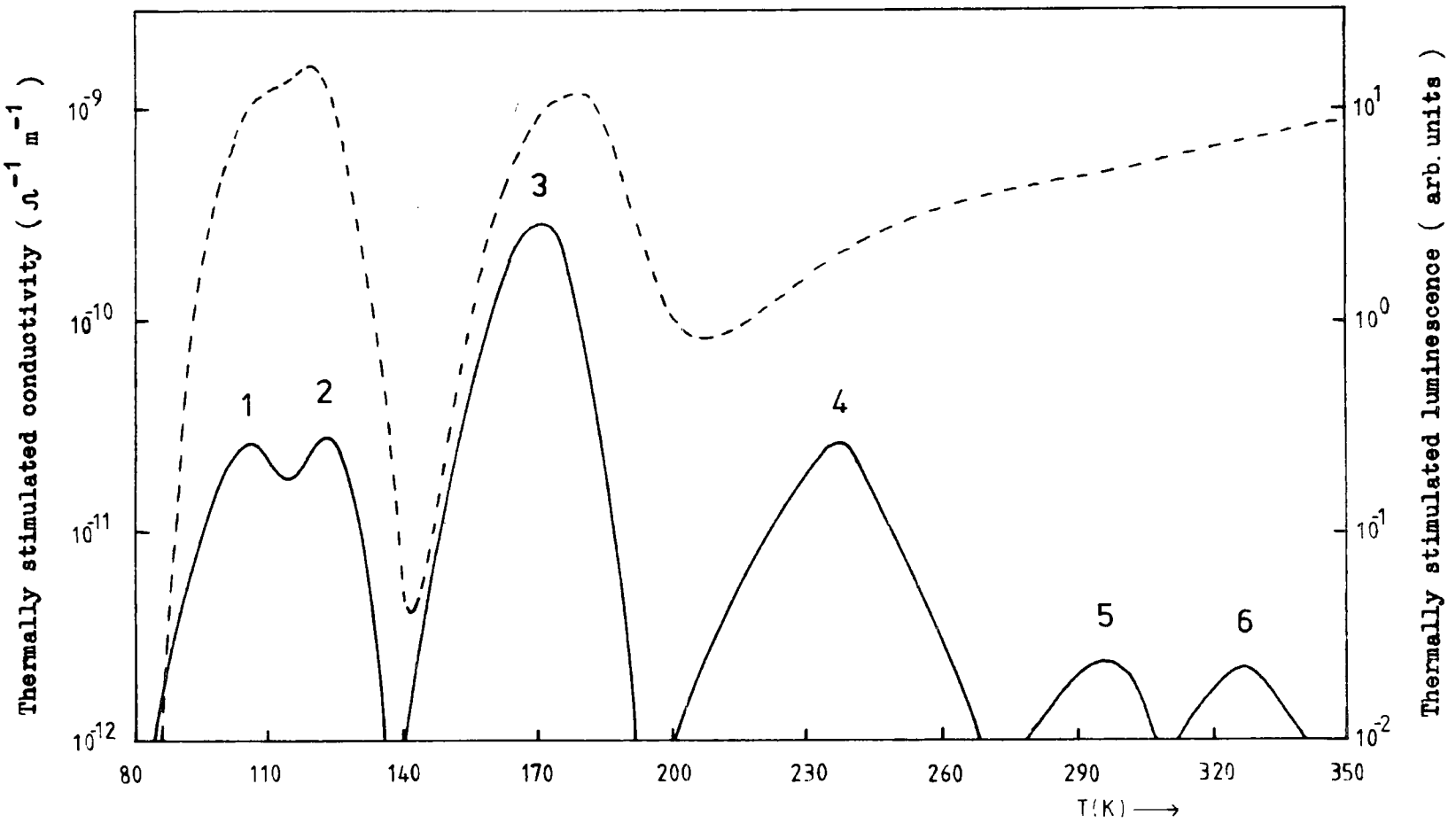

Figure 8.2.5 Comparison of the TSC and TL spectra for the crystal BS18(S) after quenching from 600°C .

TL ——— TSC - - - -

temperature the TSC turning value occurs at a higher temperature than the TSL maximum. The recombination lifetime is related to the amount of thermally disconnected charge in the material at a given temperature and will be discussed later in this chapter.

The relative magnitudes of the TSC and TL peaks for a given crystal, as shown in figures 8.2.2, 8.2.3, 8.2.4 and 8.2.5, were different for all cases investigated. These spectra can be interpreted with reference to the photoluminescence results of chapter 6 for the four types crystal examined. The area under each TSC or TL curve represents the amount of charge released during the thermal ionisation of a given trapping centre and the relative magnitudes can only be determined if the recombination lifetime is known as a function of temperature. Knowledge of the total effective recombination lifetime of all the recombination centres in the samples allows the TSC curve to be interpreted, whereas the thermoluminescence is only sampling the slower radiative recombination path. Two regions of the TSC/TL correlation can be understood in terms of the photoluminescence model proposed in chapter 6. The region above 200 K can be interpreted in terms of the thermal quenching of the photoluminescence centre where the probability of thermal ionisation of an electron in a Cr^{3+} excited state increases as the temperature rises. This explains why the TL peaks 5 and 6 are two orders of magnitude lower than the peak number 3, whilst the TSC peaks 3,4,5 and 6 are of comparible magnitude in all the crystals examined. It is worth noting that if the Cr^{3+} luminescent centre were the dominant recombination centre in the rutile crystals, the TSC and TL curves would be expected to decrease together with increasing temperature.

The second region below 200 K can again be explained with reference to section 6.6. The low temperature efficiency of the radiative centre is affected by a competitive recombination process which increases with increasing shallow trap population, possibly an Auger event. Table 8.2.6

	RATIO = $\frac{\text{magnitude peak 3}}{\text{magnitude peak 2}}$		
	TSC a	TL b	$\frac{b}{a}$
BS18(S)	3.6	3.7	1.03
BS18(NS)	21.5	62.5	2.91
CA3(NL)	78	205	2.63
BS18(S) quenched	0.68	9.3	13.68

Table 8.2.6 Comparison of the relative magnitudes of the TSC and TL spectra for different types of rutile crystal .

gives a comparison of the relative magnitudes of the TSC and TL peaks 3 and 2. If the ratio of the TSC peaks represents the ratio of the trap densities between centres 3 and 2 then it can be used to normalise the ratio of TL peaks to estimate the variation of radiative lifetime in the two temperature regimes. This calculation is an approximate but informative qualitative simplification of the trapping and recombination kinetics of the system. The crystals BS18(NS) and CA3(NL), which show similar photoluminescence temperature dependence, have reduced TL at low temperatures. Crystal BS18(S) which has the lowest TSC magnitudes for peaks 1 and 2, indicating lower trap densities, shows the least temperature dependence of photoluminescence below 200 K. When the shallow trap population is increased by quenching at 600°C the difference between the TSC and TL magnitudes of peaks 1, 2 and 3 change dramatically (see figures 8.2.4 and 8.2.5).

8.3 EXPERIMENTAL DETERMINATION OF TRAP DEPTHS FROM TL DATA

The same approximate methods of TSC and TL curve analysis described in chapters 2 and 7 were used to determine the trap depths from the TL data. Table 8.3.1 shows the results obtained for the 176 K peak for crystals BS18(S), BS18(NS) and CA3(NL). Remarkable agreement between most of the methods was obtained and the methods of Hoogenstraaten, Haering and Adams, Chen and Winer, and Garlick and Gibson gave self consistent values of trap depth. The difference between the TSC and TL peak maximums were 7.1 and 7.0 degrees for the crystals BS18(NS) and CA3(NL) respectively, and 6.2 degrees for crystals BS18(S).

A summary of the results obtained for all the traps observed in the CA3(NL) crystal is given in table 8.3.2. Again the methods of Hoogenstraaten, Chen and Winer, Haering and Adams gave self consistent results. The methods of Chen, Luschik and Grossweiner which are derived from the geometrical shape of the curve show reasonable agreement for the low

	BS18(NS) non-stoichiometric crystal + oxidation	BS18(S) stoichiometric as-grown crystal	CA3(NL) National Lead crystal
Hoogenstaaten	0.36 ∓ 0.01	0.36 ∓ 0.01	0.36 ∓ 0.01
Haering,Adams	0.37 ∓ 0.01	0.37 ∓ 0.01	0.37 ∓ 0.01
Chen,Winer	0.37 ∓ 0.02	0.37 ∓ 0.02	0.37 ∓ 0.02
Unger	0.37 ∓ 0.01	0.37 ∓ 0.01	0.37 ∓ 0.01
Garlick,Gibson 10%	0.38 ∓ 0.01	0.38 ∓ 0.02	0.38 ∓ 0.02
Garlick,Gibson 20%	0.38 ∓ 0.02	0.38 ∓ 0.02	0.38 ∓ 0.02
Boiko,Rashba,Trof.A	0.32 ∓ 0.02	0.33 ∓ 0.02	0.33 ∓ 0.02
Boiko,Rashba,Trof.B	0.33 ∓ 0.02	0.33 ∓ 0.02	0.33 ∓ 0.02
Chen 1	0.32	0.32	0.32
Chen 2	0.32	0.32	0.32
Chen 4	0.37	0.38	0.37
Chen 5	0.28	0.27	0.27
Chen 6a	0.40	0.42	0.40
Chen 6b	0.37	0.39	0.38
Luschik	0.29	0.28	0.28
Grossweiner	0.39	0.40	0.39
TSC - TSL	7.1 ∓ 0.4	6.2 ∓ 0.4	7.0 ∓ 0.4
λ	9.0	8.8	9.0
σ	8.6	8.8	8.8
ω	17.6	17.6	17.8

Table 8.3.1 Experimental TSL analysis for the 176 K peak .

TL peak	100 K	118 K	169 K	239 K	296 K	328 K
Hoogenstraaten	0.13 ∓ 0.01	0.24 ∓ 0.01	0.37 ∓ 0.01	0.50 ∓ 0.01	0.58 ∓ 0.04	0.67 ∓ 0.03
Haering,Adams	0.13 ∓ 0.02	0.24 ∓ 0.02	0.37 ∓ 0.02	0.51 ∓ 0.02	0.59 ∓ 0.02	0.68 ∓ 0.03
Chen,Winer	0.13 ∓ 0.01	0.25 ∓ 0.02	0.37 ∓ 0.01	0.51 ∓ 0.01	0.62 ∓ 0.02	0.69 ∓ 0.02
Unger	0.13 ∓ 0.01	0.23 ∓ 0.01	0.36 ∓ 0.01	0.51 ∓ 0.03	0.61 ∓ 0.02	-
Garlick,Gibson 20%	0.16 ∓ 0.03	0.25 ∓ 0.02	0.38 ∓ 0.02	0.53 ∓ 0.02	-	-
Boiko,Rashba,Trof.A	0.13 ∓ 0.01	0.22 ∓ 0.02	0.31 ∓ 0.02	0.48 ∓ 0.03	0.54 ∓ 0.03	0.63 ∓ 0.04
Chen 1	0.14	0.22	0.32	0.50	0.77	1.04
Chen 2	0.14	0.22	0.32	0.50	0.72	1.00
Chen 4	0.16	0.27	0.37	0.44	0.80	1.31
Chen 5	0.12	0.20	0.27	0.32	0.67	0.90
Chen 6a	0.18	0.31	0.40	0.41	0.80	1.45
Chen 6b	0.17	0.29	0.38	0.39	0.75	1.35
Luschik	0.12	0.18	0.28	0.33	0.69	0.84
Grossweiner	0.17	0.29	0.39	0.47	0.84	1.35
TSC - TSL	3.0	2.0	7.0	6.0	4.1	1.9

Table 8.3.2 Thermal ionisation of the six traps in the crystal CA3(NL) calculated from TSL data .

temperature peaks but there is serious disagreement with the heating rate methods for the high temperature peaks. Although the temperature difference between TSC and TL peak maxima varies from trap to trap there appears to be good agreement for a given trap from different crystals.

A comparison of results obtained from TSC and TL analysis for crystals BS18(S), BS18(NS) and CA3(NL) is given in table 8.3.3. However, there are several questions which remain unanswered. The analysis techniques used to obtain information from the TSC and TL data have all assumed the simple insulator model which includes only one recombination centre. The model proposed for single crystal rutile includes more than one centre, where recombination via the radiative centre is slower than that through the other non-radiative centres. In what follows an attempt is made to obtain a better appreciation of the rutile system by using the Kivits theory described in the previous chapter.

8.4 COMPARISON OF THE THEORETICAL AND EXPERIMENTAL TL ANALYSIS FOR PEAK 3

In the previous chapter a series of theoretical TSC curves was generated using the Kivits theory, and in this section the curve fitting will be extended to the thermoluminescence data. Table 8.4.1 shows the values of ξ (the ratio of deep and shallow trapped charge) obtained from the TSC curves for the three different types of crystal examined. Values of trap depth calculated from the theoretical input data, E=0.37 eV ; FREQ=7.39E+9 ; ξ =1.0E-3,0.85,8.5,; δ =1.0E-2,0.1,1.0,3.0 ; are given in table 8.4.2. It can be seen that the theoretical predictions of trap depth from most of the approximate methods give good agreement with the 0.37 eV input value. The temperature difference of the TSC and TL maxima is very sensitive to both the retrapping ratio (δ) and the ratio of deep to shallow trapped charge (ξ).

The dependence of the shape of the TL curve on retrapping ratio is

BS18(S)				BS18(NS)				CA3(NL)			
TSC		TL		TSC		TL		TSC		TL	
103K	0.13	100K	0.13	103K	0.13	100K	0.13	104K	0.13	100K	0.13
120K	0.24	117K	0.24	120K	0.24	119K	0.23	121K	0.24	118K	0.24
176K	0.37	168K	0.37	176K	0.37	168K	0.37	176K	0.37	169K	0.37
245K	0.51	238K	0.51	245K	0.51	239K	0.51	245K	0.51	239K	0.51
294K	0.61	293K	0.60	-	-	-	-	300K	0.61	296K	0.59
326K	0.69	328K	0.70	340K	0.81	334K	0.74	330K	0.69	328K	0.68

Table 8.3.3 Comparison of experimental TSC and TL results .

TSC peak temperature	Stoichiometric crystal BS18(S) ξ	Non-stoichiometric crystal BS18(NS) ξ	National Lead crystal CA3(NL) ξ
106	$4\ 10^3$	$1.78\ 10^2$	$1.85\ 10^3$
121	$2\ 10^3$	$9.70\ 10^1$	$1.85\ 10^3$
169	7.0	0.18	0.85
241	2.5	1.67	0.88
296	1.5	-	-
336	-	-	-

Table 8.4.1 Comparison of the ratio of deep to shallow charge (ξ) for the three different types of rutile crystal .

TSL method	HS = 2.0E+17 HD = 2.0E+14 ξ = 1.0E-3				HS = 1.7E+17 HD = 2.0E+17 ξ = 0.85				HS = 1.7E+18 HD = 2.0E+17 ξ = 8.5			
Retrapping ratio, δ	10^{-2}	0.1	1.0	3.0	10^{-2}	0.1	1.0	3.0	10^{-2}	0.1	1.0	3.0
Hoogenstraaten	.371	.371	.372	.372	.370	.372	.371	.370	.369	.369	.371	.371
Haering,Adams	.372	.372	.374	.372	.370	.373	.371	.371	.370	.370	.372	.372
Chen,Winer	.370	.370	.372	.372	.368	.371	.369	.369	.368	.368	.371	.370
Boiko,Rashba,Trof.A	.350	.350	.350	.350	.349	.350	.350	.349	.349	.349	.351	.351
Boiko,Rashba,Trof.B	.350	.349	.351	.352	.348	.351	.349	.349	.348	.348	.350	.350
Unger	.371	.370	.369	.370	.372	.371	.371	.371	.372	.371	.371	.370
Garlick,Gibson 10%	.368	.369	.368	.369	.368	.368	.368	.367	.367	.367	.367	.367
Garlick,Gibson 20%	.367	.367	.366	.367	.367	.360	.366	.364	.365	.365	.365	.364
Chen 1	.368	.266	.263	.265	.368	.325	.294	.279	.368	.363	.356	.334
Chen 2	.363	.349	.268	.247	.364	.325	.310	.282	.364	.365	.350	.334
Chen 3	.405	.399	.346	.320	.401	.381	.351	.310	.401	.397	.393	.378
Chen 4	.377	.371	.315	.286	.372	.351	.303	.276	.372	.368	.364	.348
Chen 5	.361	.334	.225	.201	.367	.303	.291	.287	.367	.362	.351	.324
Chen 6a	.830	.822	.712	.620	.826	.784	.720	.637	.826	.818	.809	.778
Chen 6b	.780	.768	.664	.579	.771	.731	.672	.595	.771	.764	.755	.726
Luschik	.370	.343	.231	.292	.376	.310	.300	.294	.376	.370	.360	.332
Halperin,Braner 1	.433	.426	.369	.310	.428	.406	.382	.330	.428	.424	.419	.403
Halperin,Braner 2	.494	.487	.421	.406	.489	.464	.410	.378	.489	.484	.479	.461
Grossweiner	.398	.392	.336	.292	.394	.372	.332	.296	.394	.389	.385	.370
TSC - TSL	8.4	8.8	10.6	14.0	1.8	2.2	2.8	3.4	0.30	0.30	0.30	0.30

Table 8.4.2 Values of trap depth calculated from theoretical curves for different ξ and δ.

Theoretical input data : E, 0.37 eV ; FREQ, 7.39E+09 .

shown in figure 8.4.3 and it is possible to obtain a best fit for the TSC and TL curves for a given peak provided E, ξ and α are known. Figure 8.4.4 shows a comparison between the experimental and theoretical TL curves for peak 3 with retrapping ratios 3.0, 1.0, 0.5 and 10^{-2}. The value 0.37 eV was used as the trap depth and the recombination lifetime was calculated from the photoconductive gain measurements. As explained in the previous chapter the values of E and s are the primary parameters which determine the position of the glow curve temperature maximum and, therefore, an order of magnitude estimate can be obtained for the trapping frequency, s, for E=0.37 eV. The values of ξ and δ do have a secondary effect on the absolute value of the glow curve maximum but as we are only interested in an order of magnitude estimate of trapping frequency these can be ignored to simplify the problem. Measured values of ξ of 7.0, 0.18 and 0.85 were obtained for the crystals BS18(S), BS18(NS) and CA3(NL) respectively. It can be observed in figure 8.4.4 that the best geometrical fit was obtained for a retrapping ratio of δ =0.5, which agrees with the TSC fit for peak 3 shown in figure 7.5.2. However, it should be observed that the difference in TSC and TL temperature maxima has been obtained using a value of ξ=0.085 which is an order of magnitude lower than the experimentally determined estimate of ξ =0.85. To demonstrate the effect of varying the value of ξ on the TSC and TL curves, the experimental and theoretical curves have been plotted in figure 8.4.5 for ξ=0.85 and ξ=8.5. It is interesting to note that crystal BS18(S) which has the smallest value of (TSC-TL) for peak 3, also has the largest value of ξ indicating a larger amount of trapped charge below trap 3 than the other crystals.

The values of trap depth estimated from the approximate methods of TL analysis have been calculated using the Kivits theory and table 8.4.6 compares the experimental values of trap depth for CA3(NL) with the theoretical predictions for ξ =0.85 and ξ=0.085. It can be seen that good agreement is obtained for most methods.

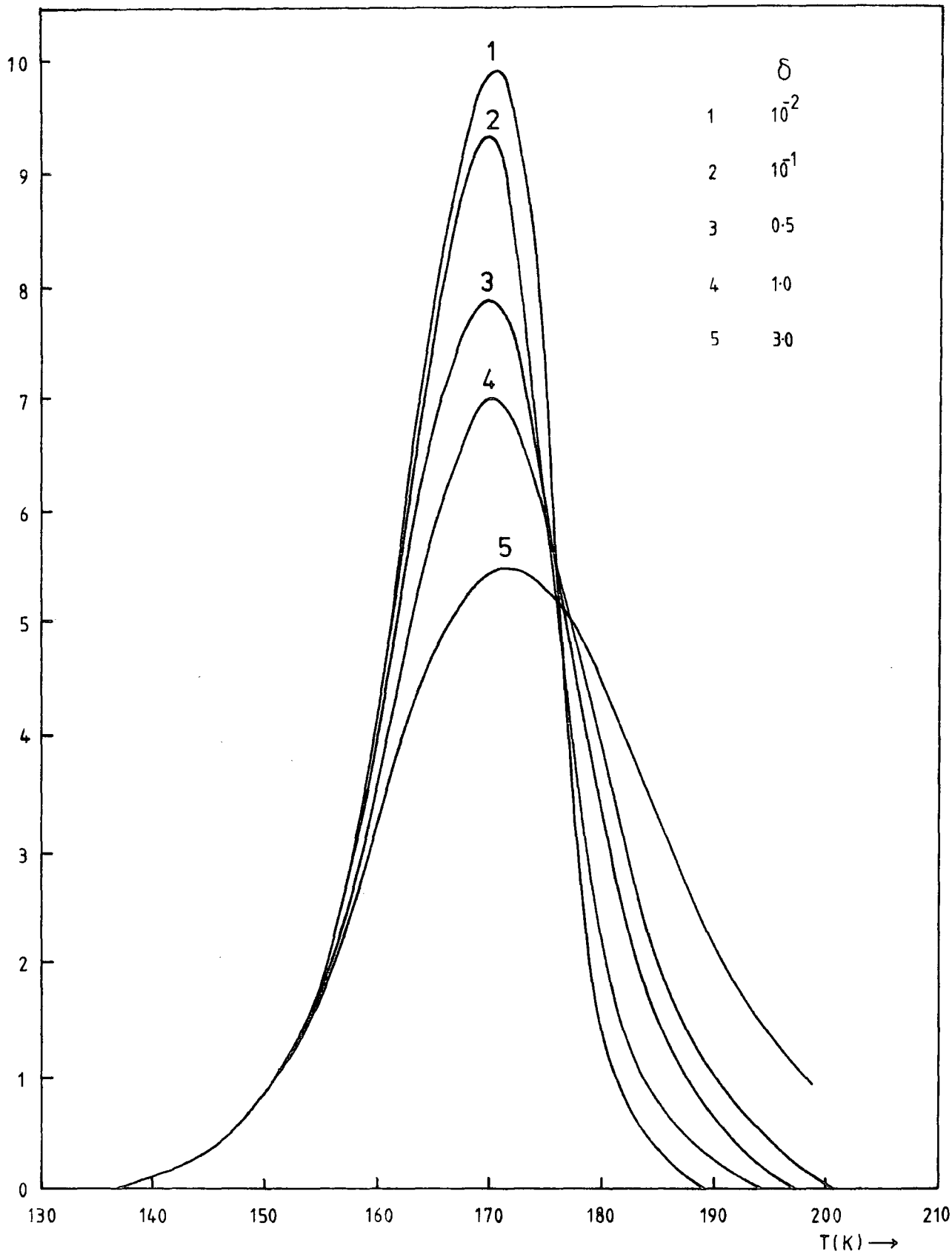

Figure 8.4.3 Variation of TSL with the retrapping ratio δ .

E = 0.37 eV ; hs = 2.0 10^{17} cm^{-3} ; hd = 1.7 10^{16} cm^{-3} ; $\tau = 10^{-8}$ s^{-1} ;

FREQ = 7.39 10^{9} s^{-1} ; $\beta = 0.5$ °/s.

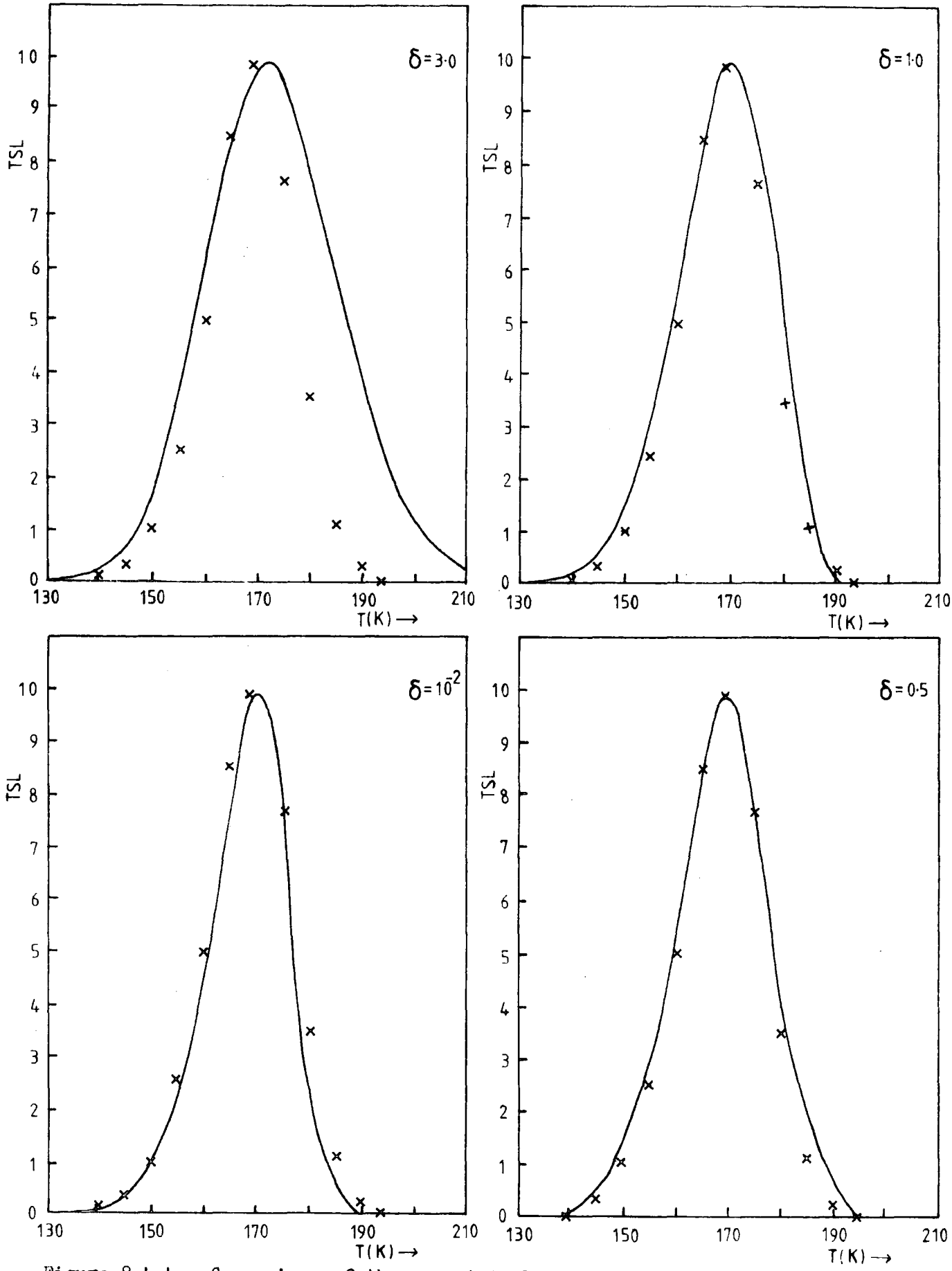

Figure 8.4.4 Comparison of the geometrical shapes of TSL curves for different retrapping ratios, δ. E = 0.37 eV ; hs = $2.0\ 10^{17}$ /cm^3 ; hd = $1.70\ 10^{16}$ /cm^3 ; $\tau = 10^{-8}$ s ; s = $7.39\ 10^9$ /s ; β = 0.5 °/s .

theoretical data ——— experimental data for CA3(NL) ×

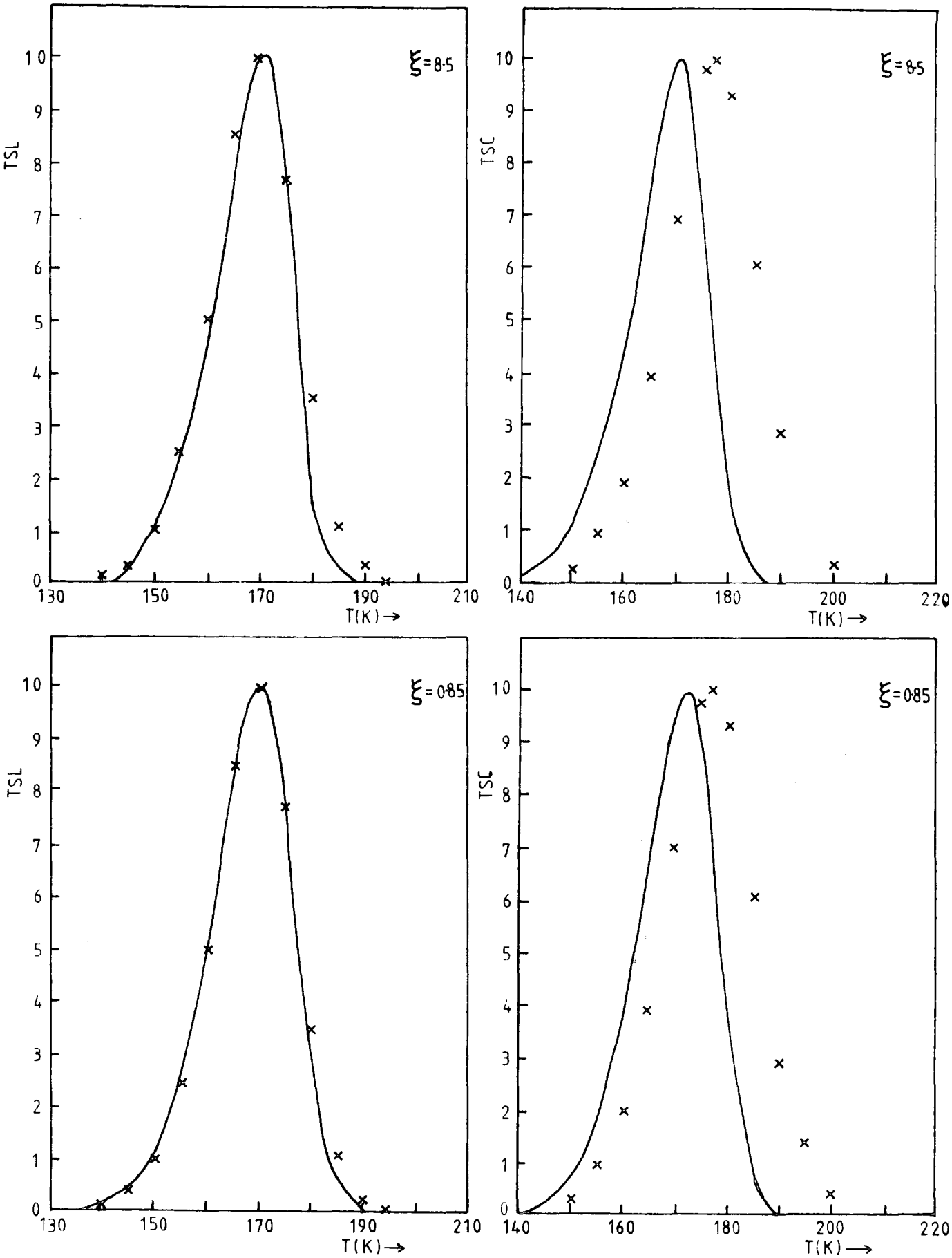

Figure 8.4.5 Comparison of the TSC and TSL curves for $\xi = 8.5$ and $\xi = 0.85$.

$E = 0.37$ eV ; $\tau = 10^{-8}$ s ; $s = 7.39\ 10^{9}$ /s ; $\beta = 0.5$ °/s .

theoretical curve —— experimental data for CA3(NL) ×

TSL method	Experimental crystal CA3(NL)	Theoretical HS = 2.00E+17 HD = 1.70E+17 ξ = 0.85	Theoretical HS = 2.00E+17 HD = 1.70E+16 ξ = 0.085
Hoogenstraaten	0.36 ∓ 0.01	0.3712 ∓ 0.0001	0.3723 ∓ 0.0001
Haering,Adams	0.37 ∓ 0.01	0.3735 ∓ 0.0001	0.3734 ∓ 0.0001
Chen,Winer	0.37 ∓ 0.02	0.3713 ∓ 0.0001	0.3724 ∓ 0.0001
Unger	0.37 ∓ 0.01	0.3713 ∓ 0.0001	0.3724 ∓ 0.0001
Garlick,Gibson 10%	0.38 ∓ 0.02	0.3682 ∓ 0.0001	0.3703 ∓ 0.0001
Garlick,Gibson 20%	0.38 ∓ 0.02	0.3663 ∓ 0.0001	0.3693 ∓ 0.0001
Boiko,Rashba,Trof.A	0.34 ∓ 0.02	0.3513 ∓ 0.0001	0.3532 ∓ 0.0001
Boiko,Rashba,Trof.B	0.33 ∓ 0.02	0.3512 ∓ 0.0001	0.3503 ∓ 0.0001
Chen 1	0.32	0.325	0.308
Chen 2	0.32	0.325	0.301
Chen 4	0.37	0.351	0.335
Chen 5	0.27	0.303	0.248
Chen 6a	0.40	0.784	0.390
Chen 6b	0.38	0.731	0.365
Luschik	0.28	0.310	0.251
Grossweiner	0.39	0.372	0.357
TSC - TSL	7.0 ∓ 0.4	2.2	6.2

Table 8.4.6 Comparison of trap depths from theoretical and experimental data for the 176 K peak .

Theoretical input data : E, 0.37 eV ; DELTA, 0.5 ; FREQ, 7.39E+09 .

8.5 LIMITATIONS OF THE SIMPLE INSULATOR MODEL

The two low temperature peaks 1 and 2 were estimated to have ξ values larger than 100, indicating that the lifetime remains constant during the thermal ionisation of these traps. If the simple insulator model is to explain the trapping and recombination kinetics of these two traps then the TSC and TL maxima would be expected to peak at identical temperatures. Obviously, the model does not produce a perfect fit with the observed (TSC-TL) difference of 3°, 3°and 4° for crystals BS18(S), BS18(NS) and CA3(NL) respectively.

Although a number of reasons for the failure of the simple insulator model can be constructed it is not possible to explain these discrepancies with any real conviction. Firstly, the TSC spectra of the two traps do overlap and the assumption that they are both thermally disconnected from each other and peak 3, may not be correct. If full compensation in the rutile crystal is assumed it is difficult to see why a 3° shift between the TSC and TL maxima is observed because there still appears to be a large amount of deep charge below trap 3. This would effectively hold the lifetime constant with temperature.

Previous results have led to the development of a model for rutile involving one radiative recombination centre having a lifetime of 35 μsec and at least one other centre having a lifetime of about 10^{-8} sec. It is interesting to consider the effects of two recombination paths on the TSC and TL analysis and this will be discussed in the next section. Finally, the possibility of an Auger event causing competitive radiationless recombination may also influence the model. Evidence of these types of events has been observed in the photoluminescence phenomena described previously.

The simple insulator model does appear to fit peak 3 as described in the previous section, apart from predicting a value of ξ one order of

magnitude lower than suggested by the experimentally determined photoconductive gain measurements. The same curve fitting procedure has been used to describe peak 4 as shown in figures 8.5.1 and 8.5.2 which demonstrate the variation of the retrapping ratio on the shape of the TSC and TL curves. A best fit is obtained for a value of $\delta = 0.1$, $\xi = 8.9.10^{-2}$ and a trapping frequency of $3.5.10^{9}$/sec. Again the value predicted by theory is an order of magnitude below the TSC determined value of $\xi = 0.88$. In conclusion, the curve fitting for both peak 3 and peak 4 suggests that the estimates of trap densities at progressively higher temperatures are at least an order of magnitude too large. Estimates of the free electron lifetime have been determined experimentally, by measuring the photoconductive gain factor under conditions of steady-state illumination when the photocurrent was comparable in magnitude to the TSC peak under investigation. It has been assumed that the lifetime measured in this way is identical with the mean time an electron remains free following detrapping in the TSC experiment. This assumption is more likely to be correct at the lower end of the temperature range where the photocurrent is independent of temperature, and the occupancy of the recombination centres with holes was more probably identical in the two different experiments.

Above 200K an extension to the simple model is required to account for thermal quenching of the radiative centre. Curve fitting for peaks above number 4 was difficult due to the increased uncertainities in the estimates of deep trapped charge.

8.6 THE CASE OF ONE TRAPPING CENTRE AND TWO RECOMBINATION CENTRES

The energy level scheme shown in figure 8.6.1 is a better general approximation to the rutile system. Assuming full compensation the neutrality condition requires that

$$a_1^+(t) + a_2^+(t) = n(t) + h_1^-(t) + h_2^-(t) \qquad (1)$$

when no free holes are present.

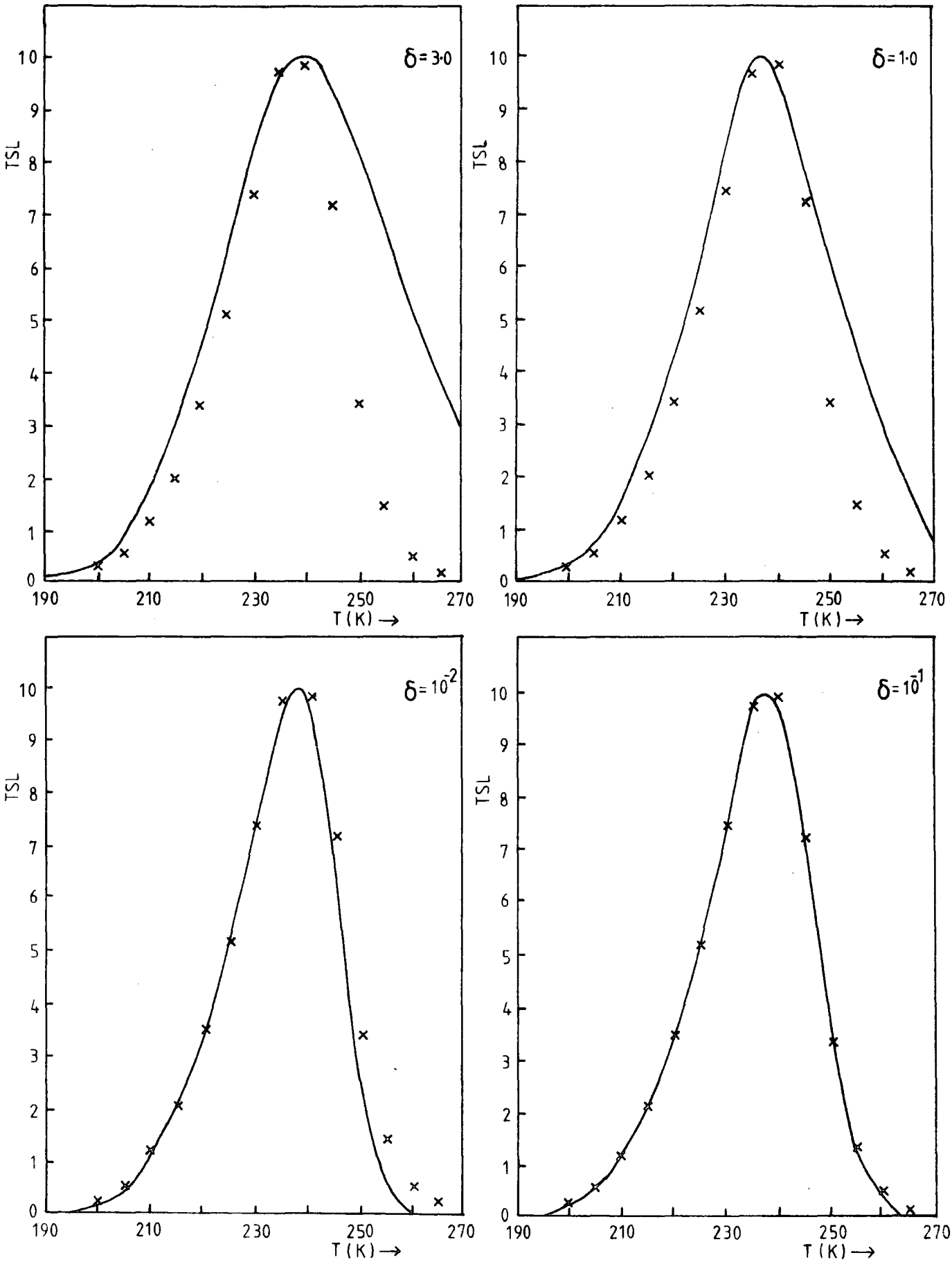

Figure 8.5.1 Comparison of the geometrical shapes of TSL curves for different retrapping ratios, δ. E = 0.51 eV ; hs = 9 10^{15} /cm^3 ; hd = 8.0 10^{14} /cm^3 ; τ = 10^{-8} s ; FREQ = 3.5 10^9 /s ; β = 0.5 °/s .

theoretical curve —— experimental data for CA3(NL) ×

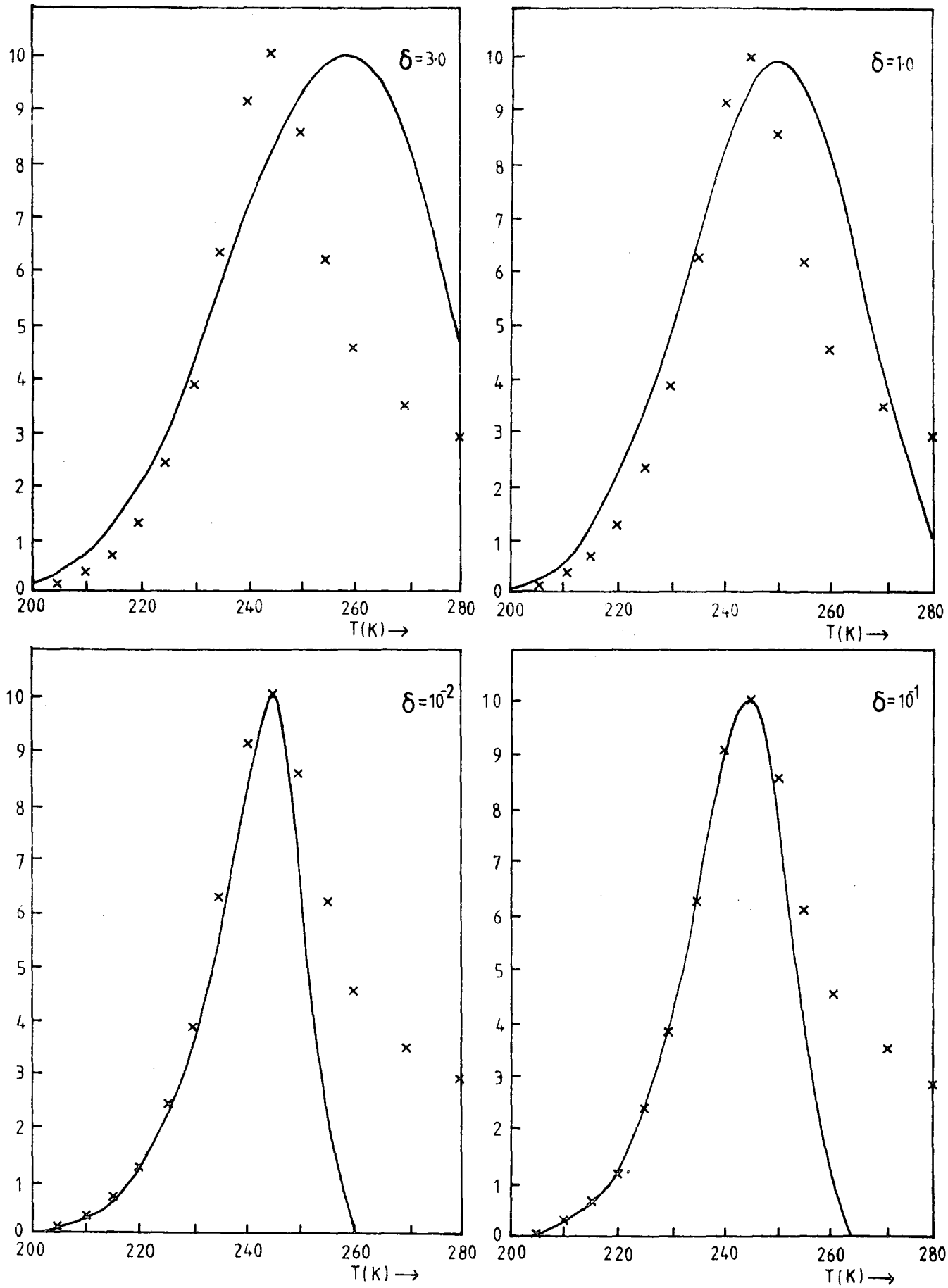

Figure 8.5.2 Comparison of the geometrical shapes of the TSC curves for for different retrapping ratios, δ. E = 0.51 eV ; hs = 9 10^{15} /cm^3 ; hd = 8.0 10^{14} /cm^3 ; τ = 10^{-8} s ; FREQ = 3.5 10^9 /s ; β = 0.5 °/s .

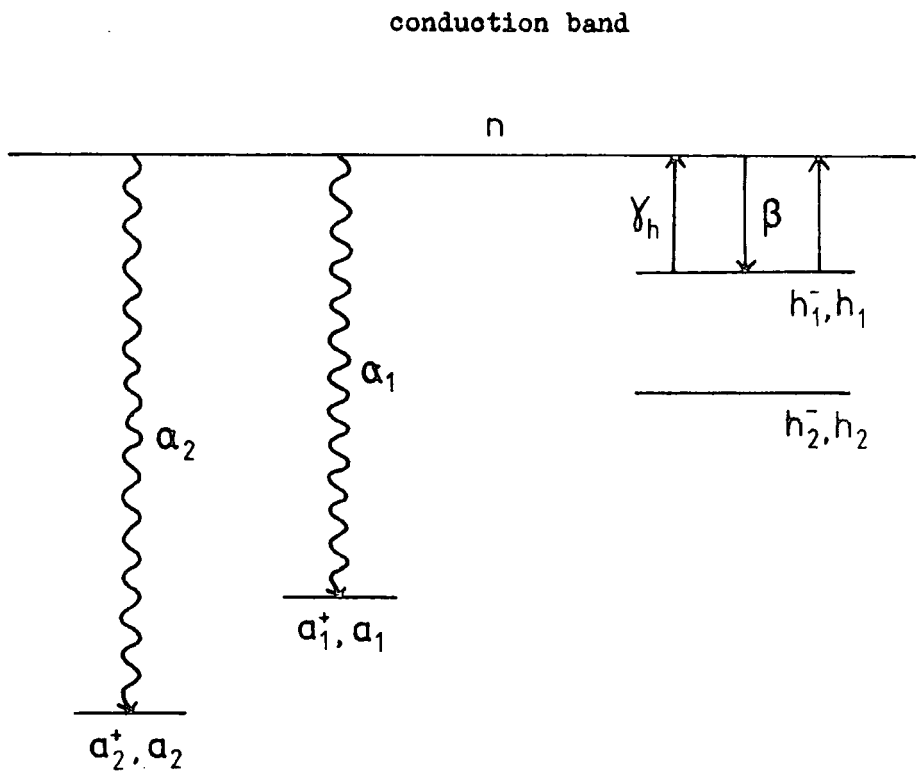

Figure 8.6.1 Energy level scheme with two acceptor centres involved in the recombination process .

The differential equations for this model are

$$\frac{dh_1^-}{dt} = -h_1^- + n(h_1 - h_1^-) \qquad (2)$$

$$\frac{dn}{dt} = -\frac{dh_1^-}{dt} - {}_1na_1^+ - na_2^+ \qquad (3)$$

$$\frac{da_1}{dt} = -na_1^+ \qquad (4)$$

$$\frac{da_2}{dt} = -na_2^+ \qquad (5)$$

With the initial conditions $a_1^+(T_0) = a_1$ and $a_2^+(T_0) = a_2$ it follows from (4) and (5) that

$$\frac{a_1^+}{a_1} = \left(\frac{a_2^+}{a_2}\right)^{\psi} \qquad (6)$$

where

$$\psi = \frac{\alpha_1}{\alpha_2}$$

Combining (1),(5) and (6) we find

$$\frac{da_2^+}{dt} = -\alpha_2 a_2^+ \left[a_2^+ + a_1\left(\frac{a_2^+}{a_1}\right)^{\psi} - h_1^-\right] . \qquad (7)$$

This system can be solved numerically (Kivits 1978) by a similar method used by Kivits on the simple insulator model. When da_2^+/dt and a_2^+ are known as a function of temperature, the values of da_1^+/dt and a_1^+ can be calculated with

$$\frac{da_1^+}{dt} = \frac{\psi a_1 a_2^{+(\psi-1)}}{a_2^{\psi}} \frac{da_2^+}{dt} . \qquad (8)$$

Unfortunately, the solution of the TSC and TL rate equations for the rutile system with two recombination centres is beyond the scope of this thesis.

Kivits has made some general points regarding the effects of more than one recombination centre on the shape of TSC/TL curves. Provided the recombination rate constant, $\alpha' > 10^4$, the shape of the TSC/TL curves will not

be affected (Hagebeuk and Kivits 1976). If $\alpha' < 10^4$ the TSC curve depends strongly on the value of α' and the TL curve shows some dependence. A situation can arise for a system containing two recombination centres, say one with a value $\alpha' > 10^4$ and another with $\alpha' < 10^4$, where double peaks are observed in the TSC and TL spectra from the thermal ionisation of a single discrete trapping centre.

8.7 DISCUSSION

Previous work described in this thesis has led to the development of a model for the single crystal rutile containing a Cr^{3+} radiative recombination centre with a lifetime of 35μsec and at least one other centre having a recombination lifetime of about 10^{-8} sec. The total chromium content in any of the crystals examined has been determined at between 0.1 and 0.9 ppm by mass spectrographic analysis. Evidence will be presented in the next chapter which suggests that Fe is present in quantities of between 3.0 and 27 ppm and acts as a fast recombination centre in the rutile lattice. Values of α' for these vary from 10^6 for the Cr^{3+} centre to 10^{10} for the Fe^{3+} centre. As a result we would not expect the type of double peaks that were discussed in the previous section to be present in the rutile spectra.

Although the simple insulator model is not a complete description of the single crystal rutile system, there does appear to be a remarkable agreement between the theoretical and experimental results for both TSC and TL. It would seem reasonable to consider why these results are self consistent.

The curve fitting procedure described previously for the TSC and TL curves led to the conclusion that the value of retrapping ratio was similar in both cases for all the traps considered. This is not surprising as the faster recombination centres will control the recombination kinetics. The Cr^{3+} radiative centre can be visualised as a 'leakage' recombination path for the free carriers and the influence of this centre on the TSC and TL

kinetics will depend on its concentration and its capture cross sections for electrons and holes, compared to the other fast centres that are present in the single crystal rutile examined. If a rutile crystal could be grown containing fewer impurities but with comparable chromium content then the shape of the TSC and TL curves might be expected to change and more carrier retrapping would be observed. Further studies of the TSC and TL spectra in pure and chromium doped flux-grown crystals (Berkes et al 1965, Wakin 1973) would be an interesting extension of this present work.

Kivits has shown that the conventional model for TL and TSC curves contains five essential parameters E,s,δ,α and ξ. Both the values of α and ξ have been determined using the photoconductive gain measurement and represent a weak source of information about the rutile crystals. The value of the trap depth E has been taken to be the value obtained from a number of self consistent analysis methods which have been supported by a more exacting theoretical analysis. Having obtained E the trapping frequency has been estimated by fitting the temperature maxima of the TSC and TL peaks. Finally, the retrapping ratio has been determined by curve fitting the experimental curves. Although self consistent values of trap depths have been obtained from various analysis techniques it must be stressed that these values have not been verified by other experimental techniques.

The present TSC and TL work has been interpreted in conjunction with photoconductivity and photoluminescence information. However, there still remains a number of experiments that are necessary to extend the interpretation of these results. The measurement of the carrier mobility would be an important addition to this work, the similarity in the TSC and TL shapes infers little temperature dependence, certainly not an exponential behaviour such as when the mobility decreases exponentially with temperature due to polaron scattering at optical phonons (Low and

Pines 1955). The problems encountered during this work have been a direct consequence of the complex recombination and trapping kinetics resulting from the indirect trap-spectrographic techniques of TSC and TL. Future work should centre on devising experiments that reduce the complexity of the recombination traffic. High field experiments (Simmons and Taylor 1972) photocapacitance (White 1976) and DLTS (Lang 1974) measurements using a Schottky barrier junction to simply the recombination and retrapping kinetics would be ideal. However, the difficulty of making a Schottky barrier to rutile remains a problem.

In conclusion, the values of trap depths derived from the TL experiments do not contradict the TSC values and the capture cross sections shown in table 7.6.3 are identical to the estimates obtained from the TL data. The thermoluminescence experiments have provided additional information towards the development of a two centre recombination model for the rutile system. In addition, they have confirmed that all the TSC peaks are derived from the transport of charged carriers. The trap densities calculated in the TSC analysis for the higher temperature traps, however, have probably been overestimated by at least an order of magnitude. Table 8.7.1 shows a comparison between the measured TSC values and the suggested theoretical curve fitting values.

	BS18(S)		BS18(NS)		CA3(NL)	
	TSC measured	TL theory	TSC measured	TL theory	TSC measured	TL theory
103K	$2\ 10^{13}$	$2\ 10^{13}$	$6\ 10^{14}$	$6\ 10^{14}$	$3\ 10^{14}$	$3\ 10^{14}$
120K	$4\ 10^{13}$	$4\ 10^{13}$	$1\ 10^{15}$	$1\ 10^{15}$	$4\ 10^{14}$	$4\ 10^{14}$
176K	$1\ 10^{16}$	$1\ 10^{16}$	$9\ 10^{16}$	$9\ 10^{16}$	$2\ 10^{17}$	$2\ 10^{17}$
245K	$2\ 10^{16}$	$7\ 10^{15}$	$6\ 10^{15}$	$2\ 10^{15}$	$9\ 10^{16}$	$2\ 10^{16}$
294K	$2\ 10^{16}$	$2\ 10^{15}$				
326K	$3\ 10^{16}$	$3\ 10^{14}$	$1\ 10^{16}$	$3\ 10^{14}$	$8\ 10^{16}$	$2\ 10^{15}$

Table 8.7.1 Comparison of trap densities calculated from TSC data derived from the TSC/TL theoretical data .

CHAPTER 9

DOPED RUTILE CRYSTALS

9.1 INTRODUCTION

In the previous chapters the optical and electrical properties of 'pure' rutile crystals have been discussed. To extend these studies a number of rutile crystals which were doped with Al, Nb, Fe and Mn during the plasma growth process, and another series of crystals diffusion doped with the transition metals Cr, Fe, Ni, Mn and Co have been examined using the photoconductivity, photoluminescence, TL and TSC techniques developed for the 'pure' crystals.

9.2 GENERAL OPTICAL AND ELECTRICAL PROPERTIES OF DOPED CRYSTALS

A summary of the doped crystals examined is given in table 9.2.1. The diffusion samples were prepared from the National Lead Verneuil boule CA3(NL) as described in chaper 3 and subsequently oxidised in a stream of oxygen at 1200°C for 24 hours, and cooled to room temperature over a period of 80 hours. Crystal BS15 was an iron doped crystal grown by the plasma flame fusion method which showed variation in colour across the boule and along its length. After oxidation the crystal was light yellow in the centre and varied from orange to red at the outside of the boule. Three crystals FE(Y), FE(O) and FE(R) were cut at different positions across the boule. The manganese (BS14) and niobium (BS12, BS19) doped plasma grown boules appeared to be more uniformly doped. All the plasma grown doped crystals were grown in the non-stoichiometric form and were subjected to a post growth oxidation similar to the NL doped crystals.

The optical spectra shown in figures 9.2.2 and 9.2.3 were obtained using an Optika double beam absorption spectrometer. All the dopants introduced absorption centres in the visible part of the spectrum and produced yellow, orange, red, brown, green and blue crystals. In the IR - region the lattice cut off occured at 1500 cm^{-1} and an OH vibration absorption line

CRYSTAL	DOPANT	METHOD OF DOPING
C1(NL)	Cr	diffusion ; 24 hrs at 1050 °C
C2(NL)	Cr	diffusion ; 24 hrs at 1150 °C
FE(NL)	Fe	diffusion ; 24 hrs at 1050 °C
FE(Y)	Fe	plasma grown crystal (BS15) ; iron dopant
FE(O)	Fe	plasma grown crystal (BS15) ; iron dopant
FE(R)	Fe	plasma grown crystal (BS15) ; iron dopant
MN(NL)	Mn	diffusion ; 24 hrs at 900 °C
MN(BS14)	Mn	plasma grown crystal (BS15) ; manganese dopant
CO(NL)	Co	diffusion ; 24 hrs at 1050 °C
NI(NL)	Ni	diffusion ; 24 hrs at 1050 °C
BS12	Nb	plasma grown crystal ; 477 ppma niobium
BS19	Nb	plasma grown crystal ; 140 ppma niobium

Table 9.2.1 Summary of the doped single crystal rutile .

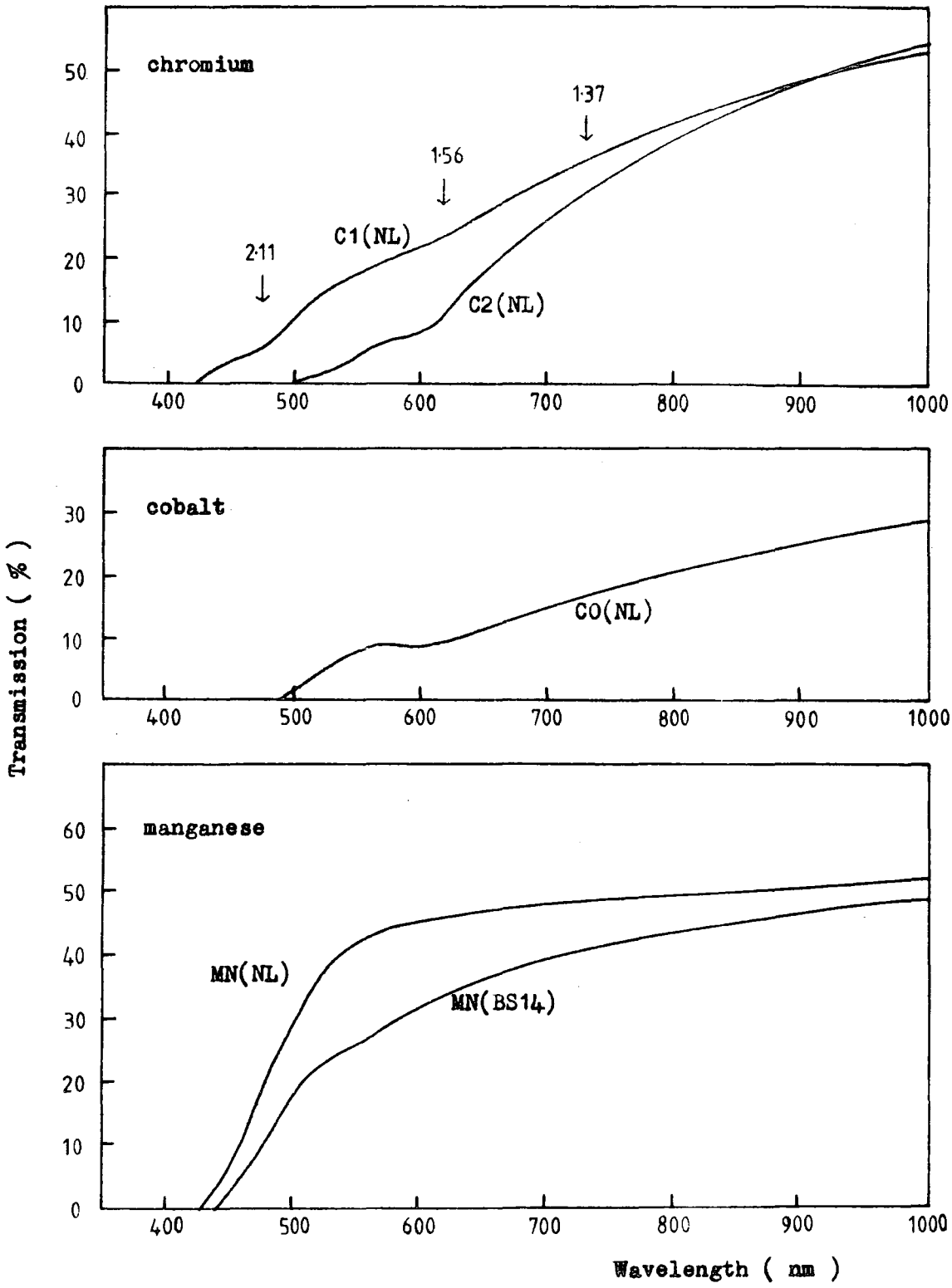

Figure 9.2.2 The optical transmission spectra of the chromium, cobalt and manganese doped rutile crystals at 300K .

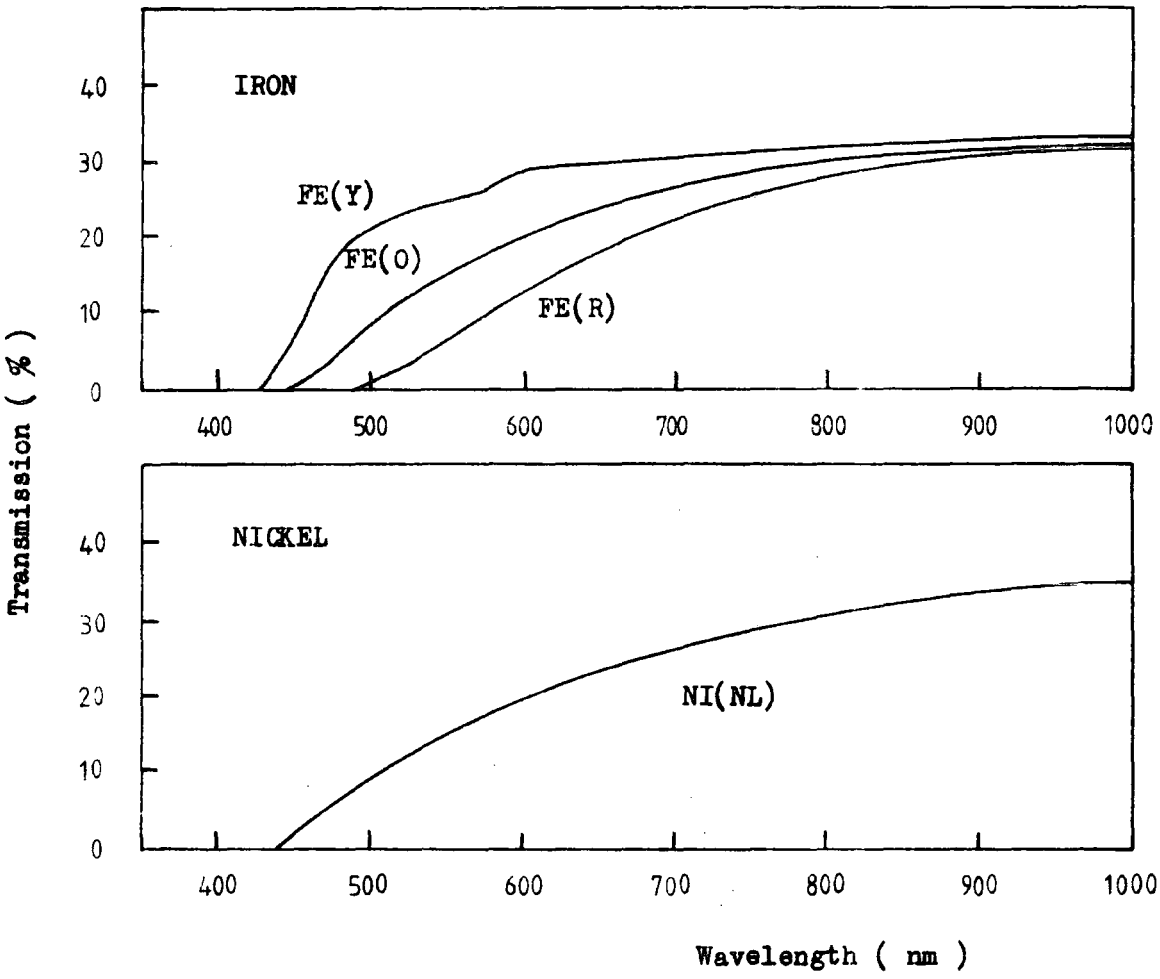

Figure 9.2.3 The optical transmission spectra of the iron and nickel doped crystals at 300 K.

was observed at 3286 cm^{-1}.

Samples with dimensions of 6 x 3 x 1 mm^2 were prepared with 2 mm diameter evaporated silver contacts on either side of the 1 mm thick samples. A potential of 25 V dc was applied across the samples and the variation of the current was recorded between the temperatures 160 K and 360 K. Figure 9.2.4 shows the thermal activation energy plots obtained for the doped rutile crystals. Mobilities were not measured and values reported by Bogolomov and Zhuze (1964) for partially reduced undoped rutile have therefore been used. All the transition metal dopants increased the resistivity of the rutile crystals which led to problems in measuring the high temperature thermally stimulated current spectra. Very little conductivity data has been previously reported, the best known being the 'Influence of Impurities on Electrical Conductivity in Rutile' by Johnson (1953). He measured the conductivity of a series of doped rutile ceramics and found a change in conductivity when transition metal dopants were added. However, the resistivity of his 'undoped' samples was about 10^7 Ω cm. Nickel, iron and cobalt all increased the resistivity to about 5 10^8 Ω cm, while chromium decreased the resistivity to about 4 10^6 Ω cm. These results do not agreee with the observations in the present work. Anderson et al (1973) report some room temperature resistivities for Fe doped crystals as 5 10^9, 2 10^9 and 8 10^8 Ω cm for red, orange and yellow crystals respectively. These values do not conflict with the present data.

After the resistivity measurements had been made the Ag contacts were removed, the crystals were again subjected to a 30 minute etch in boiling sulphuric acid and the silver contacts were vacuum deposited on the 3 x 1 mm faces of the samples. The specimens were mounted in the vacuum cryostat and cooled to 77 K in the dark after previously being heated to 400 K for 10 minutes. The samples were then illuminated with light from a 450 W Xenon light passing through an Oriel G-774-4450 filter and a 10% copper sulphate

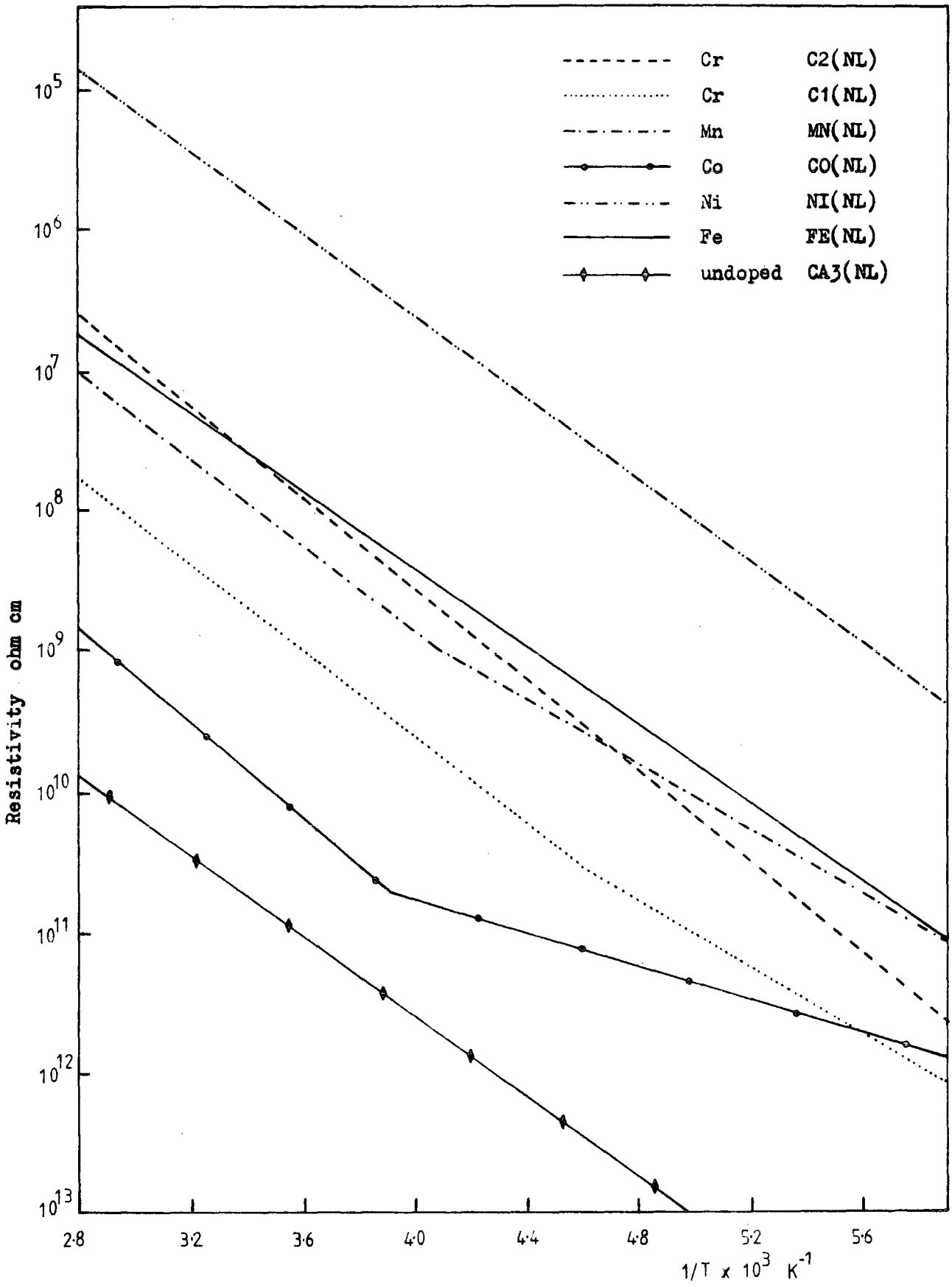

Figure 9.2.4 Thermal activation energy plots of the resistivity of the doped rutile crystals.

solution. Thus photocurrents and photoluminescence intensities were measured at an intensity of excitation of $\sim 10^{15}$ photons/s and the results are shown in figure 9.2.6 for all the rutile crystals investigated. All crystals examined showed a linear dependence of PC and PL intensity with the intensity of illumination at 77 K.

The temperature dependence of the photoluminescence emission intensity was measured and the results for crystals CO(NL), BS19, MN(NL) and NI(NL) are shown in figures 9.2.7 and 9.2.8. Activation energies extracted from a plot of $\ln (1 - \eta / \eta)$ against 1/T agree favourably with the 0.18 ± 0.02 eV level obtained from the 'undoped' crystals described in chapter 6. The photoluminescence results for chromium and iron doped crystals will be discussed later in this chapter.

9.3. ABSORPTION SPECTRA OF CHROMIUM DOPED CRYSTALS

The IR spectra of chromium doped rutile show the lattice cut off at 1500 cm^{-1} and an OH vibration absorption line at 3286 cm^{-1}. In the optical spectra at room temperature three weak absorption lines centred at 475 nm (21 10^3 cm^{-1}), 615 nm (16.3 10^3 cm^{-1}) and 730 nm (13.7 10^3 cm^{-1}) are seen (see figure 9.2.2). There is also an indication of a line hidden in the electronic absorption edge at around 420 nm (23.8 10^3 cm^{-1}).

Muller (1963) found at 30 K two absorption lines at 17.5 10^3 cm^{-1} (571 nm) and 24.4 10^3 cm^{-1} (410 nm) in chromium doped rutile which he assigned to transitions from the $^4A_2$ ground state to the $^4T_2$ and $^4T_1$ excited states of the Cr^{3+} ion. The present measurements were made at room temperature. When the crystal is cooled the decreased dimension of the lattice results in higher binding energies and the increased perturbation from the crystal field results in larger energy level splitting of the impurity ion. Tentatively, the absorption lines at 615 nm and 420 nm at room temperature may be identified with lines found by Muller at 17.5 10^3

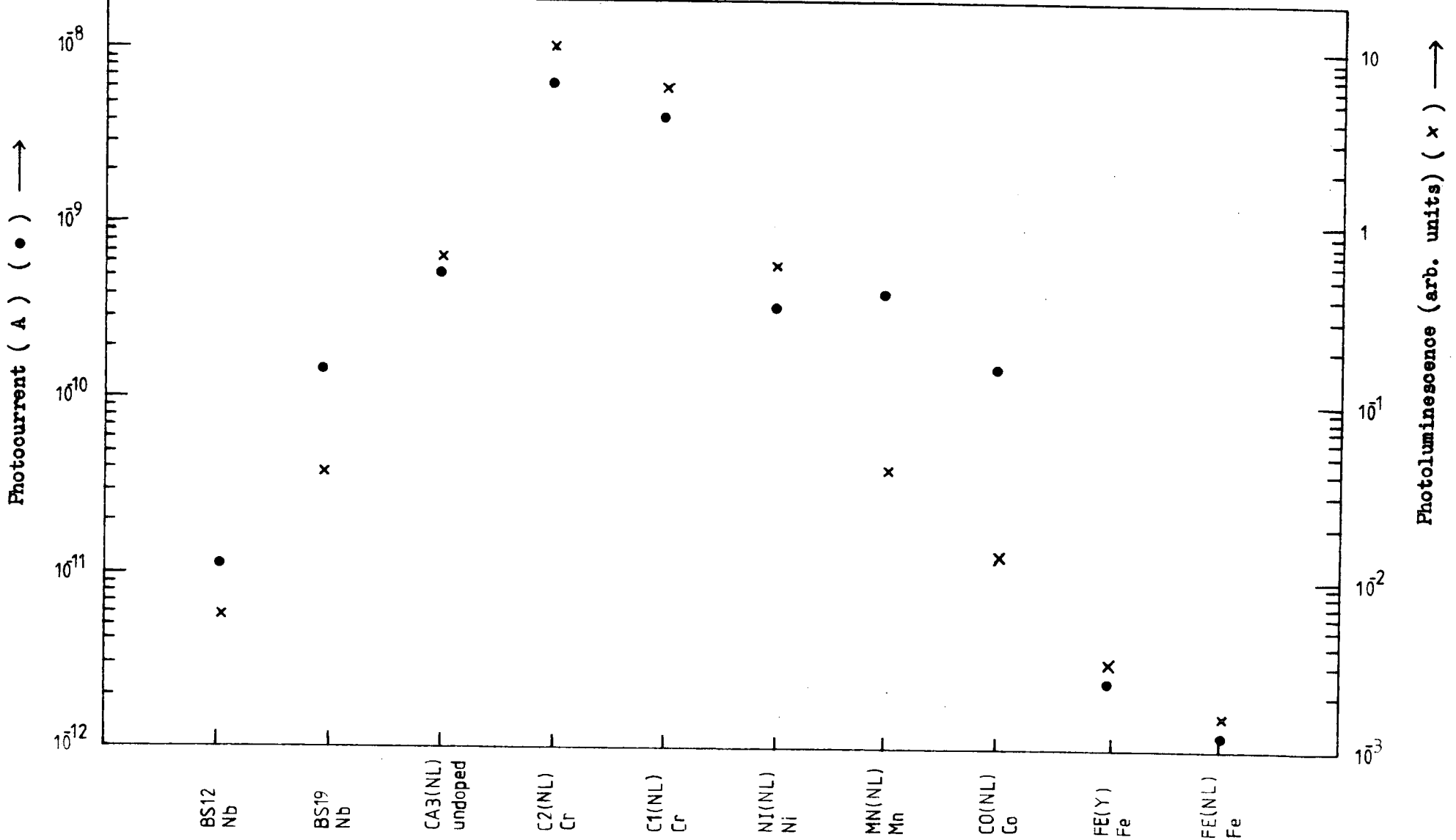

Figure 9.2.6 Comparison of the photoconductivity and photoluminescence data for the doped rutile crystals at 77 K.

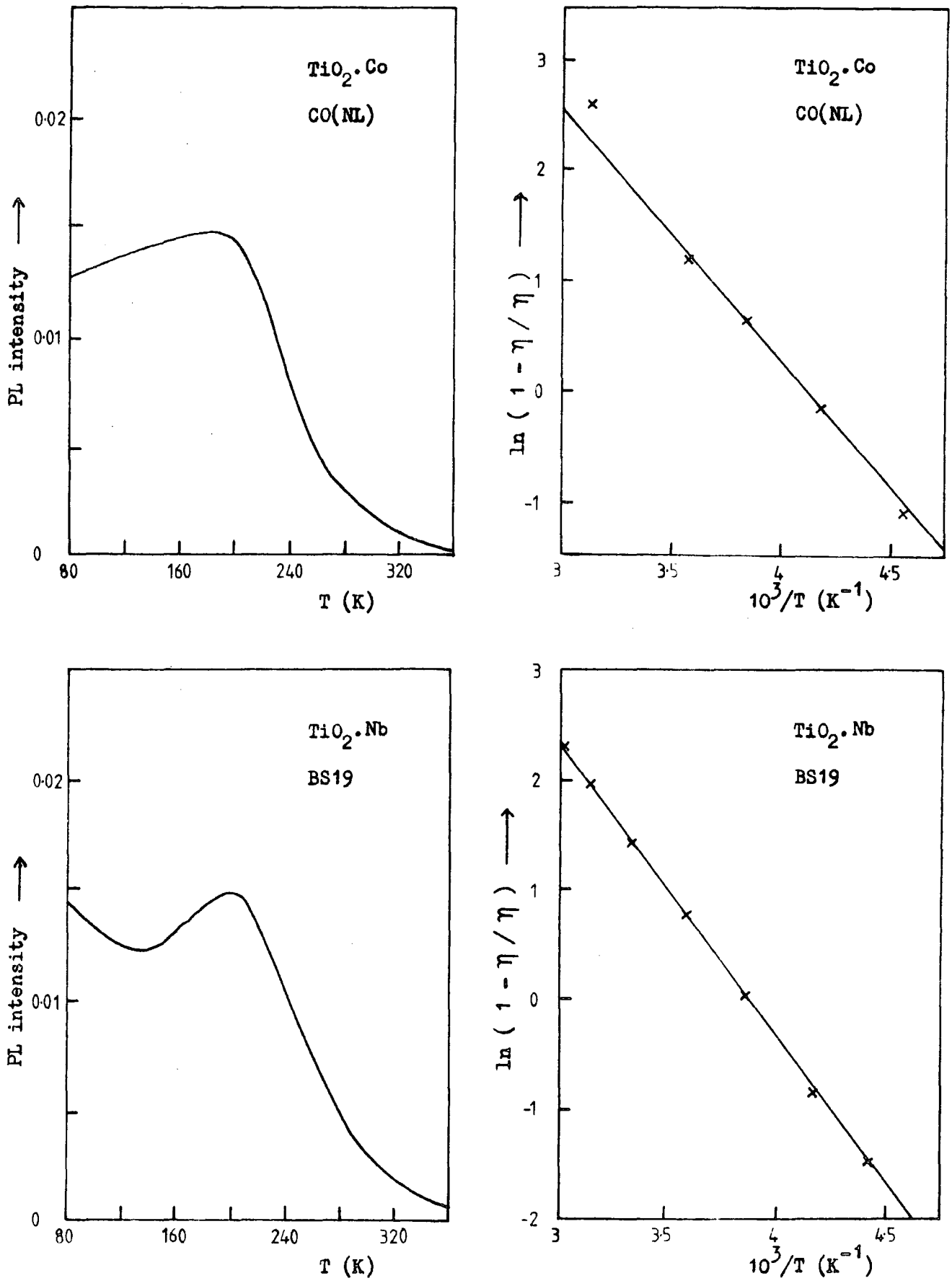

Figure 9.2.7 The temperature dependence of the photoluminescence emission intensity for crystals CO(NL) and BS19 .

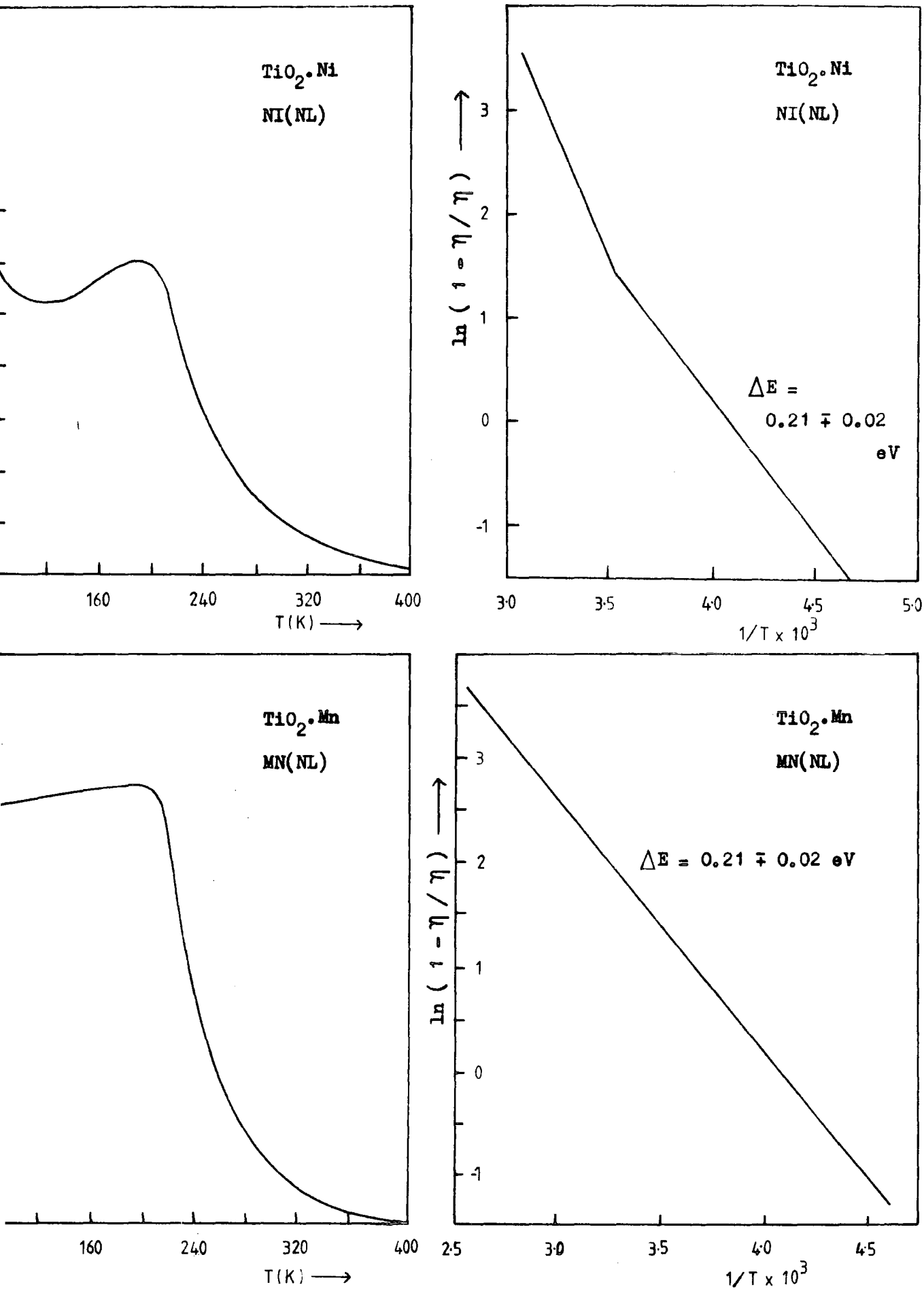

Figure 9.2.8 The temperature dependence of the photoluminescence emission intensity for the crystals NI(NL) and MN(NL).

CRYSTAL	DOPANT	ACTIVATION ENERGY
C2(NL)	Cr	0.34 eV
C1(NL)	Cr	0.36 eV ; 0.21 eV
MN(NL)	Mn	0.32 eV ; 0.23 eV
CO(NL)	Co	0.44 eV ; 0.21 eV
NI(NL)	Ni	0.37 eV
FE(NL)	Fe	0.28 eV
CA3(NL)	undoped	0.27 eV

Table 9.2.5 Activation energies of the doped rutile crystals from the resistivity / temperature measurements .

cm^{-1} and 24.4 10^3 cm^{-1} at 30 K. Muller did not observe the absorption lines at 13.5 10^3 cm^{-1} and 21.3 10^3 cm^{-1}.

Grabner (1970) observed two sharp no-phonon lines at 12685 cm^{-1} and 12732 cm^{-1}, and vibronic sidebands. In emission a splitting of 1.4 cm^{-1} (42 Ghz) of the 12685 cm^{-1} line facilitated identification of this line as due to substitutional Cr^{3+}.

The vibronic sideband in absorption is centred at 13.8 10^3 cm^{-1} and thus corresponds to the absorption found at 730 nm (13.7 10^3 cm^{-1}). Grabner assigned the observed sharp no-phonon lines to transitions between the $^4A_2$ ground state and the $^4T_2$ excited state of the Cr^{3+} ion. Moreover, Grabner believed that the absorption lines seen by Muller are due to 'background absorption' associated with some unknown defect.

Mirlin et al (1970) found that if a voltage of about 50V was applied to a chromium-doped rutile crystal held at 500-600°C in air, then original uniform reddish brown colouring became divided into two regions of a different colour with a sharp line between them after some 5-10 minutes. The cathode became light orange, while the anode region turned black. Absorption in the 500-700 μm region increased in the anode region and decreased in the cathode region.

At elevated temperatures the applied field gave rise to a drift of positively charged compensation defects in the direction of the cathode. As a result, the cathode region became enriched with compensation defects favouring the transition of Cr^{4+} into the Cr^{3+} state. According to Mirlin the black colour of the anode was due to electronic transitions from the 2p valence band to acceptor levels associated with Cr^{4+} (filled Cr^{4+} acceptors are equal to Cr^{3+} ions and charge compensation defects).

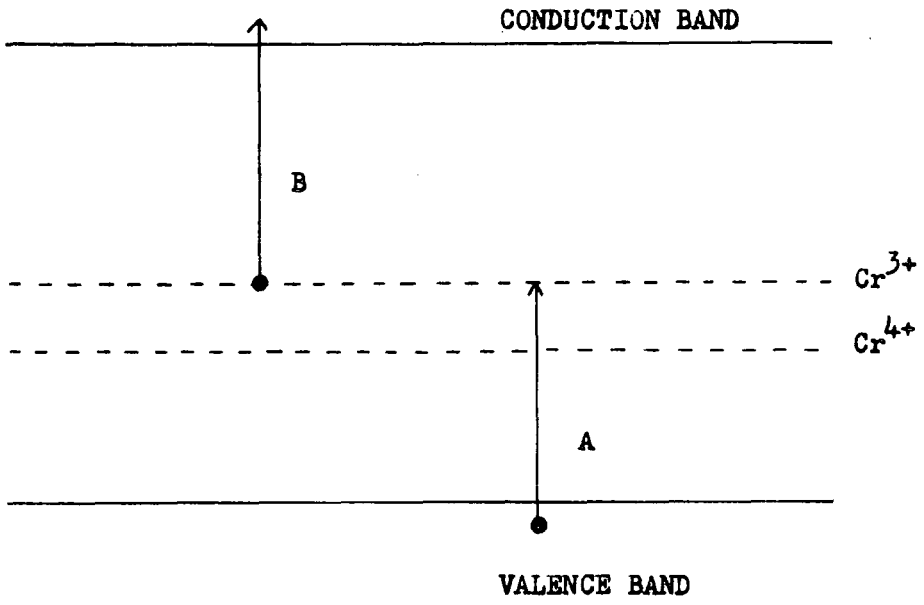

The transition marked A illustrates the excitation of an electron from the valence band to empty Cr^{3+} states (= Cr^{4+} ions). These transitions probably produce the black colour. The transition marked B illustrates the excitation of an electron from the Cr^{3+} state to the conduction band. The number of A transitions per unit time is proportional to the number of empty Cr^{3+} states. When no Cr^{4+} ions are present, the crystal has an orange colour probably due to transitions of the type B.

9.4 TSC AND TL OF CHROMIUM CRYSTALS

The as-grown C1(NL) had a resistivity of 10^2 ohm cm and a thermal activation energy of 0.04 eV, whilst crystal C2(NL) had a resistivity of 10 ohm cm and a thermal activation energy of 0.01 eV. After subsequent annealing in oxygen the TSC and TL spectra were measured. Figures 9.4.1 and 9.4.2 show the spectra obtained before and after chromium doping of the NL boule CA3(NL). It can be seen that the introduction of chromium into the rutile lattice increases the intensity of the TSC and TL spectra, and two new peaks appear. Peak 7 appears at a temperature slightly below peak 1 (0.14 eV) and peak 8 appears at a temperature above peak 3 (0.37 eV). Table 9.4.3 contains a summary of the thermal activation energies obtained using a few of the TSC/TL methods described previously. Good agreement was found

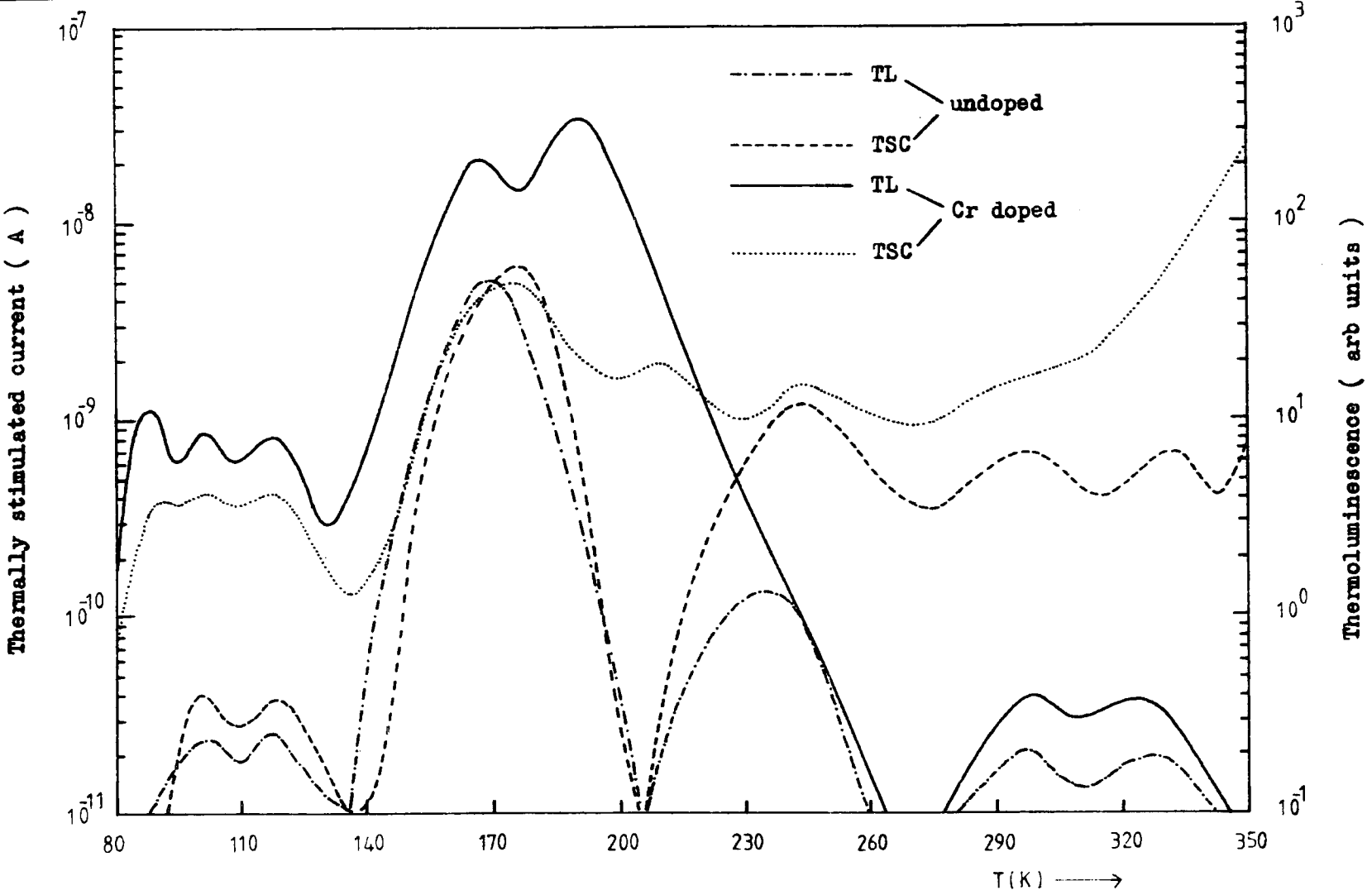

Figure 9.4.1 Comparison of the TSC and TL spectra for crystal C1(NL) before chromium doping and after doping for 4 hours at 1050°C .

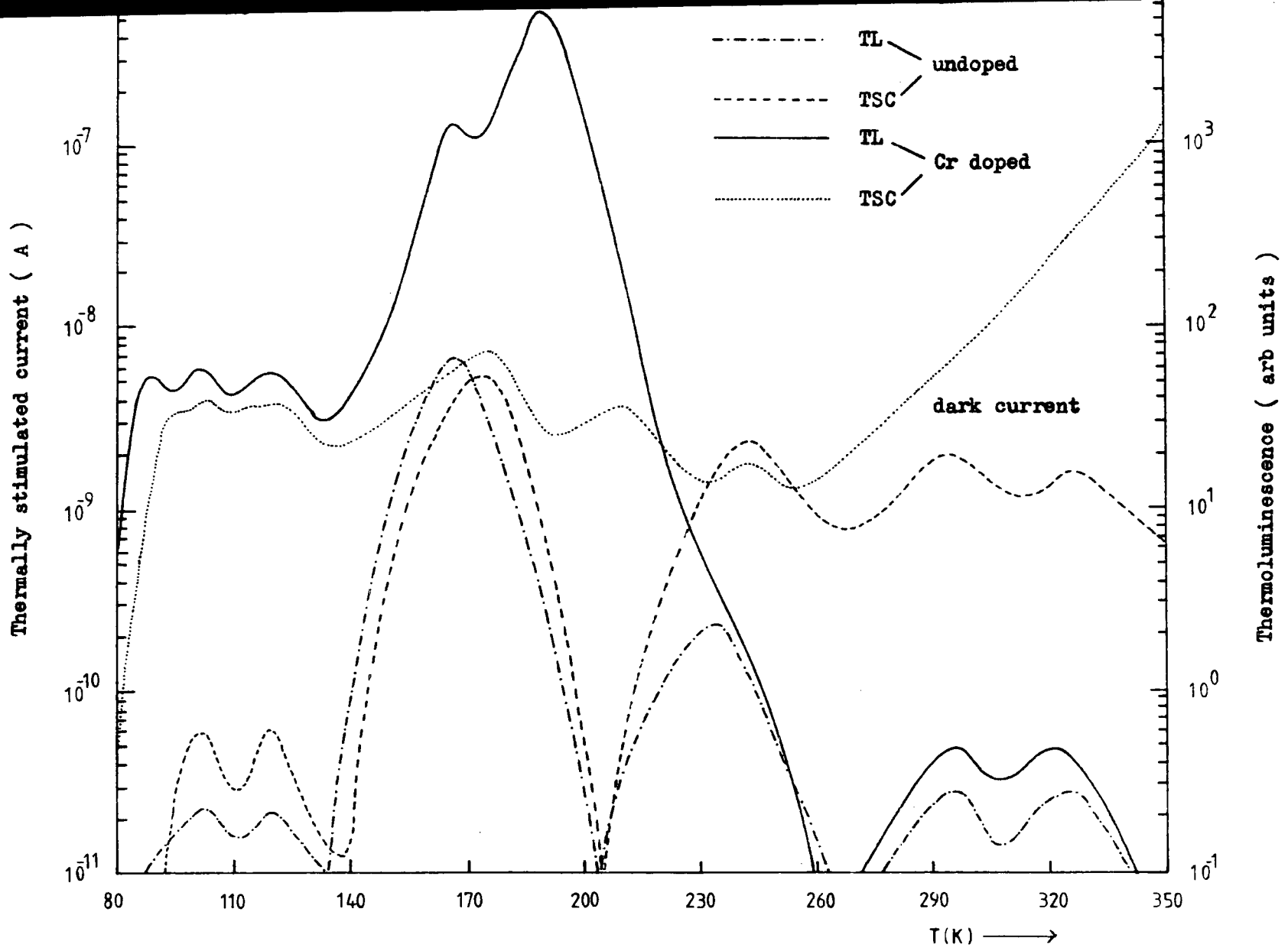

Figure 9.4.2 Comparison of the TSC and TL spectra for crystal C2(NL) before and after chromium doping for 24 hours at 1150 °C .

	PEAK 7		PEAK 1		PEAK 2	
	TSC	TL	TSC	TL	TSC	TL
Temp. maximum	92	89	103	101	119	118
Hoogenstraaten	0.18±.02	0.18±.02	0.14±.01	0.13±.02	0.23±.02	0.23±.02
Haering, Adams	0.19±.02	0.18±.01	0.14±.01	0.14±.02	0.24±.01	0.23±.02
Chen, Winer	0.19±.02	0.18±.02	0.13±.02	0.13±.02	0.23±.02	0.24±.02
Garlick, Gibson	0.20±.05	0.19±.03	0.17±.03	0.18±.04	0.24±.02	0.25±.02
Cross-section Kivits theory (cm^{-2})	10^{-18}		10^{-21}		10^{-18}	

	PEAK 3		PEAK 8		PEAK 4	
	TSC	TL	TSC	TL	TSC	TL
Temp. maximum	176	167	211	191	244	238
Hoogenstraaten	0.37±.02	0.36±.01	0.41±.01	0.42±.02	0.50±.01	0.52±.02
Haering, Adams	0.38±.02	0.37±.02	0.41±.02	0.42±.02	0.51±.03	0.51±.02
Chen, Winer	0.37±.02	0.37±.02	0.42±.02	0.42±.02	0.51±.02	0.52±.02
Garlick, Gibson	0.38±.04	0.39±.04	0.45±.04	0.46±.03	0.53±.03	0.51±.03
Cross-section Kivits theory (cm^{-2})	10^{-18}		10^{-18}		10^{-19}	

	PEAK 5		PEAK 6	
	TSC	TL	TSC	TL
Temp. maximum	?	299	?	324
Hoogenstraaten	-	0.61±.04	-	0.73±.04
Haering, Adams	-	-	-	0.72±.03
Chen, Winer	-	-	-	0.71±.05
Cross-section Kivits theory	?		?	

Table 9.4.3 Summary of TSC and TL analysis for chromium doped crystal C1(NL).

although some difficulty was encountered when thermally cleaning peak number 8 due to its close proximity to peak 3.

The trap densities for levels 1 to 8 have been estimated from the areas under the TSC curves and the photoconductive gain. Table 9.4.4 shows the increase in trap densities for each level before and after doping crystals C1(NL) and C2(NL) with chromium. The total trap density increases from 4 10^{17} cm^{-3} to 5.3 10^{18} cm^{-3} in crystal C1(NL) and from 3.8 10^{17} cm^{-3} to 7.6 10^{18} cm^{-3} in crystal C2(NL) after chromium doping.

The magnitude of the TSC and TL spectra at low temperatures can be understood in terms of the photoluminescence versus temperature curves to be presented in the next section. However, the relative magnitudes of the TSC and TL peaks for trap 8 are not completely explained in terms of either the Auger mechanisms or thermal ionisation of the Cr^{3+} excited state discussed in chapter 8. In both the C1(NL) and the C2(NL) crystal the TL magnitude appears to be larger than the TSC magnitude.

Impurity centres may be expected to have excited states. The evidence available from infrared absorption measurements (Blakemore 1962, Kivits 1978) suggests that excited states of deep impurities tend to be near the semiconductor band edges. This implies that the wave function of an electron in an excited state has a much larger spatial extent than the wave function of an electron in the ground state, especially for deep trapping centres. The excited states contribute to the free electron capture process via the cascade model of Lax (1960) and they may be of importance in the thermoluminescence process (Gransul et al 1970, Williams and Eyring 1947). It would seem likely that the trapping centre corresponding to peak 8 provides some recombination via excited states of the centre. This would explain why a larger signal is obtained from thermoluminescence rather than TSC for peak 8. However, it must be remembered that the trapping

PEAK NO.	7	1	2	3	8	4	5	6
UNDOPED	-	$5\ 10^{14}$	$5\ 10^{14}$	$3\ 10^{17}$	-	$6\ 10^{16}$	$3\ 10^{16}$	$4\ 10^{16}$
C1(NL)	$7\ 10^{15}$	$6\ 10^{15}$	$6\ 10^{15}$	$2\ 10^{17}$	$9\ 10^{16}$	$7\ 10^{16}$	$7\ 10^{16}$	$1\ 10^{17}$
UNDOPED	-	$7\ 10^{14}$	$8\ 10^{14}$	$2\ 10^{17}$	-	$4\ 10^{16}$	$8\ 10^{16}$	$6\ 10^{16}$
C2(NL)	$9\ 10^{16}$	$1\ 10^{17}$	$1\ 10^{17}$	$3\ 10^{17}$	$1\ 10^{17}$	$7\ 10^{16}$	?	?

Figure 9.4.4 Comparison of trap densities (cm^{-3}) for the chromium doped crystals before and after chromium doping . Data taken from TSC curves .

processes in rutile are further complicated because the thermoluminescence is only sampling a fraction of the recombination traffic.

Figure 9.4.5 shows the thermoluminescence peak height after 20 minutes excitation (0.015 $\mu W/mm^2$) at various excitation energies for crystal C2(NL) before and after chromium doping. The filling of the traps at energies below the band gap for the chromium doped crystal shows that deep levels have been introduced as a direct consequence of the chromium doping. Electrons are excited from these deep levels into the conduction band to provide another route for filling the traps.

Finally, crystal C1(NL) was heated to 600°C in a stream of oxygen and quenched to room temperature by removing it from the furnace whilst still in the oxygen flow. The TSC spectra (see figure 9.4.6) increased showing that the density of the low temperature traps increased by approximately an order of magnitude and the density of trap 3 almost doubled after quenching from 600°C. As the dark current increased after quenching it was not possible to examine the high temperature traps. Figure 9.4.7 shows the dependence of the shallow trap densities on the quenching temperature for crystal C1(NL). These curves are similar to the ones obtained for the 'pure' crystals (see figure 7.7.2) except that the density of the traps is larger in the chromium doped crystal.

9.5 PL AND PC OF THE CHROMIUM DOPED CRYSTALS

Both the chromium doped crystals (see figure 9.2.6) showed an approximate order of magnitude increase in photocurrent at 77 K after chromium doping. This increase in lifetime is probably due to the retrapping of carriers and the trap densities in the last section have probably been underestimated by an order of magnitude.

The temperature dependence of the photoconductivity for crystal C1(NL) is shown in figure 9.5.1 before and after chromium doping. Similar curves

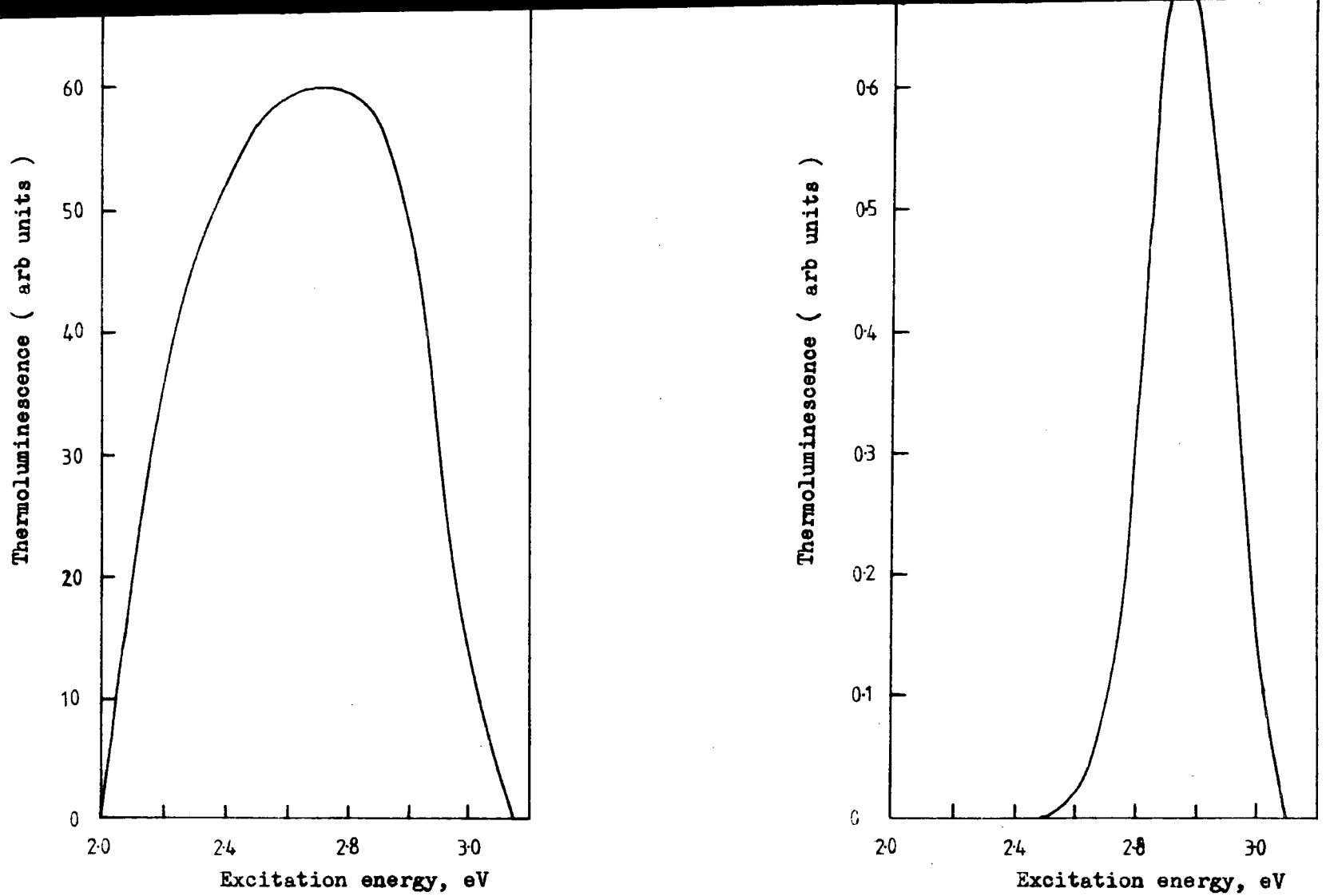

Figure 9.4.5 Thermoluminescence peak height after 20 mins excitation (0.015 $\mu W/mm^2$) at various excitation energies for crystal C2(NL) before and after chromium doping .

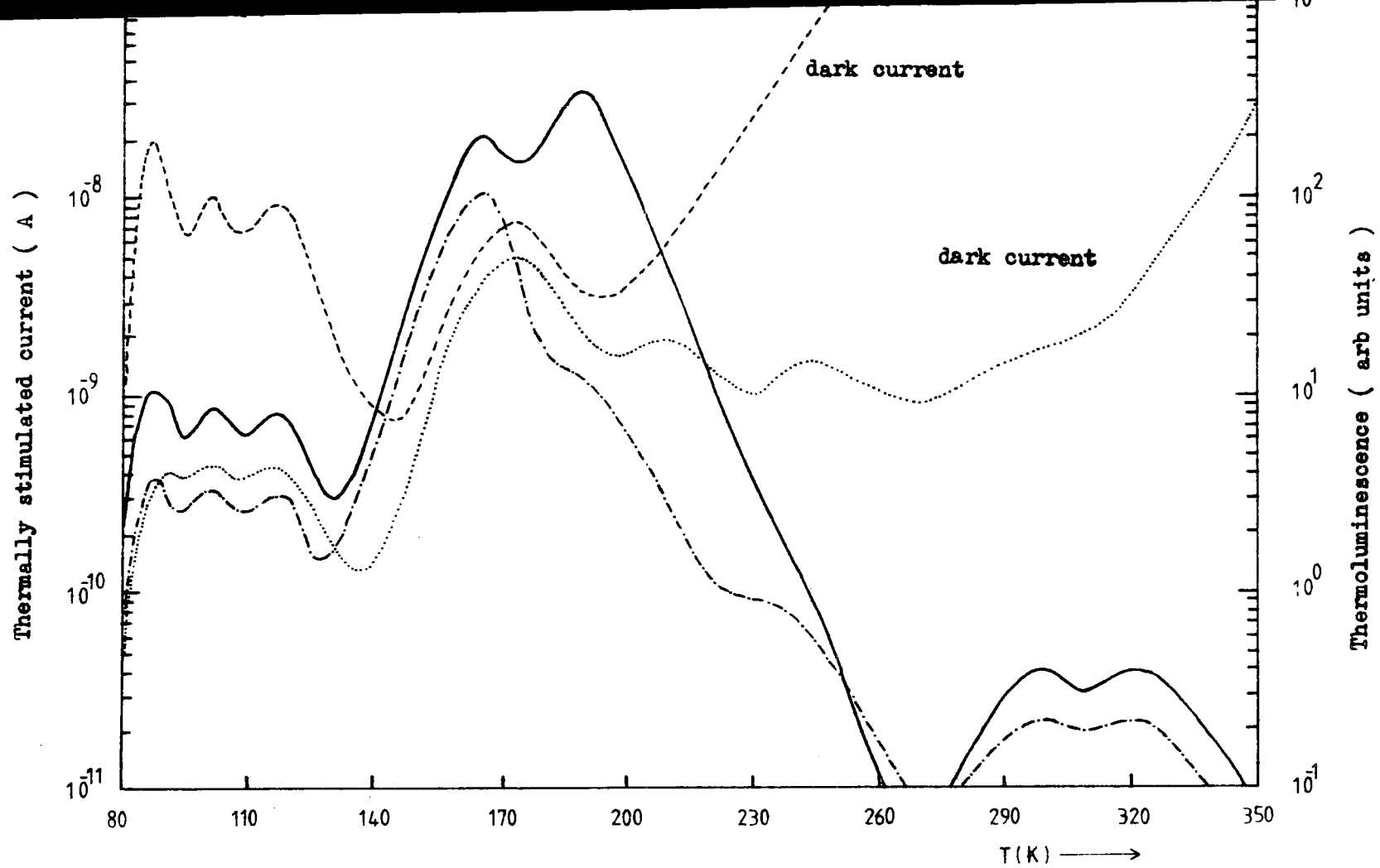

Figure 9.4.6 Comparison of the TSC and TL spectra for chromium doped crystal C1(NL) before and after thermal quenching at 600 °C .

TL, TSC — unquenched

TL, TSC — quenched

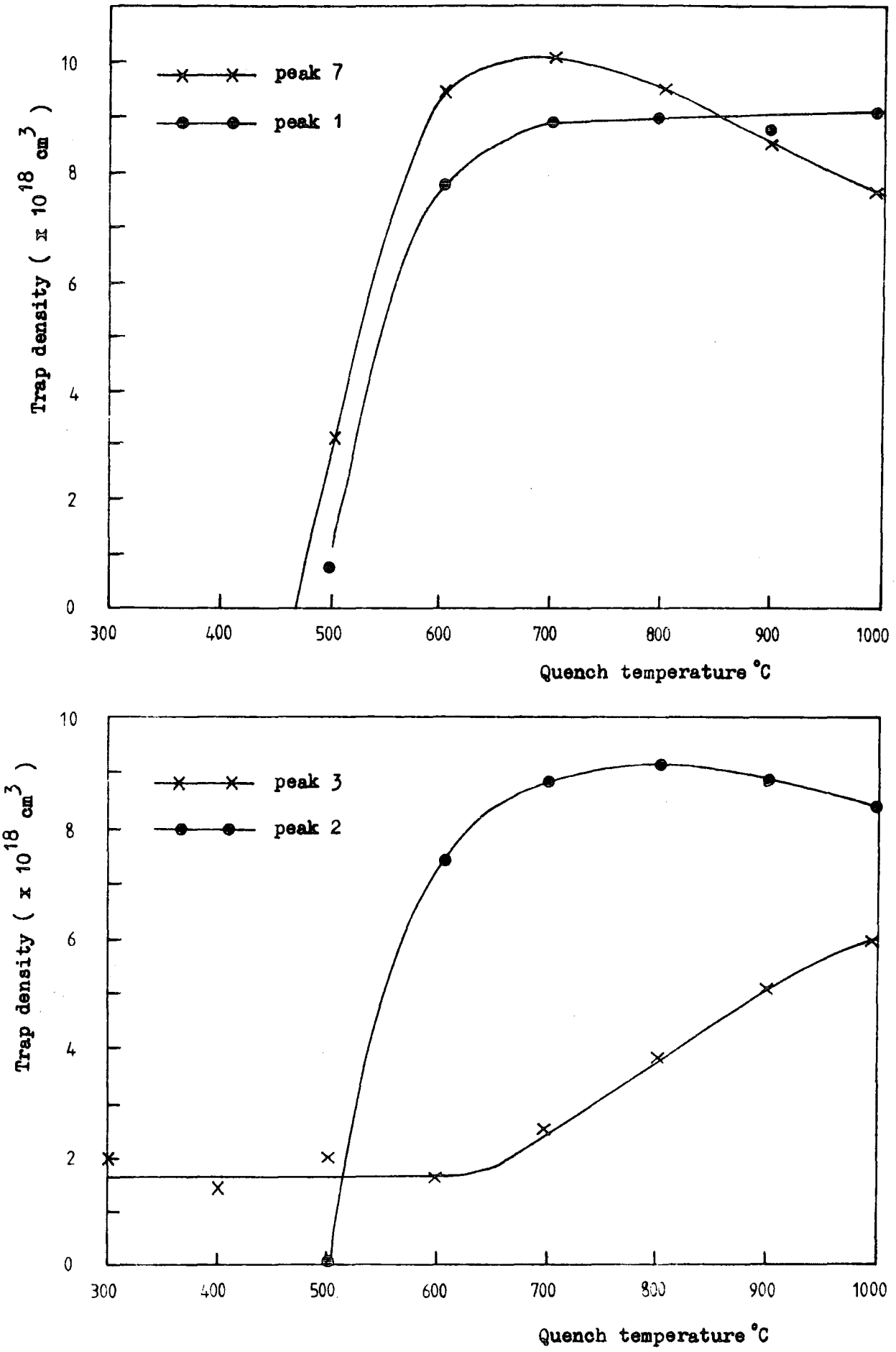

Figure 9.4.7 **Densities of the shallow traps in the chromium doped crystal** C1(NL) after quenching from T°C.

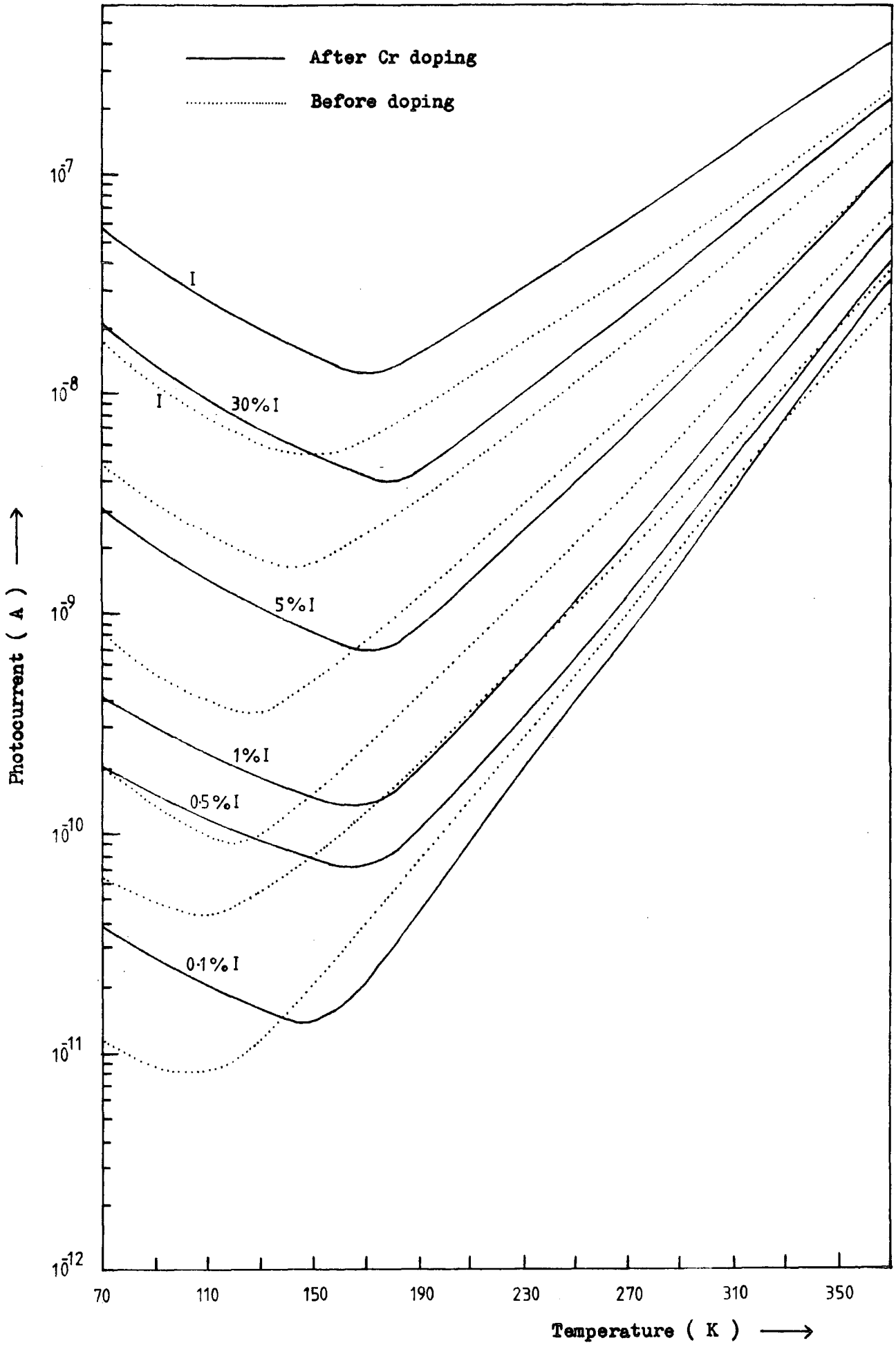

Figure 9.5.1 The temperature dependence of the photoconductivity for crystal C1(NL) .

were obtained in chaper 5 for the 'pure' crystals. The difference in the temperature snift of the curve minima can be interpreted as being due to the presence of a large density of shallow traps in the Cr doped sample, a similar case to that of the thermally quenched 'pure' crystal described in chapter 5.

The PSC spectra of both the chromium doped crystals were investigated and the results for crystal C1(NL) are shown in figure 9.5.2. As with the nominally pure crystals the PSC peak at 1 eV, which appears to be associated with the same level 3 seen in the TSC spectra, is clearly visible. However, it is interesting to observe that thermal cleaning at 205 K does not remove this peak as in the 'pure' crystals. The cleaning temperature had to be raised to 240 K before the 1 eV peak began to disappear. The presence of peak 8 in the Cr doped crystals appears to be responsible for this effect.

As already described in section 6.8 diffusion of chromium into the rutile lattice increases the photoluminescence emission intensity of these crystals. The emission spectra show the same characteristic emission at 850 nm with an indication of another emission at 820 nm. Figure 9.5.3 shows the excitation spectrum for crystal C1(NL) of the total emission, that is the no-phonon line plus the vibronics. Grabner et al (1970) have measured the excitation spectrum of the no-phonon line of TiO_2.Cr and found it to be identical to the vibronic emission. They concluded that the Cr^{3+} emission originates from a single excited state. It can be seen by comparison with the absorption spectrum (see figure 9.2.2) that the sub band gap absorption is duplicated in the excitation spectrum. In addition to the excitation at about 3 eV, where free carriers are produced, excitation of the Cr^{3+} ions is derived mainly from traps which are filled by charge carriers, rather than from direct excitation of the Cr^{3+} ion.

The temperature dependence of the intensity of the PL emission in Cr doped crystals shows a different activation energy at high temperatures

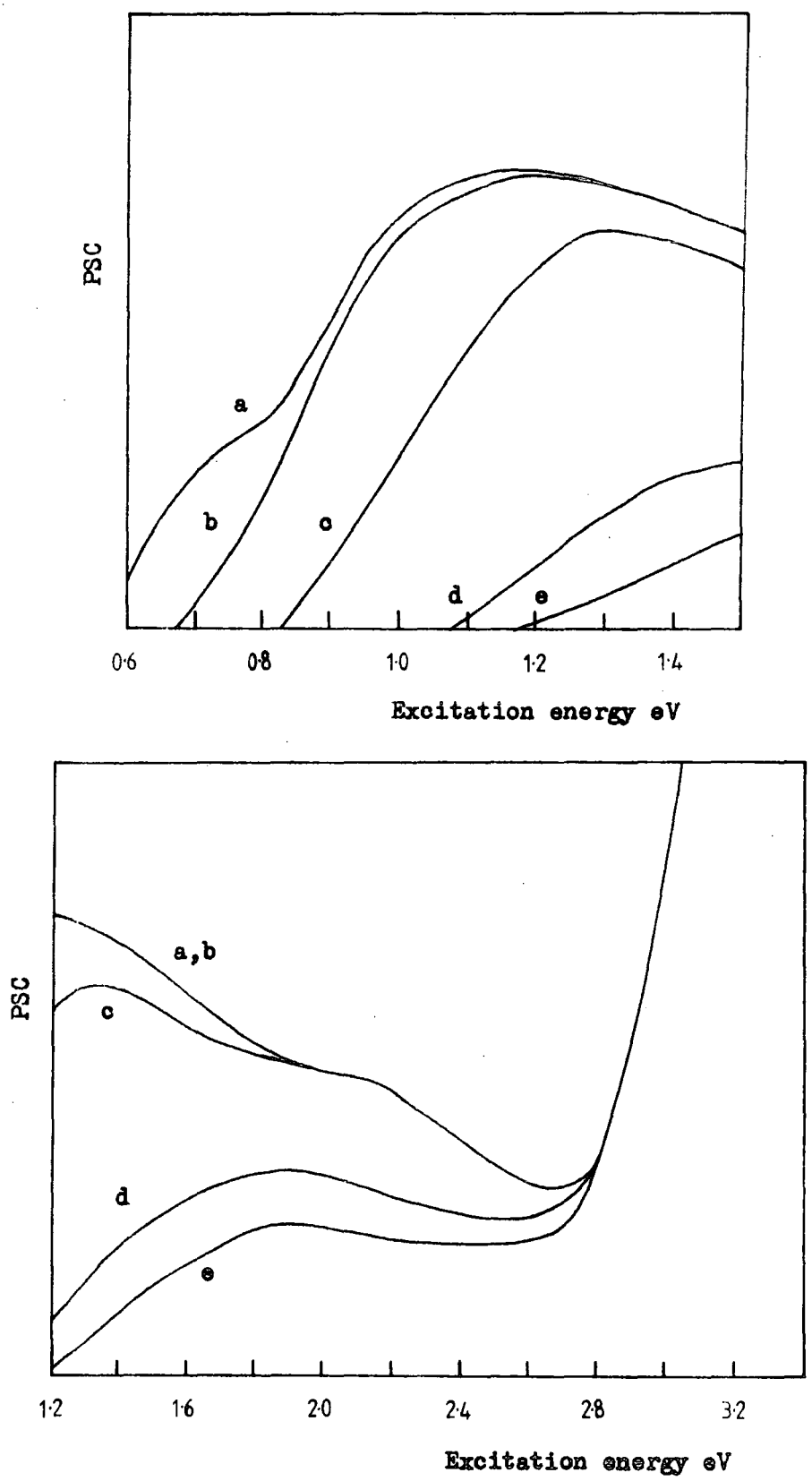

Figure 9.5.2 PSC spectra for crystal C1(NL) after chromium doping (after spectral correction) .

a traps filled b thermally cleaned at 140K c thermally cleaned at 205K d thermally cleaned at 240K e thermally cleaned at 400K

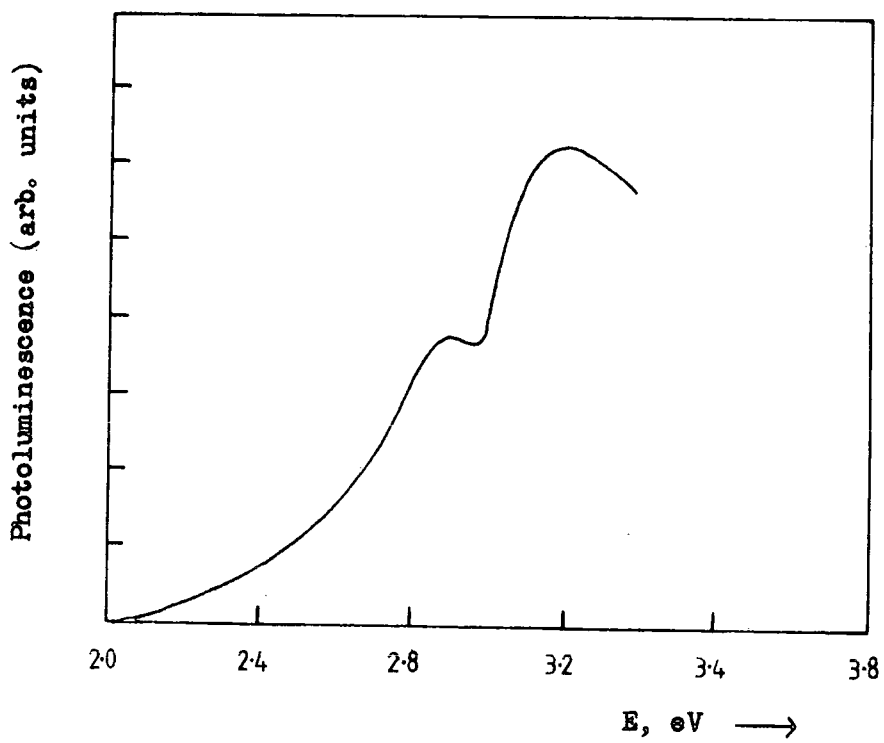

Figure 9.5.3 Photoluminescence excitation spectra for crystal C1(NL) at 77 K (after spectral correction).

compared with that of the 'pure' crystals (see figure 9.5.4). An activation energy of 0.34 ± 0.02 eV was observed in the Cr doped crystals investigated, whilst an activation energy of 0.20 ± 0.02 eV was observed at lower temperatures. The lifetime of the Cr^{3+} excited state was measured as 36 ± 1 μsec and similar activation energies were obtained from $\ln(1/\tau - 1/\tau_L)$ plots (see figure 9.5.5). The 0.34 eV activation energy is difficult to explain but could be a result of thermal excitation of an electron from the Cr^{3+} excited state to the conduction band M minima, whilst the lower 0.20 eV activation energy respresents a transition to the conduction band R minima.

9.6 DEEP LEVELS IN CHROMIUM DOPED RUTILE

The EPR spectrum of Cr^{3+} ions which substitute for Ti^{4+} ions is well known (Gerritsen et al 1959). In rutile crystals doped with substitutional trivalent metal impurities, compensation of the effective negative charge of these sites is achieved by defects in the rutile lattice. In principle, it is possible to have different types of compensating defects, e.g. oxygen vacancies or interstitial ions of titanium or chromium. Kingsbury et al (1968) have shown that compensation of trivalent impurities present in rutile as contaminants is carried out by interstitial Ti^{4+} ions, the energy levels of which are located near the conduction band. Ikebe et al (1969) have detected two EPR spectra in TiO_2.Cr crystals which they have attributed to complexes consisting of a Cr^{3+} ion with an oxygen vacancy in 2nd and 3rd coordination spheres . The first of these spectra has also been observed by Sochava et al (1970) in vacuum reduced TiO_2.Cr (at a temperature of 500-700°C). Mirlin et al (1970) found an absorption at 1.1 eV with a dichroism of $\alpha_\perp/\alpha_\parallel \sim 1.8$, where $\alpha_{\perp,\parallel}$ correspond to the normal and parallel orientation of E to the c axis of the crystal, which indicated the presence of deep electron traps in TiO_2.Cr. Sochava et al (1970) measured the dependence of the relative intensity of the EPR spectrum II and the maximum optical absorption coefficient in the 1.1 eV band on the reduction temperature of the TiO_2.Cr crystal (see

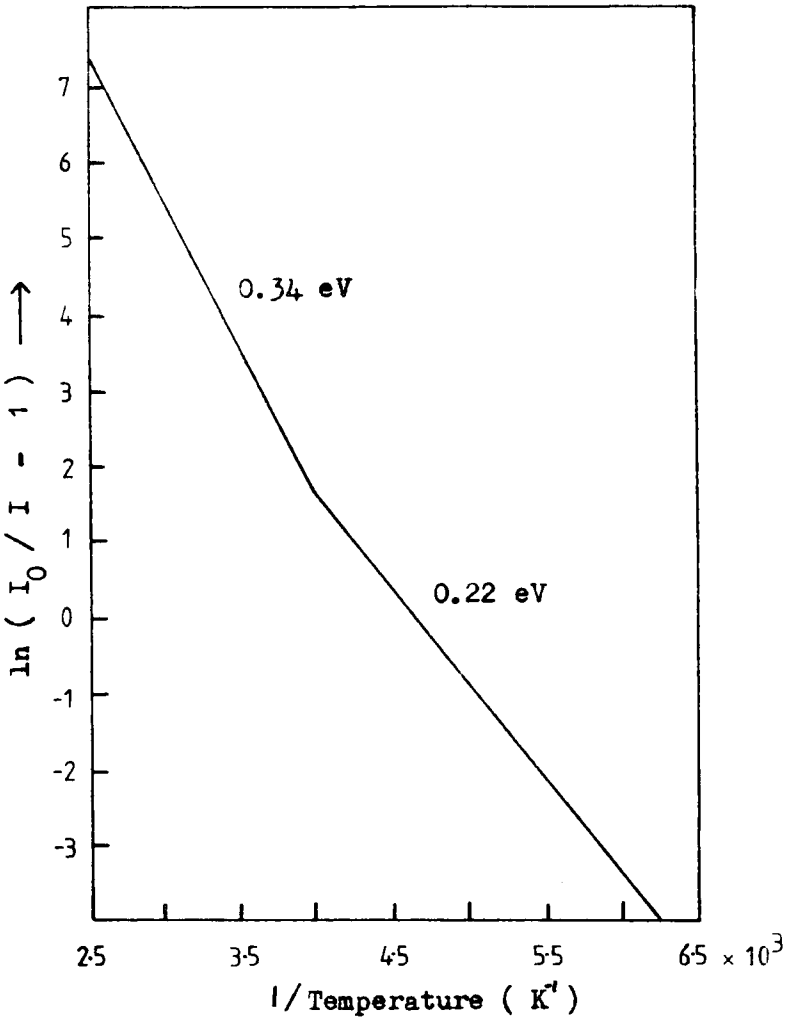

Figure 9.5.4 Temperature dependence of the photoluminescence intensity for crystal C1(NL).

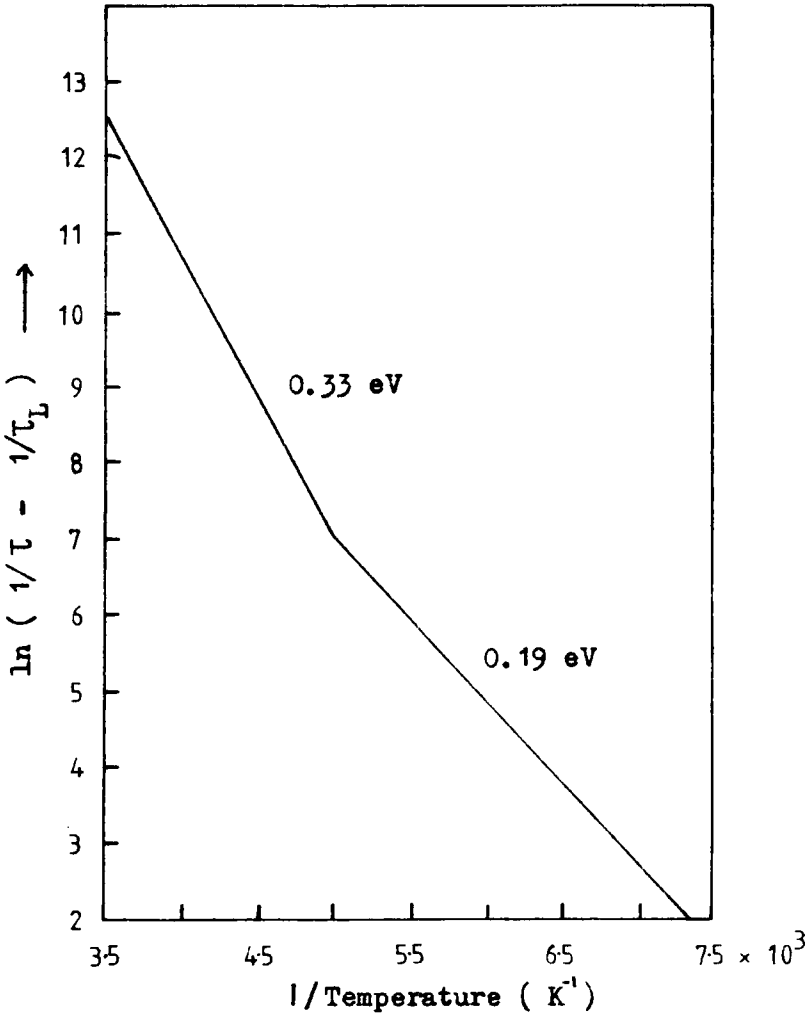

Figure 9.5.5 Temperature dependence of the luminescence lifetime for crystal C1(NL) .

figure 9.6.1 and 9.6.2). Spectrum I is the normal substitutional Cr^{3+} line as established from the hyperfine structure pattern and spectrum II is the Ikebe spectra attributed to the Cr^{3+} ion with an oxygen vacancy in the 2nd coordination sphere.

Sochava et al concluded that the decrease in J_{II} on reduction is caused by the trapping of free electrons by the chromium-vacancy complexes which become available in the reduced crystal due to the ionisation of shallow donors (Frederiske 1961). At first, with weak reduction, the electrons are trapped by low-lying acceptor levels (Ghosh et al 1973), for example Cr^{4+}. After these levels are filled, the electrons begin to fill the levels of the chromium vacancy complexes and this leads to the disappearance of the EPR spectrum II . Sochava et al also diffused molybdenum into TiO_2.Cr crystals. A change in the colour of the crystals as a result of the diffusion indicated reduction of the Cr^{4+} ions (Mirlin et al 1970), while the attenuation of spectrum II showed that the levels of the chromium-vacancy complexes were being partly filled by electrons.

The 1.1 eV absorption spectrum observed by Sochava et al is clearly the structure observed in the Cr doped crystals C1(NL) and C2(NL). However, the absorption spectra did not resolve the two trapping centres, peaks 3 and 8, which are present in the 1.1 eV band. In addition the three low temperature traps, peaks 7,2 and 1, also are very sensitive to the degree of reduction of the rutile crystal (see figure 9.4.7). Although the increase of peak 3 at a quenching temperature of 700°C rather than 500°C for peaks 7,1 and 2 compares well with Sochava's data, the correlation between spectrum J_{II} and the 1.1 eV band may not be as simple and conclusive as it would at first appear. Further investigation of photo-EPR and TSC/TL in TiO_2.Cr at different quenching temperatures is necessary to understand the nature of these trapping centres.

The investigation of the chromium doped rutile crystals has led to a

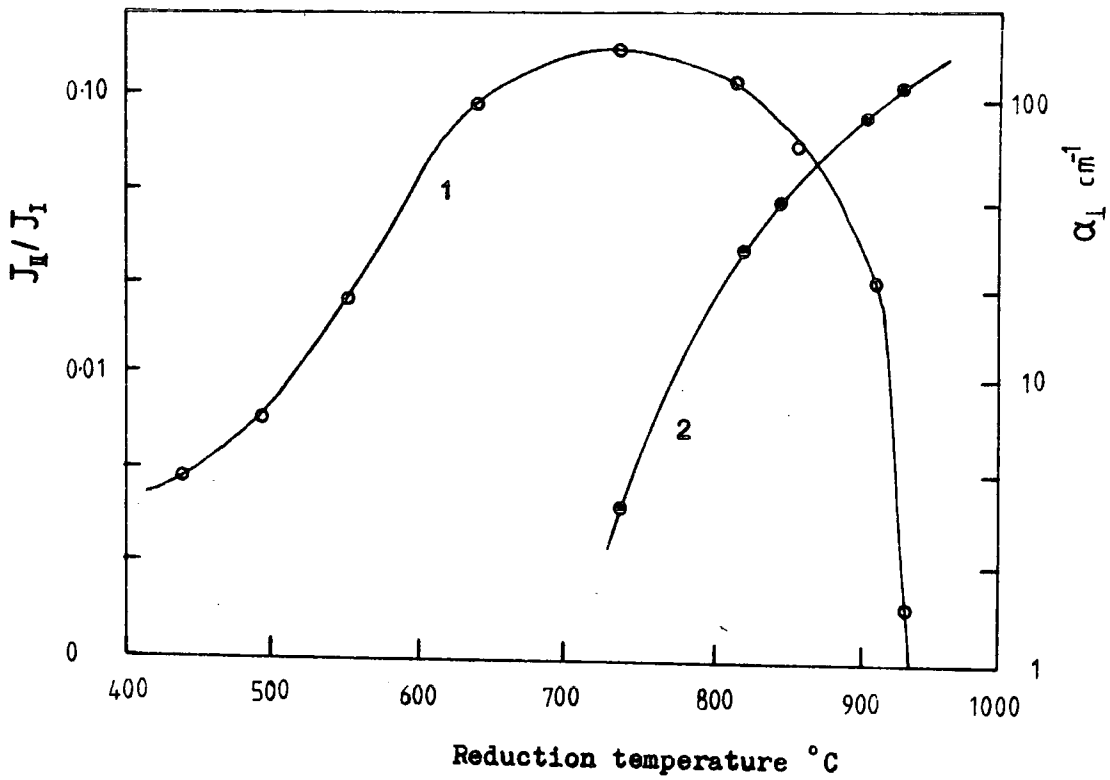

Figure 9.6.1 Dependence of (1) relative intensity of EPR spectrum II and (2) maximum optical absorption coefficient in the 1.1 eV band on the reduction temperature of the TiO_2.Cr crystal (after Sochava et al 1969) .

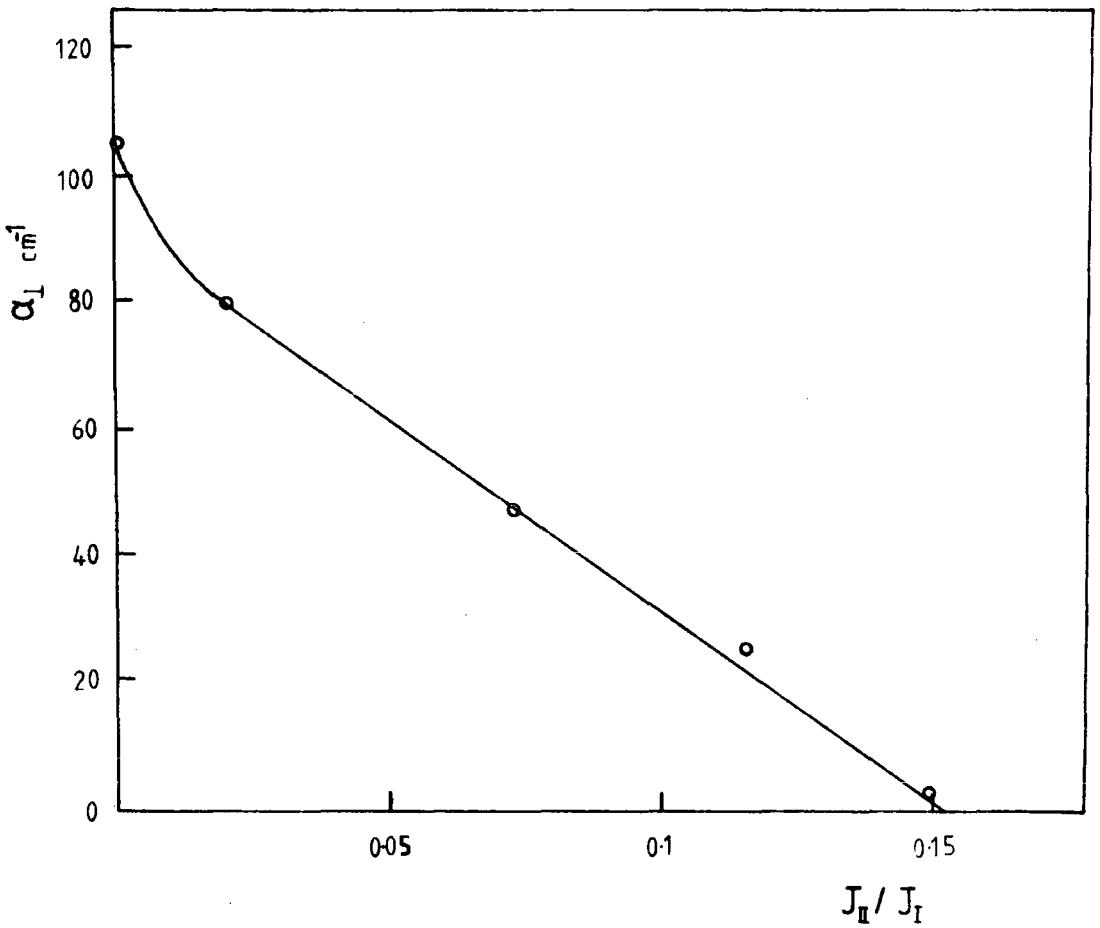

Figure 9.6.2 Relative intensity of EPR spectrum II versus the optical absorption coefficient $\alpha_\perp$ at the maximum of the 1.1 eV band for a TiO_2:Cr crystal (after Sochava et al 1969) .

better understanding of the TSC/TL data presented by Ghosh et al (1973). Comparison of the nominally 'pure' crystals with the spectra presented by Ghosh for his 'undoped' crystals show that peaks 7 and 8 were present in his crystals. In conclusion his crystals presumably had a considerable quantity of unintentional chromium present as an impurity which would have made observation of the TL with an S1 photomultiplier a good deal easier than in nominally 'pure' crystals.

9.7 ELECTRICAL AND OPTICAL PROPERTIES OF TiO_2.Fe

The IR spectra of iron doped rutile show the lattice cut off at 1500 cm^{-1} and the OH vibration absorption line at 3286 cm^{-1}. In the optical spectra at 300 K an absorption line was observed at about 550 nm (see figure 9.2.3). Anderson et al (1973) reported a broad line at 1.93 10^4 cm^{-1} (518 nm) which increased in intensity with increasing concentration of iron and this absorption appeared to be the same centre producing a reddening of the TiO_2.Fe crystals. The reddening of the crystals is probably due to precipitation of iron ions at dislocations (Andersson et al 1974). When rutile is reduced, oxygen deficient lamellae of crystallographic shear planes parallel to (132) and (101) are created (Bursill et al 1969). The former are the so called Wadsley defects with displacement vectors $\frac{1}{2}[011]$ arising from an oxygen deficiency, while the latter ones are the antiphase boundaries with displacement vectors $\frac{1}{2}[101]$.

Rudolph (1959) has shown that rutile doped with 0.2 and 0.02 at % Fe exhibits a transition from n-type to p-type conductivity as a function of partial pressure. The solubility of iron in rutile ranges from 3 at % at 1350°C to 1 at % at 800°C in rutile equilibrated in 1 atm O_2 (Rudolph 1959). Wittke (1966) found that the a and b lattice parameters were unaffected by the addition of 1.5 at % iron. Studies by Webster and Bright (1961) suggest that the solubility of iron was essentially constant between 1 and 10^{-3} atm O_2 , but decreased at reduced pressures. From the available results it does

not appear possible to determine whether iron dissolves substitutionally or interstitially or both. The results of the electrical conductivity studies by Rudolph suggest that substitutionally dissolved iron predominates.

EPR by Gerritsen et al (1963) and Carter et al (1966) have shown that most chromium ions are in the trivalent state at Ti^{4+} sites. It has also been suggested that iron in TiO_2 may also exist in valence states other than 3+. Sandim and Keesom (1969) have pointed out that the iron concentration of vacuum reduced 'pure' rutile measured by a mass spectrometer is much larger than the Fe^{3+} concentration obtained from specific heat data. EPR measurements performed by Purcell and Weeks (1971) on TiO_2 before and after γ irradiation indicate that only a small percentage of the iron present in 'pure' rutile is in the Fe^{3+} state, most being in the Fe^{2+} state. EPR experiments on pure rutile reported by Johnson (1953) also indicate that the Fe^{3+} concentration is diminished on lithium doping (reduction). Faughan and Kiss (1968) explain the photochromism of $SrTiO_3$, a compound which in many respects is similar to TiO_2, by transfer of electrons from Fe^{3+} to Mo^{6+} forming Fe^{4+} and Mo^{5+}, thus proving that Fe^{4+} can also exist. Energy level diagrams proposed to explain the photochromic behaviour in $SrTiO_3$ and TiO_2 are shown below.

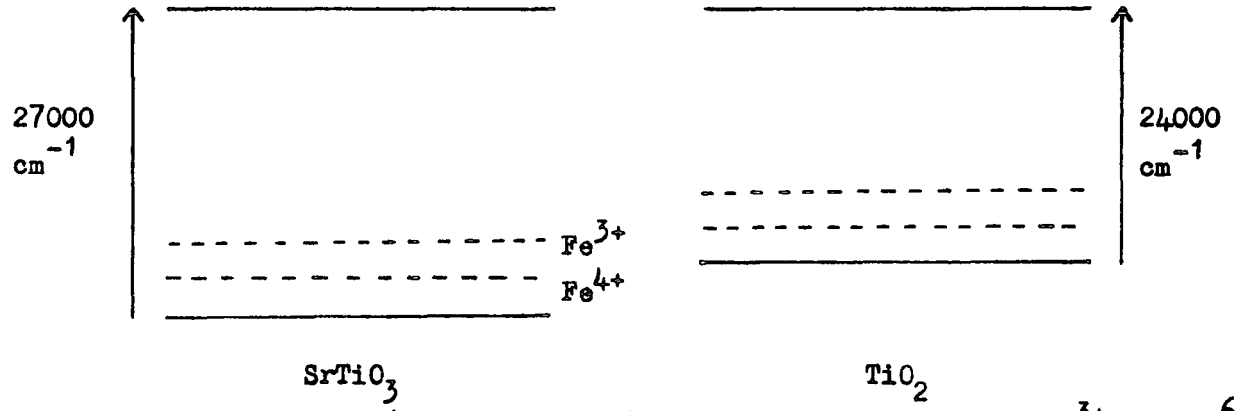

$SrTiO_3$ TiO_2

Before irradiation (0.39-0.43 μm) the ions are present as Fe^{3+} and Mo^{6+}. After irradiation with blue light charge transfer takes place through either valence or conduction band, and Fe^{4+} and Mo^{5+} are created. When a photon is absorbed and an electron in an Fe^{3+} ion is expelled it is converted to Fe^{4+}

and the electron is trapped by Mo^{6+}, or other impurity centres when no Mo is present.

It has already been reported (see figure 9.2.6) that the diffusion of iron into the rutile lattice reduces both the photoconductivity and the photoluminescence by over two orders of magnitude. Figure 9.7.1 shows the TL spectra for crystal FE(NL) before and after iron doping. The decrease in thermoluminescence is accompanied by a drop of more than two and a half orders of magnitude in the intensity of the photoluminescence and the photoconductivity at 77 K. Similar TL spectra were obtained from the yellow, orange and red samples cut from the plasma grown boule BS15 (see figure 9.7.2). These samples showed the same low photoluminescence signal as crystal FE(NL). The temperature dependence of the PL is shown in figure 9.7.3.

Analysis of the TL data for the TiO_2.Fe crystals using the Garlick and Gibson method did not prove successful. Straight lines were not obtained for ln I versus 1/T plots for the initial rise. It is difficult to offer any physical interpretation of this effect because of the problems of measuring the low intensity TL signals. Similar problems were encountered with the heating rate methods and only a limited number of data points were obtained because at low heating rates the TL signal was lost in the system noise. A summary of the trap depths obtained is given in table 9.7.4. Although no activation energies were obtained there was evidence at different heating rates to suggest that the 110 K peak was in fact two trapping peaks, possibly peaks 1 and 2 seen in 'pure' crystals. In fact it seems that the peaks at 172 K, 202 K and 236 K are those numbered 3, 8 and 4, all seen previously in the Cr doped crystals.

Investigation of the photoluminescence emission and excitation spectra of the Fe doped crystals showed the same characteristic 850 nm emission from the Cr^{3+} centre as observed in nominally 'pure' crystals. Therefore, it

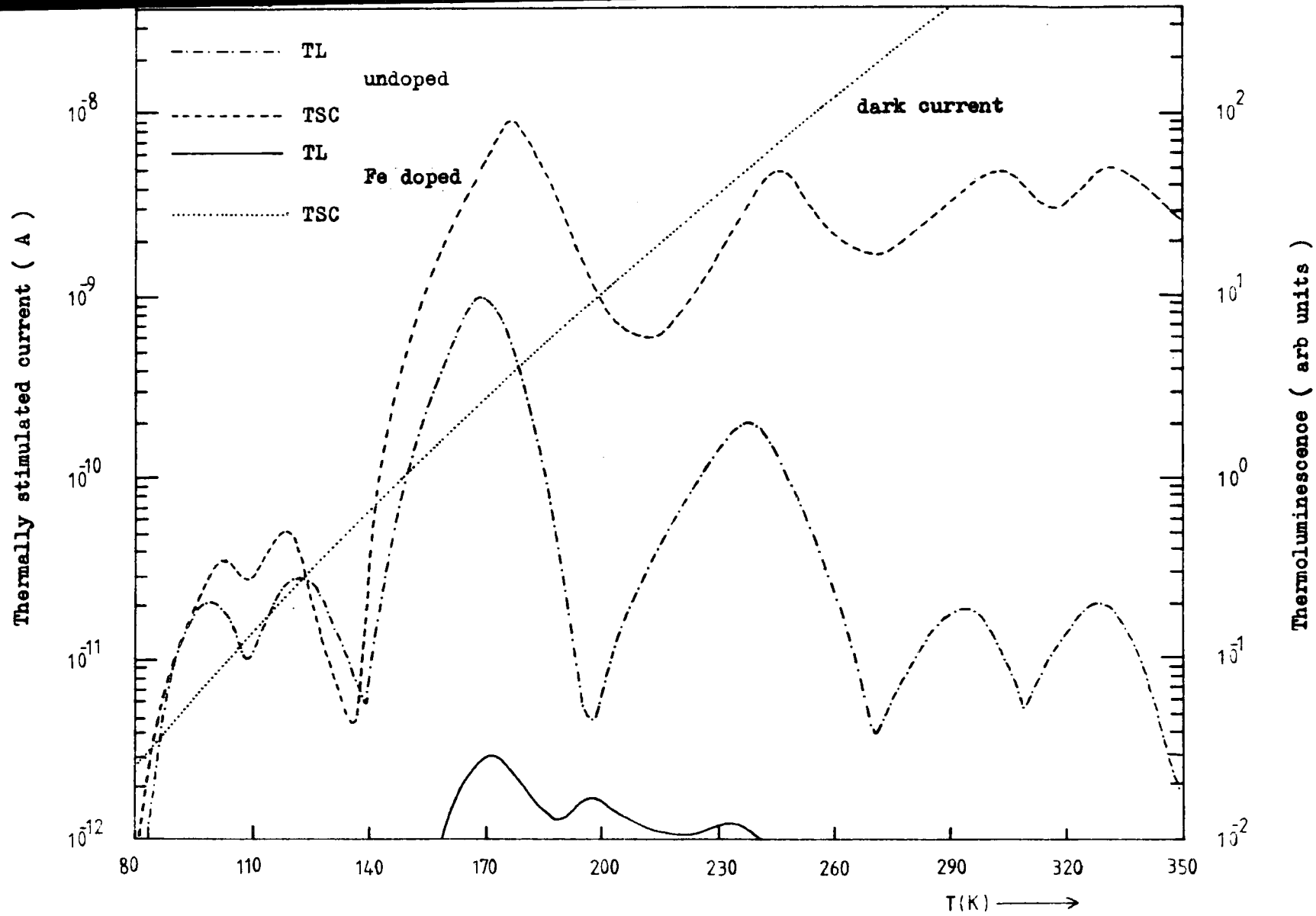

Figure 9.7.1 Comparison of the TSC and TL spectra for crystal FE(NL) before and after Fe doping .

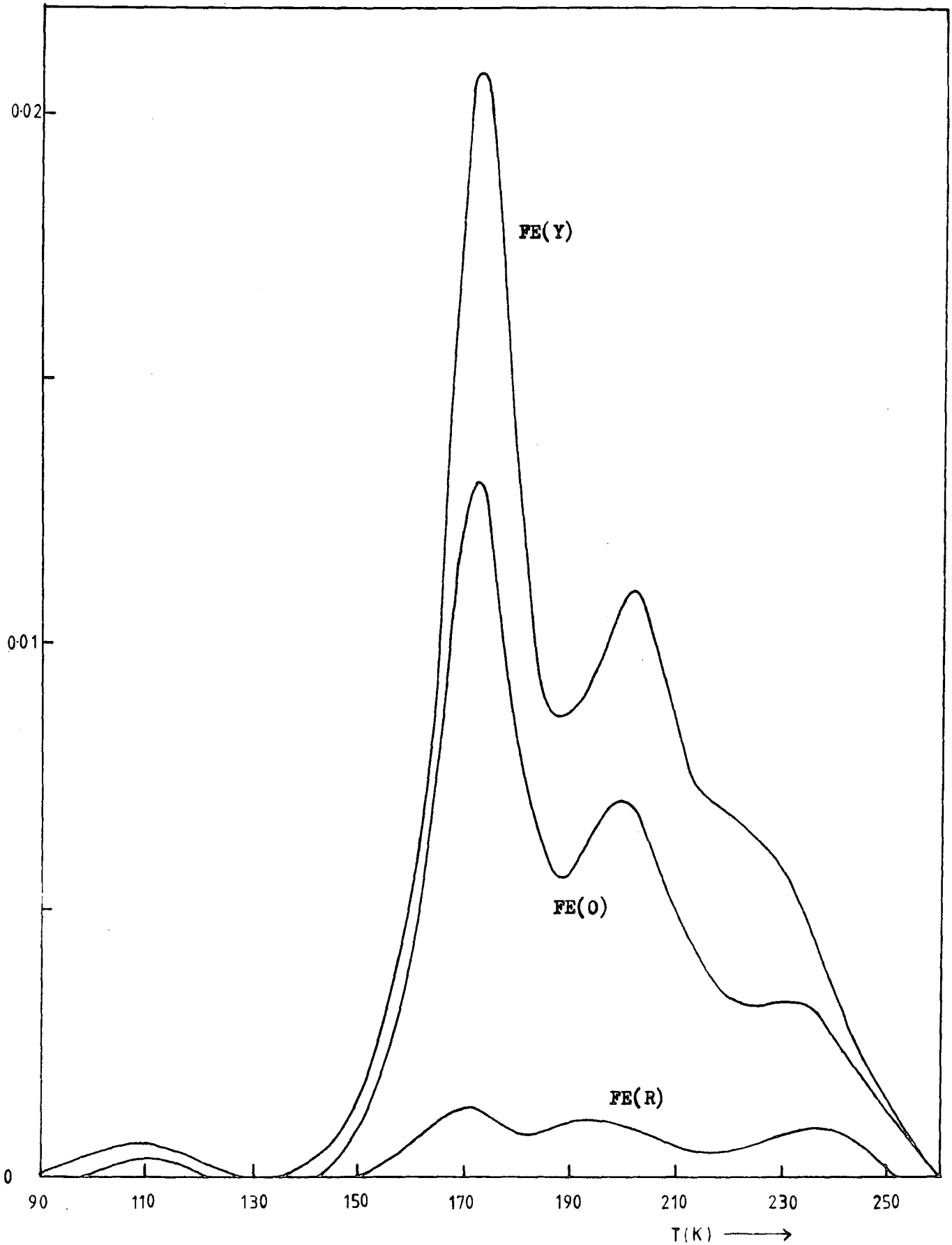

Figure 9.7.2 Thermoluminescence spectra for three samples cut from the iron doped plasma grown boule BS15 .

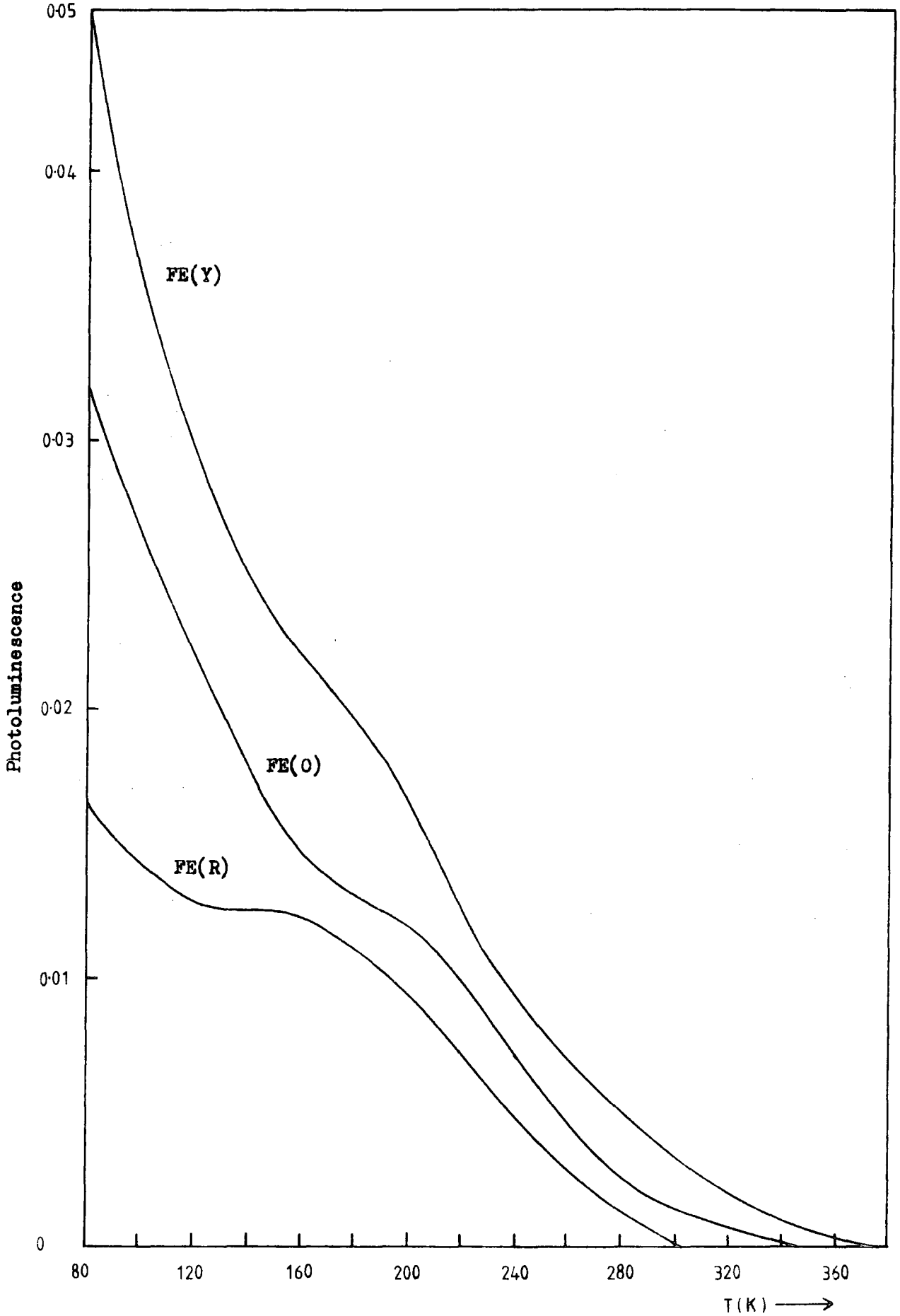

Figure 9.7.3 Photoluminescence versus temperature curves for three samples cut from the iron doped plasma grown boule BS15 .

TL PEAK		110 K	172 K	202 K	236 K
Hoogenstraaten	Y	-	0.37±0.03	0.42±0.04	0.56±0.04
	O	-	0.37±0.03	0.38±0.04	0.51±0.04
	R	-	0.34±0.04	0.39±0.06	0.55±0.03
Haering, Adams	Y	-	0.34±0.03	0.42±0.04	0.62±0.04
	O	-	0.34±0.03	0.43±0.03	0.58±0.03
	R	-	0.39±0.04	0.41±0.04	0.57±0.04
Chen, Winer	Y	-	0.37±0.02	0.44±0.03	0.54±0.02
	O	-	0.34±0.02	0.46±0.04	0.55±0.03
	R	-	0.34±0.02	0.42±0.04	0.51±0.02

Table 9.7.4 Summary of the trap depths obtained from TL data for crystals FE(Y), FE(O) and FE(R) .

appears that Fe acts as a recombination centre in the rutile lattice with a large electron capture cross-section compared to Cr^{3+} centre, and which provides an efficient recombination route for carriers that are excited into the conduction band. This also provides an explanation for the reduced photoconductivity in Fe doped rutile. It is difficult to explain the shape of the temperature dependence of the PL in these crystals although it would appear that the efficiency of the Fe centre changes with increasing temperature.

TSC spectra were not measured in the TiO_2.Fe samples due to the high dark current induced by the Fe dopant. It would normally be expected that the dark current should decrease rather than increase on the introduction of a recombination centre with a large capture cross section. This effect warrants further investigation, but it would appear that Fe doping introduces compensating and non-compensating defects into the rutile lattice. The formation of Fe precipitates, the investigation of the conductivity type and the mobility in TiO_2.Fe crystals would all be interesting subjects for further investigation.

9.8 DEEP LEVELS IN TiO_2.Fe

Since in rutile iron and chromium substitute for Ti^{4+} primarily as Fe^{3+} and Cr^{3+}, respectively, a charge compensation mechanism must be present. As already mentioned oxygen vacancies (Vo-centres) and Ti^{3+} interstitials have been proposed as the most probable compensators. Also, other positive interstitial ions such as H^+ may also compensate the charge.

In this context it is interesting to discuss briefly how the charge compensation mechanisms work. Let us first assume the crystal lattice to be absolutely perfect except for some titanium ions that are replaced by chromium or iron ions. In that event, the iron and chromium ions must have the valence state +4 since the crystal must be microscopically as well as macroscopically neutral. However, the crystal prefers to convert the Fe^{4+}

and Cr^{4+} to Fe^{3+} and Cr^{3+}, respectively, and this can be done in various ways. (A) Oxygen vacancies could be created and the oxygen ions would diffuse to the surface where they would leave the crystal as neutral oxygen atoms. Hence, positive holes (2+) would be created at the oxygen vacancies and two electrons ($2e^-$) would be released. Each oxygen vacancy would then convert two Fe^{4+} ions to Fe^{3+} ions and charge compensate for two Fe^{3+} ions.

(B) Interstitial ions might be created by diffusion of neutral titanium atoms which would occupy interstitial sites as Ti^{4+} (or Ti^{3+}). Hence, four (three) electrons are released and each interstitial Ti^{4+} (Ti^{3+}) ion would convert four (three) Fe^{4+} ions acting as a charge compensating centre.

Notice that upon diffusion doping of neutral iron into a perfect TiO_2 single crystal, Ti^{4+} substitutional ions are converted to Ti^{4+} (Ti^{3+}) interstitial ions when Ti^{4+} is substituted for Fe^{3+}. Some Ti^{4+} may then stay as interstitial ions and act as charge compensating centres while some Ti^{4+} ions may diffuse to the surface of the crystal and build another layer of TiO_2 unit cells. If Ti^{4+} interstitials were the only charge compensating centres for Fe^{3+} substitutional ions, $\frac{1}{4}$ of the substitutional Ti^{4+} ions should stay within the crystal as interstitial ions.

Anderson et al (1973) found three extra spectra in addition to the main Fe^{3+} spectrum reported by Carter and Okaya (1966). They found that one spectrum (spectrum I) is caused by Fe^{3+} substitutional ions at a $(\frac{1}{2},\frac{1}{2},\frac{1}{2})$ site with one proton approximately at the $(\frac{1}{2},0,0)$ site and equivalent interstitial sites. For each spectrum I complex, there is 'one' hydrogen electron available for converting a Fe^{4+} ion to a Fe^{3+} ion and the proton may charge compensate for one Fe^{3+} ion. Hence, the Fe^{3+} ions may be considered as locally charge compensated. Another spectrum (spectrum II) is associated with Fe^{3+} substitutional ions with one nearest neighbour oxygen vacancy (Fe^{3+}-V_O centres). Therefore $2N_{II}$ electrons and $2N_{II}$ positive charges associated with spectrum II are available for charge conversion

($Fe^{4+} \rightarrow Fe^{3+}$) and charge compensation, respectively. The origin of the third spectrum (spectrum III) is not firmly established. Its dependence upon heat treatment and iron concentration and the few data on symmetry properties indicate it is associated with Fe^{3+} substitutional ions with Ti^{3+} nearby. A similar behaviour has been found for Co^{2+} ions associated with Ti^{4+} in rutile (Miyako 1971). Andersson et al (1973) also suggested a charge compensation mechanism which behaves as if it involved charged dislocations. These defects not only act as charge compensation centres, but also as traps for iron and the formation of iron precipitates.

9.9 ELECTRICAL AND OPTICAL PROPERTIES OF TiO_2.Ni

The nickel diffusion doped crystal NI(NL) was deep orange in colour and similar in appearance to sample FE(O), but all other properties of these two crystals were different in most respects. As can be observed from figure 9.2.6 the introduction of nickel into the rutile lattice had minimal effect on the photoconductivity or photoluminescence intensity.

The temperature dependence of both the PL and PC show little change from the 'undoped' crystals indicating that the same shallow trapping centres present in the 'undoped' crystals dominated the electronic properties of these crystals. The spectral response of the PC and the excitation spectra of the PL in TiO_2.Ni (see figure 9.9.1) show the characteristic response near 3 eV. However, the sub band gap spectra in both PL and PC indicate the presence of deep levels which were introduced as a direct consequence of the nickel doping.

The TSC and TL spectra for the NI(NL) crystal are shown in figure 9.9.2 before and after nickel doping. There was little change in the TL spectra or in the activation energies obtained using the standard analytical techniques described previously. The observation of TSC for the nickel doped crystal was obscurred by the presence of a large dark current.

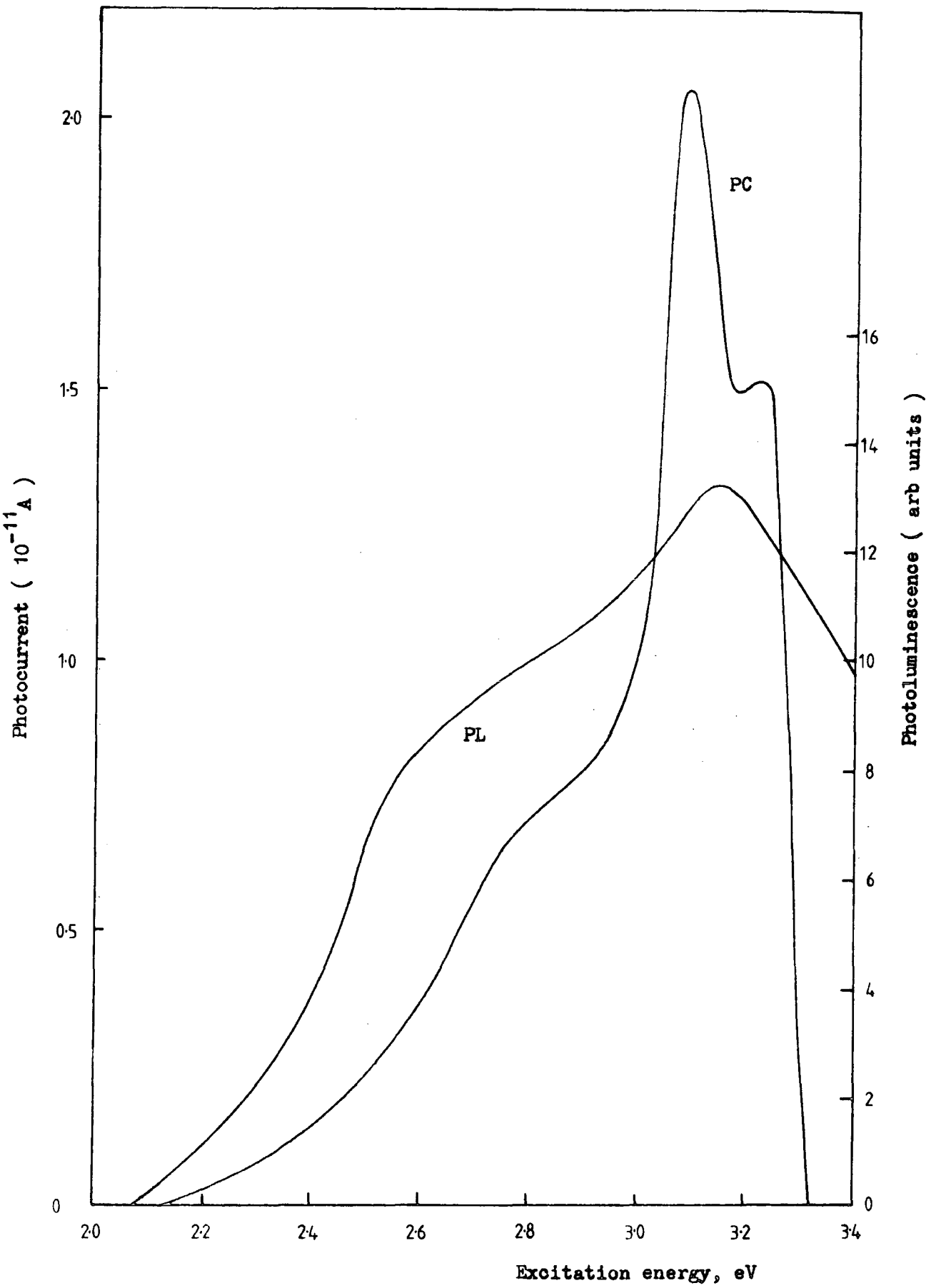

Figure 9.9.1 PC spectral response and PL excitation spectra for the TiO_2.Ni crystal NI(NL) at 77K .

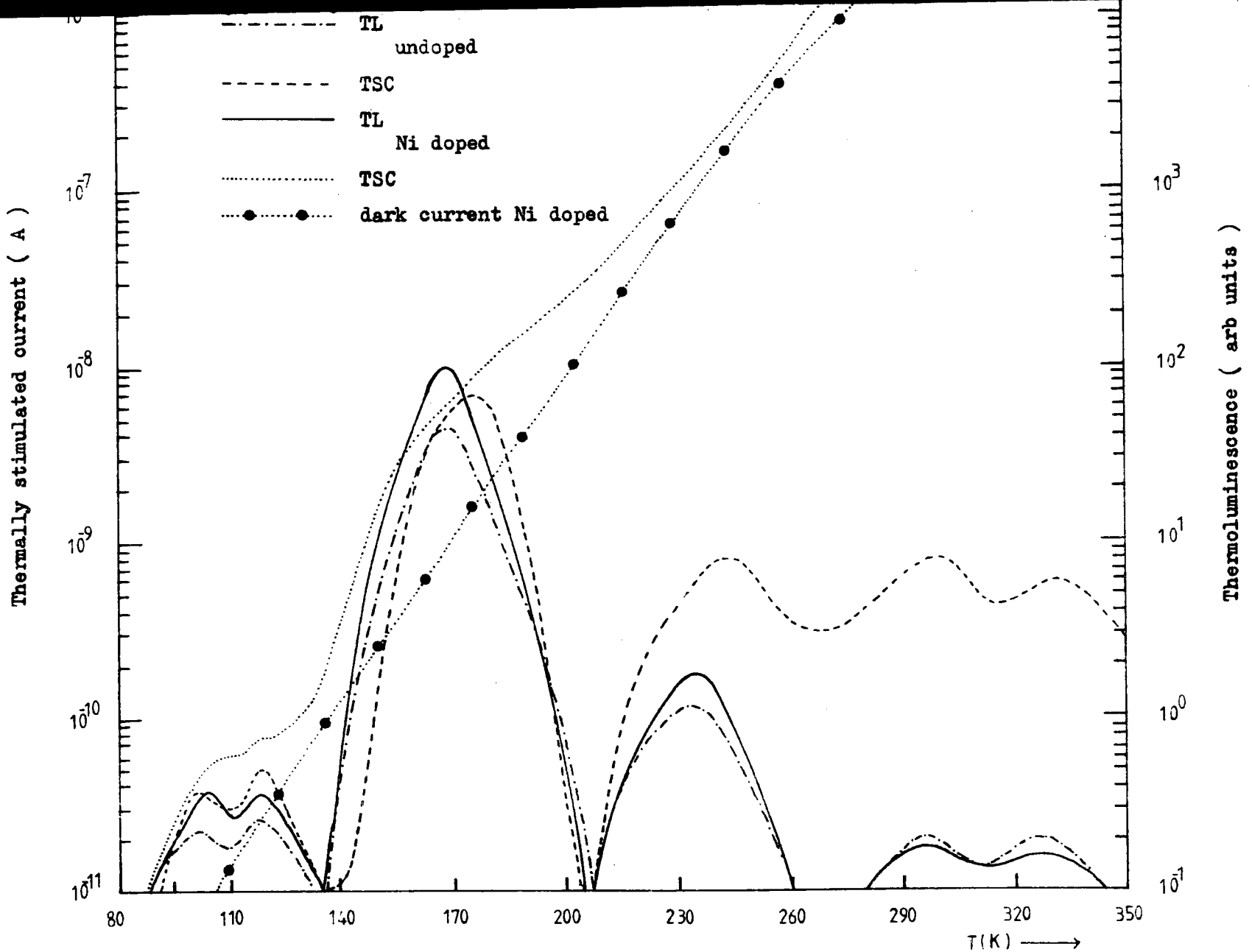

Figure 9.9.2 TSC and TL spectra for the TiO_2.Ni crystal NI(NL) before and after nickel diffusion.

After thermal quenching from 600 °C the shallow traps increased in magnitude and another TL peak appeared at 88 K (see figure 9.9.3). This TL peak had an activation energy of 0.16 ± 0.02 eV and an estimated capture cross section of 10^{-18} cm^2. It is believed that this centre is the peak 7 observed in chromium doped crystals. The TSC spectra of the quenched crystal was completely obliterated by the dark current.

In summary, nickel doping does not introduce any significant change in the shallow trap densities. It does, however, introduce deep levels near the valence band. If nickel does introduce a deep level into the rutile band gap it must have a small capture cross section for electrons and holes compared with the dominant centres already present in the nominally 'pure' crystals.

9.10 DEEP LEVELS IN TiO_2.Ni

Gerritsen et al (1963) have shown that the majority of nickel in rutile is in the divalent state and the ions occupy interstitial positions. In the RCA crystals they investigated containing 0.01 at % nickel, 80 ppma was Ni^{2+}, 5 ppma Ni^{3+} and 2 ppma was a light generated spectrum.

When Gerritsen et al (1963) illuminated the crystal at room temperature and immediately cooled it to 77 K they found another narrow line spectrum in addition to the Ni^{3+} spectrum. This spectrum is referred to as the 'light generated nickel'. With sufficient illumination, this spectrum can be made to have an intensity comparable to that of the Ni^{3+}. The same effect was found using unfiltered tungsten light or with a filter that cut off at wavelengths shorter than 5000 Å. This means that band gap radiation did not cause this phenomenon, but rather light of much longer wavelength.

9.11 ELECTRICAL AND OPTICAL PROPERTIES OF TiO_2.Co

The IR spectra of cobalt doped rutile showed the lattice cut off at 1500

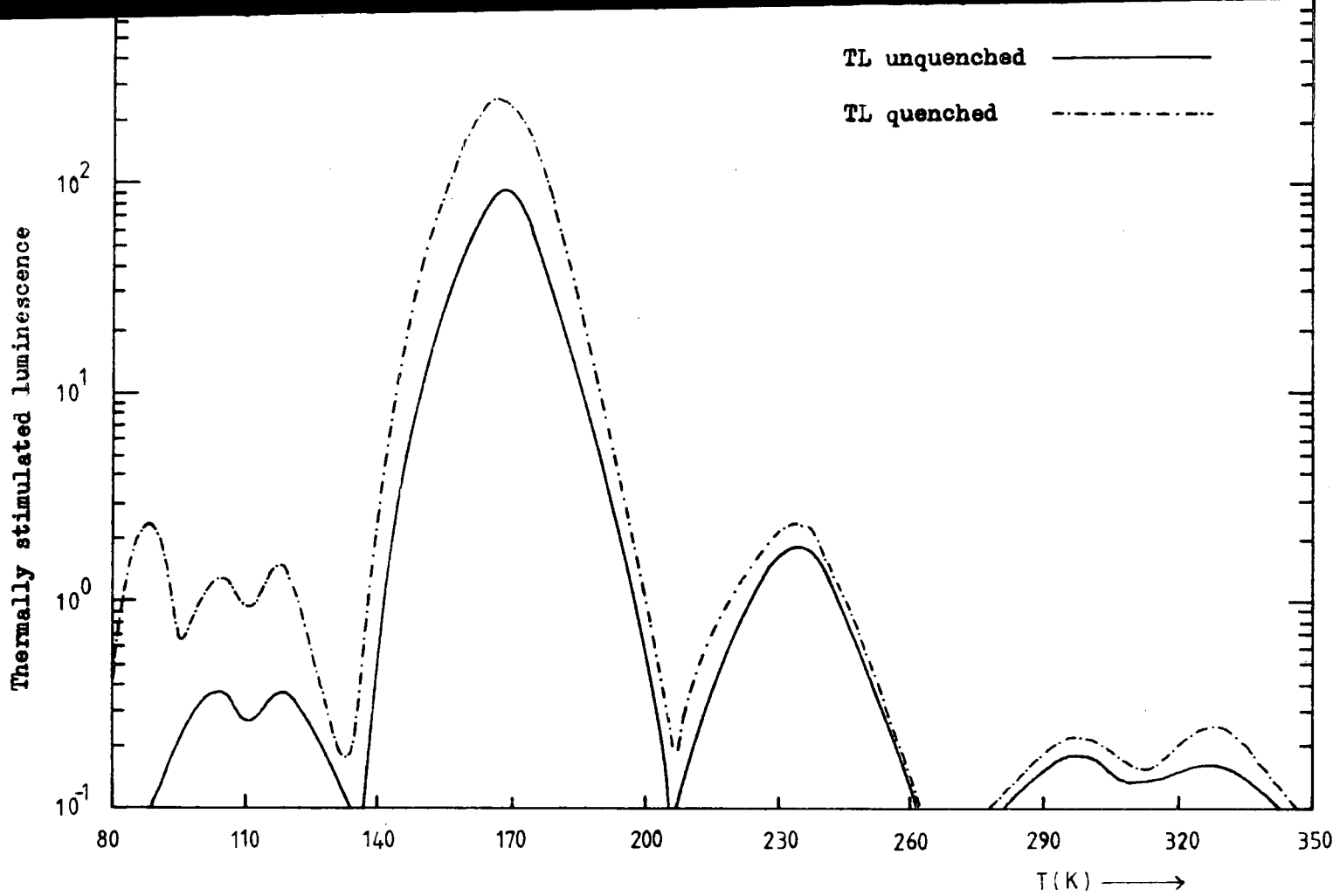

Figure 9.9.3 TL spectra for the TiO_2.Ni crystal NI(NL) before and after thermal quenching at 600 °C .

cm^{-1} and an OH vibration absorption at 3286 cm^{-1}. In the optical absorption spectrum at room temperature two absorption lines were apparent at 2.0 eV and 2.5 eV with strong absorption near the 3 eV band edge (see figure 9.2.2). The crystal CO(NL) appeared dark green in colour after cobalt diffusion and subsequent oxidation.

Both the PC and PL of CO(NL) showed a decrease after cobalt diffusion (see figure 9.2.6). Figure 9.11.1 shows the PC spectral response and the PL excitation spectrum for CO(NL). Again the characteristic absorption at 3 eV was observed but sub-band gap structure appeared in the PL and PC spectra. The 2.7 eV peak in the PC spectrum was particularly well defined and was still present at 400 K.

The TSC and TL spectra for crystal CO(NL) before and after cobalt doping are shown in figure 9.11.2. The magnitude of both the TL and TSC were reduced after doping and a new peak at 200 K appeared. Table 9.11.4 shows a summary of the data obtained from the TSC analysis of the CO(NL) crystal. The peak at 200 K had an activation energy of 0.42 ± 0.03 eV and a cross section of 10^{-18} cm^2 which appears to be the same centre 8 observed in Cr doped crystals. Trap densities were estimated from the lifetime obtained from photoconductive gain measurements and mobilities for 'undoped' crystals were used. On thermal quenching from 600 °C the concentrations of the shallow traps increased by about an order of magnitude but no extra trapping centres were observed.

In conclusion, it appears that cobalt acts as a fast recombination centre in the rutile lattice. Although no mass spectrographic analysis was performed on these crystals it would appear that the cobalt centre is not as efficient as the Fe centre but drastically reduces the free carrier lifetime. This reduction is observed in PC, PL, TSC and TL experiments. Cobalt doping also introduces centre 8, seen previously in Fe and Cr doped crystals, into the rutile lattice.

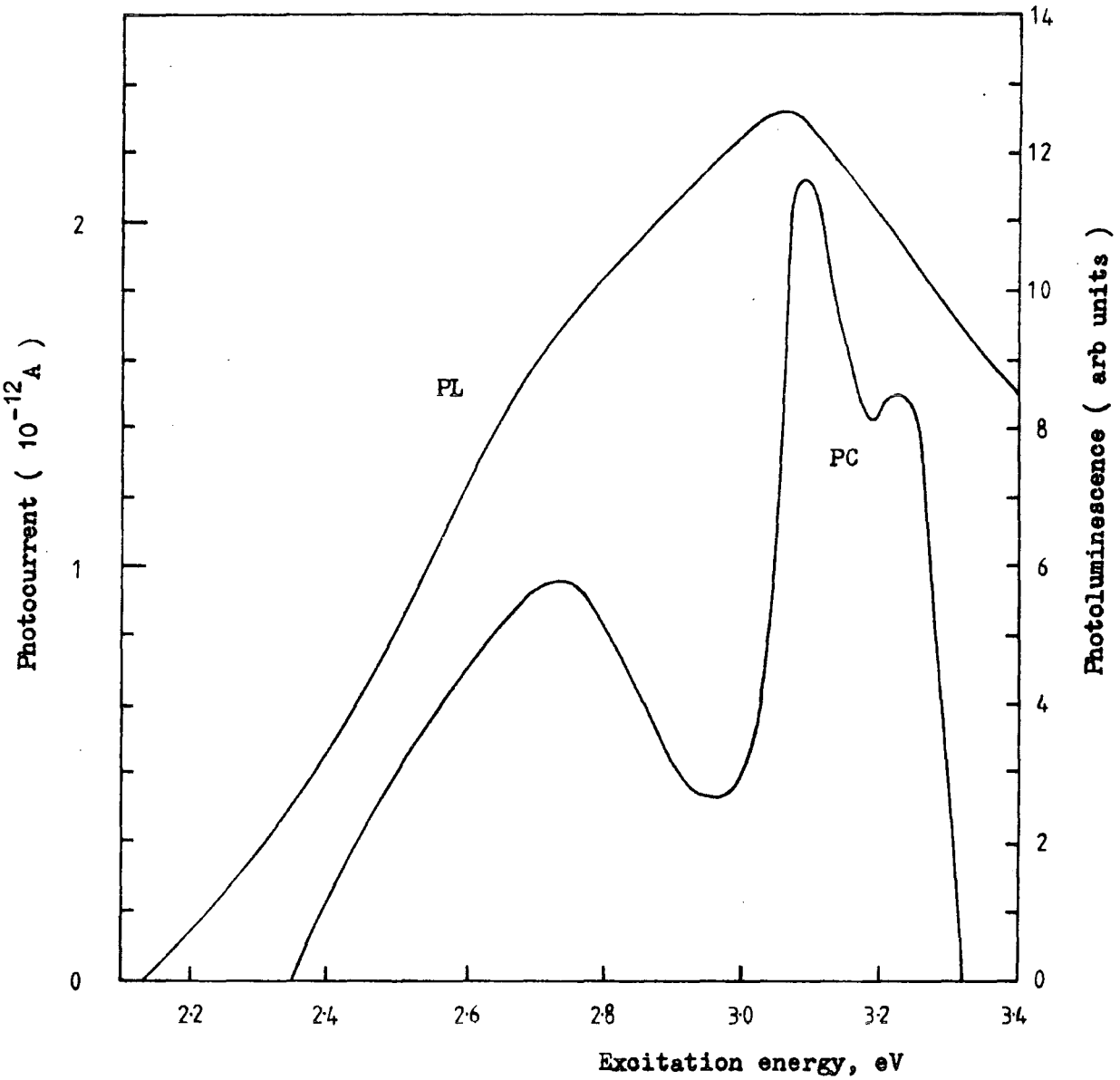

Figure 9.11.1 PC spectral response and PL excitation spectrum for cobalt doped crystal CO(NL) at 77K (after spectral correction).

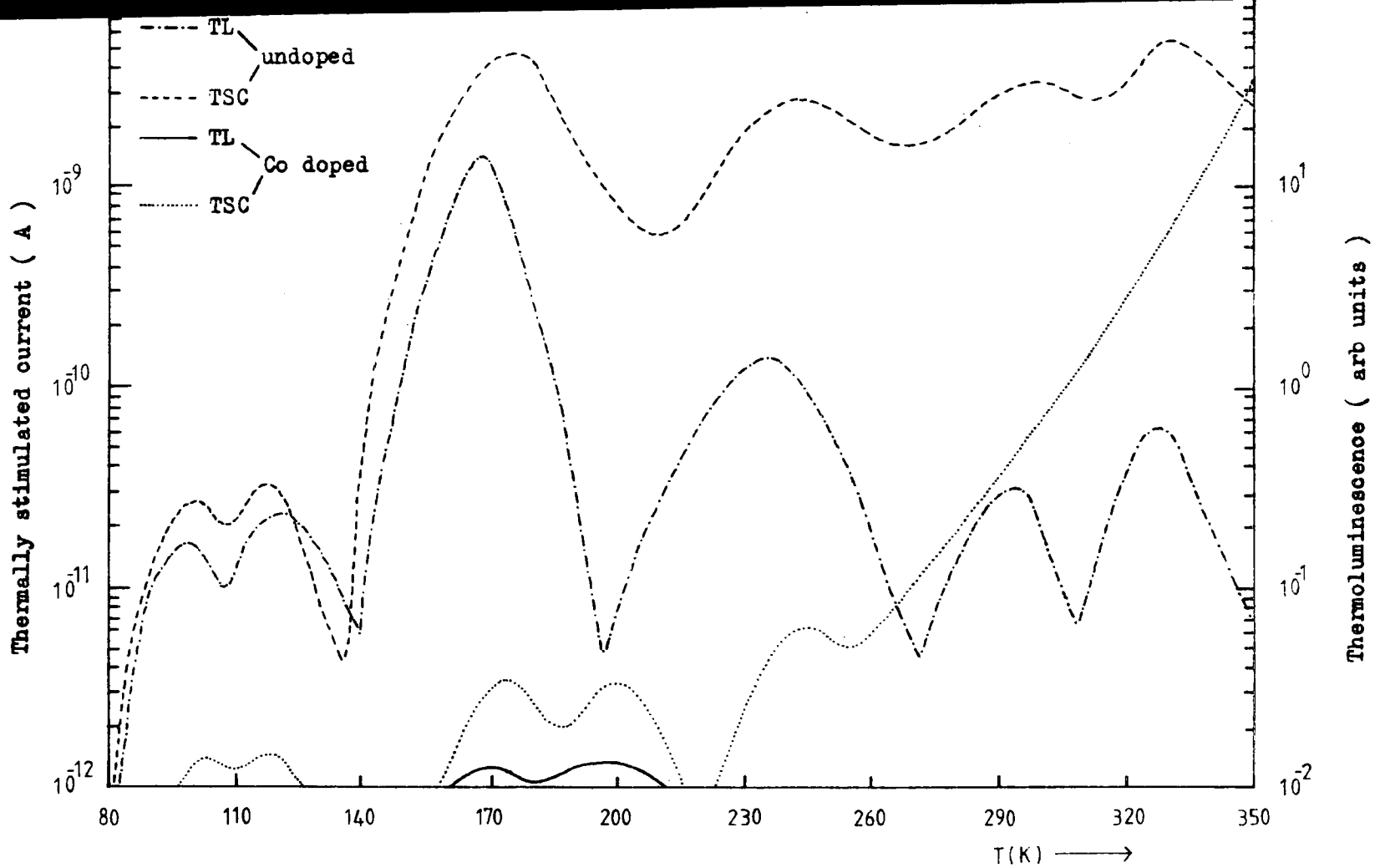

Figure 9.11.2 Comparison of the TSC and TL spectra for crystal CO(NL) before and after cobalt diffusion .

PEAK NO.	1	2	3	8	4	5	6
UNDOPED	$4\ 10^{14}$	$5\ 10^{14}$	$2\ 10^{17}$	-	$6\ 10^{16}$	$7\ 10^{16}$	$6\ 10^{16}$
CO(NL)	$2\ 10^{14}$	$3\ 10^{14}$	$5\ 10^{15}$	$5\ 10^{15}$	$1\ 10^{15}$	?	?

Table 9.11.4 Comparison of trap densities (cm^{-3}) before and after cobalt doping for crystal CO(NL). Data taken from TSC curves .

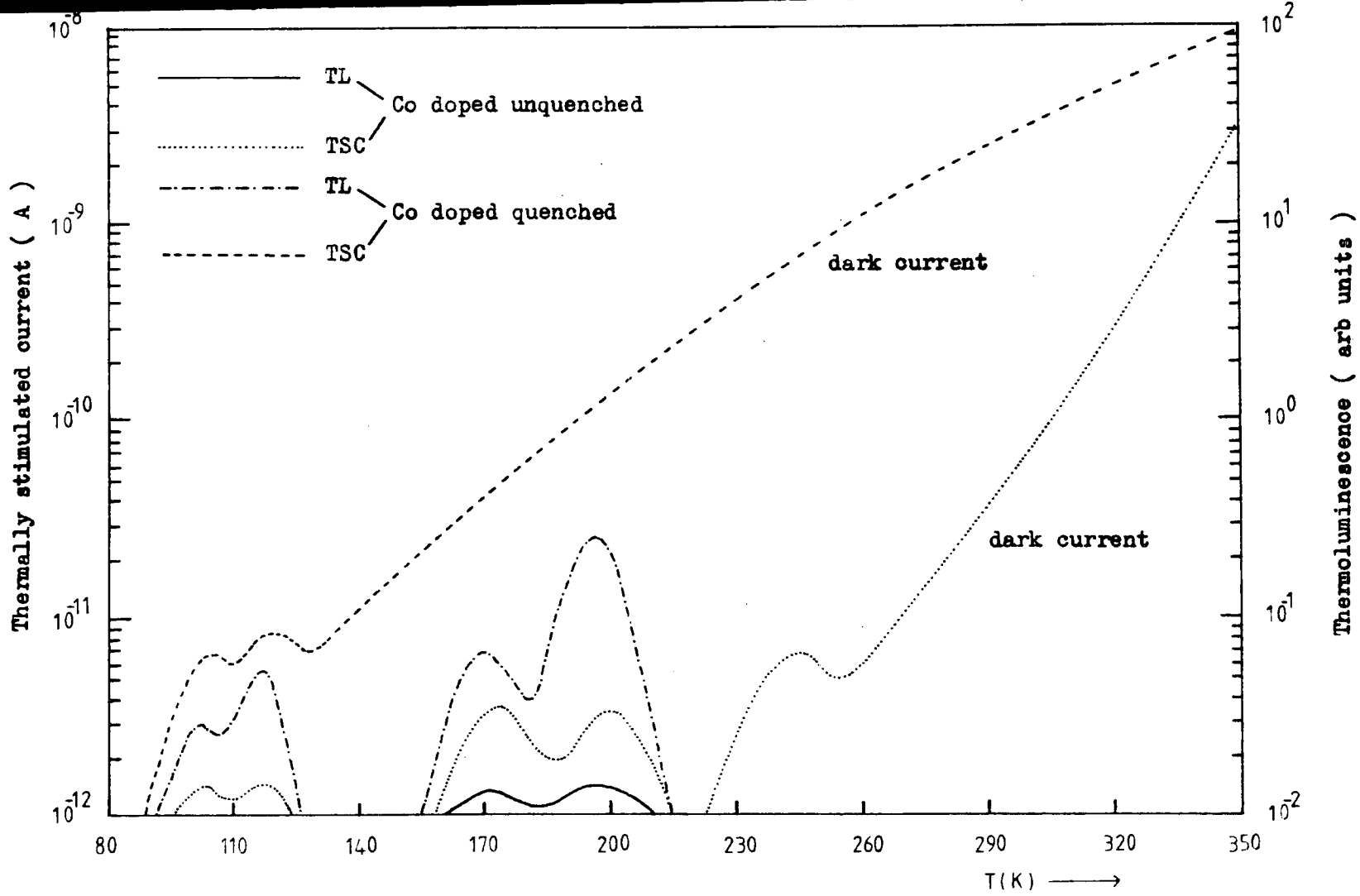

Figure 9.11.3 Comparison of the TSC and TL spectra for crystal CO(NL) before and after thermal quenching at 600°C .

9.12 DEEP LEVELS IN TiO_2. Co

Miyako (1967) has shown using ESR that Co^{2+} substitutes for Ti^{4+} in the rutile lattice. Two groups of weak signals were observed apart from the strong signals associated with substitutional Co^{2+} (Miyako 1971), and these were denoted as GI and G II.

GI was determined as the complex which was composed of the substitutional Co^{2+} ion combined with the second nearest neighbour oxygen vacancy (Miyako and Kazumata 1971). After ENDOR experiments Miyako (1967) concluded that G II represents a Co^{2+} ion that has substituted into a regular Ti^{4+} site and couples with defects at interstitial positions which are in fact Ti^{4+} ions.

It is known that the cobalt ion substitutes into the regular Ti^{4+} sites as Co^{2+}. To satisfy charge neutrality in rutile containing cobalt, an oxygen vacancy is produced in the second co-ordination sphere or an excess cation is introduced in an interstitial position. In 'nearly' stoichiometric rutile, lack of positive charge seems to be compensated preferably by interstitial Ti^{4+} rather than by oxygen vacancies. This follows from a comparison of the magnitudes of GI and G II (see figure 9.12.1).

Johnson et al (1968) have studied the optical spectra of various OH complexes in rutile as a function of impurity concentration. They have suggested that the H^+ occupies sites in the basal plane displaced somewhat from $(\frac{1}{2},0,0)$ and can associate with three subsitutional cations. The complex Co^{2+} - OH seems more probable than the complex Co^{2+} - Ti^{4+}, because the radius of the proton is much smaller than that of Ti^{4+}. Miyako (1967) et al tried to find an ENDOR signal due to the hyperfine interaction with a proton in rutile with a cobalt ion, but they could not detect a signal.

An interesting experiment would be to repeat the oxidation reduction experiment (see figure 9.12.1) and examine to TSC/TL spectra in the same crystals.

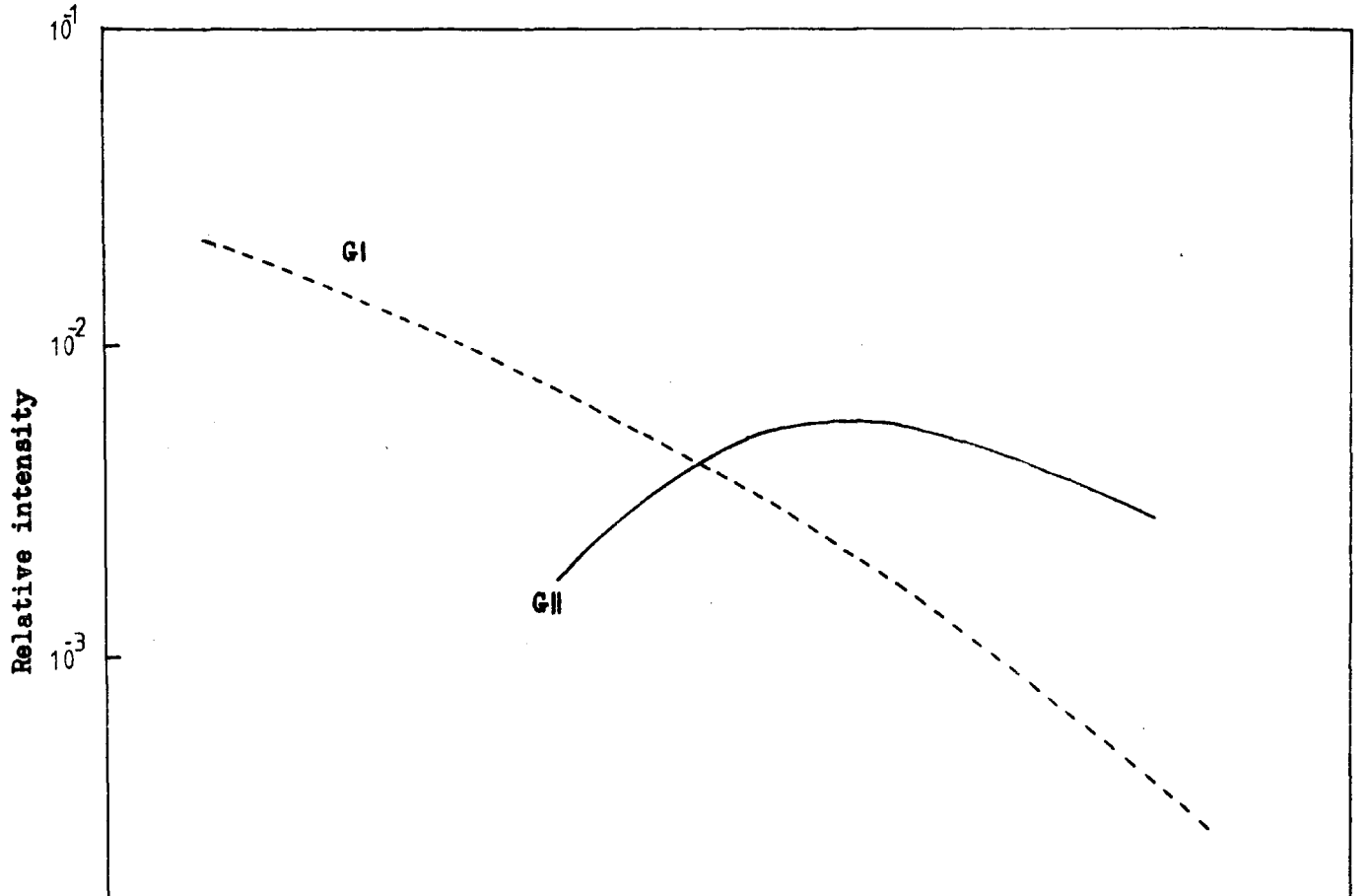

Figure 9.12.1 The change of the ESR absorption intensity for GII compared with the substitutional Co^{2+} line as a function of the times of annealing (oxidation) for the sample which was reduced in the vacuum of $10^{-2} \sim 10^{-3}$ torr at 800°C for 30 minutes (after Miyako 1971) .

9.13 ELECTRICAL AND OPTICAL PROPERTIES OF TiO_2.Mn

Crystal MN(NL) doped with manganese had a light brown colour after growth and a yellow brown appearance after post-growth oxidation. The room temperature optical spectra shown in figure 9.2.2 indicated absorption bands at 2.2 eV and 2.7 eV with strong absorption in the region of the band edge.

The PL intensity in MN(NL) shows over an order of magnitude decrease after manganese doping indicating that a recombination centre has been introduced which is considerably faster than the Cr^{3+} luminescence centre. The PC intensity was only reduced by a factor of two indicating that the dominant recombination centres present in the 'pure' crystal were still controlling the free carrier lifetime. The curves in figure 9.13.1 show some structure in the PC spectral response and PL excitation spectra at about 2.7 eV but they are dominated by the 3 eV band edge structure.

TL spectra for the TiO_2.Mn crystal MN(NL) before and after manganese diffusion are shown in figure 9.13.2. The decrease in the magnitudes of peaks 1 and 2 is a consequence of the reduction in luminescence efficiency of the Cr^{3+} centre due to additional competition from Mn recombination centres. The magnitude of peak 3 in the doped crystal MN(NL) cannot be fully explained by a change of lifetime and it would appear that the density of traps associated with this peak is actually reduced. On thermal quenching, see figure 9.13.3, there is a small increase in the densities of the shallow traps but no new centres appear.

The TSC spectra for the MN(NL) crystal were not investigated because of the high dark current. However, an interesting phenomenon was observed whilst attempting to measure the TSC spectra. After cooling to 77 K the sample was illuminated with a 250 W compact mercury source using an OX1 Chance glass filter and 10% copper sulphate solution. The sample was then placed in the dark and a large dark current was now present. This dark current remained

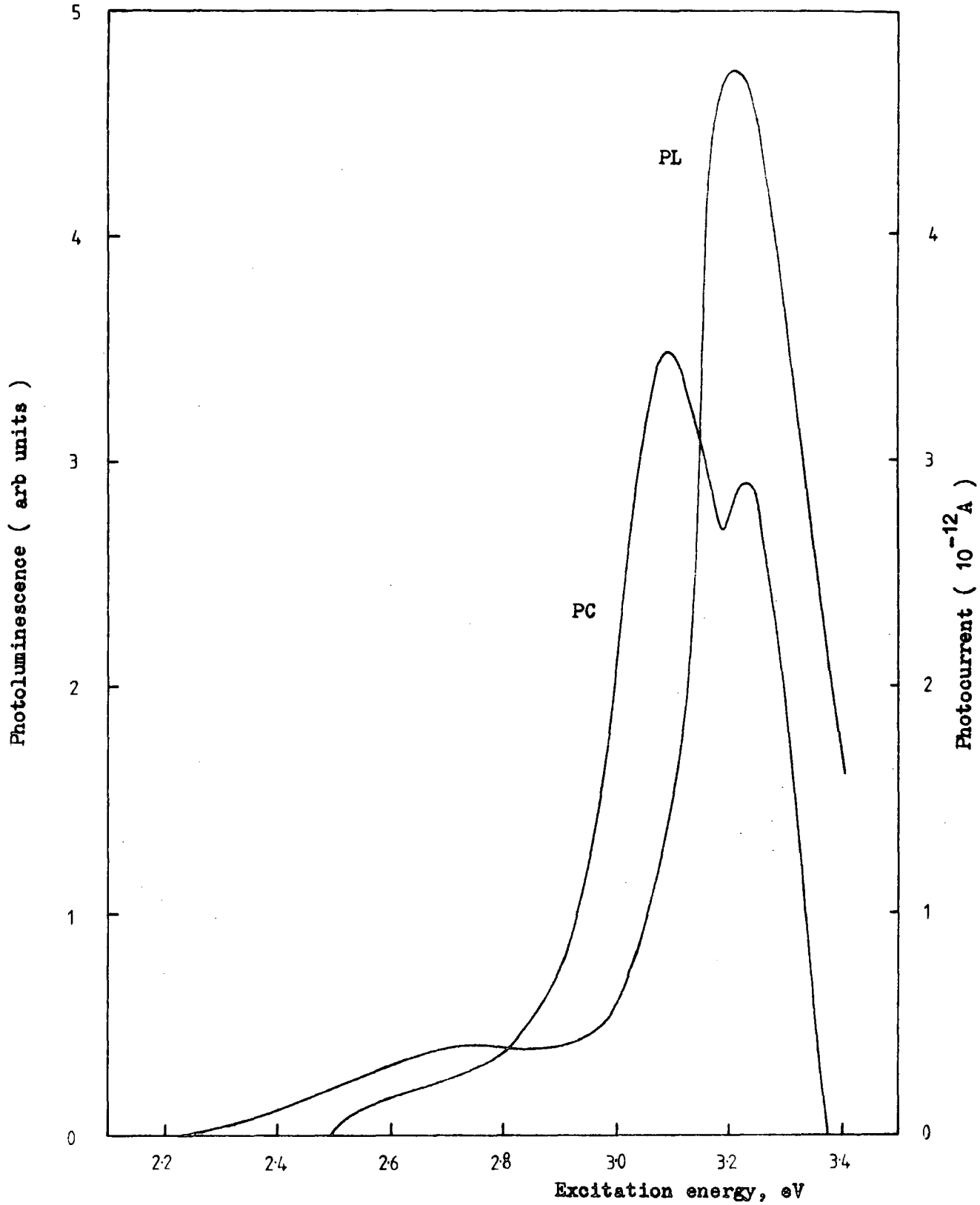

Figure 9.13.1 PC spectral response and PL excitation spectrum for the manganese doped crystal MN(NL) at 77K (after spectral correction) .

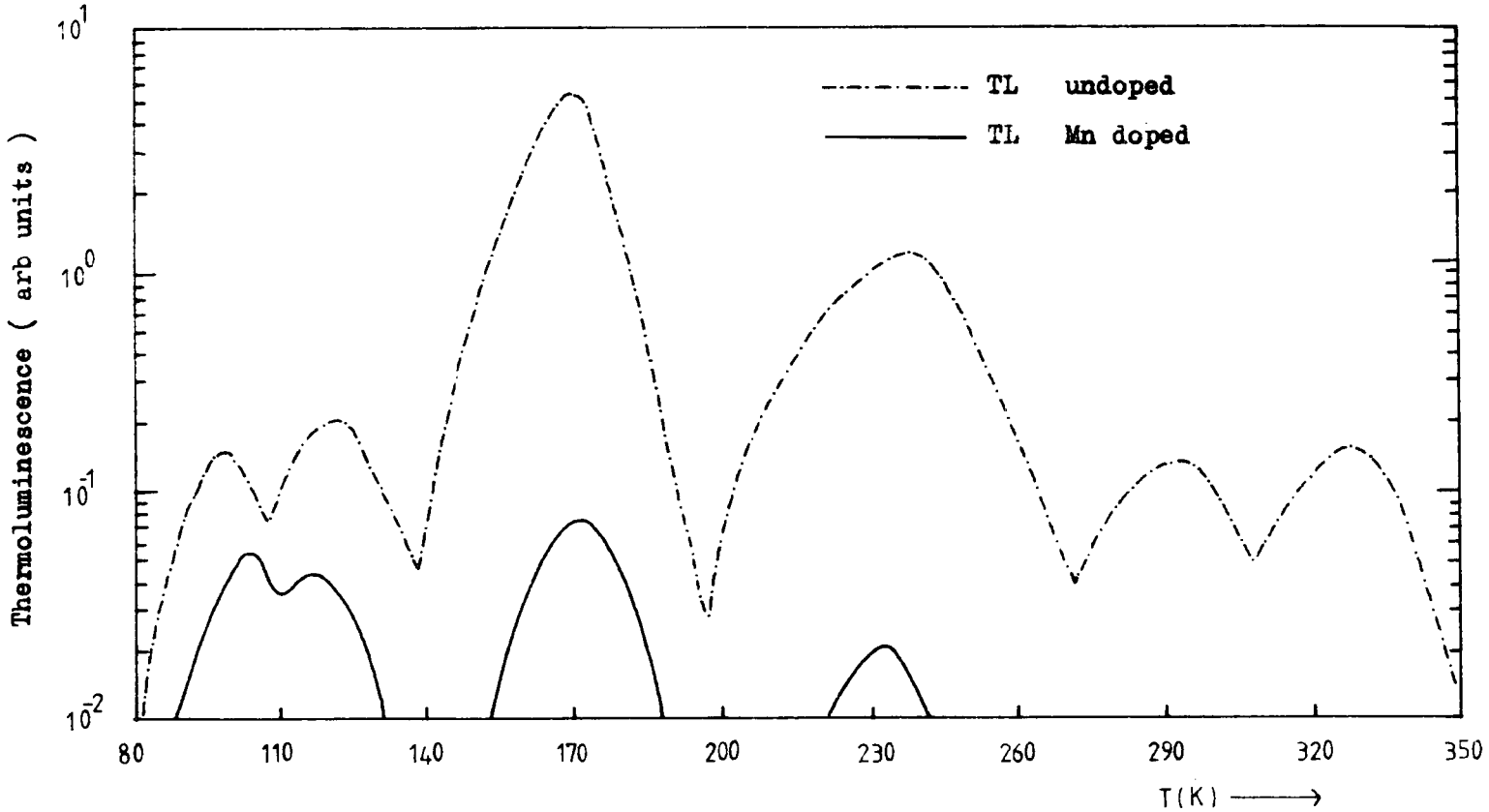

Figure 9.13.2 Thermoluminescence spectra for the TiO_2.Mn crystal MN(NL) before and after manganese doping .

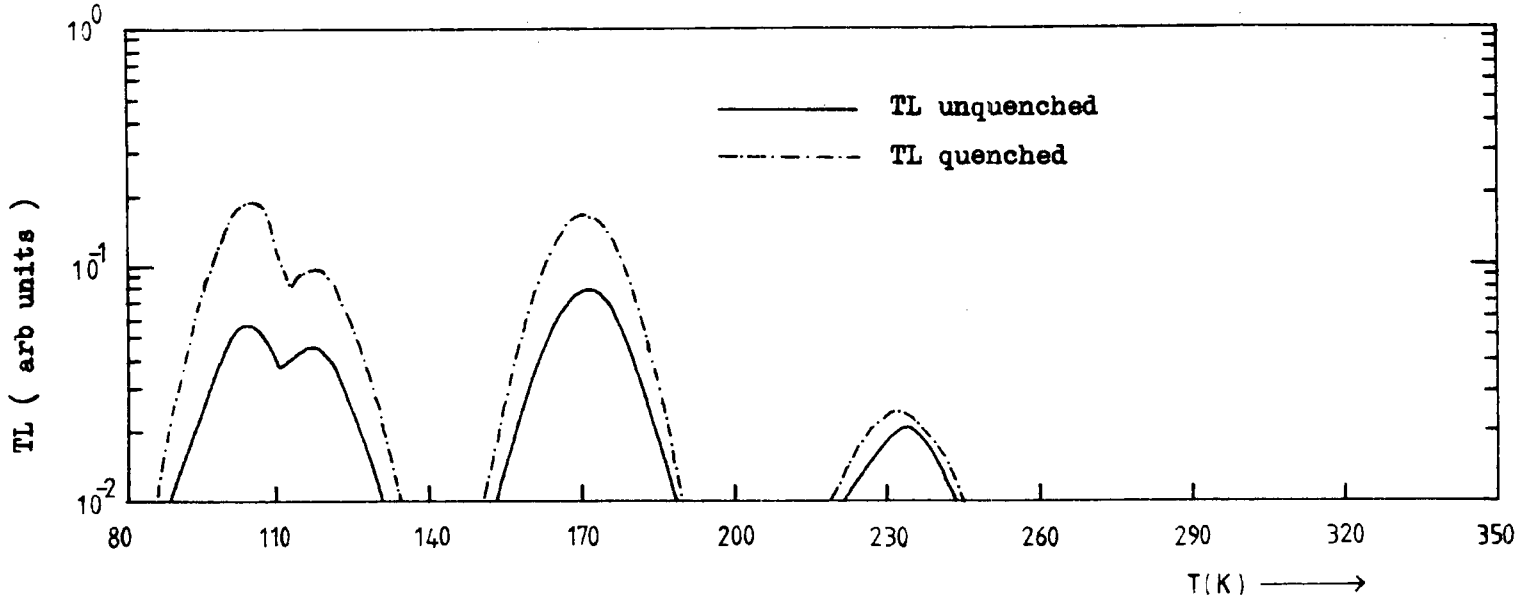

Figure 9.13.3 TL spectra for the TiO_2.Mn crystal MN(NL) before and after thermal quenching from 600°C .

the same value after 15 hours at 77 K. Figure 9.13.4 shows the activation energy plots for the crystal MN(BS14) before illumination (0.32 eV and 0.23 eV) and after illumination (0.08 eV and 0.06 eV). The stored conductivity could be removed by heating to 400 K for 30 minutes and the whole process repeated.

The phenomenon of 'stored conductivity' has been observed in CdS, GaAs and ZnO (Wright et al 1968, Kulp 1965 and Litton and Reynolds 1960). To explain this phenomenon a model was developed for CdS (Wright et al 1968) which involves a storage level from which electrons are excited while the collection of these electrons by a receiving level is accompanied by local crystal deformation allowing the quasi-equilibrium state, which stored conductivity represents, to be set up. It has been proposed that an interstitial impurity, properly situated below the plane of the S atoms, could be ionised, deform the lattice by attracting cadmium and repelling S ions. A rock-salt structure is then formed locally in the wurzite crystal lattice providing the variation in impurity energy levels that the phenomenon requires. No similar model is proposed for TiO_2.Mn but it is a possible area for further investigation.

The EPR spectrum of substitutional Mn^{4+} in TiO_2 ($3d^3$ with $S = 3/2$) is the only spectrum that is visible at room temperature (Low 1962). At and below 77 K the presence of Mn^{3+} can be observed (Gerritsen and Sabisky 1963). The crystals studied by Gerritsen and Sabisky contained 50 ppma Mn and had comparable amounts of tetravalent and trivalent substitutional manganese.

9.14 ELECTRICAL AND OPTICAL PROPERTIES OF TiO_2.Nb

The resistivities of the as-grown crystals BS12 (477 ppma Nb) and BS19 (140 ppma Nb) were measured using the four point contact method described by Van der Pauw (1958). This method eliminates contributions due to contact resistance and allows one to choose, with some limitations, arbitarily shaped

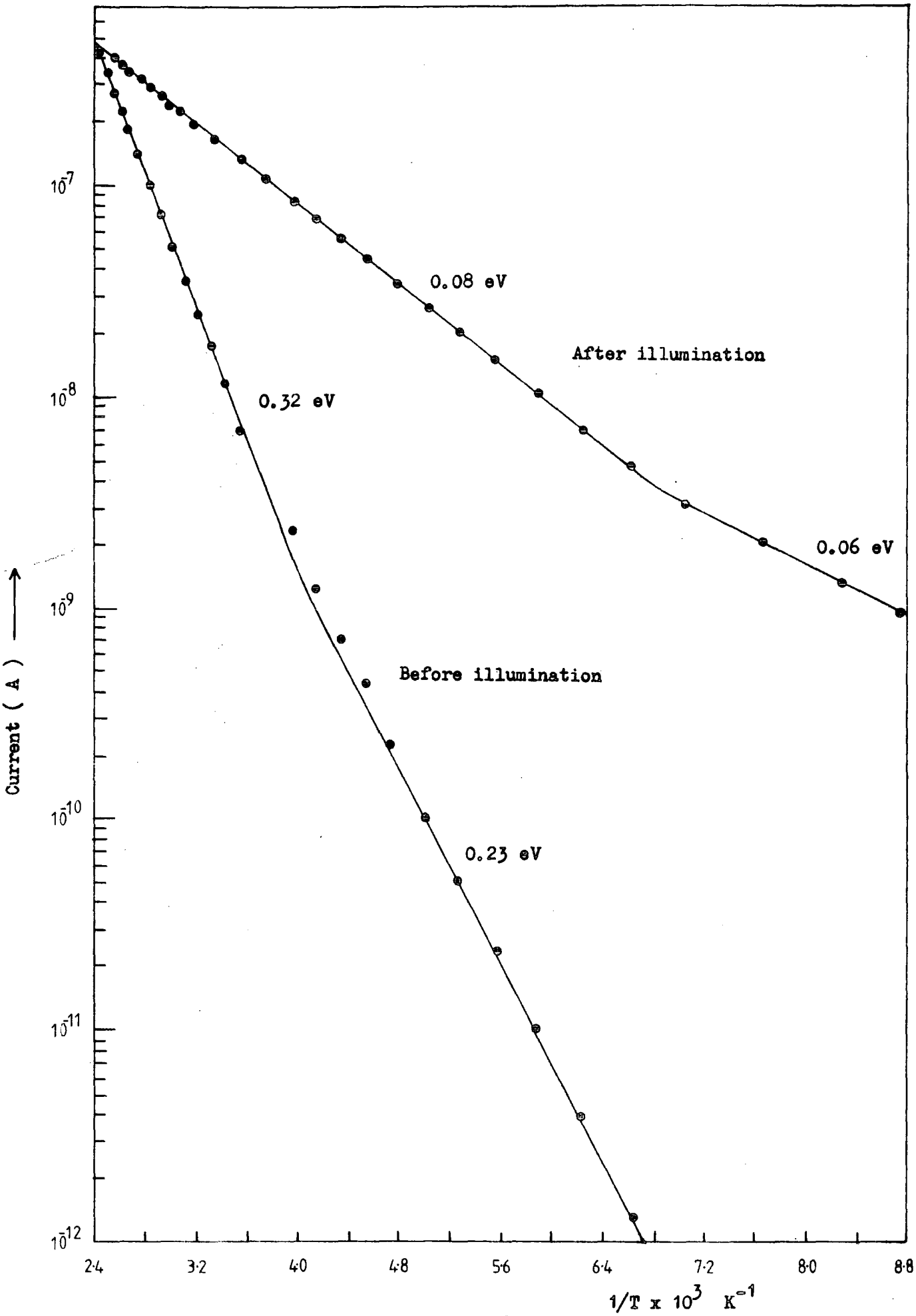

Figure 9.13.4 Conductivity storage in TiO_2.Mn crystal MN(NL).

discs of crystal material and contact configurations. The Van der Pauw method is only usable if the contacts are ohmic. Good ohmic contacts were provided by In-Sn dots alloyed onto samples approximately 8 mm x 8 mm x 0.5 mm.

Figure 9.15.1 shows the temperature dependence of the resitivities of crystals BS12 and BS19 before and after post growth oxidation. After growth the 300 K resistivities of BS19 and BS12 were 8 10^{-2} ohm cm and 10^{-1} ohm cm, respectively, and both were opaque and blue-black in appearance. After post growth oxidation the resistivities of BS19 and BS12 at 300 K increased to 8 ohm cm and 1.1 ohm cm, respectively. Crystal BS19 was light blue and transparent, whilst BS12 was dark blue and semi-transparent. The thermal activation energy of both reduced niobium crystals was 0.03 eV whilst after post growth oxidation BS12 and BS19 had activation energies of 0.10 eV and 0.12 eV respectively.

It is well known that rutile doped with elements of group V and VI, similarly to partly reduced rutile, has semiconducting properties. Bogoroditskii et al (1967) have studied the electrical properties of doped Verneuil grown crystals and showed that niobium doping increases the conductivity. They also concluded that the semiconducting properties of rutile induced by doping are much more stable toward changes in oxygen pressure at elevated temperatures than those of reduced rutile. The ionisation energies of donor centres, found from the temperature dependence of the Hall constant, for samples with different niobium concentrations lie between 0.03 and 0.12 eV at 300 K. The results presented in this section are in excellent agreement with those of Bogoroditskii et al, although the 0.03 eV activation energy might be associated with interstitial titanium donors rather than niobium donors.

Because of the large dark current in the niobium doped crystals no TSC spectra were recorded. The photoconductivity of the niobium crystals was measured at 77 K by mechanically chopping the incident light and using

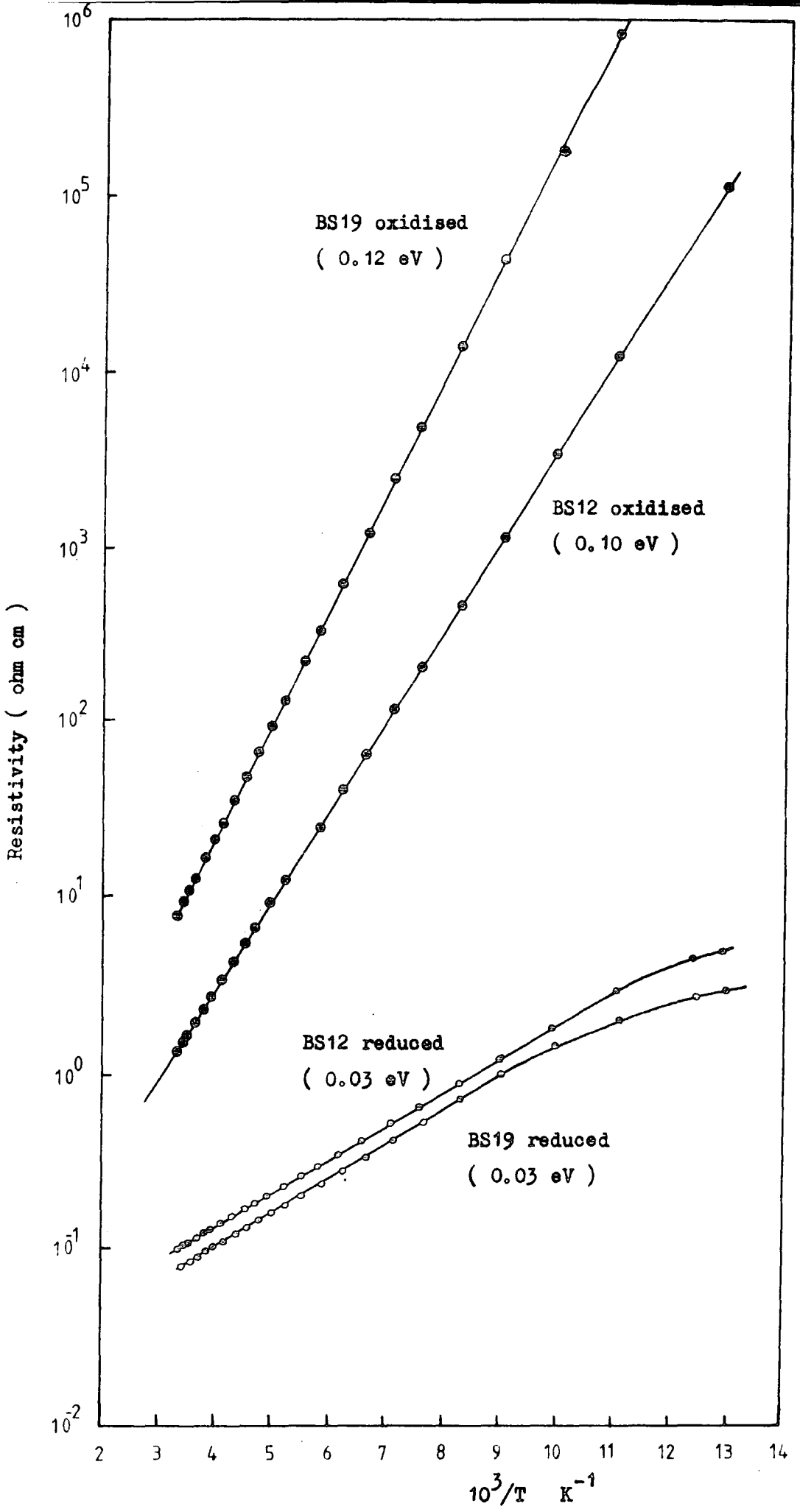

Figure 9.15.1 Temperature dependence of resistivity in niobium doped single crystal rutile .

a phase sensitive detector to record the photocurrent from a Keighley 602 electrometer. As shown in figure 9.2.6 the photoconductivities of the crystals BS12 and BS19 were lower than those of the undoped NL crystal. However, a comparison is difficult because of the differences in unintentional impurity content shown in table 3.3.

The photoluminescence emission spectra for the oxidised crystals BS19 and BS12 showed the characteristic 850 nm Cr^{3+} emission. This was rather surprising since no luminescence was observed in reduced NL or plasma grown crystals with resistivities below a value of about 10^8 ohm cm (see figure 6.7.2). It must be concluded that the behaviour of semiconducting niobium doped rutile is substantially different from that of reduced rutile. If the Auger mechanism proposed in section 6.7 is responsible for the reduction in PL intensity in reduced crystals, it would seem relevant to examine the shallow trapping density in niobium doped crystals. It might be expected that the density of the shallow traps 1, 2 and 3 would not increase as the conductivity of the crystal increased following the introduction of niobium centres.

Although the TSC spectra could not be investigated, it was possible to examine the TL spectra of BS12 and BS19. Figure 9.15.2 shows the TL spectra for BS18(S),BS19 and BS12, the spectrum for BS18(S) is included because the niobium doped crystals were grown from the same starting material DN5. The 477 ppma Nb crystal BS12 has a lower TL spectra intensity than the 140 ppma Nb crystal BS19. In view of the lower PL and PC at 77 K in BS12 (see figure 9.2.6) the reduction in the TL spectra is probably due to a decrease in the free carrier lifetime rather than a larger trap density. No extra shallow traps were observed, but peak 2 was not observed in any of the TiO_2.Nb crystals investigated.

The EPR spectrum of niobium doped rutile has been reported by Chester (1961). His experimental results indicate that niobium occupies

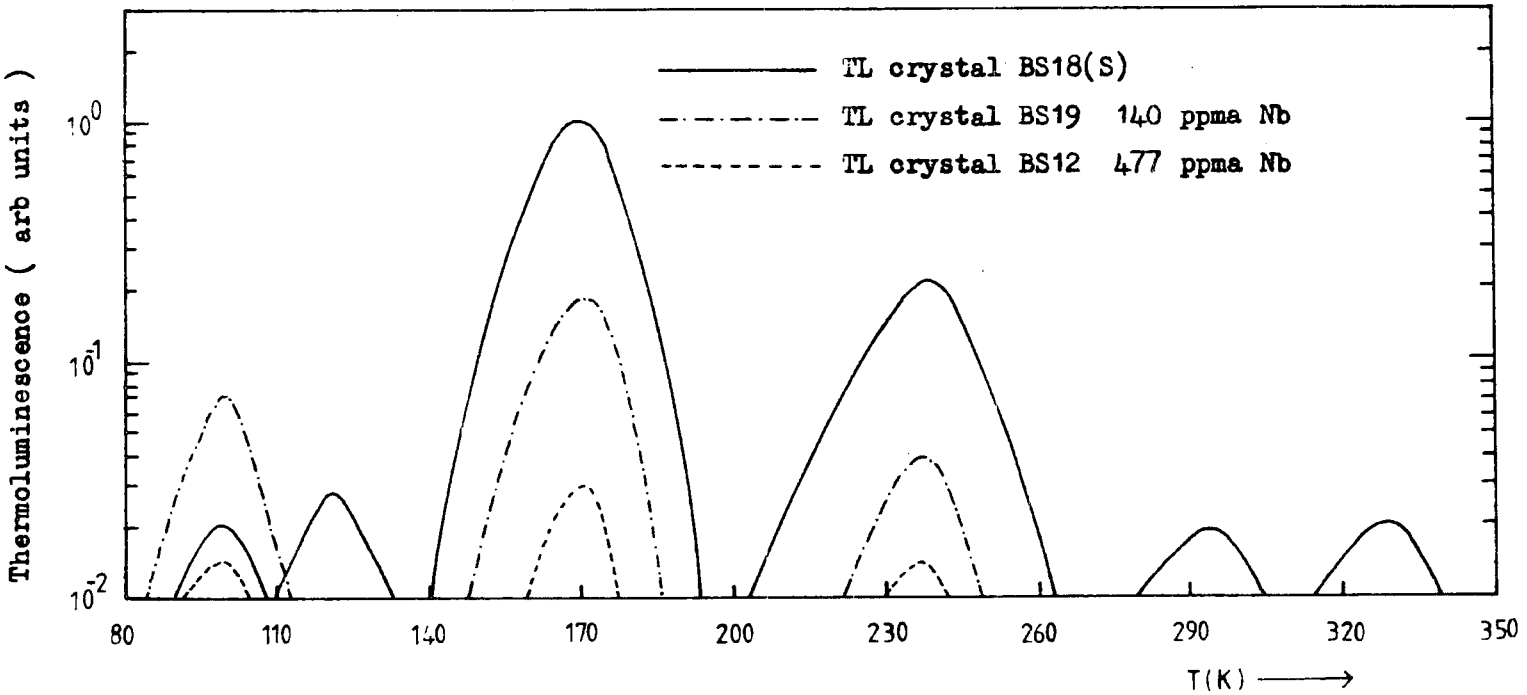

Figure 9.15.2 Comparison of TL spectra for the niobium doped crystals BS12 and BS19 and the 'undoped' crystal BS18(S) .

substitutional Ti^{4+} sites in the form Nb^{4+} ($4d^1$). At 4.2 K he observed a ten line hyperfine spectrum for each of the two inequivalent substitutional sites. These are appropriate to the I = 9/2 nuclear moment of Nb^{93}.

9.15 ALUMINUM AND SILICON IMPURITIES IN RUTILE

Aluminum was present as an unintentional impurity in the NL and plasma grown crystals in quantities ranging from 4-40 ppma, and crystals BS11 and BS16 were doped with 53 ppma and 1060 ppma of aluminum respectively. Silicon was present as an unintentional impurity in quantities ranging from 47-200 ppma.

A number of workers have studied the charge compensation mechanism for aluminum. Yahia (1963) assumed that Al^{3+} enters as a substitutional impurity, replacing Ti^{4+}, accompanied by oxygen vacancies which are either empty or filled with one or two electrons. According to this author the Al^{3+} charge might be locally compensated by a hole trapped on a neighbouring oxygen ion. The possibility of charge compensation with oxygen vacancies was also mentioned by Haul and Dumbgen (1965) in connection with their data on oxygen diffusion. As an alternative possibility Slepetys and Vaughan (1958) suggested that the charge compensation could occur where Al^{3+} ions were situated in the lattice on substitutional sites as well as interstitial sites in a 3:1 ratio. These authors concluded that this charge compensation by interstitial Al^{3+} ions was the more likely to occur on the basis of their experiments on the solid solubility of Al_2O_3 in rutile, as investigated by X-ray determination of the c unit cell parameter and by measurements of the charge density. They could not decide whether the interstitial Al^{3+} ions are either isolated in the lattice or associated with substitutional Al^{3+} ions, the latter seeming favourable regarding the opposite effective charges of these defects. The occurrence of Al^{3+} ions on interstitial sites was mentioned earlier by Forland (1964), also from solid solubility determinations.

Kerrsen and Volger (1973) have studied the EPR spectra of slightly reduced rutile crystals containing 20-150 ppma Al impurity. Two spectra B and B_{12} were found in slightly reduced samples ($5\ 10^{-4} < \sigma < 1\ 10^{-2}$ $ohm^{-1}cm^{-1}$). On the basis of their work and using the model of Slepetys and Vaughan, they proposed the following model for the B-centre and the reduction process below about 650°C. On heating in a vacuum, oxygen is lost from the surface region of the rutile sample according to reactions of the type

$$TiO_2 \longrightarrow TiO_{2(1-x)} + xO_2 + 2xV_O^{2+} + 4xe^-.$$

The oxygen vacancies subsequently created diffuse into the bulk of the crystal (Iguchie and Yajima 1972). The excess electrons created by the reactions are responsible for the conductivity of the undoped crystals. In aluminum doped samples the 25% of the Al^{3+} ions which are located on interstitial sites act as acceptor centres in such a way that an electron is trapped on one of the two Ti^{4+} ions which are nearest to an Al^{3+} interstitial, changing the valence state to Ti^{3+}. For example, Al^{3+} on a $00\frac{1}{2}$ site and Ti^{3+} on a 000 site ($Ti^{3+} - Al^{3+}$ model). As mentioned previously it seems energetically favourable for the interstitial Al^{3+} ions to be associated with substitutional ones. If this is the case, the most favourable Ti^{4+} ion for trapping an electron is that at a 000 site when the Al^{3+} ions are located at $0\frac{1}{2}0$ and 010 sites respectively ($Ti^{3+} - Al^{3+} - Al^{3+}$). Additional evidence was presented to suggest that the B signal and B_{12} signal were due to one or two electrons, respectively, which are trapped at Ti^{4+} ions near $Ti^{3+} - Al^{3+} - Al^{3+}$ complexes.

B signal : $Ti^{3+}(000) - Al^{3+}(0\frac{1}{2}0) - Al^{3+}(010)$

B_{12} signal : $Ti^{3+}(000) - Ti^{3+}(\frac{1}{2},\frac{1}{2},\frac{1}{2}) - Al^{3+}(0\frac{1}{2}0) - Al^{3+}(010)$

Two crystals BS11 and BS16 were doped with aluminum during the plasma growth process as described in chapter 3. Crystal BS11 contained 53 ppma Al which was not significantly different from the 40 ppma Al content of the

nominally pure NL crystal CA3. In fact both crystals BS11 and BS16 (1060 ppma) had similar properties to the undoped crystals. The TSC spectra of both crystals showed similar behaviour on reduction as described for the 'undoped' crystals in section 7.7. The two low temperature traps, 1 and 2, increased some four orders of magnitude from 10^{14} cm^{-3} to 10^{18} cm^{-3} as the reduction process changed the resistivity from 10^{13} ohm cm to 10^{6} ohm cm. Trap 3 increased from 10^{16} cm^{-3} to over 10^{18} cm^{-3} during the same reduction process. Crystal BS11 showed a similar photoluminescence intensity to BS18(NS), whilst crystal BS16 exhibited the lowest photoluminescence emission of all the crystals examined in their oxidised state. This phenomenon was also reflected in the low chromium content obtained from mass spectroscopy (see table 3.3). Photoluminescence was not observed in either crystal below a resistivity of 10^{6} ohm cm.

The only property observed in the aluminum crystal BS16 which was not typical of an undoped crystal was the long decay time in the dark current after illumination at 77 K. A period of three minutes was necessary before beginning the heating ramp for the TSC experiments. This seems to indicate the presence of shallow trapping centres which thermally ionise below 77 K. Kerssen and Volger could only observe the B and B12 signals below 60 K indicating the presence of shallow traps in slightly reduced rutile. It was concluded that TSC and TL experiments below 77 K were necessary to examine the shallow trapping centres in aluminum doped rutile. These measurements were beyond the scope of this present work.

Kerssen and Volger (1973), Chester (1961) and Kingsbury et al (1968) have all reported an A-signal in rutile which has been associated with a Ti^{3+} ion on an interstitial site of the type $0\frac{1}{2}0$. Kingsbury et al (1968) found support for this explanation from ruling out other possibilities and from a calculation of the lattice potential around the interstitial site which is occupied by the Ti^{3+} ion.

There are two ways in which the A-centres can be created. In nonreduced rutile crystals Ti^{4+} ions might be present at interstitial sites as a charge compensation for three-valent impurities. Upon reduction these ions might trap one electron and become Ti^{3+}. Secondly, Ti^{3+} ions can be produced at interstitial sites by reactions of the type

$$TiO_2 \longrightarrow (1-x)\ TiO_2 + x\ O_2 + x\ Ti^{4+} + 4x\ e^-,$$

followed by a diffusion of the thus formed Ti^{3+} into the bulk of the crystal. Such a diffusion occurs through the open channels along the c direction (Bourgoin and Corbett 1972). This mechanism for the production of Ti^{3+} interstitials is strongly supported by the density measurements of a number of workers (Kofstad 1962, Forland 1964).

The effective charge of substitutional Si^{4+} is zero, but the ionic radius (0.400 Å) is only about $\frac{2}{3}$ that of Ti^{4+} (0.605 Å). Kerrsen and Volger have pointed out that the oxygen ions of an oxygen octahedron surrounding a $0\frac{1}{2}0$ - type interstitial site may more easily be shifted outward to provide room for a Ti^{3+} ion when this octachedron is located next to a substitutional Si^{4+} ion. For these reasons they ascribe the A-centre to associates of the type Si^{4+} (000) - Ti^{3+} $(0\frac{1}{2}0)$. They also provided evidence to suggest that the hyperfine structure that accompanies the A-signal arises due to the 2.5% abundance of the ^{29}Si nucleus.

9.16 SUMMARY OF IMPURITY LEVELS IN SINGLE CRYSTAL RUTILE

A comparison of the trap densities derived from the TSC curves for crystals BS18(S), CA3(NL), C1(NL), C2(NL) and CO(NL) is given in table 9.16.1. Data for the Ni, Mn, Fe and Nb doped crystals could not be obtained because of the excessive dark current. Thermoluminescence data was available for the whole range of dopants and figure 9.16.2 shows a comparison of the as-measured TL peak height intensities. As previously discussed the model for single crystal rutile contains more than one recombination centre. Although the

TSC PEAK NO.	7	1	2	3	8	4	5	6
C1(NL)	$7\ 10^{15}$	$6\ 10^{15}$	$6\ 10^{15}$	$2\ 10^{17}$	$9\ 10^{16}$	$7\ 10^{16}$	$7\ 10^{16}$	$1\ 10^{17}$
C2(NL)	$9\ 10^{16}$	$1\ 10^{17}$	$1\ 10^{17}$	$3\ 10^{17}$	$1\ 10^{17}$	$7\ 10^{16}$	-	-
CO(NL)	-	$2\ 10^{14}$	$3\ 10^{14}$	$5\ 10^{15}$	$5\ 10^{15}$	$1\ 10^{15}$	-	-
BS18(S)	-	$2\ 10^{13}$	$4\ 10^{13}$	$1\ 10^{16}$	-	$2\ 10^{16}$	$2\ 10^{16}$	$3\ 10^{16}$
CA3(NL)	-	$3\ 10^{14}$	$4\ 10^{14}$	$2\ 10^{17}$	-	$9\ 10^{16}$	$6\ 10^{16}$	$8\ 10^{16}$

Table 9.16.1 Comparison of trap densities determined from TSC data .

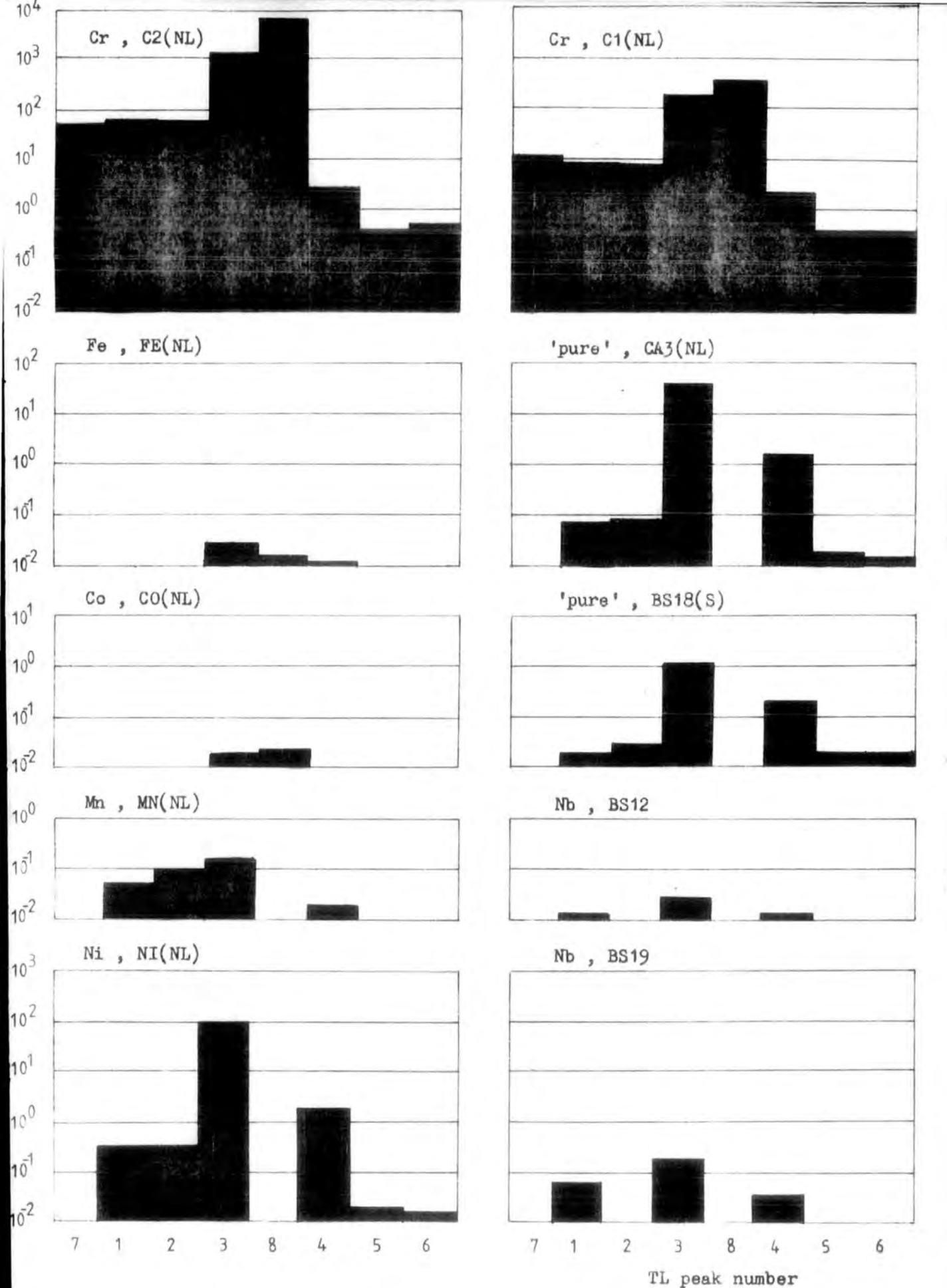

Figure 9.16.2 Comparison of the as-measured TL intensities .

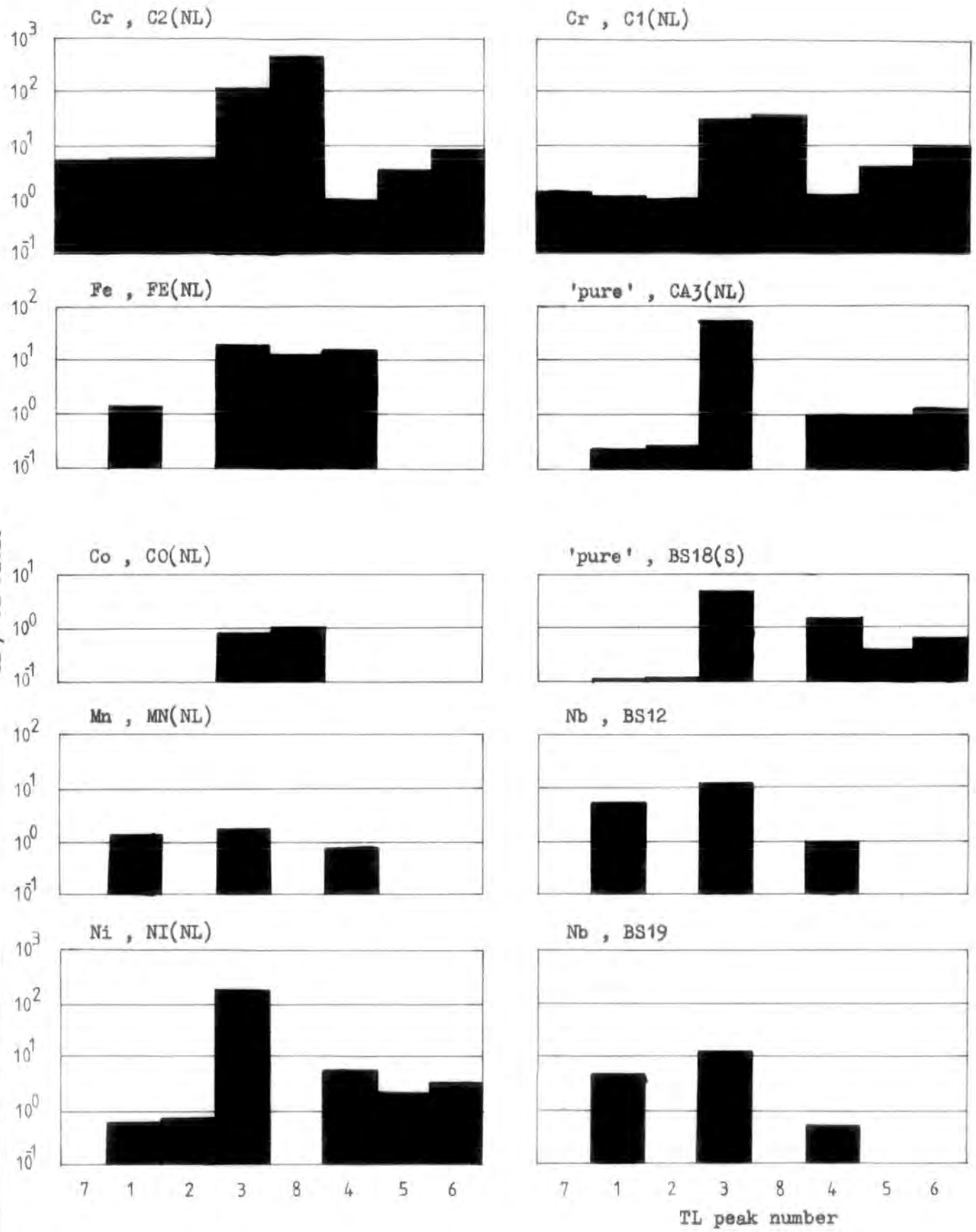

Figure9.16.3 Comparison of the TL peak intensities after normalisation by the PL intensity .

simple insulator model with one recombination centre seems to provide a good approximate model for activation energy analysis, the existence of other recombination centres must be taken into account when determining trap densities. In order to obtain a qualitative understanding of the relative number of centres in the different doped crystals the TL data was normalised by dividing by the PL signal at the given TL peak temperature maximum (see figure 9.16.3). It is instructive to compare trap densities derived from TSC and TL measurements for crystals C1(NL), C2(NL), BS18(S), CA3(NL) and CO(NL). Although there is not exact agreement, the fact that the trap densities have increased considerably in chromium doped material and decreased in the cobalt doped crystal is apparent from both sets of data. Furthermore, crystal NI(NL) which had a similar photoconductive gain before and after nickel doping is shown to have a similar trap density to the undoped crystal. The iron doped crystal FE(NL) produces prehaps the most striking result. After normalising the TL data with the PL intensity it is apparent that there is still a large number of traps present in TiO_2.Fe, comparable if not greater than in the undoped crystal.

Eight different trapping centres have been detected in single crystal rutile. The density of these different centres is influenced by the introduction of various chemical impurities. In annealed samples centre 7 was only observed in chromium-doped samples, however, it was also observed in quenched nickel and chromium crystals. Centre 8 appeared in the chromium, iron and cobalt doped crystals. The examination of the intentionally doped crystals has not established the identity of any particular centre. However, the preceding sections discuss some suggested photo-ESR, TL/TSC experiments that would be an interesting development of the present work. Unfortunately not all defects are suited for resonance measurements because they do not have unpaired electrons, or the spectra are too complex, different spectra overlap or the lines are quenched by the microwave power needed for ESR.

Mizushima et al (1973) have investigated rutile crystals doped with V, Cr, Mn and Fe impurities. They controlled the location of the Fermi level in TiO_2 by doping with lithium. The induced change of valence of the transition metal impurities was studied by photosensitive ESR. Figure 9.16.4 (a) shows the results obtained with signal intensities normalised to that of the Cr^{3+} centre. They classified the location of the impurity levels of the iron group ions into three groups (a), (b) and (c), according to their location relative to the bands of the host lattice. In the fully oxidised crystal, the impurities will exist as M_a^{+j}, M_b^{+k} and M_c^{+l}, with levels below the Fermi level of the sample. With the increase of the Li shallow donor concentration the Fermi level will gradually rise and finally reach the bottom of the conduction band. In this process the M_a^{+j} impurity will not change its valence because the location of the $M_a^{+(j-1)}$ level is higher than the bottom of the conduction band (see figure 9.16.4 (b)). M_b^{+k} will change to $M_b^{+(k-1)}$, and type (c) will first change to $M_c^{+(l-1)}$ and then to $M_c^{+(l-2)}$. The observed stable character of the Cr^{3+} signal indicates that the Cr^{2+} level exists above the bottom of the conduction band. The work of Mizushima et al is summarised in figure 9.16.4 (c).

Tanaka et al (1972) have estimated the impurity levels of the iron group ions in TiO_2 using the method of Allen (1964), who calculated the energy levels of divalent ions in ZnS, using parameters such as the crystalline field splitting obtained from optical measurements. The values of crystalline field splittings obtained from optical measurements were too large to fit the observations of Muzishima et al and a tentative correction was used to reduce the values of crystalline field splitting by 20%. The results are shown in figure 9.16.5, where is can be observed that the locations of the levels of the same valence ions have a tendency to decrease with the increase of the number of d electrons. In figure 9.16.5 it is noticed that the energy seperations in pairs of (Ti^{3+}, Ti^{2+}), (V^{3+}, V^{2+}), (V^{4+}, V^{3+}), (Cr^{4+}, Cr^{3+}), (Mn^{3+}, Mn^{2+}), (Fe^{4+}, Fe^{3+}) and (Ni^{3+}, Ni^{2+}) are small. In contrast, the energy seperations

between Cr^{3+} and Cr^{2+}, and Fe^{3+} and Fe^{2+} are large. These results explain the metallic behaviour of $Ti^{3+}O_3$, $V_2^{3+}O_3$, $V^{4+}O_2$, $Cr^{4+}O_2$, $(La_{1-x}Ca_x)MnO_3$ and $SrFe^{4+}O_3$, as well as the insulative behaviour of oxides consisting of Cr^{3+} or Fe^{3+} ions, such as Cr_2O_3 and Fe_2O_3.

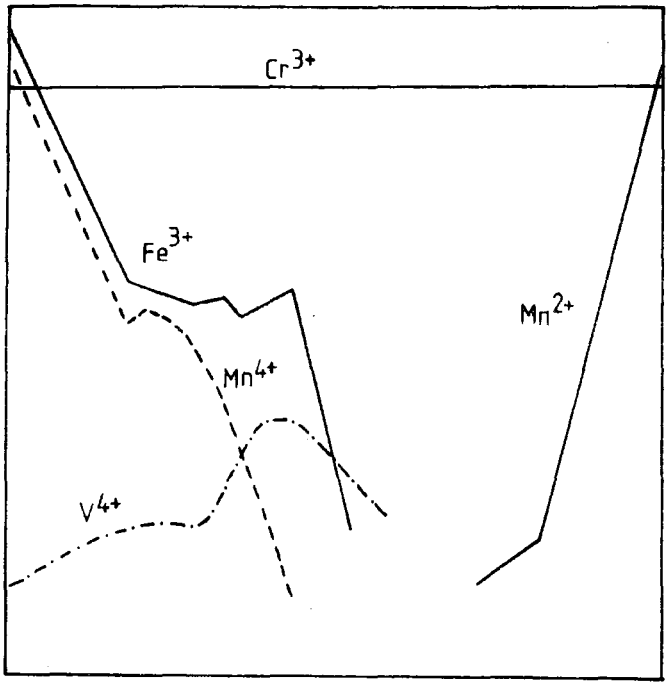

Figure 9.16.4(a) Signal intensities of various ions which are normalised to that of Cr^{3+} (Mizushima 1973).

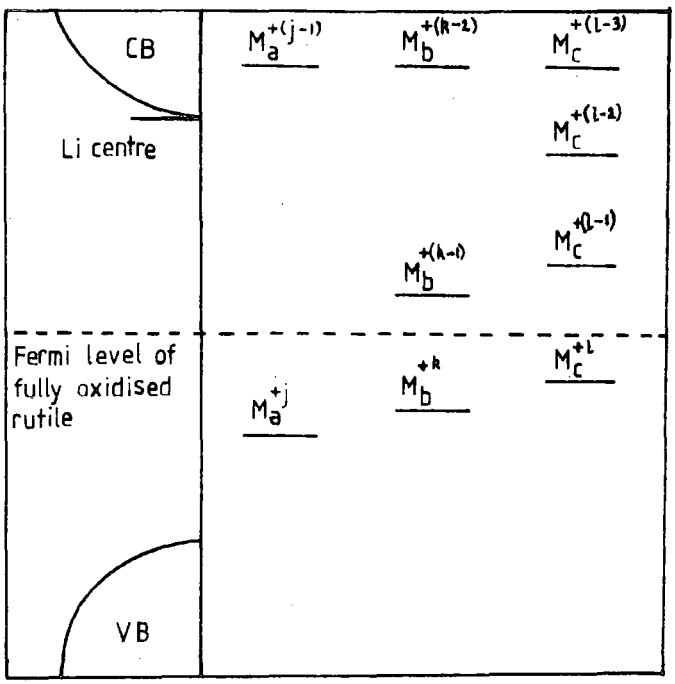

Figure 9.16.4(b) Possible three types of impurity levels (Mizushima 1973).

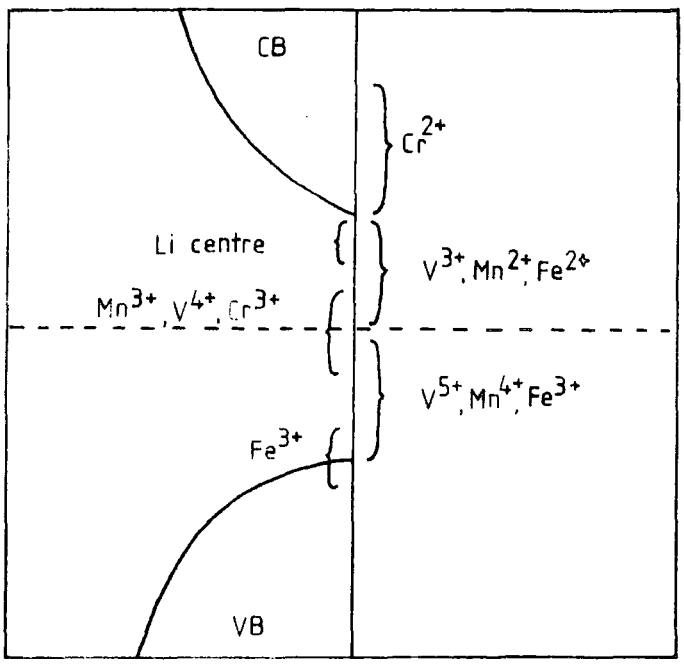

Figure 9.16.4(c) Proposed energy level schemes of the transition metal ions in TiO_2 (Mizushima 1973).

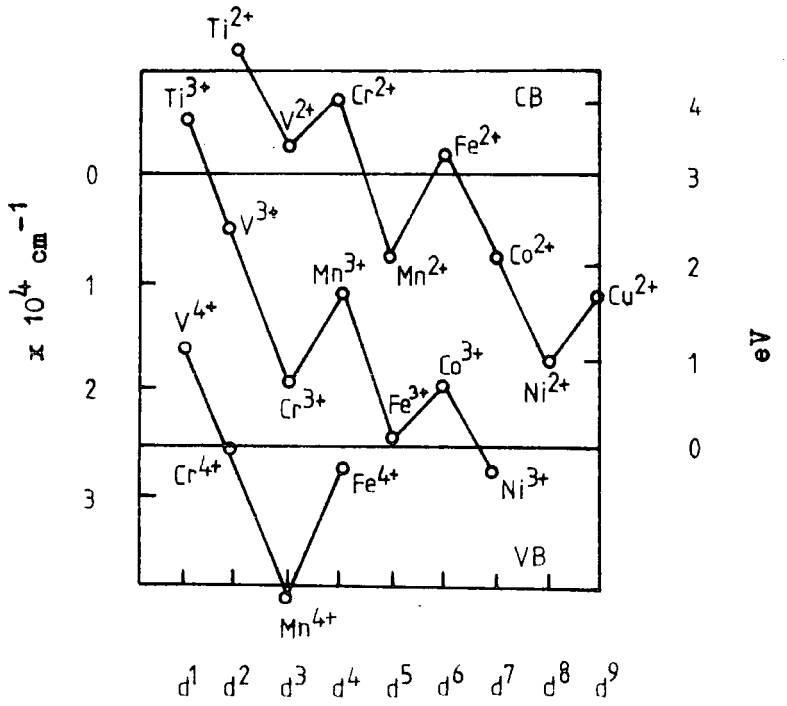

Figure 9.16.5 Calculated energy levels of the transition metal ions in TiO_2. The levels M^{+j} and $M^{+(j-1)}$ which are near mutually are enclosed with dotted lines (Tanaka et al 1972).

CHAPTER 10

POWDERS, PIGMENTS AND PAINTS

10.1 INTRODUCTION

The object of the studies on the powders, pigments and paints was to try and identify whether the defect centres observed in the single crystal were active in the pigments, and thus, establish if the single crystal results were at all relevant to the understanding of the properties of rutile pigments.

A number of workers have proposed a surface barrier model based on surface state charging and discharging, in an attempt to explain photoeffects in titanium dioxide pigments. Addiss and Wakim (1969), using flame fusion TiO_2 powders, reported that measured photocurrents were related directly to changes in surface coverage associated with photodesorption of adsorbed surface species. These results led to a proposed model for photoconduction in TiO_2 similar to that derived for photoconduction in ZnO (Melnick 1957). Vohl (1969) conducting contact potential measurements on films containing powders dispersed in an organic binder, arrived at similar conclusions and proposed a surface barrier model based on the adsorption of gas atoms in at least two different levels.

Geisler and Filipovich (1971) have studied TSC in anatase powder compacts and concluded that in addition to the surface effects which have been reported, it is also necessary to consider bulk effects, probably sited in the physical surface of the particle, in order to account for the observed kinetics of the photocurrent decay. They found TSC peak maxima at 271 K, 244 K, 193 K, 173 K and 163 K, and noted that the TSC spectra were significantly different for the range of anatase powders studied. Gray and Lowery (1971) have also studied TSC in titanium dioxide powder compacts and found evidence of a 170 K TSC peak.

Measurement of TSC on powder compacts is difficult and analysis of the results is extremely precarious. Lauer et al (1971) have examined TSC and

photocurrent decay curves in rutile pellets of greater than 95% theoretical density, which were fired in oxygen at 900 °C for six hours. Ultrasonically soldered indium contacts covered both faces of the 1.3 cm diameter circular pellets. They observed a 310 K (0.88 eV) trap in rutile. However, the effect that this trap had on the photocurrent response was not clear. The initial portion of the photocurrent decay followed a simple Elovich equation (Addiss and Wakim 1969) suggesting that the decay in this region is determined primarily by surface recombination for which the electrons must surmount a varying Schottky barrier, rather than by trap-emptying kinetics. When the photocurrent had decayed sufficiently so that the magnitude of the photocurrent was comparable to the magnitude of the current arising from the release of trapped charge, deviations from the Elovich decay were observed. At this point the decay was neither Elovich nor exponential, but was a combination of both processes.

As the object of the present work is to study pigments and paint films, it was felt that any measurement which involved the firing of samples at high temperatures was undesirable. For this reason the experiments on powders concentrated on the investigation of photoluminescence and thermoluminescence, which did not require contacts.

10.2 EXAMINATION OF THE PHOTOLUMINESCENCE AND THERMOLUMINESCENCE OF SOME TITANIUM DIOXIDE PIGMENTS

A large number of rutile pigments were examined using the PL and TL techniques developed for the single crystal rutile. From these pigments, four samples were selected as being typical of different types of TL and PL behaviour. Pigment RH472 was a Laporte high durability commercial pigment. RD2A and E1822 R/D were two BTP 'chloride' pigments and SPF552 was a BTP 'sulphate' pigment. The properties of these four pigments and that of the 'sandy' rutile powder DN5 will now be described in some detail and a comparison

will be made with a larger number of samples, later in this chapter.

Known quantities of the pigments were weighed and mixed with a small quantity of 5% cellulose in butyl acetate solution. The solution was then evenly spread over a 1 cm^2 area of a glass silica slide and allowed to dry in air into a thin powder film. A thermocouple was soldered with indium to the glass slide and the sample was mounted into the cryostat as described previously for the single crystal. Less than 1% powder was removed from the film after more than five 77 K to 400 K temperature cycles.

All the powders, pigments and paint films examined showed the characteristic PL emission at 850 nm, attributed to Cr^{3+}, as observed in the single crystal rutile. Emission intensities varied by over three orders of magnitude for the complete series of pigments examined. The lowest emission was found in the 'sandy' rutile powder DN5 which had 0.4 ppma Cr from MS7 analysis. Unfortunately no mass spectrographic analysis was available for the pigments examined and no further comparison was possible.

The PL and TL spectra for DN5 is shown in figure 10.2.1 where temperature maxima at 108 K, 120 K, 180 K and 196 K were observed in the as-prepared 'sandy' rutile. These peaks have similar temperature maxima to events 1,2,3 and 8 observed in the single crystal work. Unfortunately the TL signal was too low in intensity to perform any meaningful activation energy analysis.

Throughout the work presented in this chapter the TL and PL spectra can be compared with each other. The PL measurements were made using a photomultiplier supply voltage of 1000 volts and the anode current was measured as a voltage across a 1 MΩ resistor. Conversion to this voltage can be made by dividing the PL scale by 100. Thermoluminescence was measured with a supply voltage of 2000 volts and a conversion to find the voltage across the 1 MΩ resistor can be made by dividing the TL scale value by 10.

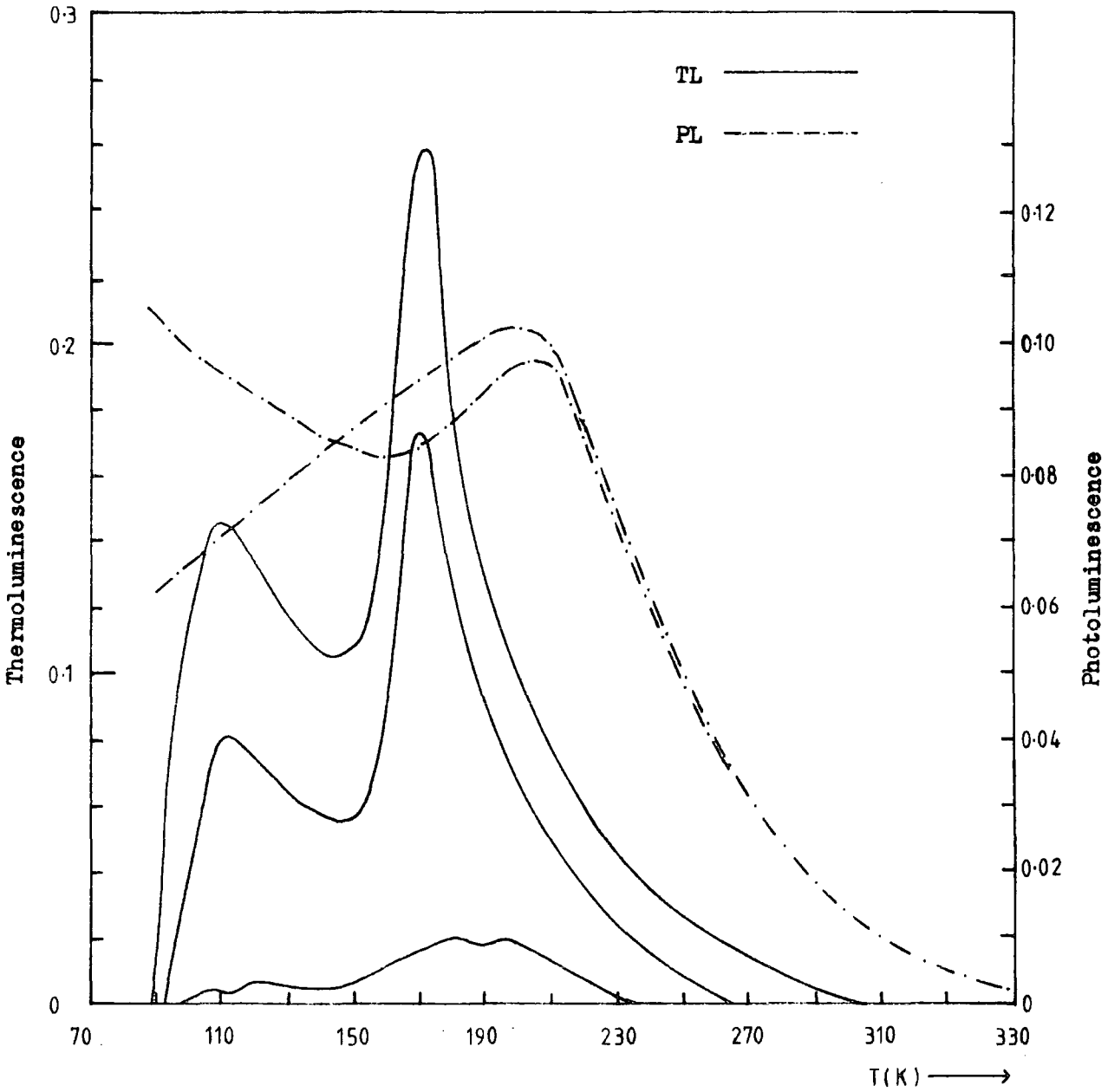

Figure 10.2.1 **Photoluminescence and thermoluminescence spectra for the 'sandy' rutile powder DN5 (a) as-prepared (b) quenched from 500°C (c) quenched from 1000°C.**

Figures 10.2.2 to 10.2.5 show the TL/PL spectra for the pigments RH472, RD2A, E1822 R/D and SPF552 respectively. These spectra demonstrate the typical range of PL and TL intensities, as well as the various types of PL versus temperature responses, that can be observed in rutile pigments. Attempts were made to analyse the TL spectra using the methods successfully applied to single crystal rutile. Unfortunately little success came from these experiments and the methods of Garlick and Gibson, and Hoogenstraaten invariably did not give straight lines.

A plot of $\ln ((1-\eta)/\eta)$ versus $1/T$ for DN5 gave an activation energy of 0.19 ∓ 0.02 eV whilst a plot of $\ln (1/\tau - 1/\tau_L)$ versus $1/T$ gave an activation energy of 0.22 ∓ 0.02 eV, with a luminescence lifetime at 77 K of about 36 μs. These values are similar to the values obtained for the single crystal rutile. Luminescence lifetimes at 77 K for SPF552, RH472, RD2A and E1822 R/D were measured as 57 μs, 52 μs, 48 μs and 36 μs respectively. Plots of $\ln ((1-\eta)/\eta)$ and $\ln (1/\tau - 1/\tau_L)$ versus $1/T$ gave two activation energies, one of about 0.36 eV and another of about 0.22 eV. Similar plots were obtained for the TiO_2:Cr crystals (see figure 9.5.4), although for these crystals a lifetime of 36 μs was observed at 77 K.

10.3 PROPERTIES OF QUENCHED POWDERS AND PIGMENTS

Small quantities of the pigments RH472, RD2A, E1822 R/D and SPF552 were heated in oxygen for 24 hours at various temperatures up to 1000°C. The pigments were then removed from the furnace and allowed to cool to room temperature. Temperatures of 1000°C, 900°C, 800°C, 700°C, 600°C, 500°C, 400°C and 300°C were used in these experiments.

Figure 10.3.1 shows the TL spectra for the pigment RH472 after quenching from temperatures of 600°C, 800°C and 1000°C. The behaviour of the low temperature peaks is similar to that described for the single crystal rutile and the 120 K peak increases as the quenching temperature is raised. Variation of the TL peak heights with quenching temperature is shown in

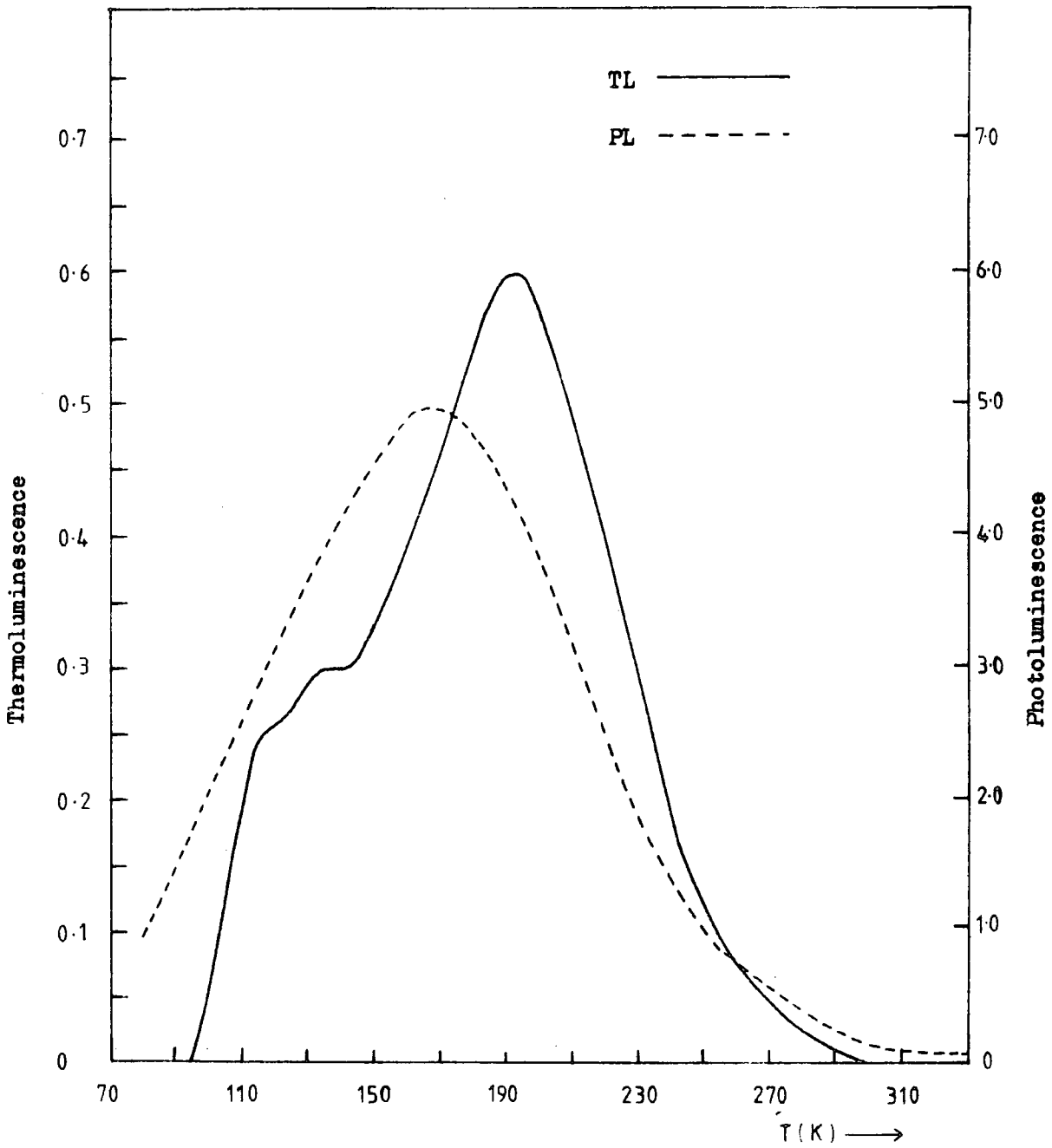

Figure 10.2.2 Photoluminescence and thermoluminescence spectra for the rutile pigment RH472, as-prepared.

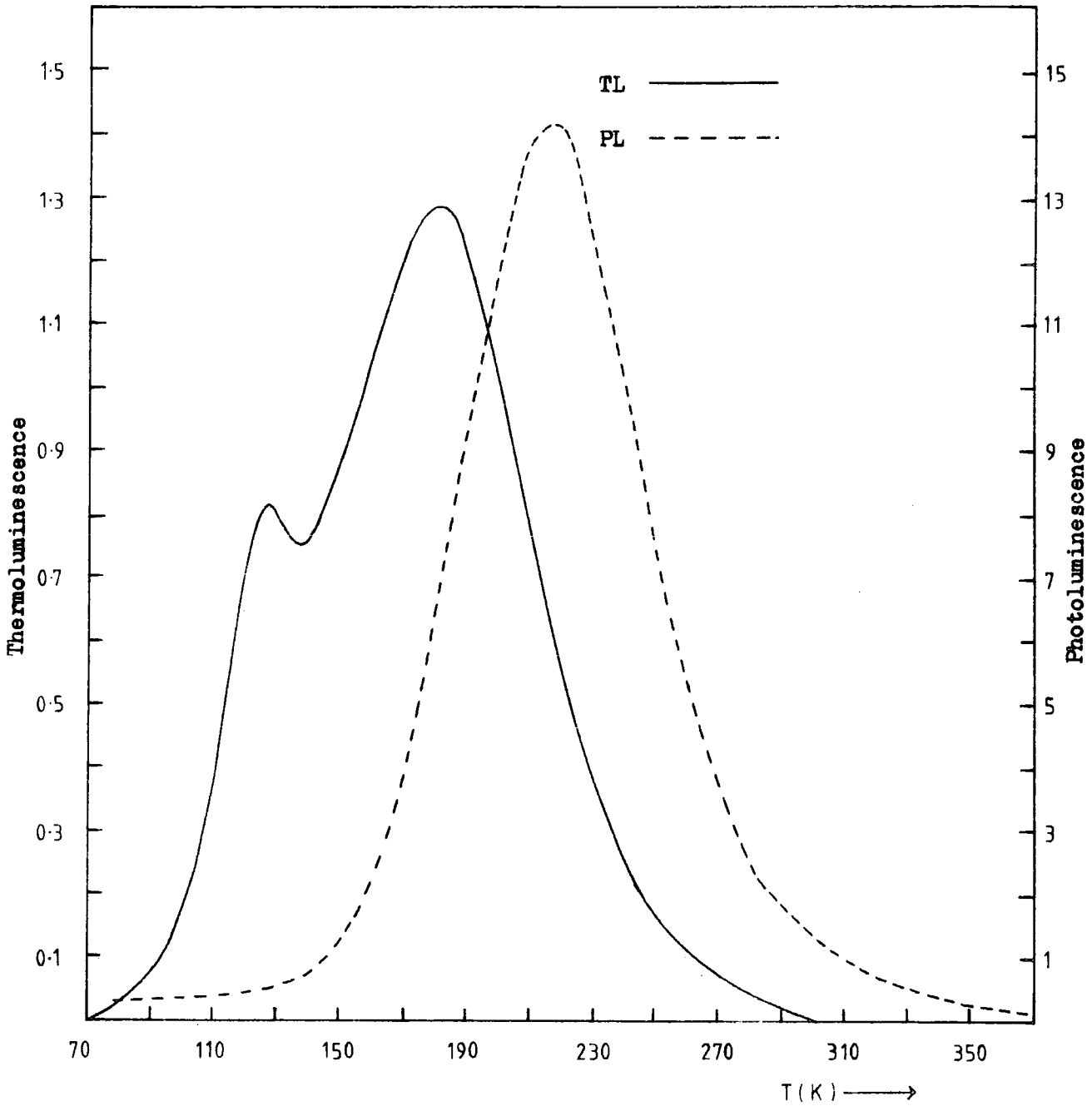

Figure 10.2.3 Photoluminescence and thermoluminescence spectra for the rutile pigment RD2A, as-prepared .

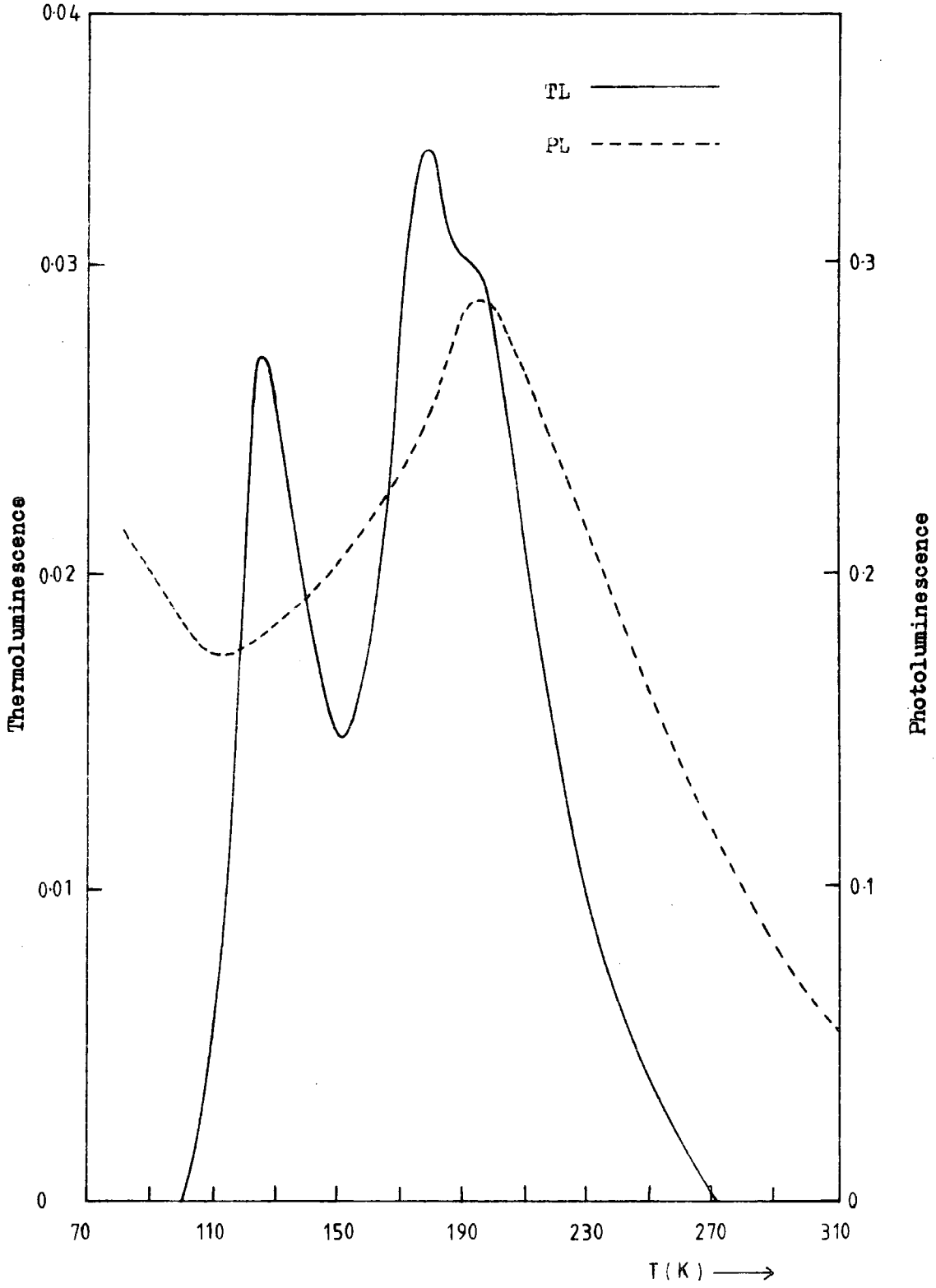

Figure 10.2.4 Photoluminescence and thermoluminescence spectra for the rutile pigment E1822 R/D, as-prepared .

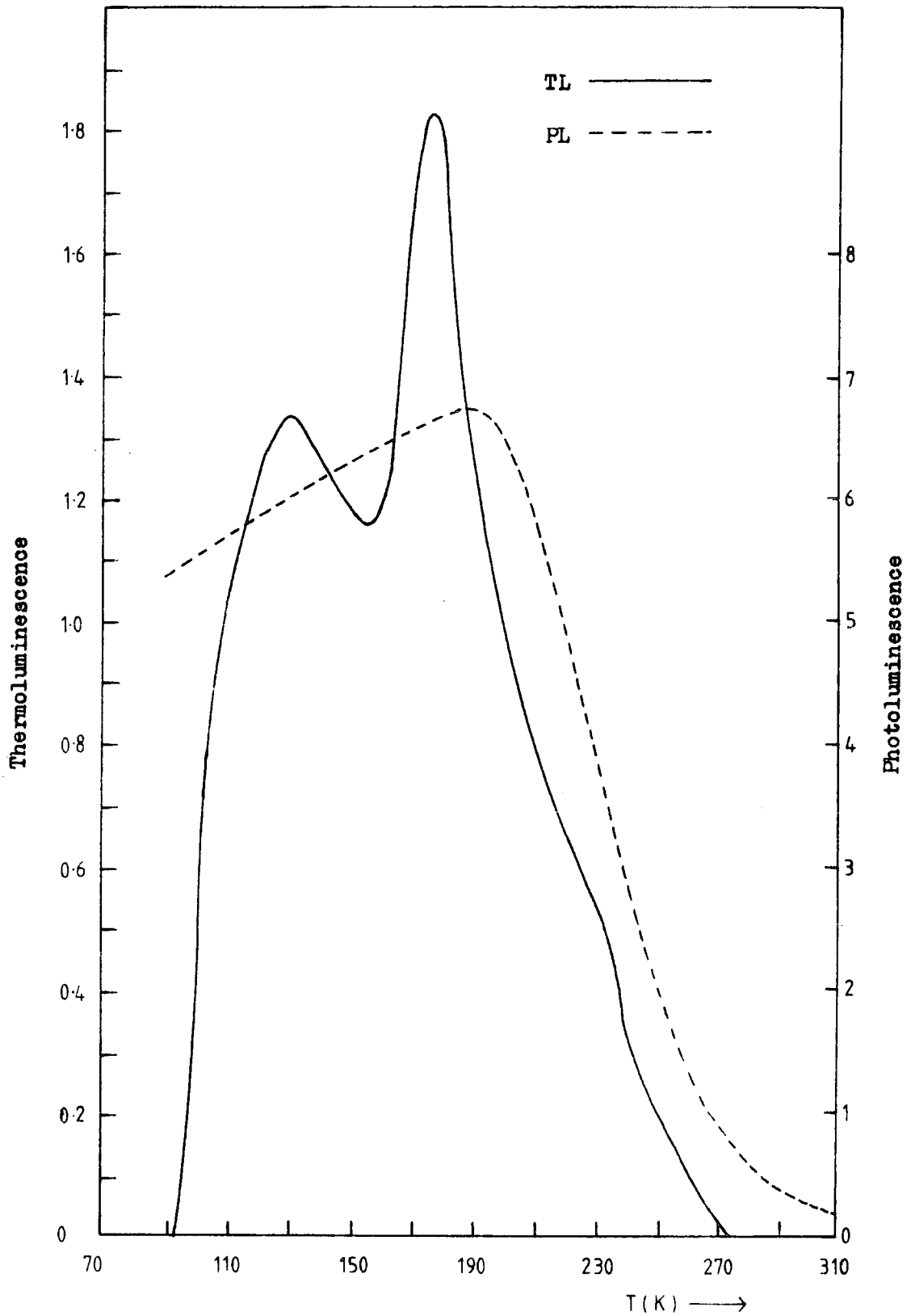

Figure 10.2.5 Photoluminescence and thermoluminescence spectra for the rutile pigment SPF552, as-prepared .

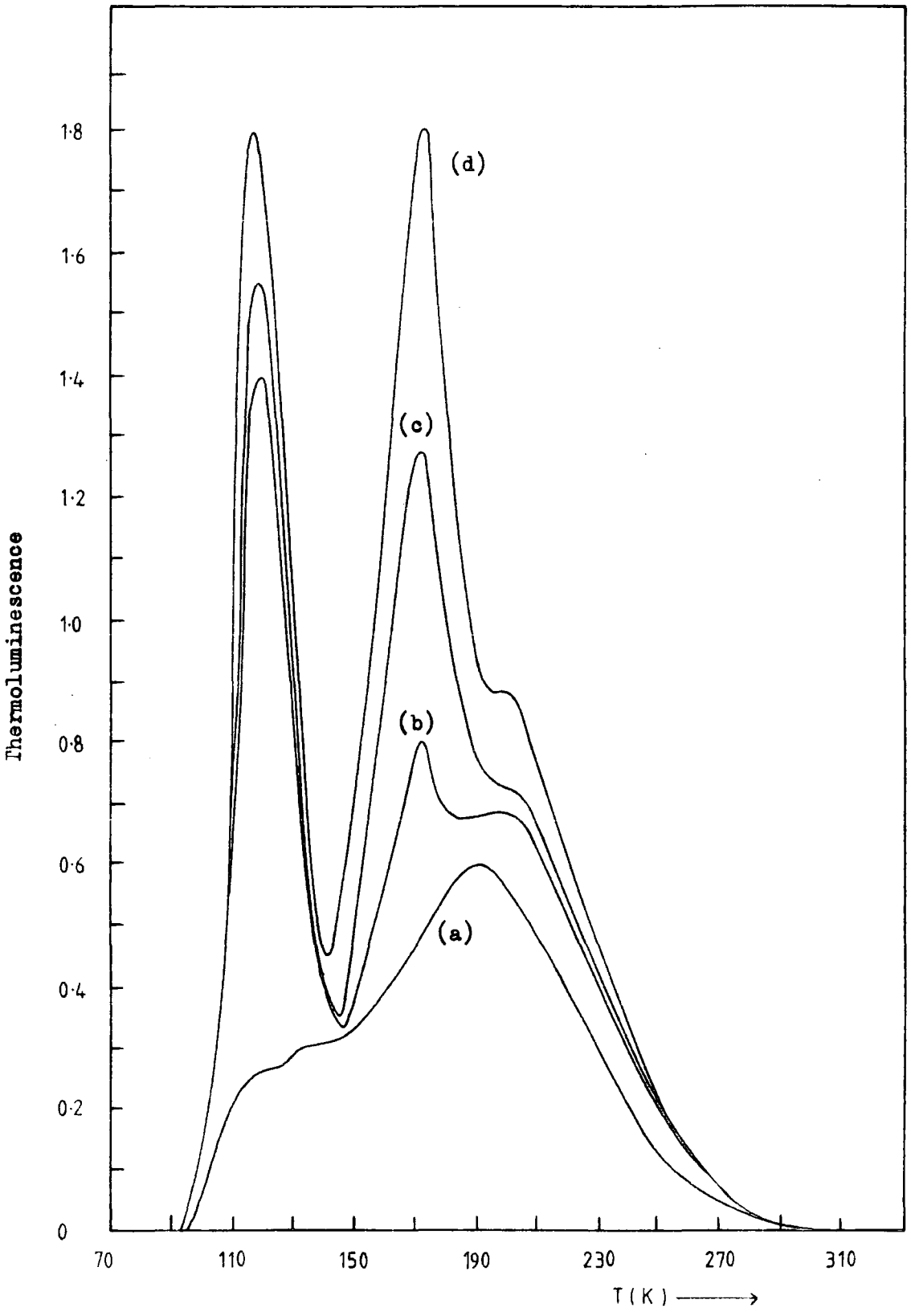

Figure 10.3.1 TL spectra for the rutile pigment RH472 (a) as-received and after quenching from a temperature of (b) 600°C (c) 800°C (d) 1000°C .

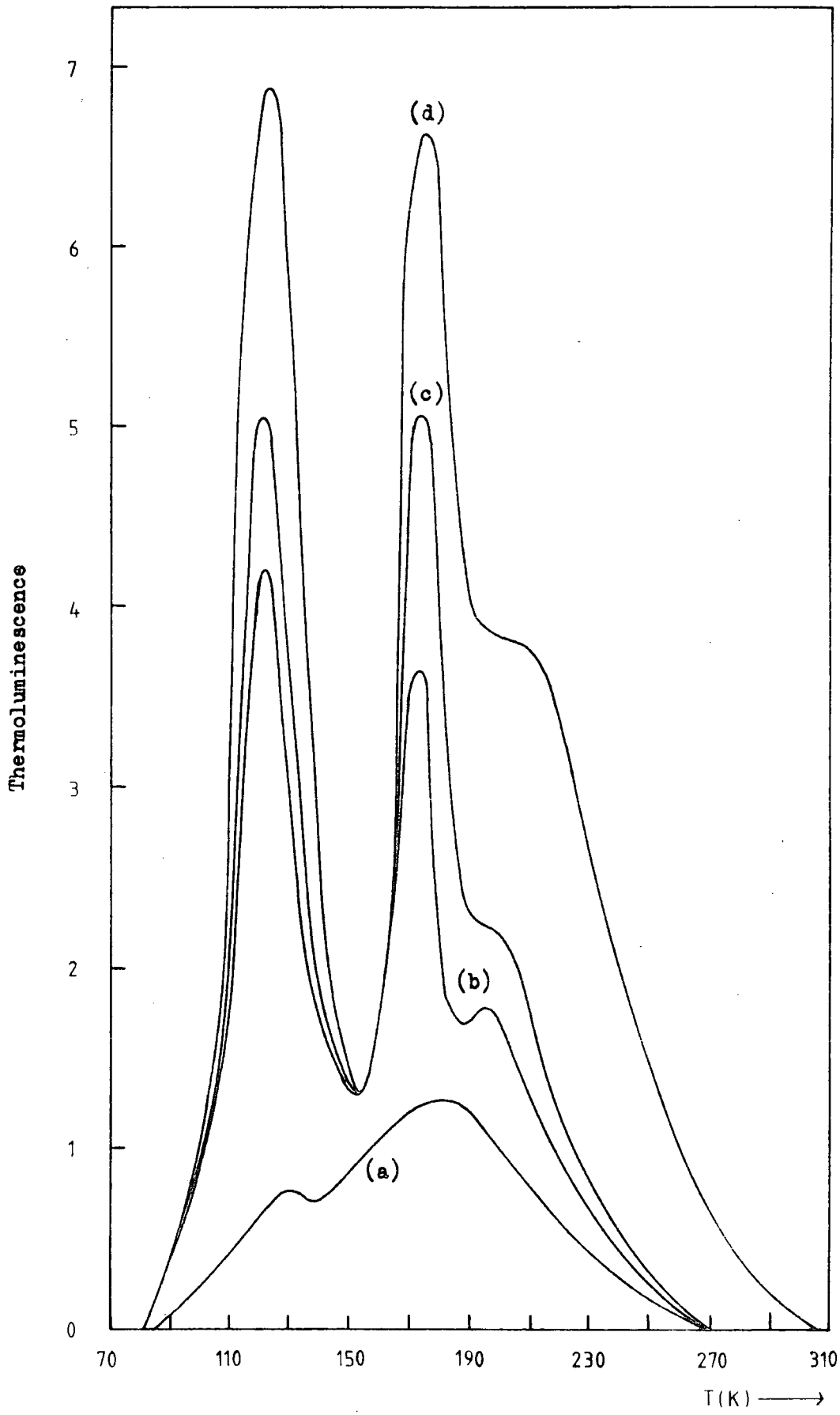

Figure 10.3.2 TL spectra for the rutile pigment RD2A (a) as-received and after quenching from a temperature of (b) 600°C (c) 800°C (d) 1000°C.

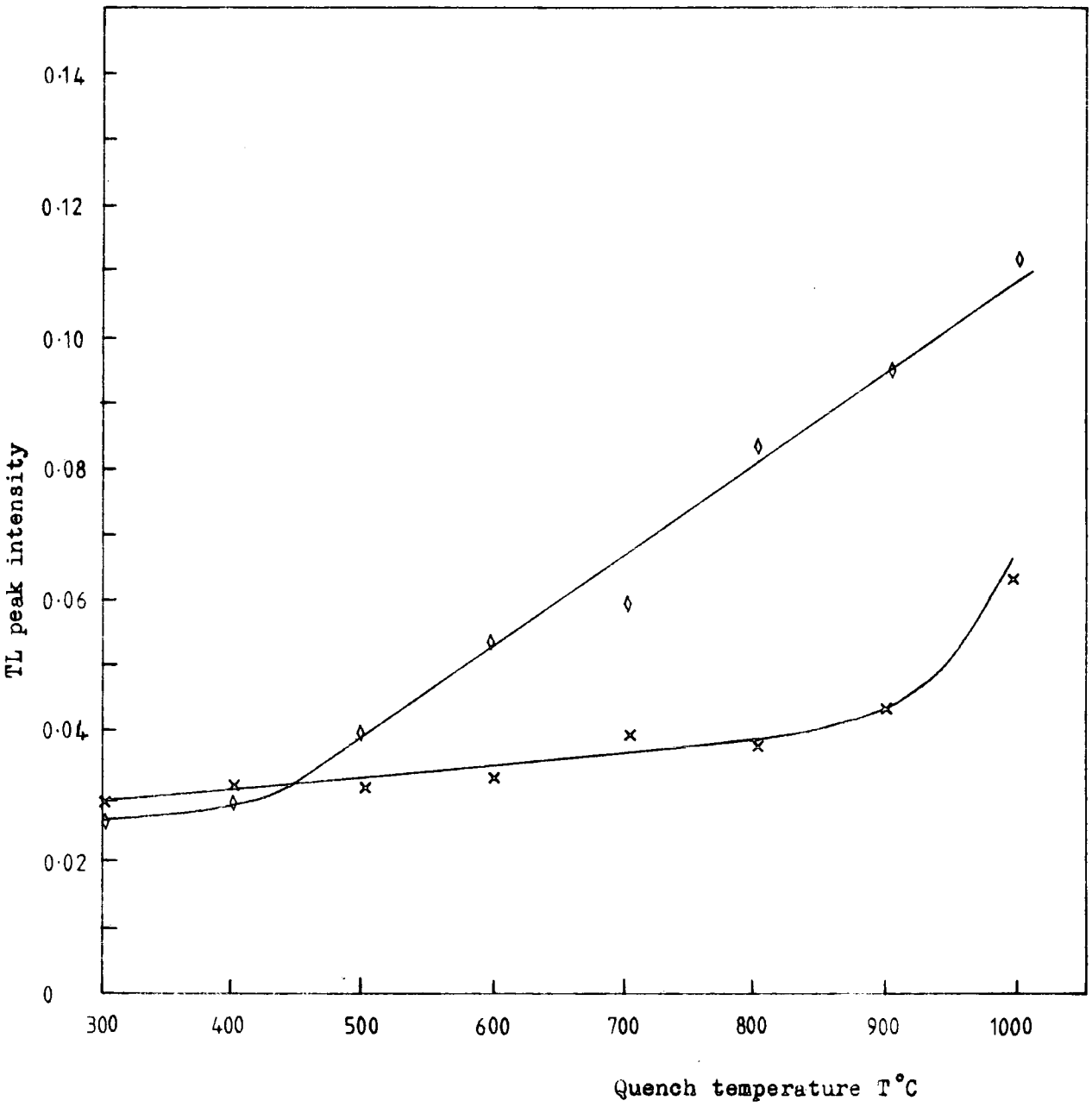

Figure 10.3.3 Variation of the TL peak intensity for pigment E1822 R/D after quenching from T°C . ◊ 125 K peak ⨯ 170 K peak

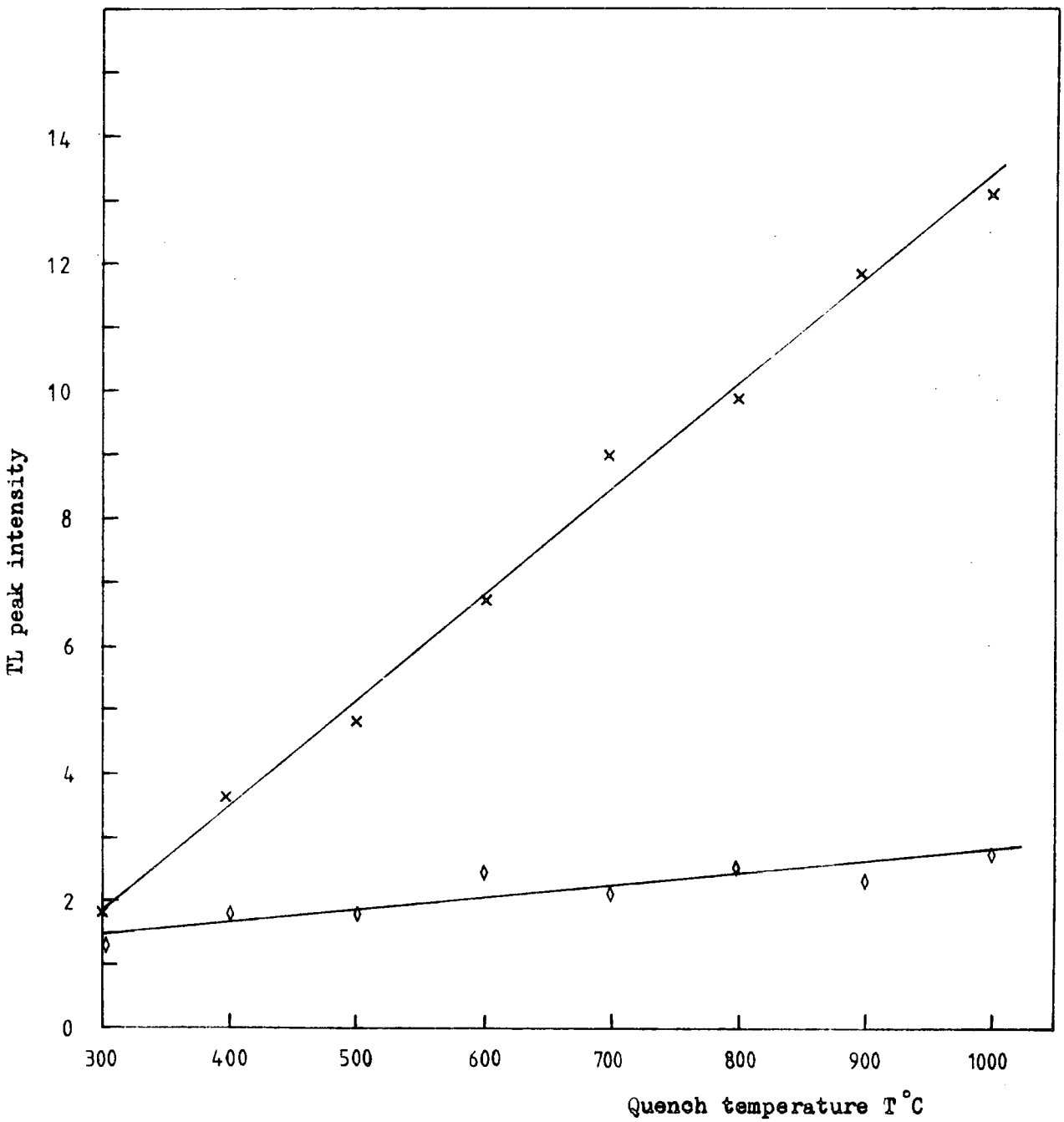

Figure 10.3.4 Variation of the TL peak height for pigment SPF552 after quenching from T°C . × 175 K peak ◊ 130 K peak

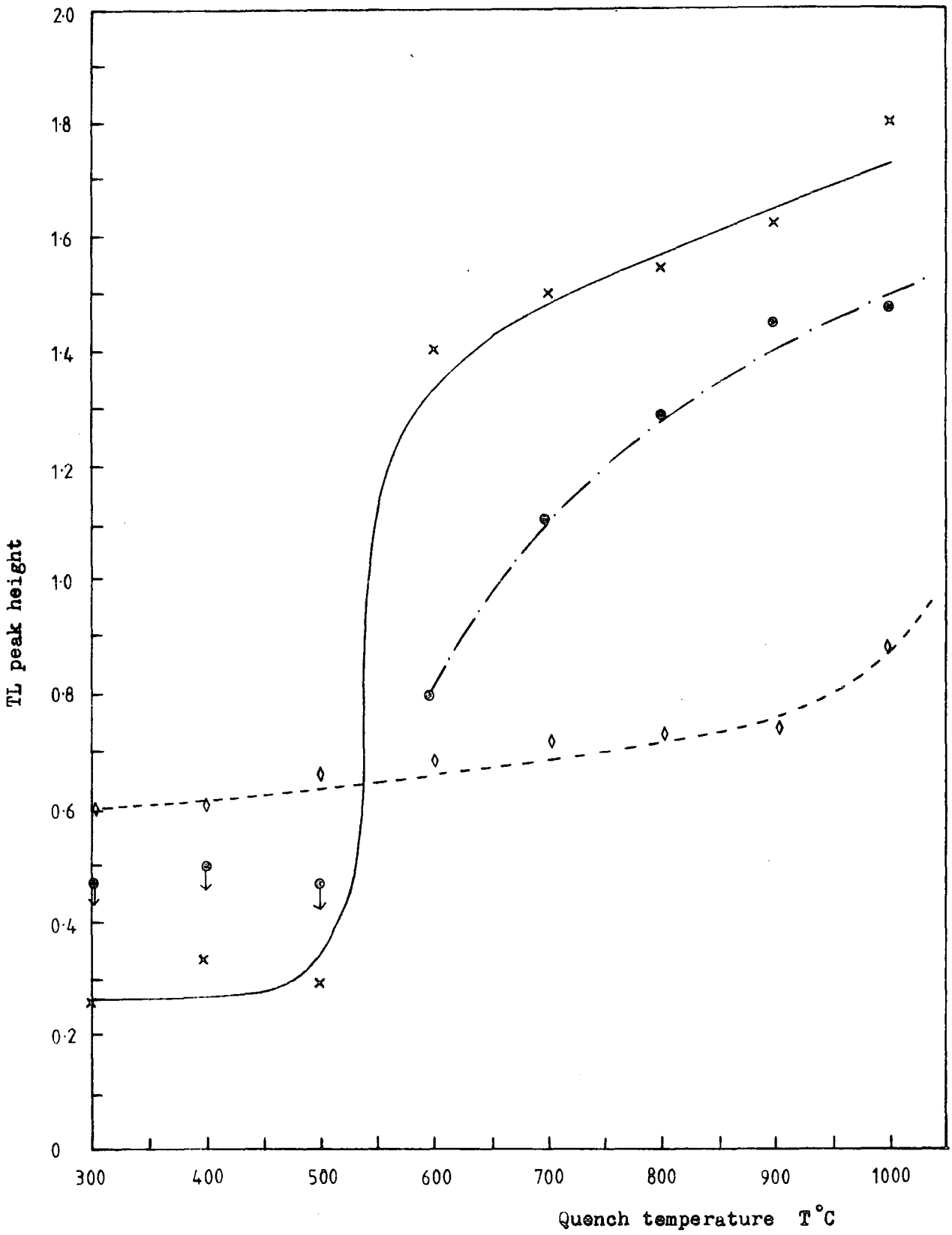

Figure 10.3.5 Variation of the TL peak height for pigment RH472 after quenching from T°C . ◊ 200 K peak × 120 K peak ⊛ 175 K peak

figure 10.3.5. The spectra shown in figure 10.3.1 demonstrate that the 190 K peak observed in the as-prepared pigment is in fact a combination of the 175 K and 200 K peaks. This explains some of the problems encountered when trying to apply the methods of Garlick and Gibson, and Hoogenstraaten to the as-received pigments. Analysis of some selected pigments, where individual peaks were well isolated, will be described in the next section.

One major difference between the PL behaviour in single crystal rutile and pigments is that no reduction in luminescence was observed as the result of temperature quenching. As shown in figure 6.7.1 for single crystal rutile an order of magnitude reduction in PL intensity was observed after quenching from 1000°C. Powder DN5 showed a reduction of approximately a half after quenching from 1000°C.

Figure 10.3.2 shows the TL spectra for pigment RD2A after quenching from 600°C, 800°C and 1000°C. The variation of the TL peak heights with quenching temperature is very similar to RH472. Pigment E1822 R/D has a different type of quenching behaviour, as shown in figure 10.3.3. The 170 K peak increases slowly until about 900°C when it begins to show a slight increase. However, the 125 K peak shows a linear increase between 500°C and 1000°C, unlike the sudden rapid increase at about 600°C observed in pigments RH472 and RD2A. The 'sulphate' pigment SPF552 exhibits a completely different behaviour as shown in figure 10.3.4. The 130 K peak shows little variation with quenching temperature, whilst the 175 K peak shows a linear increase between 300°C and 1000°C.

10.4 ANALYSIS OF TL CURVES FROM POWDERS

Many of the powders and pigments examined had too low a TL emission to apply the heating rate methods over a wide enough range of temperatures to establish good activation energy plots. As previously mentioned analysis of TL peaks such as the 195 K peak shown in figure 10.3.1 were

difficult because of overlapping TL peaks, as demonstrated by the growth of the 170 K peak with increase in quenching temperature. However, analysis of the isolated 170 K peak even did not produce consistent results, in contrast with the corresponding peaks in single crystal rutile. Table 10.4.1 shows the results obtained by applying some of the TL methods previously described in chapters 2 and 8. When the TL geometrical shape methods of Chen and Grossweiner were tried it was observed that the TL width varied with heating rate. From the results obtained it is tempting to conclude that the 170 K peak is the same as the peak 3 seen in single crystal rutile. The variation of the TL halfwidth could well have been due to the problems of heat transfer in the vacuum cryostat. Careful experiments in a helium gas exchange cryostat would be necessary to determine if the heat transfer affect is the primary reason for large errors in the activation energy analysis, or whether some other explanation is necessary such as trap distributions in powders or invalidity of the simple insulator model.

Analysis of the two low temperature peaks was not successful. As shown in figure 10.3.1 the two TL peaks observed in the as-received RH472 pigment, merged into one large TL peak as the quenching temperature was raised. This behaviour was similar to that observed for peaks 1 and 2 in single crystal rutile. Coupled with the observation that with temperature quenching the two low temperature peaks increase in magnitude, becoming comparable to the 170 K peak, it is tempting to suggest that these peaks are in fact the same peaks 1 and 2 observed in single crystal rutile. Application of the initial rise method to the two low temperature peaks produced a range of activation energies from 0.09 eV to 0.25 eV as the TL peaks were thermally cleaned. Again it was not possible to distinguish between the possibility of overlapping TL peaks, trap distributions, limitations of the simple insulator model and experimental heat transfer problems. More experimental work is necessary to distinguish

	170 K PEAK RH472	170 K PEAK RD2A
Hoogenstraaten	0.34 ∓ 0.04	0.33 ∓ 0.05
Unger	0.32 ∓ 0.06	0.31 ∓ 0.06
Garlick, Gibson 10%	0.36 ∓ 0.03	0.34 ∓ 0.04
Boiko, Rashba, Trofimenko A	0.31 ∓ 0.06	0.30 ∓ 0.05
Chen, Winer	0.33 ∓ 0.04	0.34 ∓ 0.04
Haering, Adams	0.29 ∓ 0.06	0.30 ∓ 0.07

Table 10.4.1 Trap depths obtained from TL analysis for the RH472 and RD2A pigments that were temperature quenched from 800 °C .

between these effects.

Although a good deal of qualitative evidence has been presented to suggest that traps 1, 2, 3, 8 and 4 have been observed in both single crystal and powdered rutile, no quantitative activation energy analysis can be cited to support this view. One obvious experiment that could now be applied to this problem would be progressively to grind up a single crystal and measure the TL spectra as a function of the particle size.

10.5 SUMMARY OF THE PIGMENT RESULTS

The TL and PL spectra of fifty nine pigments were examined during the course of this investigation. These pigments were provided by BTP Stockton and their labels have been used throughout this chapter. Although the full details of their history were not disclosed by the manufacturer, the durabilities of twelve of these pigments were known. Some of the labels used are not significant in the context of this present work, but it is hoped that the information may be useful when correlated with other properties obtained by workers at BTP. It is for this reason that the BTP labels have been retained.

The values of durability ratio, D, were measured using the Marr twin-carbon-arc rotating drum accelerated weathering machine. This equipment provides a hostile enviroment of water and uv radiation in which to assess the durability of the paint film. For the purposes of the present work it is only important to note that the lower the durability ratio the better the durability and vica versa. For example, the sulphate pigment SPF552 had poor durability with D = 0.8 and the chloride pigment RD2A had good durability with D = 0.45.

The durability ratios of SPF552, E1822 R/D, RD2A and RH472 were 0.8 0.65, 0.45 and 0.40 respectively. Figure 10.5.1 shows the TL and PL spectra of four rutile pigments with mediocre durabilities, whilst figure 10.5.2 shows the spectra of four pigments with good durabilities. Pigment RX

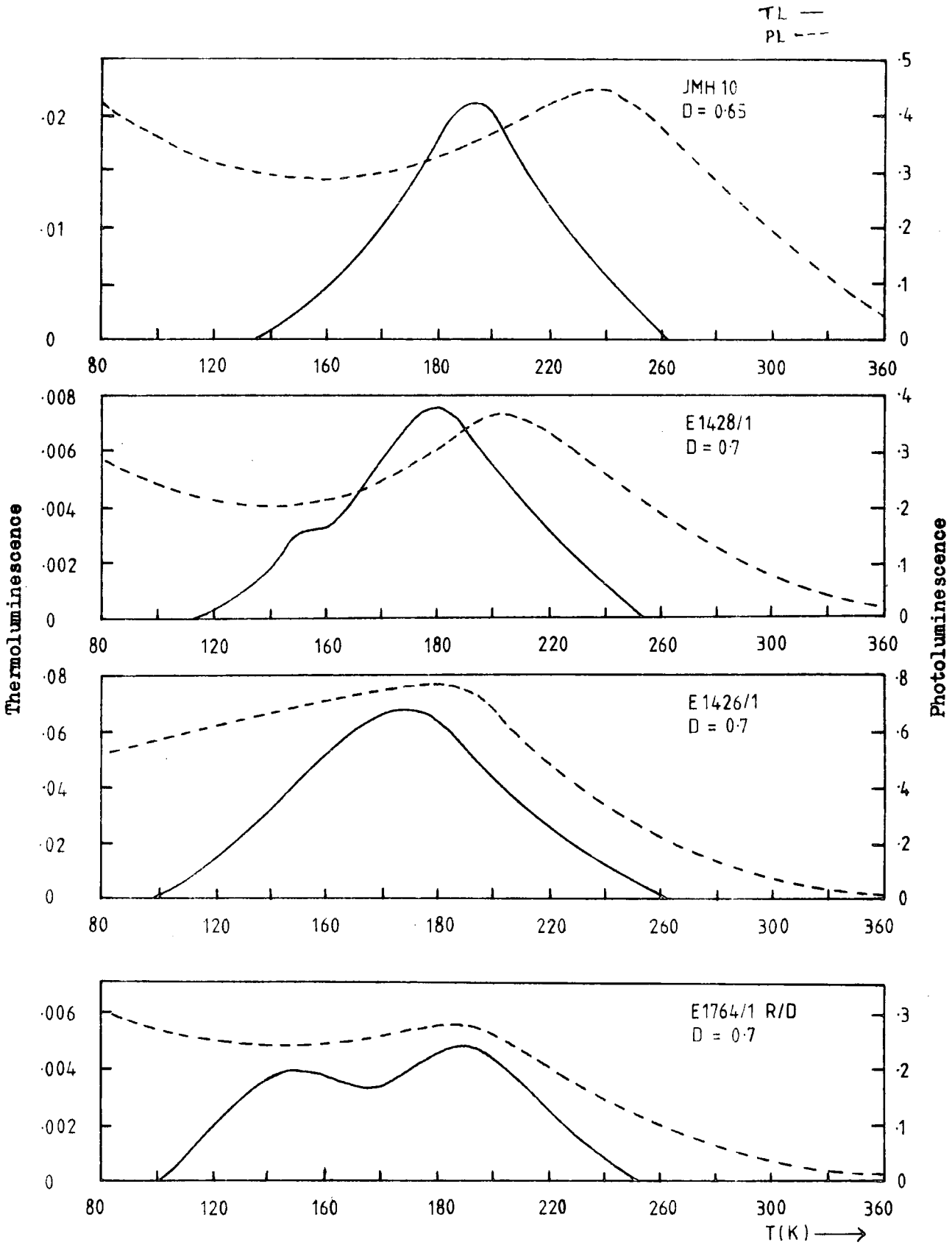

Figure 10.5.1 TL and PL spectra for the four rutile pigments JMH10, E1428/1, E1426/1 and E1764/1 R/D .

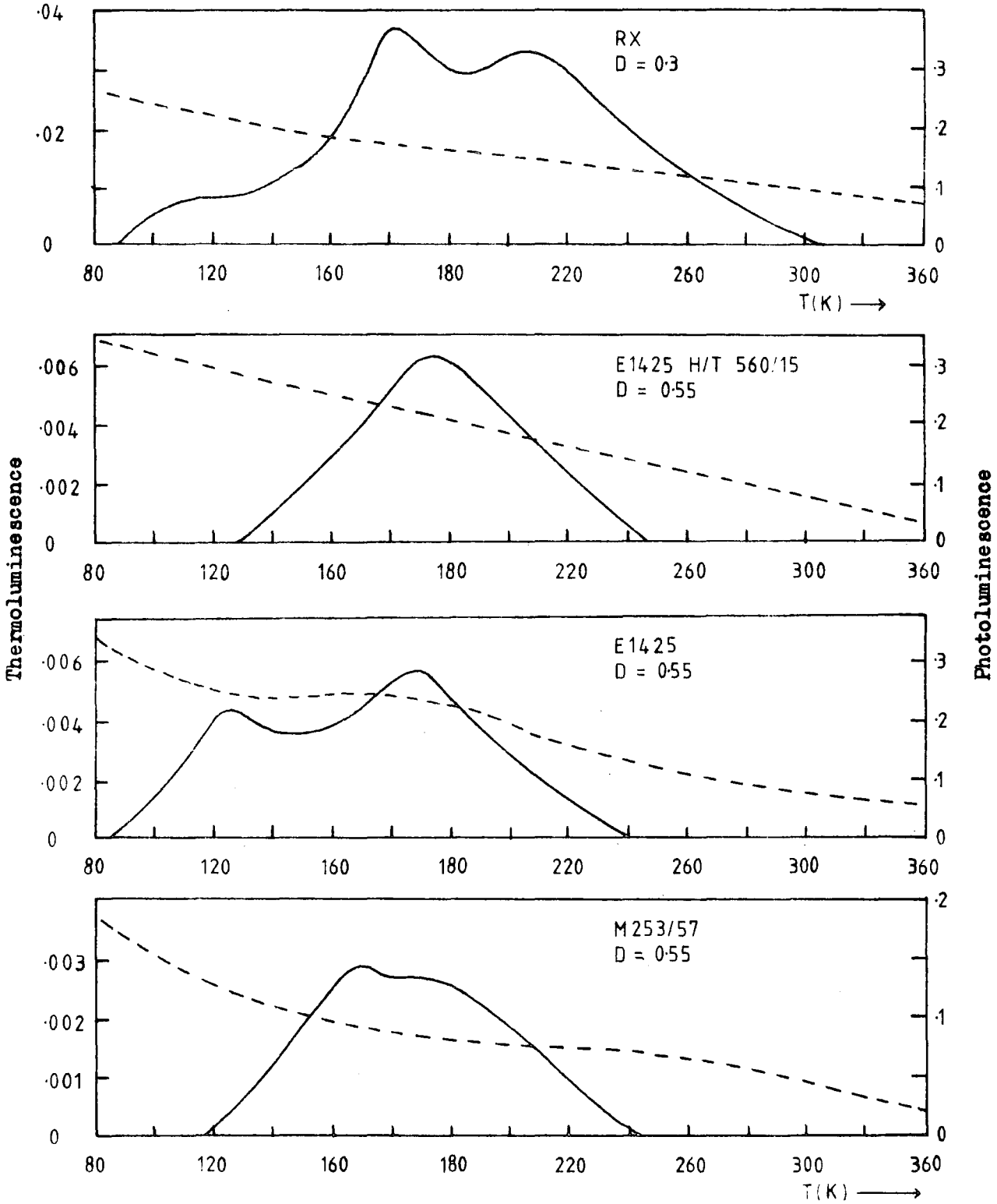

Figure 10.5.2 TL and PL spectra for the four rutile pigments RX, E1425 H/T 560/15, E1425 and M253/57 .

had an exceptionally high durability of 0.3. Before discussing the possible interpretations of these results it is interesting to plot the maximum TL peak height against the maximum emission for all the pigments examined. Figure 10.5.3 shows this information for all the fifty nine pigments measured. As can be observed, there is approximately three orders of magnitude variation in PL intensity and four orders of magnitude variation in TL intensity.

The area under the TL curve represents the amount of trapped charge released during the TL measurement. To obtain trap densities it is necessary to know the lifetime of the carriers and the recombination traffic via the radiative centre. We know from the work on single crystal rutile that the Cr^{3+} centre is not the dominant impurity centre as regards the recombination kinetics in rutile. The PL emission intensity for the Cr^{3+} centre is a measure of the efficiency of this centre in competition with other centres present in the pigment. Therefore, high TL intensity does not necessarily imply a large trap density and the efficiency of the Cr^{3+} centre in the pigment must be considered. In general, as can be observed in figure 10.5.3, pigments with high PL intensity tend to have high TL intensity. However, it is pertinent to ask whether low PL intensity is the result of low chromium content or the presence of a large quantity of fast competitive recombination centres such as iron.

A glance at figure 10.5.3 might at first sight suggest little correlation between durability and the TL/PL ratio. High and low durability pigments have both low and high TL/PL ratios. However, there is more information contained in the PL versus temperature data which allows a more complete hypothesis to be presented.

Pigments RD2A and RH472, although from different sources appear to have a similar defect composition. Both pigments have high PL and TL intensities suggesting high chromium content with little competition

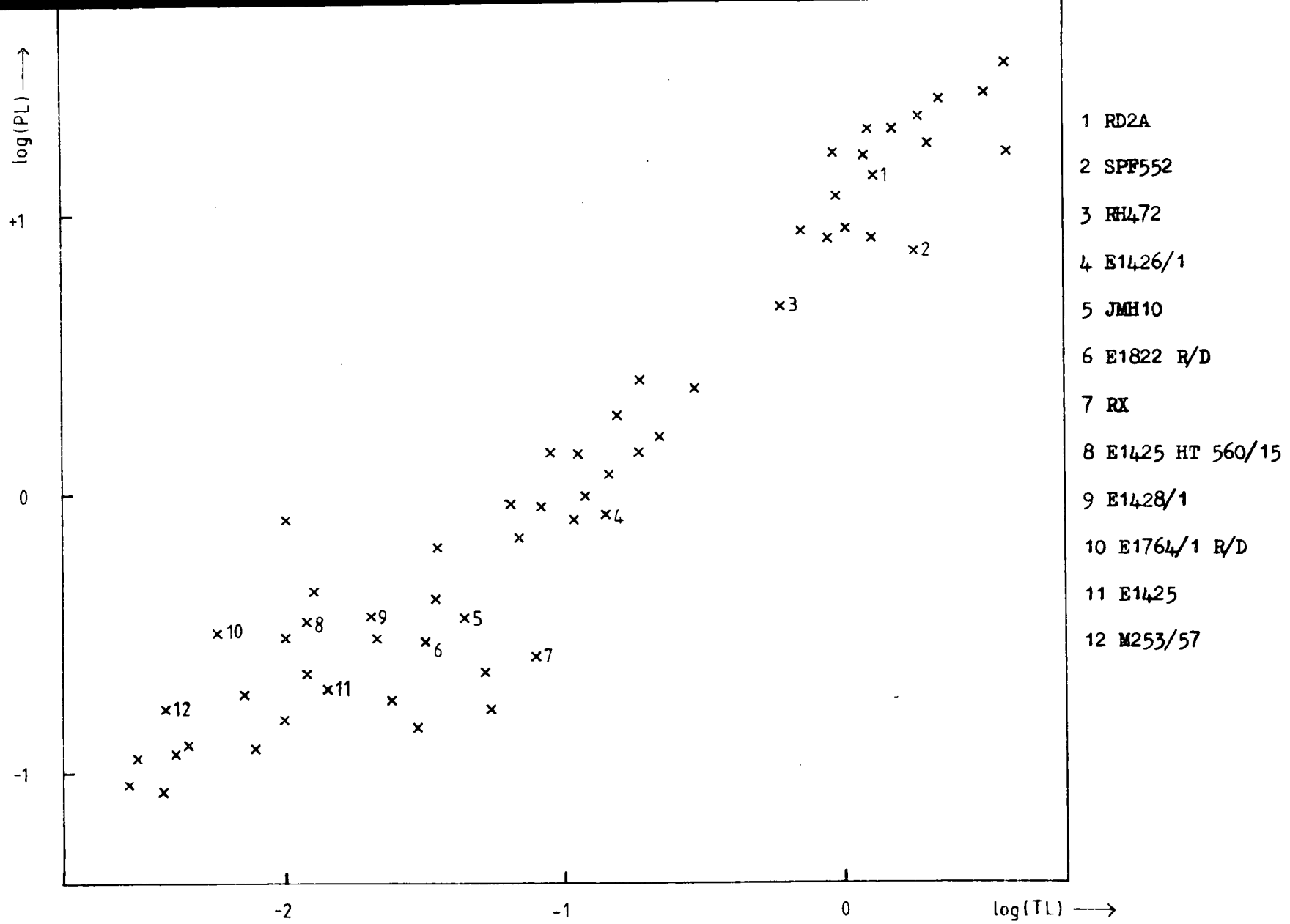

Figure 10.5.3 Variation of the maximum TL peak height with maximum PL emission for 59 pigments .

from fast recombination centres. The large reduction in PL intensity at low temperatures has been explained previously for single crystal rutile as being due to Auger recombination, and hence we may conclude that these pigments have large densities of shallow traps. These centres trap any charge that is produced by uv radiation preventing it reaching the surface of the pigment particle, where it may participate in the degradation processes described in the preface. On the otherhand, the sulphate pigment SPF552 has equally large TL and PL values but the shape of the PL versus temperature curve suggests a low density of shallow traps.

Figure 10.5.1 shows four pigments with low TL and low PL intensities, and they display typical PL versus temperature curves. These pigments appear to have low chromium luminescence efficiency due to low chromium content, low density of competitive recombination centres and a low density of shallow traps. The durability of these pigments is mediocre.

Figure 10.5.2 shows four pigments with low PL and TL intensities, but that display PL versus temperature curves that have only previously been observed in iron doped single crystal rutile (see figure 9.7.3). These pigments would appear to have a set of dominant fast iron recombination centres which effectively 'mop' up any free carriers created by band gap radiation. It is proposed that it is the recombination kinetics rather than the shallow trapping centres that produce the good durability ratios in these pigments.

One encouraging aspect of the TL/PL measurements is the fact that there is a wide range of solid state properties contained within a commercial range of pigments. The TL and PL properties of these pigments reflect the manufacturing history of each individual pigment. Although the hypothesis proposed has not been tested on a large enough data base, there does appear to be encouragement for continued work on shallow and deep levels in rutile. We might expect to find a correlation between TL/PL ratio and durability

ratio for pigments with constant Cr^{3+} luminescence efficiency.

One of the missing experiments in the present exercise is the comparison of pigments with 'normal' and iron doped type PL/temperature spectra with their respective MS7 analysis. It would also be interesting to compare the brightness and tone of these two different categories of pigments with their respective iron content. Further work should also include studies on chromium and iron double doped single crystal rutile. Although the PL versus temperature curves shown in figure 10.5.2 have only been observed in iron doped single crystal rutile there may be some other mechanism responsible for this effect. It may also be possible to grind up these crystals and remeasure their TL/PL spectra as a function of particle size. A study of the quenching behaviour of these crystals may also elucidate why the increase in the concentrations of defects upon quenching is not the same in different pigments.

Finally, it should be mentioned that two anatase pigments were examined. Low photoluminescence emission identical to the Cr^{3+} emission in rutile was observed, and low PL/TL spectra were obtained similar to those shown in figure 10.5.2 for rutile pigments. It is concluded that these pigments contained a percentage of rutile pigment that was formed during its manufacture.

CHAPTER 11

CONCLUSIONS

11.1 IN CONCLUSION

Thermally stimulated current and thermoluminescence curves have been measured for National Lead flame fusion crystals, non-stoichiometric as-grown plasma crystals and stoichiometric as-grown plasma crystals. These measurements reveal the presence of six discrete sets of electron traps with ionisation energies of 0.13, 0.24, 0.37, 0.51, 0.61 and 0.69 eV. Crystals from different sources all contain the same three trapping levels with ionisation energies of 0.13, 0.24 and 0.37 eV, and the density of these traps increases as the crystals are chemically reduced.

The TSC curves have been analysed in detail following the procedure advocated by Hagebeuk and Kivits, and also by using a large number of analysis methods, the reliability of which has recently been discussed by Kivits and Hagebeuk. The methods of Hoogenstraaten, Haering and Adams, Chen and Winer, Unger, and Garlick and Gibson, yield consistent values of the trap depths which are taken to be correct. The procedure for the determination of the values of the trap depth, detrapping frequency, recombination rate constant, retrapping ratio and the ratio of thermally disconnected to thermally connected traps has been discussed in detail for the 176 K peak.

The consistency of the results obtained by analysing both the TSC and TL curves shows that the simple insulator model applies quite well to rutile. In particular it is clear that it is realistic to speak of discrete traps. However, it has been pointed out in chapter 8 that there are at least two recombination centres present in the nominally 'pure' crystals from both the BTP Stockton and National Lead sources. Since the Cr^{3+} radiative centre has a recombination time of 35 μs, at least one other centre with a recombination lifetime of 10^{-8} s appears to be involved. The subsequent in-diffusion of ions from the first transition series showed that iron drastically reduces the PC and PL, whereas chromium increases both the PC and PL. These experiments

confirm the need for a two centre recombination model to describe the single crystal rutile system. The total chromium content in our crystals was determined to be between 0.1 and 0.9 ppma by solid source mass spectroscopy, whereas Fe was present in quantities between 3 and 27 ppma.

Examination of single crystal rutile doped with Cr, Fe, Co, Ni, Nb, Mn or Al showed that peak 7 (0.19 eV) appeared only in the chromium doped crystals, and peak 8 (0.41 eV) appeared in the Cr, Fe and Co doped crystals. The nominally 'pure' crystals investigated by Ghosh et al (1968) revealed the presence of all eight trapping centres. Ghosh et al did not comment on the concentration of any chromium in their crystals but it seems likely that Cr was present in their crystals in appreciable amounts (> 1 ppma). Our investigations do not provide any meaningful speculation as to the atomic nature of the trapping centres. Ghosh et al thought there was some evidence to indicate that the trap to which we assign an activation energy of 0.37 eV was associated with oxygen vacancies. Our observation of this centre and its dependence on the degree of reduction would not conflict with this assignment. In fact, the appearance of most of the centres 1 to 7 in a wide range of doped and undoped crystals suggests that these shallow trapping centres are associated with oxygen vacancies or interstitial titanium and are more complex than simple point defects. Photo-ESR experiments in conjunction with TSC/TL experiments might well provide information regarding their atomic nature.

Theoretically, perfect crystals in terms of perfect lattices are thermodynamically impossible. Thermal energy provides the means of forming vacant lattice sites by transfer of an atom or ion to an interstitial or surface site (Frenkel and Schottky defects respectively). All titanium dioxide pigments are heated to about 1000 °C at some stage in their manufacture and at this temperature there will be about 1 in 14000 defective oxygen sites.

During cooling these defects (mostly Schottky-type) decrease in number. At around 500 °C the remaining defects are 'frozen-in'. A sphere of rutile 0.2

μm in diameter contains about 100 vacancies at room temperature if it is cooled very slowly. At faster cooling rates more vacancies, between 10^2 and $1.4\ 10^4$ will be frozen into the rutile lattice.

On the surface of TiO_2 raised to a high temperature, oxygen ions are capable of associating to form molecules, volatilising and leaving the crystal oxygen-deficient. This oxygen deficiency differs from the oxygen vacancies caused by Schottky defects, because the latter do not give rise to a seperation of electrical charge.

The defects so far discussed lead to the concept of a TiO_2 grain at room temperature that contains vacant oxygen sites at a concentration of greater than about one in two million oxygen lattice points. Associated with some of these vacancies are Ti^{3+} ions or electrons trapped near the sites.

It is impossible, and usually undesirable, to make TiO_2 entirely free from impurities, and the impurities generally encountered are in the form of positive ionic species that occupy titanium lattice sites. For some impurities the host lattice is very receptive, but for others the enviroment is less accommodating, in which case the process of crystal growth is one of rejection. Impurities that have a strong effect on the absorption of visible light are in practise reduced to a minimum during processing in order to obtain the whitest products.

Other impurities (or, more correctly, conditioning agents) are added during processing for their benefical effects on durability, colour, and opacity; or as promoters for formation of rutile; examples of such impurities are Al^{3+} and Zn^{2+} and P^{5+}. Impurities such as Nb^{5+} are also present in pigments where the raw material used in manufacture contains the element in question.

The approximate numbers of ions and defects present in a typical

pigment grain 0.2 μm in diameter, are as follows:

O^{2-}	270×10^6
$Ti^{4+}(Ti^{3+})$	135×10^6
Oxygen vacancies(Schottky)	10^2 to 10^4
Cr^{3+}	200
Fe^{3+}	2000

and in certain cases, Al^{3+}, Zn^{2+}, P^{5+}, Nb^{5+} 10^5 to 10^6.

Although no quantitative data has been obtained from the TL analysis of rutile pigments, the TL spectra are very similar to those observed for single crystal rutile. If we can consider a 0.2 μm diameter pigment grain to be a replica of a large rutile crystal then the total number of shallow trapping centres would vary from about 10^2 to 10^4. These values can be regarded as minimum values of shallow trap concentrations expected in pigment particles. In the example previously given it should commented that a concentration of Fe^{3+} ions exceeding 100 in a 0.2 μm pigment grain would be expected to dominate the trapping and recombination kinetics, because of the apparently large electron and hole capture cross sections of the Fe^{3+} impurity. This example refers to a pigment manufactured by the 'sulphate' process where the main raw material is the iron based ore ilmenite. If the level of iron can be reduced substantially, by say the 'chloride' process, then one can envisage a situation where the shallow trapping centres become an important mechanism for preventing free carriers reaching the surface of the pigment particle and participating in oxidation of the binder. In such a situation it may be necessary to control the rate of cooling of the pigment and the presence of chromium, which by enhancing the shallow trap population, may prove a beneficial impurity.

11.2 SUGGESTIONS FOR FURTHER WORK

(1) Measure the Hall mobility in stoichiometric rutile crystals and doped crystals using the Hall voltage and the Hall current technique (Dobrovol'skii and Gritsenko, Sov Phys - Solid State 4 (1963) 2025; Pethig and Morgan, Nature 214 (1967) 177). The mobility could be measured in a crystal at various stages of reduction.

(2) Investigate the TL spectra of powder, pigments and paints in a helium gas exchange cryostat. The various TL analysis techniques could be applied to a crystal as it is successively ground to smaller particle sizes.

(3) Study the TSC/TL spectra of single crystal rutile, especially aluminum doped, below 77 K.

(4) Investigate the photo-ESR and TSC/TL spectra in TiO_2. Cr and attempt to resolve the two peaks 3 and 8 in 1.1 eV absorption band observed by Sochava et al.

(5) Examine the possibility of using a Schottky barrier diode to examine deep levels in single crystal rutile using photocapacitance and DLTS measurements.

(6) Repeat the EPR/reduction experiments of Miyako (1967) on TiO_2.Co but with associated TSC/TL measurements.

(7) Investigate the infra red quenching of PC and PL in the doped rutile crystals. Double diffusion doped Cr-Fe crystals might be an interesting system to examine.

(8) Continue to correlate durability and the PL/TL ratio for various pigments. Information from mass spectroscopy concerning the Fe and Cr content would be valuable in this exercise.

APPENDIX 1

LISTING OF FILE TSCL1 14:05:37 JUL 7, 1978

```
1    C TSC AND TSL CURVES ARE GENERATED BY KIVITS THEORY FOR SIMPLE
2    C INSULATOR MODEL
3    C TSC AND TSL DATA REQUIRED: EV,HS,HD,RATE,FREQ,TO,ALPHA,BETA
4    C TSC AND TSL ANALYSIS IS PERFORMED USING GENERAL METHODS
5          SUBROUTINE CURVE(SS,E,DELTA,ALFA,SKSI,P,Q,T,A,FIFN,FN,DFN,DA,K,IX
6         1,L,FNN,DAA,HS,HD,ALPHA,BETA,EV,TEMP)
7          IMPLICIT REAL 8 (A-H,O-Z)
8          DIMENSION P(1001),Q(1001),T(1001),A(1001),TEMP(1001),FIFN(1001),
9         1FNN(1001),DAA(1001),FN(1001),DFN(1001),DA(1001)
10   C E,ALFA,DELTA,SKSI,S ARE DIMENSIONLESS QUANTITIES
11   C EV IS THE THERMALLY CONNECTED TRAP OF DENSITY HS(/CM  2),BOLTZ IS
12   C BOLTZMANN'S CONSTANT,TO IS THE INITIAL TEMP.(80K),RATE IS THE HEATING
13   C RATE IN K/SEC,FREQ IS THE FREQUENCY FACTOR,HD IS THE DENSITY OF THERMALLY
14   C DISCONNECTED TRAPS,ALPHA IS THE RECOMBINATION RATE (CM  2/SEC),BETA IS
15   C THE RETRAPPING RATE
16   C
17         DO 1002 I=1,L
18         FNN(1)=0.0
19         DAA(1)=0.0
20    1002 CONTINUE
21         GO TO 1001
22    1000 L=L-1
23    1001 DT=1.25D-3
24         DO 10 I=1,L
25         T(I)=1.0D0-1.25D-3+I*DT
26         TEMP(I)=79.9+DFLOAT(I)/10.0
27         X=E/T(I)
28         GE=DLOG(1.00D1)
29         S=DLOG10(SS)
30         P(I)=DEXP(GE*S-X)
31         Q(I)=T(I)*P(I)*(1.0D0-((X+4.0364D0)*X+5.03637D0)
32        1X+4.19160D0))
33         A(I)=1.0D0/(1.0D0+Q(I))
34         FN(I)=P(I)/(1.0D0+Q(I))
35         T(I)=80.0D0*T(I)
36         ZZ=DFLOAT(I)/10.0D0
37         IZZ=IFIX(SNGL(ZZ))
38         IZ=IZZ*10
39         IF(P(I).GE.1.0D3.AND.IZ.EQ.L) GO TO 10
40       10 CONTINUE
41         K=3
42         FIFN(1)=0.0
43         FIFN(2)=0.0
44         DO 40 J=1,20
45         IX=L-1
46         GO TO 90
47       80 K=K+1
48       90 DO 20 M=2,IX
49         DFN(M)=(FN(M+1)-FN(M-1))/DT/2.0D0
50       20 CONTINUE
51         DO 30 N=K,IX
52         FIFN(I)=FIFN(N-2)+4.0D0*FN(N-1)+FN(N))*DT/3.0D0
53         XX=FIFN(N)
54         IF(DABS(XX).GE.1.74D2) GO TO 1000
```

```
55          A(N)=(1.0D0+SKSI)*DEXP(-XX)
56          W=A(N)+DELTA*(1.0D0+SKSI-A(N))
57          R=P(N)*(A(N)-SKSI)-FN(N)*W-(DFN(N)+FN(N)*(P(N)+DELTA*FN(N)))/ALFA
58          RR=W+(P(N)*2.0D0*DELTA*FN(N))/ALFA
59          FNS=R/RR
60          FN(N)=FN(N)+7.0D-1*FNS
61          IF(FN(N).LT.0.0) GO TO 30
62          FNN(N)=FN(N)*HS/ALFA
63          DA(N)=A(N)*FN(N)
64          DAA(N)=(DA(N)*HS**2)/ALFA
65          IF(FN(N).GE.1.0D-4) GO TO 50
66       50 IF(K.NE.N) GO TO 30
67          XXX=1.0D-4*(1.0D0+DABS(XX))
68          IF(DABS(FNS).GE.XXX.OR.XX.GE.1.0D-4) GO TO 30
69       30 CONTINUE
70          ITER=J
71          IF(J.GE.24.OR.K.GE.L-2) GO TO 40
72       40 CONTINUE
73          RETURN
74          END
75     C FIND TSC AND TSL MAXIMUM VALUES
76     C DAMAX IS THE TSL MAX.,FNMAX IS THE TSC MAX.,CTMAX AND OTMAX ARE THE
77     C TEMPS. OF THE TSC AND TSL MAXIMUMS
78     C
79          SUBROUTINE SORT(FNN,DAMAX,DAA,IX,FNMAX,CTMAX,OTMAX)
80          IMPLICIT REAL 8 (A-H,O-Z)
81          DIMENSION FNN(1),DAA(1)
82          IXX=IX-1
83          DO 405 M=K,IXX
84          IF(FNN(M).GT.FNN(M+1)) GO TO 406
85       405 CONTINUE
86       406 FNMAX=FNN(M)
87          CTMAX=DFLOAT(M)/10.0+79.9
88          DO 407 M=K,IXX
89          IF(DAA(M).GT.DAA(M+1)) GO TO 408
90       407 CONTINUE
91       408 DAMAX=DAA(M)
92          OTMAX=DFLOAT(M)/10.0+79.9
93          RETURN
94          END
95     C FIND TSC AND TSL HALF VALUES
96     C FNHALF IS THE TSC HALF VALUE,DAHALF IS THE TSL HALF VALUE
97     C CTHALF AND OTHALF ARE THE LOW TEMP. VALUES OF THE HALF VALUES
98     C
99          SUBROUTINE THALF1(FNN,DAA,FNMAX,DAMAX,FNHALF,DAHALF,K,IX
100        1CTHALF,OTHALF)
101         IMPLICIT REAL 8 (A-H,O-Z)
102         DIMENSION FNN(1),DAA(1)
103         DO 411 I=K,IX
104         FNHALF=FNMAX/2.0
105         IF(FNN(I).GT.FNHALF) GO TO 412
106      411 CONTINUE
107      412 CTHALF=DFLOAT(I)/10.0+79.9
108         DO 413 I=K,IX
109         DAHALF=DAMAX/2.0
110         IF(DAA(I).GT.DAHALF) GO TO 414
111      413 CONTINUE
```

```
112    414 OTHALF=DFLOAT(I)/10.0+79.9
113        RETURN
114        END
115    C FIND TSC AND TSL HIGH TEMP. HALF VALUES
116    C CTHAB AND OTHAB ARE THE TSC AND TSL HIGH TEMP. HALF VALUES
117    C
118        SUBROUTINE THALF2(FNN,DAA,FNHALF,DAHALF,CTMAX,OTMAX,IX,
119       1CTHAB,OTHAB)
120        IMPLICIT REAL 8 (A-H,O-Z)
121        DIMENSION FNN(1),DAA(1)
122        M=IFIX(SNGL(CTMAX-79.9))*10
123        DO 415 I=M,IX
124        IF(FNN(I).LT.FNHALF) GO TO 416
125    415 CONTINUE
126    416 CTHAB=DFLOAT(I)/10.0+79.9
127        M=IFIX(SNGL(OTMAX-79.9))*10
128        DO 417 I=M,IX
129        IF(DAA(I).LT.DAHALF) GO TO 418
130    417 CONTINUE
131    418 OTHAB=DFLOAT(I)/10.0+79.9
132        RETURN
133        END
134    C GARLICK AND GIBSON 10% METHOD
135    C
136        SUBROUTINE GG10(FNN,DAA,K,IX,FNMAX,DAMAX,FTGG10,FGG10,
137       1DTGG10,DGG10,NUM1,NUM2,M,M2
138        IMPLICIT REAL 8 (A-H,O-Z)
139        DIMENSION FNN(1),DAA(1),FTGG10(1001),FGG10(1001),DTGG10(1001),
140       1DGG10(1001)
141        FNO1=0.005*FNMAX
142        DO 465 I=K,IX
143        IF(FNN(I).GT.FNO1) GO TO 466
144        M=I
145    465 CONTINUE
146    466 FNO1=FNMAX*0.10
147        DO 467 I=K,IX
148        IF(FNN(I).GT.FNO1) GO TO 468
149        N=I
150    467 CONTINUE
151    468 NUM1=N-M
152        DO 469 II=M,N
153        FGG10(II)=DLOG(FNN(II))
154        FTGG10(II)=1.0/(DFLOAT(II)/10.0+79.9)
155    469 CONTINUE
156        DNO1=DNMAX*0.005
157        DO 470 I=K,IX
158        IF(DAA(I).GT.DNO1) GO TO 471
159    470 CONTINUE
160    471 M2=I
161        DA10=DAMAX 0.1
162        DO 472 I=K,IX
163        IF(DAA(I).GT.DA10) GO TO 473
164    472 CONTINUE
165    473 N2=I
166        NUM2=N2-M2
167        DO 474 I=M2,N2
168        DGG10(I)=DLOG(DAA(I))
169        DTGG10(I)=1.0/(DFLOAT(I)/10.0+79.9)
170    474 CONTINUE
```

```
171         RETURN
172         END
173   C GARLICK AND GIBSON 20% METHOD
174   C
175         SUBROUTINE GG20(FNN,DAA,K,IX,FNMAX,DAMAX,FTGG20,FGG20,
176        1DTGG20,DGG20,NUM3,NUM4,M3,M4)
177         IMPLICIT REAL 8 (A-H,O-Z)
178         DIMENSION FNN(1),DAA(1),FTGG20(1001),FGG20(1001),DTGG20(1001),
179        1DGG20(1001)
180         FNO1=FNMAX*0.005
181         DO 475 I=K,IX
182         IF(FNN(I).GT.FNO1) GO TO 476
183     475 CONTINUE
184     476 M3=I
185         FN20=FNMAX*0.2
186         DO 477 I=K,IX
187         IF(FNN(I).GT.FN20) GO TO 478
188     477 CONTINUE
189     478 N3=I
190         DO 479 I=M3,N3
191         FGG20(I)=DLOG(FNN(I))
192         FTGG20(I)=1.0/(DFLOAT(I)/10.0+79.9)
193     479 CONTINUE
194         NUM3=N3-M3
195         DNO1=DNMAX*0.005
196         DO 480 I=K,IX
197         IF(DAA(I).GT.DNO1) GO TO 481
198     480 CONTINUE
199     481 M4=I
200         DA20=DAMAX 0.2
201         DO 482 I=K,IX
202         IF(DAA(I).GT.DA20) GO TO 483
203     482 CONTINUE
204     483 N4=I
205         DO 484 I=M4,N4
206         DGG20(I)=DLOG(DAA(I))
207         DTGG20(I)=1.0/(DFLOAT(I)/10.0+79.9)
208     484 CONTINUE
209         NUM4=N4-M4
210         RETURN
211         END
212   C PLOT GARLICK AND GIBSON DATA
213         SUBROUTINE PLOTGG(FNN,DAA,K,IX,FNMAX,DAMAX,FTGGP,FGGP,
214        1DTGGP,DGGP,NUM5,NUM6,M5,M6)
215         IMPLICIT REAL 8 (A-H,O-Z)
216         DIMENSION FNN(1),DAA(1),FTGGP(1),FGGP(1),DTGGP(1),DGGP(1)
217         FNO1=FNMAX*0.005
218         DO 1205 I=K,IX
219         IF(FNN(I).GT.FNO1) GO TO 1207
220    1205 CONTINUE
221    1207 M5=I
222         FN95=FNMAX*0.95
223         DO 1208 I=K,IX
224         IF(FNN(I).GT.FN95) GO TO 1209
225    1208 CONTINUE
226    1209 N5=I
227         DO 1210 I=M5,N5
228         FGGP(I)=DLOG(FNN(I))
229    1210 CONTINUE
```

```
      NUM5=N5-M5
      DNO1=DNMAX*0.005
      DO 1211 I=K,IX
      IF(DAA(I).GT.DNO1) GO TO 1212
 1211 CONTINUE
 1212 M6=I
      DN95=DAMAX*0.95
      DO 1213 I=K,IX
      IF(DAA(I).GT.DN95) GO TO 1214
 1213 CONTINUE
 1214 N6=I
      DO 1215 I=M6,N6
      DGGP(I)=DLOG(DAA(I))
      DTGGP(I)=1.0/(DFLOAT(I)/10.0+79.9)
      NUM6=N6-M6
      RETURN
      END
C CALCULATE TSC AND TSL TRAP DEPTHS BY GENERAL METHODS
      IMPLICIT REAL 8 (A-H,O-Z)
      DIMENSION P(1001),FNN(1001),DAA(1001),Q(1001),T(1001),A(1001),
     1FIFN(1001),FN(1001),DFN(1001),DA(1001),
     1OM(9),OTM(9),OT1(9),CM(9),CTM(9),CT1(9),CT2(9),
     1CHOOG(9),OTM1(9),CTM1(9),OHOOG(9),RESULT(9),
     1COMEGA(100),OOMEGA(100),OCHENW(9),CCHENW(9),TEMP(9000),
     1CHAAD(9),OHAAD(9),CSIGMA(100),OSIGMA(100),
     1CLAMDA(100),CBOIKB(9),OBOIKB(9),CBOIKA(9),OBOIKA(9),CCHEN1(9),
     1OCHEN1(9),OCHEN2(9),CCHEN4(9),OCHEN5(9),CCHEN5(9),OCHEN4(9),
     1CCHE6A(9),OCHE6B(9),CCHEN3(9),OCHEN3(9),CLUSCH(9),OLUSCH(9),
     1CHB1(9),CGROSS(9),OLAMDA(9),CCHEN2(9),CCHE6A(9),OGROSS(9),
     1DIFF(9),CCHE6B(9),OHB1(9),CHB2(9),OHB2(9),DGGE(9),FGGE(9),OT11(9),
     1CT11(9),DGGE(9),FGGE(9),FTGG10(1001),FGG10(1001),DTGG10(1001),
     1DGG10(1001),FTGG20(1001),FGG20(1001),DTGG20(1001),DGG20(1001),
     1FTGGP(1001),FGGP(1001),DTGGP(1001),DGGP(1001)
      READ(5,410) RATE,EV,HS,BETA
      READ(5,410) FREQ,TO,HD,ALPHA
  410 FORMAT(4D10.2)
      DATA BOLTZ/8.617D-5/
      DATA BOLTZ2/1.38D-23/
      DATA EMASS/9.109D-31/
      READ(5,500) L,NN
  500 FORMAT(2I6)
      READ(5,1380) XLOW
 1380 FORMAT(D10.2)
      RATE=0.55
      WRITE(6,457)
  457 FORMAT(1H ,34H                DATA                    )
      WRITE(6,451) EV
  451 FORMAT(1H ,4H EV=,D10.4,3H EV)
      WRITE(6,452) HS
  452 FORMAT(1H ,4H HS=,D10.4,6H CM  2)
      WRITE(6,453) HD
  453 FORMAT(1H ,4H HD=,D10.4,6H CM  2)
      WRITE(6,454) ALPHA
  454 FORMAT(1H ,7H ALPHA=,D10.4,9HCM  2/SEC)
      WRITE(6,455) BETA
  455 FORMAT(1H ,6H BETA=,D10.4,9HCM  2/SEC)
      WRITE(6,459) FREQ
  459 FORMAT(1H ,6H FREQ=,D10.4,6H SEC-1)
      WRITE(6,458)
  458 FORMAT(1H ,34H                                        )
```

```
290         WRITE(6,1375) XLOW
291    1375 FORMAT(1H ,'TEMP. PLOTTING MIN.=',D10.2)
292         WRITE(6,1376) L
293    1376 FORMAT(1H ,'NO. OF PLOTTING POINTS=',I6)
294         WRITE(6,1377) NN
295    1377 FORMAT(1H ,'NO. OF HEATING RATES=',I6)
296         WRITE(6,458)
297         XPLOT=(XLOW-80.0) 10.0
298         NPLOT=IFIX(SNGL(XPLOT))
299         KSYMB=0
300         YO=5.5
301         SPACE=10
302         CALL PLTXMX(80.0)
303         DO 1 I=1,NN
304         RATE=RATE-5.00D-2
305         SS=(FREQ*TO)/RATE
306         E=EV/(BOLTZ*TO)
307         DELTA=BETA/ALPHA
308         ALFA=(ALPHA*HS*TO)/RATE
309         SKSI=HD/HS
310         CALL CURVE(SS,E,DELTA,ALFA,SKSI,P,Q,T,A,FIFN,FN,DFN,DA,K,IX,L,FNN,
311        1DAA,HS,HD,ALPHA,BETA,EV,TEMP)
312         CALL SORT(FNN,DAA,IX,K,DAMAX,FNMAX,CTMAX,OTMAX)
313         CALL THALF1(FNN,DAA,FNMAX,DAMAX,FNHALF,DAHALF,K,IX,CTHALF,OTHALF)
314         CALL THALF2(FNN,DAA,FNHALF,DAHALF,CTMAX,OTMAX,IX,CTHAB,OTHAB)
315         CALL GG10(FNN,DAA,K,IX,FNMAX,DAMAX,FTGG10,FGG10,DTGG10,DGG10,
316        1NUM1,NUM2,M,M2)
317         CALL GG20(FNN,DAA,K,IX,FNMAX,DAMAX,FTGG20,FGG20,DTGG20,DGG20,
318        1NUM3,NUM4,M3,M4)
319         CALL PLOTGG(FNN,DAA,K,IX,FNMAX,DAMAX,FTGGP,FGGP,DTGGP,DGGP,
320        1NUM5,NUM6,M5,M6)
321         LL=L-NPLOT
322         IF(I.GT.1) GO TO 1007
323         TTT=CTMAX
324    C NC IS THE DENSITY OF STATES IN THE COND. BAND,TVEL IS THE THERMAL
325    C VELOCITY OF THE CARRIERS,CROSS IS THE CAPTURE CROSS SECTION
326         NC=4.32D23*(TTT*1.5)
327         TVEL=((2*BOLTZ2*TTT)/EMASS)**0.5
328         CROSS=FREQ/(NC*TVEL)
329         WRITE(6,1392) CROSS
330         FORMAT(1H ,'CAPTURE CROSS-SECTION=',D10.2,'M  2')
331    C PLOT TSC AND TSL CURVES FOR NN HEATING RATES USING  PLOTSYS
332         CALL PSCALE(8.0,1.0,YMIT,DAA(1),L,2)
333         CALL PSCALE(8.0,1.0,YMIX,YX,FNN(1),L,2)
334         CALL PSCALE(8.0,1.0,YMIN,YF,FGGP(M5),NUM5,2)
335         CALL PSCALE(10.0,1.0,XMIN,XF,FTGGP(M5),NUM5,2)
336         CALL PSCALE(8.0,1.0,YMIY,XY,DTGGP(M6),NUM6,2)
337         CALL PSCALE(10.0,1.0,XMIY,XY,DGGP(M6),NUM6,2)
338         CALL PAXIS(18.0,1.0,'TEMPERATURE DEG K',-17,10.0,0.0,XLOW,10.0
339        1,1.0)
340         CALL PAXIS(18.0,1.0,'TSC  FNN-VALUES',15,8.0,90.0,YMIX,YX,1.0)
341         CALL PAXIS(36.0,1.0,'1/TEMPERATURE',-13,10.0,0.0,XMIN,XF,1.0)
342         CALL PAXIS(36.0,1.0,'LN(FNN)',7,8.0,90.0,YMIN,YF,1.0)
343         CALL PAXIS(4.0,1.0,'TEMPERATURE DEG K',-17,10.0,0.0,XLOW,10.0,1.0)
344         CALL PAXIS(4.0,1.0,'TSL  DAA-VALUES',15,8.0,90.0,YMIT,YT,1.0)
345         CALL PAXIS(48.0,1.0,'1/TEMPERATURE DEG K',-17,10.0,0.0,XMIY,XY,1.0)
346         CALL PAXIS(48.0,1.0,'LN(DAA)',7,8.0,90.0,YMIY,YY,1.0)
347         CALL PSYMB(6.0,10.0,-0.2,'TSL FOR NN HEATING RATES',0.0,23)
348         CALL PSYMB(24.0,10.0,-0.2,'TSC FOR NN HEATING RATES',0.0,23)
349         CALL PSYMB(42.0,10.0,-0.2,'GARLICK GIBSON',0.0,29)
```

```
      CALL PNUMBR(6.0,9.5,0.10,EV,0.0,'''EV='',DE1.3,''EV'' ')
      CALL PNUMBR(6.0,9.0,0.10,HS,0.0,'''HS='',DE1.3,''/CM  3'' ')
      CALL PNUMBR(6.0,8.5,0.10,HD,0.0,'''HD='',DE1.3,''/CM  3'' ')
      CALL PNUMBR(6.0,8.0,0.10,ALPHA,0.0,'''ALPHA='',DE1.3,''CM  2/SEC''
     1 ')
      CALL PNUMBR(6.0,7.5,0.10,BETA,0.0,'''BETA='',DE1.3,''CM  2/SEC'' '
     1)
      CALL PNUMBR(6.0,7.0,0.10,FREQ,0.0,'''FREQ='',DE1.3,''CM  2/SEC'' '
     1)
      CALL PSYMB(6.0,6.0,-0.10,'HEATING RATES',0.0,13)
1007  CALL PLTOFS(XLOW,10.0,YMIT,YT,4.0,1.0)
      CALL PLINE(TEMP(NPLOT),DAA(NPLOT),LL,2,300,KSYMB,1.0)
      CALL PLTOFS(XLOW,10.0,YMIX,YX,18.0,1.0)
      CALL PLINE(TEMP(NPLOT),DAA(NPLOT),LL,2,300,KSYMB,1.0)
      CALL PLTOFS(XMIN,XF,YMIN,YF,36.0,1.0)
      CALL PLINE(FTGGP(M5),FGGP(M5),NUM5,2,SPACE,KSYMB,1.0)
      CALL PLTOFS(XMIY,XY,YMIY,YY,48.0,1.0)
      CALL PLINE(DTGGP(M6),DGGP(M6),NUM6,2,SPACE,KSYMB,1.0)
      CALL PSYMB(6.0,YO,-0.10,KSYMB,0.0,-3)
      CALL PNUMBR(6.5,YO,0.10,RATE,0.0,'DE1.2',''K/SEC'' ')
      IF(I.LT.NN) GO TO 1004
      CALL PNUMBR(6.0,6.5,0.10,NN,0.0,'''NN='',I2,''HEATING RATES'' ')
      CALL PLTEND
1004  KSYMB=KSYMB+1
      YO=YO-0.25
      SPACE=SPACE+1
      DIFF(I)=CTMAX-OTMAX
      CM(I)=DAMAX
      OTM(I)=OTMAX
      OT1(I)=OTHALF
      OT2(I)=OTHAB
      CM(I)=FNMAX
      CTM(I)=CTMAX
      CT1(I)=CTHALF
      CT2(I)=CTHAB
      OTM1(I)=1.0/OTMAX
      CTM1(I)=1.0/CTMAX
      OT11(I)=1.0/OTHALF
      CT11(I)=1.0/CTHALF
      COMEGA(I)=CTHAB-CTHALF
      COMEGA(I)=OTHAB-OTHALF
      CSIGMA(I)=CTHAB-CTMAX
      OSIGMA(I)=OTHAB-OTMAX
      CLAMDA(I)=CTMAX-CTHALF
      OLAMDA(I)=OTMAX-OTHALF
      CHOOG(I)=DLOG(CTM(I)**2/RATE)
      OHOOG(I)=DLOG(OTM(I)**2/RATE)
      CHAAD(I)=DLOG(FNMAX)
      OHAAD(I)=DLOG(DAMAX)
      CCHENW(I)=DLOG((CTMAX**4*FNMAX)/RATE*2)
      OCHENW(I)=DLOG((OTMAX**4*DAMAX)/RATE*2)
      CBOIKA(I)=DLOG(FNMAX/CTMAX**1.5)
      OBOIKA(I)=DLOG(DAMAX/OTMAX**1.5)
      CBOIKB(RATE/CTMAX**3.5)
      OBOIKB(I)=DLOG(RATE/OTMAX**3.5)
      CCHEN1(I)=2.0*BOLTZ*CTMAX*(1.25*CTMAX/COMEGA(I)-1.0)
      OCHEN1(I)=2.0*BOLTZ*OTMAX*(1.25*OTMAX/OOMEGA(I)-1.0)
      CCHEN2(I)=2.29*BOLTZ*(CTMAX*2)/COMEGA(I)
      OCHEN2(I)=2.29*BOLTZ*(OTMAX*2)/OOMEGA(I)
      CCHEN4(I)=1.52*BOLTZ*(CTMAX*2)/CLAMDA(I)-3.16*BOLTZ*CTMAX
```

```
      OCHEN4(I)=1.52*BOLTZ*(OTMAX*2)/OLAMDA(I)-3.16*BOLTZ*OTMAX
      CCHEN5(I)=0.976*BOLTZ*(CTMAX*2)/CSIGMA(I)
      OCHEN5(I)=0.976*BOLTZ*(OTMAX*2)/OSIGMA(I)
      CCHE6A(I)=3.0*CSIGMA(I)*BOLTZ*(CTMAX*2)/(CSIGMA(I)*CLAMDA(I))
      OCHE6A(I)=3.0*OSIGMA(I)*BOLTZ*(OTMAX*2)/(OSIGMA(I)*OLAMDA(I))
      CCHE6B(I)=2.8*CSIGMA(I)*BOLTZ*(CTMAX*2)/(CSIGMA(I)*CLAMDA(I))
      OCHE6B(I)=2.8*OSIGMA(I)*BOLTZ*(OTMAX*2)/(OSIGMA(I)*OLAMDA(I))
      CCHEN3(I)=(1.548*BOLTZ*(CTMAX*2)/CLAMDA(I)*(1.0-3.16/E)
      OCHEN3(I)=(1.548*BOLTZ*(OTMAX*2)/(OLAMDA(I)*(1.0-3.16/E))
      CLUSCH(I)=BOLTZ*(CTMAX*2)/CSIGMA(I)
      OLUSCH(I)=BOLTZ*(OTMAX*2)/OSIGMA(I)
      CHB1(I)=(1.72*BOLTZ*(CTMAX*2)/CLAMDA(I))*(1.0-5.16/E)
      OHB1(I)=(1.72*BOLTZ*(OTMAX*2)/OLAMDA(I))*(1.0-5.16/E)
      CHB2(I)=(2.0*BOLTZ*(CTMAX*2)/CLAMDA(I)(1.0-6.0/E)
      OHB2(I)=(2.0*BOLTZ*(OTMAX*2)/OLAMDA(I)(1.0-6.0/E)
      CGROSS(I)=1.51*BOLTZ*CTMAX*CTHALF/CLAMDA(I)
      OGROSS(I)=1.51*BOLTZ*OTMAX*OTHALF/OLAMDA(I)
      IFAIL=0
      CALL GO2CAF(NUM1,FTGG10(M),RESULT,IFAIL)
      FGGE(I)=RESULT(6)*BOLTZ
      WRITE(6,425) (RESULT(6))
      WRITE(6,785) (RESULT(3))
      CALL GO2CAF(NUM2,DTGG10(M2),DGG10(M2),RESULT,IFAIL)
      DGGE(I)=RESULT(6)*BOLTZ
      WRITE(6,425) RESULT(5)
      WRITE(6,785) RESULT(3)
      CALL GO2CAF(NUM3,FTGG20(M3),RESULT,IFAIL)
      FGGE(I)=RESULT(6)*BOLTZ
      WRITE(6,425) RESULT(5)
      WRITE(6,785) RESULT(3)
      CALL GO2CAF(NUM4,DTGG20(M4),DGGE(M4),RESULT,IFAIL)
      DGGE2(I)=RESULT(6)*BOLTZ
      WRITE(6,425) RESULT(5)
      WRITE(6,785) RESULT(3)
    1 CONTINUE
      WRITE(6,1379) (1,DIFF(I),I=1,NN)
 1379 FORMAT(1H ,'TEMP.DIFF. TSC-TSL=(',I3,')=',D10.2)
      IFAIL=0
      CALL GO2CAF(NN,CTM1,CHOOG,RESULT,IFAIL)
      ENERGY=RESULT(6)*BOLTZ
      WRITE(6,424) ENERGY
  424 FORMAT(1H ,' TSC,HOOG. METHOD, TRAP DEPTH=',D10.4,3H EV)
      WRITE(6,425) RESULT(5)
      WRITE(6,785) RESULT(3)
  785 FORMAT(1H ,'STANDARD DEVIATION=',D10.4,'EV')
  425 FORMAT(1H ,'REGRESSION COEFF. ERROR',D10.4)
      CALL GO2CAF(NN,OTM1,OHOOG,RESULT,IFAIL)
      ENERGY=RESULT(6)*BOLTZ
      WRITE(6,425) ENERGY
  426 FORMAT(1H ,'TSL, HOOG. METHOD, TRAP DEPTH=',D10.4,'EV')
      WRITE(6,425) RESULT(5)
      WRITE(6,785) RESULT(3)
      CAL GO2CAF(NN,CTM1,CHAAD,RESULT,IFAIL)
      ENERGY=RESULT(6)*BOLTZ
      WRITE(6,427) ENERGY
  427 FORMAT(1H ,' TSC,HAERING ADAMS METHOD, TRAP DEPTH=',D10.4,3H EV)
      CALL GO2CAF(NN,OTM1,CHAAD,RESULT,IFAIL)
      ENERGY=RESULT(6)*BOLTZ
      WRITE(6,428) ENERGY
  428 FORMAT(1H ,' TSL,HAERING ADAMS METHOD, TRAP DEPTH=',D10.4,3H EV)
```

```
      WRITE(6,425) RESULT(5)
      WRITE(6,785) RESULT(3)
      CALL GO2CAF(NN,CTM1,CCHENW,RESULT,IFAIL)
      ENERGY=RESULT(6)*BOLTZ
      WRITE(6,429) ENERGY
  429 FORMAT(1H ,' TSC,CHEN WINER METHOD, TRAP DEPTH= ',D10.4,'EV')
      WRITE(6,425) RESULT(5)
      WRITE(6,785) RESULT(3)
      CALL GO2CAF(NN,OTN1,OCHENW,RESULT,IFAIL)
      ENERGY=RESULT(6)*BOLTZ
  430 FORMAT(1H ,' TSL,CHEN WINER METHOD, TRAP DEPTH= ',D10.4,'EV')
      WRITE(6,425) RESULT(5)
      WRITE(6,785) RESULT(3)
      CALL GO2CAF(NN,CTM1,CBOIKA,IFAIL)
      ENERGY=RESULT(6)*BOLTZ
      WRITE(6,431) ENERGY
  431 FORMAT(1H ,' TSC BOIKO RASHBA TROFIMENKO, TRAP DEPTH= ',D1
     10.4,'EV')
      WRITE(6,425) RESULT(5)
      WRITE(6,785) RESULT(3)
      CALL GO2CAF(NN,OTM1,OBOIKA,RESULT,IFAIL)
      ENERGY=RESULT(6)*BOLTZ
      WRITE(6,432) ENERGY
      FORMAT(1H ,' TSL BOIKO RASHBA TROFIMENKO METHODA,TRAP DEPTH= ',D1
     10.4,'EV')
      WRITE(6,425) RESULT(5)
      WRITE(6,785) RESULT(3)
      CALL GO2CAF(NN,CTM1,CBOIKB,RESULT,IFAIL)
      ENERGY=RESULT(6)*BOLTZ
      WRITE(6,433) ENERGY
  433 FORMAT(1H ,' TSC BOIKO RASHBA TROFIMENKO,TRAP DEPTH= ',D1
     10.4,'EV')
      WRITE(6,425) RESULT(5)
      WRITE(6,785) RESULT(3)
      CALL GO2CAF(NN,OTM1,OBOIKB,RESULT,IFAIL)
      ENERGY=RESULT(6)*BOLTZ
      WRITE(6,434) ENERGY
  434 FORMAT(1H ,' TSL BOIKO RASHBA TROFIMENKO,TRAP DEPTH= ',D1
     10.4,'EV')
      WRITE(6,425) RESULT(5)
      WRITE(6,785) RESULT(3)
      CALL GO2CAF(NN,CT11,CHAAD,RESULT,IFAIL)
      ENERGY=RESULT(6)*BOLTZ
      WRITE(6,700) ENERGY
  700 FORMAT(1H ,' TSC UNGER TRAP DEPTH= ',D10.4,'EV')
      WRITE(6,425) RESULT(5)
      WRITE(6,785) RESULT(3)
      CALL GO2CAF(NN,OT11,CHAAD,RESULT,IFAIL)
      ENERGY=RESULT(6)*BOLTZ
      WRITE(6,701) ENERGY
      FORMAT(1H ,' TSL UNGER TRAP DEPTH= ',D10.4,'EV')
      WRITE(6,425) RESULT(5)
      WRITE(6,785) RESULT(3)
      WRITE(6,495) (I,FGGE(I),I=1,NN)
  495 FORMAT(1H ,'TSC G G 10% TRAP DEPTH( ',I1,')+ ',D10.4,'EV')
      WRITE(6,496) (I,DGGE(I),I=1,NN)
  496 FORMAT(1H ,'TSL G G 10% TRAP DEPTH( ',I1,')= ',D10.4,'EV')
      WRITE(6,497) (I,FGGE2(I), I=1,NN)
      FORMAT(1H ,'TSC G G 20% TRAP DEPTH( ',I1,')= ',D10.4,'EV')
```

```
529         WRITE(6,498) (I,DGGE2(I), I=1,NN)
530     498 FORMAT(1H ,'TSL 20% G G TRAP DEPTH(',I1,')=',D10.4,'EV')
531         WRITE(6,435) (I,CCHEN1(I), I=1,NN)
532     435 FORMAT(1H ,'TSC CHEN1(',I1,')=',D10.4,'EV')
533         WRITE(6,436) (I,OCHEN1(I), I=1,NN)
534     436 FORMAT(1H ,'TSL CHEN1(',I1,')=',D10.4,'EV')
535         WRITE(6,437) (I,CCHEN2(I), I=1,NN)
536     437 FORMAT(1H ,'TSC CHEN2(',I1,')=',D10.4,'EV')
537         WRITE(6,438) (I,OCHEN2(I), I=1,NN)
538     438 FORMAT(1H ,'TSL CHEN2(',I1,')=',D10.4,'EV')
539         WRITE(6,439) (I,CCHEN3(I), I=1,NN)
540     439 FORMAT(1H ,'TSC CHEN3(',I1,')=',D10.4,'EV')
541         WRITE(6,440) (I,OCHEN3(I) I=1,NN)
542     440 FORMAT(1H ,'TSL CHEN3(',I1,')=',D10.4,'EV')
543         WRITE(6,441) (I,CCHEN4(I), I=1,NN)
544     441 FORMAT(1H ,'TSC CHEN4(',I1,')=',D10.4,'EV')
545         WRITE(6,442) (I,OCHEN4(I), I=1,NN)
546     442 FORMAT(1H ,'TSL CHEN4(',I1,')=',D10.4,'EV')
547         WRITE(6,443) (I,CCHEN5(I), I=1,NN)
548     443 FORMAT(1H ,'TSC CHEN5(',I1,')=',D10.4,'EV')
549         WRITE(6,444) (I,OCHEN5(I), I=1,NN)
550     444 FORMAT(1H ,'TSL CHEN5(',I1,')=',D10.4,'EV')
551         WRITE(6,445) (I,CCHE6A(I), I=1,NN)
552     445 FORMAT(1H ,'TSC CHEN6A('I1,')=',D10.4,'EV')
553         WRITE(6,446) (I,OCHE6A(I), I=1,NN)
554     446 FORMAT(1H ,'TSL CHEN6A('I1,')=',D10.4,'EV')
555         WRITE(6,447) (I,CCHE6B(I), I=1,NN)
556     447 FORMAT(1H ,'TSC CHEN6B(',I1,')=',D10.4,'EV')
557         WRITE(6,448) (I,OCHE6B(I), I=1,NN)
558     448 FORMAT(1H ,'TSL CHEN6B('I1,')=',D10.4,'EV')
559         WRITE(6,449) (I,CLUSCH(I), I=1,NN)
560     449 FORMAT(1H ,'TSC LUSCHIK TRAP DEPTH(',I1,')=',D10.4,'EV')
561         WRITE(6,450) (I,OLUSCH(I), I=1,NN)
562     450 FORMAT(1H ,'TSL LUSCHIK TRAP DEPTH(',I1,')=',D10.4,'EV')
563         WRITE(6,702) (I,CHB(I), I=1,NN)
564     702 FORMAT(1H ,'TSC HALPERIN BRANER1 TRAP DEPTH(',I1,')=',D10.4,'EV')
565         WRITE(6,703) (I,OHB1(I), I=1,NN)
566     703 FORMAT(1H ,'TSL HALPERIN BRANER1 TRAP DEPTH(',I1,')=',D10.4,'EV')
567         WRITE(6,704) (I,CHB2(I), I=1,NN)
568     704 FORMAT(1H ,'TSC HALPERIN BRANER2 TRAP DEPTH(',I1,')=',D10.4,'EV')
569         WRITE(6,705) (I,OHB2(I), I=1,NN)
570     705 FORMAT(1H ,'TSL HALPERIN BRANER2 TRAP DEPTH(',I1,')=',D10.4,'EV')
571         STOP
572         END
```

TSL FOR NN HEATING RATE

EV= 3.700E-01EV

HS= 2.000E+16/CM**3

HD= 1.700E+17/CM**3

ALPHA= 5.882E-10CM**2/SEC

BETA= 2.941E-10CM**2/SEC

FREQ= 7.390E+09CM**2/SEC

NN= 9HEATING RATES

HEATING RATES

□	5.00E-01K/SEC
◇	4.50E-01K/SEC
△	4.00E-01K/SEC
+	3.50E-01K/SEC
×	3.00E-01K/SEC
◇	2.50E-01K/SEC
+	2.00E-01K/SEC
⊼	1.50E-01K/SEC
Z	1.00E-01K/SEC

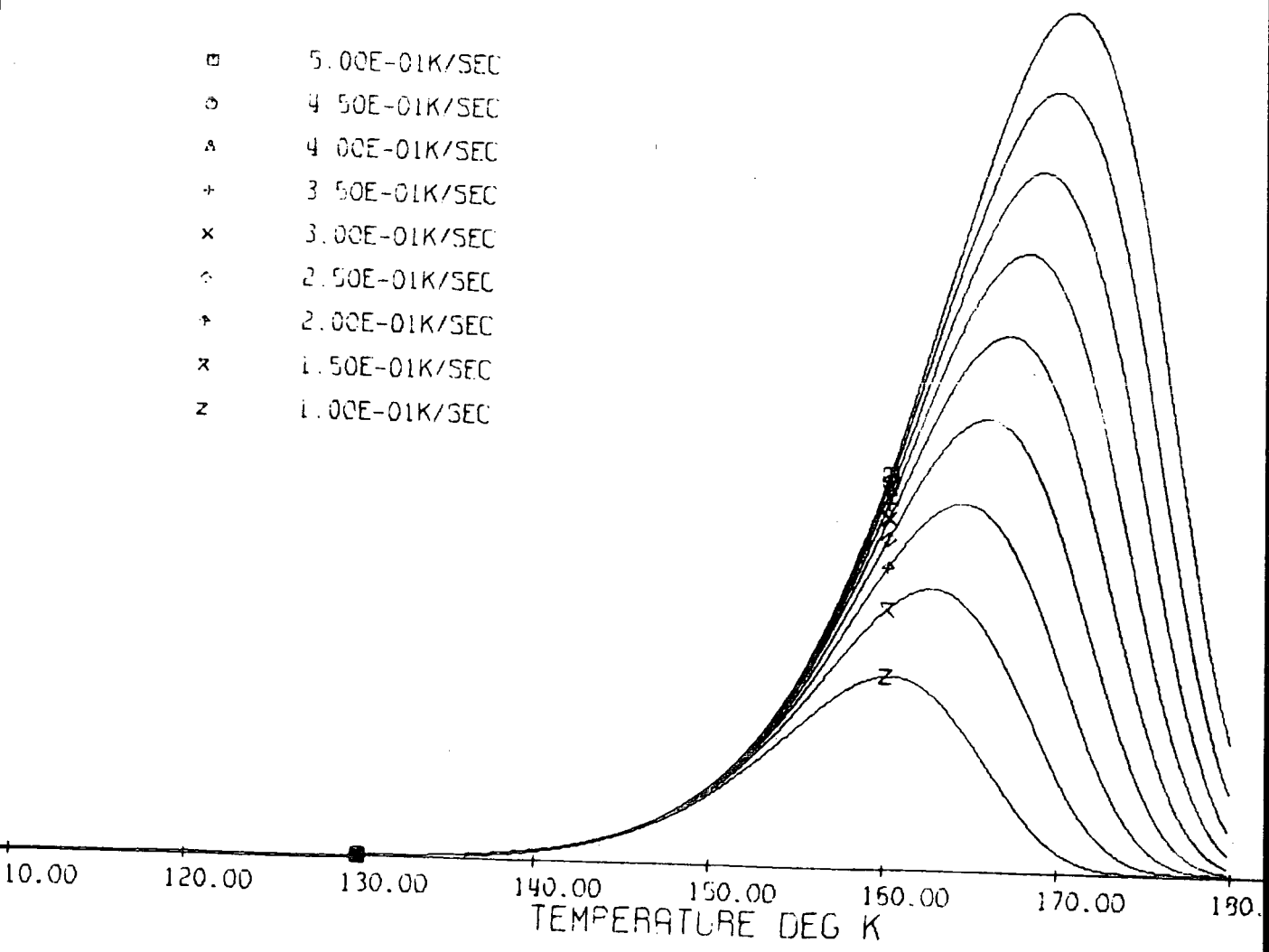

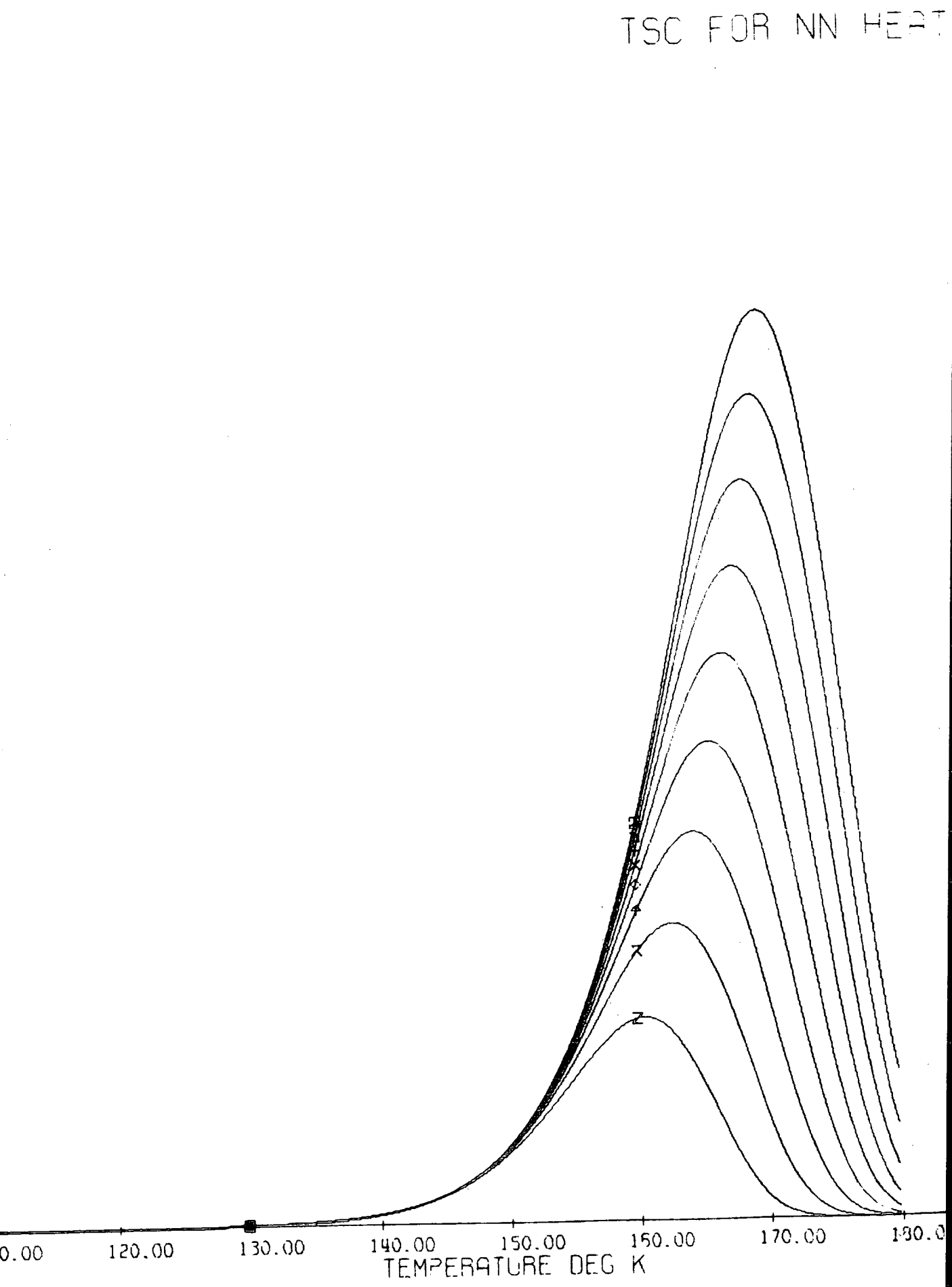
TSC FOR NN HEAT
0.00
120.00
130.00
140.00
150.00
160.00
170.00
180.0
TEMPERATURE DEG K

APPENDIX 2

ALGOL 66 PROGRAM TO SOLVE THE TSC/TL DIFFERENTIAL EQUATIONS

```
100     'PROCEDURE'CURVE(E,S,ALFA,DELTA,KSI,T,A,DA,DDA,IN,N,DN,L,ITER);
200     'REAL'E,S,ALFA,DELTA,KSI; 'ARRAY'T,A,DA,DDA,IN,N,DN;
300     'INTERGER'L,ITER;
400     'BEGIN''ARRAY'P,Q(0:L); 'INTERGER'I,J,K; 'REAL'X,DI,NS,LGE,W;
500       DT:=1/80; LGE:=LN(10);
600       'FOR'I:=0'STEP'1'UNTIL'L'DO'
700       'BEGIN'T(I):=1+I*DT; X:=E/T(I); P(I):=EXP(LGE*S-X);
800         Q(I):=T(I)*P(I)*(1-((X+4.03640)*X+1.15198)/
900                 ((X+5.03637)*X+4.19160));
1000        A(I):=1/(1+Q(I)); N(I):=P(I)/(1+Q(I)); T(I):=80 T(I)
1100        'IF'P(I)>1000'AND'L'/''10 10=L'THEN'L:=I;
1200      'END'I; K:=2; IN(0):=IN(1):=0;
1300      'FOR'J:=0,J+1'WHILE'J<25'AND'K<L-1'DO'
1400      'BEGIN''FOR'I:=1'STEP'1'UNTIL'L-1'DO'DN(I):=(N(I+1)-N(I-1))/DT/2;
1500        'FOR'I:=K'STEP'1'UNTIL'L-1'DO'
1600        'BEGIN'IN(I):=IN(I-2)+(N(I-2)+4*N(I-1)+N(I)*DT/3;
1700          A(I):=(1+KSI)*EXP(-IN(I));
1800          W:=A(I)+DELTA*(1+KSI-A(I));
1900          NS:=(P(I)*(A(I)-KSI)-N(I)*W-(DN(I)+N(I)*(P(I)+DELTA
2000              N(I)))/ALFA)/(W+P(I)+2*DELTA*N(I))/ALFA);
2100          N(I):=N(I)+0.7*NS;
2200          'IF'N(I)<0'THEN'N(I):=0;
2300          'IF'(ABS(NS)<0.0001*(1+ABS(N(I)))'OR'N(I)<0.0001)'AND'K=I
2400          'THEN'K:=K+1;
2500        'END'I;
2600      'END'J;
2700      ITER:=J; A(I):=KSI; N(0):=N(1):=DN(0):=DA(0):=
2800      DA(1):=DDA(0):=DDA(1):=0; IN(L):=IN(L-1);
2900      'FOR'I:=1'STEP'1'UNTIL'L-1'DO'DA(I):=A(I) N(I);
3000      'FOR'I:=1'STEP'1'UNTIL'L-1'DO'DDA(I):=(DA(I+1)-DA(I-1))/DT/2;
3100    'END''CURVE';
```

REFERENCES

Abernethy J, Wireless World (Dec 1970).

Acket G and Volger J, Physica 32 (1966) 1680.

Addiss R and Wakim F G, Photogr Sci Eng 13 (1969) 111.

Adler D, Solid State Physics ed Seitz F, Academic Press N Y (1968) 193.

Agekyan V T and Stepanov Yu A, Fiz Tverd Tela 17 (1975).

Allen J W, Proc of 7th Int Conf Semiconductors Paris (1964) 781.

Anderson S and Collen B, Acta Chem Scand 11 (1957) 1641.

Anderson J and Khan A, J Less Common Metals 22 (1970) 219.

Anderson P O, Kollberg E L and Jelenski, J Phys C 7 (1974) 1868.

Andersson P O, Jelenski A and Kollberg, Research Rept 107 Onsala Space Observatory Gothenburg (1973).

Arkad'eva E N, Kasmoya R S and Ryvkin S M, Sov Phys Solid State 3 (1962) 1755.

Arntz F and Yacobi Y, Phys Rev Lett 17 (1966) 857.

Atlas L and Schlehman G, Am Cer Soc 48 (1965) 384.

Austin I and Mott N, Advance in Physics 18 (1969).

Barbanel V I, Bogolovmov V N, Borodin S A and Budarina S I, Sov Phys Solid State 11 (1969) 431.

Barkhalov B S and Lutsenko E, Phys Stat Sol (a) 11 (1972) 433.

Baur W H, Acta Cryst 9 (1956) 515.

Becker J and Hosler W R, Proc Int Conf on Crystal Lattice Defects (1962).

Becker J and Hosler W R, Phys Rev 137 (1965) 1872.

Berkes J S, White W and Roy R, J Appl Phys 36 (1965) 3276.

Bhattacharya P K and Majerfeld A, Appl Phys Lett 34 (1978) 211.

Blakemore I S, Semiconductor Statistics Pergamon Press N Y (1962).

Blumenthal R, Kirk J and Hirthe W, Phys Chem Solids 28 (1967) 1077.

Blumenthal R and Whitmore P, J Electrchem Soc 110 (1963) 92.

Boer K, Oberlander S and Voigt J, Ann Lpz 2 (1958) 130.

Bogomolov V N, Sov Phys Solid State 5 (1964) 1468.

Bogomolov V N, Kudinov E and Firsor Yu A, Sov Phys Solid State 9 (1968) 2502.

Bogolomov V N, Kudinov E, Mirlin D and Yu A, Sov Phys Solid State 9 (1968) 1630.

Bogomolov V N and Mirlin D N, Phys Stat Sol 27 (1968) 443.

Bogomolov V N and Zhuze V, Sov Phys Solid State 5 (1964).

Bogomolov V N and Zhuze V, Sov Phys Solid State 8 (1967) 1904.

Bogoroditskii N P and Kristya V, Sov Phys Solid State 9 (1967) 187.

Bohm M and Scharmann, Phys Stat Sol (a) 5 (1971) 563.

Bohm M and Scharmann A, Phys Stat Sol (a) 11 (1972) 433.

Bohun A, Czech J Phys 4 (1954) 91.

Boiko I, Rashba E and Trofimenko A, Sov Phys Solid State 2 (1960) 99.

Booth A, Canad J Chem 32 (1954) 214.

Bourgois J C and Corbett J W, Phys Lett 38A (1972) 135.

Bransky I and Tannhauser D, Sol State Comm 7 (1969) 245.

Breckenridge R G and Hosler W R, Phys Rev 91 (1953) 793.

Breckenridge R G and Hosler W R, Phys Rev 137 (1965) A1872.

Brodribb J D, Hughes D M and Lewis T J, Electrets, Charge Storage and Transport in Dielectrics ed Perlmann, Electrochem Soc (1972).

Brodribb J D, O'Colmain and Hughes D M, J Phys D (1975) 856.

Bube R, J Chem Phys 23 (1955) 18.

Bube R, Photoconductivity of Solids Wiley (1964).

Bursill, Hyde, Terasaki and Watanabe, Phil Mag 20 (1969) 347.

Cardona M and Harbeke G, Phys Rev 137 (1965) A1467.

Carter D L and Okaya A, Phys Rev 118 (1960) 1485.

Cath and Peasbody, Anal Chem 43 (1971) 91.

Chandrashekhar G V and Title R S, J Electrochem Soc 123 (1976) 392.

Chase J D and van Ruyven L J, J Cryst Growth 5 (1969) 294.

Chen R, Chem Phys 11 (1969) 371.

Chen R, Chem Phys 6 (1970) 125.

Chen R, Chem Phys 11 (1971) 371.

Chen R and Fleming R, J Appl Phys 44 (1973) 1393.

Chen R and Winer S, J Appl Phys 41 (1970) 5227.

Chester P F, J Appl Phys 32 (1961) 866.

Cowell T A and Woods J, Brit J Appl Phys 18 (1967) 1045.

Cronemeyer D C, Phys Rev 87 (1952) 876.

Curie D, Luminescence in Crystals Methnen (1963).

Devore J R, J Opt Soc Am 41 (1951) 416.

Dittfeld H and Voigt J, Phys Stat Sol 3 (1963) 1941.

Donskoi A V and Dresvin S V, Electrothermics 5 (1963).

Dresvin S V and Donskoi A V, Tep Vyso Temp 3 (1965) 627.

Dussel G A and Bube R H, Phys Rev 155 (1967) 764.

Farrell E F and Lins A, Chem Bull 54 (1975) 1017.

Faughan B W and Kiss Z J, Phys Rev Lett 21 (1968) 1331.

Fischer D, Phys Rev B5 (1972) 4219.

Forland K, Acta Chem Scand 18 (1964) 1267.

Franks J and Keating P, J Phys Chem Sol 22 (1961) 25.

Frederikse H P, J App Phys Suppl 32 (1961) 2211.

Gansul G J, Marteus M, Mehrkam L and Williams F E, J Lumin 12 (1970) 94.

Garlick G and Gibson A, Proc Phys Soc 60 (1948) 574.

Geisler C H and Filopovich G, Second Int Conf on Electrophotography (1971) 129.

Gerritsen H J, Paramagnetic Resonance ed Low W, Academic N Y (1963) 3.

Gerritsen H J, Harrison S E, Lewis H and Wittke J, Phys Rev Lett 2 (1959) 153.

Gerritsen H J, Harrison S E and Lewis H R, J App Phys 31 (1960) 1566.

Gerritsen H J and Sabisky E S, Phys Rev 132 (1963) 1507.

Ghosh A R, Lauer R B and Addiss RR, Phys Rev B 8 (1973) 4842.

Ghosh A R, Wakim F G and Addiss RR, Phys Rev 184 (1969) 979.

Goodenough J B, Metallic Oxides Solid State Chemistry 5.

Grabner L, Stokowski S E and Brower W S, Phys Rev B 2 (1970) 590.

Gray T J and Amigues, Surface Science 13 (1968) 209.

Gray T J and Lowery N, Discussion Faraday Soc 52 (1971) 132.

Grossweiner L, J Appl Phys 24 (1953) 1306.

Grushko N S and Gutkin A A, Sov Phys Semiconductor 9 (1975) 37.

Haering R and Adams E, Phys Rev 117 (1960) 451.

Halperin A and Braner A, Phys Rev 117 (1960) 408.

Hasiguti R R, Minami K and Yunemitsu H, J Jap Phys Soc 16 (1961) 2223.

Haul R and Dumbgen G, Z Elektrochemie 66 (1962) 636.

Haul R and Dumbgen G, J Phys Chem Sol 26 (1965) 1.

Haul R and Dumbgen G, Proc 4th Int Symp on Reactivity of Solids, Amsterdam (1960).

Hagebeuk H J and Kivits P, Physica 83B (1976) 289.

Henry C and Lang D V, Proc 12th Conf on Physics of Semiconductors, Stuttgart (1974) 411.

Hermann R C and Hafstadter R, Phys Rev 57 (1940) 932.

Hird M, J Coatings Technology (USA) (Sept 1976).

Hirthe W, Adsit N and Brittain J, Symp on Imperfections in Crystals, Am Inst of Mining and Metallurgical Engineers, N Y Interscience (1961) 617.

Hirthe W and Brittain J, J Amer Ceram Soc 45 (1962).

Holt J, Brit J Appl Phys 16 (1965) 639.

Hoogenstraaten W, Phil Res Repts 13 (1958) 515.

Hughes W, 10th FATIPEC Congress, Austr OCCA Proc (1974).

Huntingdon H B and Sullivan G A, Phys Rev Lett 14 (1965) 177.

Hutchins M T, Solid State Physics 16 (1963) 227.

Iguchi E and Yajima K, J Phys Soc Jap 32 (1972) 1415.

Ikebe M, Miyako Y and Date M, J Phys Soc Jap 26 (1969) 43.

Itakura M, Niizeki N and Iwasaki H, J App Phys Jap 6 (1967) 311.

Johnson G H, J Amer Ceram Soc 36 (1953) 97.

Johnson O W, Phys Rev 136A (1964) 284.

Johnson O W, Ohlsen W P and Kingsbury P J, Phys Rev 175 (1968)1102.

Kaempf G, Papenroth W and Holm R, J Paint Techl 46 (1974) 56.

Kahn A and Leyendecker A, Phys Rev 135 (1964) 1321.

Keating P, Proc Phys Soc 78 (1961) 1408.

Keithley, Electrometers (1972).

Kelly P and Laubitz M J, Phys Rev B4 (1960) 1971.

Kerssen J and Volger J, Physica 69 (1973) 535.

King A, Plastics and Polymers (June 1968).

Kingsbury P J, Ohlsen W P and Johnson O W, Phys Rev 175 (1968) 1091.

Kivits P, J Lumin 16 (1978) 119.

Kivits P and Hagebeuk H, J Lumin 15 (1977) 1.

Klick C L and Schulman J H, Solid State Physics ed Seitz F and Turnbull D, Academic Press N Y 5 (1957).

Klinger M, Sov Phys Solid State 4 (1963) 2260; Phys Stat Sol 11 (1965) 499; 12 (1965) 765.

Kofstad P, J Phys Chem Sol 23 (1952) 1579; J Phys Chem Sol 23 (1962) 1579; J Less Common Metals 13 (1967) 635.

Kressel H, Havryco F Z and Buiocchi C J, J Appl Phys 39 (1968) 5139.

Kroger F and Vink H, Solid State Physics, Chemistry of Imperfect Crystals Wiley (1964).

Kudinov E, Mirlin D and Yu A, Fiz Tverd Tela 11 (1969) 2789.

Kulp B A, J Appl Phys 36 (1965) 553.

Kuznetzov V, J Cryst Growth 3 (1968) 405.

Kwietniak M and Piekarczyk W, Electron Technology 5 (1972) 65.

Lang D V, J Appl Phys 45 (1974) 3014.

Lauer R B, Addiss R R and Ghosh A K, J Appl Phys 42 (1971) 3508.

Lax M, J Phys Chem Sol 8 (1959) 66; Phys Rev 119 (1960) 1502.

Litton C W and Reynolds D C, Phys Rev 125 (1960) 516.

Lorang R and Perry G, J Chim Phys 63 (1966) 833.

Low F and Pines D, Phys Rev 98 (1955) 414.

Low W, Paramagnetic Resonance, Proc 1st Int Conf Jerusalem (1962).

Low W and Offenbacher E, Solid State Physics 17 (1965) 135.

Luschik, Dok Akad Nauk SSSR 101 (1955) 641.

Majerfeld A and Bhattacharya, Appl Phys Lett 33 (1978) 261.

Majerfeld A and Wada O, Appl Phys Lett 33 (1978) 957.

Melnick D A, J Chem Phys 26 (1957) 1136.

Mirlin D N, Reshina II and Sochava L, Sov Phys Solid State 11 (1970) 1995.

Miyako Y, Phys Lett 24A (1967) 635.

Miyako Y, J Phys Soc Jap 31 (1971) 1732.

Miyako Y and Kazumata Y, J Phys Soc Jap 31 (1971) 1727.

Mizushima K and Tanaka M, AIP Conf (USA) Part 18 (1973) 1044.

Moch P, Balkanski M and Aigfain P, C R Acad Sci 251 (1960) 1373.

Moore C H, Mini Engng 1 (1949) 194.

Morin F, Phys Rev 96 (1954) 28.

Moser J, Blumenthal R and Whitmore D, Amer Cer Soc 48 (1965) 384.

Muller K A, Proc 1st Int Conf Trans Element Ions, Jerusalem (1963).

Nassau K and Broyer A, J Amer Cer Soc 45 (1968) 474.

Neville G, Encyclopedia of Chemical Technology 20 (1969) 380.

Nicholas K H and Woods J, Brit J App Phys 15 (1964) 783.

NL Titanium Pigment Division Rept (1965) NL Industries South Amboy N J.

Parfianovitch I, J Exp Theor Phys SSSR 26 (1954) 696.

Pak J, Sov Phys Solid State 16 (1975) 2023.

Perny G and Lorang R, J Chim Phys 63 (1966) 2211.

Piekarczyk W, Study of purification and crystallisation processes in rutile Ph D Thesis ITE PAN Warszawa (1969).

Pragin A and Nichols R, Proc IRE 48 (1960) 771.

Purcell T and Weeks R A, J Chem Phys 54 (1971) 2800.

Ranby B and Rabek J F, Photodegradation, Photo-oxidation and Photostabilisation of Polymers, Interscience N Y (1975).

Randall J T and Wilkins M, Proc Roy Soc A184 (1945) 390.

Reboux J, Engng Techn 166 (1963) 109.

Reed T B, J Appl Phys 32 (1961) 821; 32 (1961) 2534.

Robbins D J and Dean P J, Advances in Physics 27 (1978) 499.

Rose A, Concepts of Photoconductivity and Allied Problems, Interscience (1963).

Rudolph J, Z Naturforschung 14 (1959) 727.

Ryvkin S M, Photoelectronic effects in semiconductors, Consultants Bureau N Y (1964).

Samoc M and Samoc A, Phys Stat Sol (a) 51 (1979) K195.

Sandin T R and Keesom P A, Phys Rev 117 (1969) 1370.

Sandomirskii V and Zhdan A, Sol St Electr 13 (1970) 69.

Saunders I J, J Phys C 2 (1969) 2181.

Schon M, Tech Wiss 7 (1958) 175.

Shannon R and Prewitt C T, Acta Cryst B25 (1969) 925.

Simmons J and Taylor G, Phys Rev B 5 (1972) 1619.

Slater J and Koster G, Phys Rev 94 (1954) 1498.

Slepetys R A and Vaughan P A, J Phys Chem 73 (1958) 2157.

Sochava L S, Reshina I I and Mirlin D N, Sov Phys S S 12 (1970) 946.

Soffer B, J Chem Phys 35 (1961) 940.

Stepanov A and Agekyan V, Fiz Tverd Tela 17 (1975) 3676.

Stokowski S and Schawlow A, Phys Rev Lett 21 (1968) 965.

Sturge M D, Solid State Physics 20 (1967) 91.

Suchan H and Drickamer H, J Phys Chem Sol 10 (1959) 343.

Tanaka M, Mzushima K, J Phys Soc Jap 132 (1972) 1519.

Thomas J M and Williams J, Trans Far Soc 64 (1968) 2496.

Tioxide Pigments (1977) A guide to selection, BTP guide 182, Tioxide International.

Torluachi S, Barcucci U and Zorzella G, Cent Ric Pigmenti Montecatini Edison Italy 24 (1974) 10.

Tsang J C, Phys Rev 173 (1968) 172.

Unger K, Phys Stat Sol 2 (1962) 1279.

Urbach F, Sitzber Akad Wiss Wein Math-Natavio Klasse 139 (1930) 353.

Van der Pauw L J, Phil Res Rept 13 (1958) 1.

Van Raalte J A, J Appl Phys 36 (1965) 3365.

Venkatu D L and Poteat L E, Mater Eng Sci Eng, 5 (1970) 258.

Verneuil M, C R Acad Sci 135 (1902) 791.

Vohl P, Photogr Sci Eng 13 (1969) 120.

Voigt J, Diplomarbeit (1958).

Von Hippel A, Kalnoys J and Westphal W, J Phys Chem Sol 23 (1962) 779.

Vos K, J Phys C 10 (1977) 3917.

Vos K and Krusemeyer H, Solid State Comm 15 (1974) 949.

Waff H S and Park K, Phys Lett 32 (1970) 109.

Wahlbeck P G and Gilles P W, J Amer Cer Soc 49 (1966) 180.

Walsh PS and Lightowlers, J Lumin 4 (1971) 393.

Wakim F G, J Appl Phys 44 (1973) 496.

Webster A H and Bright N, J Amer Cer Soc 44 (1961) 110.

White A M, J Appl Phys 47 (1976) 3230.

Williams F E and Eyring H, J Chem Phys 15 (1947) 289.

Wittke J P, J Electrochem Soc 113 (1966) 193.

Wolkenstein T and Karpenko I, J Appl Phys 33 (1962) 460.

Wright H, Downey R and Canning J, Brit J Appl Phys 1 (1968) 1593.

Yahia J, Phys Rev 130 (1963) 1711.